UNIVERSITÀ DELLA CALABRIA

UNIVERSITY OF CALABRIA

DEPARTMENT OF CHEMISTRY AND CHEMICAL TECHNOLOGIES

"Bernardino Telesio" – Doctorate School of Science and Technique

Curriculum: "Mesophases and Molecular Materials" - CHIM/02

XXVIII CICLO

With the contribution of "Fondo Sociale Europeo" (FSE)
Polo di innovazione regionale: Tecnologie dei materiali e della produzione

"Transport Properties in polymer nanocomposite membranes"

Supervisor
Dr. Isabella Nicotera

Coordinator
Prof. Carlo Versace

Director
Prof. Roberto Bartolino

Candidate
Dr. Cataldo Simari

Academic Year 2014/2015

To my family,

for their unconditional love,

encouragement and support.

Transport Properties in Polymer Nanocomposite Membranes

Cataldo Simari

PhD Dissertation

Laboratory: PC_SM “Mario Terenzi”
Department of Chemistry and
Chemical Technologies - CTC
University of Calabria
Ponte P. Bucci, 14D
87036-Rende (CS)
Italy

ABSTRACT

The aim of this thesis has been to prepare and characterize innovative composite membranes for polymer electrolyte fuel cells (PEMFCs) applications. Among the different energy conversion devices based on polymer electrolytes, PEMFCs, both hydrogen (DHFC) and direct methanol (DMFC), seems to be one of the most promising clean energy technologies. As electrochemical devices able to directly convert the chemical energy of a fuel into electrical energy, PEMFCs offer interesting advantages in vehicular or portable applications , as the quick start, the high energy conversion efficiency (~ 50%), the reduced environmental impact for the low CO_2 emissions (zero in the case where the primary fuel is hydrogen) and the flexibility respect to the fuel, in fact, besides hydrogen (DHFC), they can be fed for example with methanol (DMFC).

However, considerable efforts are still needed to be able to achieve satisfactory performance in terms of efficiency, durability and cost for mass deployment of such technology. It is necessary to deal with some problems that concern the electrolyte membrane, such as the degradation of the materials, the low proton conductivity at low relative humidity (RH) and poor mechanical properties at temperature higher than 130 °C.

Therefore, the development of high-performance proton conducting polymer electrolyte membranes is critical for the optimal power density and efficiency a PEMFC can achieve because membrane ohmic loss is the major cause of overpotential in the operational current range of the fuel cell. In recent years, increasing interest has been devoted to the development of **high temperature proton conducting polymer electrolyte** fuel cell systems. In fact, most of the shortcomings associated with the low-temperature PEMFC technology based on perfluorosulfonic acid (PFSA) membranes can be solved or avoided by developing alternative membranes with suitable ionic conductivity and stability up to 150 °C. The increasing the operational temperature would result in increased performance of the cell because of easier and more efficient water management, higher reaction rates to the electrodes, improved CO tolerance by the anode electro-catalysts, faster heat rejection rates and better systems integration.

It has been mentioned the possibility to feed PEMFCs systems with other fuel respect to hydrogen. In particular, direct methanol fuel cells (DMFCs) combine the merits of polymer electrolyte fuel cells fueled by H_2 with the advantages of a liquid fuel, such as easy handling and high energy density. However, despite these advantages, also regard this devices there are still technical barriers to overcome for their widespread commercialization such as methanol crossover from anode to cathode through the proton exchange membrane.

From the above, it is thus highly important to enhance the proton conductivity of the electrolyte membrane under low RH in order to accomplish higher PEMFCs performance. On the other hand, is essential to develop polymer electrolytes with reduced methanol cross-over for DMFC.

The work presented in this thesis is the result of a Ph.D. project carried out during a period of about three years from 2012 – 2015, in the Physical Chemistry Soft Matter Laboratory "Mario Terenzi" (PC_SM Mario Terenzi) at the Department of Chemistry and Chemical Technologies in the University of Calabria. The thesis was written as part of the requirements for obtaining the doctor of philosophy degree.

The overall objective of this doctoral thesis was to design, synthesize and evaluate innovative composite electrolytes with specific properties suitable for PEM fuel cells that operate at high temperatures (above 100 ° C) and low RH and/or with low methanol permeability.

To this purpose, three main classes of materials have been explored as nanoadditives to create nanocomposite membranes: (i) organo-modified TiO_2 nanoparticles, (ii) layered materials based on clays (anionic and cationic) and graphene oxide and (iii) hybrids clays-carbon nanotubes. While, as concern the ionomers, perfluorosulfonic acid (Nafion®) and polyaromatic polymers (sulfonated Polyether Ether Ketone and Polybenzimidazole) have been evaluated.

In my doctoral porject an attempt was made to conjugate an intense basic research in order to understand the molecular mechanisms at the basis of ionic conduction in such complex systems, and the design, synthesis and more comprehensive characterization of new nanocomposites with opportune requisites. For this purpose an deep study of the transport properties of the water confined within the electrolyte membranes has been performed by NMR spectrocopy (diffusometry, relaxometry and ^1H spectral analysis)

together to a wide physico-chemical, mechanical and electrochemical characterization in order to achieve a systematic understanding at a fundamental level of the effects of dimensionality, architecture and organization of these nanofillers on the properties of the ionomers and to exploit this knowledge for the preparation of high performance electrolytes.

Some of the electrolytes membranes investigated during my PhD thesis were prepared and studied in the framework of the PRIN Project: NAMED-PEM "Advanced nanocomposite membranes and innovative electrocatalysts for durable polymer electrolyte membrane fuel cells".

The last part of this thesis concerns a research work arisen from a collaboration with ITM-CNR of the University of Calabria, on the Ion Exchange Membranes for Reverse Electrodialysis (RED) process. Here, the NMR techniques were used to study the water dynamics in anion- and cation- exchange membranes (AEMs and CEMs) in order to achieved additional important insights about the effect of the electrolyte solution, on membrane microstructure and its transport and electrical properties.

The results of this research have been published in scientific international Journals and reported in appendix to the end of the thesis.

During these years I have spent two stages periods abroad:

1) in the "Department of Materials Science and Engineering of the University of Ioannina, Ioannina (Greece)", where I worked under the supervision of Prof. D. Gournis, my research has been focused on the synthesis of novel carbon-based materials as additives for nanocomposite membranes;

2) in Department of Physics & Astronomy of the Hunter College, New York (USA), where I worked under the supervision of Prof. S. Greenbaumn, I performed the High Pressure NMR investigation of water and methanol transport properties in sPEEK-based nanocomposite electrolytes.

Two scientific papers, based on the results obtained during these stages, have been recently submitted and also reported in appendix.

SUMMARY OF PAPERS

The first two papers deal with the investigation of the transport properties of novel Nafion-based nanocomposite membranes as electrolyte for Direct Hydrogen Fuel Cells (DHFCs). In **paper I** a new class of hybrid materials based on carbon nanotubes (CTNs) rooted on smectite clay (SWy) has been synthesized and, after opportune side-wall chemical oxidation and organo-functionalization of CNTs, was tested as additive in the polymer matrix. The experimental results demonstrated as this class of hybrid material allow the creation of a well connected path for proton conductivity: a conductivities of $\mathbf{7\times10^{-2}\ S\ cm^{-1}}$ @ 120 °C and 30% RH has been obtained for membrane containing nanotubes decorated with sulfonic acid groups.

Paper II is a study about the effect on water molecular dynamics of the dispersion of sulfated Titania nanoparticles within Nafion matrix. In this work, a "two-sites" model for the quantitative analysis of the self-diffusion coefficients data have been also proposed. The presence of the filler has found to improve both the water retention and diffusion in composite membranes with a significant impact in the region of high temperatures and very low water content. On the other hand, the model proposed allowed a good estimation of the hydration number on both pristine and composite membranes.

In **paper III**, Polybenzimidazole (PBI) was proposed as alternative electrolyte for High Temperature PEMFC. In particular, a deep investigation about the effect of the monomer sulphonation on the proton dynamics and the mechanical properties of the membranes has been conducted. The experimental data proved that sulphonation causes the formation of inter-chain crosslinks, resultin in a reduced proton mobility and, consequently, the ionic conductivity.

The fourth and the fifth paper are devoted to the investigation of the effect of 2D-layered additives on methanol cross-over. Nanocomposite membranes were prepared and tested as electrolyte in Direct Methanol FCs (DMFCs). In **Paper IV,** tailored organo-modified graphene oxide nanolayers bearing sulfonated functional groups were tested as additives in Nafion matrix. A procedure to attempt some preferential orientation of the graphene nanoplatelets in the polymer matrix has been also experienced. It has been proved that the different preparation methods of the

nanocomposites led to characteristic morphology, transport properties and barrier effect to methanol. The resulting membrane showed a significant reduction of the diffusion of methanol and however, a high mobility of the water at high temperatures was still guaranteed.

Paper V refers about the investigation of Nafion-composite membranes obtained by dispersion of anionic (LDH) and cationic (Laponite) nano-clays within polymer matrix. Nanocomposite membranes showed enhanced water retention capability and reduced methanol permeability, leading to improved performances of the DMFCs. Remarkable results were obtained on the composite Nafion-LDH.

In **Paper VI** sPEEK-based membranes have been proposed as alternative electrolyte for high temperature DMFCs. For the preparation of the nanocomposite membranes, an organically functionalized titania, TiO_2-RSO_3H, was evaluated as filler. The experimental results demonstrated that sPEEK-based membranes represent an interesting alternative for DMFC application, when opportunely modified with nanoadditives. Remarkable improvements were found when using the sPEEK/TiO_2-RSO_3H composite membrane as electrolyte in a DMFC, in terms of reduced methanol crossover and higher current and power density delivered.

Paper VII is devoted to a systematic study, by EIS, about the effect of the solution concentration on on the electrical resistance of anion- and cation- exchange membranes (AEMs and CEMs) and interfaces (electrical double layer and diffusion boundary layer). In this study, NMR techniques have been applied in order to obtain additional important insights about the effect of the electrolyte solution and membranes fixed charges concentration, on membrane microstructure and its mass and electrical transport properties.

LIST OF PAPERS

1. Nicotera, I., Simari, C., Coppola, L., Zygouri, P., Gournis, D., Brutti, S., Minuto, F.D., Aricò, A.S., Sebastian, D., Baglio, V.
   "Sulfonated graphene oxide platelets in nafion nanocomposite membrane: Advantages for application in direct methanol fuel cells"
   Journal of Physical Chemistry C, **2014**, *118* (42), pp 24357-24368;

2. Fontananova, E., Zhang, W., Nicotera, I., Simari, C., Van Baak, W., Di Profio, G., Curcio, E., Drioli, E.
   "Probing membrane and interface properties in concentrated electrolyte solutions"
   Journal of Membrane Science, **2014**, *459*, pp 177–189;

3. Nicotera, I., Kosma, V., Simari, C., D'Urso, C., Aricò, A.S., Baglio, V.
   "Methanol and proton transport in layered double hydroxide and smectite clay-based composites: influence on the electrochemical behavior of direct methanol fuel cells at intermediate temperatures",
   Journal of Solid State Electrochemistry, **2014**, *19* (7), pp 2053-2061;

4. Nicotera, I., Kosma, V., Simari, C., Angioni, S., Mustarelli, P., Quartarone, E.
   "Ion Dynamics and Mechanical Properties of Sulfonated Polybenzimidazole Membranes for High-Temperature Proton Exchange Membrane Fuel Cells",
   Journal of Physical Chemistry C, **2015**, *119* (18), pp 9745–9753;

5. Nicotera, I., Kosma, V., Simari, C., Ranieri, G. A., Sgambetterra, M., Panero, S., Navarra, M.A.
   "An NMR study on the molecular dynamic and exchange effects in composite Nafion/sulfated titania membranes for PEMFCs",
   International Journal of Hydrogen Energy, **2015**, 40 (2), pp 14651–14660.

6. De Bonis, C., Simari, C., Kosma, V., Mecheri, B., D'Epifanio, A., Allodi, V., Mariotto, G., Brutti, S., Suarez, S., Pilar, K., Greenbaum, S., Licoccia, S., Nicotera, I.
   "Enhancement of proton mobility and mitigation of methanol crossover in sPEEK fuel cells by an organically modified titania nanofillers",
   Under revision in *Journal of Solid State Electrochemistry*.

7. Simari, C., Potsi, G., Policicchio, A., Perrotta, I., Nicotera, I.
   "Hybrids Clay-Carbon Nanotubes for Nanocomposite Membranes with Enhanced Proton Conductivity Under Low Humidification"
   Submitted to *Journal of Membrane Science*

Other relevant papers not included in this thesis

- ✓ Nicotera, I., Oliviero Rossi, C., Simari, C., Turco Liveri, V., Calandra P.
  "bis(2-ethylhexyl)phosphoric acid/bis(2-ethylhexyl)amine mixtures as solvent media for lithium-ions: a dynamical study"
  In press to *Colloids and Surfaces A* - DOI: 10.1016/j.colsurfa.2015.11.021

- ✓ S. Scalese, S., Nicotera I., D'Angelo, D., Filice, S., Libertino, S., Simari, C., Privitera, V.
  "Cationic and anionic azo-dye removal from water by sulfonated graphene oxide nanosheets in Nafion nanocomposite membranes"
  Submitted to *New Journal of Chemistry*

- ✓ Boutsika, L.G., Enotiadis, A., Nicotera, I., Simari, C., Charalambopoulou, G., Steriotis, T.A.
  "Nafion nanocomposites using Nanoscale Ionic Materials for high temperature proton exchange membrane fuel cells"
  Submitted to *International Journal of Hydrogen Energy*

CONTRIBUTIONS TO CONFERENCES

- ✓ **Nicotera, I.**, Simari, C., Gournis, D.
  Oral presentation: "*The effect of functionalized Graphene Oxide platelets on the transport properties of proton and methanol in Nafion nanocomposite membranes"*
  GEI 2013- Giornate dell'Elettrochimica Italiana, 22 – 27 September 2013, Pavia, Italy;

- ✓ **Fontananova, E.**, Wenjuan, Z., van Baak, W., Nicotera, I., Simari, C., Di Profio, G., Curcio, E., Drioli, E.
  Oral presentation. "*Probing membranes and interfaces properties by impedance spectroscopy*"
  Advances in Science and Engineering for Brackish Water and Seawater Desalination II; An ECI Conference Series, September 29 – October 3, 2013 Cetraro (Calabria), Italy;

- ✓ **Nicotera, I.**, Angjeli, K., Simari, C., Coppola, L., Ranieri G. A.
  Oral presentation*: "Enhanced Proton Transport and Water Retention in Nanocomposite Membranes for HT-PEMFCs using Organo-Modified Layered nanostructures*"
  CIMTEC 2014, 15-19 June 2014- Montecatini Terme, Italy;

- ✓ **De Bonis, C.**, D'Epifanio, A., Mecheri, B., Cozzi, D., Nicotera, I., Licoccia, S.
  Oral presentation: "*SPEEK/Functionalized Titanium Oxide Nanocomposite Proton Exchange Membranes*"
  CIMTEC 2014, 15-19 June 2014- Montecatini Terme, Italy;

- ✓ **Nicotera, I.**, Angjeli, K., Simari, C., Kosma, V., Coppola, L., Baglio, V.
  Oral presentation: "*Layered nanostructures for composites hybrid membranes in fuel cell application: investigation of water and methanol transport prop*erties"
  XXV CONGRESSO DELLA SOCIETA' CHIMICA ITALIANA, 7-12 September 2014, Rende (CS), Italy;

- ✓ **Filice, S.**, D'Angelo, D., Libertino, S., Kosma, K., Simari, C., Gournis, D., Nicotera, I., Barberio, M., Privitera, V., Scalese, S.
  Oral presentation: "*CNT-TiO_2 composites in Nafion membranes for efficient dye degradation in water*"
  IEEE Nanotechnology Materials and Devices Conference, 12-15 October 2014, Aci Castello, Italy;

- ✓ **Kosma, V.**, Simari, C., Coppola, L., Ranieri, G.A., Nicotera, I.
  Oral presentation: "*Hybrid nanocomposite membranes based on lamellar fillers: a study on methanol and water transport properties for DMFC applications"*
  EmHyTeC2014, 9-12 December 2014, Taormina, Italy;

- ✓ Rossi, C.O., Calandra, P., Nicotera, I., Simari, C., Ranieri, G.A.
  Poster presentation: "*Dynamics of the Lithium ion confined in HDEHP/BEEA local structures as probed by Pulsed Field Gradient NMR*"
  5th International Colloids Conference, 21 - 24 June 2015, Amsterdam, Netherlands.

- ✓ **Nicotera, I.**, Simari, C., Coppola, L., Ranieri, G.A.
  Oral presentation: "*Novel Clay-Carbon nanotubes as fillers for hybrid nanocomposite membranes: a study on water transport properties for PEMFC applications*"
  V Iberian Symposium on Hydrogen, Fuel Cells and Advanced Batteries, 05-08 July 2015, Tenerife, España;

- ✓ Boutsika, L.G., Enotiadis, A., Nicotera, I., Simari, C., Charalambopoulou, G., Theodore A. Steriotis, T.A.
  Poster presentation: "*Development of nanocomposite polymer electrolyte membranes for fuel cell applications using novel nanofillers*"
  E-MRS Fall Meeting and Exhibit, 15-18 September 2015, Warsaw University of Technology.

CONTENTS

APPENDIX B

SECTION I

POLYMER ELECTROLYTE MEMBRANES: OVERVIEW AND APPLICATIONS

This Section is divided in three main Chapters:

(1) Hydrogen and Fuel Cells;

(2) Proton exchange fuels cells: properties and materials

(3) Reverse Electrodialysis;

In the first part concerning the fuels cells is reported a comprehensive overview about the main topic in which polymer electrolyte membranes found application, i.e. the proton exchange membrane fuel cells (PEMFCs) that are one of the most promising clean energy technologies. A review of different fuel cell technologies with their working principles, advantages, disadvantages and suitability for several kind of application are also illustrated.

The second part is devoted to the Reverse electrodialysis (RED) technique, another emerging membrane-based energy conversion process, used to extract electricity by mixing two water streams of different salinities. A brief panning about the aspects related to this particular process is also reported.

1.1 HYDROGEN AND FUEL CELLS

This Chapter deals with the main aspects related to hydrogen energy and fuel cells. As main topic of my PhD research, particular emphasis is given to fuel cells based on polymeric membranes as electrolyte (PEMFCs). The state of the art and the main shortcomings hampering the large scale diffusion of this technology have been extensively discussed.

1.1.1 Hydrogen as fuel

Today depletion of petroleum-based energy resources, climate change and environmental pollution has turned into a great problem for human. As main route to solve these problems, vast efforts to replace fossil fuels with other energy sources such as its connotation clean fuel have been taken. A promising possibility is to exploit the energy potential of the most plentiful element in the known universe: **hydrogen**. As known, hydrogen is the simplest element (only one proton and one electron) that constitutes about 75% of all normal matter in the universe and nearly 90% of all atoms. At room temperature and pressure, this diatomic molecule (H_2) is colorless, tasteless, odorless, slightly soluble in water and safe even if highly explosive.
Hydrogen combustion with oxygen can generate a huge amount of energy:

$$2H_2 + O_2 \rightarrow 2H_2O + \textbf{\textit{572 kJ/mol}}$$

Furthermore, we need to consider that hydrogen has an energy density of 39 kWh kg^{-1}, which means that 1 kg of hydrogen contains 130 times more energy than 1kg of batteries, and at least three times larger than that of other chemical fuels (for example, the equivalent value for liquid hydrocarbons is 13 kWh kg^{-1}). This makes hydrogen universally recognized as a green synthetic fuel that could replace fossil fuel, especially for transport applications. Despite its simplicity and abundance, hydrogen doesn't occur naturally as a gas on the earth. Due to its low density (*0.08988 g/L*), it is not retained by the force of gravity and thus tends to escape from the terrestrial atmosphere: hydrogen is not in and of itself an energy source, because it is not naturally occurring as a fuel but it

is always combined with other elements. Water, for example, that is a combination of hydrogen and oxygen (H_2O), can be considered unlimited resources of hydrogen.

Fig 1 shows a clean way, based on hydrogen, to produce energy starting from water and sunlight through the combined action of photovoltaic cells and water electrolysis. Solar panels, wind turbines or any other form of renewables could be used to generate electricity to locally power homes and domestic industries, and any excess electricity can be used for splitting water into hydrogen and oxygen, with the hydrogen stored for later use. The stored hydrogen can then be converted back into electricity or other forms of energy when needed, via a fuel cell or direct combustion. Besides water, hydrogen is the main component of many other organic compounds, notably the "hydrocarbons" that make up many of our fuels such as gasoline, natural gas, methanol and propane[1] from which it can be separated from through the application of heat via a process known as reforming. However, unlike hydrocarbons, hydrogen cannot be destroyed, is carbon-free, non-toxic, and its thermal or electrochemical combustion with oxygen yields nothing but energy and water[2, 3].

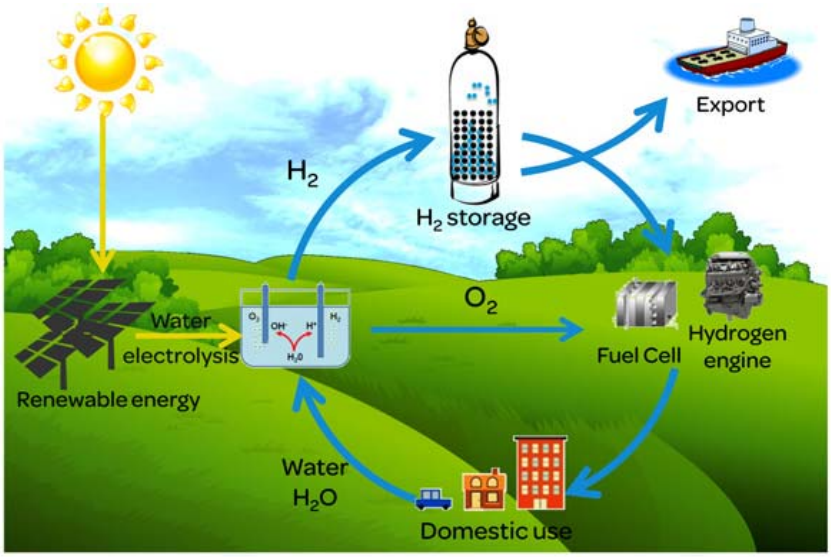

Figure. 1. Hydrogen cycle for green generation of electrical power.

Water is the only waste product deriving from hydrogen combustion; this is the great advantage replacing methane, gasoline and other fossil fuels with hydrogen. The combustion of these substances actually produces carbon dioxide (CO_2), the main

greenhouse gases in the atmosphere. The increase of carbon dioxide and other greenhouse gases in the atmosphere is believed to be the cause of global warming and numerous environmental and climate problems (such as melting glaciers and rising sea levels). To cope with these environmental threats, the international community has decided to take very important economic measures, e.g., the Treaty on the reduction of greenhouse gas emissions, known as the "Kyoto Protocol". Unfortunately, even if hydrogen seems to provide the solution to environmental pollution and dwindling fossil fuels[1-3], up to now the "*green revolution*", so called because foresees a shift from an economy based on fossils fuels to one based on clean and renewable sources of energy, it has not occurred yet. In fact, the scientific world must still overcome several obstacles in order to make hydrogen become the major energy resource: pure hydrogen is currently more expensive than traditional energy sources; the production efficiency (the amount of energy or feedstock used to produce hydrogen) still needs to be improved; lack of infrastructure able to produce and distribute in a capillary way large amounts of hydrogen and lack of technologies suitable to store it safely.

Nonetheless hydrogen represents a lifeline for the future of our planet: an engine that burns pure hydrogen produces almost no pollution. A system based on hydrogen as fuel provides a path for effectively harvesting renewable energy and a sustainable path for unlimited clean energy in which the inherent energy of the stored hydrogen can be released and converted into electrical energy when needed with the only emission of pure water. All of this can be done by another type of electrochemical device, better known as **Fuel Cell**.

1.1.2 Fuel cells

Due to their particular properties, Fuel Cells are on the verge of creating a vast revolutionary change in the electricity's field. A fuel cell is an electrochemical device, which can continuously and directly convert the chemical energy of a fuel, without fuel combustion, into electrical energy. Therefore, in a fuel cell system, the chemical energy related to electrochemical reaction of the fuel with oxidant directly change into water, electricity and heat[4]. Fuel cells are often compared to batteries: both convert the energy produced by a chemical reaction into usable electric power. However, the fuel cell

produces electricity as long as fuel (hydrogen) is supplied, never losing its charge. Fig. 2 shows a comparison of fuel cell performance with other energy conversion systems. As it is possible to see, the efficiency of fuel cell systems is in any case higher if compared with conventional system: fuel cell converts up to 40–60% of available fuel to electricity. Beside the high efficiency of energy conversion that allow savings in fossil fuels, comparing a fuel cell with other distributed generation technologies, it offers more others advantages: zero emission, reduced noise pollution, modularity, scalability, quick installation and gives good opportunities for cogeneration operations[5, 6] (increasing the efficiency at 90% with heat recovery). All these aspects render fuel cells preferable over other energy conversion devices and a promising technology for use as a source of heat and electricity for buildings, and as an electrical power source for electric vehicles.

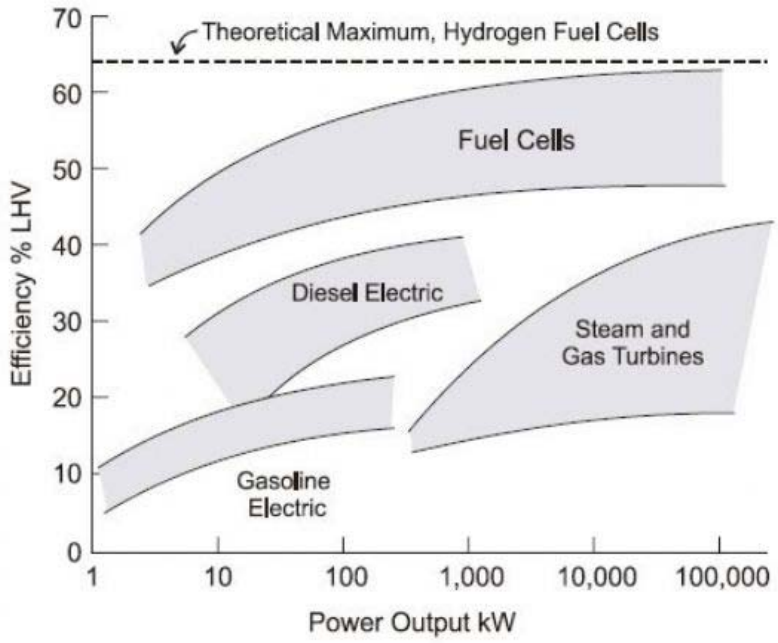

Figure 2. Comparison of fuel cell performance with other energy conversion systems.

Fuel cells operate best on pure hydrogen. But fuels like natural gas, methanol, or even gasoline can be reformed to produce the hydrogen required for fuel cells. Reforming these fuels to create hydrogen will allow the use of much of our current energy infrastructure -gas stations, natural gas pipelines, etc.- while fuel cells are phased in. Some fuel cells even can be fueled directly with methanol, without using a reformer.

Although fuel cells are not a recent development, the use of polymeric membranes as electrolytes has received an incredible impetus in the recent past. It is because of this development that fuel cells are the premier candidates as portable source of power for light duty vehicles and buildings and as replacement for rechargeable batteries[7]. In fact, among the different type of fuel cells, **proton-exchange membrane fuel cells** (**PEMFCs**) are considered to be one of the most promising technology for a clean and efficient power generation in the twenty-first century. Despite PEMFCs have already found a wide range of applications there are still some barriers that must be overcome to promote their rapid commercialization: developing membrane that complies with the basic requirements of fuel cells and is inexpensive at the same time has been the principal goal of research.

In this section, after a description of the general principles of the Fuel Cells and their classification, we'll focus our attention on Proton Exchange Membrane Fuel Cells and the proton transport properties of these electrolytes, ending with an analysis of a possible strategy to improve PEMFC performances: the synthesis of composite membranes.

Historical outline

The basic principles of a fuel cell had effectively been demonstrated at the beginning of nineteenth century by Humphry Davy. This was followed by pioneering work on what were to become fuel cells by the scientist Christian Friedrich Schönbein in 1838. However, is William Grove, that is generally credited with inventing the fuel cell in 1839. Grove conducted a series of experiments, which ultimately proved that electric current could be produced from an electrochemical reaction between hydrogen and oxygen over a platinum catalyst[8]. The term fuel cell was first used in 1889 by Charles Langer and Ludwig Mond, who researched fuel cells using coal gas as a fuel, but the technology generally remained obscure.

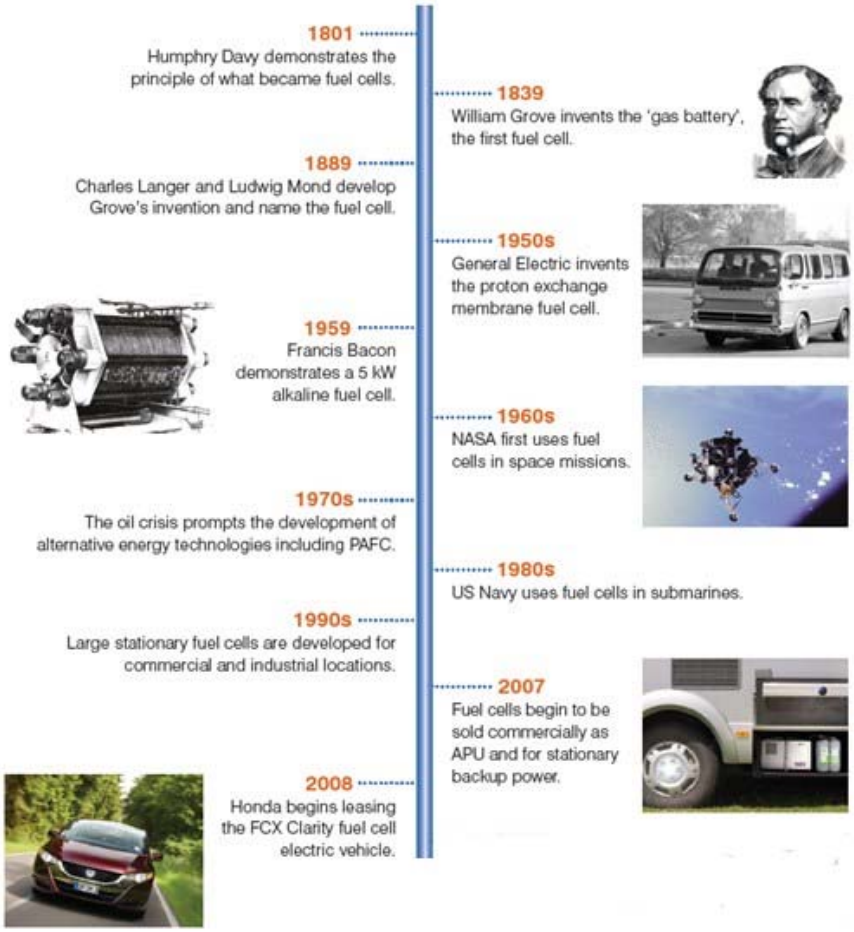

Figure 3. Historical review of fuel cells[10].

In 1932, Cambridge engineering professor Francis Bacon modified Mond's and Langer's equipment to develop the first Alkaline Fuel Cells (AFC) but it was only in 1959 that Bacon demonstrated a practical 5 kW fuel cell system. In the late 1950s and early 1960s NASA, in collaboration with industrial partners, began developing fuel cell generators for manned space missions. Within this collaboration, Willard Thomas Grubb at General Electric (GE) created the first PEMFC unit. Another GE researcher, Leonard Niedrach, refined Grubb's PEMFC by using platinum as a catalyst on the membranes. The Grubb-Niedrach fuel cell was further developed in cooperation with NASA, and was used in the Gemini space program of the mid-1960s. International Fuel Cells (IFC, later UTC Power) developed a 1.5 kW AFC for use in the Apollo space missions. The fuel cell provided electrical power as well as drinking water for the astronauts for the whole duration of their mission. IFC subsequently developed a 12 kW AFC, used to

provide onboard power on all space shuttle flights. Beginning in the mid-1960s, the research work was focused on further development of various fuel cells for applications like stationary powers and transportations. Prompted by concerns over energy shortages and higher oil prices, in the 1970s, many national governments, mainly USA, Canada and Japan and large companies initiated research projects to develop more efficient forms of energy generation[9] resulting in important advances in Phosphoric Acid Fuel Cell (PAFC) technology, in particular in stability and performance. In the 1990s, attention turned first to PEMFC and Solid Oxide Fuel Cell (SOFC) technology, particularly for small stationary applications, moving then to Direct Methanol Fuel Cell (DMFC), as PEMFC technology was adapted for direct methanol portable devices, and to Molten Carbonate Fuel Cell (MCFC) technologies, for large stationary applications. During the last two decades, due to the increasing concerns on the part of governments, business and consumers over energy security, energy efficiency, and carbon dioxide (CO_2) emissions, the attention has turned once again to fuel cells as one of main potential technology capable of delivering energy efficiency and CO_2 savings while reducing dependence on fossil fuels. Not surprisingly, fuel cells began to become commercial in a variety of applications in 2007. First they started to be sold to end-users with written warranties and service capability, in particular, thousands of PEMFC and DMFC auxiliary power units (APU) were commercialized in leisure applications, such as boats and campervans, with similarly large numbers of micro fuel cell units being sold in the portable sector in toys and educational kits. Then Honda presented the model FCX Clarity at Los Angeles automobile saloon. This model is available for the consumer since the summer of 2008. This is the first fuel cell vehicle platform-exclusive in the world manufactured in series[10].

The types of Fuel Cells

As already explained, a fuel cell is an electrochemical device able to convert the chemical energy of a reaction directly into electricity with byproduct of water and heat. There are several types of fuel cell but they are all based around a central design. A fuel cell unit consists of a stack, which is composed of a number of individual cells. The structure of a simplified fuel cell is shown in Fig. 4 [11]. Each cell within the stack has two electrodes, one positive (anode) and one negative (cathode), which sandwich the

membrane electrode assembly (MEA). The MEA consists of an appropriate electrolyte with catalysts on both sides. The hydrogen fuel is fed continuously to anode electrode and the oxidant (or oxygen from air) is fed continuously to the cathode electrode. Through a reaction occurring at the anode, hydrogen fuel is decomposed into positive ions (protons) and negative ions (electrons). The intermediate electrolyte permits only to the appropriate ions to flow from anode to cathode side and acts as an insulator for electrons. If free electrons or other substances could travel through the electrolyte, they would disrupt the chemical reaction. In fact, free electrons, in order to reach the other side of the membrane and ensure the stability to the system, must move to the cathode side through an external electrical circuit. The recombination of the positive and negative ions with oxidation takes place at the cathode to form depleted oxidant (or) pure water.

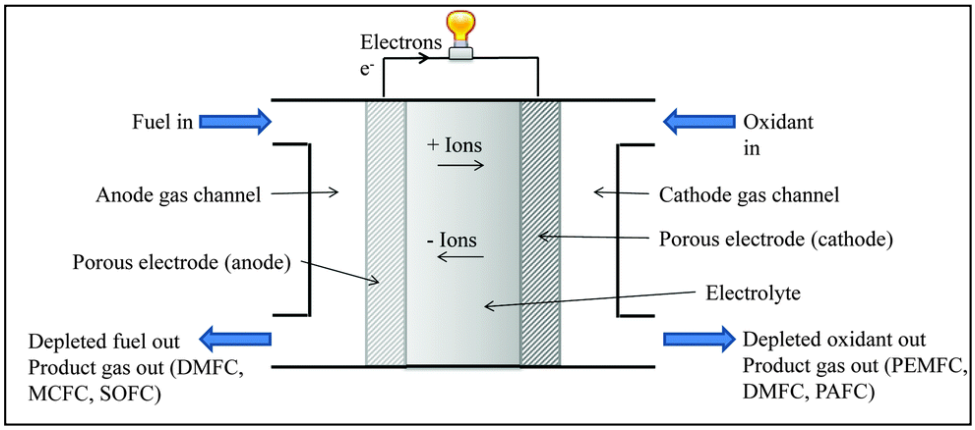

Figure 4. Schematic design of a Fuel Cell.

Based on the nature of the electrolyte, fuel cells may generally be distinguished into four main categories: Proton Exchange Membranes, Alkaline, Solid Oxide and Molten Carbonate fuel cells. Each type has its own unique chemistry, such as different operating temperatures, catalysts and electrolytes (see Fig. 5). According to their operational temperature range, a further classification can also be done as:

High Temperature Fuel Cells:

- Molten Carbonate fuel cells (MCFCs)
- Solid Oxide fuel cell (SOFCs)

Low Temperature Fuel Cells:

- Proton Exchange membrane fuel cells (PEMFCs):
  - ✓ Direct Hydrogen FC (DHFC)
  - ✓ Direct methanol FC (DMFC)
  - ✓ Phosphoric Acid FC (PAFCs)

- Alkaline fuel cells (AFCs)

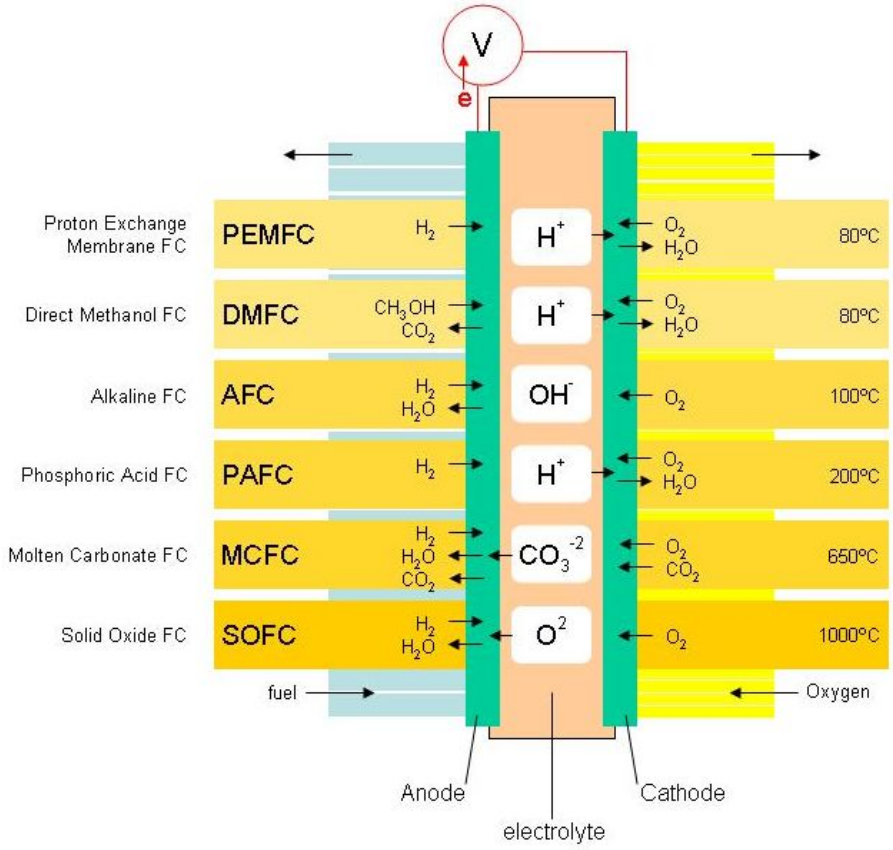

Figure 5. Schematic representation of different fuel cell types: Proton Exchange Membrane (PEM) fuel cell, Direct Methanol fuel cell (DMFC), Alkaline fuel cell (AFC), Phosphoric Acid fuel cell (PAFC), Molten Carbonate fuel cell (MCFC) and solid Oxide fuel cell (SOFC).

According to the review conducted[12-17] and the above described classification, the main advantages, disadvantages and suitability of application of all the different fuel cells are briefly described below.

Special emphasis will be given in the next section to proton exchange membrane (PEM) fuel cells, the type of fuel cell studied in this thesis.

Molten Carbonate Fuel Cells (MCFCs) are high temperature fuel cells, working at temperatures about 600–700 °C, that use an electrolyte composed of a molten carbonate salt mixture suspended in a porous, chemically inert ceramic lithium aluminum oxide matrix. By this electrolyte circulating carbonate ions (CO_3^{2-}) from the cathode to the anode (the reverse of most fuel cells), see Fig. 6.

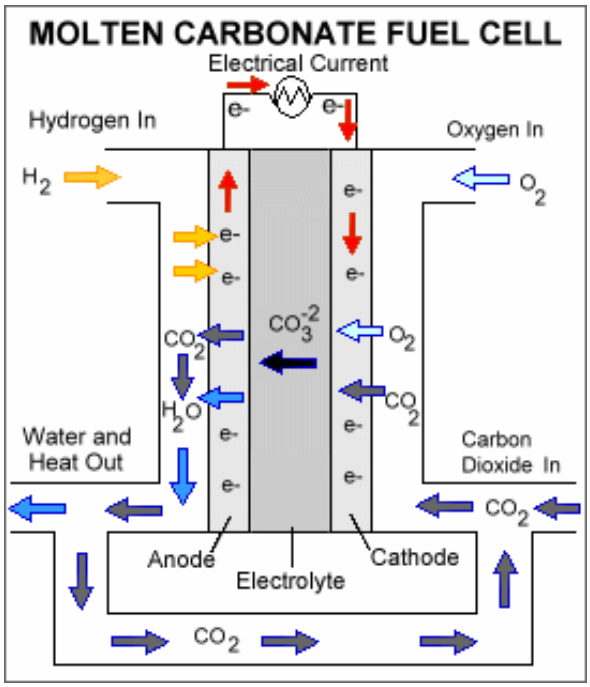

Figure 6. Schematic illustration of a Molten Carbonate FC.

Anode reaction: $2H_2 + 2CO_3^{2-} \rightleftharpoons 2H_2O + 2CO_2 + 4e^-$ (1)

Cathode reaction: $O_2 + 2CO2 + 4e^- \rightleftharpoons 2CO_3^{2-}$ (2)

The lower cost of a MCFC compared with other fuel cells is probably the main advantage of this kind of cell. The high operational temperatures, allow the replacement of platinum with other non precious metals as catalysts at the anode and cathode. Beside, unlike alkaline, phosphoric acid, and PEM fuel cells, MCFCs do not require an external reformer to convert fuels such as natural gas and biogas to hydrogen. Methane and other light hydrocarbons in these fuels are converted to hydrogen within the fuel cell itself by a process called internal reforming, which enables the use of a variety of fuels and reduces the cost associated with adding a reformer to the system. Improved efficiency (50–60%) is another reason MCFCs offer significant cost reductions over

phosphoric acid fuel cells[12]. The primary disadvantage of current MCFC technology is durability. The high temperatures at which these cells operate and the corrosive electrolyte used accelerate component breakdown and corrosion, decreasing cell life. This cell is intolerant to sulfur and slow start up is another of its drawbacks. Molten carbonate fuel cells are currently being developed for natural gas and coal based power plants for electrical utility, industrial, and military applications. It is mainly used for medium and large power applications[13].

The **Solid Oxide Fuel Cell (SOFC)** is another type of high temperature fuel cell, operating temperature of about 1000 °C. Fig. 7 shows the basic structure and working principles of a SOFC. In a SOFC, the electrolyte is a solid ceramic material based on sintered yttria or scandia stabilized zirconia. Because the oxide ions travel through the electrolyte, fuel cell can be used to oxidize any combustible gas.For the electrodes, platinum is replaced by lower price metals such as nickel or cobalt.

Anode reaction: $2H_2 + 2O^{2-} \rightleftharpoons 2H_2O + 4e^-$ (3)

Cathode reaction: $O_2 + 4e^- \rightleftharpoons 2O^{2-}$ (4)

The main advantages of the SOFC is that they are operated at high efficiency of 50–60%. In addition, waste heat can be recycled to make additional electricity by cogeneration operation, overall fuel use efficiencies could top 85%. As for MCFC, a SOFC does not require a separate reformer to extract hydrogen from the fuel due to its internal reforming capability[12, 14].

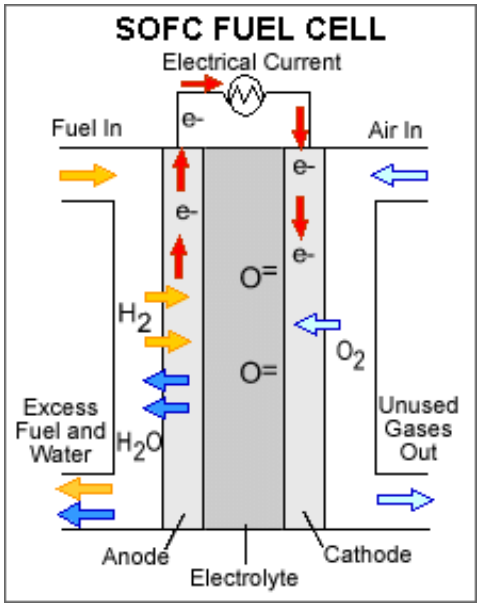

Figure 7. Scheme of a SOFC.

The high operating temperature improves the catalytic activity of alternative metallic or ceramic materials, this means that the system does not need noble metal catalysts, e.g. platinum, and then reduction of cost. Unlike MCFC, SOFCs can tolerate several orders of magnitude more sulfur than other cell types can and they are not poisoned by carbon monoxide, which can even be used as fuel. Hence SOFCs can use natural gas, biogas, and gases made from coal. However high temperature operation has also its disadvantages. First it results in a slow start up and requires significant thermal shielding to retain heat and protect personnel, which may be acceptable for utility applications but not for transportation. Not less important, the high temperatures also place stringent durability requirements on materials. Here because one of the most fascinating challenge about this technology is the development of low cost materials with high durability at cell operating temperatures. The SOFC is mainly used for medium and large power applications. This type of fuel cells is used in stationary applications or such as auxiliary power systems (APU)[15].

The **Alkaline Fuel Cells (AFCs)** have been one of the first fuel cell technologies developed, and they were the first type widely used in the U.S. space program to produce electrical energy and water Onboard spacecraft. Formerly it is also called as

Bacon fuel cell after its British inventor. Despite an AFC operates at temperature very close to that of PEMFC (around 100 °C), it has an higher efficiency of conversion, reaching even 60–70%. The better performance of AFCs is due to the rate at which electrochemical reactions take place in the cell (see Eqs. 5-6).

Anode reaction: $2H_2 + 4OH^- \rightleftharpoons 4H_2O + 4e^-$ (5)

Cathode reaction: $O_2 + 2H_2O + 2e^- \rightleftharpoons OH^-$ (6)

These fuel cells use a solution of potassium hydroxide (KOH) in water as the electrolyte and can use a variety of non precious metals as a catalyst at the anode and cathode. In recent years, novel AFCs that use a polymer membrane as the electrolyte have been developed. These fuel cells are closely related to conventional PEM fuel cells, except that they use an alkaline membrane instead of an acid membrane. It transports negative charged ions from anode to cathode and releases water as its byproduct, Fig 8.

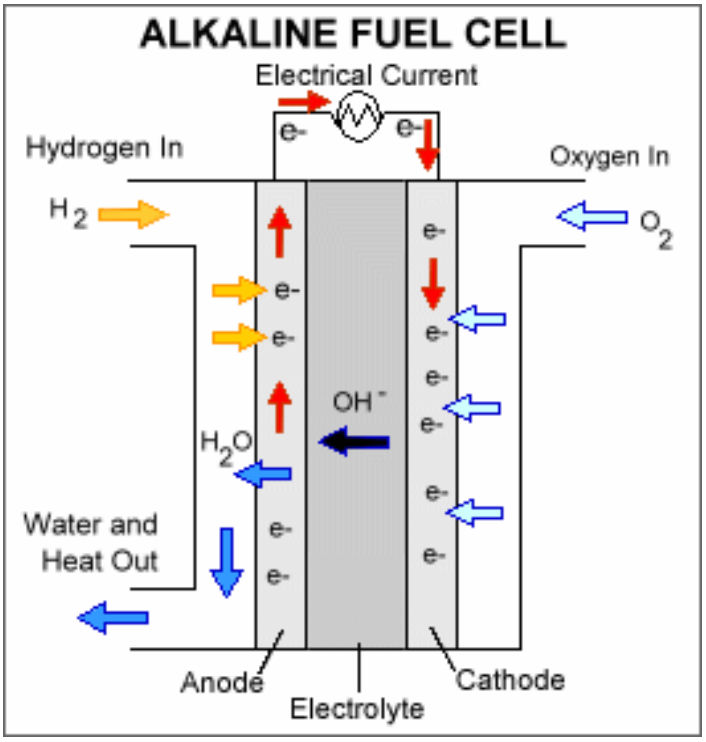

Figure 8. Schematic illustration of an Alkaline FC.

One of the advantages of this fuel cell system is the quick start. Furthermore it is also possible to use electrodes made of non-noble and relatively cheap materials such as nickel or nickel based compounds. The major disadvantage is that it is easily poisoned

by carbon dioxide (CO_2) since it takes more time to react and consumes the alkaline in the electrolyte thereby reducing the concentration of hydroxide ion during chemical reactions[12,13]. This means that even the small amount of CO_2 in the air can affect this cell's operation, making it necessary to purify both the hydrogen and oxygen used in the cell: it needs an expensive separate system to remove the CO_2 from the air. Susceptibility to poisoning also affects the cell's lifetime (the amount of time before it must be replaced), further adding to cost.

The **Polymer electrolyte membrane fuel cell (PEMFC)**, also called proton exchange membrane fuel cells, foresees a solid polymer as electrolyte, which is an excellent conductor of protons and an insulator for electrons, interposed between two porous carbon electrodes containing a platinum or platinum alloy catalyst. They are typically fueled with pure hydrogen, supplied from storage tanks or reformers, oxygen from air, and water. At the interface between anode and the electrolyte, the fuel is converted into protons (H^+) and electrons (e^-), a process which is made possible by a catalyst that is typically Pt-based. Polymer electrolyte membrane allows protons to flow through, but prevents electrons from passing through it. Electrons travel to the cathode through an external circuit producing electrical current, while H^+ ions (protons) pass through the membrane from anode to cathode, where they combine with oxygen molecules and electrons to produce water and heat. Figure 9 shows a scheme of this process. PEM fuel cells operate at relatively low temperatures, around 80°C (in specific configurations around 180 °C). The chemical reactions involved in anode and cathode sides and their overall reactions are given in Eqs. (7)–(9)[16].

Anode reaction: $H_2 \rightleftharpoons 2H^+ + 2e^-$ (7)

Cathode reaction: $1/2O_2 + 2H^+ + 2e^- \rightleftharpoons H_2O$ (8)

Overall reaction: $H_2 + 1/2O_2 \rightleftharpoons H_2O$ (9)

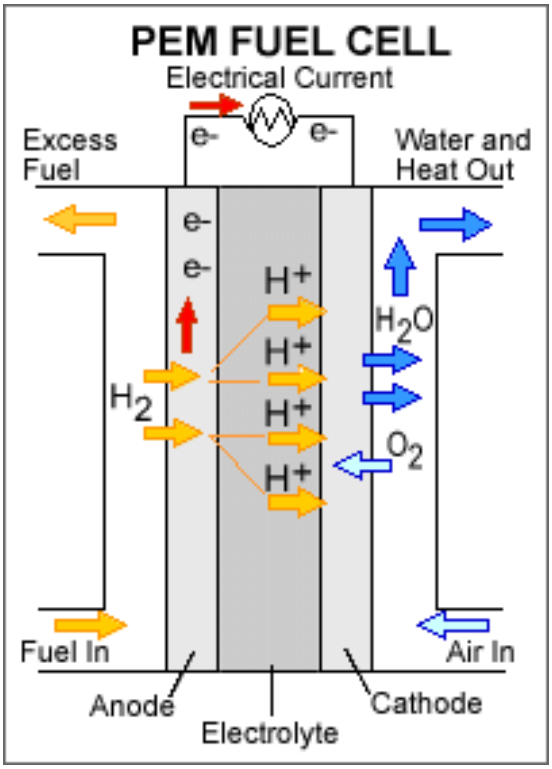

Figure 9. Schematic representation of a PEMFC.

A PEM Fuel Cell, compared with other fuel cells, delivers high power density, despite its low weight and volume. Besides, the low temperature operation allows them to start quickly (less warm up time) resulting in less wear on system components and then in better durability. However, the presence of platinum as catalyst to separate the hydrogen's electrons and protons, from one side cause an increase to system cost, from the other side the platinum catalyst is extremely sensitive to carbon monoxide poisoning, making it necessary to employ an additional reactor to reduce carbon monoxide in the fuel gas if the hydrogen is derived from a hydrocarbon fuel. Due to their fast startup time and favorable power to weight ratio, PEM fuel cells are particularly suitable for use in passenger vehicles, such as cars and buses[12] and some stationary applications.

The **Direct Methanol Fuel Cell (DMFC)** technology is relatively new when compared to rest of the fuel cells. Like PEM fuel cell, also in a DMFC the electrolyte is a polymer able to conduct protons from one electrode to the other. However, in a

DMFC system, the fuel cell anode is directly fed by pure methanol in appropriate mixture with water (Fig. 10). Via chemical reactions, the anode directly catalyzes the production of hydrogen and electrons from liquid methanol (CH_3OH): this system does not need an external reformer. At the cathode, the negative ions, coming from the anode through an external circuit, and protons, that have passed through the electrolyte, are combined with oxidized air to produces water as a byproduct:

Anode reaction: $CH_3OH + H2O \rightleftharpoons CO_2 + 6H^+ + 6e^-$ (10)

Cathode reaction: $3/2\ O_2 + 6H^+ + 6e^- \rightleftharpoons 3H_2O$ (11)

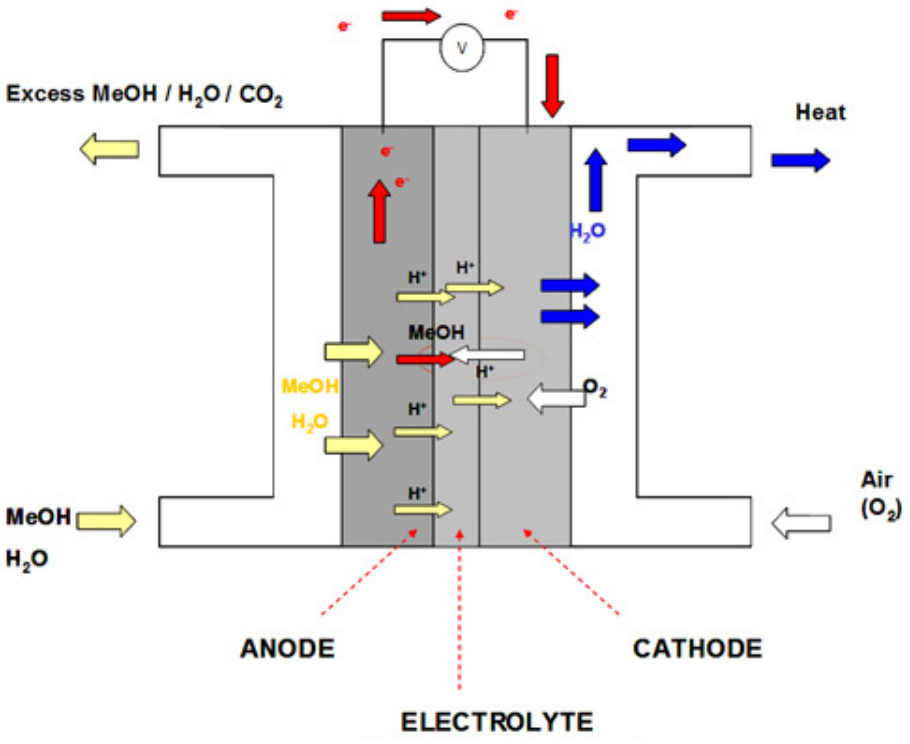

Figure 10. Schematic diagram of a Direct Methanol FC.

As novel technology, direct methanol fuel cells offer a series of advantages compared with other fuel cell systems. For example, despite the system is very similar to a PEMFC, a DMFC do not have many of the fuel storage problems typical of a fuel cell that need pure hydrogen as fuel: methanol has a higher energy density than hydrogen. Being liquid, like the fuels currently used, methanol is easier to transport and supply to the public using our current infrastructure. Unfortunately, the diffusion of this

technology on an industrial scale is hampered by two important shortcomings that limit DMFC performances: the slow oxidation kinetics of methanol below 100 °C and the crossover of methanol, resulting in a drop in efficiency of fuel utilization upon 50%[17]. Methanol crossover can be ascribed to the high affinity between methanol and polymer used as electrolyte; methanol diffuses through the membrane from the anode side to the cathode. It has been found that nearly 30%–40% of methanol can be wasted due to this crossover to the cathode depending on operating conditions like temperature, concentration of methanol in the anode feed, and current density in the cell[18, 19]. The direct consequence of this phenomenon is a reduction of DMFC efficiency: both because there is a fuel leak (the crossed-over methanol is essentially wasted), and because the carbon atoms of the methanol induce cathode's catalyst poisoning. To minimize the negative impact of the methanol crossover, fuel cell developers are forced to (1) use thicker membranes that reduce the fuel crossover but increase the specific cell resistance; (2) limits methanol concentrations at the anode compartment to around 2–5 wt%, that, however, limit the overall DMFC efficiency to around 15–20% and the power density to around 30 mW/cm^2. Despite these limits, Direct Methanol fuel cells are slowly replacing traditional batteries in applications for relatively low-power energy sources like small electronic equipment: i.e., notebooks, cameras and video cameras, DVD players, and some medical devices. In fact, by virtue of the higher lifetime compared to the lithium ion battery and the possibility to recharge them by simply changing the cartridge of fuel there is an increasing interest in such systems in the market of portable applications. So far, another potential field of application of DMFC as power sources for electric vehicles is too remote. Work is needed to achieve the futures of longer lifetime and greater efficiency[20].

The **Phosphoric Acid Fuel Cell (PAFC)** operates at temperature almost double as compared to that of PEM fuel cell, about 175–200 °C. The electrolyte, a liquid phosphoric acid within a matrix of silicon carbide, conducts hydrogen ions (H^+) from the anode to the cathode (Fig. 11). The chemical reaction involved in this fuel cell is same as PEM fuel cell , see Eqs. 7-9, where pure hydrogen is used as its input fuel[12].

Unlike the PEM and AFC, which are easily "poisoned" by carbon monoxide (it binds to the platinum catalyst at the anode, decreasing the fuel cell's efficiency), PAFCs are more tolerant of impurities in fossil fuels that have been reformed into hydrogen: reformed hydrocarbon fuels may use air directly from the atmosphere. The high operating temperature allow energy cogeneration and the potential available for hot water supply as well as electricity depends on the heat and electricity load profile. Not surprisingly, PAFCs are more than 85% efficient when used for the cogeneration of electricity and heat but they are less efficient at generating electricity alone (37% – 42%). Unfortunately this systems are still affected by a series of disadvantages. First, PAFCs are less powerful than other fuel cells, given the same weight and volume. As a result, these fuel cells are typically large and heavy.

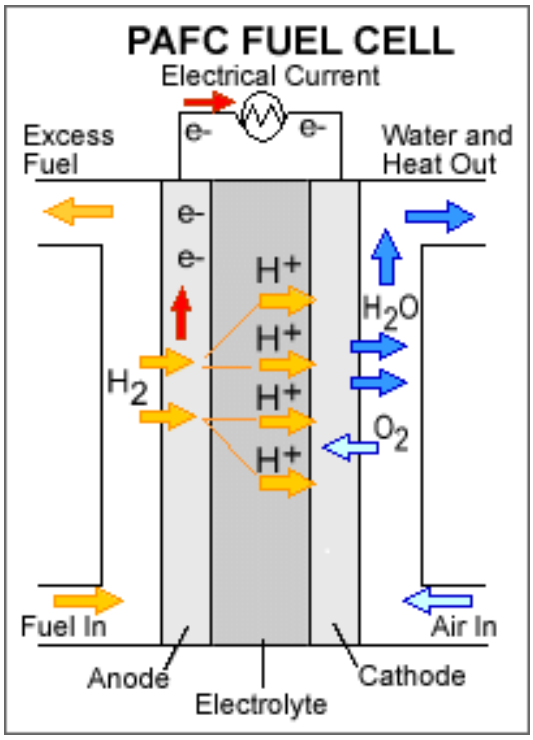

Figure 11. Scheme of a PAFC.

PAFCs are also expensive: they require much higher loadings of expensive platinum catalyst than other types of fuel cells do, which raises the cost. Finally, they utilize as electrolyte a liquid which is corrosive to average temperatures, involving handling and safety problems. However, PAFC is one of the most mature cell types to be used

commercially. This type of fuel cell is typically used for stationary power generation, but some PAFCs have been used to power large vehicles such as city buses. The 100, 200 and 500 kW size plants are available for stationary and heat applications. A 1.3MW system is already tested in Milan[13]. More over PAFC have been installed at 70 sites in Europe, USA and Japan.

1.2 PEMFCs: PROPERTIES AND MATERIALS

It was in 1959 when General Electric (GE) first incorporated an ion exchange resin as an electrolyte for space application. Those resin were phenolic membranes obtained polymerizing phenol-sulfonic acid with formaldehyde. Since then, an intensive research has been focused on PEM fuel cell system as clean alternative for energy production. However, it was the discovery of Du Point to give further impetus to the development of devices for a large scale use as energy storage or conversion system (fuel cell)[21]. In 1970s, he developed a stable cation-exchange membrane based on sulfonated polytetrafluoro-ethylene, called "Nafion®", characterized by a specific conductivity two order higher than previous polymer electrolytes for PEM fuel cells able, also, to extend the lifetime of the device by four orders of magnitude (10_4–10_5 h). Nafion membrane has immediately become a standard for PEMFC and remains so till today. This enabled the PEMFC over a period to surpass the solar cells and other alternatives. Based upon its perceived simplicity of design and weight advantages, combined with optimum compatibility[22].

From what above, it appears clear as the central core of a PEM fuel cell is the so called Membrane Electrode Assembly (MEA). Fig. 12 shows in details all the components of a PEM fuel cell. As is possible to see, the MEA consists of a polymeric membrane squeezed between the two porous, electrically conductive electrodes (electrocatalyst), and is the place where electrochemical reaction occurs to produce free electrons and protons from the appropriate fuel. These electrodes are typically made out of carbon cloth or carbon fiber paper. At the interface between the porous electrode and the polymer membrane there is a layer with catalyst particles, typically platinum supported on carbon. The membrane, which acts as the electrolyte, must possess particular characteristics. In fact, this solid polymer electrolyte must form a thin but sound electronic insulator and gas barrier between the two electrodes, preventing the direct contact between hydrogen and oxygen and the resulting efficiency losses due to direct chemical reaction (chemical short-circuit), and, at the same time, must provide the transportation pathway for the hydrogen ions from the anode to the cathode side of the cell, allowing high current densities[23].

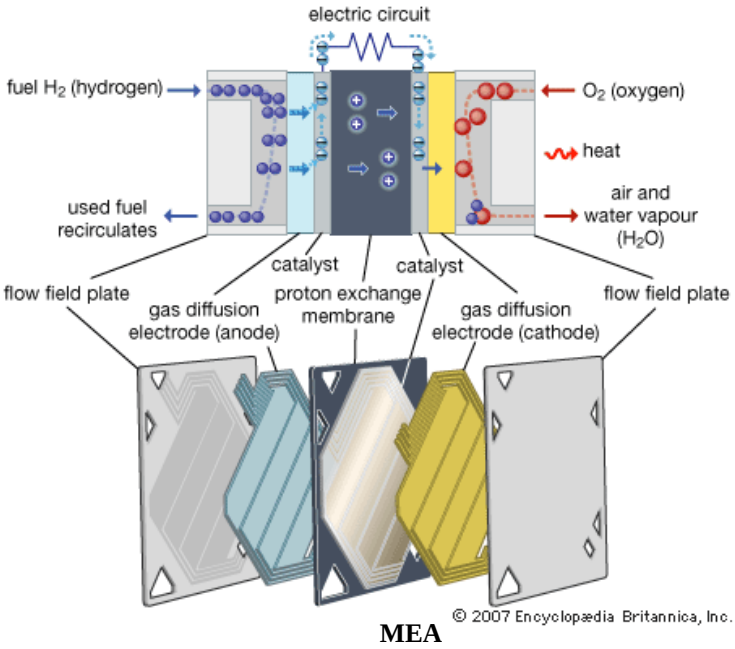

Figure 12. Schematic representation of a PEM fuel cell.

Although interest in synthesizing polymers for fuel cell applications has been observed for about a century, major developments in this field were made only in the recent past[24]. In fact, there is considerable application-driven interest in lowering the membrane cost and extending the operating window of PEMs. Current PEMFC technology is based on Nafion, an expensive perflourinated proton-exchange membranes (PEMs), that operate effectively only under fully hydrated conditions: it is well known the proton conductivity of proton exchange membranes is strictly related to the extent of the humidity of the membrane. Higher proton conductivity, and so high fuel cell performance, achieve by the higher extent of the humidity. Besides the level of hydration, another factor affects the performance of a proton exchange membrane, it is the thickness of the membrane. A strategy to avoid water drag or water crossover is to reduce the membrane thickness thereby enabling an improvement in the fuel cell performance. Other advantages of reduced thickness include lower membrane resistance (and therefore an enhancement in membrane conductivity), lower cost and rapid hydration. However, there is a limit to the extent to which membrane thickness can be reduced because of difficulties with durability and fuel by-pass. To reduce PEMFC system complexity, the road currently being undertaken by researchers foresees the development of 'water-free' electrolytes that do not require hydration; such kind of

electrolytes could definitively open interesting path for the large-scale implementation of this technology. A polymer that can work with no needs of humidification, can also enable the PEMFC to be operated under 'warm' conditions (i.e. above 100 °C) thus further improving its efficiency and capital cost could also be further reduced because at warmer conditions less Pt could be used. To achieve high efficiency the membrane must possess the following desirable properties[25]:

- high proton conductivity;
- zero electronic conductivity;
- chemical and electrochemical stability under operating conditions;
- extremely low fuel or oxygen by-pass to maximize coulombic efficiency;
- adequate mechanical strength and stability;
- moisture control in stack;
- compatibility
- availability;
- production costs compatible with intended application.

As already said, the role of polymeric membrane between electrodes is the conduction of the produced proton from anode to cathode[23]. In order to support high currents with minimal resistive losses, a proton conductivity above 10^{-2} S cm^{-1} is required. At the same time, the membrane has to be electronically insulating, in order to avoid short circuit of the cell, and a good barrier for the reactants: reactant cross-over decreases the efficiency and results in voltage losses in fuel cells. Besides to alteration of the performance of the fuel cell, an high crossover rate entails safety issues resulting from the formation of explosive gas mixtures. Another key feature that the membrane must necessarily possess is a high resistance under the condition of the operating cell. For example the polymer matrix has to withstand to the harsh oxidative stress, i.e. aggressive radicals, high potentials, extreme pH and eventually high temperatures. Advances in the synthesis and characterization of polymers are also aimed to improvements in thermal and mechanical properties and flexibility of the polymers. Thermal cycling of the electrochemical cell will induce stresses in contact points between different cell components, which ultimately might lead to physical membrane failure. Moreover, in order to allow a good reaction kinetics, compatibility of the

membrane with the cell hardware as well as the electrode materials is required. Finally, but not less important, in order to reach widespread commercial utilization of the PEM technology, the cost of the membrane material has to be minimized[26, 27].

Towards the development of the PEMFC, several new PEMs as well as variants on the Nafion structure have been developed over the last decade. Generally, the materials used in synthesis of the polymer electrolyte membranes can be classified into three vast groups:

- ✓ perflourinated ionomers (or partially perflourinated);
- ✓ non-flourinated hydrocarbons (including aliphatic or aromatic structures);
- ✓ acid-base complexes[28].

1.2.1 Polymers used in the PEM

Perfluorinated sulfonic acid (PFSA) and Nafion polymers

The PFSA membranes are currently the reference polymer for portable fuel cell applications. This class of membranes is characterized by a perfluorinated backbone with attached sulfonic acid groups ($-SO_3H$)[29]. The perfluorinated polymer used most extensively goes by the trade name of Nafion®, a copolymer of variable amounts of unsaturated perfluoroalkyl sulfonyl fluoride and tetrafluoroethylene (Teflon®), developed by Du Pont in 1970s. In the recent past, a series of alternative polymers with a shorter pendant side-chain (SSC) carrying the sulphonic group than Nafion have been investigated for fuel cell operation, see Fig. 13. Similar polymers are Flemion® produced by Asahi Glass, 3M®, Aciplex-S®, Aquivion® produced by Solvay-Solexis, etc[30-32]. However, because of its high proton conductivity, good chemical stability and mechanical strength, the DuPont product is considered to be superior among the three major types of PFSA membranes[42].

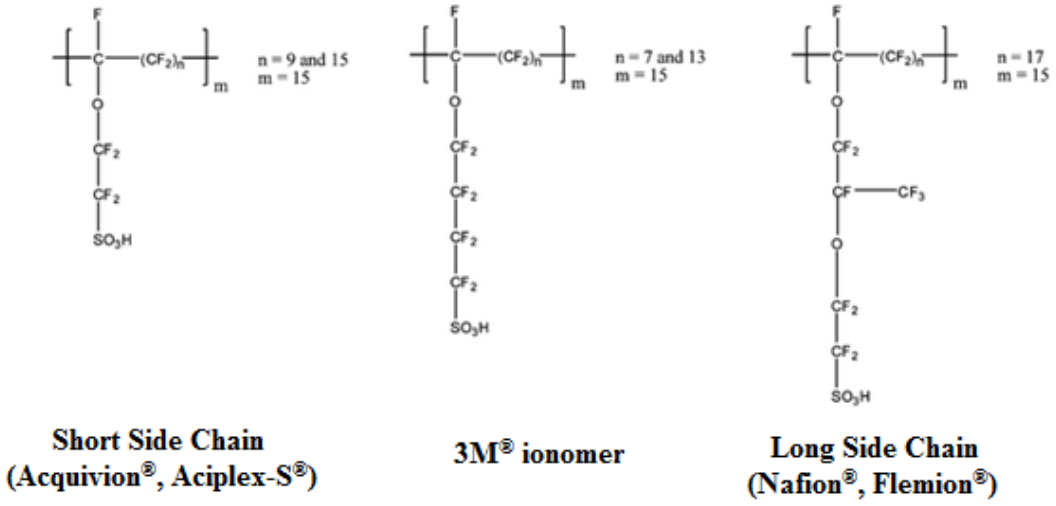

Figure 13. Chemical structures of LSC and SSC perfluorinated ionomers

The chemical-physical properties of this polymer are closely related to its chemical structure. Teflon backbone of this structure gives the hydrophobic nature for membrane while the hydrophilic sulfonic acid groups (HSO_3^-), chemically grafted into the backbone, are involved in the absorption of the large amount of water by polymer and therefore, lead to hydration of the membrane. Hence, according to Kreuer[34], perfluorosulfonic polymers naturally combine, in one macromolecule, the extremely high hydrophobicity of the perfluorinated backbone with the extremely high hydrophilicity of the sulfonic acid functional groups. Such amphoteric feature, in presence of water, lead to some hydrophobic/hydrophilic nano-separation. While the sulfonic acid functional groups aggregate to form a hydrophilic domain responsible for the transport of protons and water, the hydrophobic domain provides the polymer with the morphological stability and prevents the polymer from dissolving in water.

Due to the high ionic conductivity and chemical stability under operating environment, that make Nafion® a suitable electrolyte for fuel cell applications, during the recent years an increasing interest has been focusing on this ionomer. It is clear that the tuning of these materials for optimum performance requires a detailed knowledge of chemical microstructure and nanoscale morphology.

Structurally, Nafion® is complex. Although the exact structure is not known, several models have been proposed since the early 1970s, to describe the way in which ionic

groups aggregate within the Nafion® polymer. The basis for all these models is the description of the microscopic structure of the polymer that was proposed in the early 1980s by Gierke and Hsu[35], according to which Nafion morphology can be described as an inverted micellar structure in which the ion-exchange sites (the sulfonate-ended perfluoroalkyl ether groups) are separated from the fluorocarbon backbone thus forming spherical clusters (pores), connected by short narrow channels. The model was hence termed as 'cluster network' model[26, 37], shown in Figure 14. Other similar model have been subsequently proposed. According to the "random network model"[38], for example, a structure where hydrated regions are distributed randomly in the polymer matrix has been suggested. Such structures facilitates quicker transport of protons upon the rotation of these side chains and has been proved to be generally acceptable, especially in the region of 9–34% relative humidity[39].

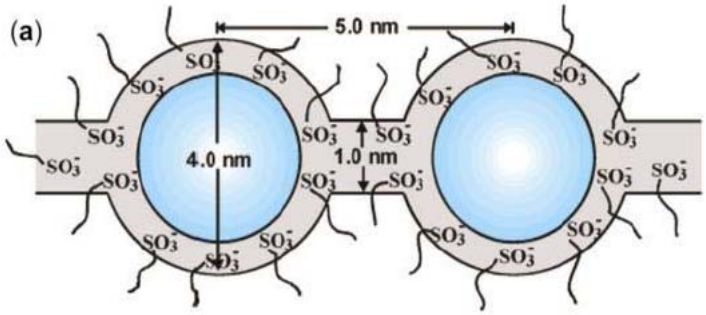

Figure 14. Cluster-network model[36] for the morphology of hydrated Nafion.

Yeager and Steck, instead, proposed a model, whose representation has shown in Fig. 15, based on a three-phase clustered system with interconnecting channels within the polymer. The three regions consist of (A) a fluorocarbon backbone, some of which is microcrystalline, (B) an interfacial region of relatively large fractional void volume containing some pendant side chains, some water, and those sulfate or carboxylic groups and counter ions which are not in clusters, (inhomogeneous matrix phase) and (C) the clustered regions where the majority of the ionic exchange sites, counter ions, and sorbed water exists[40, 41].

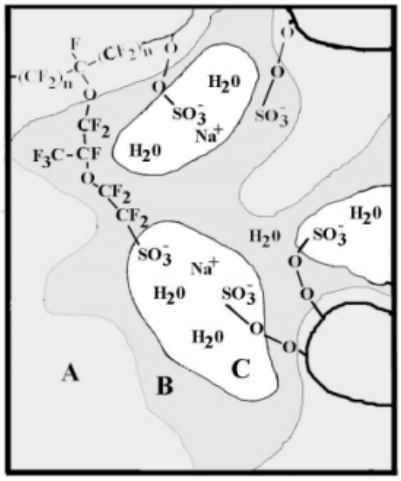

Figure 15. The Yeager 3 phase model[40] of Nafion® clusters, region A, B and C are the fluorocarbon backbone, the interfacial and the clustered regions respectively.

.

About 15 years later Gierke's theories, Litt[42] first proposed a re-evaluation of Nafion morphology reframing a lamellar model consistent with the bilayer structure in order to explain the reversibility of the swelling/deswelling behavior of Nafion membranes. Such lamellar model was then refined by Haubold et al[43]. After performing experiments on dry samples in air and samples equilibrated with water, methanol, and a range of water/methanol mixtures using an in situ flow cell, Haubold proposed a layered model whose basic structure element (i.e., the scattering particle) is a "sandwich" (Figure 16). The side chains, including the sulfonic acid groups, compose the "shell" (external portion) of the sandwich, while the inner liquid portion (the "core") consists of the water/methanol molecules. To provide channels that serve as conduction pathways for protons through the membrane, these structural elements were proposed to be juxtaposed in a linear fashion so that the liquid core regions are contiguous.

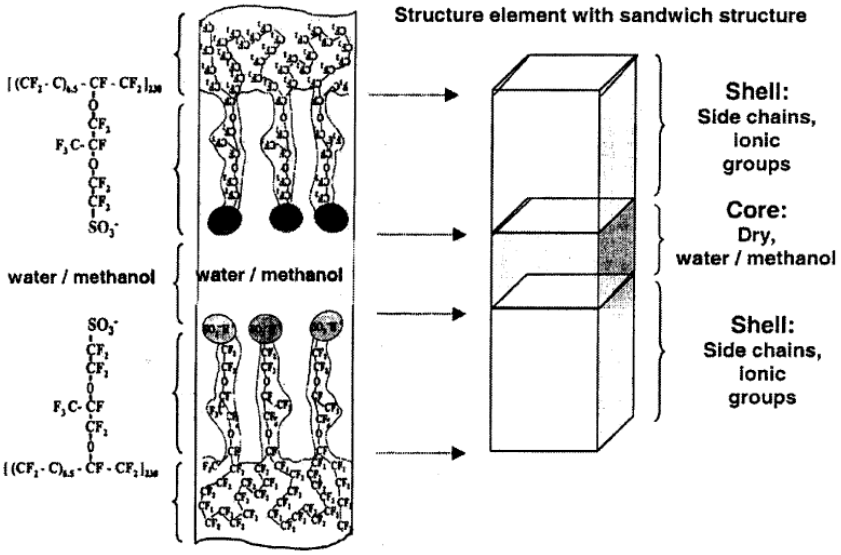

Figure 16. Sandwich-like structural element proposed for the morphological organization of Nafion[43].

Among the different model, a plausible mechanism for the evolution in structure from the widely accepted concept of isolated clusters, for membranes containing relatively low water contents, to rod-like structures in solution, was offered by Gebel, and is shown schematically in Figure 17[44]. According to this qualitative model, the dry membrane is considered to contain isolated, spherical ionic clusters with diameters of ~1.5 nm and a center-to-center separation distance of ~2.7 nm. The absorption of water induces a progressive clusters swelling until the membrane "dissolves" into solution. The rodlike structures separate to yield a colloidal dispersion of isolated rods: the structure of highly swollen membranes is very close to that of the Nafion solution.

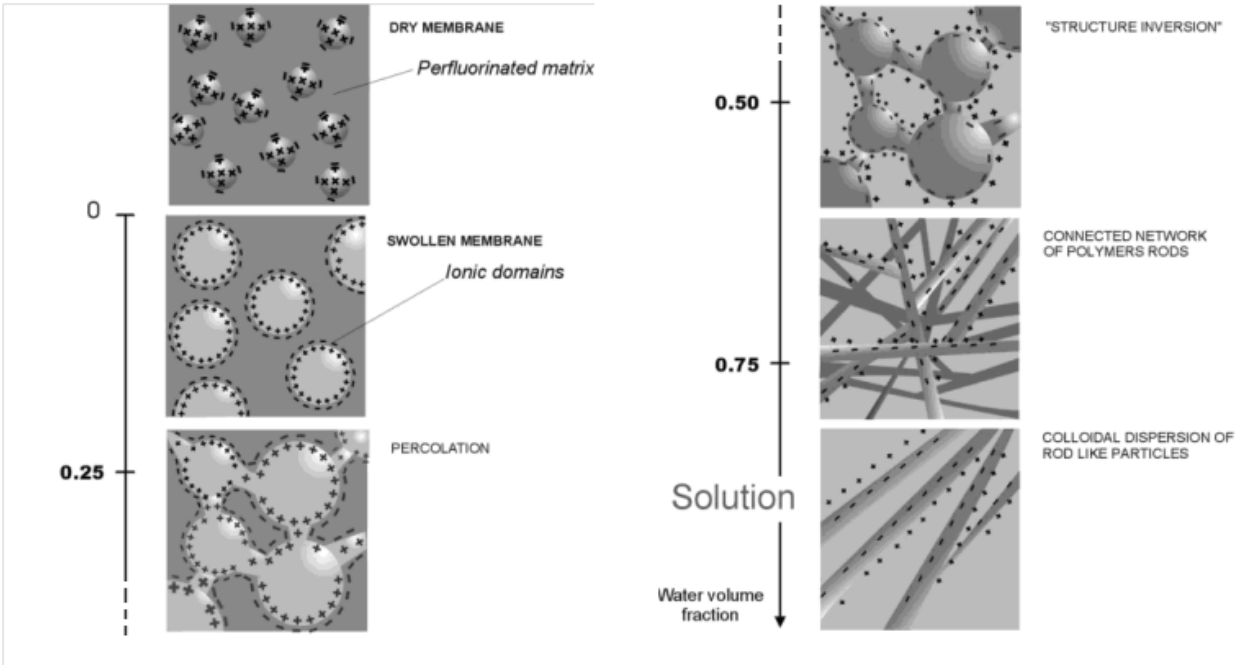

Figure 17. Conceptual model fot the morphological reorganization and continuity of the ionic domains in Nafion as the dry membrane is swollen with water.

One of the latest models for Nafion morphology has been proposed in 2007 by Schmidt-Rohr and Chen[45]. The application of a recently introduced algorithm to the small-angle scattering data present in litterature allowed them to propose a water-channel model for Nafion structure. According to this model, the structure of Nafion at a hydration level of 20 vol% (11 wt%) water, is made up of water channels (cylinders), whose diameter ranges between 1.8 and 3.5 nm, with an average of ~ 2.4 nm, lined with hydrophilic side groups, Fig. 18a,b. Such channels, that are locally parallel to their neighbours and can be considered as cylindrical inverted micelles, are stabilized on the outside by the relatively straight helical backbone segments. The stiffness of the helical backbone segments[46, 47], can stabilize the long cylindrical structures. The water-channel model naturally accounts for many of the outstanding properties of Nafion, in particular its high proton conductivity and water permeability[48] as well as the large permeation, diffusion coefficient and electro-osmotic drag[49].

Currently, this simple water-channel model seems to provide a unified view of the structure of Nafion.

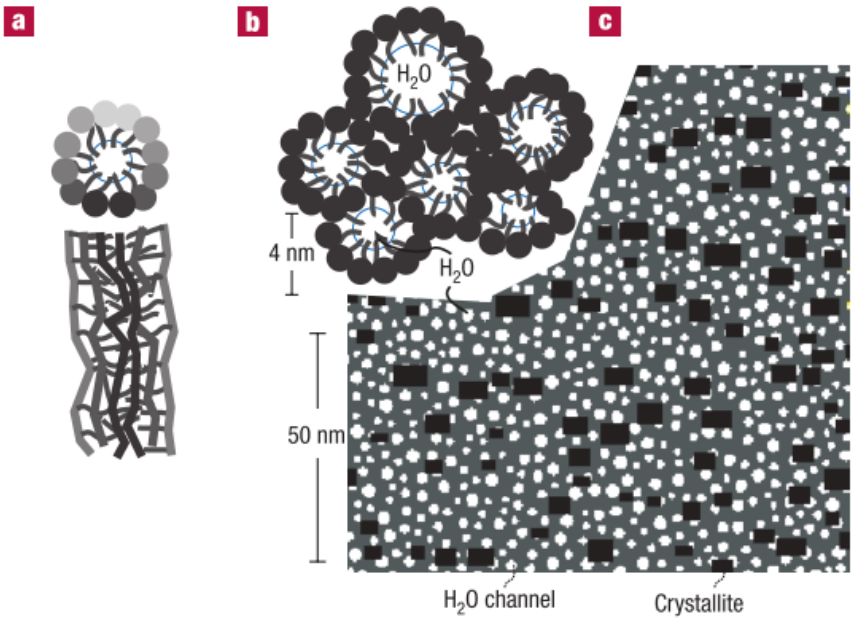

Figure 18. Parallel water-channel (Inverted micelle cylinder) model of Nafion. **a**, Two views of an inverted-micelle cylinder, with the polymer backbones on the outside and the ionic side groups lining the water channel. Shading is used to distinguish chains in front and in the back. **b**, Schematic diagram of the approximately hexagonal packing of several inverted-micelle cylinders. **c**, Cross-sections through the cylindrical water channels (white) and the Nafion crystallites (black) in the non-crystalline Nafion matrix (dark grey), as used in the simulation of the small-angle scattering curves.

As we have just seen, these models have led to a much clearer understanding about morphology and transport features of ionic domains in Nafion. In contrast, the nature of the crystalline component has received little attention: the relevance of this morphological feature to the technologically important properties of the membranes is still unclear. However, since the initial studies on Nafion morphology, the crystalline component has been recognized as an important structural feature and often considered as a necessary component that provides mechanical integrity and a barrier to solvent swelling: it is crucial for mechanical properties, acting as physical crosslinks[50]. Therefore, acting on the crystalline part of the polymer, for example by redissolution in appropriate solvent[51], one can generate distinct ordered structures in the clusters and form a network between clusters using the short channels that connect the aggregates. Upon doing so, the original ionomer properties can be altered and tailored to specific uses and needs, such as, specific gas and liquid separations and fuel cell operations.

Two main research areas currently of interest on Nafion® are the transport phenomena within the membrane and in particular modifications made to the membrane to increase its performance as well as water retention capacity. PFSA-based fuel cell technology, in fact, still suffers of several shortcomings, primarily due to the use of Nafion membranes:

- ✓ the high cost of membrane amounting to US$ 700 per square meter[52];
- ✓ lack of safety during its manufacture and use[53];
- ✓ requirement of supporting equipment[54], e.g. the hydration system adds considerable cost and complexity to the vehicle;
- ✓ temperature related limitations[55];
- ✓ methanol crossower[56].

Despite its shortcomings, Nafion® is still the polymer of choice for most PEFC and DMFC applications. However, it is likely that Nafion® will be replaced by an alternative membrane in the future[57]. To overcome few of the disadvantages enumerated above, the researchers are carrying out an intensive research work to identify promising alternatives[58]. Rikukawa and Sanui[55] suggest that in order to produce materials that are less expensive than Nafion, some sacrifice in material lifetime and mechanical properties may be acceptable, provided the cost factors are commercially realistic. Hence, the use of hydrocarbon polymers, even though they had been previously abandoned due to low ionic conductivity, has attracted renewed interest[34].

Non-fluorinated hydrocarbon polymers

Promising candidates for proton exchange membrane synthesis are *non-fluorinated hydrocarbon* polymers. These can be aliphatic or aromatic polymers bringing benzene ring structures in the polymeric backbone of membrane or in the bulky pendant groups from this membrane polymeric backbone. Presently, one of the most promising routes to high-performance proton conducting polymer electrolyte membranes is the use of hydrocarbon polymers for polymer backbones[59]. Hydrocarbon membranes provide some definite advantages over perfluorinated membranes: from one side they can be synthesized with relatively inexpensive and commercially available

monomers as well as easy to recycle by conventional methods; from the other side the polymer structures can be built with desired properties using various functional monomers or via introduction of polar sites as pendant groups, i.e. in order to increase the water uptake.

Among the aforementioned opportunities, several studies pointed out that sulfonated Polyetheretherketone polymer (sPEEK) seems to constitute a real alternative to commercial Nafion since, in some cases, it shows comparable (or superior) proton conductivity performances to Nafion as well as a superiority in terms of thermo-chemical properties, lower fuel crossover and, particularly, lower costs[60]. PEEK is a colourless semicrystalline thermoplastic polymer, in the polyaromatic family, available commercially, with excellent mechanical and chemical resistance properties that are retained to high temperatures.

Due to its low proton conductivity, however, pristine PEEK cannot be employed as such in a fuel cell system: to improve its ionic conductivity, protogenic groups (generally a sulfonic acid groups) must be introduced into the polymer. Accordingly, since the polymer sulfonation procedure is the most significative parameter affecting S-PEEK behaviours, several strategies for PEEK sulfonation have been developed during these years, each one showing a series of benefits and drawbacks[61]. The most used procedure for S-PEEK synthesis, whose structure is shown in Fig. 19, foresees the direct electrophilic sulfonation by using concentrated sulphuric acid or chlorosulphuric acid. However PEEK sulfonation may be also performed introducing directly the sulfonic acid group onto the polymer backbone[62] as well as by modification or via polymerization of the sulfonated monomers[63].

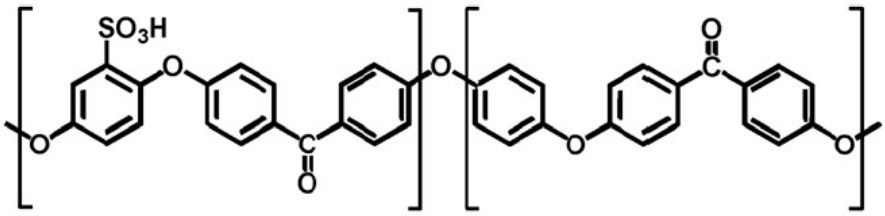

Figure 19. Formula of sPEEK.

It has already mentioned that the sulfonation of PEEK, due to the reduction of the cristallinity, affects the chemical character of the polymer, and consequently several important parameters. The glass transition temperature (*Tg*), for example, increases with DS, depending on the gradual introduction of SO_3H groups into the PEEK polymer. This increases both the intermolecular interaction due to the hydrogen bonding of SO_3H groups (ionomer effect), then the molecular bulkiness. An increased number of sulfonic groups lead also to enhanced proton conductivity of the polymer both because this acid groups are direct involved in proton transport mechanism and because of the polymer becomes more hydrophilic and absorbs more water, which also facilitates the proton transport. However, high sulfonation, in particular for uncrosslinked sulfonated membranes, results in high swelling, which leads to poor mechanical properties and low ion permselectivity, especially at higher operating temperatures. Finally, also the methanol permeability tends to increase with increasing values of DS. In fact, due to its microstructure, PEEK has a low intrinsic methanol permeability. However, as mentioned above, since with increasing DS the crystallinity decreases, sPEEK solubility changes when the sulfonation degree is modified[64].

Most of the differences between sPEEK and Nafion in term of the hydration behavior, the transport of protonic charge carrier and water can be qualitatively explained by differences in the microstructures and the acidity of the sulfonic acid functional groups, as Kreuer[34] first suggested. In Nafion membranes, with water absorption, the sulfonic acid functional groups aggregate to form a hydrophilic domain, giving rise to some hydrophobic/hydrophilic nano-separation. When this hydrophilic domain is hydrated, protonic charge carriers form within inner space charge layers by dissociation of the acidic functional groups, and proton conductance assisted by water dynamics occurs. The situation in sulfonated polyetherketones was found to be distinctly different with respect to both transport properties and morphological stability. In sPEEK, the backbone is less hydrophobic and at the same time the sulfonic acid group is less acidic and, therefore, less polar; this leads to a smaller hydrophilic/hydrophobic difference that associated with the smaller flexibility of the polymer backbone makes the separation into a hydrophilic and a hydrophobic domain less pronounced. In addition, in sPEEK the sulfonic acid groups are directly attached to the phenyl ring along the backbone of the polymer and there is little flexibility to allow the phase separation as suggested for

Nafion. The random position of the sulfonic acid groups and minimal flexibility of the PEEK backbone results in small clusters. The poor packing leaves free volume where water sorbs; since sorbed water can occupy free volume surrounding the sulfonic acid, the polymer does not need to swell to accommodate water. Finally, the sulfonic acid groups are suggested to either be isolated or in small clusters of two or three interacting sulfonic groups[65]. From what discussed, hydrophilic domains in Nafion and sPEEK have different topologies and so different response to water absorption. As schematically illustrated in Fig. 20, the water filled channels in sulfonated PEEK are narrower compared to those in Nafion. Additionally, they are less separated, poorly connected and more branched with more dead-end "pockets". These features correspond to the larger hydrophilic/hydrophobic interface and, therefore, also to a larger average separation between the sulfonic acid groups.

An important consequence of the narrow channels in sulfonated PEEK is that the electro-osmotic drag as well as the permeation coefficient are distinctly lower than in well separated perfluorosulfonic polymer for a given water content[66]. In fact, also the different methanol permeance through sPEEK and Nafion may be accounted for the difference in their microstructures. In Nafion membrane, the hydrophilic domains are interconnected and, not only proton and water but also a smaller polar molecules such as methanol can go through them, leading to the methanol crossover. With respect to Nafion, the microstructure of sPEEK leads to a separation into hydrophilic and hydrophobic domains less pronounced and, for this reason, their methanol permeances are lower than the Nafion ones[67]. However, by increasing DS, the selectivity decreases.

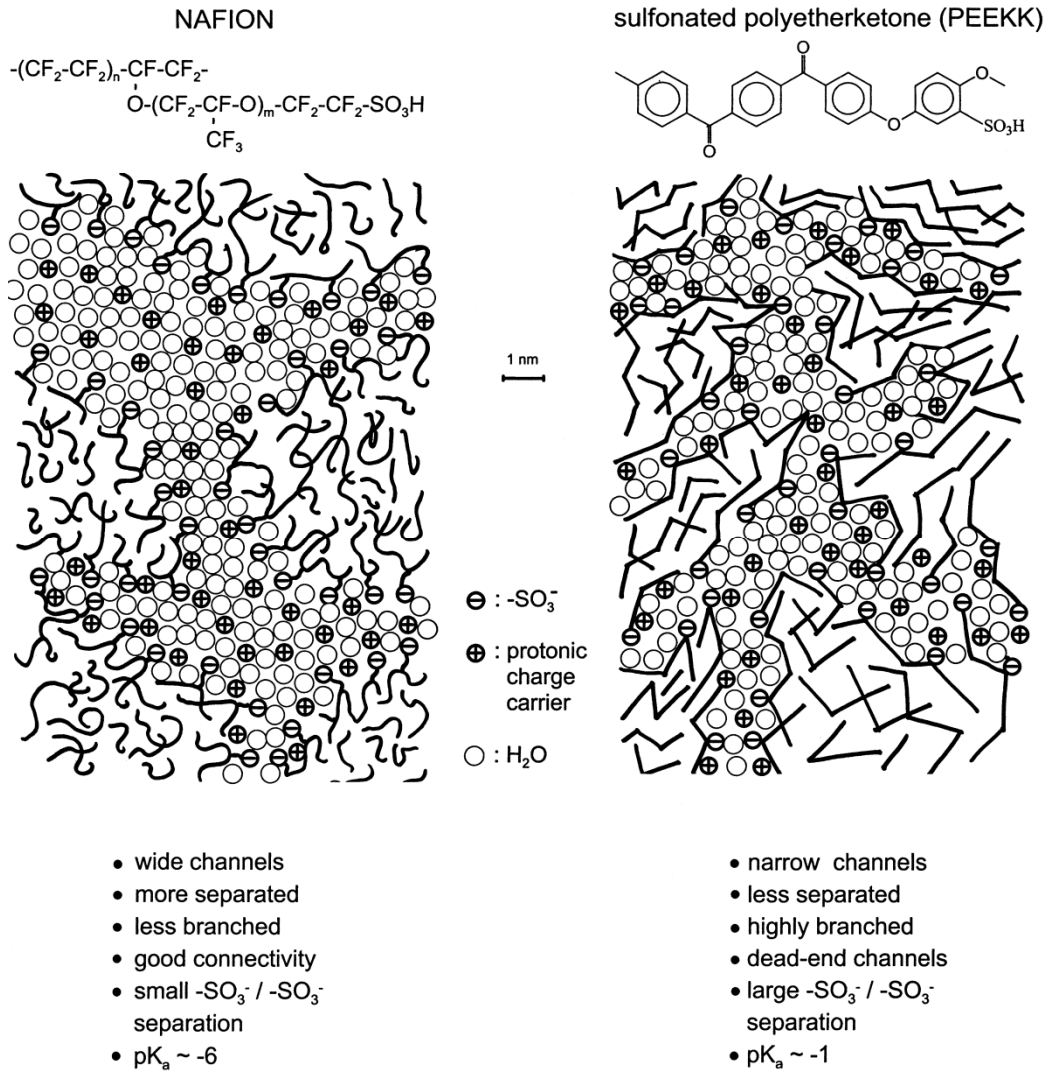

Figure 20. Schematic representation of the microstructures of NAFION and a sulfonated polyetherketone[34].

As membrane materials for fuel cells, plain sulfonated polyetherketones apparently have some advantages that have made it particularly attractive. It is cheaper than Nafion and can be easly recycled by conventional methods; after sulfonation ensures a high water uptake over a wide temperature range, may be durable enough under fuel cell operating conditions[34] and with a long life-time (sometimes >3000 h). Besides, the low drag coefficients facilitate the water management under operating conditions[68], and the low solvent (water and methanol) crossover, is of advantage especially in direct methanol fuel cells[69]. However, to increase the low proton conductivity of pristine PEEK, a strong sulfonation process is required: depending on the variation of the sulfonation

degree (DS), the mechanical properties and methanol permeability of sPEEK membranes could deteriorate progressively.
Based on the above analyses, researchers are moving through several different chemical and microstructural modifications in order to improve the transport properties of such polymer without sacrificing mechanical and chemical stability[70].

During this doctoral work, in the framework of the Project NAMED-PEM "Advanced nanocomposite membranes and innovative electrocatalysts for durable polymer electrolytemembrane fuel cells", several sPEEK based membranes, prepared by Dr. De Bonis C. of Department of Chemical Science and Technologies, University of Rome "Tor Vergata", were tested as polimer electrolyte for application in high temperature direct methanol fuel cells. Details about the experimental results are reported in paper VI in the appendix of this thesis.

Acid–base complexes

All the sulfonated membranes, perfluorinated, non-fluorinated or partially fluorinated, still require to be fully hydrated to keep a high proton conductivity, consequently maximum working temperatures are still too low. Among the polymers of choice for the development of High Temperature PEM fuel cells[71], acid-doped polybenzimidazole (PBI/H_3PO_4) membrane seems so far the most successful system. This acid-base complex, in fact, seem to offer an optimal combination of properties such as mechanical stability, higher values of conductivity at elevated temperatures without suffering from dehydration effects[71, 72] and the tolerance towards fuel impurities at temperatures up to 200 °C.
Polybenzimidazoles are fully aromatic heterocyclic polymers, having benzimidazole moieties in their backbone. The chemical structure is shown in Fig. 21. Among them, the acronym PBI is reserved for the only commercial polybenzimidazole type polymer, the poly[2,20-(m-phenylene)-5,50-dibenzimidazole], produced by Celanese Corporation since 1983[73].

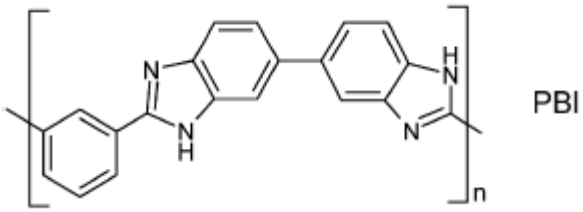

Figure 21. Chemical structure of polybensimidazole (PBI).

Regarding its use in fuel cell technology, is well known that pristine PBI is not a proton conducting polymer, and cannot be used as solid electrolyte. One of the ways to increase significantly the proton conductivity of a PBI membrane is to treat it with strong acids. This results in a nano-impregnation, ambiguously named in the literature as "doping", at a molecular level similar to that taking place for water in Nafions, which is well beyond just wetting the membrane. Chemically, indeed, PBI is a basic polymer (pKa= 5.5 as protonated)[74] and can readly react with a strong acid. Various inorganic acids have been investigated such as H_2SO_4[75], H_3PO_4[76], $HClO_4$[77], HNO_3[77] HBr[75] HCl[77] as well as organic acids like CH_3SO_3H, $C_2H_5SO_3H$[78]. However it seems that a high conductivity can only be obtained with amphoteric acids, wich act both as donors and acceptors in proton transfer and therefore allow for proton migration along the anionic chain. From this it derives that water is not necessary in the working membranes to achieve good performances, though some humidity enhances proton conductivity. Moreover, the higher thermal stability of these acids, compared to water (much more easily evaporated) allows the membranes to work at temperatures as high as 180–200 °C for PA-doped PBI.

Due to its high proton conductivity and thermal stability, among all the acids investigated, H_3PO_4 is the most most widely studied and the most interesting. The strong interaction between PBI and acid results in the absorbed acid immobilisation in the polymer. By immersing a PBI membrane in a phosphoric acid solution, the weight gain of the membrane is due to both water uptake and acid doping. However, the absorbed water can be removed by drying the resulting membrane at 110 °C until a constant sample weight is reached. In this way the amount of water and that of acid can be separately derived. Consequently, the doping level can be determined as the number of molecules H_3PO_4 per repeat units of PBI. The doping level, and consequently the

mechanical and ion transport properties of the membrane, strongly depends on the procedures followed for membranes preparations. The first method, the most widely used for the preparation of membranes, is based on the casting from a PBI solution (10–20%) in dimethylacetamide (DMAc)[79] by evaporation of the solvent. Finally, after a cleaning/activation step, the acid-PBI blend in formed by soaking the membranes in a concentrated phosphoric acid bath[80]. The first two H_3PO_4 molecules absorbed by the membrane form a salt by protonation of the imine N group at the imidazole ring (Fig. 22): the imine N is very important for the acid doping of the membrane. Further acid molecules absorbed are incorporated as free acid[81]. According to this procedure, the amount of absorbed acid as well as the water content depends on the bath concentration. An alternative methods allow the preparation of phosphoric acid doped membranes in a single step, i.e. through direct acid casting from solutions of PBI and the desired amount of phosphoric acid in trifluoroacetic (TFA)[82]. Finally, phosphoric acid doped PBI membranes can also be directly prepared through a sol–gel process, involving hdrolysis of Polyphosphoricacid (PPA) into PA. This strategy, first proposed by Benicewicz, simplifies the fabrication of PA-doped PBI membranes with higher levels of PA and ionic conductivities than previously reported, while maintaining mechanical integrity[82].

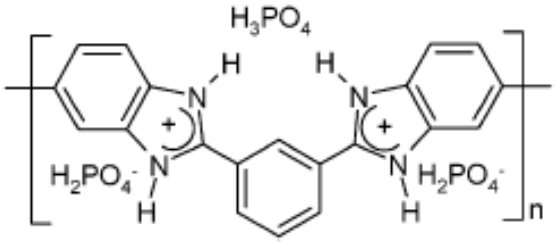

Figure 22. Poly-salt formed by phosphoric acid doping of PBI.

An alternative approach to enhance proton conductivity of pristine PBI foresees the introduction of sulfonic acid groups attached on the polymeric backbone. Sulfonated PBIs can be prepared either sulfonating preformed polymers via direct treatment with sulfuric acid or polymerizing sulfonated monomers. However, the conductivity of those membranes in not high enough to be used directly in PEMFCs[84].

According with the most used procedure for acid-doped PBI membranes, the doping level, and then the proton conductivity, depends on the concentration of the doping acid solutions; increasing DA level can be achieved by increasing concentration of the doping solution. It has been mentioned that the proton conduction mechanism for the PA-PBI complex does not involves water molecules. Proton conduction, indeed, happens via a Grotthus mechanism, deeply described in the next paragraph, according to which proton moves through the electrolyte hopping between two molecules (acid–acid, acid–water, or acid–benzimidazole ring). Despite some proton conductivity has been reported for PBI under humidified conditions[85], proton hopping from one nitrogen site to another, as for example in non-doped PBI, contributes little to the conductivity; mobile (or ‘‘free’’) acid between the polymers chains is a major factor affecting the ion conduction due to its unique proton conduction mechanism by self-ionization and self-dehydration[86]. This conductivity mechanism allows these membranes to work at temperatures as high as 200 °C without humidification, only hydrated by water produced in the cathode of PEMFC[72].

Beside the high proton conductivity at low relative humidity and temperature up to 200 °C, other advantages make PA-doped polybenzimidazole (PBI) promising candidate for low-cost and high performance fuel cell membrane material. The electro-osmotic drag for this kind of membranes is almost zero, this confirm that they can operate without humidification. Even the input of water in the system, in order to further improve the proton conductivity, is less critical since at temperature above the boiling point water does not condense and block the electrodes. This fact considerably simplifies the fuel cell construction and operation compared with Nafion cells: water management is not mandatory for PBI cells. The higher operating temperature leads also to a partial suppression of the CO poisoning effect for platinum catalyst. This opens to the use of reformed methanol as fuel, directly from a simple reformer with only one reactor. In fact, steam reforming of methanol, that usually takes place at 230-250 °C, is possible also at temperatures below 200 °C. At these temperatures, the shift reaction that converts CO into CO_2 proceeds along with the reformer, and the CO level will consequently not be higher than 1 vol%: the methanol reformate gas produced, containing hydrogen, CO_2 and CO, directly enters into the fuel cell[87]. Finally, the high

temperature provides a pratical energy efficient way for heat supply and is therefore expected to improve the overall system efficiency.

At present, the main problems associated with polybenzimidazole PEMFCs seem to be acid leaching and catalyst degradation processes which dramatically decrease the fuel cell performances[88]. Besides, at least for automotive application, this technology is still far from the spread on industrial scale: (i) the high operating temperature do not allow for a rapid start-up as required for vehicles; (ii) the power densities that can be achieved with these membranes appear lower than those obtained with perfluorosulfonic acid (PFSA) membranes.

In the framework of the Project NAMED-PEM "Advanced nanocomposite membranes and innovative electrocatalysts for durable polymer electrolytemembrane fuel cells", during this PhD thesis, membranes with increased number of sulfonic groups within the monomer structure have been prepared by Dr. Quartarone E. of the Department of Chemistry, University of Pavia and INSTM. In order to investigate the effect of the sulphonation on the proton dynamics and the mechanical properties of the membranes, modified membranes were compared to pristine 5N-PBI (see paper III in appendix).

1.2.2 Proton Conduction Mechanisms in PEM

The study of proton transport in aqueous solution has received considerable attention for over a century because of its paramount importance in chemical, biological, and electrochemical systems. In particular, for proton exchange membrane fuel cells proton conduction is usually the first characteristic considered when evaluating membranes for potential fuel cell use: resistive loss is proportional to the ionic resistance of the membrane and high conductivity is essential for the required performance especially at high current density.

Is well known that, the dominant intermolecular interaction in water is hydrogen bonding so that, in aqueous solutions of acids, the proton exists as hydronium ion (H_3O^+), which is itself hydrated, e.g., as $H_5O_2^+$ or H^9O^{4+} [89, 90]. Therefore, the introduction of an extra proton can be more appropriately described as a delocalized electronic charge defect spanning multiple molecules, that leads to the contraction of hydrogen bonds in the vicinity of such a defect. The spread of this charge defect blurs the identity of the excess "proton" among several likely candidates, each of which corresponds to a different classical hydronium-like character and chemical bond arrangement. One consequence of this behavior is that the mobility of the excess proton is abnormally higher as compared with other cations of similar size and charge. It is this charge delocalization and dynamic chemical bonding that is at the heart of the interesting solvation and transport properties of the hydrated proton. The transport of delocalized protonic charge defects is a complicated process involving the coordinated rearrangement of several water molecules over which the charge density is distributed.

At a molecular level, the proton transport in hydrated polymeric matrices is in general described on the basis of either of the two principal mechanisms: (i) proton hopping, or shuttling, between molecules and (ii) a vehicular component involving the translational diffusion of the hydrated proton solvation structure[91, 92]. The time scales for the hopping and vehicular components are both intimately coupled to the dynamics of the water hydrogen-bond (H-bond) network. As widely proven, in a polymer electrolyte fully hydrated two different water environments it can usually be distinguished[93-95]. For instance, the water in the middle region of the pore is referred to as "bulk water", through which the mobility of protons is fast. However, water near the pore surface along the array of acid groups is referred to as "surface water", and the

proton mobility through the surface is considerably smaller than that in the bulk, due to the strong electrostatic attraction of acid groups hung along the polymer chain.

The proton hopping, mechanism was first discussed in a paper by ***Grotthuss*** over two centuries ago, and it has since been termed the "Grotthuss mechanism"[96]. Fig. 23 shows a simple scheme of the above mechanism[97]: protons hop from one hydrolyzed ionic site ($SO3^-$ and $H3O^+$) to another across the membrane. *Grotthuss diffusion coefficient* includes: (i) the hydrogen-bond cleavage between the proton accepting site molecule and a nearby water molecule; (ii) reorientation of the proton-accepting molecule toward the hydronium ion to be in a receptive orientation. Through this mechanism, the produced proton by oxidation of hydrogen in anode adheres to water molecule than the provisional hydronium ion is formed and one different proton from same hydronium ion hops on the other water molecule. In completely swollen perflourinated sulfonic acid membranes, such as Nafion, the hopping mechanism has little contribution to conductivity: proton transport mechanism through a PEM is basically conduction through water.

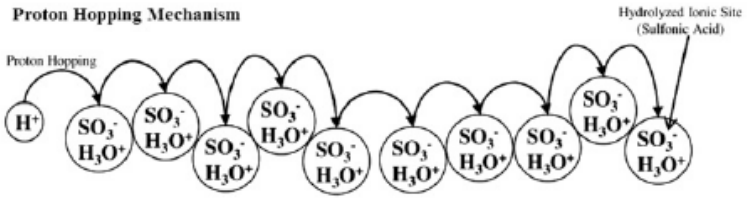

Figure 23. Scheme of the proton hopping mechanism[68].

The second mechanism is a diffusion mechanism, also called "vehicular" since water act as vehicle. In this mechanism, as a consequence of the electrochemical difference, the hydrated proton (H_3O^+) diffuses through the aqueous medium. In vehicular mechanism, the water connected protons ($H^+(H_2O)_x$), in the result of the electro-osmotic drag, carry the one or more molecules of water through the membrane and itself are transferred with them. The formation of the vehicular mechanism is promoted by the existence of the free volumes within polymeric chains in proton exchange membrane which allow the transferring of the hydrated protons through the membrane. Besides,

the hydrophobic nature of Teflon backbone facilitates the water transfer through the membrane because the surfaces of the hydrophobic holes tend to repel the water molecules[97]. The schematic design of the vehicular mechanism in membranes has been shown in the Fig. 24.

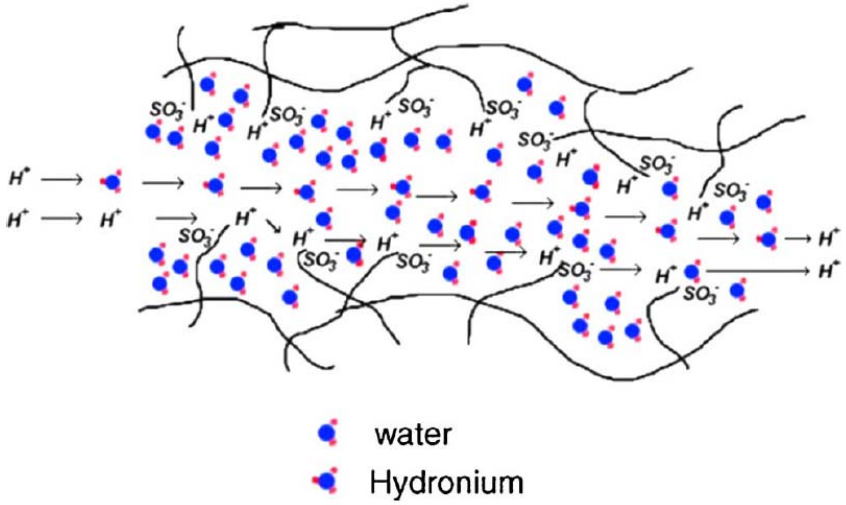

Figure 24. Schematic design of the Vehicular Mechanism as proton conduction in pristine membrane[71].

The mechanism for proton transport in water does not occur within a single step. In fact, excess protons can be a part of a dimer ($H_5O_2^+$, "Zundel" ion) or a part of a hydrated hydronium ion ($H_9O_4^+$, "Eigen" ion). However, the central bond of $H_5O_2^+$ (≈250 pm) in an aqueous medium is noticeably contracted compared to the average hydrogen bond length in bulk water (≈280 pm) but elongated compared to an isolated dimer (≈240 pm). While, in case of $H_9O_4^+$, the central bond is less contracted (≈260 pm) than $H_5O_2^+$. These empirical data demonstrate that most of the time the complex must be considered to be only Zundel- or Eigen-ion-like with rapid variations between these two regimes (≈10^{-13} s). The structure of the solvated proton during vehicular mechanism is then best described as a distorted, non symmetric Eigen cation[98], with one H-bond considerably shorter than the others at any given instant, as illustrated in Figure 25. This process or changing and rearrangement of H-bond, known as "Eigen-Zundel-Eigen" (EZE) mechanism, or "special-pair dance", is the preparatory stage for proton transport with

rapid partner exchanges, randomizing the proton hop direction, until the final partner is found and a successful proton transfer occurs[99].

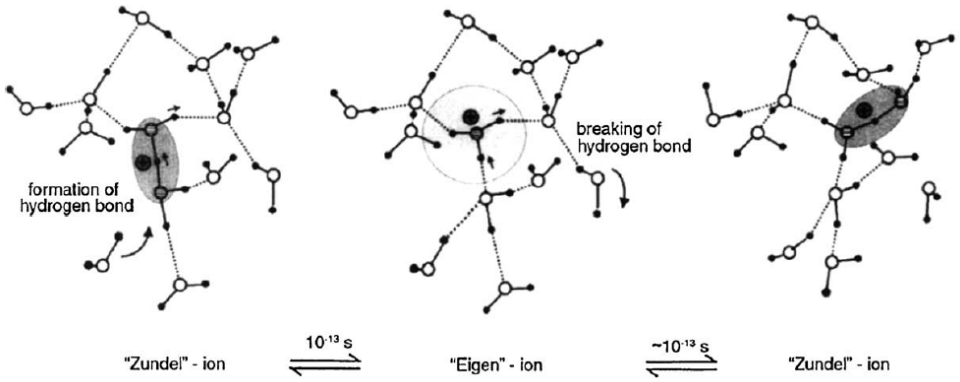

Figure 25. Transport mechanism of Protonic defect in water [71].

The reason for the low activation enthalpy of the overall process is due to the fact that the two reaction steps, i.e. molecular reorientation and proton displacement within hydrogen bonds, are strongly coupled within the surrounding aqueous environment. Due to the presence of additional hydrogen bonds in bulk water, the central bond of such complexes is weakened to some extent[100]: the binding power of a water molecule depends on the number of hydrogen bonds it is already involved in. This also leads to relaxation effects in the neighboring hydrogen bonds as a response to the formation and cleavage of hydrogen bonds: when a hydrogen bond is formed, the surrounding bonds are weakened, while the cleavage of a hydrogen bond leads to a strengthening of neighboring bonds[101]. As a consequence, the effective energy for breaking a hydrogen bond in bulk water is significantly lower than the average hydrogen bond energy.

Summing up, the transport of protons in PEMs is strongly dependent upon the structure and physicochemical nature of the polymer with the level of hydration: at low water contents, proton transfer, is limited primarily to the surface region; at high water contents, however, the properties of water in electrolyte polymer approach those of bulk water. In any case, the measured proton conductivity of PEM at given water content is the result of weighted average of the surface and bulk conductivities, depending upon the radial distribution of protons and water content in the polymer, and can vary by two or more orders of magnitude as the RH is increased from dry conditions to saturations. To conclude, we can assume that the transport of protons in PEM is carried out via (*i*) a

Grotthuss mechanism occurring close to the pore wall or under low water activity, *i.e.*, in a layer of around 1 nm from the pore wall[102], and (*ii*) a vehicular mechanism prevailing in the central region of the pore or under high water activity condition[94, 95, 103].

As already said, the researchers have focused to reach proton exchange membrane with high proton conductivity at high temperatures and at low relative humidity. One of the main approach to reach this target is via synthesis of nanocomposite membranes, obtained by the addition of a filler to the polymeric electrolyte. The mechanism of proton transport in these hybrid membranes is even more complex than pristine ones, since it involves both the surface and chemical properties of the inorganic and organic phases. A schematic representation of the proton transport in nanocompostie membranes has been shown in the Fig. 26. The incorporation of hydroscopic inorganic filler (e.g., silica) may result in an increase in membrane swelling at lower relative humidity, and offer resistance to fuel crossover playing a blocking-effect: the transport of protons through the membrane becomes easier and reduces the methanol permeability. On the other hand, a composites based on the polymer matrix and an alternative proton transporter, i.e., use of heteropolyacids, allow to immobilize a highly conducting acid in the polymer so that proton conduction is independent of hydration and the electro osmotic drag is reduced.

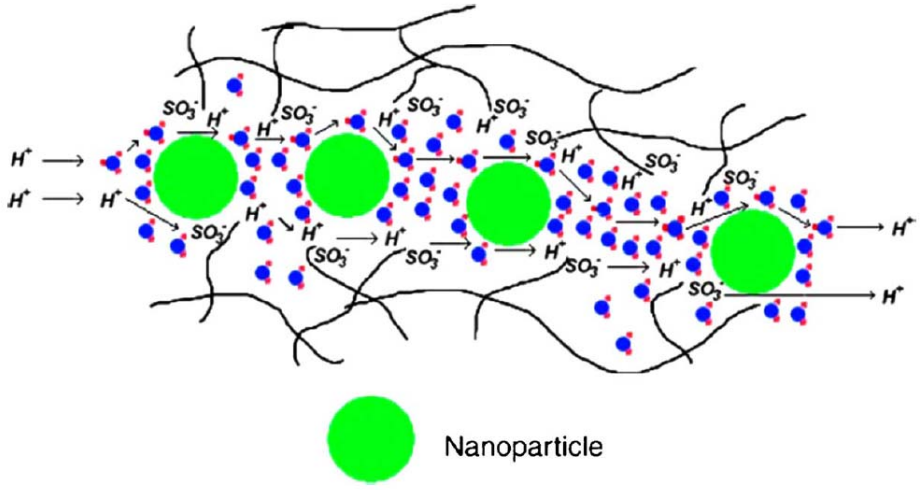

Figure 26. Proton transport in nanocomposite membranes[101].

1.2.3 Nanocomposite Electrolyte Membranes

In the recent years, increasing efforts have been devoted to the development of polymeric electrolyte able to ensure good proton conductivity and energy conversion efficiency at higher temperature respect to the typical operative temperature of PEM-FC.

As already mentioned, current technology foresees the use of perfluorosulfonic acid (PFSA) polymer membranes, limiting the application of this system in a temperature range between 50 and 90 °C. Such low temperature range is strictly related to most of the main issues and shortcomings of the PEM fuel cell described shortly here:

Water management. As already explained, due to the electro-osmotic drag, during operation of the PEM there is a dehydration of the membrane at the anode side and resulting in a dramatic decrease of the conductivity. At the same time, any change in the water content could lead to the deterioration of the membrane-catalyst interface as a consequence of the swelling and shrinkage of membranes. Accordingly, an effective and intensive humidification of both the fuel steam and the oxidant is needed. Additionally, due to the presence of the water, high water vapor pressure in the feed-gas stream is a necessity, which in turn requires a high total pressure, if operational temperature above 100 °C are required. From the above, careful management of the water balance is one of the key issues for the system design and operation.

CO Poisoning Effect. Another critical effect associated with a low operational temperature is the reduced tolerance to fuel impurities, e.g., CO in the hydrogen steam. If the concentration of CO is excessive (~10 ppm), it will strongly adsorb to the platinum (Pt) surface and poison the platinum electrocatalyst[104, 105] (Figure 27). As a consequence very pure hydrogen is needed for operation of PEMFCs. This poisoning effect has been shown to be very temperature-dependent: since adsorption of CO on Pt is associated with high negative entropy, its adsorption is favored at low temperatures and disfavored at high [81].

Direct Hydrogen. Beside hydrogen production and purification, another issue related to the direct hydrogen FC is the fuel storage. Novel complexes based on hydrides, such as $NaAlH_4$, show a good storage capacity[106, 107]. However, to desorb hydrogen from this complexes, the heat should be provided in a temperature range of

100-200 °C: due to the low operating temperature, such a high-capacity H_2 storage tank cannot be integrated into a PEMFC system.

Reformate and direct methanol as fuel. The use of methanol is an efficient and economical way to bring hydrogen into a fuel cell system. When used in an indirect way, i.e., via reforming, the reformate gas contains hydrogen, carbon dioxide, carbon monoxide, and residual water and methanol as well[108, 109]. Because of the above-mentioned CO poisoning effect, even with reformed methanol careful purification of the reformed hydrogen is necessary to remove the CO traces. However, the installation of an on-board fuel processing system results in increased cost, weigh and complexity as well as a reduced start up of the system. From the other side, direct use of methanol as fuel is a preferable option for propulsion of vehicles and other purposes. However, as already mentioned, the direct methanol fuel cell based on PFSA membrane is affected by two key issues[110, 111]. First, PFSA membranes have a large methanol crossover rate resulting in not only waste of fuel but also considerably lowered energy efficiency and cell performance due to the mixed electrode potential[112]. Secondly, the anodic catalyst is not sufficiently active, both because of the slow kinetics of the methanol oxidation that for the strong poisoning effect of the intermediate species (CO) from methanol oxidation. Both effects could be considerably improved by increasing the operational temperature of DMFC.

Thermal balance. Another complication with PEMFCs is the cooling of the system. In fact, a PEM operating at 80 – 90 °C produces a large amount of heat that has to be removed in order to maintain the working temperature: an advanced cooling system is needed.

Heat Recovery. The heat energy from a PEMFC stack at around 80 °C is of little value to recover, either for stationary or for mobile applications. An increasing of the operating temperature, for example 200 °C, could allow the production of water steam of up to 15 atm. This heat could be directly used for heating so that the overall efficiency will be improved for stationary purposes. It can also be used to operate the system at high pressures or to produce steam for fuel reforming.

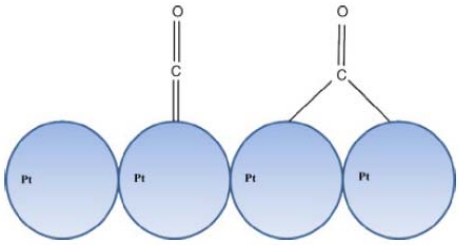

Figure 27. Adsorption of CO on Pt[73].

From what above, increasing interest have been focused to the development of high temperature proton conducting polymer electrolyte for fuel cell: most of the shortcomings associated to PEM fuel cell based on PFSA membranes can be solved or avoided by developing membranes operating at temperature above 100 °C. In particular, the US Department of Energy (DOE) has set as main objective the development of new membranes with suitable ion conductivity and stability under low humidification at temperature up to 120 °C[113]. Higher temperature operation includes the following:

(i) The kinetics for both electrode reactions will be enhanced. This is of special importance for the direct oxidation of methanol in DMFC;

(ii) Above the boiling point of water, operation of PEMFCs involves only the water vapor, resulting in a simplified system;

(iii) Due to the increased temperature gradient between the fuel cell stack and the coolant, the required cooling system will be simple and practically possible;

(iv) The heat can be recovered as, e.g., steam, which in turn can be used either for direct heating or steam reforming or for pressurized operation. In this way the overall system efficiency will be significantly increased;

(v) The operational temperature of a fuel cell around 200 °C would be close to temperatures for methanol reforming and for hydrogen desorption of the newly developed high capacity storage materials. This will allow for an integration of the fuel cell with a methanol reformer or a high-capacity hydrogen storage tank.The CO tolerance will be dramatically enhanced: from 10-20 ppm of CO at 80 °C, to 1000 ppm at 130 °C, and up to 30000 ppm at 200 °C[114].

In particular for the latter aspect, with such high CO tolerance a fuel cell could use hydrogen directly from a simple reformer, so that the hydrogen purification apparatus for the CO cleanup can be eliminated from the fuel processing system.

The main efforts to develop these higher temperature membranes include (i) the modification of the conventional host polymers, e.g., developing organic-inorganic composites, or (ii) by developing alternative new polymer systems[115, 116]. In particular, the homogeneous dispersion of organic/inorganic particles into the polymeric matrix seems to be the best strategy for the development of polymer electrolyte able to ensure a good proton conductivity in a dehydrating environment. Hydrophilic ceramic/inorganic fillers, such as SiO_2, TiO_2, ZrO_2, zeolites, etc. have been added to Nafion matrix to improve water retention in the composite membrane at higher temperatures and low humidity[117, 118]. These hydrophilic inorganic materials, when incorporated with Nafion, increase the binding energy of water as well as the number and strength of acid sites: the filler particles have affinity to absorb and retain water in the Nafion matrix. This can be attributed to the hydrophilic nature of the acidic inorganic additives within the pores of Nafion-membrane and the increased acidity and surface areas of nanoparticles. In other words, the water interacting with the surface of the filler is more likely to be retained than loosely bonded water in unmodified-Nafion, and it is still mobile enough to allow fast proton transport. Finally, but not least, the inclusion of inorganic fillers improves the mechanical properties of the nanocomposite. The mechanical reinforcement of the membrane, and hence the reduction of the swelling properties play an important role, especially in the temperature range 90-110°C, where high humidification conditions can be still obtained at acceptable pressures of the cell. Moreover the properties of the final composite membranes not only depend on the ionomer and the solid used but also on the composite's procedure of synthesis and on the amount, homogeneous dispersion, size, and orientation of the solid particles dispersed in the polymeric matrix. In the literature, membranes with inorganic fillers have been fabricated by a variety of techniques. One method includes impregnating inorganic oxide particles as fine powders into the Nafion ionomers and fabricating a composite membrane[119]. Another method includes addition of a precursor, generally as acidic metal alkoxides solution, into the Nafion ionomer for fabricating a composite membrane, and then converting the precursor material into the

desired proton conducting oxide[120]. Beside the aspects related to the improvement of proton conductivity in stringent environmental conditions, Nafion-composite membranes suitably modified with ceramic/inorganic fillers, as SiO_2, TiO_2, ZrO_2, zeolite etc[121-123] are particularly interesting due to their capacity to inhibiting the direct permeation of reaction gases or fuel by increasing the transport pathway tortuousness[124]. As shown in Fig. 28, the components are chosen so that protons are transported through both the dispersed phase and the polymer matrix. However, if the dispersed material is impermeable to methanol, protons will have a more direct and shorter path compared to methanol[125]. Composite membranes based on hygroscopic inorganic fillers could enhance the proton selectivity, while reducing methanol crossover.

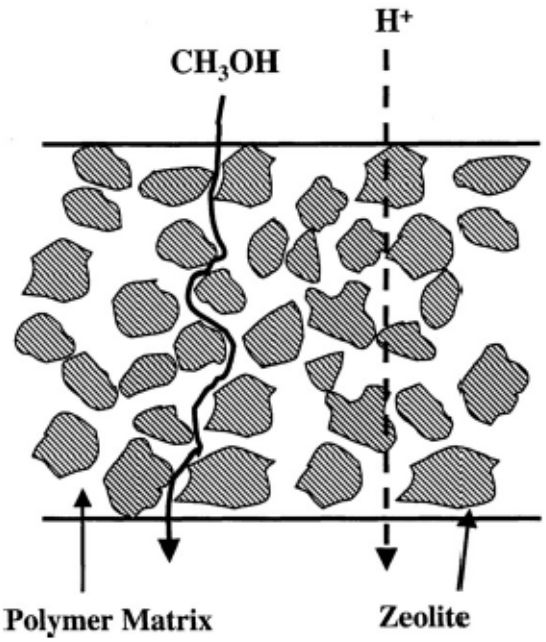

Figure 28. H^+ and methanol ions passing way in the polymer matrix of the filled membranes with zeolite[125].

As already said, the Direct Methanol fuel cell (DMFC) technology is still far from satisfactory because of the large fuel crossover that involves PFSA polymeric membranes: membrane with low methanol crossover must be developed to fully develop this technology. To this purpose, researchers have shown increasing interest in two dimensional (2D) layered material, such as Clays[126, 127], Graphite Oxide[128] and Layered Double Hydroxide (LDHs)[129]. Beside the attractive hydrophilic properties and

good thermal stability at high temperature this class of filler can be further modified in order to best suit these materials to fuel cell application. For example, through the organic modification from one side can be improved the compatibility with the polymer, i.e., to have a good interface bonding between polymer and organic/inorganic filler surface and at the same time it can aid the proton conductivity of the whole composite membrane system. Additionally, the introduction of this layered material into a polymer electrolyte might provides a remedy to methanol crossover. In fact, the complete exfoliation of such 2D-layered materials and their organization into an ordered structure (alignment) inside the polymeric matrix should from one side create an additional pathway for proton conduction and from the other side should play a blocking effect to methanol diffusion. In Figure 29 is schematically shown the effect of all the above properties to the performance of the nanocomposite membrane, in this images is shown the increase of the tortuous path encountered by a given diffusing species with increasing degree of exfoliation and/or lamellar particles[130].

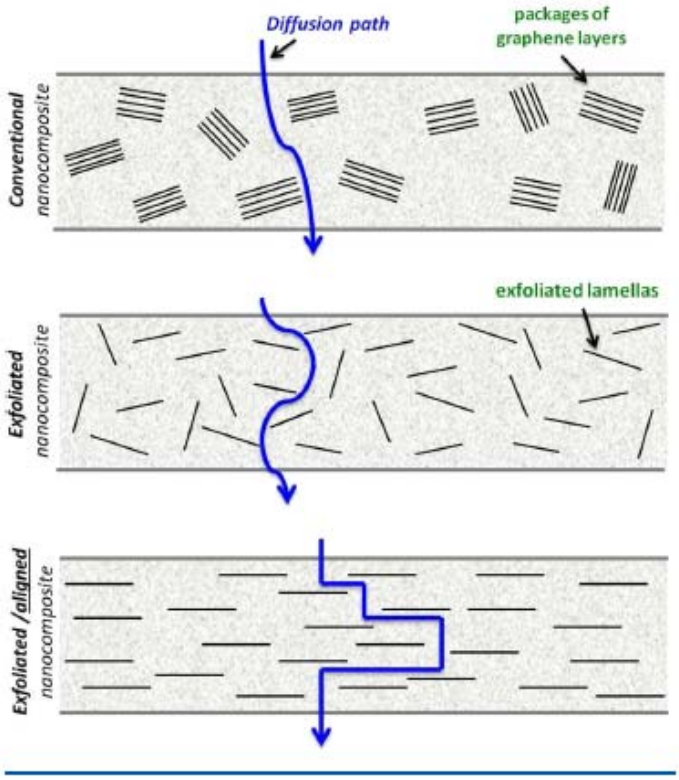

Figure 29. Representation of the Diffusion Pathway of Methanol Molecules through a Conventional, Exfoliated and Exfoliated/Aligned Nanocomposite Membrane, Respectively[130].

During my PhD two family of materials have been tested as nanoadditives for the preparation of Nafion-based electrolyte: 2D layered fillers, such as Grapgene oxide (GO), Smectite Clays and Layeder Double Hydroxide (LDH), and hybrid organic/inorganic material, i.e. Clay-CNTs and acid modified TiO_2. Properties and the main aspects related to the application of these material into fuel cells technologies are extensively discussed in the next section.

1.3 REVERSE ELECTRODIALYSIS: FROM SALINITY GRADIENT TO SUSTAINABLE ENERGY.

As mentioned in the previous chapter, the huge risk of climate change and pollution associated with the use of fossil fuels, global warming, increasing fuel prices and depletion of fossil fuel stocks forces the developments in the direction of alternative energy sources. The development of renewable and sustainable energy conversion technology is widely recognized as an important strategy for global energy security, resulting most probably one of the main topic of the scientific world over the XXI century. Among the different so-called "green energy" sources, the ocean represents a renewable and clean energy resource, but still largely untapped: oceans and surface waters, only partially contribute to these types of energy such as thermal, waves and tidal power. However, another route to gain energy from the sea, though less known, is the exploitation of the **salinity gradient power** (SGP), which is the energy available from mixing of two aqueous solutions of different salinities, such as seawater and river water. In other word, the chemical potential ensuing from mixing sea and river water can be converted into electrical energy. Salinity gradient energy has been estimated to be the second largest marine-based energy source. The amount of available energy due to the salinity gradient of seawater mixed with river water is equivalent to the energy obtained from a waterfall that is ~270 m high[131-133], with a total estimated global potential for power production of about 2.4-2.6 TW, which exceeds the global electricity demand for 2011 (2.3 TW)[134, 135]. Salinity gradient energy, also called "blue energy", has become recognized as a nonpolluting (no emissions of CO_2, SO_2, or NO_x) and sustainable energy source, and its viability is further assured by the abundance of river and seawater: salinity gradient power can be utilized worldwide in places where salt solutions of different salinity mix, for instance, where river water flows into the sea, or where industrial brine is discharged.

This paragraph deals with the main aspects related to salinity gradient energy technology.

1.3.1 Salinity Gradient Power (SGP).

The concept of SGP is already known for a long time and e.g. described in 1953[132]. In his study[132] Pattle indicates "When a volume V of a pure solvent mixes irreversibly with a much larger volume of a solution the osmotic pressure of which is *P*, the free energy lost is equal to *PV*. The osmotic pressure of seawater is about 20 atmospheres, so that when a river mixes with the sea, free energy equal to that obtainable from a waterfall 200 m high is lost." Unfortunately, until now utilization has been considered to be neither economically feasible nor technically attractive when compared to fossil fuel systems. In fact, these membrane-based conversion techniques has found in the high price of membranes their main drawback. However, the increasing prices of fossil fuels as well as the decreasing prices of membranes for desalination and water reuse applications make salinity-gradient power attractive in near future. The salinity gradient power is based on the difference between the chemical potential of concentrated and dilute solutions of salt. This difference is also referred to be caused by the difference in "osmotic pressure" between both salt solutions: solution with a high salt concentration has a high osmotic pressure and therefore contains a considerable amount of energy.

The theoretically available amount of energy obtainable from the controlled mixing of a relatively concentrated salt solution (e.g. sea water) and a diluted salt solution (e.g. river water) can be calculated from the Gibbs free energy, where the total amount of energy available from mixing 1 m^3 of a concentrated and 1 m^3 of diluted salt solution can be determined from the Gibbs energy of the system after mixing, subtracted by the Gibbs energy before mixing Fig. 30, Eq 12[136, 137]:

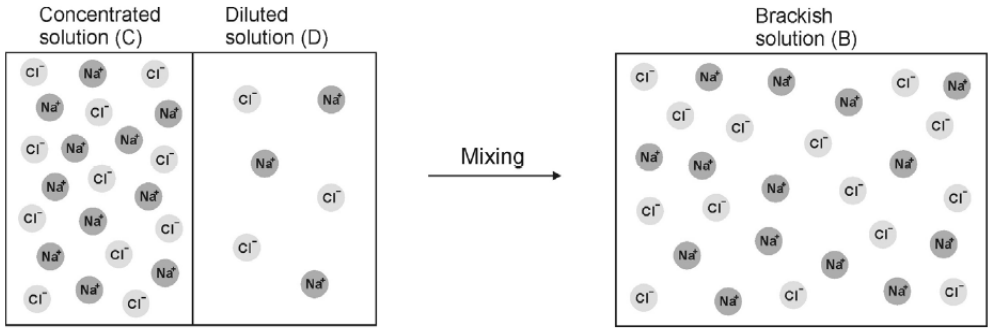

Figure 30. The mixing of a concentrated and a diluted solution giving a brackish solution.

$$\Delta G_{mix} = G_b - (G_c - G_d) \quad \text{(Eq. 12)}$$

where ΔG_{mix} is the free energy of mixing ($J \cdot mol^{-1}$), ΔG_b is the Gibbs energy of the mixture, the brackish water ($J \cdot mol^{-1}$), G_c is the Gibbs energy of the concentrated salt solution (e.g. seawater) ($J \cdot mol^{-1}$) and G_d is the Gibbs energy of the diluted salt solution (e.g. river water) ($J \cdot mol^{-1}$).

The Gibbs energy of an ideal solution is the sum of chemical potentials of the individual chemical components present in that solution:

$$G = \Sigma \mu_i \cdot n_i \quad \text{(Eq. 13)}$$

In this equation, G is the Gibbs energy of the system ($J \cdot mol^{-1}$), μ_i is the chemical potential of component i in the solution ($J \cdot mol^{-1}$), and n_i is the number of moles of component i in the solution. The chemical potential of the component i (μ_i) in an ideal solution can be simplified when no pressure change or charge transport is considered upon mixing of a concentrated and a diluted salt solution:

$$\mu_i = \mu_i^0 + RTlnx_i \quad \text{(Eq. 14)}$$

where μ_i^0 is the molar free energy under standard conditions ($J \cdot mol^{-1}$), R is the universal gas constant ($8.314\ J \cdot (mol \cdot K)^{-1}$), T is the absolute temperature (K), x_i is the mol fraction of component i. When Eq. (14) is substituted in Eq. (14) and n is replaced by solution concentration c ($mol \cdot m^{-3}$) and volume V (m^3), the final Gibbs free energy of mixing can be described as follows:

$$\Delta G_{mix} = \Sigma[c_{i.c}V_cRTln(x_{i,c}) + c_{i.d}V_dRTln(x_{i,d}) - c_{i.b}V_bRTln(x_{i,b})] \quad \text{(Eq. 15)}$$

Because the mixing of two solutions is a spontaneous process, the Gibbs energy of mixing is negative: energy is released when two solutions are mixed. With Equation (15) the theoretical available amount of energy from the mixing of two solutions can be calculated, and thus the theoretical amount of energy from salinity gradients can be determined. The work or energy theoretically obtainable from the mixing of 1 m^3 of sea water (0.5 M NaCl) with 1 m^3 of river water (0.01 M NaCl) at a temperature of 293 K as calculated from Equation 15 is 1.4 MJ, but if we assume that this cubic meter of river water is mixed with an "infinite" amount of cubic meters of sea water, 2.3 MJ can be extracted[138, 139]. However, in practice, the chemistry of seawater and river water is much more complex since it does not consist of only pure sodium chloride. In addition, factors such as mass transfer limitations, pressure drop, and other restrictions such as resources availability, limit the energy really recovered to a part of this theoretical energy, but it is still a huge renewable energy source. Several methods do exist for the extraction of salinity gradient energy. Two of the most widely studied of these techniques are based on selective membranes: **pressure retarded osmosis** (PRO) **and reverse electrodialysis** (RED). A selective membrane, also called semi-permeable membrane, is a media through which the crossing is limited to one of the components, either the solvent, i.e. water, or solutes, i.e. dissolved salts. In a pressure-retarded osmosis system for example, the two solutions of different salinity are brought into contact by a membrane (Fig. 31) that allows only the solvent molecules (i.e. water) to permeate and retains the solute (i.e. dissolved salts). The chemical potential difference between the solutions causes water transport from the diluted salt solution to the more concentrated salt solution. This generally lead to an increased total volume of more concentrated solution, however, if hydrostatic pressure is applied to the concentrated solution, the water transport will be partly retarded. The transport of water from the low-pressure diluted solution to the high-pressure concentrated solution results in a pressurization of the volume of transported water. This pressurized volume of transported water can be used to generate electrical power in a turbine.

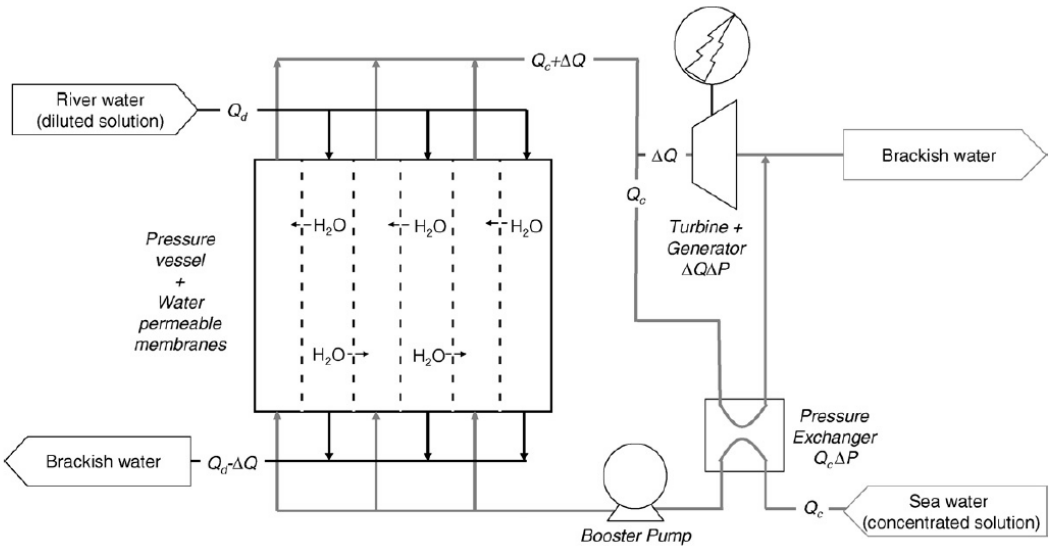

Figure 31. Conceptual representation of an energy conversion scheme using pressure-retarded osmosis; Q is the volumetric solution flow (m^3/s), ΔQ the transported amount of water in time through the membranes (m^3/s), ΔP the applied hydrostatic pressure difference between both solutions (Pa), whereas the power generated by means of a turbine and generator is $\Delta Q \, \Delta P$ (W).

The reverse electrodialysis systems instead, a technology that will be further deepened in the following paragraphs, are based on ion selective membranes that allow selective transport of ions in the solution only: water cannot cross the membrane. Each of these technologies is used in different salinity conditions. In fact, it has been proved that the maximum power density of pressure-retarded osmosis is more sensitive to the concentration of the concentrated solution and less sensitive to the concentration of the diluted solution when compared to reverse electrodialysis which is more sensitive to the concentration of the diluted solution (i.e. more horizontal oriented isohypses). Thus, current reverse electrodialysis seems to have a higher maximum power density than pressure-retarded osmosis for applications on seawater and river water, while pressure retarded osmosis is more suitable for application on brines.

1.3.2 Reverse electrodialysis process (RED).

With the initial aim of demineralizing sugar syrup, Maigrot and Sabates, in 1890, first demonstrated the principle of ED[140]. However, only in 1954, Pattle[132] first developed the principle of RED. He proved that RED could be used as technology to extract electricity from salinity gradients. Pattle's approach was further developed in the late 1970's by Weinstein et al.[141] and later by Lacey[142]. Both converged on the idea that semi-permeable membranes with low electrical resistance and high selectivity are necessary to maximize the net output voltage from RED cells for a large-scale energy conversion. Today the RED system has been developed such that it may be combined with hybrid system such as with the seawater desalination systems[143], the pressure retarded osmosis[144] and the microbial power cell[145].

In a reverse electrodialysis system, a number of **cation exchange membranes** (CEM) and **anion exchange membranes** (AEM) are stacked in an alternating pattern between a cathode and an anode (Fig. 32). The stack is similar to that of conventional electrodialysis[146-148], however, in this case the compartments between the membranes are alternately filled with a concentrated salt solution and a diluted salt solution. The ion exchange membranes inside the stack are separated by spacers consisting of a non-conductive fabric. The spacer net prevents the membranes from touching each other and direct the flow. At the same time however, they reduce the active membrane area available for ionic transfer because of the non-conducting character of the spacers, which is undesired. Within the stack, the difference in chemical potential between both solutions acts as driving force for a ionic migration through the membranes from the concentrated solution to the diluted solution. For a sodium chloride solution, chloride ions (Cl^-) migrate through the AEM towards the anode, and sodium ions (Na^+) permeate through the CEM in the direction of the cathode. The salinity gradient results in a potential difference (e.g. 80 mV for seawater and river water) over each membrane, the so-called membrane potential. The electric potential difference between the outer compartments of the membrane stack is the sum of the potential differences over each membrane.

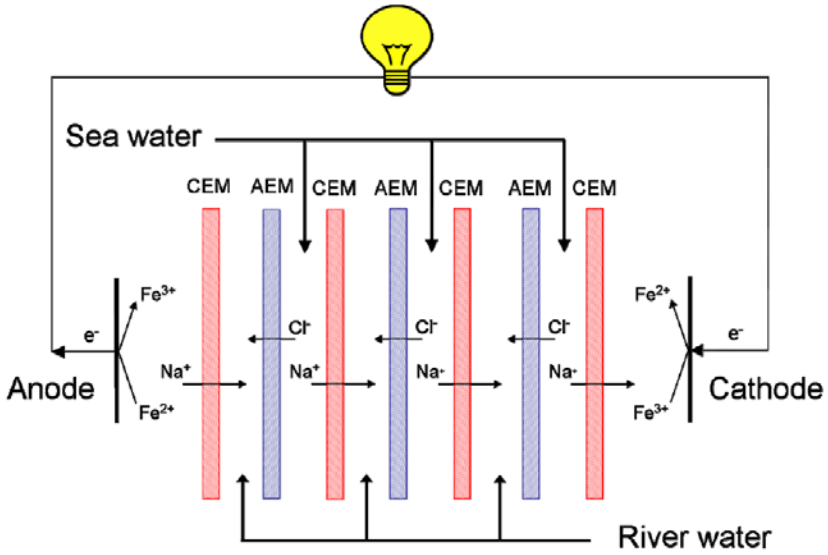

Figure 32. Principle of Reverse Electrodialisys (RED); in this representation AEM i san anion Exchange membrane, CEM a cation Exchange membrane.

To maintain electroneutrality, at the electrodes redox reactions occur to convert this electrochemical potential directly into electricity. As a redox pair, often a homogeneous $K_4Fe(CN)_6/K_3Fe(CN)_6$ redox system can be chosen, because it does not cause net chemical reactions and therefore the power losses are low. The iron(III) complex is reduced at the cathode surface and the iron(II) complex is reoxidized at the anode surface:

$$Fe(CN)_6^{3-} + e^- \rightleftharpoons Fe(CN)_6^{4-} \qquad \text{(Eq. 17)}$$

As results, electrons migrate from anode to cathode through an external electrical circuit. This electrical current and the potential difference over the electrodes can be used to generate electrical power, when an external load or energy consumer is connected to the circuit.

The theoretical value of the potential over an ion exchange membrane for an aqueous monovalent ion solution (e.g. NaCl) can be calculated using the Nernst equation[136, 142]:

$$\Delta V^0 = N \frac{2\alpha RT}{zF} ln\left(\frac{a_c}{a_d}\right) \qquad \text{(Eq. 18)}$$

where ΔV^0 is the theoretical stack potential (V), α is the average membrane permselectivity of an anion and a cation exchange membrane pair (-), N is the number

of membrane cells (-), R is the gas constant (8.314 J mol^{-1} K^{-1}), T is the absolute temperature (K), z is the electrochemical valence, F is the Faraday constant (96485 C mol^{-1}), a_c is the activity of the concentrated salt solution (mol l^{-1}) and a_d is the activity of the diluted salt solution (mol l^{-1}). The power produced is related to the electrochemical potential drop across the membrane, ΔV^0, and an external load resistance resulting in:

$$W = I^2 R_{load} = \frac{(V^0)^2 R_{load}}{(R_{stack}+R_{load})^2} \quad \text{(Eq. 19)}$$

In this equation, I is the current (A), R_{load} is the resistance of the load (Ω), R_{stack} is the stack resistance (Ω) and V^0 is the open stack circuit potential (V). The stack resistance is the sum of the resistances of the anion and cation exchange membranes, the feed water compartments (i.e. seawater and river water compartments), the electrodes and their compartments:

$$Rstack = \frac{N}{A} \cdot \left(R_{aem} + R_{cem} + \frac{d_c}{\kappa_c} + \frac{d_d}{\kappa_d}\right) + R_{el} \quad \text{(Eq. 20)}$$

where A is effective membrane area (m^2), R_{aem} is the anion exchange membrane resistance (Ω·m^2), R_{cem} is the cation exchange membrane resistance (Ω·m^2), d_c is the thickness of the concentrated saltwater compartment (m), d_d is the thickness of the diluted saltwater compartment (m), κ_c is the conductivity in the concentrated saltwater compartment (S · m^{-1}), κ_d is the conductivity in the diluted saltwater compartment (S · m^{-1}) and R_{el} is the ohmic resistance of both electrodes and their compartments (Ω). The maximum power output of the system is obtained when R_{load} is equal to the resistance of the stack (R_{stack})[141, 142]. Thus, the maximum power output can be simplified into:

$$W_{max} = \frac{(V^0)^2}{4R_{stack}} \quad \text{(Eq. 21)}$$

Consequently, the power density (power output per unit membrane area, W_{gross}) can be calculated from W_{max}:

$$W_{gross} = \frac{W_{max}}{2 \cdot A \cdot N} \quad \text{(Eq. 22)}$$

where W_{gross} is the maximum gross power density ($W \cdot m^{-2}$), W_{max} is maximum power output (W), A is effective area of a single membrane (m^2) and N is number of membrane cells.

As is possible to see from Eq. 18, the membrane permselectivity is one the main dominating membrane related factors in the maximum power density in a RED stack; it directly affects the membrane potential, since it is an explicit factor in Eq. 16. Other two important factors are the membrane resistance and the resistance of the river water compartments (which affect mainly the stack resistance, Equation (20)[141, 142, 149]. Consequently, it can be easily understood as the ion exchange membrane properties play a significant role in determining the RED performance.

1.3.3 Ion Exchange Membranes for RED.

In general, a membrane is defined as a permselective barrier between two phases. This means that, under the influence of a driving force, a membrane allows the selective transport of certain species from a feed mixture, while others are rejected. In the case of RED, the core of the stack is based on ion exchange membranes (IEMs), scilicet membranes with fixed anionic or cationic exchange groups that are able to transport cations or anions. All the specific properties of ion exchange membranes are related to the presence of these charged groups. Based on the type of fixed charge group, ion exchange membranes can be divided into two types: Cation Exchange Membranes (CEM) and Anion Exchange Membranes (AEM), whose basic structures has been showed in Fig 33. The polymer matrix of CEMs bears negatively charged groups, e.g. sulfonic acid ($–SO_3^{2–}$) or carboxylic acid groups ($–COO^–$), in the membrane structure; while positive charged groups, e.g. ammonium groups ($–NR_3^+$, $–NH_4^+$, $–NH_2$, =NH, ≡N), are attached to the polymer matrix of AEM. Amount, type and distribution of ion exchange groups determine the most important membrane properties. Ions with the same charge as the fixed charged groups in the membranes are called co-ions, while ions with a charge opposite to the fixed charges of the membranes are denoted as counter ions. Theoretically, co-ions are excluded and cannot pass through the membrane, while the counter ions can pass freely through the membrane, due to the effect known as Donnan exclusion[149]. Taking as example a cation exchange

membrane, when it is in contact with a diluted electrolyte solution, the concentration of the cation (counter ion) in the membrane will be much higher than the cation concentration in the solution, due to the presence of the fixed charges in the cation exchange membrane. On the other hand, the concentration of anions (co-ions) in the membrane will be much lower than in the solution. These concentration differences lead to the migration of ions from one side to another, in order to maintain electro neutrality in the membrane and the bulk solution. This thus creates an electric field in the direction opposite to the direction of the diffusional flow.

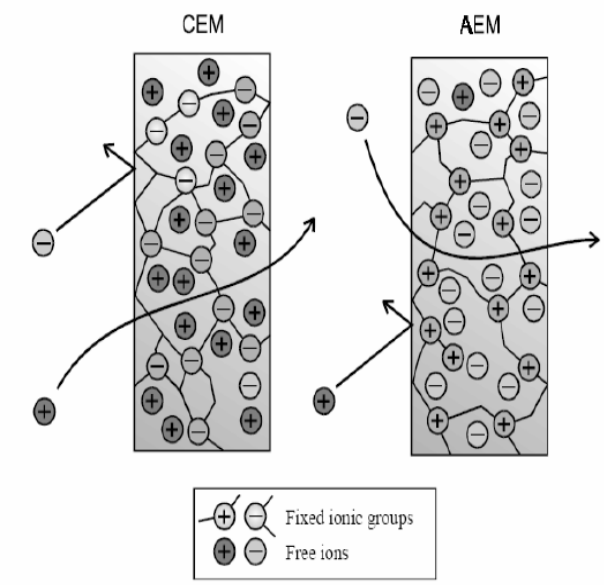

Figure 33. Schematic rapresentation of cation (left) and anion (right) exchange membranes.

As already stated, RED performances strongly depend on IEMs electrochemical properties. Among these, the ion exchange capacity (IEC) is widely recognized as a crucial parameter which affects almost all other membrane properties. The IEC is the number of fixed charges inside the ion exchange membrane per unit weight of dry polymer. The IEC, expressed in milli equivalent of fixed groups per gram of dry membrane (mequiv./g membrane), is usually determined experimentally according to the titration method using a strong acid or base of HCl for CEMs and NaOH for AEMs, respectively. Another important electrochemical property of ion exchange membranes, directly related to IEC, is the fixed charge density, expressed in milli equivalent of fixed groups per volume of water in the membrane (mequiv./l). This parameter strongly depends on the IEC and the swelling degree of the membrane: in the swollen state, the

distance between the ion exchange groups increases thus reducing the fixed charge density. Finally, the permselectivity of a membrane describes its ability to prevent co-ions from passing through the membrane. Theoretically, a perfect IEM would have a permselectivity of one when the complete exclusion of the co-ions from the membrane is achieved; however, according to Donnan′s theory, a certain amount of co-ions could contribute to the transport current[150]. Thus, the permselectivity would decrease below the ideal value of 1 as the solution concentration increases[151]. However, for RED systems, it is not necessary to achieve both high permselectivity and low ionic resistance because an RED system can tolerate moderate permselectivity. After all, the main goal is to produce electricity and not to separate solutions[152]. Commercial membranes currently employed for RED were designed specifically for other applications, such as electrodialysis, diffusion dialysis, and electrodeionization. These other applications normally require different physical and electrochemical characteristics of membranes; hence, most currently available commercial membranes cannot meet RED membranes′ required conditions. Although some commercial membranes contain a few desired properties needed for RED (e.g., high permselectivity), their high prices are still a significant hindrance in the smooth transition to commercialization of RED power generation. Cost reduction is possible as global demand increases. However there are some requirements that ion exchange membranes in a RED system must fulfill[147, 153]:

- ✓ high permselectivity, i.e. ion exchange membrane should have a permselectivity of more than 95%;
- ✓ low electrical resistance, i.e. ion exchange membranes should have an area resistance of maximum 3 $\Omega \cdot cm^2$;
- ✓ a good mechanical and form stability, i.e. the membranes should be mechanically strong enough to construct a RED stack, as thin as possible to have low area resistance, have a low degree of swelling or shrinking in transition from dilute to concentrated ionic solutions;
- ✓ a reasonable chemical stability, i.e. no special requirements for chemical stability due to mild membrane environment e.g. seawater and river water. Lifetime should be at least 5 years:
- ✓ low cost, i.e. the membranes should be as cheap as 2 €/m^2.

References

[1] Momirlan M, Veziroglu TN. *International Journal of Hydrogen Energy* **2005**, 30, 795.

[2] Schlapbach L, Zuttel A. *Nature* **2001**, 414, 353.

[3] Schlapbach L. *Nature* **2009**, 460, 809.

[4] Peighambardoust SJ, Rowshanzamir S, Amjadi M. *International Journal of Hydrogen Energy* **2010**, 35, 9349.

[5] Boudghene Stambouli, Traversa E. *Renewable and Sustainable Energy* **2002**, Reviews 6, 295.

[6] Kirubakaran, Jain S, Nema R. K. *Renewable and Sustainable Energy* **2009**, Reviews 13, 2430.

[7] Babir F, Gomez T. *Int. J. Hyd. Energy* **1996**, 21, 891.

[8] Brian, C. *IEEE Proc* **2002**, 205.

[9] Alberti G, Casciola M. *Annual Review of Materials Research* **2003**, 33, 129.

[10] Andújar J M, Segura F. *Renewable and Sustainable Energy* **2009**, Reviews 13, 2309.

[11] Huang X, Zhang Z, Jiang J. *IEEE Symposium on Industrial Electron* **2006,** 8, 1613.

[12] Farooque M, Maru HC. *IEEE Proc* **2001**, 89, 1819–29.

[13] U.S. Dept. of Energy. *Fuel cell hand book*, 7th ed., West Virginia: Office of Fossil Fuel, National Energy Technology Laboratory; October 2000.

[14] Swider-Lyons KE, Carlin RT, Rosenfeld RL, Nowak RJ. *Proceedings of the 2002 workshop on autonomous underwater vehicle* **2002**, 61–64.

[15] Yakabe H, Sakuri T, Sobue T, Yamashita S, Hase K. *IEEE Int. Conf. Ind. Inform.* **2006**, 369–374.

[16] Ellis MW, Von Spakovsky MR, Nelson DJ. *IEEE Proc* **2001**, 89, 1808–18.

[17] Garcia BL, Sethuraman VA, Weidner JW, White RE, Dougal R. *J Fuel Cell Sci Technol* **2004**, 43–8.

[18] Apanel G, Johnson E. *Fuel Cells Bulletin* **2004**, 12.

[19] Neburchilov V, Martin J, Wang H, Zhang J. *Journal of Power Sources* **2007**, 169, 221.

[20] Dillon R, Srinivasan S, Aricò AS, Antonucci V. *Journal of Power Sources* **2004,** 127, 112.

[21] Grot WG. *U.S. Patent* **1973**, 3, 770, 567.

[22] Guarau V, Barbir F, Liu H. *J. Electrochem. Soc.* **2000**, 147 (7), 2468.

[23] Ahmad MI, Zaidi SMJ, Rahman SU. *Desalination* **2006**, 193, 387-97.]

[24] Bouchet R, Miller S, Deulot M, Sonquet JL. *Solid State Ionics* **2001**, 145, 69-78.

[25] Sridhar P. Perumal R, Rajalakshmi N, Raja M, Dhatatreyan KS. *J. Power Sources* **2001**, 101, 72–78.

[26] Li Q, He R, Jensen JO, Bjerrum NJ. *Chemistry of Materials* **2003**, 15, 4896.

[27] Li Q, Jensen JO, Savinell RF, Bjerrum NJ. *Progress in Polymer Science* **2009,** 34, 449.

[28] Smitha, Sridhar S, Khan AA, *Journal of Membrane Science* **2005,** 259, 10.

[29] Steck AE, Stone C, in: Savadago O, Roberge PR. (Eds.), *Proceedings of the Second International Symposium on New Materials for Fuel Cell and Modern Battery Systems, Montreal*, July 6–10, **1997**, p. 792

[30] Ghielmi, Vaccarono P, Troglia C, Arcella V. *Journal of Power Sources* **2005,** 145, 108.

[31] Arcella V, Troglia C, Ghielmi A. *Industrial & Engineering Chemistry Research* **2005,** 44, 7646.

[32] Arico S, Baglio V, Di Blasi A, Antonucci V, Cirillo L, Ghielmi A, Arcella V. *Desalination* **2006,** 199, 271.

[33] Motupally S, Becker AJ, Weidner JW. *J. Electrochem. Soc.* **2000**, 147 (9) 3171–3177

[34] Kreuer KD. *Journal of Membrane Science* **2001,** 185, 29.

[35] Gierke TD, Hsu WY, in: A. Eisenberg, H.L. Yeager (Eds.), *Perfluorinated Ionomer Membranes, ACS Symposium Series No. 180, American Chemical Society*, Washington, DC, **1982**, p. 283.

[36] Gierke TD, Munn GE, Wilson FC. *J. Polym. Sci., Polym. Phys.* **1981**, 19, 1687.

[37] Hsu WY, Gierke TD. *Macromolecules* **1982**, 15, 101.

[38] Eikerling M, Kornyshev AA, Stimming U. *J. Phys. Chem. B* **1997,** 101, 10807.

[39] James PJ, McMaster TJ, Newton JM, Miles MJ. *Polymer* **2000**, 41, 4223–4231.

[40] Yeager HL, Steck A. *J. Electrochem. Soc.* **1981**, 128, 1880.

[41] Yeager HJ, Eisenberg A. in: *Perfluorinated Ionomer Membranes; eds. A. Eisenberg and H. L. Yeager, ACS Symp. Ser. No.180, American Chemical Society*, Washington, DC, **1982**, pp. 1-6, 41-63.

[42] Litt MH. *Polym. Prepr.* **1997**, 38, 80.

[43] Haubold HG, Vad T, Jungbluth H, Hiller P. *Electrochim. Acta* **2001**, 46, 1559.

[44] Gebel G. *Polymer* **2000**, 41, 5829.

[45] Schmidt-Rohr K, Chen Q. *Nature Materials* **2008**, 7, 75-83.

[46] Chu B, Wu C, Buck W. *Macromolecules* **1989**, 22, 831–837.

[47] Rosi-Schwartz B, Mitchell GR. *Polymer* **1996**, 37, 1857–1870 (1996).

[48] Choi P, Jalani NH, Datta R. *J. Electrochem. Soc*. **2005,** 152, E123–E130.

[49] Ise M, Kreuer KD, Maier. *J. Solid State Ion.* **1999**, 125, 213–223.

[50] Moore RB, Martin CR. *Macromolecules* **1988**, 21, 1334-1339.

[51] Moore RB, Martin CR. *Anal. Chem.* **1986**, 58, 2569.

[52] Gilpa X., Hogarth M., *Department of Trade and Industry (UK)* Homepage, 2001. Available on: http://www.dtigov. uk/renewable/pdf/f0200189.pdf. Last retrieved November 2, **2001**.

[53] Ion Power Homepage, Nafion® Material Safety Data Sheet (MSDS) Available on: http://ion-power.com/nafion/naf001.html. Last retrieved November 2, **2001**.

[54] Larminie J., Dicks A. *Fuel Cell Systems Explained*, Wiley, West Sussex, **2000.**

[55] Rikukawa M., Sanui K. *Prog. Polym. Sci.* **2000,** 25, 1463–1502.

[56] Sakari T., Takenaka H., Wakabayashi N., Kawami Y., Tori K. *J. Electrochem. Soc.* **1985,** 132, 1328.

[57] Watkins D.S., in: L.J.M.J. Blomen, M.N. Mugerwa (Eds.), *FuelCell Systems, Plenum Press*, New York, **1993**, p. 493.

[58] Smitha S., Sridhar, Khan A.A. *J. Membr. Sci.* **2003**, 225, 63–76.

[59] Rikukawa M, Sanui K. *Prog Polym Sci*, **2000**, 25, 1463-502.

[60] Intaraprasit N, Kongkachuichay P. *J Taiwan Inst Chem Eng* **2011**, 42, 190-5.

[61] Li X, Wang Z, Lu H, Zhao C, Na H, Zhao C. *J Membr Sci* **2005**, 254, 147-55.

[62] Jin X, Bishop MT, Ellis TS, Karasz FE. Br Polym J 1985;17:4e10.

[63] Wang F, Hickner M, Kim YS, Zawodzinski TA, McGrath JE. *J Membr Sci* **2002**, 197, 231-42.

[64] Bailly C, Williams DJ, Karasz FE, MacKnight WJ. *Polymers* **1987**, 28, 1009.

[65] Xuemei Wu, Xiaowen Wang, Gaohong He, Jay Benziger, *Journal of Polymer Science part B: polymer physics* **2011**, 49, 1437–1445.

[66] Ise M. *Ph.D. Thesis*, University of Stuttgart, **2000**.

[67] Li L, Zhang J, Wang Y. *J Membr Sci* **2003**, 226, 159-67.

[68] Eikerling M., Kharkats Y.I., Kornyshev A.A., Volfkovich Y.M., *J. Electrochem. Soc.* **1998,** 145, 2684.

[69] Sundmacher K., Scott K. *Chem. Eng. Sci.* **1999,** 54, 2927.

[70] Kreuer K.D., Dippel Th., Maier J.. *Proc. Electrochem. Soc.* **1995**, 95-23, 241.

[71] Li Q., He R., Jensen J. O., Bjerrum N. J. *Fuel Cells* **2004**, 4, 147–159.

[72] Li Q., Hjuler H. A, Bjerrum N. J. *J. Appl. Electrochem.* **2001**, 31, 773–779.

[73] Buckley, Stuez E. D., Serad G. A. in *Encyclopedia of Polymer Science and Engineering, ed. H. F. Mark, Wiley*, New York, **1988**, 11, 572–601.

[74] Wainright J.S., Wang J.-T., Weng D., Savinell R.F., Litt M., *J. Electrochem. Soc.* **1995**, 142, L121.

[75] Glipa X., Hadda M.E., Jones D.J., Roziére J. *Solid State Ionics* **1997**, 145, 61.

[76] Fontanella J.J., Wintersgill M.C., Wainright J.S., Savinell R.F., Litt M. *Electrochem. Acta* **1998**, 43, 1289.

[77] Xing B., Savadogo O., *J. New Mater. Electrochem. Sys.* **1999**, 2, 95.

[78] Kawahara M., Morita J., Rikukawa M., Sanui K., Ogata N., *Electrochem. Acta* **2000**, 45, 1395.

[79] Trouw N. S., Gillette N. J. *US Pat.* **1987**, 4, 693-825.

[80] Wainright J. S., Wang J. T., Weng D., Savinell R. F., Litt M. *J. Electrochem. Soc.* **1995**, 142, L121–L123.

[81] Asensio J. A., *PhD Thesis*, Institut Quìmic de Sarrià , UniversitatRamon Lull, **2003**.

[82] Wainright J. S., Litt M. H., Savinell R. F. *Handbook of Fuel Cell, Fundamentals, Technology, and Applications*, ed. W. Vielstich, A. Lamm and H. A. Gasteiger, John Wiley & Sons, **2003**, 3, 436.

[83] Xiao L., Zhang H., Scanlon E., Ramanathan L. S., Choe E.-W., Rogers D., Apple T., Benicewicz B. C. *Chem. Mater.*, **2005**, 17, 5328–5333

[84] Staiti P., Lufrano F., Aricò A. S., Passalacqua E., Antonucci V. *J. Membr. Sci.* **2001**, 188, 71–78.

[85] Hoel, Grunwald E. *J. Phys. Chem.* **1977**, 81, 2135.

[86] Schechter, Savinell R. F., Wainright J. S., Ray D. *J. Electrochem. Soc.*, **2009**, 156, B283–B290.

[87] Gottesfeld S., Pafford J. *J. Electrochem. Soc.* **1988**, 135, 2651.

[88] Mustarelli P., Quartarone E., Magistris A., in: *J. Garche, et al. (Eds.), Encyclopedia of Electrochemical Power Sources, Elsevier*, **2009**, ISBN: 0-444-52093-7.

[89] Wicke, Eigen M., Ackermann T. *Z. Phys. Chem. (Munich),* **1954,** 1, 340.

[90] Zundal, Metzger H. *Z. Phys. Chem. (Munich)* **1968**, 58, 225.

[91] Weber AZ, Breslau JBR, Miller IF. *Ind Eng Chem Fundam* **1971,** 10, 554-65.

[92] Kreuer KD, Paddison SJ, Spohr E, Schuster M. *Chem Rev* **2004**, 104, 4637-78.

[93] Eikerling M., Kornyshev A. A., Kuznetsov A. M., Ulstrup J., Walbran S. *J. Phys. Chem. B,* **2001**, 105, 3646.

[94] Paddison S. J., Paul R. *Phys. Chem. Chem. Phys.,* **2002**, 4, 1158.

[95] Mafe S., Manzanares J. A., Ramirez P. *Phys. Chem. Chem. Phys.,* **2003**, 5, 376.

[96] Grotthuss, C. J. T. d. Ann. Chim. (Paris) 1806, 58, 54–74

[97] Deluca NW, Elabd YA. *J Polym Sci Part B Polym Phys* **2006,** 44, 2201-13.

[98] Swanson JMJ, Simons J. *J. Phys. Chem. B* **2009**, 113, 5149.

[99] Chandra A, Tuckerman M.E, Marx D. *Phys. Rev. Lett.* **2007**, 99, 145901.

[100] Kreuer K.D., Chem. Mater. **1996**, 8, 610.

[101] Hogarth WHJ, Diniz da Costa JC, Lu GQ. *J Power Sources* **2005,** 142, 223–37.

[102] Spohr E., Commer P., Kornshev A. A. *J. Phys. Chem. B,* **2002**, 106, 10560.

[103] Ennari J., Elomaa M., Sundholm F. *Polymer,* **1999**, 40, 5035.

[104] Barbir, Gómez T. *International Journal of Hydrogen Energy* **1996,** 21, 891.

[105] Pettersson L. J. , Westerholm R, *International Journal of Hydrogen Energy* **2001**, 26, 243.

[106] Bogdanovic B, Schwickardi M. *J. Alloys Compd*. **1997**, *253-254*, 1.

[107] Jensen CM, Gross K. J. *Appl. Phys.* **2001**, *A72*, 213.

[108] Thomas CE. *Int. J. Hydrogen Energy* **1998**, *23*, 507.

[109] Peppley BA, Amphlett JC, Kearns LM, Mann RF. *Appl. Catal*. **1999**, *179*, 21 - 31.

[110] Hogarth MP, Hards GA. *Eur. Fuel Cell News* **1997**, *4*, 14.

[111] Wasmus S, Kuever A. *J. Electroanal. Chem*. **1999**, *461*, 14.

[112] Heinzel A, Barragan VM. *J. Power Sources* **1999**, *84*, 70.

[113] Marcinkoski J., Kopasz J. P., Benjamin T. G. *International Journal of Hydrogen Energy* **2008,** 33, 3894.

[114] Li Q, He R, Gao J, Jensen J. O, Bjerrum N. J. *J. Electrochem. Soc.* **2003**, 150, A1599.

[115] Malhotra S, Datta R. J Electrochem Soc **1997**, 144(2), L23-6.

[116] Ramani V, Kunz HR, Fenton JM. *J Membr Sci* **2004**, 232(1-2), 31-44.

[117] Miyake N, Wainright J S, Savinell R F. *J. Electrochem. Soc.* **2001**, 148, A898.

[118] Panero S, Fiorenza P, Navarra M A, Romanowska J and Scrosati B *J. Electrochem. Soc.* **2005**, 152, 2400.

[119] Baglio V, Aricò AS, Blasi AD, Antonucci V, Antonucci PL, Licoccia S, Traversa E, Fiory F S. *Electrochim. Acta* **2005**, 50, 1241.

[120] Aparicio M, Castro Y, Duran A. *Solid State Ionics* **2005**, 176, 33.

[121] Watanabe M, Uchida H, Seki Y, Emori M. *J. Phys. Chem.* **1998**, B102 3129.

[122] Adjemian KT, Lee SJ, Srinivasan S, Benziger J, Bocarsly AB. *J. Electrochem. Soc.* **2002**, 149, A256.

[123] Sacca A et al. *J. Power Sources* **2005**, 142, 385.

[124] Mex L, Sussiek M, Muller J. *Chem Eng Commun* **2003**,190,1085-95.

[125] Libby B, Smyrl WH, Cussler EL. *AIChE J* **2003**, 49 (4), 991-1001.

[126] Nicotera I, Enotiadis A., Angjeli K., Coppola L, Gournis D. *International Journal of Hydrogen Energy* **2012,** 37, 6236-6245.

[127] Nicotera I, Enotiadis A., Angjeli K., Coppola L., Ranieri G., Gournis D. *Journal of Physical Chemistry B* **2011**, 115(29), 9087-9097.

[128] Enotiadis A, Angjeli K., Baldino N., Nicotera I., Gournis D. *Small* **2012**, 8, 3338-3349.

[129] Angjeli K., Nicotera I., Baikousi M., Enotiadis A., Gournis D., Saccà A., Passalacqua E., Carbone A. *Energy Conversion and Management* **2015**, 96, 39–46.

[130] Nicotera, I., Simari, C., Coppola, L., Zygouri, P., Gournis, D., Brutti, S., Minuto, F.D., Aricò, A.S., Sebastian, D., Baglio, V. *Journal of Physical Chemistry C*, **2014**, *118* (42), 24357-24368.

[131] Logan B. E., Elimelech M., *Nature* **2012**, 488, 313–319.

[132] Pattle R., *Nature* **1954**, 174, 660.

[133] Ramon G. Z., Feinberg B. J., Hoek E. M. V. *EnergyEnviron.Sci.* **2011**, 4, 4423.

[134] Turek M., Bandura B. *Desalination* **2007**, 205, 67.

[135] Koter S. *Journal of Membrane Science* **1995**, 108, 177.

[136] Jagur-Grodzinski R. K. J. *Ind. Eng. Chem. Process Des. Dev.* **1986**, 443-449.

[137] Tongwen X., Weihua Y. *Journal of Membrane Science* **2001**, 190, 159.

[138] Post J.W., Hamelers H.V.M., Buisman C.J.N. *Environmental Science and Technology* **2008**, 42, 5785-5790.

[139] *EIA, International Energy Outlook 2010*, in, Washington DC, **2010.**

[140] Shaposhnik V., Kesore K. *J. Membr. Sci.* **1997**, 136, 35–39.

[141] Weinstein J.N., Leitz F.B. *Science* **1976**, 191, 557.

[142] Lacey R. E. *Ocean Eng*. **1980**, 7, 1–47.

[143] Brauns E. *Desalination*, **2008**, 219, 312-323

[144] Achilli, Cath T.Y., Childress A.E. *Journal of Membrane Science*, **2009**, 343, 42-52.

[145] Cusick R.D., Kim Y., Logan B.E. *Science*, **2012**, 335, 1474-1477.

[146] Mulder M. *Kluwer Academic Publishers*, Dordrecht, **1996**.

[147] Strathmann H. Elsevier, 1 ed., **2004**.

[148] Strathmann H., Giorno L., Drioli E., *CNR Servizio Pubblicazioni*, **2006.**

[149] Strathmann H. *Membrane Science and Technology Ion-Exchange Membrane Separation Processes*, 9, 1st Edition, Elsevier, **2004.**

[150] Strathmann H., Grabowski A., Eigenberger G., *Ind. Eng. Chem. Res.* **2013**, 52, 10364–10379.

[151] Sata T., *The Royal Society of Chemistry*, Cambridge, **2004**.

[152] Dlugolecki P., Nymeijer K., Metz S., Wessling M. *J. Membr. Sci.* **2008**, 319, 214–222.

[153] Post J.W. Wageningen University, Wageningen, **2009.**

SECTION II

MATERIALS:

FILLER NANOSTRUCTURED AND NANOCOMPOSITES

The first part of this section is devoted to a broad overview about the nanostructured material investigated as additives in polymer matrix. Specificcaly, 2D-layered materials [Graphite Oxide (GO), Smectite Clays and Layered Double Hydroxides (LDHs)] and hybrid organic-inorganic material [Clay-CNTs and sulfonated TiO_2].

In the second part of the section, a brief panning about the aspects related to the preparation of nanocomposite membranes and a description of the procedures followed during this research are also reported.

2.1 NANOFILLERS

2.1.1 Graphene and Graphite Oxide

If the 20th century was the age of plastics, the 21st century seems set to become the age of **graphene**, a recently discovered material made from a one-atom-thick planar sheet comprising an sp2-bonded **carbon** honeycomb structure that has emerged as a rapidly rising star in the field of material science[1, 2]. Ever since its discovery in 2004[3], graphene has been making a profound impact in many areas of science and technology due to its remarkable physicochemical properties, as for example the exceptionally high crystal and electronic quality. It's well known that carbon is the fourth most aboundant element in the universe by mass (over 95% of all known chemical compounds are "carbon compounds"), and is also the second abundant element by mass in human body. In other word, it is the base of DNA and all life on the earth. However, what makes carbon the most fascinating element in the periodic table is its ability to bond to itself essentially without limits through single (average bond energy ~350 kJ mol^{-1}), double (~ 610 kJ mol^{-1}), or triple (~840 kJ mol^{-1}) bonds[4]. Due to this ability, carbon can exist in several forms defined "allotropes". Allotropes are structurally different forms of the same element, in which the same atoms bond together in different ways, resulting in different properties. The well-known allotropes of carbon are amorphous carbon, diamond, graphite, fullerenes and carbon nanotubes (CNTs). Figure 1 shows crystallographic structures of these allotropes. Amorphous carbon, such as soot and black carbon, does not have any crystalline structure (Fig. 1a). Diamond and graphite (Fig 1b and 1c respectively) both have a three-dimensional structure, though it's completely different: in diamond, the atoms are tightly bonded in three-dimensional tetrahedrons, whereas in graphite, atoms are bonded tightly in two-dimensional layers, which are held to the layers above and below by relatively weak forces. **Diamond** consists of pure *sp*3 hybridized carbon atoms, each of which is covalently bonds to four others (Fig. 1b), extending three-dimensionally as an array of tetrahedra.

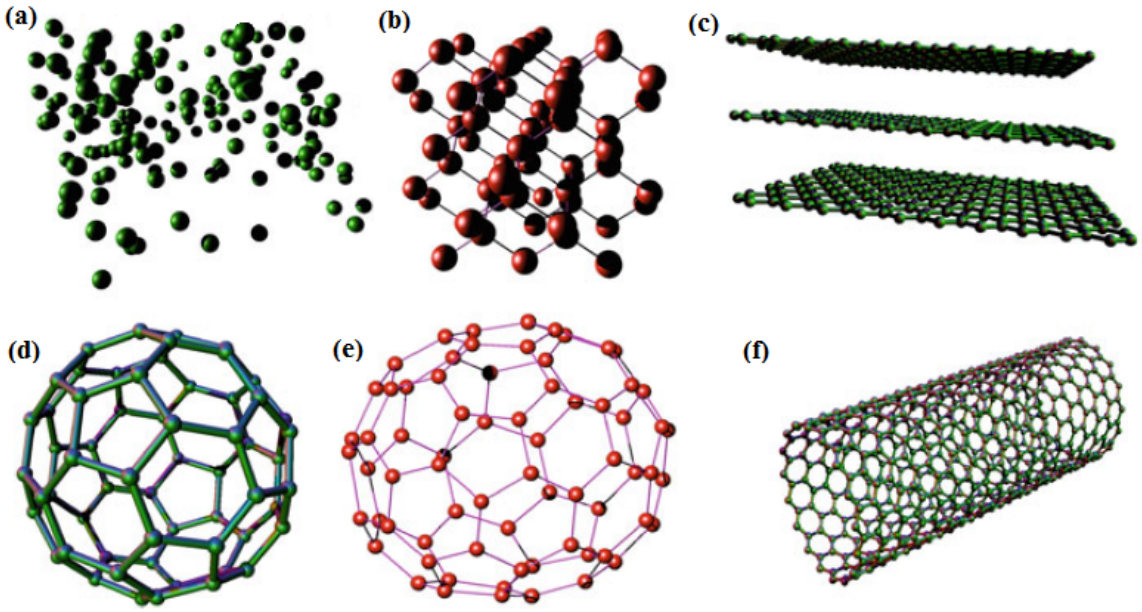

Figure 1. Allotropes of carbon. **a** Amorphous carbon. The carbon atoms are randomly arranged. **b** Diamond. The carbon atoms are bonded together in a tetrahedral lattice arrangement. The carbon atoms are *sp*3 hybridized. **c** Graphite. The carbon atoms are bonded together in sheets of a hexagonal lattice. Van der Waals force bonds the sheets together. The atoms are *sp*2 hybridized. **d** Spherical fullerene, C60. The carbon atoms of fullerenes are bonded together in pentagons and hexagons. **e** Ellipsoidal fullerene, C70. The carbon atoms are bonded together in an ellipsoidal formation. **f** Tubular fullerene, SWCNT. The carbon atoms are in a tubular formation.

Ideally, **graphite** comprises infinite layers of sp2- hybridized carbon atoms (Fig. 1c). Within a layer (called a graphene sheet), each C atom bonds to three others, forming a planar array of fused hexagons (honeycomb structure) with a lattice parameter of 0.142nm. The weak Van der Waals force holds the layer together, leading to a distance between planes of 0.335 nm[5], making graphite the softest natural materials with Mohs hardness of 1. Owing to its particular structure, graphite is a good electrical and thermal conductor in the plane directions (due to the delocalized π band and the σ bonds, respectively), and a poor electrical and thermal conductor in the stacking direction (due to the van der Waals force between the layers)[5]. Recently, other allotropic forms of carbon have been reported, such as 0-dimensional **fullerenes** (including C_{60} and C_{70})[6, 7] and quasi-one-dimentional **nanotubes**[8, 9].

As previously reported, graphene is, basically, a single atomic layer of graphite. The term *graphene* was coined as a combination of *graphite* and the suffix *-ene* to describe single-layer carbon foils in 1962[10]. As is possible to see in Fig. 2, theoretically

graphene can be considered as mother of all graphitic forms: the graphene can be wrapped up into 0D buckyballs, rolled into 1D nanotubes, or stacked into 3D graphite. However, using electron microscopy it has been observed that within graphene monolayers small ripples exist. It is speculated that these imperfections on the surface of graphene are what help to keep it from rolling into nanotubes or other carbonic structures[3]. All the main properties of graphene directly derive from its honeycomb framework. First, this structure creates an immensely strong 2D-material, so strong (breaking strength of 42 N/m) that it is two hundred times the strength of steel: graphene is the strongest material ever tested. Addictionally, graphene shows a high specific surface area (theoretically 2630 m^2/g for single-layer)[1, 11], extraordinary electronic properties and electron transport capabilities[12], unprecedented pliability and impermeability[13], strong mechanical strength[14] and excellent thermal and electrical conductivities (ten times higher thermal conductivity than copper)[15]. Owing to these large number of unique properties, graphene based nanocomposites have been widely investigated within a panoptic array of applications[16-19]. Graphene within the polymer matrix act as fillers which improves the engineering capabilities of a composite. The filler loading is a crucial factor which determines the flexibility chemical affinity, stability and functionality of the composite for various applications. Based on the interaction between the filler and the matrix, properties like electronic, optical, mechanical, magnetic and thermal of the composite improves significantly[20, 21]. The bonding effect between the surface of graphene and the polymer results in diverse polymeric structures which help in elevating graphene from lower work scale to the higher work scale (i.e., laboratory to nanotechnological) applications.

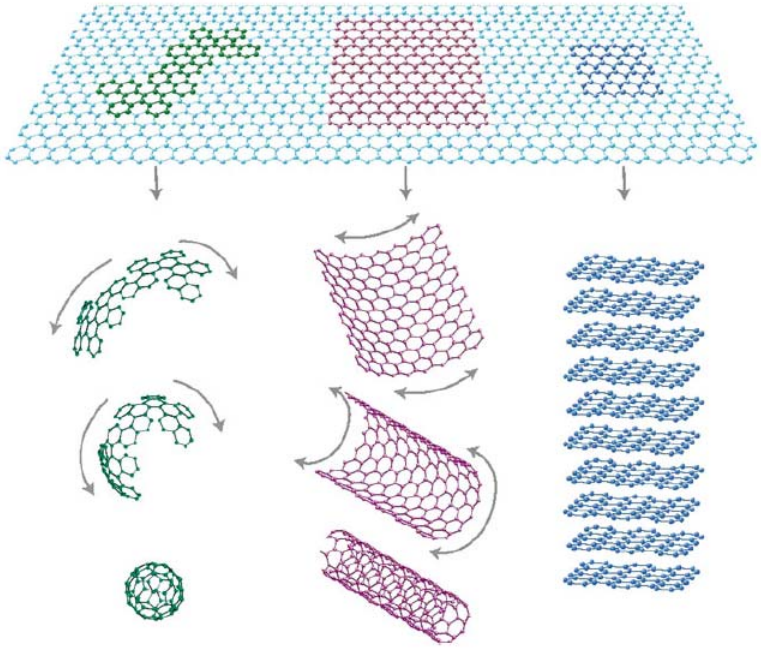

Figure 2. Mother of all graphitic forms. Graphene is a 2D building material for carbon materials of other dimensionalities[1]. It can be wrapped up into 0D buckyballs (*left*), rolled into 1D nanotubes (*middle*) or stacked into 3D graphite (*right*).

Unfortunately, the major obstacle that must be overcome, with respects to the development of a nano-dispersion of graphene, is the tendency of GO to agglomerate in a polymer matrix reducing the use of this material. This phenomenon is due to the fact that pristine graphite is inaccessible in the interlayer space. To avoid this problem, the functionalization of graphite by chemical oxidation is a particularly attractive solution: the resulting material is a hydrophilic graphite derivative with covalently attached oxygen-containing groups (hydroxyl, epoxy and carboxyl) to its layers called **graphite or graphene oxide (GO)**[22]. The presence of these polar groups both improves the solubility and processability and enhance the interactions with organic and inorganic guest molecules. The most common source of graphite used for chemical reactions, including its oxidation, is flake graphite, which is a naturally occuring mineral that is purified to remove heteroatomic contamination[23]. As such, it contains numerous, localized defects in its π-structure that may serve as seed points for the oxidation process. The chemical oxidation of graphene can be achieved by Brodie, Staudenmaier or Hummers method. In 1859, Brodie first attempted to grapheme oxidation via a series of sequential oxidative treatments obtained by addition of potassium chlorate ($KClO_3$)

to a slurry of graphite in fuming nitric acid (HNO_3)[24]. Since the final material was dispersible in pure or basic water, but not in acidic media, Brodie termed it "graphic acid". Staudenmaier improved Brodie's $KClO_3$-fuming HNO_3 preparation both through the addition of concentrated sulfuric acid in order to increase the acidity of the mixture and, and adding the chlorate in multiple aliquots over the course of the reaction, rather than in a single addition as Brodie had done. This slight change in the procedure resulted in an overall extent of oxidation similar to Brodie's multiple oxidation approach (C:O ~ 2:1), but performed more practically in a single reaction vessel[25]. Nearly 60 years after Staudenmaier, Hummers and Offeman developed an alternate oxidation method by reacting graphite with a mixture of potassium permanganate ($KMnO_4$) and concentrated sulfuric acid (H_2SO_4), again, achieving similar levels of oxidation[26]. The Brodie and Staudenmaier approaches both use $KClO_3$ and nitric acid (most commonly fuming [> 90% purity]), whose combination generates the strongest oxidation conditions known at the time. Nitric acid is a common oxidizing agent (e.g. aqua regia) and is known to react strongly with aromatic carbon surfaces, including carbon nanotubes[27]. The reaction results in the formation of various oxide-containing species including carboxyls, lactones, and ketones. However, oxidations by HNO_3 result in the liberation of gaseous NO_2 and/or N_2O_4 (as demonstrated in Brodie's observation of yellow vapors)[28]. Likewise, potassium chlorate is a strong oxidizing agent commonly used in blasting caps or other explosive materials. $KClO_3$ typically is an in situ source of dioxygen, which acts as the reactive species[28]. The Hummers method, instead, uses a combination of potassium permanganate and sulfuric acid. Permanganate is a commonly used oxidant (e.g. dihydroxylations). The active species is, however, diamanganese heptoxide (Mn_2O_7). This particular oxidating agent can selectively oxidize unsaturated aliphatic double bonds over aromatic double bonds, which may have important implications for the structure of graphite and reaction pathway(s) occuring during the oxidation[29]. Aside from the operative oxidative mechanism, the precise chemical structure of GO has been the subject over the years, and even to this day no unambiguous model exists. This is primarily due to the complexity of the material: GO incarnates various nanoscale inhomogeneities. Others reasons are the uncertainty pertaining the distribution of the oxygen-containing functional groups[30], its nonstoichiometric atomic composition, and the lack of sufficiently sensitive analytical

techniques for characterizing the GO structure. Despite this obstacles, with respect to its structure, there have been several conflicting structural models[31, 32] proposed over the years. Among them, the most well-know is certainly the one proposed by Lerf and Klinowsky. According to their model, the oxygen functional groups are mostly in the form of hydroxyl and epoxy groups on the basal plane, with smaller amounts of carboxy, carbonyl, phenol, lactone, and quinone at the sheet edges[32, 33].

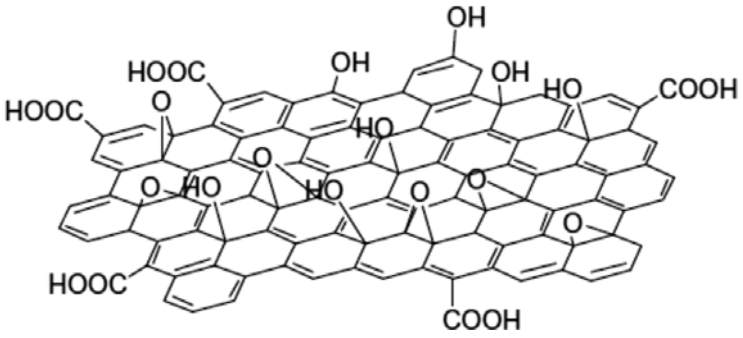

Figure 3. Structural models of GO according to ref [32].

Despite the fact that currently the precise atomic structure of GO is still uncertain and remains to be fully elucidated, al the models agree about the fact that, unlike graphene sheet which consists of only trigonally bonded *sp*2 carbon atoms[34], the GO sheet consists of a hexagonal ring-based carbon network having both (largely) *sp*2-hybridized carbon atoms and (partly) *sp*3-hybridized carbons bearing oxygen functional groups[35]. Besides, in GO, the carbon atoms that are covalently bonded with oxygen functional groups (such as hydroxyl, epoxy, and carboxy) are *sp*3 hybridized. These can be viewed as oxidized regions, and they disrupt the extended *sp*2 conjugate network of the original honeycomb-lattice structured graphene sheet. The latter can be viewed as the unoxidized regions[36]. These *sp*3 hybridized carbon clusters are uniformly but randomly displaced slightly either above or below the graphene plane[37]. The presence of these functional groups provides potential advantages for using GO in numerous other applications. From one side the polar oxygen functional groups of GO render it strongly hydrophilic, confering to GO good dispersibility in many solvents, particularly in water[38]. From the other side, using well-known chemistry strategies, these functional groups serve as sites for chemical modification or functionalization of GO, which in

turn can be employed to immobilize various electroactive species through covalent or noncovalent bonds for the design of sensitive electrochemical systems. Therefore, the chemical composition of GO, which can be chemically, thermally, or electrochemically engineered, allows the tenability of its physicochemical properties[33, 39].

In my doctoral work, 3-amino-1-propanesulfonic acid has been covalently bound via the amide functionality on the GO surface and the resulting organo-modified GO nanofillers were incorporated in Nafion by solution intercalation.

For the preparation of the nanomaterial, graphite powder was first oxidized to aqueous dispersions of graphene oxide by using a modified Staudenmaier's method[25]. The typical synthesis foresees the addition of the appropriate amount of powdered graphite to a misture of concentrated sulfuric acid and nitric acid (3/1 v/v%) while cooling in an ice-water bath. To this mixture, potassium chlorate powder is slowly added in small portions while stirring and cooling. The reaction is quenched after 18 h by pouring the mixture into distilled water. The oxidation product is washed until the pH reaches 6.0 and finally dried at room temperature.

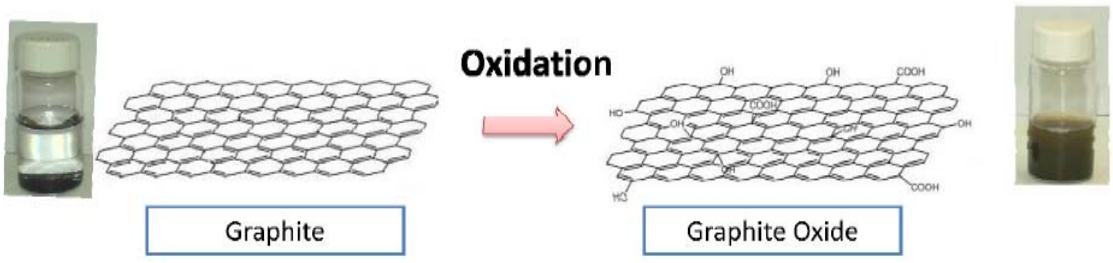

Figure 4. Chemical oxidation of GO.

For the preparation of the organo-modified nanomaterial, an aliquot of GO was first dispersed in pure water. A solution of the above mentioned ammine in pure water have been therefore added to the acqueous dispersion of Graphene Oxide.

After stirring for 24 h, the organo-modified GO was washed with water, separated by centrifugation and air-dried by spreading on glass plates. A schematic representation of the reactions followed for the organo-modification of GO is presented in Figure 5.

Details about the whole synthetic procedure and results are given in the paper IV in appendices.

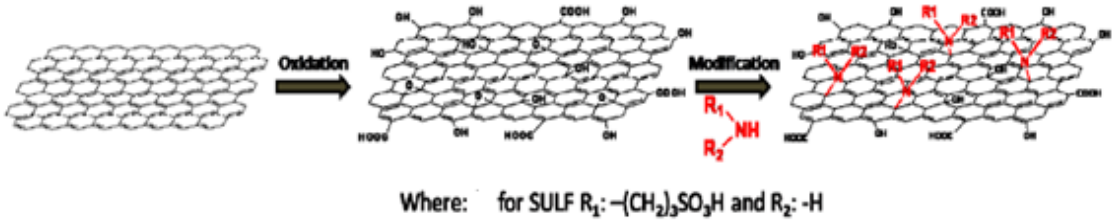

Figure 5. Schematic representation of the synthetic procedure for organo modified GO preparation.

2.1.2 Clays

Among the inorganic compounds suitable for the organic matrix, the clay family is a promising candidate due to their unique combination of swelling, intercalation, and ion exchange properties. Indeed, layered aluminosilicate, like smectite clays[40, 41], show attractive hydrophilic properties and good thermal stability at high temperature[42]. Smectite clays consist of layers of negatively charged oxygen atoms within which several types of positively charged cations are fixed in specific positions: oxygen atoms coordinate cations such as Si, Al, Mg, and Fe to form two-dimensional "sheets". The coordination of cations in adjacent sheets typically alternates between tetrahedral and octahedral. Tetrahedral sheets (also abbreviated as "T"), which commonly contain Si, consist of hexagonal or ditrigonal rings of oxygen tetrahedral linked by shared basal oxygens. The apical oxygens of these tetrahedra help form the base of octahedral sheets (abbreviated as "O") commonly containing Al. A regular repeating assemblage of sheets *(e.g.,* tetrahedral-octahedral or tetrahedral-octahedral-tetrahedral) is referred to as a layer, and can be composed by two, three or four sheets. Smectite clays having two tetrahedral sheets around the central octahedral sheet in each layer (Figure 6) are known as 2:1 phyllosilicates (T-O-T type), with a total thickness of about 1nm[43, 44]. On the other hand, exist also clays with one tetrahedral and one octahedral sheet in each layer, T-O type (1:1 phyllosilicate), as well as the type 2:2 or 2:1:1. As the apical oxygens from the tetrahedral sheet form ditrigonal or hexagonal rings, one oxygen from the octahedral sheet is located in the center of each ring and is protonated to yield a structural hydroxyl. Perhaps the most unique property of smectite clays is the presence of exchangeable cations that are primarily adsorbed on interlamellar surfaces. In fact, the isomorphous substitution of cations having different valences, e.g., Mg^{2+} for Al^{3+} in the octahedral sheet and Al^{3+} for Si^{4+} in the tetrahedral sites, can lead to charge imbalances within a sheet. These may be partly balanced by the opposite type of charge imbalance in the adjacent sheet *(e.g.,* a positively charged octahedral sheet may offset some of the negative charge associated with a tetrahedral sheet). The net charge imbalance on a 2:1 layer, if it occurs, is negative. This charge is referred to as the *layer charge* of the mineral and is balanced by the incorporation of larger cations *(e.g.,* Na^{+}, K^{+}, Ca^{2+}, and Mg^{2+}) that coordinate to the basal surfaces of the tetrahedral sheets from adjacent layers. The electrically neutral sheets are bonded together by relatively weak

dipolar and van der Waals forces. Besides, because these charge-balancing cations are located between adjacent 2:1 layers, they are referred to as "interlayer exchangeable cations".

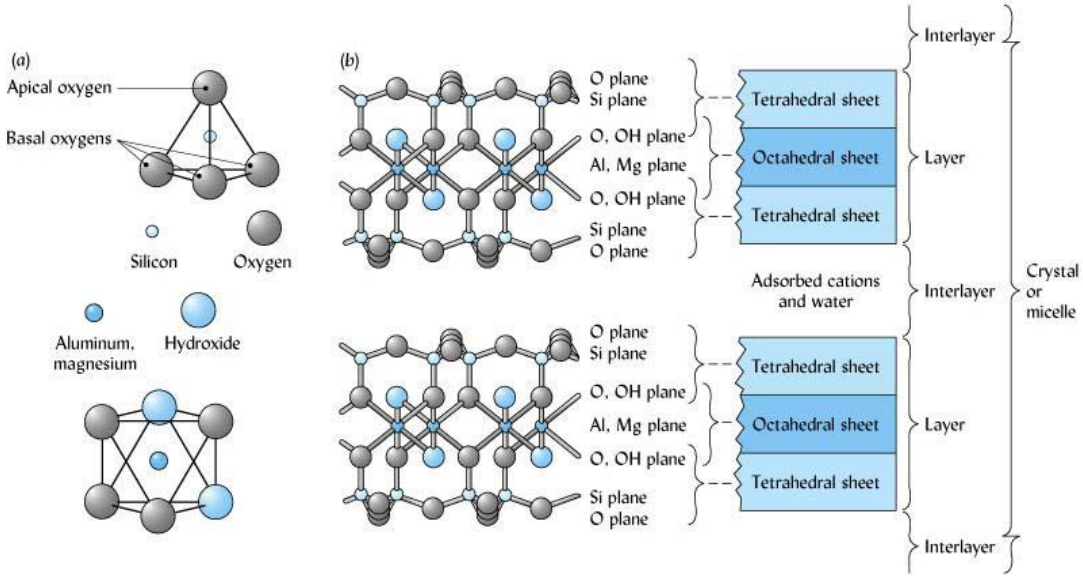

Figure 6. Schematic structure of smectite clay 2:1 minerals[44].

The unique physicochemical properties displayed by smectite clays are the result of (i) extremely small crystal size, (ii) variations in internal chemical composition, (iii) structural characteristics caused by chemical factors, (iv) large cation exchange capacity, (v) large surface area that is chemically active, (vi) variations in types of exchangeable ions and surface charge, and (vii) interactions with inorganic and organic liquids. Among the materials with a layer lattice structure, only in the smectite clays there is the simultaneous presence of interlayer cations exchangeable and interlayer surfaces and cations hydratable. The ions located between the clay layers allow the absorption of polar solvent, like water (figure 7), with good retention capacity so, when incorporated into a polymer membrane, they help to prevent the loss of the hydration water not only at high temperatures but also under low relative humidity environment. Although hydration and dehydration occur regardless of the type of exchangeable cation present, the degree of hydration is dependent on the species of exchangeable ion, on the size and charge of the cations, and on the magnitude and location of the layer charge of

the adjacent silicate sheets. Presently, it is generally accepted that the hydration of the interlamellar surfaces of smectite clays occurs in a series of steps when these clays are subjected to increasing relative humidity levels. At high humidity levels between one and four layers of water molecules may be formed, depending on the cation adsorbed. Besides, the arrangement of the water molecules and the thickness to which oriented water layers could develop strongly depend on the type of exchangeable cations, and in particular on their tendency to hydrate.

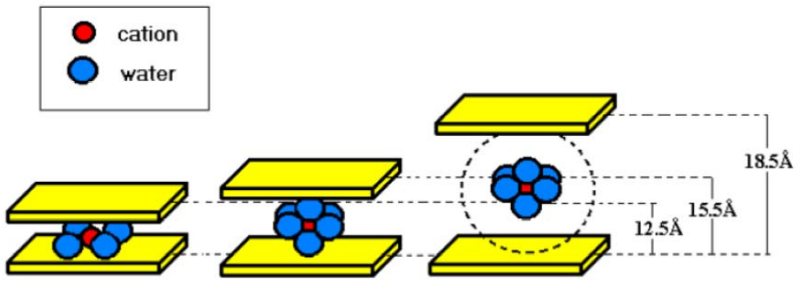

Figure 7. Schematic representation of the swelling of one clay layer.

The reversibility of the swelling, however, limits the application of clays. In fact, depending on the temperatures, two forms of water can be lost from smectite clays, adsorbed and crystalline. When they are heated at relatively low temperatures (100- 200 °C) the adsorbed water loss occurs, most of which is interlayer water. This leads to precipitation of the sheets, reducing the interlayer space. However, if smectite clays are not heated much above 200 °C, most will rehydrate completely in the presence of liquid water, despite generally there are some effects on certain properties such as swelling and, or, dispersion. When heated at temperature above 300-400 °C, loss of OH or lattice water occurs: the OH loss involves a breakdown of the silicate structure. It has been demonstrated that, in the presence of liquid water, smectite clays will generally rehydrate to some degree even after heating[45] to temperatures as high as 500-700 °C. However, the degree of rehydration depends mainly on the degree of structural change owing to loss of OH lattice water. What really matters is the fact that, at low water content, smectite clays are poor proton conductor. Their incorporation inside Nafion® for example, which is highly proton conductive, can lead to a reduction of the global

proton conductivity of the membrane. The introduction of proton conductive bulky cations within the interlayer space seems to be a fruitful strategy in order to prevent the collapse of the interlayer space, since then they act as pillar keeping the aluminosilicate sheets apart, and, at the same time, in order to enhance the proton conductivity of the hybrid material (also under low relative humidity), without losing the benefits brought by the inorganic particles. The intercalation process in these systems is equivalent to ion exchange, and unlike the intercalation compounds of graphite, it does not involve necessarily charge transfer between the guest and host species[46]. The preparation process of the pillared clays, occurs through a cationic exchange reaction of countervailing cations that lead to the intercalation of the pillar. After incercalation, the calcination of the intercalates is needed. During this step, the complexes inserted in the clay interlayer space are transformed into metal oxide pillar. These latter support the silicate sheets and keep them apart even at elevated temperatures (up to about 600 °C) [47]. In the figure 8 is presented the intercalation process of the pillared clays. Naturally, the cation substitution within the interlayer space, results in changes on the layers and thus on many fundamental properties of the clays, including water holding cation fixation, swelling ability, cation exchange capacity and specific surface area: using simple chemical methods such as intercalation with organic or inorganic guest molecules, the properties of the smectite nanoclays can be tailored according to the specific needs for a wide range of application.

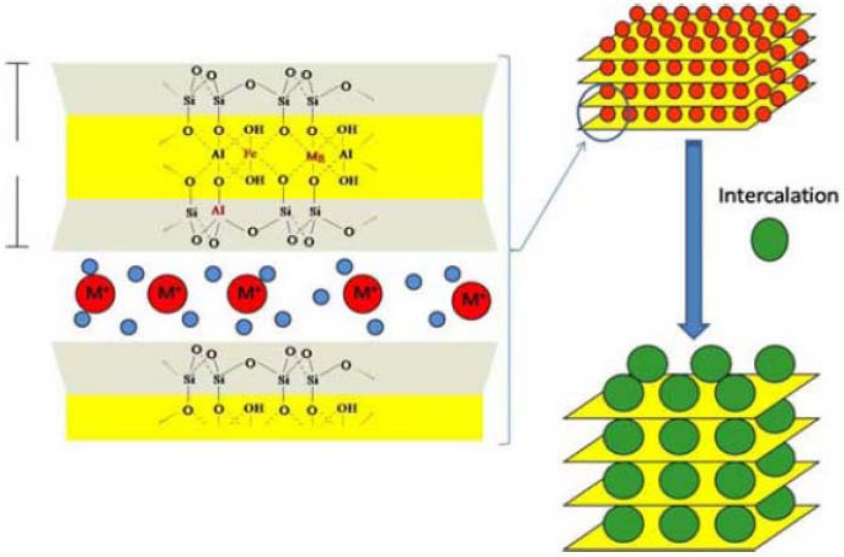

Figure 8. Simple illustration of the intercalation process[46].

Within this doctoral thesis the effect on the transport properties of Nafion nanocomposite membranes of two different Clays, differing for the particle size and the CEC, were investigated. A synthetic trioctahedral hectorite, named Laponite (Lap), has been directly introduced into the polimer matrix. The effect of the introduction of such 2D-layered material on water and methanol transport properties of the nanocomposite membrane has been deeply investigated (details are available in paper V in the appendices). Besides, a natural smectite montmorillonite Wyoming clay, SWy-2, has been used as substrate for the preparation of a novel Clay-CNTs hybrid material, whose properties and preparation procedure are deeply described in the next paragraph.

2.1.3 Carbon Nanotubes (CNTs) and Clay - CNTs hybrid

As already discussed in paragraph 2.1.1, carbonaceous nanofillers such as grapheme and carbon nanotubes (CNTs) play a very promising role for a wide range of applications, due to their better structural and functional properties such as high aspect ratio, high mechanical strength high electrical properties etc. than others[48, 49]. Carbon nanotubes (CNTs) are fullerene-related nanostructures which can be described as rolled-up sheets of graphite, with the carbon atoms arranged in a honeycomb-like hexagonal structure[50]. These hollow graphene cylinders can be open-ended or closed at either end with caps containing pentagonal rings, which are isostructural to a half fullerene molecule. Based on the number of graphene sheets which constitute them, single-wall and multi-wall structures can be differentiated: single walled nanotubes (SWNTs), can be considered as single graphene sheet rolled into a cylinder; multi-wall carbon nanotubes (MWNTs), which are more easily formed, can be considered as stacking of concentric layers of several graphene layers in the form of cylinders with an interspacing of 0.36 nm[51, 52]. In Fig. 9 a structure presentation of both type of carbon nanotubes has shown.

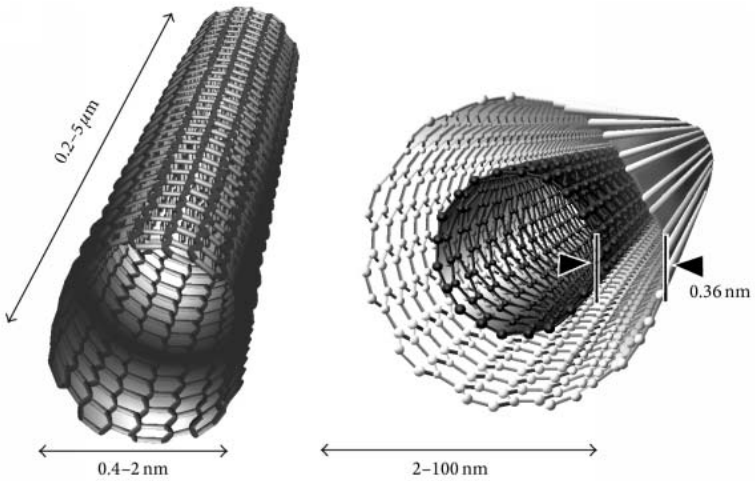

Figure 9. Carbon nanotubes: single-walled carbon nanotubes (SWCNTs) on the left; and multiwalled carbon nanotubes (MWCNTs) on the right.

Owing to their outstanding properties, arising from combination of unique dimensional, structural and topological features[50, 53], CNTs have been termed "materials of the twenty-first century". Indeed, they exhibit exceptional electrical and mechanical properties, which combined with their elongated shape and nanoscale dimensions enable the design and development of novel nanodevices and nanocomposite materials[54, 55]. In addition to these excellent mechanical and electrical properties, CNTs exhibit high thermal stability, surviving up to temperatures as high as 2800 °C under vacuum conditions, optoelectronic properties, low density, open pipe framework and relative chemical inertness.

Among the numerous potential applications of carbon nanotubes, their use in polymer-reinforcement has found increasing interest in the recent years[56, 57]. However, regard the use of CNTs as additives, two main problems must still be overcome. First, the fabrication of well-defined and organized arrays of carbon nanotubes, in sufficient quantities and at a low cost, is of high importance, since then their unique properties originate from their nano-scale structure[58]. Nowadays three mainly techniques are widely used to synthesize CNTs: laser ablation[59], arc discharge[60] and catalytical chemical vapour deposition (CVD)[61]. Via laser ablation and arc discharge high quality material can be produced. However, both methods suffer from several drawbacks: in relation to the size of the carbon source (the anode in arc-discharge and the target in laser ablation) there is a limitation in the volume of sample that can be produced; the high temperature requirement results in prohibitive costs for scale-up mass production of carbon nanotubes. Only CVD allows large scale production of CNTs at relatively low cost[62]. In brief, the method comprises the catalytic decomposition of carbon-containing gases (methane, ethane, and acetylene), at rather high temperatures, over a catalyst containing nanoparticles of transition metal (Fe, Co, Ni) or of the related oxide, embedded in solid matrices or supported on the surfaces of porous materials[61, 63]. Besides the possibility of mass production at a low cost, another important advantage of CVD is that diameter, length and morphology of the nanotubes can be controlled by altering the size of the nanoparticles and the deposition conditions. However, in order to facilitate the large scale production of CNTs, support material should have a threefold action: i) reduces the amount of byproducts (amorphous carbon, graphite nanospheres

etc.) at minimum levels; ii) inhibits the aggregation of catalytic centers; iii) allows its removal from the resulting CNTs using simple chemical procedures.

The other drawback related with the use of CNTs is due to the lack of solubility and dispersibility of carbon nanotubes in organic solvents or water. This solubility problem can be partially coped via functionalization or modification of carbon nanotubes surfaces. Two main paths are usually followed for the functionalization of carbon nanotubes. The first foresees the attachment of organic moieties to carboxylic groups that are formed by oxidation of CNTs with chemicals such as HNO_3, $KMnO_4$, H_2O_2, NaClO, H_2SO_4, KOH, and NaOH[64]. According to this method, single-walled carbon nanotubes (SWNT) are first derivatized[65] by adding amines to the carboxylic groups, previously activated by $SOCl_2$. Following, similar reactions gave other functionalized carbon nanotubes soluble in organic solvents, such as chloroform, tetrahydrofuran, carbon disulphide[66]. CNTs solubility in organic solvents can also be enhanced by direct bonding to the surface double bonds[67, 68]. However, despite the activation of CNTs plays an important role in enhancing the maximum adsorption capacity because of the modification in the surface morphology and surface functional groups, the main disadvantage of both these paths of modification is however the shortening of carbon nanotubes size during the formation of carboxylic groups in the oxidation step.

Recently, different studies have appeared in literature related to the synthesis of Clay–carbon nanotubes hybrids[61, 69, 70]. Indeed, smectite clays represent an attractive support for the synthesis of carbon nanotubes. As described in paragraph 2.1.2, owing to the unique swelling, ion-exchange and intercalation properties smectite clays can be easily, uniformly and reproducibly loaded with metal cations, such as iron, nickel and cobalt[61, 69], or oligonuclear metal oxide clusters that can function as catalysts in the growth of carbon nanotubes. After a calcination process, they are converted into metal oxide particles, which are effectively immobilized between the layers and on the surface of the clay. The use of MgO as support material minimizes the formation of amorphous carbon as the main impurity[71] and deters the metal particles from aggregating. Furthermore, it has been reported that the use of MgO increases the yield of the synthesized CNTs compared to other support materials like alumina or silica. The use of bimetallic systems of transition metal oxides results, moreover, in higher yields of synthesized CNTs, since the synergistic action of the two metals enhances the total

catalytic activity[72, 73]. Besides being an efficient path for the synthesis of well-defined and organized arrays of CNTs, carbon nanotubes rooted on smectite layers show high solubility in a wide range of organic solvents and water. At the same time, clay can be directly exfoliated into random silicate platelets when CNTs are used as the intercalating agent. This method greatly simplifies the overall procedure of preparation of polymer nanocomposites containing both clays and CNTs, with improved mechanical properties. In has been proved, in fact, that when small amounts of clay particles are fully exfoliated and well-dispersed in a polymer[74, 75] give composites with outstanding mechanical, thermal, optical and other properties that increase their technological value. The synthesis of Clay– CNT hybrids is, thus, of high interest due to the combination of remarkable mechanical and physical properties of carbon nanotubes (1D material) and smectite clay (2D-layered) which originate from their unique 3D nano-scale structure[76] (see Fig. 10). Finally, the electrochemical properties of this particular hybrid material can also be easily tuned by appropriate functionalization of the CNTs surface: through simple reactions of organic chemistry, in fact, a wide range of organic molecules and functional groups may be introduced on the surface of CNTs. In this frame, one would expect that the combined action of clay–carbon nanotubes in polymer matrixes would provide outstanding functionalities to the resulting composite materials.

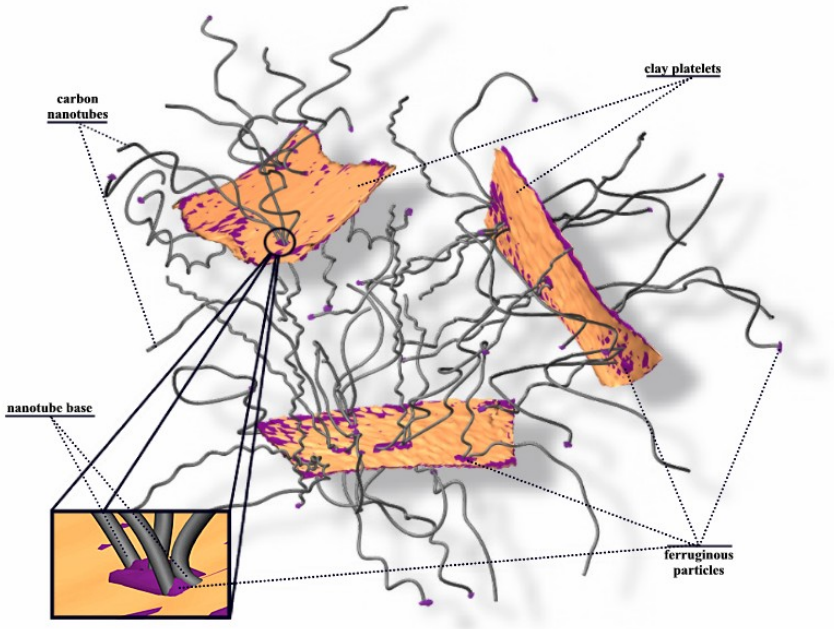

Figure 10. Schematic illustration of the clay–carbon nanotube composite[76].

During this doctoral work, starting from a natural Smectite montmorillonite Wyoming clay (SWy-2), opportunely fractionated and purified, carbon nanotubes (CTNs) were rooted on the surface of the Clay by catalytic chemical vapor deposition (CCVD) method, and studied to be introduced in a perfluorosulfonic acid (Nafion®) membrane, as effective way to improve the transport properties of the polimer electrolyte. Side-wall chemical oxidation and organo-functionalization of the CNTs was performed using organic ester molecules containing hydrophilic groups (-RSO_3H).
The synthetic procedure, described in detail below, was performed during my period in the Department of Materials Science and Engineering of the University of Ioannina, where I worked under the supervision of Prof. D. Gournis..

Synthesis of Clay-CNTs hybrid materials

The synthetic procedure (illustrated in the Figure 11) for the production of the clay-CNTs hybrid nanofillers used in this work consists of four steps, and retraces, for the initial two stages, those described by Tsoufis et al.[77]:
1) metal-exchange reaction for the preparation of an appropriate clay-substrate with catalytic metal centres (Fe and Ni);
2) growth of the CNTs on such clay-substrates;
3) oxidation reaction to obtain oxidized CNTs (ox-CNTs);
4) organo-functionalization reaction to obtain SWy-oxCTNs–RSO_3H.
For the first step, an homogeneous clay suspension in water was reacted with aliquots of nickel chloride and iron chloride aqueous solution ($NiCl_2{\times}6H_2O$ and $FeCl_3{\times}6H_2O$), concentration 0.1 M, such that, the amount of Ni-Fe cations added corresponds to 5 times the CEC of the clay. This allows to exchange all of the Na^+ ions present into the clay-galleries with bimetallic cations, obtaining a catalyst in which Fe^{2+} and Ni^+ ions are incorporated in the clay's structure. The final Ni-Fe-exchanged clay was separated by centrifugation, rinsed repeatedly with distilled−deionized water, and dried at room temperature in air. The resulting solid part was then subjected to calcinations at 450 °C for 4 hours, collected and grounded in fine powder.

This powder was, in a second step, used as substrate for the growth of the CNTs via Chemical Vapor Deposition by catalytic decomposition of acetylene in a fixed bed flow

reactor at a temperature of 700 °C. In a typical run, a certain amount of catalyst powder was placed in an alumina crucible within a quartz tube, located in a horizontal tubular furnace and was heated up to the 700 °C under nitrogen atmosphere with acetylene as a carbon precursor. After the completion of acetylene flow, the ceramic boat was cooled down to room temperature.

Based on different reaction times in CVD (15 min and 30 min) it was possible to obtain two aliquots of hybrid materials loaded with different percentage of CNTs, as confirmed by thermogravimetric analysis showed later.

In the third step, an aliquot of Swy-CNTs powder was oxidized through refluxing in an acid solution of H_2SO_4-HNO_3 (3:1) mixture, to obtain the SWy-oxCNTs material. The oxidation of the CTNs is necessary for the organo-functionalization (fourth step) through, before an esterification reaction by reflux in thionyl chloride ($SOCl_2$) in dimethylformamide (DMF), and then followed by the addition of aliquots of propane amino sulfonic acid. After stirring for 24 h, the organo-modified CNTs were washed with water, separated by centrifugation and air-dried, obtaining the SWy-oxCNTs-RSO_3H powder. At the end of the procedure, three types of hybrid materials were collected and tested as nanoadditives in a Nafion polymer matrix: SWy-CNTs, SWy-oxCNTs and SWy-oxCNTs-RSO_3H.

The materials were characterized by a combination of techniques (TGA, Raman, FT-IR, SEM, TEM) and all the results of the experimental study are discussed in the **paper I**, recently submitted, and reported in the appendix to the thesis.

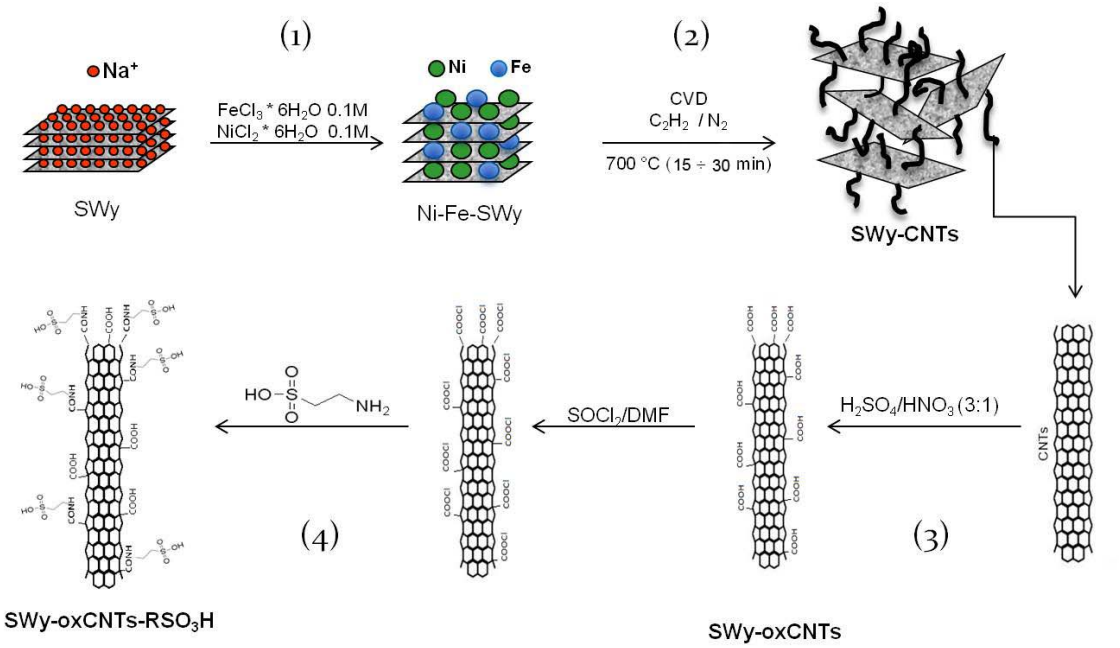

Figure 11. Synthetic procedure for the production of clay-carbon nanotubes hybrid materials used as nanoadditives in Nafion polymer.

2.1.4 Layered Double Hydroxide (LDH)

Layered Double Hidroxides (LDHs) form a typical class of layered minerals that are frequently termed **anionic clay minerals** or **hydrotalcite-like compounds**. These are a broad class of 2-D inorganic compounds with basic character and a high capacity for anion intercalation. Accordingly, LDHs can be used as storage matrix (hosting), and control the release of different anionic species[78, 79]. In this case, anion species (guests) are intercalated between the lamellae of the LDH, which is called interlayer space. Although not abundant in nature, the layered double hydroxides may be synthesized in the laboratory at a relatively low cost.

As previously mentioned, the LDHs are also widely known as hydrotalcite-like compounds, recalling their structural similarities to hydrotalcite, a mineral with the formula $Mg_6Al_2(OH)_{16}CO_3{\cdot}4H_2O$. The hydrotalcite structure results from the stacking of brucite-like layers [$Mg(OH)_2$] containing a positive residual charge arising from the partial isomorphous substitution of Mg^{2+} cations by Al^{3+} cations. This positive excess charge is balanced by the carbonate anions, which reside in the interlamellar spaces[80, 81]. Like clay minerals, also LDH have two-dimensional structures[78, 79]. Such materials may by represented by the following general chemical formula:

$$[M_{(1-x)}^{II} M_x^{III} (OH)_2](A^{n-})_{x/n}{\cdot}mH_2O]$$

where M^{II} represents a divalent metal ion, e.g., Mg^{2+}, Ca^{2+}, Zn^{2+}, etc, and M^{III} represents a trivalent metal ion, e.g., Al^{3+},Cr^{3+}, Fe^{3+}, Co^{3+}, etc, which can be accommodated in the octahedral holes in the brucite-like layers. The ionic radius of both kind of metallic ions should not be too different from that of Mg^{2+}. In the formula, x is the metal ratio $M^{3+}/(M^{2+}+M^{3+})$. A broad range of x values have been claimed for synthesizing an LDH structure; however, the pure LDH phase contains a narrow range of x values: $0.2 \leq x \leq 0.33$[82]. The species A^{n-} in the interlamellar region can be any charge compensating anion (organic or inorganic) e.g., Cl^-, CO_3^{2-}, NO_3^-,etc., and m is the amount of water present in the same region[83]. Due to the similarities in terms of chemical structures between LDH and brucite, a comparative analogy would be very helpful in this context. In Fig. 19 a schematic illustration comparing the structures of brucite and LDH has shown. Brucite, as clearly visible from this figure, consists of a hexagonal close packing of hydroxyl ions with alternate octahedral sites occupied by Mg^{2+} ions. It is well known

that the metal hydroxide sheets in the brucite crystal structure have neither a positive nor a negative charge, and they are linked with each other via weak Van der Waals forces, producing a basal spacing of approximately 0.48 nm. In contrast, in the LDH structure, some of the divalent cations of the brucite-like sheets are isomorphously replaced by a trivalent cation. Consequently, the mixed metal hydroxide layer, i.e., $[M_{(1-x)}^{II}\ M_x^{III}\ (OH)_2]^{x+}$, that is formed attains a net positive charge. For the electroneutrality of the system, this excess positive charge on the metal hydroxide layers is neutralized via incorporation of anions in the interlayer region. Besides, water molecules can be coupled bot with the interlayer anions (water of hydration) than also between crystallites (adsorbed water environment). In the first case, the water molecules act stabilizing the crystal structure of HDL while the second quantity depends on the relative humidity of the atmosphere with which HDL is in contact[84]. Thus, the lamellae are not only linked by hydrogen bonds, as in the case of the brucite, but also by electrostatics interaction between the positively charged plates and interlayer anions. The simultaneous presence of anions and water molecules ultimately causes an increase of the basal spacing from 0.48 nm in brucite to approximately 0.77 nm in Mg-Al LDH (Fig. 12). By varying the choice of metallic cations isomorphously substituted within the surface, their ratio and the interlayer anions, it can be formed a great number of LDH types. Besides, LDH containing more than one divalent and/or trivalent cation can also be synthesised. Furthermore, virtually almost any conceivable cation might be able to balance the positive residual charge of LDH lamellae. However, it is not easy to obtain pure and crystalline materials. In general, simple inorganic anions with a higher charge/radius ratio are more likely to get in. This is because these anions have increased electrostatic interaction with the inorganic layers. For organic anion intercalation, especially anionic polymers, it should be taken into account factors such as anion geometry, interaction to each other, their size and the relationship between their size and charge.

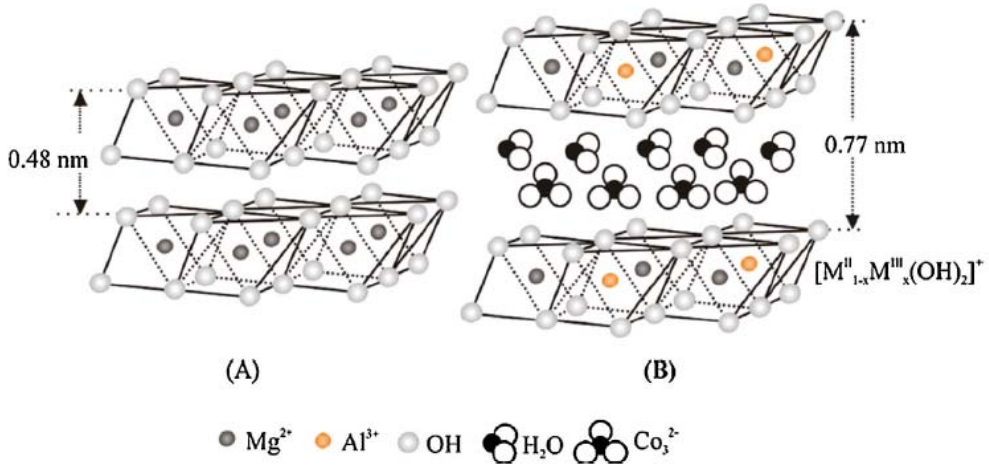

Figure 12. Schematic rapresentation of layered structures: (A) brucite-like sheets and (b) Mg Al LDH.

In this contest of structural discussions, another analogy needs to be mentioned. Both LDHs and clays layered silicates, such as montmorillonite (MMT), possess layered crystalline structures and substitutable interlayer ionic species; however, they are not identical with respect to their chemical and structural features[85]. Figure 13 shows the difference in terms of crystal structures between LDH and MMT. From the earlier discussions, it is clear that LDHs have positively charged layers with anionic interlayer species (thus, they are called anionic clays)[86]; the layered silicates instead, have a completely opposite nature (hence, they are called cationic clays). Furthermore, also with regard to composition, geometries and layer thickness LDHs completely differ from layered silicates. As explained earlier, in LDHs each crystal layer is composed of a single octahedral metal hydroxide sheet, whereas in layered silicates, the structure consists of two or more tetrahedral-silicate sheets organized over an octahedral metal oxide layer. As clearly appers from Fig. 13, the crystal layer in MMT is composed of three sheets: one octahedral sheet containing Fe, Al, Mg, etc. that is sandwiched between two tetrahedral-silica sheets. This difference in the layer structure eventually results in a considerably lower crystal layer thickness and rigidity in LDH-type clays.

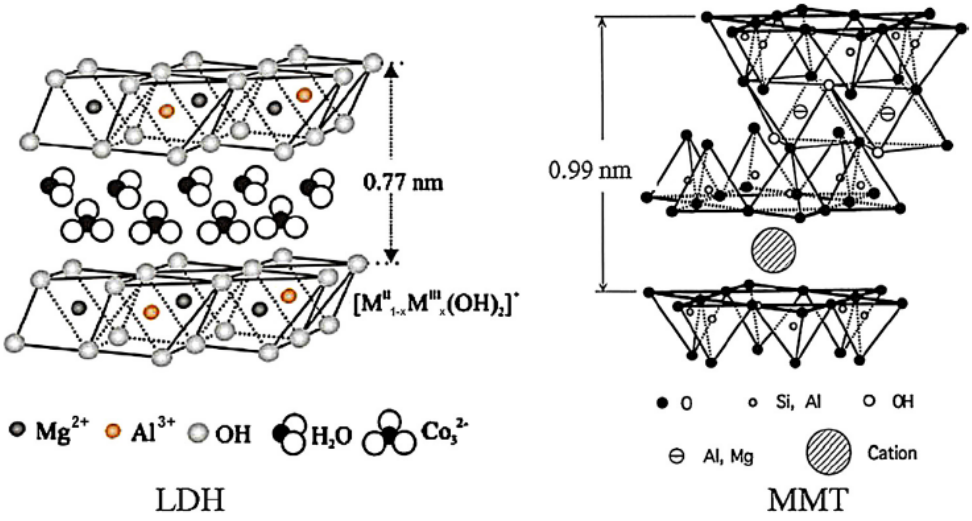

Figure 13. Comparison between layered structures: (left) LDH; (right) montmorillonite (MMT)[85].

Given the low abundance in nature, most of the commercially available LDHs are generally the result of synthesis in laboratory. It is not very easy to prepare pure LDHs, but several different techniques can be employed to obtain the desired LDH composition[87]. The synthesis of such solids, for both commercial and scientific purpose, can occur through direct methods, as for example coprecipitation[78, 83], according to which to a basic solution containing the anions to be intercalated is added the solution containing the metal cations (M^{II} and M^{III}) at a constant pH value in the range of 8–10[87]; homogeneous precipitation method, which normally uses "urea hydrolysis" leading to LDHs containing CO_3^{2-} anions with a high degree of crystallinity and a narrow particle size distribution; sol-gel synthesis[88], and hydrothermal crystallization[89] which results in the crystallization of an amorphous trivalent metal oxide ($M_2^{III}O_3$) precursor in the presence of a suitable divalent metal oxide ($M^{II}O$), producing a combination of two different types of valency among the metal oxides. Beside the direct synthesis of the specific LDHs, various organo-modified LDHs can be obtained after incorporation of a wide variety of anionic organic species into the LDH interlayer regions[90, 91]. In this case, however, the affinity of the anions to such an interchange reaction is completely dependent on their charge and size. Practically, the original LDH, used as a precursor, is dispersed in an aqueous solution of the desired

anionic species. The dispersion is stirred at room temperature for several hours to obtain the desired product.

Due to the great number of possible compositions and metal anion combination as well as to their tunable structural homogeneity[92], LDHs have been extensively investigated for a wide range of applications. In this Doctoral work, a Mg^{2+}:Al^{3+} LDH whose metal ratio was adjusted to 2:1, (details are given in paper V), has been incorporated in Nafion by solution intercalation in order to investigate its effect on water and methanol transport properties of the resulting nanocomposite membrane.

2.1.5 Titanium Dioxide and Sulfated titania

In the research of higher-temperature proton-exchange membrane with adequate performances at low relative humidity (RH), among the several strategies explored, the dispersion of hygroscopic inorganic fillers into the polymeric matrix, to fabricate organic-inorganic composite membranes, has attracted much interest[93, 94]. These particular membranes has been specifically designed to promote internal self-humidification effects that can increase polymeric electrolyte water retention properties and ease water management even at high temperature and low humidity conditions. According to this specific strategy, the addition of metal oxides, in the form of nano- or sub-micrometric particles, has demonstrated to be particularly effective since it results in simultaneus improvement of several interesting polymer properties, such as proton conductivity, water retention, thermal and mechanical stability[95, 96]. Considering that the observed improvements are usually related to the polymer/inorganic phase interfacial properties, theoretically, the higher is the interface interaction between the polymer and the dispersed particles, the greater is the filler influence on the original characteristics of the polymer[97, 998]. Accordingly, due to their larger specific surface area, nanoparticles are expected to modify the original characteristics to a greater extent than microparticles. A large variety of ceramic compounds, such as SiO_2, TiO_2, and ZrO_2, have been already investigated as fillers to a Nafion matrix[99-101]. Among them, hydrated titanium dioxide powder, for example, exhibits high conductivity at a relatively low humidity, being one of the most effective compounds in retaining water[102]. **Titanium dioxide**, also known as **titanium(IV) oxide** or **titania**, is the naturally occurring oxide of titanium, chemical formula TiO_2, a very useful semiconducting transition metal oxide material that exhibits unique characteristics such as low cost, easy handling, non-toxicity, biocompatibility and resistance to photochemical and chemical erosion. These advantages make TiO_2 a good material in solar cells, chemical sensors, for hydrogen gas evolution, energy production, as pigments, self-cleaning surfaces and environmental purification applications[103]. One of the most common method for the production of titanium dioxide utilizes the mineral ilmenite. However, considering that the chemical and physical properties exhibited by these materials depend, among others, on both the composition and the degree of homogeneity, other different synthesis strategies have been developed[104]. Among

them, the sol-gel route has demonstrated a high potential for controlling the bulk and surface properties of the oxides[105].

Titanium dioxide exists in both crystalline and amorphous forms and mainly exists in three crystalline polymorphos, namely anatase, rutile and brookite, wich unit cells are shown in Fig. 14. Anatase and rutile have a tetragonal structure, whereas brookite has an orthorhombic structure[106].

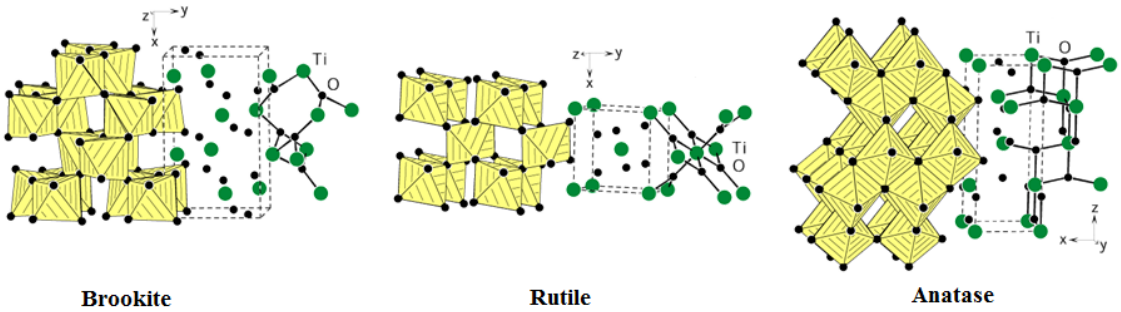

Figure 14. The crystal structures of orthorhombic brookite (space group *P*bca), tetragonal anatase ($I4_1$/amd), and tetragonal rutile ($P4_2$/mnm). The edge- and corner-sharing TiO_6 octahedra and the more or less distorted trigonal-planar environments of the oxygen atoms are emphatised.

The main structural differences among the different crystalline polymorphos are related to the number of shared octahedral, i.e. two in rutile, three in brookite and four within anatase structure. Obviously these structural differences involve also different properties. Rutile, for example, shows the highest thermal resitance and is also the most used for industrial purpose, while anatase is metastable and, among the three crystalline form, has the highest photocatalytic activity. Thus is the is the most technologically used crystal form.

The main product obtained through mosto of the synthetic procedures is amorphous TiO_2, whose structure have not any long range order[107]. Amorphous TiO_2 can be converted in crystalline form via thermic treatment. Generally, a first cristallization into anatase form can be obtained after few thermal cycles at relatively low temperature. The conversion into rutile phase, instead, occurs at higher temperatures, i.e. 600 °C.

The extraordinary properties resulting from the interaction between the organic moiety and the inorganic moiety, led to an increased interest toward organic-inorganic materials[108, 109]. In fact, in most of the case, composite membrane shows better physicochemical properties than pristine polymer. In some nanocomposites, however, one can observe a reduction of the proton conductivity with increasing filler content. This can be due both to the rather low proton conductivity of the fillers themselves[110] that to the interaction between the additives with proton-exchange groups in the original polymer matrix. Therefore, modifying inorganic fillers by inorganic sulphonic acid has become a promising way to enhance proton conductivity of membranes under intermediate temperature and low relative humidity or even anhydrous conditions[111, 112]. In general, the incorporation of acid modified inorganic fillers in conventional Nafion type membranes is of primary interest, having the dual function of improving water retention as well as providing additional acidic sites[113]. Accordingly, sulfated nanoparticles are expected to show better performance to improve the proton conductivity than unmodified filler, when they dispersed in suitable polymer matrices[114]. Besides, it has been proved that the interaction between acid modified titania and polymer enhances the thermal stability of the nanocomposite membranes. However, it has been demonstrated that the proton conductivity of sulfated titania, as well as its surface and crystallographic properties, varies largely depending on the method of preparation, in particular on the thermal treatments[115, 116]. About that, sulfonic groups on the titania surface can be principally added by two different methods: "in situ generation" and impregnation. The impregnation method foresees the dispersion of TiO_2 particles into an aqueous solution of sulfuric acid. The "in situ generation" procedure, instead, requires the addition of sulfuric acid directly into the reactant system in the presence of the TiO_2 precursor. Sulfonated TiO_2 particles can also be obtained by an indirect way, i.e. by grafting a suitable organic species bearing sulfonic acid groups onto the surface of a selected ceramic oxide, that is nanostructured titania.

During my Doctoral work, in the framework of the Project NAMED-PEM "Advanced nanocomposite membranes and innovative electrocatalysts for durable polymer

electrolytemembrane fuel cells", two type of organically functionalized titania, TiO_2-RSO_3H, were tested as filler.

The first, prepared by Dr. M.A. Navarra of Department of Chemistry, Sapienza University of Rome via a 1-step sol-gel synthesis procedure (details are given in paper II reported in the appendices), was evaluated as inorganic additives in composite Nafion-based membranes. Briefly, the procedure foresees the addition of H_2SO_4 (0.5 M) to a mixture of the appropriate titania precursor and *i*-propanol, in order to directly obtain sulfated titania nanoparticles.

A two-steps synthetic pathway was instead used by Dr. De Bonis C., of Department of Chemical Science and Technologies, University of Rome "Tor Vergata", to prepare sulfated titania nanoparticles investigated as filler in sPEEK-based composite membranes for application in high temperature direct methanol fuel cells. (paper VI). The schematic illustration of the procedure followed has shown in Fig 15. As is possible to see: (i) due to the presence of a large number of hydroxyl groups, mercaptopropyl moieties can be easily introduced onto titania surface; (ii) by subsequent oxidation of the thiol groups into sulfonic acid groups propylsulfonic-functionalized titania can be obtained.

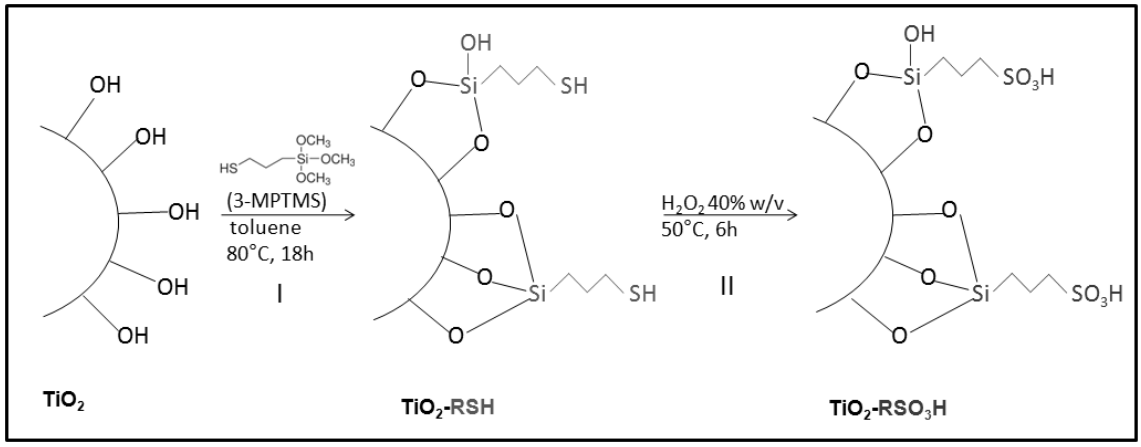

Figure 15. Synthetic pathway for the surface functionalization of TiO_2 nanoparticles used as filler in sPEEK-based membranes.

2.2 PREPARATION OF NAFION NANOCOMPOSITE MEMBRANES

Organic/inorganic composite membranes are often characterized by the incorporation of variable amount of a solid filler dispersed into a polymer that serves as the matrix component. The additive might present intrinsic proton-conduction properties or, as for example with silica, titania or zirconia, it can be used as water-retaining inorganic filler or for mechanical support. In general, the simple dispersion of an inorganic solid in a polymer solution makes use of the mixing of pre-formed inorganic proton-conductors or ceramic oxides with a polymer solution, followed by film casting and drying. In this case we need to consider that, the properties of the resulting composite membranes not only depend on the nature of the ionomer and the solid used, but also on the amount, homogeneous dispersion, size and orientation of the solid particles dispersed in the polymeric matrix. Indeed, it is well known that one of the major issue that is encountered in the dispersion of metal oxide particles in a polymer matrix is their aggregation in clusters, more or less large, which cause obstruction in the hydrophilic pores at the water mobility, and thus to the protons[117, 118]. In addition, since the proton-conduction pathway for many inorganic materials is across the surface rather than through the bulk, proton-conductivity tends to increase as the particle size is reduced. Moreover, the presence of finely divided inorganic particles also contributes to inhibiting direct permeation of reaction gases by increasing transport pathway tortuosity, by the possible interaction of diffusing species with the surface of the inorganic phase and by a molecular size exclusion effect in a porous arrangement[119]. From the above, it appears clear the importance to develop an effective procedure for the preparation of highly homogeneous composites, where the fillers particle in nanometric scales are successfully dispersed in the polymer matrix.

In addition to the above discussed aspects, particular mention should be made for the preparation of composites membranes containing 2D-layered materials as fillers. Indeed, depending on the strength of interfacial interactions between the polymer matrix and the inorganic materials, three different types of nanocomposites are thermodynamically achievable, as shown in Figure 16: (1) conventional composites,

where packages of silicate layers, keep their stacking, creating a conventional phase separated composite (microcomposite), (2) intercalated nanocomposites, where the polymer chains are intercalated between the silicate layers, therefore increasing their gallery height but maintaining their layered stacking, resulting in a well ordered multilayer with alternating polymer/silicate layers, (3) exfoliated nanocomposites, in which the individual clay layers lose their stacking and are exfoliated and dispersed in the continuous polymeric matrix[120]. The conventional procedures to prepare these nanocomposites include: i) solution[121, 122], ii) melt intercalation[123], where the polymer intercalate to the interlayer space from solution or melt respectively and iii) in situ polymerization[124], where the polymerization is started inside of the filler galleries. Despite the filler particles have found to have nanometric size in two of the three different nanocomposites, the fully exfoliation of the filler has been proven to confer the best mechanical and transport properties.

During this PhD thesis, nanodispersed and/or fully exfoliated fillers, incorporated into the polymeric matrix, have obtained easily and effectively by solution intercalation[125].

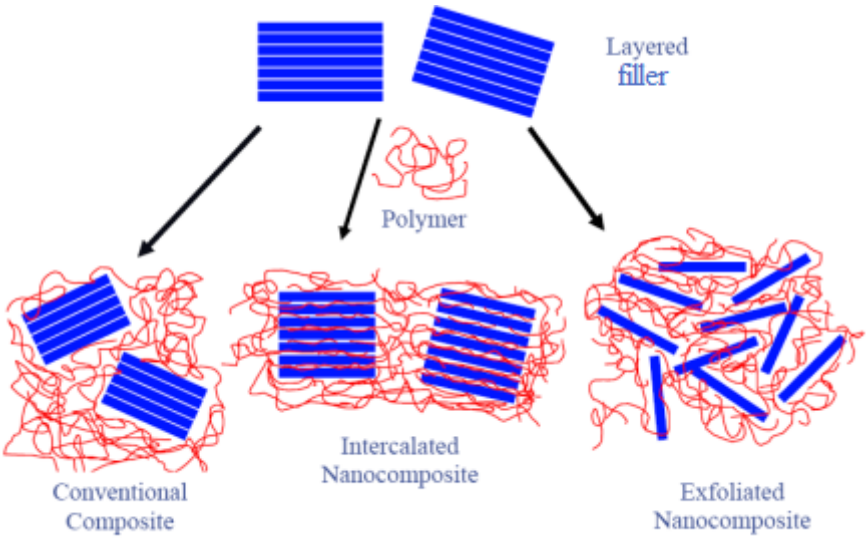

Figure 16. Schematic illustration of the three types of filler-polymer composites: conventional composites (or microcomposites), intercalated nanocomposites and exfoliated nanocomposites.

Accordingly, Nafion hybrid membranes were prepared by solvent casting method[126] by dispersing the fillers in a Nafion solution.

Depending on the nature of the filler, DMF or directly the hydroalcoholic solution of commercial Nafion has been used as solvents. The resulting dispersion is ultrasonicated for 1 day, and stirred for another day until a clear solution-like is obtained. After that, the dispersion is cast on a petri disk at 60 °C overnight to remove the solvents. The hybrid membranes is removed from the petri disk by immersing the glass plate in deionized water for several minutes. To reinforce the membrane, it is sandwiched and pressed between two Teflon plates and placed in an oven at 150 °C for about 15 min. All the membranes prepared are subsequently treated by rinsing in: 1) boiling HNO_3 solution (1 M) for 1 h to oxidize the organic impurities, 2) boiling H_2O_2 (3 vol%) for 1 h to remove all the organic impurities, 3) boiling in deionized water for 40 min three times, 4) boiling H_2SO_4 (0.5 M) for 1 h to remove any metallic impurities, and again 5) boiling in deionized H_2O for 40 min twice to remove excess acid. According to MacMillan et al.[127] an additional purification procedure was performed to ensure the removal of paramagnetic contaminants, which are particularly damaging to NMR experiments, such as the presence of copper that we found by electron paramagnetic resonance analysis. By this procedure membranes are soaked in ethylenediaminetetracetic acid (EDTA) solution (0.001 M) for 1 day followed by a thorough rinse. Then, they are soaked in HCl (2M) at 80 °C for 2 h followed by boiling in freshly distilled–deionized water to remove any residual acids, and the treatment with EDTA was repeated. Finally, rinsing in boiled deionized water is carried out three times to remove residual EDTA and the membranes are stored at room temperature in the fully hydrated state.

Detailed descriptions of the preparation procedure for each membrane prepared during this doctoral work are available in the respective papers in the appendix to the thesis.

References

[1] Geim K, Novoselov KS. *Nat. Mater*. **2007**, 6, 183.

[2] Brumfiel G. *Nature* **2009**, 458, 390.

[3] Novoselov K. S, Geim, AK, Morozov SV, Jiang D, Zhang Y, Dubonos SV, Grigorieva IV, Firsov AA. *Science* **2004**, 306, 666.

[4] Streitwieser A, Heathcock CH, Kosower EM. *Introduction to Organic Chemistry*, 4th Edition, Macmillan Publishing Company, New York, **1992**, Ch. 1 and 2.

[5] Chung DDL. *J Mater Sci* **2002**, 37, 1475–1489.

[6] Kroto HW, Heath JR, O'Brien SC, Curl RF, Smalley RE. *Nature* **1985**, 318, 162–163.

[7] Kroto HW, Allaf AW, Balm SP. *Chem Rev* **1991**, 91, 1213–1235.

[8] Rao CNR, Seshadri R, Govindaraj A, Sen R. *Mater Sci Eng R* **1995**, 15, 209–262.

[9] Iijima S. *Nature* **1991**, 354, 56–58.

[10] Boehm H.P., Clauss A., Fischer G.O., Hofmann U. *Chemie* **1962**, 316(3–4), 119–127.

[11] Stoller MD, Park S, Zhu YW, An J, Ruoff RS. *Nano Lett.* **2008**, 8, 3498.

[12] Novoselov KS, Geim AK, Morozov SV, Jiang D, Katsnelson M. I, Grigorieva IV, Dubonos SV. Firsov AA. *Nature* **2005**, 438, 197.

[13] Bunch JS, Verbridge SS, Alden JS, van der Zande AM, Parpia JM, Craighead HG, McEuen PL. *Nano Lett*. **2008**, 8, 2458.

[14] Lee C, Wei X, Kysar JW, Hone J. *Science* **2008**, 321, 385.

[15] Balandin AA, Ghosh S, Bao WZ, Calizo I, Teweldebrhan D, Miao F, Lau CN. *Nano Lett.* **2008**, 8, 902.

[16] Zhao L., Zhao F., Zeng B. *Electrochim. Acta* **2014**, 115, 247.

[17] Zhao Y., Huang Y., Wang Q. *Ceram. Int.* **2013**, 39, 6861.

[18] Zeng Y., Zhou Y., Kong L., Zhou T., Shi G. *Biosens. Bioelectron.* **2013**, 45, 25.

[19] Li R., Liu L., Yang F. *Chem. Eng. J.* **2013**, 229, 460.

[20] Sayyar S., Murray E., Thompson B.C., Gambhir S., Officer D.L., Wallace G.G. *Carbon* **2013**, 52, 296.

[21] Layek R.K., Nandi A.K. *Polymer* **2013**, 54, 5087.

[22] Bourlinos A. B., Gournis D., Petridis D., Szabó T., Szeri A., Dékány I. Langmuir **2003**, 19, 6050.

[23] Wissler M. *J. Power Sources* **2006**, 156, 142–150.

[24] Brodie B. C. *Philos. Trans. R. Soc. London* **1859**, 149, 249–259.

[25] Staudenmaier L. *Ber. Dtsch. Chem. Ges.* **1898**, 31, 1481–1487.

[26] Hummers W. S., Offeman R. E. *J. Am. Chem. Soc.* **1958**, 80, 1339.

[27] Lakshminarayanan P. V., Toghiani H., C.U.P. Jr. *Carbon* **2004**, 42, 2433–2442.

[28] Cotton F. A., Wilkinson G., Murillo C. A., Bochmann M. *Advanced Inorganic Chemistry*, Wiley India, Singapore, **200**4.

[29] Troömel M., Russ M. *Angew. Chem.* **1987**, 99, 1037–1038.

[30] Compton O. C, Nguyen S. T. *Small* **2010**, 6, 711.

[31] Dreyer DR, Park S, Bielawski CW, Ruoff RS. *Chem. Soc. Rev.* **2010**, 39, 228.

[32] Lerf A, He HY, Forster M, Klinowski J. *J. Phys. Chem. B* **1998**, 102, 4477.

[33] Eda G, Chhowalla M. *Adv. Mater.* **2010**, 22, 2392.

[34] Lui CH, Liu L, Mak KF, Flynn GW, Heinz TF. *Nature* **2009**, 462, 339

[35] Elias DC, Nair RR, Mohiuddin TMG, Morozov SV, Blake P, Halsall MP, Ferrari AC, Boukhvalov DW, Katsnelson MI, Geim AK, Novoselov KS. *Science* **2009**, 323, 610.

[36] Eda G, Mattevi C, Yamaguchi H, Kim H, Chhowalla M. *J. Phys. Chem. C* **2009**, 113, 15768.
[37] Schniepp HC, Li JL, McAllister MJ, Sai H, Herrera-Alonso M, Adamson DH, Prud'homme RK, Car R, Saville D. A, Aksay IA. *J. Phys. Chem. B* **2006**, 110, 8535.
[38] Bissessur R, Scully SF. *Solid State Ionics* **2007**, 178, 877.
[39] Mattevi C, Eda G, Agnoli S, Miller S, Mkhoyan KA, Celik O, Mastrogiovanni D, Granozzi G, Garfunkel E, Chhowalla M. *Adv. Funct. Mater.* **2009**, 19, 2577.
[40] Alonso R. H., Estevez L., Lian H. Q., Kelarakis A., Giannelis E. P. *Polymer* **2009**, 50, 2402.
[41] Nicotera I., Enotiadis A., Angjeli K., Coppola L., Gournis D. *International Journal of Hydrogen Energy* **2012**, 37, 6236.
[42] Chang J.H., Park J.H., Park G.-G., Kim C.-S., Park O.-O. *J. Power Sources* **2003**, 124, 18–25.
[43] Wang J., Merino J., Aranda P., Galvan J.-C., and H.-R. E. *J. Mater. Chem.* **1998**, 9 161.
[44] Giannelis E., Krishnamoorti R., Manias E., edited by S. Granick, et al. (*Springer* Berlin/Heidelberg, **1999**, Vol. 138, p. 107.
[45] Grim RE, Kulbicki G. *Am. Miner.* **1961**, 56, 1329-1369.
[46] Gournis D., et al. *Journal of the American Chemical Society* **2006**, 128, 6154.
[47] Petridis D., Bakas T., Simopoulous A., Gangas N. H. J. *Inorganic Chemistry* **1989**, 28, 2439.
[48] Balandin A.A., Ghosh S., Bao W., Calizo I., Teweldebrhan D., Miao F., Lau C.N. *Nano. Lett.* **2008**, 8, 902.
[49] Lee C., Wei X., Kysar J.W., Hone J. *Science* **2008**, 321, 385.
[50] Ajayan P.M. *Chem. Rev.* **1999**, 99, 1787.
[51] Bethune D.S., Kiang C.H., Devries M.S., Gorman G., Savoy R., Vazquez J., Beyers R. *Nature* **1993**, 363, 605.
[52] Iijima S. *Nature* **1993**, 363, 603.
[53] Dresselhaus MS, Dresselhaus G, Eklund PC. *New York: Academic Press*, **1996**.
[54] Paradise M., Goswami T. *Mater. Des.* **2007**, 28, 1477.
[55] Bandaru P.R. *J. Nanosci. Nanotechnol*. **2007**, 7, 1239.
[56] Tans SJ, Verschueren AR, Dekker C. *Nature* **1998**, 393(6680), 49–52.
[57] Tans SJ, Devoret MH, Dai H, Thess A, Smalley RE, Geerlings LJ, Dekker C. *Nature* **1997**, 386(6624), 474–7.
[58] Iijima S. *Physica B* **2002**, 323, 1.
[59] Guo T., Nikolaev P., Thess A., Colbert D.T., Smalley R.E. *Chem. Phys. Lett.* **1995**, 243, 49.
[60] Ebbesen TW, Ajayan PM. *Nature* **1992**, 358, 220–222.
[61] Chen B., Parker G., Han J., Meyyappan M., Cassell A.M. *Chem. Mater.* **2002**, 14, 1891.
[62] Hafner J.H., Bronikowski M.J., Azamian B.R., Nikolaev P., Rinzler A.G., Colbert D.T., Smith K.A., Smalley R.E. *Chem. Phys. Lett.* **1998**, 296, 195.
[63] Zheng F., Liang L., Gao Y., Sukamto J.H., Aardahl C.L. *Nano Lett.* **2002**, 2, 729.
[64] Liu J, Rinzler AG, Dai H, Hafner JH, Bradley RK, Boul PJ, et al. *Science* **1998**, 280, 1253–6.
[65] Chen J, Hamon MA, Hu H, Chen Y, Rao AM, Eklund PC, et al. *Science* **1998**, 282 95–8.
[66] Hamon MA, Chen J, Hu H, Chen Y, Itkis ME, Rao AM, et al. *Adv Mater* **1999**, 11(10), 834–40.
[67] Georgakilas V, Kordatos K, Prato M, Guldi DM, Holzinger M, Hirsch A. *J Am. Chem Soc* **2002**, 124(5), 760–1.

[68] Bahr JL, Yang JP, Kosynkin DV, Bronikowski MJ, Smalley RE, Tour JM. J. Am Chem Soc 2001;123(27):6536–42.
[69] Lu M, Lau KT, Qi JQ, Zhao DD, Wang Z, Li HL. *J Mater Sci* **2005,** 40(13), 3545–8.
[70] Zhang W-D, Phang IY, Liu TX. *Adv Mater* **2006**, 18(1), 73–7.
[71] Soneda Y., Duclaux L., Beguin F. *Carbon* **2002**, 40, 965.
[72] Qian W., Liu T., Wang Z., Yu H., Li Z., Wei F., Luo G. *Carbon* **2003**, 41, 2487.
[73] Qingwen L., Hao Y., Yan C., Jin Z., Zhongfan L. *J.Mater. Chem.* **2002**, 12, 1179.
[74] Lagaly G. *Appl Clay Sci* **1999**, 15(1/2), 1–9.
[75] LeBaron PC,Wang Z, Pinnavaia TJ. *Appl Clay Sci* **1999**, 15(1/2), 11–29.
[76] Gournis D., Karakassides M.A., Bakas T., Boukos N., Petridis D. *Carbon* **2002**, 40, 2641–2646
[77] Tsoufis T., Jankovic L., Gournis D., Trikalitis P. N., Bakas T. *Mater. Sci. Eng. B* **2008**, 152 (1–3), 44–49.
[78] Cavani F, Trifirò F, Vaccari A. *Catal Today*. **1991,** 11, 173-301.
[79] Forano C, Hibino T, Leroux F, Taviot-GuéHo C. *Handbook of clay science.* Amsterdam: Elsevier; **2006**, 1019-128.
[80] Allman, R, Neues Jahrb. *Mineral.,* Monatsh. **1969**, 12, 544.
[81] Allman, R. **Chimia 1970**, 24, 99.
[82] O'Leary S, O'Hare D, Seely G. *Chemical Communications* **2002**, 1506–7.
[83] Miyata S. *Clays Clay Miner.* **1975**, 23, 369 212.
[84] de Roy A, Forano C, El Malki K, Besse JP. *Anionic Clays: Trends in Pillaring Chemistry*; Occelli, M. L. and Robson, H. E.; *Synthesis of Microporous Materials, 1. ed.*, New York, Van Nostrand Reinhold, **1992**, 2, 108-169.
[85] Das A, Costa FR, Wagenknecht U, Heinrich G. *European Polymer Journal* **2008**, 44, 3456–65.
[86] Costa FR, Wagenknecht U, Heinrich G. *Polymer Degradation and Stability* **2007,** 92, 1813–23.
[87] Peng D, Wei C, Baojun QU. *Progress in Natural Science* **2006**, 16, 573–9.
[88] Lopez T, Bosch P, Ramos E, Gomez R, Novaro O, Acosta D, Figueras F. *Langmuir* **1996**, 12, 189
[89] Roy DM, Roy R, Osborn EF. *Am. J. Sci.* **1953**, 251, 337.
[90] Khan AI, O'Hare D. *Journal of Materials Chemistry* **2002**, 12, 3191–8.
[91] Malki KE, Guenane M, Forano C, De Roy A, Besse JP. *Materials Science Forum* **1992**, 91–93, 171–6.
[92] Leroux F, Besse JP. *Chemistry of Materials*, **2001**, 13, 3507–15.
[93] Jones DJ, Roziere, *J. Adv. Polym. Sci.* **2008**, 215, 219–264.
[94] Einsla ML, Kim YS, Hawley M, Lee HS, McGrath JE, Liu B, Guiver MD, Pivovar BS. *Chem. Mater.* **2008**, 20, 5636.
[95] Wieser C. *Fuel Cells* **2004**, 4, 245.
[96] Alberti G, Casciola M, Pica M, Tarpanelli T, Sganappa M. *Fuel Cells* **2005**, 5, 366.
[97] Su Y-H, Liu Y-L, Wang D-W, Lai J-Y, Guiver MD, Liu B. *J. Power Sources* **2009**, 194, 206.
[98] Alberti G, Casciola M. *Annu. Rev. Mater. Res.* **2003**, 33, 129.
[99] Sahu AK, Selvarani G, Pitchumani S, Sridhar P, Shukla AK. *J. Electrochem. Soc.* **2007**, 154, B123.
[100] Baglio V, Di Blasi A, Aricò AS, Antonucci V, Antonucci PL, Serraino Fiory F, Licoccia S, Traversa E. *J. New Mater. Electrochem. Syst.* **2004**, 7, 275.

[101] Chalkova E, Fedkin MV, Wesolowski DJ, Lvov S. *J. Electrochem. Soc.* **2005**, 152, A1742.
[102] Hara S, Takano S, Miyayama M. *J. Phys. Chem. B* **2004**, 108, 5634.
[103] Hoffmann M.R., Martin S.T., Choi W., Bahnemann D.W. *Chem.Rev.* **1995**, 95(1), 69-96 ,.
[104] Toba M., Mizukami F., Niwa S., Sano T., Maeda K., Annila A., Komppa V. *J. Molec.Catal.* **1994**, 91(2), 277-289.
[105] Ward D.A, Ko E.I. *Ind. Eng. Chem .Res.* **1995**, 34(2), 421-433.
[106] Mahshid S., Askari M., Ghamsari M.S. *J.Mater.Process.Tech.* **2007**, 189(1-3), 296-300.
[107] Hanaor D.A.H., Sorrell C.C. *J. Mater. Sci* **2011**, 46, 855-874.
[108] Mauritz K.A., Jones C.K. *J. Appl. Polym. Sci.* **1990**, 40, 1401–1420.
[109] Wen J., Mark J.E. *Polym. J.* **1995**, 27, 492–502.
[110] Suryani Y.L.L. *J. Membr. Sci.* **2009**, 332, 121–128.
[111] Wang K., McDermid S., Li J., Kremliakova N., Kozak P., Song C.J., Tang Y., Zhang J.L., Zhang J.J. *J. Power Sources* **2008**, 184, 99–103.
[112] Jin Y.G., Qiao S.Z., Diniz da Costa J.C., Wood B.J., Ladewig B.P., Lu G.Q. *Adv. Funct. Mater.* **2007**, 17, 3304–3311.
[113] Thampan TM, Jalani NH, Choi P, Datta R. *J. Electrochem. Soc.* **2005**, 152, A316–A325.
[114] Aslan A., Bozkurt A. *J. Power Sources* **2012**, 217, 158–163.
[115] Hara S, Miyayama M. *Solid State Ionics* **2004**, 168, 111–116.
[116] Li C, Li M. *J. Raman Spectrosc.* **2002**, 33, 301–308.
[117] Adjemian K. T., Dominey R., Krishnan L., Ota H., Majsztrik P., Zhang T., Mann J., Kirby B., Gatto L., Velo-Simpson M., Leahy J., Srinivasan S., Benziger J. B., Bocarsly A. B. *Chem. Mater* **2006**, 18, 2238–2248.
[118] Mohammadi G., Jahanshahi M., Rahimpour A. *Int. J. Hydrogen Energy* **2013**, 38(22), 9387–9394.
[119] Mauritz KA. *Mater. Sci. Eng. C* **1998**, 6, 121.
[120] Ray SS, Okamoto M. *Progr Polym Sci* **2003**, 28, 1539.
[121] Thomassin J. M., Pagnoulle C., Caldarella G., Germain A., Jerome R. *Polymer* **2005**, 46, 11389.
[122] Georgakilas V., Bourlinos A., Gournis D., Tsoufis T., Trapalis C., Mateo-Alonso A., Prato M. *J. Am. Chem. Soc.* **2008**, 130, 8733.
[123] Jung D. H., Cho S. Y., Peck D. H., Shin D.R., Kim J. S. *J. Power Sourc* **2003**, 118, 205.
[124] Kim Y. S., Dong L. M., Hickner M. A., Pivovar B. S., McGrath J. E. *Polymer* **2003**, 44, 5729.
[125] Cele N, Ray SS. *Macromolecular Materials and Engineering* **2009**, 294, 719.
[126] Cohen B, Huppert D. *J. Phys. Chem. A* **2003**, 107, 3598.
[127] Pavlidou S, Papaspyrides CD. *Progress in Polymer Science*(Oxford) **2008**, 33, 1119.

SECTION III

RESULTS AND DISCUSSION

Improving Fuel Cell system reliability, performances, efficiency and cost is one of the main topic in the vast field of the so called "green energy". In the recent years, the development of high performance MEAs has been devoted increasing interest, due to the critical impact of such components on the performances of the FC system. Accordingly, during my PhD research, a series of novel nanocomposite membranes has been prepared and tested as polymer electrolyte for Fuel Cell applications.

In the framework of the Project NAMED-PEM "Advanced nanocomposite membranes and innovative electrocatalysts for durable polymer electrolyte membrane fuel cells", a PFSA membrane, i.e. Nafion®, and two polyaromatic polymers, such as sulfonated Polyether Ether Ketone (S-PEEK) and Polybenzimidazole (PBI), have been used as polymer matrices to design electrolytes with improved proton conductivity and water retention capability at high temperatures, and reduced methanol cross-over in the case of membranes for DMFCs. For this aim, 2D-layered material, i.e. Graphite Oxide (GO), Smectite Clays and Layered Double Hydroxides (LDHs), and hybrid organic-inorganic material, i.e. Clay-CNTs and sulfonated TiO_2, were evaluated as additives.

Beside the synthesis and the membrane preparations, an intense investigation of water and methanol molecular dynamics within the different electrolytes have been carried out. To this purpose, the study of the transport properties of the composite membranes

prepared, which is one of the key aspects in the evaluation of these materials[1-4], was mainly carried out by NMR spectroscopy. This techniques, whose principles are widely described in appendix at the end of this thesis, has universally recognized to be a powerful tool for the non-invasive investigation of the transport properties of polymeric membranes. For this purpose, during this PhD work, the Pulse-Field-Gradient NMR (PFG-NMR) method[5] has been extensively applied for the direct measurement of the self-diffusion coefficients of water and methanol, confined in swollen membranes, in a wide range of temperatures (20-130 °C). The results obtained, together with the analysis of the ^{1}H-NMR spectra have provided a general description of water and methanol behavior: how solvent molecules are shared in the polymer structure; how the presence of the nanofillers and their surface modifications affects molecular dynamics; the interactions between water molecules and hydrophilic groups present and, finally, a quantitative estimate of the hydration number, i.e. number of water molecules solvating the hydrophilic sites both in the maximum hydration regime and in quasi-dehydration conditions[6]. Spin-lattice relaxation times (T_1), measured via Inversion Recovery sequence, were also acquired as a function of temperature and solvent uptake. Additionally, through Electrical Impedance Spectroscopy (EIS) the proton conductivity as a function of temperature and relative humidity has been also measured for all the membranes prepared. Moreover, in order to investigate the effect of the filler on the mechanical properties of the electrolyte, Dynamic Mechanical Analysis (DMA) has been performed. Finally, both pristine materials (fillers and polymers) as well as the resulting nanocomposites were also characterized by a combination of X-ray diffraction, FTIR and Raman spectroscopies, thermal analysis (DTA/TGA) and scanning/transmission electronic microscopy (SEM and TEM respectively).

This PhD research, however, was not exclusively limited to the investigation of polymeric membranes for FC applications. Indeed, in the framework of collaborations with other research groups, NMR spectroscopy has also been applied for the study of polymer electrolyte, as well as other matrices, for a wide range of application. Within one of these collaborations, PFG-NMR technique has been used to study and understand the effect of the electrolytic solution concentration on the microstructure of Ion Exchange Membranes for Reverse Electrodialysis (RED) process.

The results of these studies have been published on scientific international journals and reported in appendix at this thesis. In this section, the most important results have been articulated in the following paragraphs and discussed:

3.1 Proton exchange membranes for Direct Hydrogen Fuel Cells

Hybrid fillers for Nafion-based nanocomposites

PBI-based electrolyte for High Temperature Fuel Cells

3.2 Nanocomposite membranes for Direct Methanol Fuel Cells

Effect of layered material on methanol crossover

sPEEK based electrolyte for DMFC

3.3 Ion Exchange Membranes for Reverse Electrodialysis

3.1 POLYMER ELECTROLYTE FOR DHFC

Proton Exchange Membrane Fuel Cells (PEM-FC), as extensively discussed in chapter 1.2, are promising candidates for efficient and environmentally benign concept for electrical power generation, especially for portable and automotive applications. The key core of current PEM-FC, the polymer electrolyte, is based on an expensive PFSA membranes (Nafion® by DuPont). Most of the key issues and shortcomings of the PFSA-based PEMFC technology, such as water management, CO poisoning, cooling and heat recovery, could be solved or avoided by developing alternative membranes with suitable ionic conductivity and stability up to 120-130 °C. Accordingly, during this PhD research, hybrid organic-inorganic fillers have been used for the preparation of Nafion® nanocomposite membranes with enhanced transport properties under drastic conditions, such as high temperatures and low water content. Additionally, PBI has also been investigated as alternative electrolyte for High Temperature Fuel Cells.

3.1.1 SWy-CNTs hybrids for Nafion-based nanocomposites (PAPER I)

Carbon nanotubes rooted on smectite layers, as well as the preparation procedure, have been deeply described in chapter 2.1.3. During my PhD work this material have been proposed as hybrid nanoadditives in order to provide outstanding functionalities to the resulting composite membranes by combining the features of both the clays and CNTs materials[7]. All the results of the experimental study are discussed in the **paper I**, recently submitted, and reported in the appendix to the thesis.

As already mentioned in the chapter, concerning the preparation of this hybrid nanomaterial, the amount of CNTs growth on the clays surfaces strongly depends from the reaction times in the CVD camera. Therefore, varying the time of exposition (15 min and 30 min) two aliquots of SWy-CNTs were collected.. The percentage of carbon yield was then estimated via Thermogravimetric analysis (TGA), by the following Equation (1)[8]:

$$\%\ yield = \frac{\text{weight loss (from 400 °C to 700 °C)}}{100-\text{weight loss}} \times 100 \qquad \text{(Eq. 1)}$$

TGA curves showed in Figure 1 for the two materials demonstrate the different percentage of CNTs' loading on smectite clays, explicitly the weight loss between 400 °C and 700 °C proves a percentage yield of 32% (Fig 2a) and 5% (Fig 2b), respectively.

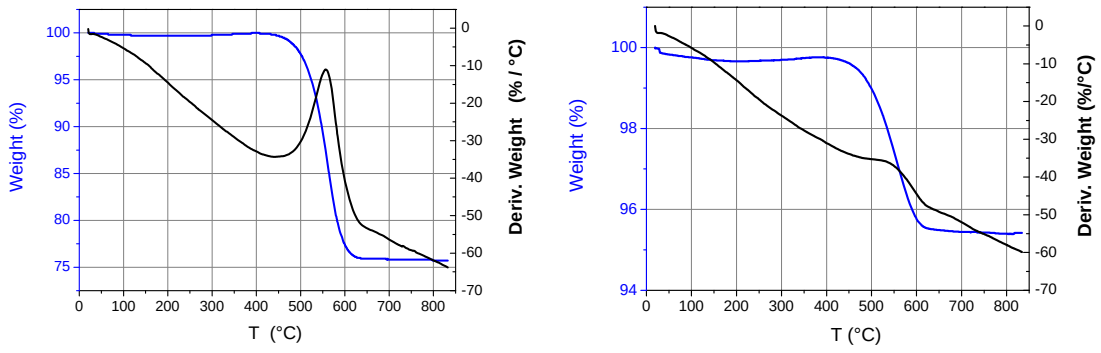

Figure 1. TG curves derived from SWy-CNTs with 32% (on the left) and 5% of yields (on the right).

Side-wall chemical oxidation and organo-functionalization of the CNTs was also performed using organic ester molecules containing hydrophilic groups (-RSO_3H). Accordingly, at the end of the procedure, three types of hybrid materials were collected: SWy-CNTs, SWy-oxCNTs and SWy-oxCNTs-RSO_3H.

Nanocomposite membranes were obtained by directly dispersion of the nanoadditives into the Nafion solution. The procedure developed by our laboratory for the preparation of Nafion composite membranes with carbon-based fillers[9], allows to obtain highly homogeneous films with an extraordinary nanodispersion of the additive, without formation of agglomerates or clusters. Nanocomposite membranes at 1 wt% of filler loading respect to the polymer were prepared for all the material synthesized. The composites with the functionalized CNTs were also prepared at higher loading, 2 wt% and 3 wt%, to investigate its effect.

For the investigation of the effect of the fillers added on the transport properties of water molecules confined in the porous structure of the Nafion-based membrane, the samples were first dried in a vacuum oven at 80 °C for 2h, and the dry mass (m_{dry}) has been measured. Membranes were thus immersed in distilled water at 30°C for 24 hours (m_{wet}).

The membrane water retention (uptake%) was calculated as:

$$\boldsymbol{uptake}_{\%} = \left[\frac{(\boldsymbol{m_{wet}} - \boldsymbol{m_{dry}})}{\boldsymbol{m_{dry}}}\right] \times \mathbf{100} \qquad \text{(Eq. 2)}$$

The water absorption ability of the composites respect to the filler free Nafion membrane is displayed in the histogram of Figure 2. As clearly appears, due to the hydrophobic character of CNTs, the presence of carbon nanotubes reduces the hydrophilic ability of the clay itself on which are grafted, so much that the composite, absorbs very low amount of water compared to the polymer recast. The oxidation and the subsequent functionalization, however, creates a highly hydrophilic material, and the composites can absorb almost 40% more water than the Nafion. The same trend observed for the water uptake behaviour can also be detected in the data of water self diffusion coefficients obtained on completely swelled membranes. It is well known, in fact, that the hydration degree is the main factor that governs the proton conductivity in

a polymer membrane, because the transport mechanism of the protons can occur through a diffusional mechanism or a "hopping" mechanism, related to its long-range and short-range mobility, respectively. The values of self-diffusion coefficients, directly measured by PFG technique, are showed in Figure 3. In the graph are reported the value obtained on hydrated membranes (at their maximum water uptake), in the temperature range 20-130 °C. For comparison, the data obtained on recast Nafion are also reported.

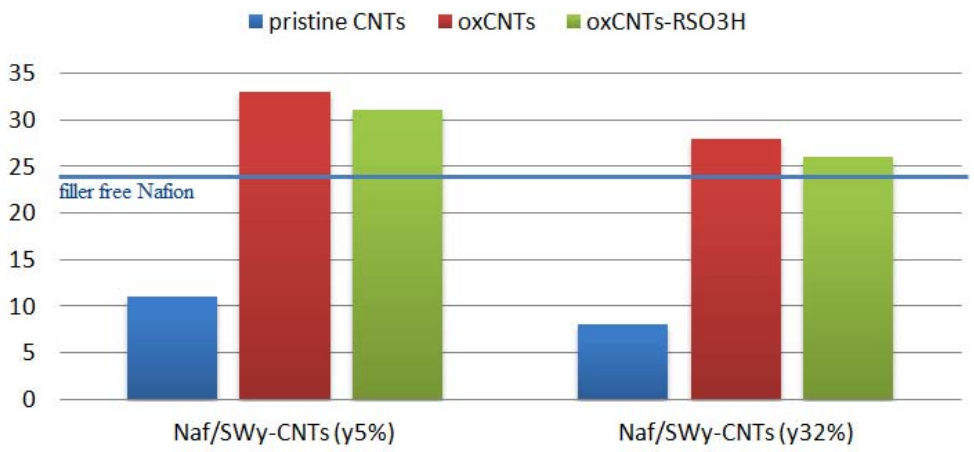

Figure 2. Water uptakes of the composites membranes.

As expected, while the SWy-CNTs additives strongly reduce the proton diffusion of the electrolytes, the oxidation of the CNTs surface, increasing the material's hydrophilicity (and thus of water uptake), lead to the improvement of water diffusion for membranes containing SWy-oxCNTs. In particular, remarkable is the behaviour of the diffusion at high temperatures. Whereas the recast Nafion exhibits a collapse of the diffusion, due to the well-known dehydration of this polymer above 80 °C, the composite membranes based on oxidized nanotubes and, even more, those organo-functionalized, are able to maintain high values of D, and this means that they can keep a certain amount of water of hydration capable of ensuring the proton transport, without any further humidification.

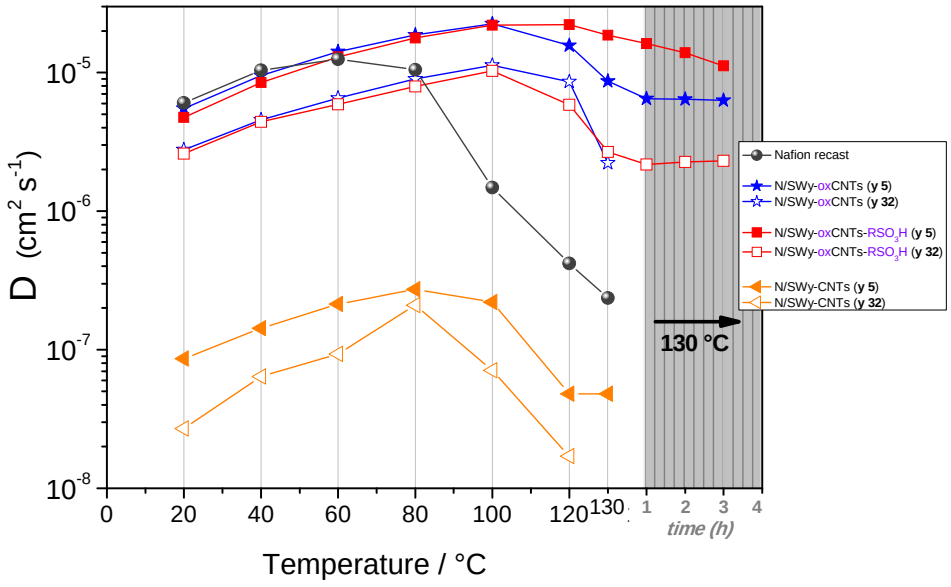

Figure 3. Self-diffusion coefficients as function of the temperature (from 20 °C up to 130 °C) of the water confined in recast Nafion and clay-CNTs composites membranes. In the graph are also plotted the data collected at 130 °C after several hours.

These interesting findings have found great feedback in the electrochemical investigation. Particularly outstanding are the results obtained on membranes containing the nanoadditives with lower yield of CNTs. In Figure 4 the proton conductivities measured in the temperature range from 30 °C up to 120 °C, and for three relative humidity conditions: 30%, 50% and 90%, have displayed. Respect to filler-free Nafion, both composites with oxidized and sulfonated CNTs demonstrate to have higher proton mobility and the difference is noteworthy as the operating conditions become more drastic, that are high temperatures and very low RH. For instance, at 120 °C and 30% RH, the Naf/SWy-oxCNTs-RSO_3H reaches a proton conductivity of **0.03 S cm^{-1}**. This is a very high value compared with composites reported in literature[10-13].

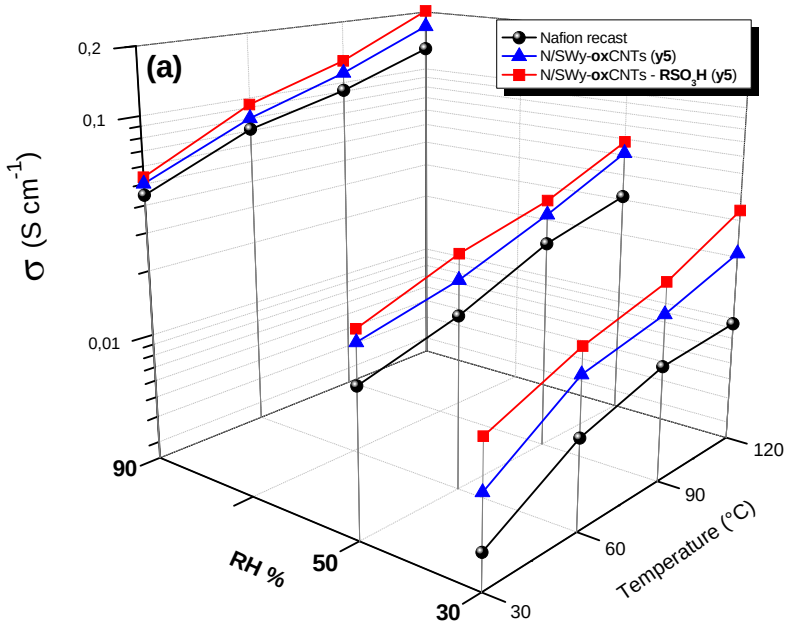

Figure 4. In-plane conductivities as a function of temperature and RH%, of three representative membranes: Nafion recast, Naf/SWy-oxCNTs (y5) and Naf/SWy-oxCNTs-RSO_3H (y5).

In "quasi-anhydrous" state of the membrane, the proton mobility can be ensured by a Grotthus-type mechanism, only if the correct network of interconnected acids sites is created inside the hydrophilic pores. This is what is expected from a material such as the one proposed, where long nanotubes (well distributed through the clay platelets), appropriately decorated with sulfonic groups, favour the formation of a network, through which protons can move.

Further details on the experimentals and on the all the results derived from this research are widely discussed in paper I reported in appendices at the thesis..

3.1.2 Nafion/Sulfated titania membranes for PEMFCs (PAPER II)

Sulfated-Titania nanoparticles has been evaluated as additive in composite Nafion-based membranes. Three different filler loadings, 2, 5 and 7%, respect to the polymer were comparatively investigated to elucidate the effect of the organic-inorganic particles on membrane peculiar properties and finally establish the most effective electrolyte composition. Membranes were thus equilibrated at three different water contents corresponded to the saturation condition (maximum membrane swelling), to a medium swelling of about 20 wt%, up to very low hydration condition, i.e. about 10 wt%, in order to explore the behaviour of each system and the effect of the nano-additive in the various hydration states. The analysis of the experimental results allowed the validation of a "***two sites model***" for the estimation of the number of water molecules involved in the hydration shell of the hydrophilic groups of both polymer and filler. Details are given in the **paper II** in the appendix to the thesis.

Sulfated titania nanoparticles used in this work demonstrated, despite to its strong acidity and hydrophilicity, a poorer performance if compared with the hybrid filler clay-CNTs seen before. This finding can be partially related to the agglomeration processes of the titania particles in the polymer matrix and consequent membrane inhomogeneity. However, it suggests that the configuration of the composite plays a key role in fuel cell performance of the membrane. In fact, mass transport in the electrolyte strongly depends on the structure at the molecular level, which determines the electrostatic interactions and the way in which ionic groups aggregate within the polymer network to form the clusters. Based on this, a one dimensional system like a CNT, homogeneously decorated acid groups, behaves very differently from the ceramic filler when dispersed in the polymer because it could interact and modify the polymeric network structure.

In any case, a great improvement respect to the filler-free Nafion in the region of high temperatures, and in particular for very low humidity condition was achieved, as we can see from the diffusion data reported in Figure 5. The data of diffusion coefficients for

recast Nafion and a representative nanocomposite membrane (M5) have been shown as a function of the temperature and the water content. In recast Nafion, a brusque drop of the water mobility of almost two order of magnitude, starting already at 60-80 °C, can be observed. Furthermore, when the water content is very low (10 %), over 100 °C the proton signal is insufficient to perform diffusion measurements while, in the composites the diffusion remain high, without any appreciable differences respect to the filler loadings. From the figure it is also clearly visible as at 130 °C the values of the diffusion coefficients to different water uptake (*wu*) converge to a value almost identical.

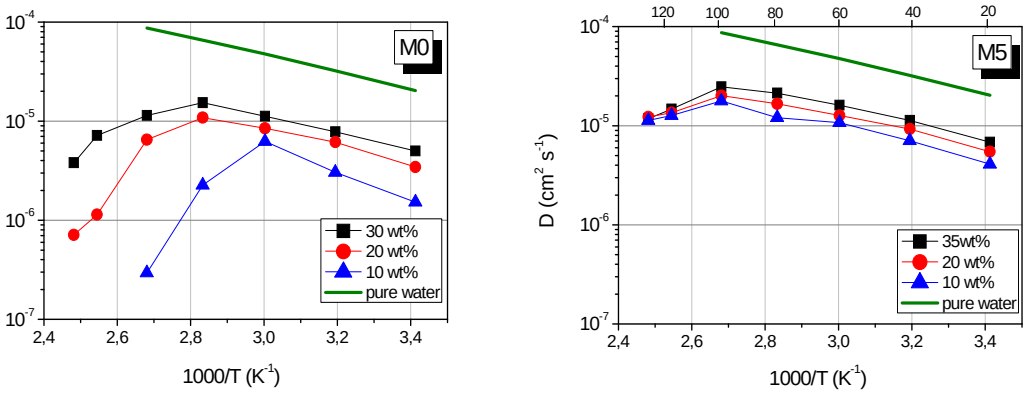

Figure 5. Arrhenius plot of the ^{1}H self diffusion coefficients of water in filler-free Nafion and a representative Nafion composites membranes (M5) swelled at three water uptake (saturation, 20 wt% and 10 wt%), in the temperature range 20-130 °C. The pure-water diffusion coefficients are also plotted.

To investigate and fully characterize the nature of water dynamics and the state(s) of the water (bound and free states) as well as its interaction with the hydrophilic polymer sites and particles surface, self-diffusion coefficients data and proton spectra were interpreted in terms of a simple "two-sites" model involving the exchange between relatively bound water and free water sites.

It is well known, in fact, that water molecule diffusion in presence of macromolecules is hampered by both the need to divert around macromolecules (obstruction effect) and any interactions with the same macromolecules that inhibit their motion (solvation or

hydration), i.e. molecules are in the "bound state"[14, 15]. According to "bound water/free water exchange" representation[15-17], we can assume that water molecules exist as "free" and "bound" water in rapid exchange compared with the NMR times involved in the experiment[18]. Due to this fast exchange, an averaged diffusion coefficient D is generally measured, which is a weighted sum of the diffusion coefficients of water molecules into bound- and free-state, as expressed by the Eq. 3:

$$D = (1-P)\, D_f + P\, D_b \qquad \text{(Eq. 3)}$$

where, D_f and D_b are the diffusion coefficients of free and bound water, respectively, while P is the molar fraction of the so-called bound water (water molecules involved in hydration of the acid groups present in the composite membrane).

Using our simple model to analyse the diffusion data is possible to determine the hydration number of the sulfonic groups, i.e. the water fraction in the bound state.

In fact, we know that the self-diffusion coefficient of free water confined in membranes is defined as $D_f = f\, D_0$, where D_0 is the diffusion of the pure water and f is the so-called obstruction factor. Furthermore, despite the evaluation of D_b is not an insignificant matter, it is generally assumed to be negligible compared to D_f and therefore approximated as zero. Accordingly, Eq. (3) simplifies to:

$$D \approx (1 - P) f \times D_0 \qquad \text{(Eq. 4)}$$

The obstruction factor reported in the formula is a geometrical parameter depending on the particular structure and on the translational freedom degrees of water molecules, and its value ranges between zero (no diffusion) and 1 (free state)[19-21], that is, by increasing the translational freedom degrees of the molecules, the obstruction factor tends to be close to unity. Based on geometrical assumptions, justified in accordance with the water-channel model proposed by Schmidt-Rohr and Chen[22, 23] for Nafion morphology in hydrated state, we were able to postulate an obstruction factor of about 0.92 (details are extensively reported in paper II). Therefore, by considering only the geometric confinement there would be a correction of only about 10% compared to free diffusion of water in bulk. This result is surely coherent for the observed water diffusion coefficient in Nafion.

From what above, the fraction of free water (1 – *P*) can now be easily calculated as:

$$(1 - P) \approx \frac{D}{f \times D_0} \qquad \text{(Eq. 5)}$$

with $f = 0.92$.

These *(1-P)* data were used to calculate both bound (χ_b) and free (χ_f) water molar fractions for all the swollen membranes by considering their initial uptake. The results are listed in Table 1. The water loss reported in the table has been calculated in accordance with the following Eq. (6):

$$\%water\ loss = \frac{free\ water(20°C) - free\ water(100°C)}{free\ water(20°C)} \times 100 \qquad \text{(Eq. 6)}$$

Table 1 - **Estimation of bound- and free-water fractions in membranes**

Membranes	***wu*** (%wt) ***at 20°C***	χ_f χ_b ***at 20°C***	χ_f ***at 100°C***	**Water loss**
M0	30	8.1 21.9	4.3	~ 47%
M2	32	9.5 22.5	8.6	~ 9.5%
M5	36	13.2 22.8	11.2	~ 15%
M7	34	12.3 21.7	10.5	~ 15%

From the values reported, it appears evident as the amount of bound-water is similar for all the membranes investigated; a little variation from its average value (ca. 22 %wt) has been observed. However, the water loss at 100 °C of the filler-free Nafion reaches almost the 50 %, while the composites retain more water, loosing no more than 15 % of their initial water uptakes.

By taking into account of the above data and the area of the spectral signals (see paper II for details), we attempted a quantitative analysis in order to estimate the number of

water molecules involved in the hydration shell of the sulfonic acid groups of Nafion polymer, as well as of the sulfate groups on the nanoparticles.

Table 2 reports a schematic description of the calculations executed, before on the filler-free Nafion membrane and then on one composite sample, i.e. M5 membrane.

Table 2: Water distribution and hydration numbers in M0 and M5 membranes

M0 *wu = 30 wt% → 16.7 mmoles of H_2O* $\left(= \frac{0.3\ gr}{18\ gr/moles}\right)$

At ***20 °C***, χ_b *=21.9 % [from Table 2]* $\Rightarrow$ ***12.2 mmoles*** $\left(= \frac{0.219\ gr}{18\ gr/moles}\right)$;

$$h_{SO_3^-} = \frac{12.2\ mmoles}{(0.9\ mmoles\ SO_3^-)} = 13.6\ \ H_2O/SO_3^-$$

At ***130 °C*** *[from normalized area of ^1H signal]* χ_b *= 6.45 %* $\Rightarrow$ ***3.59 mmoles*** $\left(= \frac{0.0645\ gr}{18\ gr/moles}\right)$

$$h_{SO_3^-} = \frac{3.59\ \ mmoles}{(0.9\ mmoles\ SO_3^-)} = 4\ \ H_2O/SO_3^-$$

M5 *wu = 36 wt% → 20 mmoles of H_2O* $\left(= \frac{0.36\ gr}{18\ gr/moles}\right)$

At ***20 °C***, χ_b *=22.8 % [from Table 2]* $\Rightarrow$ ***12.67 mmoles*** $\left(= \frac{0.228\ gr}{18\ gr/moles}\right)$;

$$h_{SO_3^-,SO_4^=} = \frac{12.67\ mmoles}{(0.9\ mmoles\ SO_3^-) + [(1.08\ \times 5\%)mmoles\ SO_4^=]} = 13.3\ \ H_2O/\ (SO_3^-, SO_4^=)$$

At ***130 °C***, *[from normalized area of ^1H signal]* χ_b *= 7.56 %]* $\Rightarrow$ ***4.2 mmoles*** $\left(= \frac{0.0756\ gr}{18\ gr/moles}\right)$

$$h_{SO_3^-,SO_4^=} = \frac{4.2\ mmoles}{(0.9\ mmoles\ SO_3^-) + [(1.08\ \times 5\%)mmoles\ SO_4^=]} = 4.4\ \ H_2O/\ (SO_3^-, SO_4^=)$$

The hydration numbers obtained by similar calculation for all the studied membranes have been found to be very similar between composites and recast Nafion; the hydration numbers are nearly to 13 H_2O/acid sites *mol/mol* in the maximum hydration state, and circa 4.5 H_2O/acid sites *mol/mol* in the very low hydration state. These values are found to be in a good agreement with those reported in literature[22-24].The application of the model to membranes equilibrated at different water content allowed the calculation of

the hydration numbers as a function of the solvent uptake. The results, shown in Figure 6, range between 8 and 10 at 20 wt%, and between 4.5 and 6 at 10 wt% of water content, respectively. This regular reduction of the number of water molecules hydrating the sulfonic/sulfate groups is expected by decreasing the dimension of the hydrophilic pores and, to date, these values are consistent with data reported in literature.

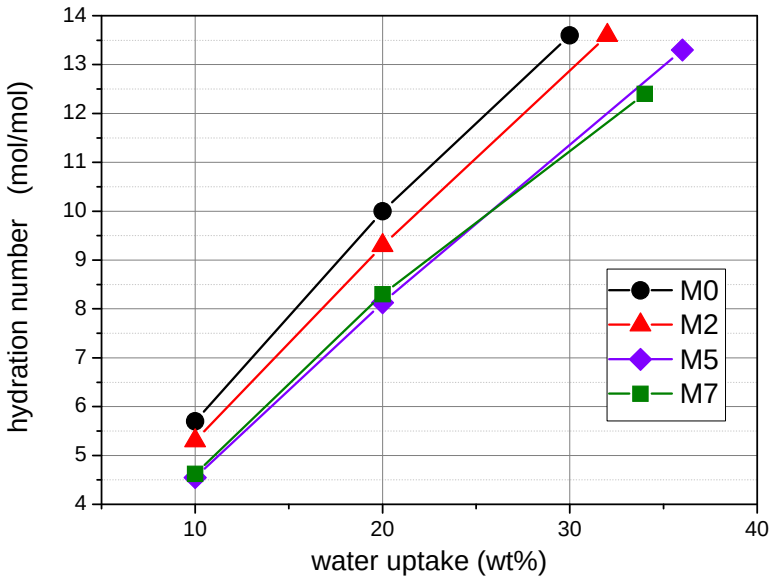

Figure 6. Hydration numbers calculated by the "two sites" model for all the membranes swelled at different water uptake at room temperature.

The results obtained are encouraging and indicate, therefore, that this relatively simple "two sites" model used to interpret the water diffusion data on pure Nafion and Nafion-composite membranes, was able to give a plausible description of the water distribution inside so complex systems.

3.1.3 PBI-based electrolyte for High Temperature PEM-FC (**PAPER III**)

One of the most fascinating challenge of the PEM fuel cell field is the development of polymer electrolyte suitable for high temperatures systems. Despite the efforts aimed to increase the operating temperatures of the PFSA-based PEMFCs, the obstacle deriving from the abrupt fall in proton conductivity at temperatures above 100 °C it has not been surmounted yet. In this scenario, phosphoric acid-Polybenzimidazole (PBI) complex seems to represent an interesting alternative electrolyte for the development of fuel cells able to work at temperature up to 200 °C and in dehydration state[25-28].

Monomer sulphonation is one of the strategies suggested to improve proton transport in these membranes. Accordingly, in the framework of the Project NAMED-PEM, membranes with increased number of sulfonic groups within the monomer structure have been prepared by Dr. Quartarone E. of the Department of Chemistry of the University of Pavia and INSTM. During this PhD research, a detailed NMR study on two sulfonated polymer electrolyte membranes, whose chemical structures have shown in Figure 7, has been conducted. To investigate the effect of the sulphonation on the proton dynamics and the mechanical properties of the membranes, the results obtained on modified membranes have been compared with those of poly(2,2'-m-(phenylene)-5,5'-bibenzimidazole) (PBI_5N), which we consider our reference matrix for fuel cell applications.

Prior to perform our NMR experiments, the membranes were doped with two different phosphoric acid concentrations, namely 50 and 70 wt%, and finally dried at 120 °C overnight to obtain the doping level, $N=n_{acid}/n_{mon}$. A deep investigation on both ^{1}H and ^{31}P nuclei was then carried out and the experimental results have been reported in paper III.

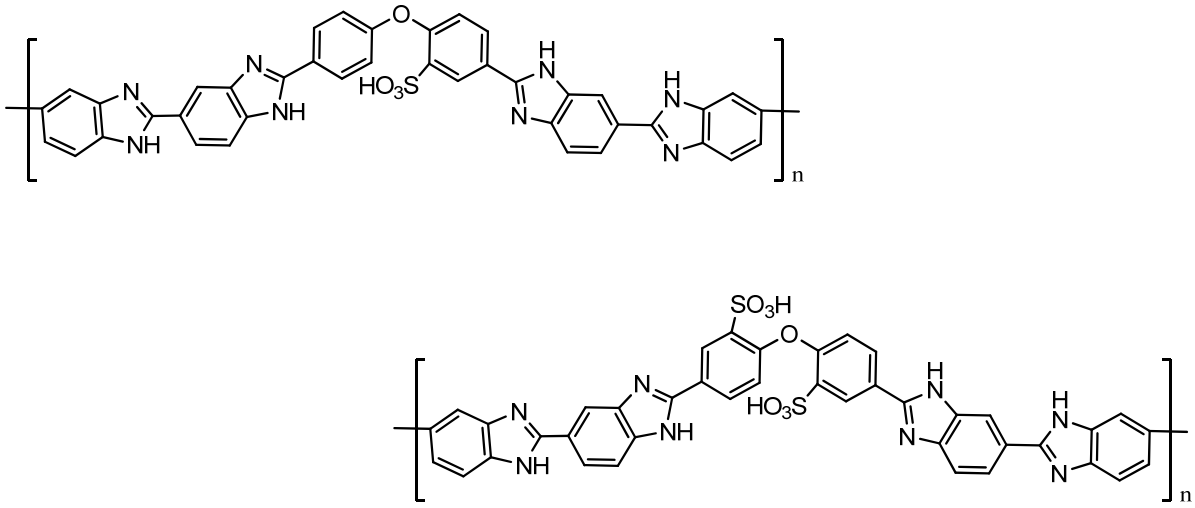

Figure 7. Illustration of the chemical structures of the polymers 2Θ-PBI-1SO_3H (top) and 2Θ-PBI-2SO_3H (down)

Figure 8 shows the Arrhenius plots of the ^1H self-diffusion coefficients measured on the membranes doped in a 50% solution of phosphoric acid. It appears evident as, in all the investigated temperatures, the proton diffusion in sulfonated membranes is slower than in pristine PBI_5N. This can be mainly to the fact that PBI_5N has found to absorbs a higher amount of acid than the 2Θ-PBI-1SO_3H and 2Θ-PBI-2SO_3H membranes, although in the sulphonated polymer should there be a higher hydration level due to -SO_3H groups. Besides, we have postulated that the presence of sulfonic groups could involve the formation of a greater cross-linking between the polymer chains, so resulting in a stiffer membrane: an higher rigidity implies more difficult segmental motions of the polymeric chains. The behaviour of the diffusion coefficients can now be interpreted as the effect of higher PA content and higher flexibility of the polymer chains in the PBI_5N sample, that favour the proton transport through a hopping-like mechanism.

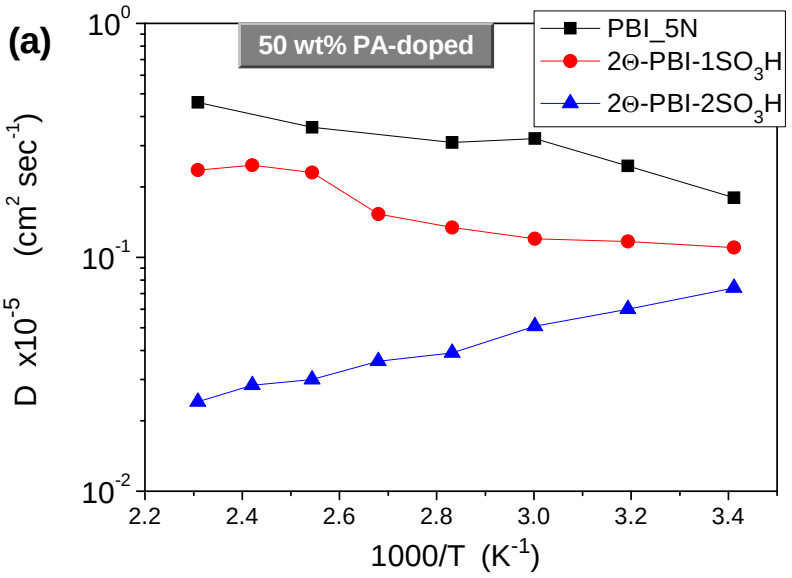

Figure 8. Arrhenius plot of the ^{1}H diffusion coefficients measured on the three membranes, PBI_5N, 2Θ-PBI-1SO_3H and 2Θ-PBI-2SO_3H, activated with 50 wt%

As mentioned, the mechanism expected for the proton diffusion is the Grotthuss one, which foresees a strong interaction among the H^+ ions and the lattice, i.e. with the phosphates and with active groups on the polymer. The analysis of the ^{1}H and ^{31}P spin-lattice relaxation times (T_1), deeply described in the paper III reported in appendices, allowed to confirm: i) a more efficient Grotthuss mechanism for PBI_5N membrane respect to both the sulfonated ones; ii) in the sulphonated membranes P nuclei do experience stronger interactions with the polymer than in the PBI_5N one, in agreement with the evidence of slower proton diffusion in the sulphonated membranes. This aspect became more evident during the analysis of the temperature evolution of the ^{31}P spectra, acquired on the three different membranes.

Figure 9 reports the ^{31}P spectra, acquired from 20 °C up to 160 °C, on the PBI_5N membrane activated with 50% PA concentration. The main peak at 0 ppm is due to orthophosphoric acid. The line width of this peak narrows as the temperature increases (see Figure 9b) because of the increased molecular mobility. Besides, the intensity of this peak increases up to about 100-120 °C, and then decreases in favor of the signals at -14 ppm and at -27 ppm, which are assigned to the condensation products of the H_3PO_4, i.e. pyrophosphates and trypoliphosphates (or metaphosphates), respectively[29].

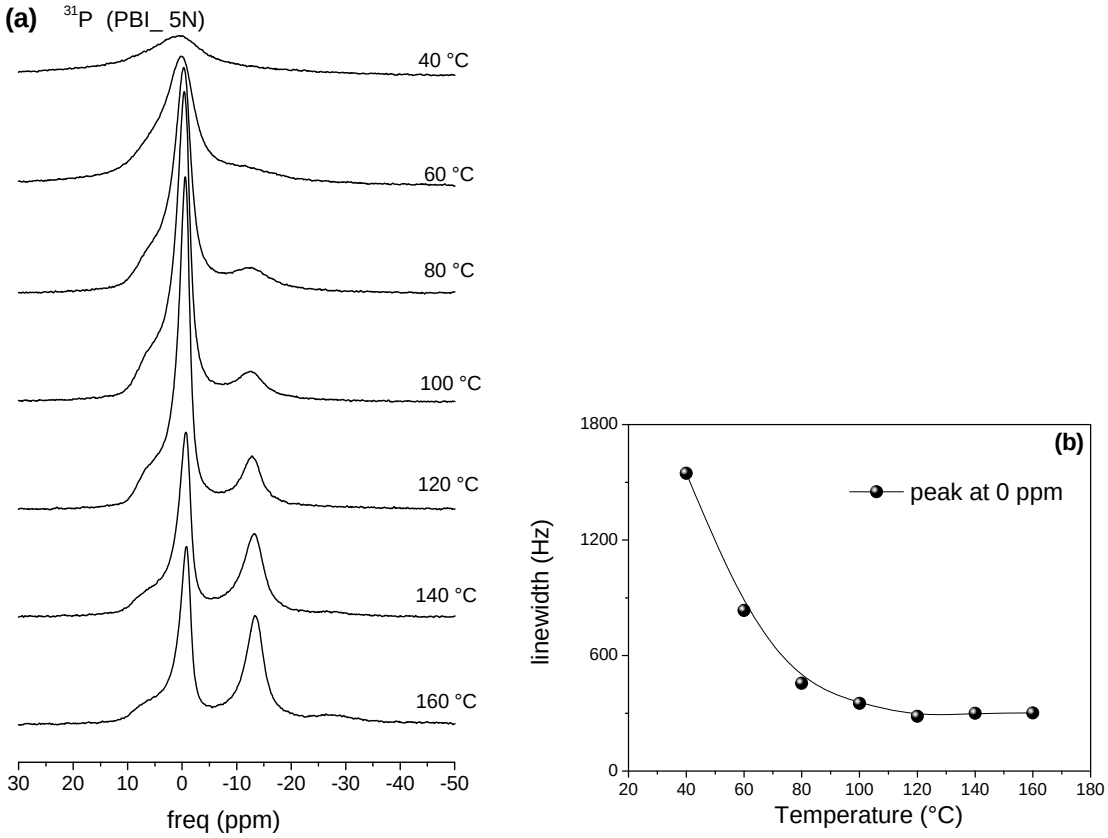

Figure 9. (a) Temperature evolution of the ^{31}P spectra, from 20°C up to 160°C, for the PBI_5N membrane activated with 50 wt% PA concentration. (b) Linewidth variations of the main peak (at 0 ppm) vs. temperature.

The ^{31}P spectra of the 2Θ-PBI-1SO_3H and 2Θ-PBI-2SO_3H, are slightly different from those of PBI_5N as we can see in the Figure 9. From the analysis of the spectra, it immediately emerges that for both sulfonated polymers the signal related to pyrophosphate species have a lower intensities than in PBI_5N. Besides, the signal with chemical shift ~5 ppm associated to phosphate molecules or anions interacting with the polymer backbone and that in the spectra obtained on PBI appeared only as a shoulder peak, here seems to be more relevant, indicating a lower mobility and/or higher disorder, and thus probably a stronger interaction. Finally, in the ^{31}P spectra obtained on both sulfonated membranes, there is no evidence of the signal at -27 ppm, due to tripolyphosphates (or metaphosphates). This is a clear indication of the fact that the presence of the sulphonic groups strongly reduce the possibility of H_3PO_4

polycondensation. Confirming the hypothesis previously drawn from the *D* and T_1 data about the stronger interactions of the PA molecules with the sulphonic groups, resulting in formation of interchain cross-links.

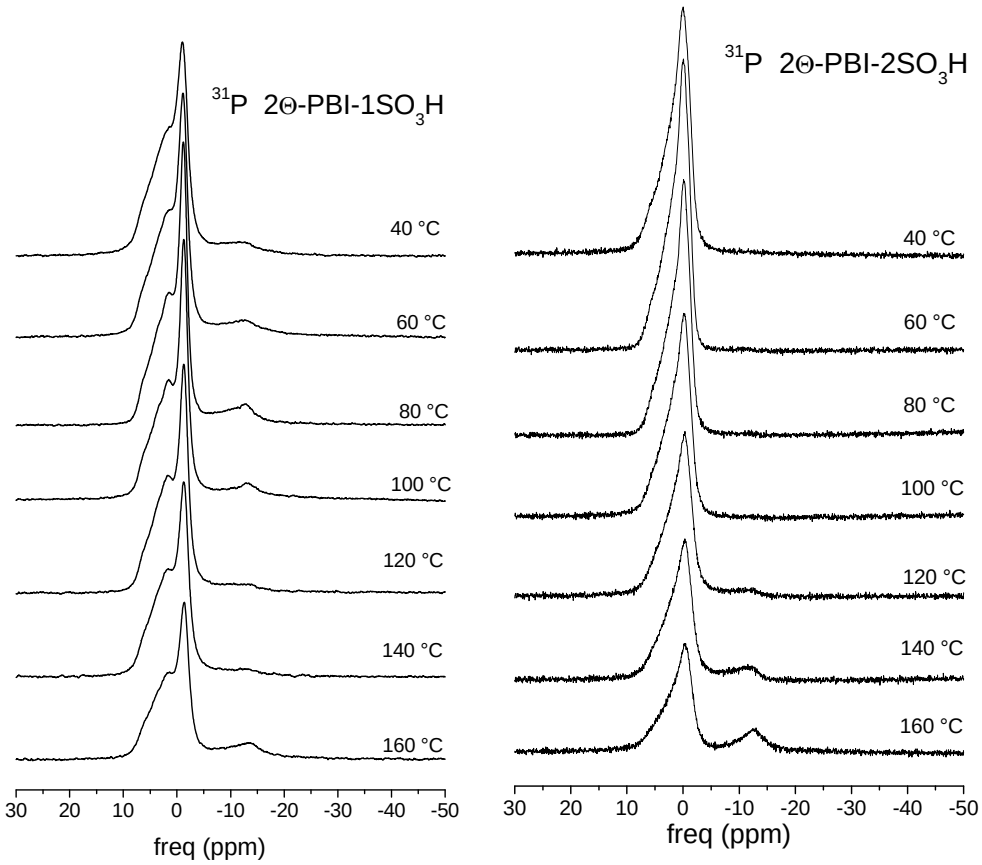

Figure 10. Temperature evolution of the 31P spectra, from 20°C up to 160°C, for 2Θ-PBI-1SO_3H (left), and 2Θ-PBI-2SO_3H (right) membranes activated with 50 wt% PA solution.

A further and final evidence about the veracity of our hypothesis was finally provided by the results obtained via Dynamic Mechanical Analysis. Figure 11, shows the evolution of the storage moduli versus temperature obtained on the membranes activated with 50 wt% PA. As is possible to see, both the sulfonated membranes exhibit higher moduli compared to the PBI_5N, and thus higher stiffness, as expected on the basis of the NMR findings. The presence of sulfonic groups does cause stronger intermolecular interactions among the polymeric chains, which in turn inhibits segmental motions.

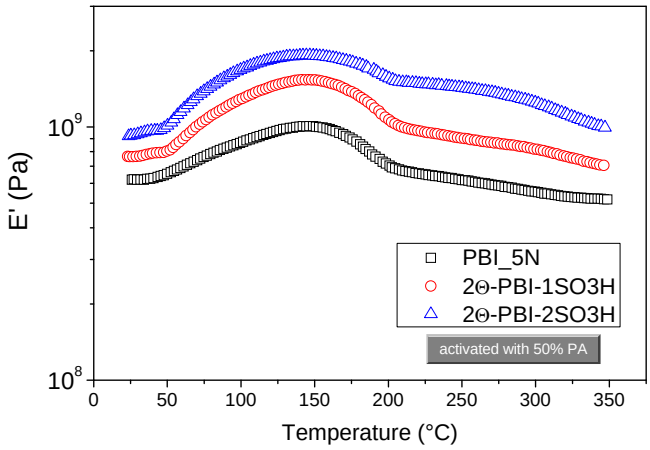

Figure 11. Storage moduli (E'), from 25 to 350 °C, obtained on the samples activated with 50% PA.

Both NMR and dynamic mechanical analysis studies of sulphonated PBI membranes for applications in polymer fuel cells demonstrated that sulphonation does increase the membrane stiffness by increasing the inter-chain crosslinks involving PA molecules and sulphonic groups. This, in turn, reduces the proton mobility with respect to PBI_5N, which is our PBI standard, where, the higher flexibility of the polymer chains favors the proton transport through a hopping-like mechanism.

3.2 NANOCOMPOSITE MEMBRANES FOR DMFC

In recent years, research is moving towards the development of high temperature DMFC systems. The direct methanol fuel cell (DMFC) is a promising alternative power source, for portable and auxiliary power unit applications[30, 31]. It combines the merits of direct hydrogen/air fuel cells with the advantages of a liquid fuel, such as convenient handling and high energy density. Despite these advantages, technical barriers still need to be overcome for their large scale commercialization of DMFCs[32]. DMFC operation at elevated temperatures increases, in fact, both methanol oxidation and oxygen reduction kinetics and simplify water and thermal management. To this purpose, the addition of a filler in the polymer matrix has been examined as possible strategy with the aim of exploiting the strong affinity between water molecules and hygroscopic additives[33-35]. In this case, the role of organic-inorganic filler is to improve the water retention in the membrane, allowing an increase of fuel cell operation temperature due to a suitable conductivity, and to reduce methanol cross-over, through a increased obstruction effect[36]. In fact, one of such technical barriers is the large methanol crossover that affect the performances of the PFSA-based DMFC. In an attempt to overcome this phenomenon, the barrier properties of several layered materials have been investigated. The presence of hydrophilic 2D platelike layers in the polymeric matrix, is of major interest due to the significant gains in thermal stability, mechanical and barrier properties of the resulting nanocomposites.[37]. These physical modifications of the ionic clusters could be exploited to reduce the methanol crossover through obstruction effect and increased tortuosity of the fuel diffusion path, though, for a similar mechanism, the proton conduction may also decrease.

For this purpose, based on the recent experience of my group of research[38], I have focused on three types of hydrophilic lamellar-type nanomaterials, for the development of hybrid membranes with improved suitable ionic conductivity, stability up to 130 °C and reduced methanol cross-over. Accordingly, Smectite Clays, Layered Double Hydroxile and Graphene Oxide have been disperded in Nafion matrix and their effect on water and methanol mobility into the nanocomposites characterized.

Besides, sulfonated PEEK and S-PEEK-based nanocomposites has also been evaluated for application in high temperature direct methanol fuel cells.

*3.2.1 Carbon-based layered materials in DMFC: a novel strategy to reduce the methanol crossover (**PAPER IV**)*

It has been proved that the dispersion of organo-modified GO into Nafion matrix lead to nanocomposite membranes with exceptional water retention capacity as well as improved mechanical and thermal resistance[9]. Therefore, the appropriate functionalization of GO surfaces with amino derivatives having terminal sulfonic acid groups, is expected to be an effective method to improve the proton transport by promoting the Grotthus-type mechanism, whereas the water "vehicular" transport mechanism, which strongly boosts the methanol crossover, may be reduced. In Figure 12 is reported a pictorial representation of the diffusion pathway of methanol molecules in three different nanocomposite membranes:

1) conventional composite membrane, where packages of layers keep their stacking; it is characterized by minimal limiting effect in the methanol diffusion and no major positive effects for the proton mobility[38, 39].

2) exfoliated nanocomposite where the exfoliation of the layers and their dispersion throughout the continuous polymeric matrix may significantly increase the obstructions for the methanol crossover;

3) exfoliated/aligned nanocomposite where the exfoliated platelets are orthogonally-oriented in respect to the diffusion path and the barrier effect could become noteworthy.

To this purpose, in my doctoral work, an amine derivative containing sulfonic functional end-group was covalently bonded via the amide functionality on the GO surfaces and the resulting organo-modified GO nanofiller was incorporated in Nafion by solution intercalation. In the resulting nanocomposite, graphene-based nanoadditives are completely exfoliated and an attempt to induce some preferential orientation to the GO_{SULF} lamellas in the polymer matrix was implemented by tuning the casting procedure of a very viscous dispersion.

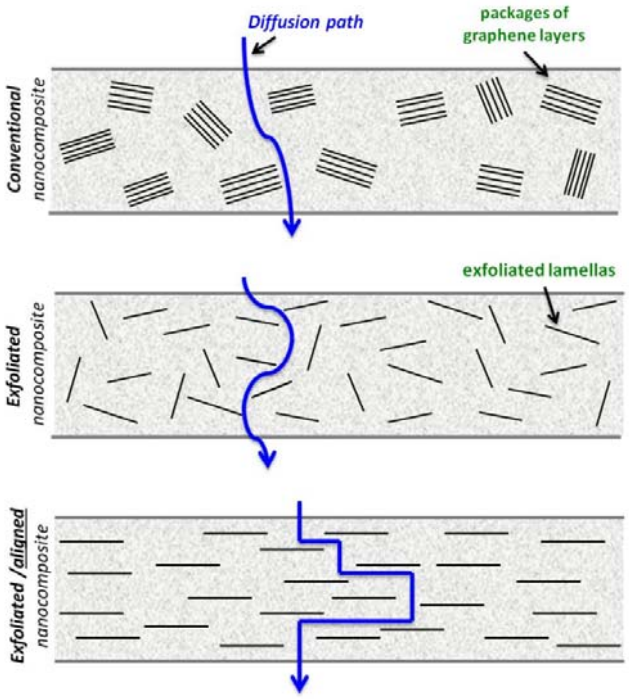

Figure 12. Representation of the diffusion pathway of methanol molecules through a conventional, exfoliated and exfoliated/aligned nanocomposite membrane, respectively.

The general procedure for the preparation of nanocomposite membranes has already been reported in chapter 2.2. The filler is first dispersed into the Nafion solution and by casting of the dispersion on a pretridish (*pd*) the nanocomposite membrane is obtained. However, in order to prepare "aligned" composites, a novel different casting procedures of the polymer dispersion were followed: a very viscous dispersion (after concentration of the initial dispersion) has been spread with a knife or doctor blade (*kn*) (Figure 13). The resulting membranes have been thus compared.

Figure 13. Casting procedures followed in order to prepare membranes: casting in a petridish (left) and spread with a knife (right).

The results of the XRD and morphological analysis, performed by SEM, TEM and AFM, confirmed that both casting procedures allowed the complete exfoliation and homogeneous dispersion of the filler within polymer (see paper IV for details).

In this context, particularly interesting are the results obtained during SEM investigation. SEM images of Naf/GO_{SULF}-*pd* and Naf/GO_{SULF}-*kn* membranes cross-section obtained by cryo-cleavage are shown in the Figure 14. As is possible to see from the images, the *kn*-membranes shows cleavage planes oriented parallel to their surface in the whole body. On the other hand, the cleavage planes in the *pd*-membranes have no preferential orientation. Moreover, the quantitative comparison of the dispersion angle of the membranes cleavage calculated for both membranes, and reported in Figure 14 (b) and (f): for *pd*-membrane there is not a preferential direction and the distribution appears almost isotropic, while the *kn*-membrane has a sharp distribution of the cleavage planes orientation.

Since the membranes differ only for the casting procedure, the result of this morphological analysis, directly related to the microstructure of the membranes, proves that apparently different morphologies of the composite membranes can be obtained by different casting procedures and a preferential direction is induced by the *knife*-casting procedure.

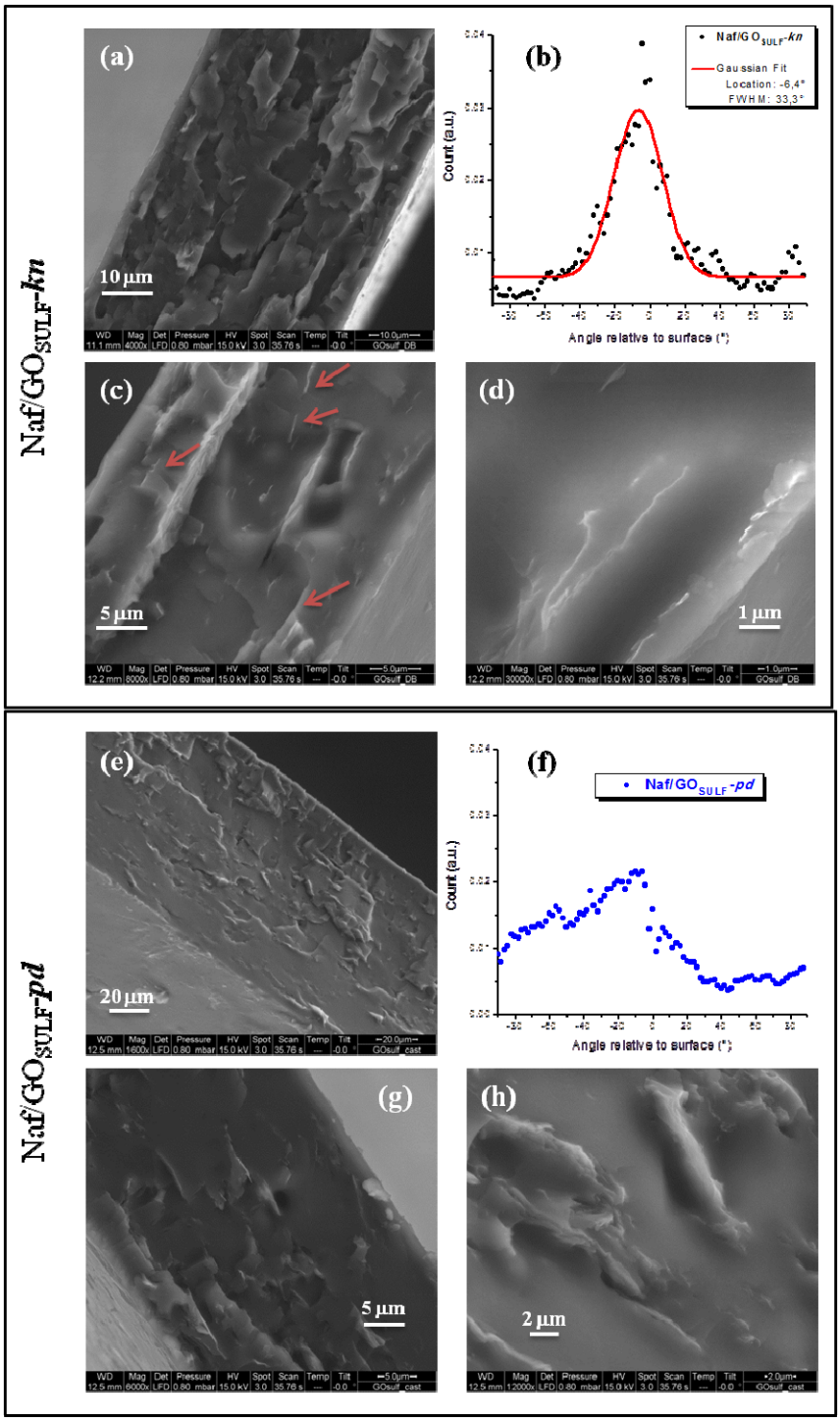

Figure 14. SEM images of the two Naf/GO$_{SULF}$-kn and Naf/GO$_{SULF}$-pd samples.

These differences in terms of morphology, have found partial empirical evidence in the results obtained by NMR investigation. First, it was found a significant difference concerning the amount of absorbed water in the two nanocomposites which is

appreciably lower in the *kn*-membrane respect to the membrane prepared by casting in petri dish (*pd*): 50 wt% and 27 wt%, respectively. However, the water self-diffusion coefficients showed in Figure 15, both for the nanocomposites and the filler-free Nafion (also it prepared by the two casting procedure), demonstrate that, independently from the procedure applied, the presence of the filler leads to composite membranes with outstanding water retention capacity, at high temperature and for several hours without any external humidification, and the difference is related to the water amount absorbed. For the filler free Nafion, the casting method does not affect the water diffusion.

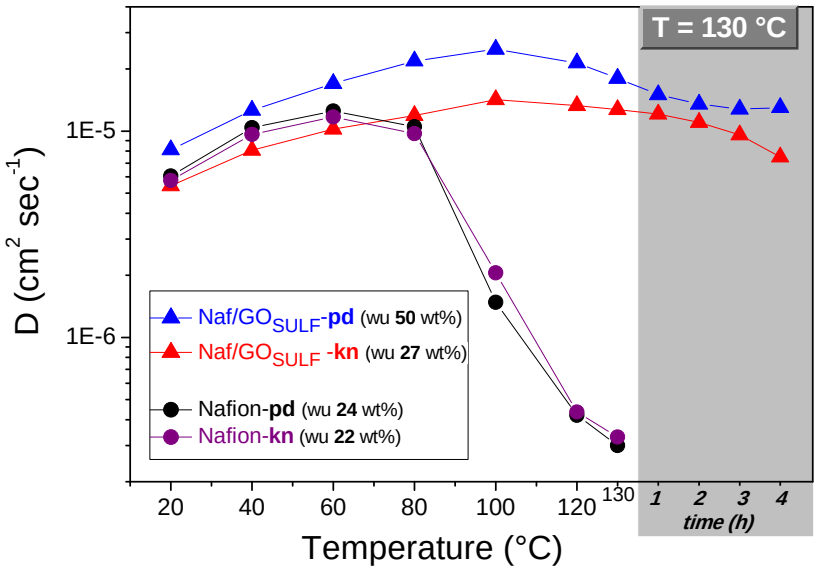

Figure 15. Water self-diffusion coefficients vs. temperature (from 20 °C up to 130 °C) in completely swelled membranes of Nafion filler-free and GO_{SULF}-nanocomposite. Samples prepared by casting in petridish (pd) and by knife (kn) are compared and the water uptake is reported in the legend. In the graph are also plotted the data collected at 130 °C after several hours.

In this scenario, the reduced water absorption, despite the same material has been dispersed in both nanocomposites, can be explained in terms of structural/morphological modification of the hydrophilic pores. On the basis of these observations, we verified the ability of these composite membranes to reduce the methanol diffusion in order to limit the crossover in the MEA, while maintaining high proton mobility.

It is well known that, due to the different distribution of methanol and water molecules in the hydrophilic domains of the polymer membrane[40, 41], in filler-free Nafion swelled in 2M solution the diffusion coefficients of methanol are higher than water, for temperature above 60 °C. The effect on water and methanol mobility of the incorporation of a layered filler in the polymeric matrix is shown in Figure 16 where the diffusion coefficients of water and methanol in 2 M solution are reported. In order to discriminate in the ^{1}H NMR spectrum between the proton signals coming from water or methanol, deuterated molecules, i.e. mixture of CH_3OD/D_2O and CD_3OD/H_2O for measuring methanol and water, respectively have been used[37, 45].

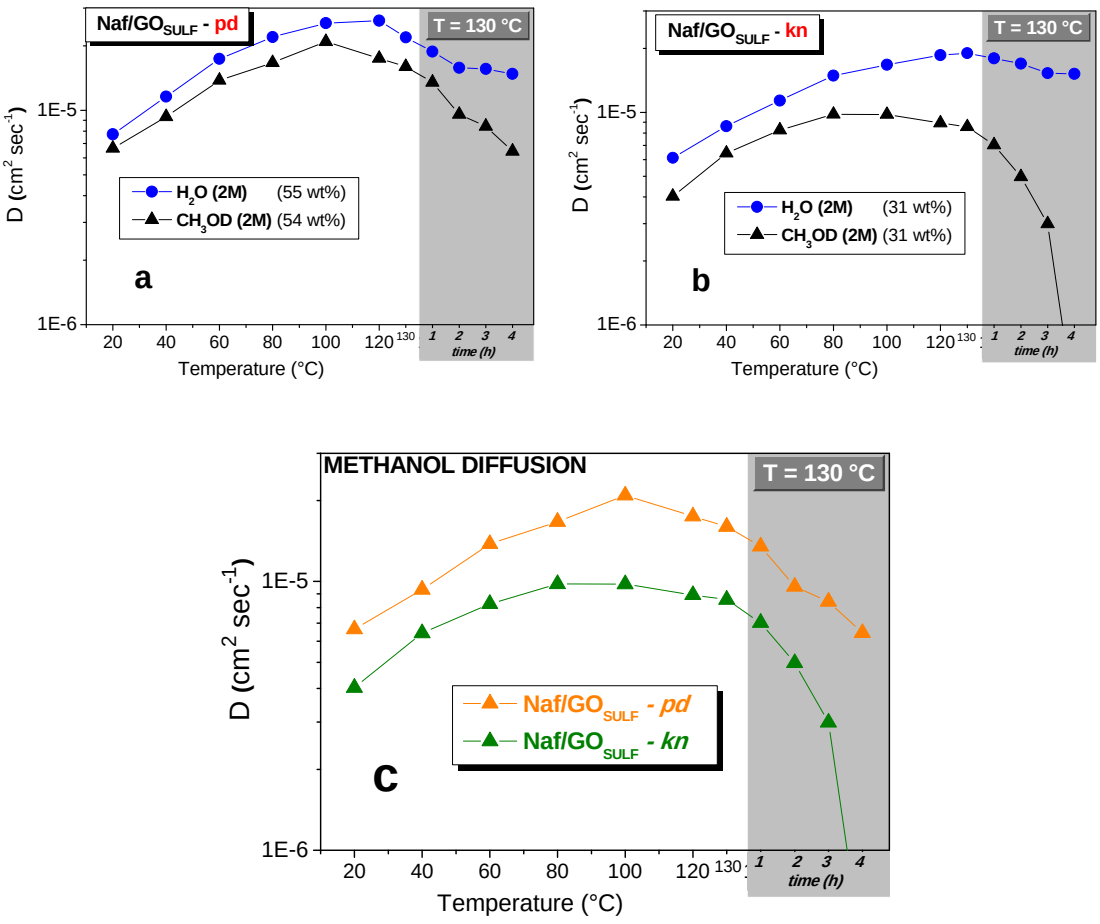

Figure 16. Self-diffusion coefficients of water and methanol in 2 M solution confined in Nafion-GO$_{SULF}$ nanocomposite membranes prepared by (a) pd and (b) kn, from 20 °C up to 130 °C. In the graphs are reported also the solution uptakes (wt%). The comparison of the methanol diffusion between the two membranes is shown in (c). In each graph the data collected at 130 °C after some hours are also plotted.

The graphs clearly demonstrate as water diffusion coefficients are higher than methanol ones in all the temperature range investigated, thus proving the beneficial blocking effect of the nanoparticles dispersed in the polymer: water diffusion in the composite membrane remains large likely due to the good retention capacity of the filler that boosts the proton transport by the Grotthus-type mechanism through the highly acid GO_{SULF} surfaces. Again, a large difference in the solution uptake must be underlined, about 55 wt% in GO_{SULF}-*pd* and about 31 wt% in GO_{SULF}-*kn*. Besides, the discrepancy between water and methanol diffusion is larger for the *kn*-sample and increases as the temperature increases. To emphasize the remarkable reduction of the methanol molecules mobility in the *kn*-membrane, in Figure 16c, a comparison between the diffusion coefficients of methanol in the two membranes has shown.

The experimental results support our hypothesis on a possible preferential orientation of the lamellae of GO in the polymer film driven by the casting procedure which induces (a) structural and morphological modification of the polymeric matrix and consequently of the hydrophilic domains, thus reducing the capability to absorb higher amount of water and/or solution; (b) an increase of the tortuosity of the diffusional paths of both water and methanol molecules.

Finally, this set of membranes has been subjected to electrochemical investigation. Figure 17 shows the polarization and power density curves obtained on the membrane-electrode assemblies (MEAs) based on the different membranes at two temperatures, 90 °C and 120 °C (Figure 17(a) and (b) respectively), feeding a 2 M methanol solution at the anode and oxygen at the cathode. The electrochemical analysis, as well as the NMR study, highlights and confirms the exceptional water retention properties at high temperatures of the organo-GO material dispersed in the polymeric matrix. In fact, the maximum power density of the DMFC equipped with both composite membranes of Naf/GO_{SULF} increases slightly with temperature, while there is a significant drop of performance of the filler-free Nafion-based cell.

The most remarkable aspect in this graph is however the variation of open circuit potential (OCP) for the cells based on the different membranes, an important parameter in order to assess the methanol permeability of a membrane. The OCP and the potential

at low current densities is higher for the cell equipped with Nafion/GO_{SULF}-*kn* membrane, confirming the blocking effect of the well-distributed particles towards methanol permeation, through an increase of the tortuosity pathway.

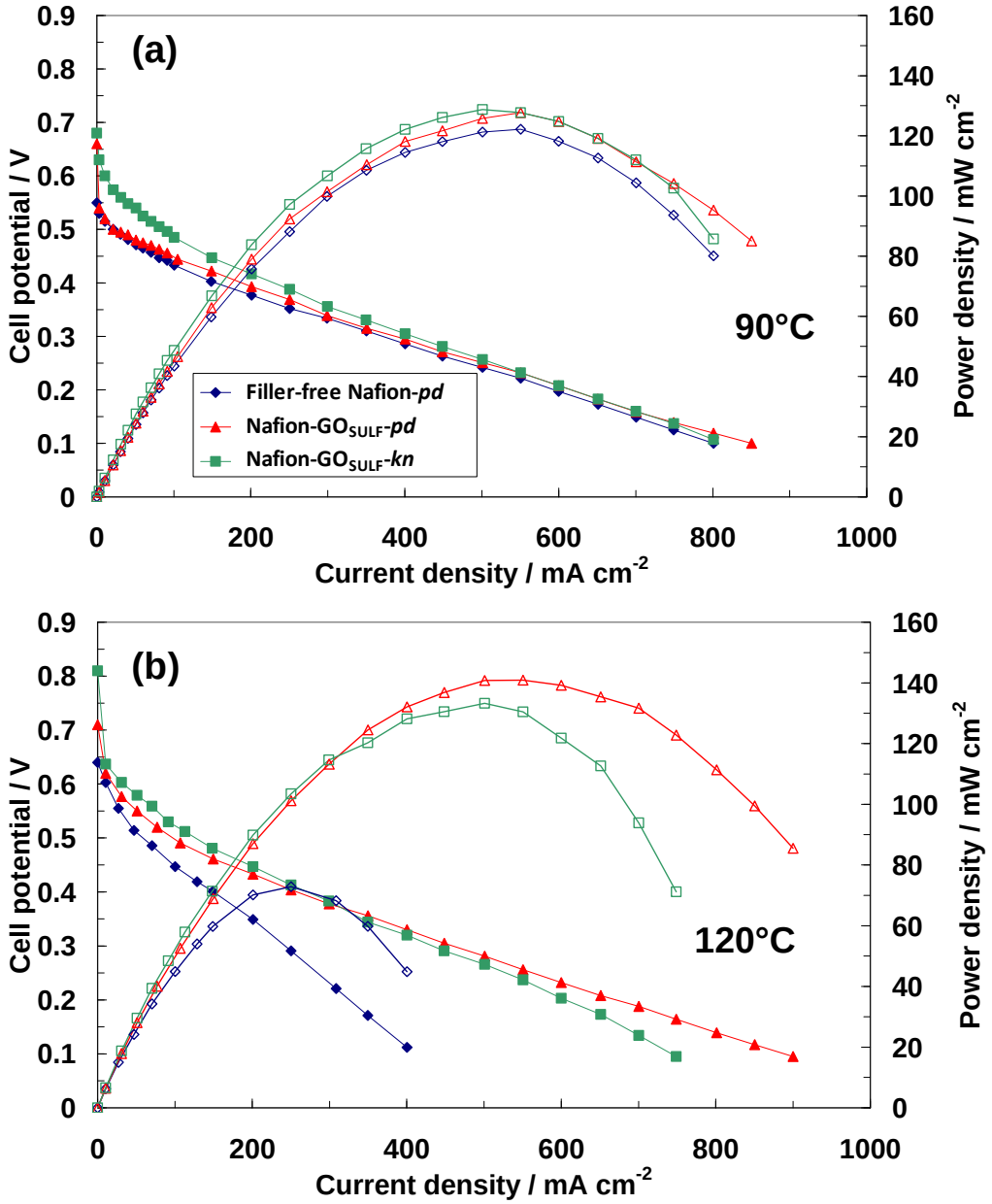

Figure 17. DMFC polarization and power density curves at 90 °C (a) and 120 °C (b) for the membrane-electrode assemblies equipped with composite and filler-free Nafion membranes.

This result is perfectly in agreement with the diffusion data observed previously: higher water diffusion and retention of the membrane prepared by petri dish ensure a lower

resistance of the membrane (thus the possibility to produce high current density in a fuel cell), whereas a larger tortuosity effect of the *kn*-membrane produces a lower methanol cross-over (thus high OCP and low potential losses at low current density). Accordingly, depending on the operating conditions selected for the DMFC stack (high voltage or high power), the most suitable preparation procedure for this kind of composite membranes may be applied..

3.2.2 Anionic and cationic clays nanocomposites for DMFCs (PAPER V)

As a consequence from the results described, other types of layered material have been also tested. In particular two type of nanoclays, one cationic and one anionic, were studied as fillers in the Nafion polymer matrix: Laponite (synthetic clay) and LDH (layered double hydroxide). For this study, it was chosen a Mg^{2+}/Al^{3+} LDH with 2:1 metal ratios and NO_3^- as interlayer anion. Both additives have been already described in Section 2, however, for convenience of presentation, their structures are again reported in Figure 18.

Composite membranes, indicated as Naf-Lap and Naf-LDH, were synthesized by solution intercalation procedure with 3% of filler loading with respect to the polymer, followed by simple casting method. These membranes were investigated in direct methanol fuel cells operating at intermediate temperatures and low oxygen partial pressure.

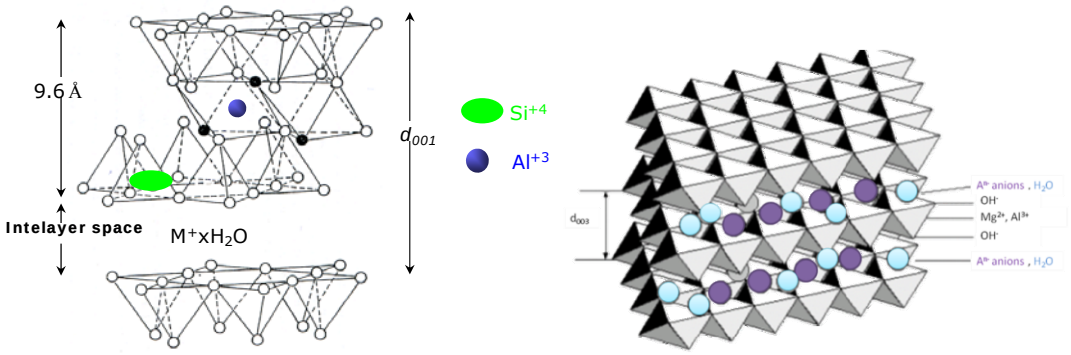

Figure 18. Schematic representations of a smectite clay (on the left) and LDH (on the right) structures.

For this set of membranes, the electrochemical investigation was carried out in a single cell by recording the ac-impedance spectra at different temperatures (from 60 °C to 110 °C) and the polarization curves in the temperature range from 90 °C to 110 °C, feeding a 2 M methanol solution at the anode and oxygen at the cathode. The results of the series resistance (high frequency intercept on the real axis in the Nyquist plot) registered

as a function of temperature are shown in Figure 19, while in Figure 20 the polarization and power density curves recorded at 90 °C and 110 °C are reported. The introduction of such fillers, in particular LDH, into the polymer matrix allow the preparation of nanocomposites with enhanced water retention capacity and reducing the cell resistance, This produces a higher performance of the MEAs based on the nanocomposites compared to the filler-free membrane.

The maximum power density of the DMFC equipped with the composite membranes slightly increases as the temperature increases, although the methanol solution is fed under atmospheric pressure and thus subjected to evaporation; whereas, a decrease in performance is recorded for the filler-free membrane-based MEA. From the other hand, also the OCP is, at both temperatures, higher for the cells equipped with filler loaded membranes, suggesting a reduced susceptibility to methanol crossover.

Particularly noteworthy is the performance achieved by using the Naf-LDH hybrid membrane, which makes these materials quite promising, in comparison to other electrolytes reported in the literature[42].

To explain the nature of this results, a thorough investigation of the molecular dynamics that govern the water and methanol transports confined in the polymer matrix is needed. Accordingly, measurements of the self-diffusion coefficients, spin-lattice relaxation times and the ^{1}H spectra have been performed on the different membranes.

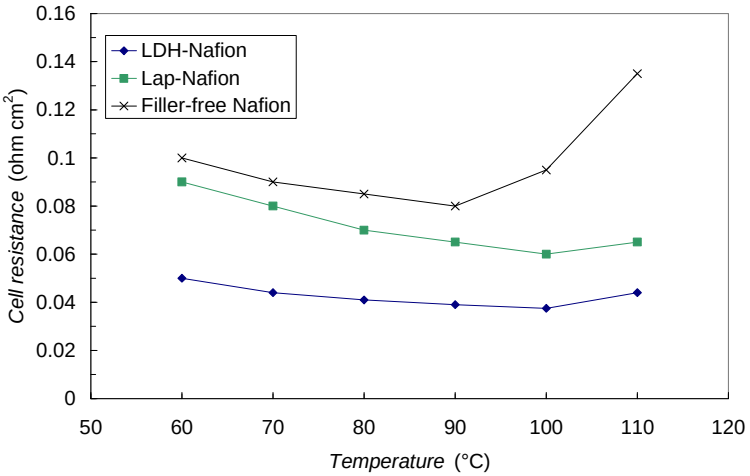

Figure 19. Cell resistance values as a function of temperature for the cells equipped with the different membranes.

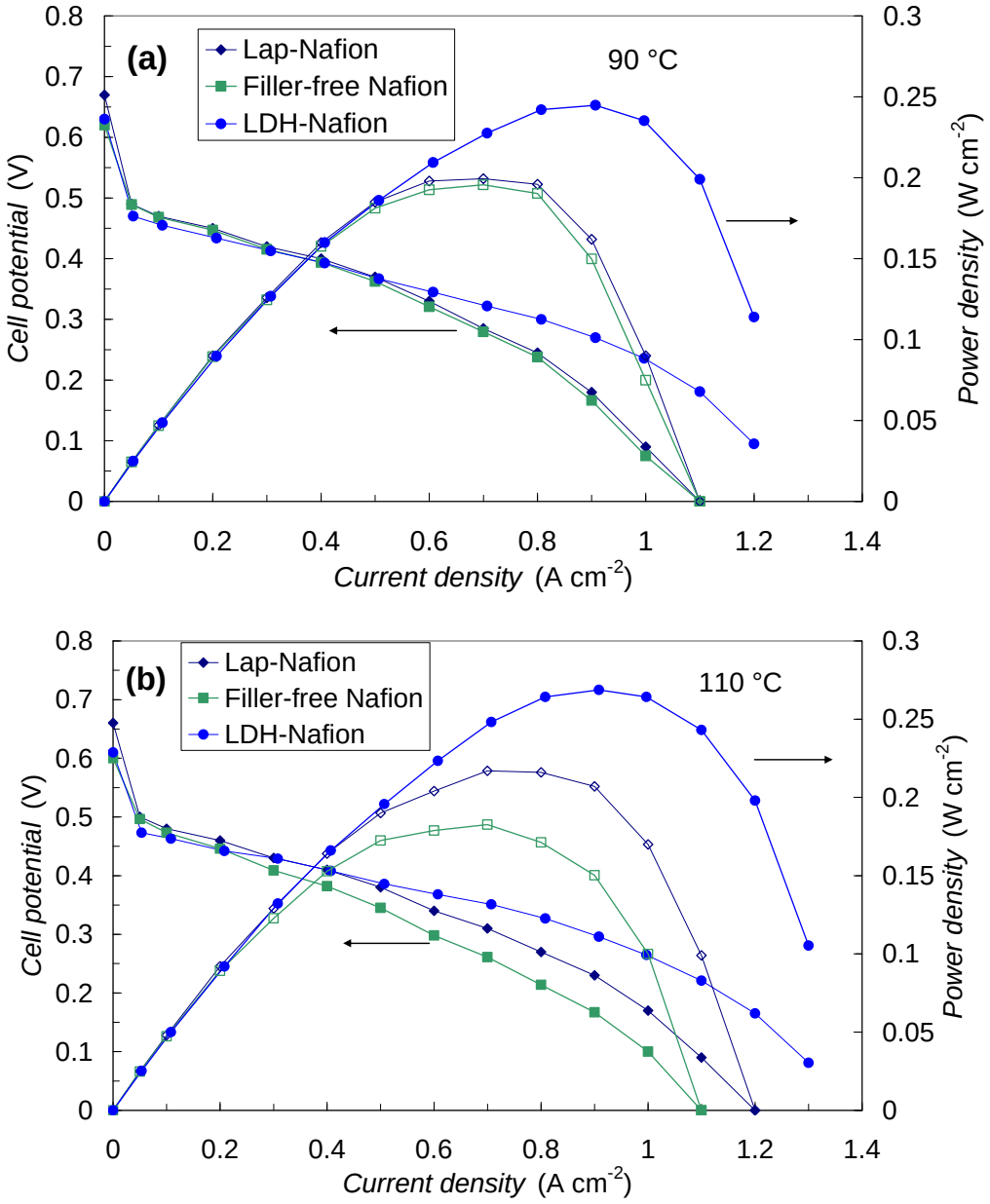

Figure 20. DMFC polarization and power density curves at 90 °C (a) and 110 °C (b) for various membrane-electrode assemblies equipped with composite and filler-free membranes.

Particularly interesting are the information derived from the study of the temperature evolution (from 20 °C up to 130 °C) of the proton spectra acquired on Naf-LDH and Naf-Lap (the details are in the paper in appendices). From the analysis of linewidth, spectral integral and chemical shift versus temperature, registered on both composite membrane emerged that water and methanol molecules strongly interact with ionic

species within the interlayer space of the nanoclays, leading to improved water retention capability of the nanocomposites respect to pristine Nafion. However, a clear difference also came out. Indeed, in Naf-Lap nanocomposite water and methanol show a similar rate of evaporation from the membrane. Conversely, in Naf-LDH membrane it has found that, for temperature above 100 °C, when a large amount of methanol evaporates from the membrane, and the remaining is strongly interacting with the polymer, a considerable water's amount still remains in the composite.

These differences observed between LDH and Laponite are likely connected to the chemical nature of the two clays, that is in case of LDH, favorable electrostatic interactions should occur between the negatively-charged Nafion and the positively-charged LDH platelets, whereas electrostatic repulsions are expected with the negatively-charged Lap mineral. This could have an impact on the nanomorfology of the hydrophilic pores the polymer matrix, leading to different interactions with water and methanol molecules and then to different transport properties.

From the water and methanol diffusion coefficients (in 2 M solutions) , showed in Figure 21, the presence of layered nanoadditives, dispersed in polymeric matrix, is able to considerably reduce the methanol mobility through an increase of the tortuosity of the diffusional paths of both water and methanol molecules.

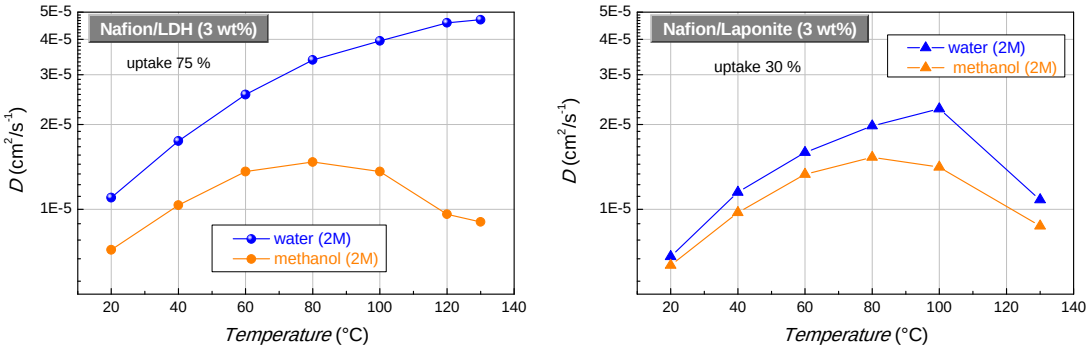

Figure 21. Self-diffusion coefficients of water and methanol in 2 M solution confined in Nafion-LDH and Nafion-Lap nanocomposite membranes, from 20 °C up to 130 °C. In the graphs are reported also the solution uptakes (wt%).

On the other hand, the anionic clay, likely due to the higher hydrophilicity and retention capability respect to cationic clay, is able to maintain a very high water diffusion at high temperatures. The superior retention capability of the LDH has also been raised from the spectral analysis. In fact, by considering the electrostatic interactions between clay materials and polymer, discussed above, the favourable interactions in the LDH-composite likely are able to originate a "bridge" for the proton diffusion, which instead is lacking with the Laponite clay.

Important information, supporting our speculation about the different nature of the interaction between anionic and cationic clays with solvent molecules, have been obtained by spin-lattice relaxation times (T_1) measurements. Figure 22 shows the temperature variation of the T_1 of (a) methanol and (b) water for the two nanocomposites. T_1 values, compared to diffusion, reflect more localized motions including both translation and rotation on a time scale comparable to the reciprocal of the NMR angular frequency (~1 ns), therefore, higher T_1 values suggest more facile molecular motions. As is possible to see, although the solution uptake of the LDH-membrane is almost double (75 wt% against 30 wt%), both water and methanol relaxation times in the Lap-membrane are much higher than of LDH-membrane in all the temperature range investigated. This from one side implies a greater local mobility (more degrees of freedom) of the molecules in the Lap-sample, which in turn can be attributed to structuring and nanomorphology of the composite, but from the other side provides additional evidence for stronger interactions between the water molecules and the LDH material, suggesting as the proton mobility at very high temperatures is ensured prevalently through the Grotthus mechanism which foresees a strong interaction between the H^+ ions and the lattice.

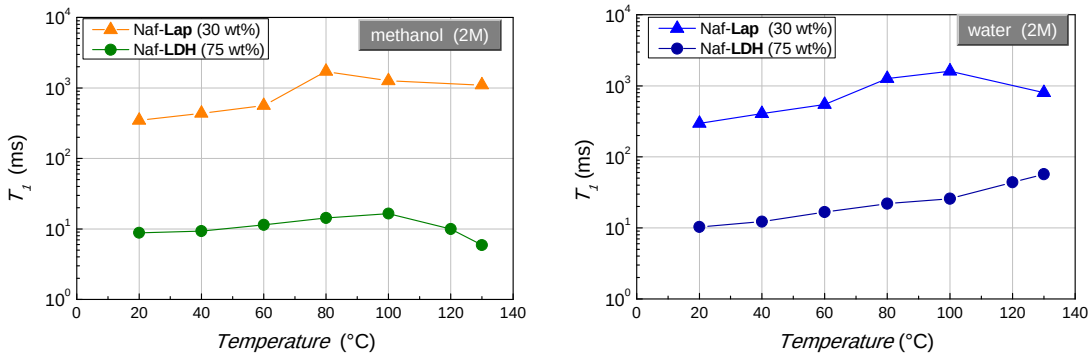

Figure 22. Longitudinal relaxation times (T_1) of the methanol (a) and water (b) measured in the LDH and Lap composite membranes swollen in 2M solution, in the temperature range from 20 °C up to 130 °C.

Nafion-LDH (kn-pd) double-layer composite membrane for high performances DMFCs.

So far we have demonstrated as the dispersion and fully exfoliation of layered materials in Nafion matrix ensures better performance to the DMFC by virtue of a good proton conductivity at high temperatures, likely due to a Grotthuss mechanism, and a reduced permeability to methanol, due to the obstruction effect of the filler particles. In this regard, the most interesting results were obtained after dispersion of anionic clay (LDH) in the polymer matrix. We have also demonstrated how an alternative procedure for membranes preparation, i.e. spreading a viscous solution by a knife (*Kn*), can be used to mechanically confer a preferred orientation to the lamellae within the electrolyte, accentuating the obstruction effect to the methanol permeation.

Due to the nature of these findings, we tried to develop a novel procedure for the preparation of membranes where the water transport properties of electrolytes obtained via simple casting procedure, and the reduced methanol permeability resulting from the preferential orientation of the 2D-layered fillers coexist. Morphological, electrochemical and transport properties characterization of this hybrid membranes is still in progress. Here I am going to discuss about some preliminary results.

In this case, the same anionic clays, i.e. LDH, has been used as additives for the preparation of Nafion composite membranes. By solution intercalation two polymeric solution with 3% of filler loading with respect to the polymer were prepared, the first of which has been spread by doctor blade, (after opportune solution's concentration). In agreement with the results obtained on membranes containing GO_{sulf} as additive, a membrane in which the lamellae have a higher degree of order was thus prepared. Such membranes was subsequently used as a lower support on which the second solution has been deposited via simple casting procedure (see Figure 23). The resulting membranes is henceforth referred to as a hybrid (*kn-pd*)_Nafion-LDH nanocomposite. For comparison a pure (*kn*)Nafion-LDH has been also prepared.

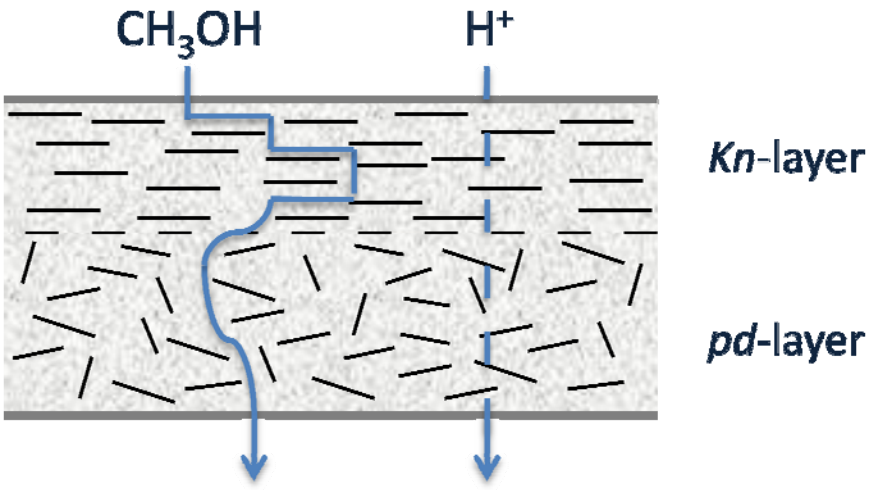

Figure 23. H^+ and methanol ions passing way in the polymer matrix of the Nafion-LDH*(kn-pd)* double-layer nanocomposite membrane

For the electrochemical investigation a MEA have been assembled with the hybrid *kn*/*pd* membrane and placed in the DMFC so that the kn-layer of the membrane could face the anodic component of the system. The series resistance, registered as a function of the temperature from 60 °C to 110 °C and carried out in a single cell by recording the ac-impedance are shown in Figure 24. For comparison, data collected on filler-free Nafion and on Nafion-LDH prepared by simple casting procedure are also shown. The values of cell resistance for DMFC assembled with *kn*/*pd* membrane are

almost comparable with those obtained for Nafion-LDH(*pd*) and proceed in parallel to the previous results during the heating. As expected, a slight increase of the resistance has been registered: the presence of a component in which the lamellae of the filler are more organized, from one side induces amendments in the pores morphology, from the other side tends to oppose a larger resistance to the crossing of diffusing species. As already observed for other LDH-nanocomposite, MEAs equipped with the hybrid membrane show a smooth increase of cell resistance passing from 100 to 110°C. In contrast, a strong increase of the resistance for the cell assembled with pristine Nafion has been observed at temperature above 90 °C. This confirms the larger water retention capability of composite membranes containing LDH.

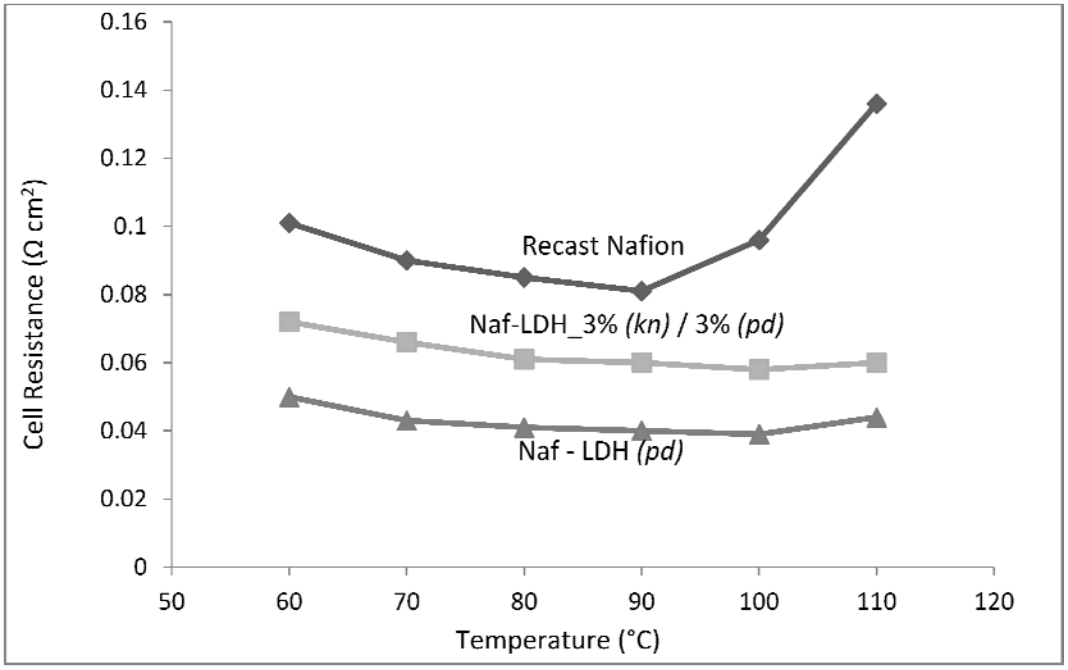

Figure 24. Cell resistance values as a function of temperature for the cells equipped with Nafion-LDH*(kn)/(pd)*. For comparison the data of MEAs assembled with recast Nafion and Nafion-LDH*(pd)* are also reported.

Figure 25 reports the polarization and power density curves at 90 °C and 110 °C, feeding a 2 M methanol solution at the anode and oxygen at the cathode. Despite the increase of the overall resistance, the MEA assembled with (*kn-pd*)_Nafion-LDH

showed improved performances: a power density of 270 mW cm^{-2} at 90 °C and extended current density have been registered. Besides, the increased of the temperature up to 110 °C resulted in a slight increase of the maximum power density. However, the most remarkable aspect in this graph is the variation of open circuit potential (OCP) for the cells based on the different membranes. It is well known that, in a DMFC, the OCP is a parameter directly related to the methanol permeability of a membrane. The assembly of the (*kn-pd*)_Nafion-LDH membrane in the DMFC produced an increase of the OCP and the potential at low current densities. This can be ascribed to the increase of the tortuosity pathway, resulting from the well-distributed particles of the kn-layer, obstructing the methanol permeation.

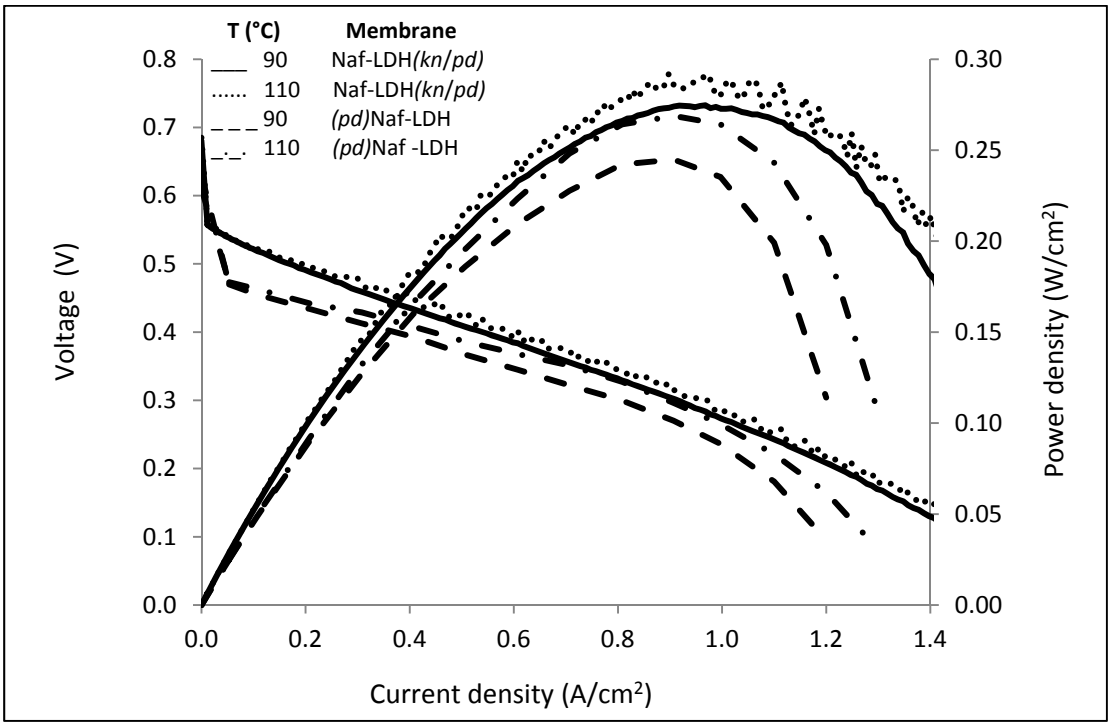

Figure 25. Comparisons between DMFC polarization and power density curves at 90 °C and 110 °C obtained on various membrane-electrode assemblies equipped with (*pd*)Naf-LDH and Naf-LDH (*kn/pd*).

These preliminary results seem to suggest that our procedure allow the preparation of a *(kn-pd)*double-layer composite membrane where an high current density (and thus high performances of the DMFC), ensured by the higher water diffusion and retention

capacity of the membrane prepared by petridish, and the lower methanol cross-over (thus high OCP and low potential losses at low current density), resulting from the larger tortuosity effect of the kn-layer of the membrane, coexist.

To verify the veracity of our hypothesis, morphological and NMR characterizations on this set of membrane are in progress.

3.2.3 sPEEK based electrolyte for DMFC (**PAPER VI**)

As we have seen, the preparation of composites containing organically modified inorganic fillers, such as silica, clays, graphene oxide is a widely covered strategy for the improvement of the performance of Nafion membranes in DMFC[43-46]. The dispersion of such kind of fillers in the polymer matrix results in the production of electrolytes with better mechanical properties, reduced methanol permeability and higher power density delivered in a DMFC, with respect to unfilled Nafion membranes[47, 48]. However, due to the high affinity between methanol and the fluorinated backbone of the PFSA polymers, the issues related to methanol crossover in DMFC are still unresolved.

The use of hydrocarbon polymers alternative to Nafion is still one of the main targets to develop cheaper proton exchange membranes and with lower methanol permeability [49], since that can be chemically modified to obtain proton-conducting electrolytes. Among them, sulfonated polyetheretherketone (sPEEK) is particularly interesting for applications in DMFCs because its microstructure, as described in chapter 1.2.1, consists of narrower and less connected water filled channels compared to those of Nafion and this can help to reduce the problems related to methanol crossover and high water drag that occur in cell operative conditions[50].

Accordingly, in the framework of the Project NAMED-PEM, Dr. C. De Bonis of the Department of Chemical Science and Technologies (University of Rome "Tor Vergata") used sPEEK, having DS=0.5, to prepare composite membranes where propylsulfonic-functionalized nanometric titania (TiO_2-RSO_3H) has been dispersed in the polymer matrix.

During this thesis, an extensive investigation of the membranes morphologies, transport properties and electrochemical characterization has been carried out, as reported in paper VI. Here the results obtained via electrochemical and NMR investigation has been pointed out.

The proton conductivity was measured by EIS on both pristine and nanocomposites sPEEK membranes. The resulting plots are shown in Figure 26. As expected, due to the non-conductive nature of the inorganic filler, its dispersion in the

polymer matrix does not improve the proton conductivity of the electrolytes. However, from the comparison of data relative to the sPEEK/TiO_2 and sPEEK/TiO_2-RSO_3H membranes emerges that the functionalization of TiO_2 avoids the reduction of the overall proton conductivity of the electrolyte: in the whole investigated temperature range, the sPEEK/TiO_2-RSO_3H membrane showed a conductivity similar to that of pure sPEEK.

To test the functioning of these membranes in a real device, DMFC single cell measurements were also carried out.

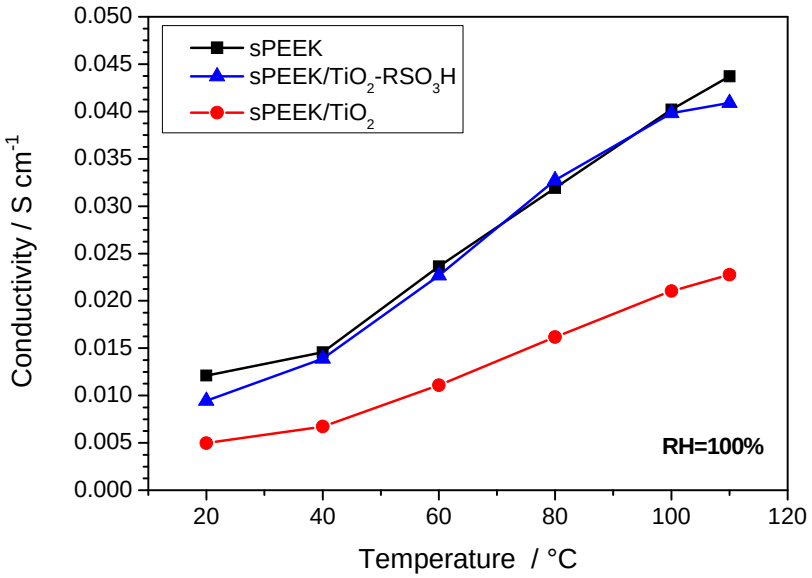

Figure 26. Proton conductivity of pure sPEEK and composite membranes.

The polarization and power density curves of the membranes, recorded at 70 °C and 1 abs bar and 90 °C and 2 abs bar, are shown in Figure 27. Independently from the operative condition applied, the sPEEK/TiO_2-RSO_3H composite showed better performance than those of the other membranes, in terms of higher power density delivered and reduced methanol crossover. Moreover, as can be observed, increasing the temperature and pressure the maximum *PD* of the cell increases for all the sPEEK-based membranes. Among them, also at higher temperature, the sPEEK/TiO_2-RSO_3H

composite has confirmed to be the most suitable electrolyte for DMFC applications; for MEA assembled with this nanocomposite a PD improvement of 20% with respect to the pure sPEEK membrane (PD_{max} = 40 mW cm^{-2}) has been registered.

To explain the apparently conflicting nature between the data of proton conductivity and those obtained by DMFC test we need to consider that, in the sPEEK/TiO_2-RSO_3H membrane, the presence of silylpropylsulfonic groups onto TiO_2 surface leads to a highly reticulated microstructure, creating tortuosity and narrowing of the diffusional paths of methanol molecules as well as of bulk water. Accordingly, from one side the contribution to proton conductivity due to vehicular mechanism, that is the diffusion of protonated water molecules, will be smaller and the relative contribution of the Grotthus-type mechanism will be larger, resulting in a lack of improvement of the proton conductivity. On the other hand, the physical cross-linking between the functionalized titania nanoparticles and the polymer chains reduce the size of the hydrophilic channels and thus effectively decreases the methanol permeability that strongly depends on the size and tortuosity of diffusional channels network[51]. Consequently, when a DMFC is assembled with this membranes, a larger tortuosity of the diffusive path produces a lower methanol crossover and lower potential losses at low current density, while the higher water mobility with respect to that of methanol and the significant contribution of the Grotthus-type mechanism to the proton conductivity ensure a higher current density.

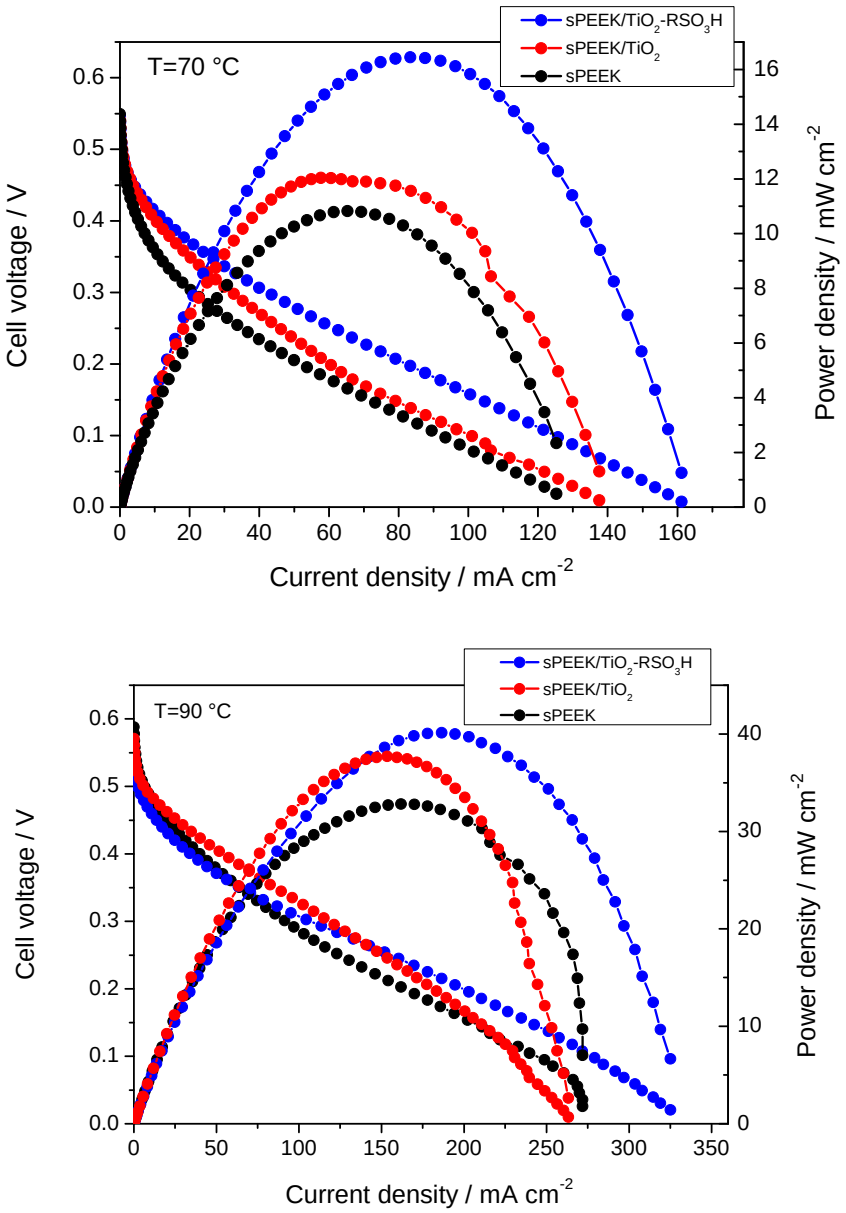

Figure 27. DMFC polarization and power density curves at 70 °C and 90 °C for the MEA equipped with composite and pure sPEEK membranes.

The results obtained by DMA investigation have given further strength to our speculations regarding the interaction between the the sulfonilic groups on the titania particles and the polymer chains, leading to an increase of the reticulation degree. Figure 28(a) reports the temperature evolution, collected in the temperature range between 25 °C and 250 °C, of storage modulus of the sPEEK membrane and of the

nanocomposites, sPEEK/TiO_2 and sPEEK/TiO_2-RSO_3H. As is possible to see, the dispersion of TiO_2 particles into the sPEEK matrix results in an improvement of the mechanical properties of the membrane, detectable to the increase of the E' values. Besides, the titania particle's functionalization with silylpropylsulfonic groups further enhances the stiffness of the final composite. This beneficial effect is likely due to a stronger intermolecular interactions between the polymeric chains.

Turning to the *tan δ* profile (Figure 28(b)), a simple alpha transition is observed for all samples in this temperature range, likely correlated to segmental motions of polymer backbone chains. Whereas for pristine sPEEK membrane, the glass transition temperature is at 228 °C, the nanocomposites both show a slight shift of the T_g to higher temperatures, in particular the sPEEK/TiO_2, and also a strong decreases in the loss tangent values from 1.6 to 0.7-0.8. This reduction is likely related to the higher stiffness of the nanocomposites respect to the filler-free membrane.

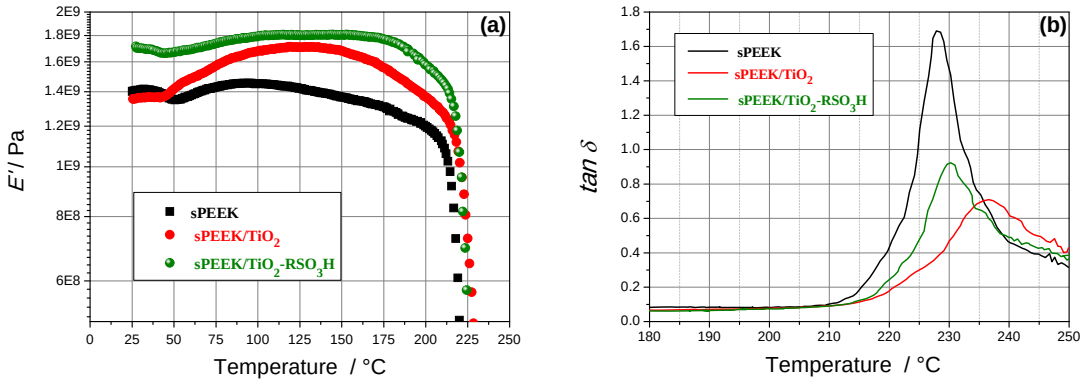

Figure 28. Storage modulus *E'* (a) and *tan δ* (b) versus temperature of pristine sPEEK and sPEEK/TiO_2 and sPEEK/TiO_2-RSO_3H nanocomposite membranes.

Finally, a more comprehensive NMR analysis was performed, including the use of hydrostatic pressure as a thermodynamic variable, in order to understand the effect of the filler on the transport properties of methanol and water, and its interaction with this polymer. Water and methanol molecular dynamics within sPEEK-based electrolytes have been characterized in terms of self-diffusion coefficient, obtained via PGSE-NMR,

spin-lattice (T_1) relaxation times, measured via Inversion Recovery sequence, and ^1H spectral analysis.

Following have been reported data obtained by High Pressure-NMR. It is well known that molecular motions and ionic diffusion are associated with volume fluctuations that can be directly probed by employing pressure as the thermodynamic variable. Accordingly, the analysis of the evolution of the diffusion coefficients under variable pressure is a powerful method to obtain an estimation of the activation volume of the diffusive phenomenon investigated.

During this study, conducted during my period in the Department of Physics & Astronomy of the Hunter College (NY) where I worked under the supervision of Prof. Greenbaumn S., the membranes were equilibrated in aqueous methanol solution at concentration of 2 M, so as to have the same conditions used in the DMFC cell.

Figure 29 reports the comparison between the methanol and water self-diffusion coefficients obtained as a function of the pressure from 1 atm. up to 2 kbar on sPEKK, sPEEK/TiO_2 and sPEEK/TiO_2-RSO_3H, respectively. The measurements were conducted at two different temperatures, 303 K and 328 K, but here only data at 328 K are shown.

It is clear from the data that, for all the pressures range examined, water self-diffusion coefficient is always higher than methanol diffusion. These data confirm that sPEEK has a low intrinsic methanol permeability, due to the particular structure of the solvent filled channels within the polymer matrix[50]. At the same time it appears evident that the dispersion of titania nanoparticles in the polymer matrix produces a structure that further inhibits the methanol transport; moreover, such obstruction effect is exacerbates by the functionalization of these particles with the RSO_3H groups.

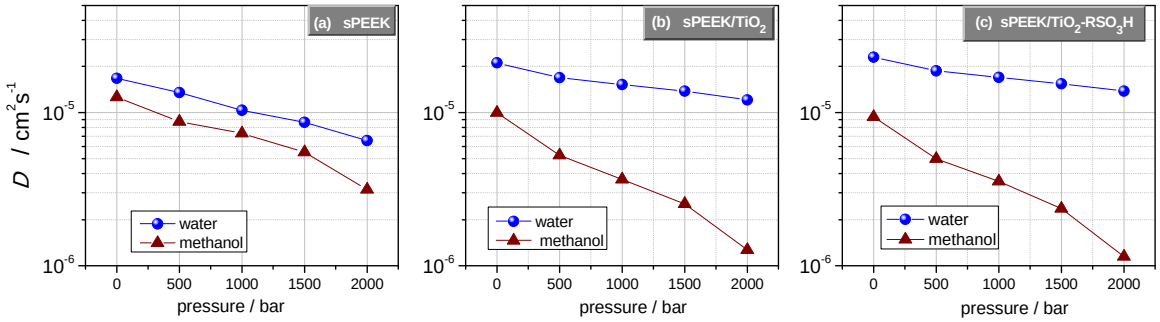

Figure 29. Self-diffusion coefficients of water and methanol in 2 M solution confined in sPEEK (a), sPEEK/TiO_2 (b) and sPEEK/TiO_2-RSO_3H (c) membranes, respectively, measured by high pressure SE–NMR technique from 0 up to 2 kbar, at 55 °C.

Table 3 reports the activation volumes of water and methanol in 2 M solution, respectively, calculated from the diffusion data for the pure sPEEK and the two composites according to Eq. 7:

$$\Delta v = -kT\left(\frac{\vartheta \ln D}{\vartheta P}\right)_T \qquad \text{(Eq. 7)}$$

Higher activation volume implies that more cooperative motion and hence larger change in local volume is required for the process of diffusion to occur within the membrane. This is consistent with interactions occurring between the methanol molecules and the surface of the nanoparticles. In fact, the activation volume of methanol increases in the composites, and the higher value is obtained for the sulfonated one. On the other hand, while the activation volume of water decreases in the composites, that of methanol increases.

Under the effect of the increasing pressure, we can speculate that an alteration of the dimensions of the diffusion channels occurs, resulting in a more difficult dynamical motion within the polymer matrix. However, protons can be transported additionally through a Grotthus-type mechanism that is likely enhanced in highly reticulated system. Additionally, we should be considered that methanol molecules have higher sterical hindrance than that of water molecules. Accordingly, sulfonated titania particles in the polymer matrix increases the ability of the hydrophilic channels to respond to such

pressure effect, allowing a good water diffusion and disfavoring the methanol permeation.

Table 3. Activation Volumes* of water (2 M) and methanol (2 M) in the three membranes and at two temperatures.

Membrane	*Activation Volume (cm^3 mol^{-1})*			
	H_2O/CD_3OD (2 M)		D_2O/CH_3OD (2 M)	
	303 K	***328 K***	***303 K***	***328 K***
sPEEK	16.5	12.0	21.5	16.7
sPEEK/TiO_2	11.6	6.8	28.6	25.1
sPEEK/TiO_2-RSO_3H	10.4	6.3	30.2	25.6

* The error bar for these volumes is around +/-0.5 (since the error on *D* values of about 3%)

This results further confirm that the dispersion of organically functionalized titania, TiO_2-RSO_3H, lead to nanocomposite membranes where the higher water mobility with respect to that of methanol is mainly ensured by a Grotthuss-type mechanism. Due to the reduced methanol crossover and higher current and power density delivered, sPEEK/TiO_2-RSO_3H membrane seems to be a promising electrolyte for DMFC application.

This last result is really outstanding if we consider that sPEEK membranes, in general show very good methanol resistance and mechanical properties but at the same time suffer from lower proton conductivity compared to Nafion. Using finally the sulfonated titania filler we have managed to achieve low methanol permeability without sacrificing the conducting performance of the membrane.

3.3 Ion Exchange Membranes for Reverse Electrodialysis

Membrane-based integrated systems opened interesting perspectives for sustainable and efficient energy conversion using natural and abundant water resources. The interest towards concentrated solutions lies, indeed, in the high salinity-gradient power (SGP) that can be extracted by membrane-based energy conversion processes like pressure-retarded osmosis (PRO) and reverse electrodialysis (RED). As discussed in chapter 1.3, RED system usually focus on the combination of fresh water, as the diluted solution, and seawater, as the concentrated solution, for the conversion of the SGP into electrical energy power. Theoretically, brine solution can be produced by reverse osmosis and/or membrane distillation of seawater[52-54], and it can be used as concentrated stream in RED stack employing as diluted stream sea or brackish water. This strategy potentially offers a huge potential for the improvement of the electrical performance of RED system: the use of concentrated solution allows to reduce the electrical resistance within the low concentration compartment of the RED stack, boosting the power that can be extracted from the SGP[55, 56]. However, at the best of our knowledge, up to now the effect of the use of concentrated solution on the transport properties of the ion exchange membranes is still unknown.

To this purpose, through EIS, a systematic study on the effect of solution concentration, temperature and flow rate, on the electrical resistance of anion- and cation- exchange membranes (AEMs and CEMs) and interfaces (electrical double layer and diffusion boundary layer), was carried out by ITM-CNR of the University of Calabria. As part of the collaboration with Dr. Fontananova E., during my PhD research Nuclear Magnetic Resonance techniques were used to obtain additional important insights about the effect of the electrolyte solution and membranes fixed charges concentration, on membrane microstructure and its mass and electrical transport properties.

3.3.1 Ion Exchange Membranes microstructures as a function of the electrolyte solution concentration ***(PAPER VII)***

The temperature evolution of the ^{1}H NMR spectra, collected from 20 °C up 100 °C on the Fuji-AEM-80045 and Fuji-CEM-80050 membranes, swelled in 0.5, 1 and 4 M solutions, are reported in Figure 15 and 16, respectively. All the spectra were acquired with the same number of scans (ns = 4) and were referenced against pure water set at 0 ppm. The NMR signal essentially originates from the water of the salt solutions absorbed from the membranes, while, the proton signals of the polymer chains are basically "invisible", both because their intensity is very small compared to the signal intensity of the water, and because the dipolar spin-spin interactions make hugely broaden the spectral lines.

As can be seen, the proton's signal obtained for both AEM and CEM, has found to be quite large and asymmetric. Such configuration is evidence of different "types" of water coexisting in the system: water was involved in the hydration "shells" of the ionic groups of the polymer matrix as well as of the sodium and chlorine ions of the solutions. However, in the case of solvents confined in membranes, due to the fast rate of proton exchange, distinguish the different states of water within the hydrophilic channels was not possible: only one peak was seen. Due to water evaporation from the membrane, the intensity of this peak decreased with increasing temperature, and as inset in each graph was shown the peak area vs. temperature.

For the Fuji-AEM-80045 (Figure 30) the proton signal of the membrane swelled with the 0.5M solution was more intense and narrow than membrane swelled in 4M. This was due to the higher solution uptakes and to the greater amount of bulk water (water molecules not involved in the hydration shells of the anions), respectively. In fact, the bulk/"free" water originates a narrower Lorentzian signal and, by heating, it was reasonable to expect that this evaporates before, while the "bound" water was more retained in the membrane pores and the strong interactions cause a broadening of the NMR signal.

Regarding the Fuji-CEM-80050 (Figure 31), the spectral line for the two concentrations, was very similar and different from that observed in the anionic membrane. Indeed, in

the CEM was present a peak quite lorentzian accompanied by a broad shoulder in the region of higher frequency. The shape of the spectral line of water confined in membrane clearly depends on the structural and morphological nature of the membrane itself, such as hydrophilic channels size and ionic functional groups present within them, as well as by the nature (size and charge) of the solvated ions. In the CEM, the hydration of the Na^+ cations involves a greater number of water molecules (hydration number is 5±1), i.e. sodium ion has a greater hydrodynamic radius, than that of the Cl^- anions (hydration number is 1±1). Furthermore, the different orientation of water molecules (H pointed toward anions and oxygen toward cations, Figure 31), which arises from the charge asymmetry of the water molecule, results in an effect on the chemical shift of water protons, as was clear from the spectra. The CEM swelled in 0.5 M solution showed a more pronounced shoulder signal than the 4M, probably imputable to the greater number of water molecules bounded to the ionic groups in the pores. Instead, the decrease of the total area of the signal in temperature follows the same trend for both concentrations.

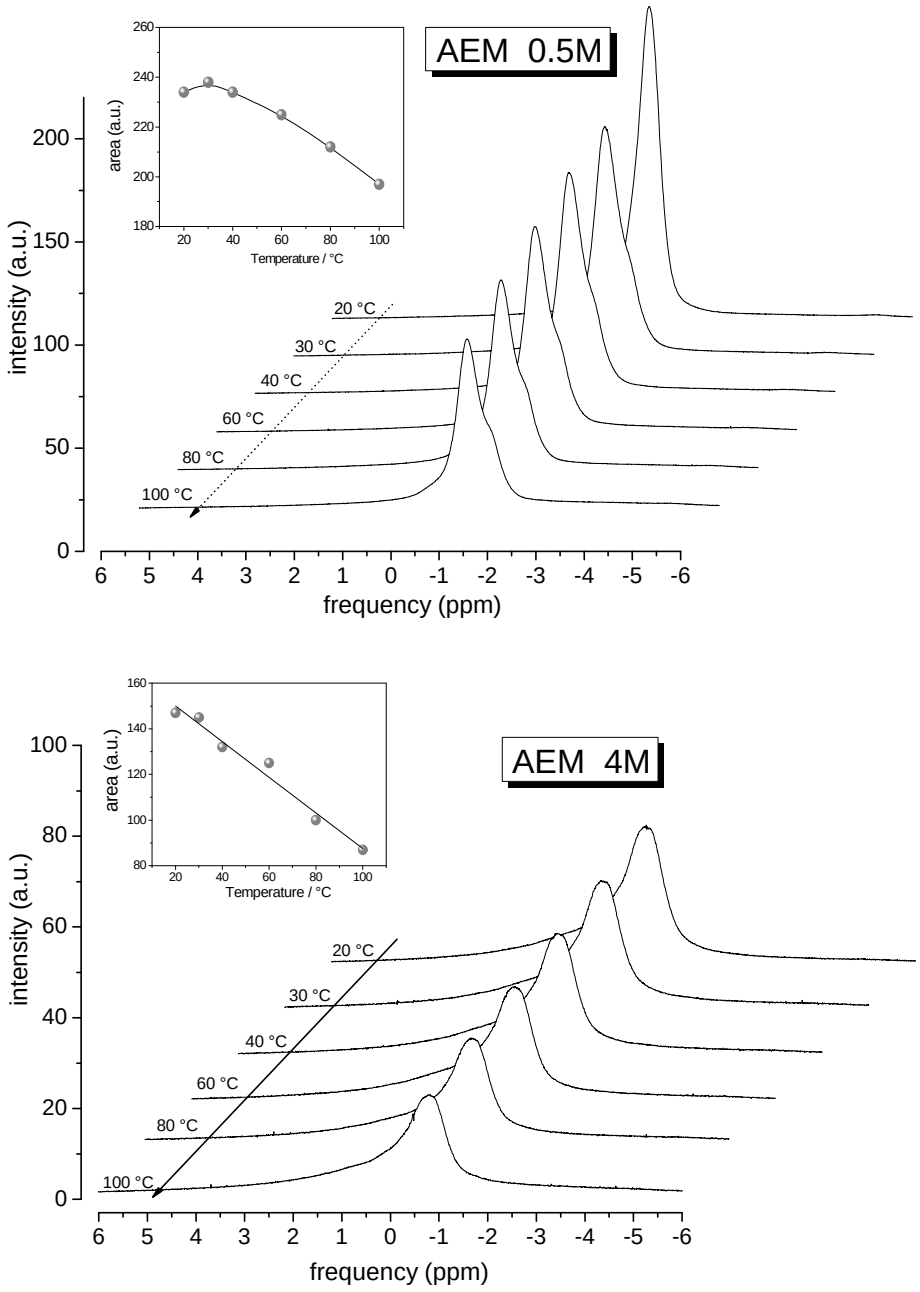

Figure 30. Temperature evolution of 1H-NMR spectra collected on the Fuji-AEM-80045 membranes swelled in water salt solution at two concentrations, 0.5 and 4 M.

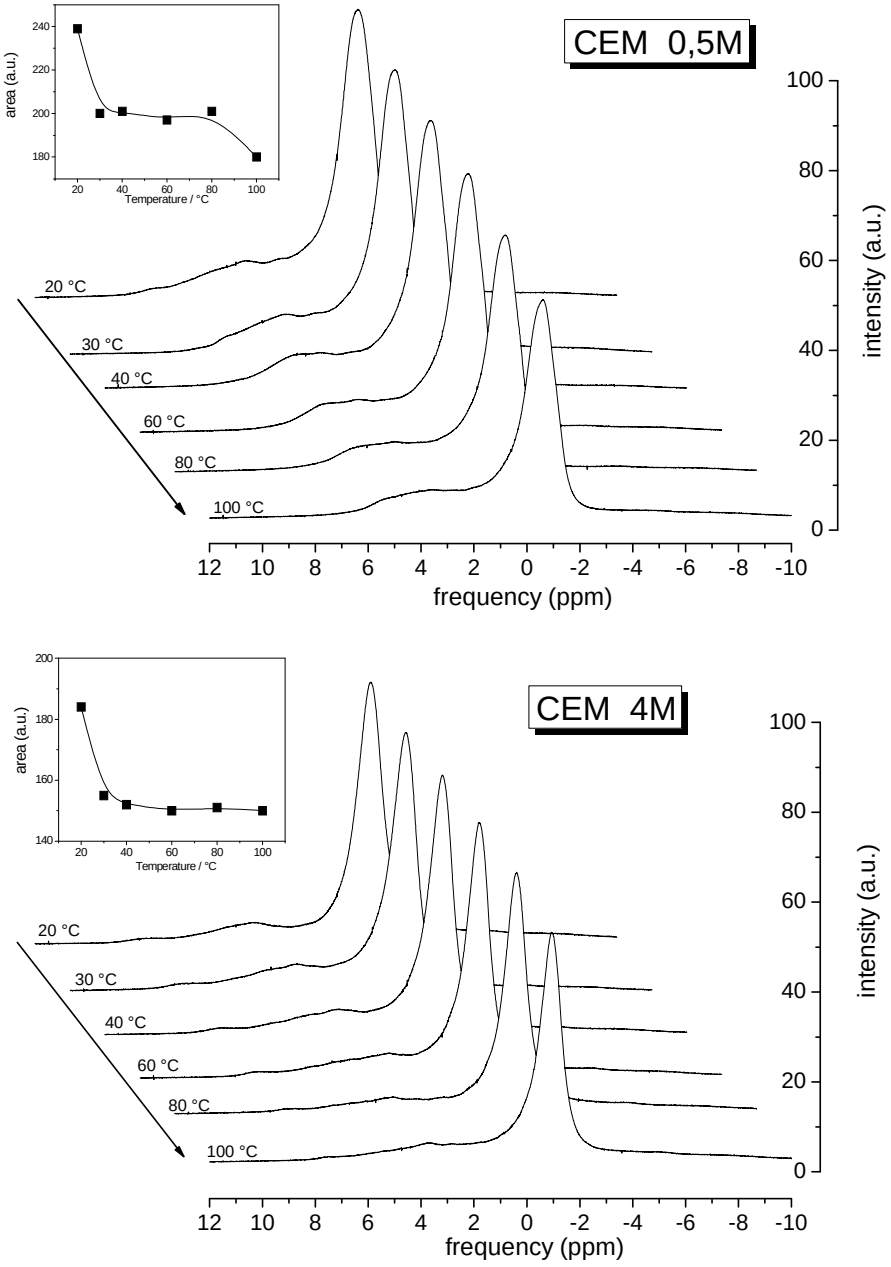

Figure 31. Temperature evolution of 1H-NMR spectra collected on the Fuji-CEM-80050 membranes swelled in water salt solution at two concentrations, 0.5 and 4 M.

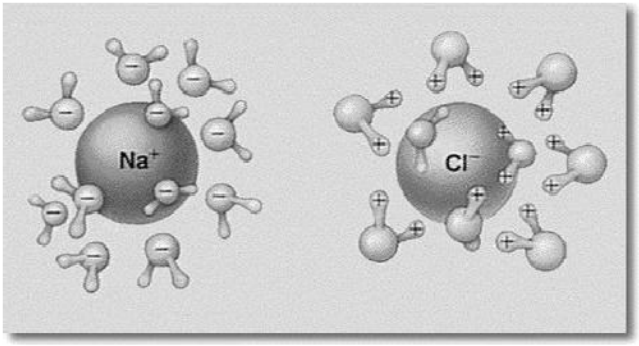

Figure 32. Schematic representation of the hydration of sodium and chlorine ions.

The self-diffusion coefficients (D) of water confined in the AEM and CEM swelled up to saturation in salt solutions at three different concentrations, 0.5M, 1M and 4 M, are reported in Figure 33 as a function of temperature, from 20 °C up to 100 °C.

It is well established that when solvent molecules (water in this case) diffuse in presence of macromolecules, their diffusion is slowed down by both the need to divert around macromolecules (obstruction effect) and any interactions with the same macromolecules that inhibit their motion[14, 15]

The latter effect, i.e. the interaction between solvent and macromolecules, may be termed solvation or hydration and we can affirm that the interacting molecules are in the "bound state". Exchange of molecules between bound- and free-state results in an averaged water diffusion coefficient *D*, which depends on the time fraction spent in each state. Additionally, in this case a salt solutions was present, so, water molecules are also involved in the hydration of sodium and chlorine ions and their transport by a vehicular mechanism.

From the data emerged that the ions mobility decreased with increasing the solution concentration while, overall, in the CEM, the water diffusion was lower than in the AEM.

The decreasing of D when the concentration of the solution increases was due to:

i) the greater amount of ions that entails a greater number of hydration water molecules, then less mobile;

ii) the reduction of hydrophilic channels size, that was correlated to the swelling of the membrane and that brings a higher obstruction effect and at a reduction of the amount of “free” water .

Finally, as expected, the water diffusion in the AEM was higher than in CEM, since in the AEM, chlorine ions have a number of hydration much smaller than that of the sodium ion in the CEM, therefore, more "free" water in the first membrane and less in the second, at the same concentration.

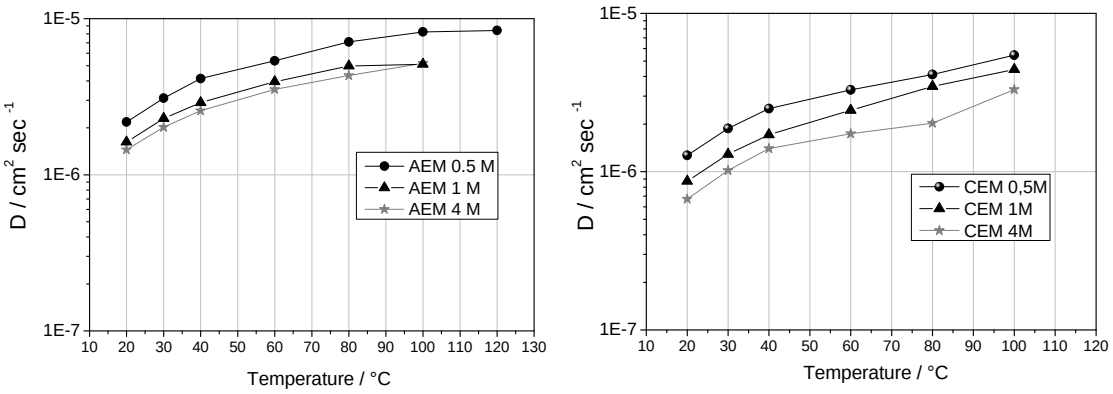

Figure 33. Self-diffusion coefficients of water confined in completely swelled membranes, from 20 °C up to 100 °C. AEM indicates the Fuji-AEM-80045; CEM indicates the Fuji-CEM-80050.

The data obtained by NMR confirmed the strong effect of the electrolytic solution concentration on membrane microstructure. In particular, from the data clearly emerged that the water self diffusion coefficient decreased with increasing the solution concentration. In parallel the strong increase of fixed charged groups density increased the resistance to the ion migration.

References

[1] Zawodzinski TAJ, Neeman M, Sillerud LO, Gottesfeld S. *J. Phys. Chem.* **1991**, A 95, 6040.

[2] Fontanella JJ, McLin MG, Wintersgill MC, Greenbaum SG, *Solid State Ionics* **1993**, **66**, 1.

[3] Nicotera I, Zhang T, Bocarsly A, Greenbaum S, *Journal of Electrochemical Society* **2007**, 154, B466.

[4] Nicotera I, Coppola L, Rossi CO, Youssry M, Ranieri GA. *J Phys Chem B* **2009**, 113, 13935.

[5] Stejskal EO, Tanner J.E. *The Journal of Chemical Physic* **1965**, 42, 288.

[6] Adjemian K. T., Srinivasan S., Benziger J., Bocarsly A. B. *Journal of Power Sources* **2002,** 109, 356.

[7] Litina K., Miriouni A., Gournis D., Karakassides M., Georgiou N., Klontzas E., Ntoukas E., Avgeropoulos A. *Eur. Polym. J.* **2006**, 42(9), 2098–2107.

[8] Karakoulia S., Jankovic L., Dimos K., Gournis D., Triantafyllidis K. *Molecular Sieves: From Basic Research to Industrial Applications, Proceedings of the 3rd International Zeolite Symposium (3rd FEZA)*, vol. 158. Elsevier, **2005**.

[9] A. Enotiadis, K. Angjeli, N. Baldino, I. Nicotera, and D. Gournis, *Small* **2012**, vol. 8, no. 21, pp. 3338–49.

[10] Kim D. J., Jo M. J., Nam S. Y. *J. Ind. Eng. Chem.* **2015**, 21, 36–52.

[11] Amiinu I.S., Li W., Wang G., Tu Z., Tang H., Pan M., Zhang H. *Electrochim. Acta* **2015**, 160, 185–194.

[12] Donnadio A., Pica M., Capitani D., Bianchi V., Casciola M. *J. Memb. Sci.* **2014**, 462, 42–49.

[13] Ketpang K., Shanmugam S., Suwanboon C., Chanunpanich N., Lee D. *J. Memb. Sci.* **2015**, vol. 493, pp. 285–298.

[14] Coppola L, Muzzalupo R, Ranieri G. *J Phys II* **1996,** 6, 657–666.

[15] Gottwald A, Creamer LK, Hubbard PL, Callaghan PT. *J Chem Phys* **2005,** 122(3) 34506.

[16] Nilson P, Lindman B. *J Phys Chem* **1983,** 87, 4756.

[17] , Nilson P, Lindman B. *J Phys Chem* **1984,** 88, 4764.

[18] Johnson C S. *J Magn Reson Ser A* **1993,** 102, 214–218.

[19] Wang J H. *J Am Chem Soc.* **1954,** 76, 855.

[20] Jonsson B, Wennerstrom H, Nilsson P, Linse P. *Colloid Polym Sci* **1986,** 264, 77.

[21] Chidichimo G, De Fazio D, Ranieri G, Terenzi M. *Chem Phys Lett* **1985,** 117, 514-517.

[22] Kreuer KD, Paddison SJ, Spohr E, Schuster M. *Chemical Reviews* **2004,** 104, 4637-4678.

[23] Schmidt-Rohr K, Chen Q.. *Nature Materials* **2008**, 7, 75-83.

[24] Choi BG, Hong J, Park YC, et al. *ACS Nano.* **2011,** 5(6), 5167-5174.

[25] DOE Fuel Cells Technical Plan, *Hydrogen and Fuel Cells Programs* **2012**, www1.eere.energy.gov/hydrogenandfuelcells/mypp/pdfs/fuel_cells.pdf.

[26] Li Q, Jensen J.O, Savinell R.F, Bjerrum N.J. *High Prog. Polym. Sci*. **2009**, *34*, 449.

[27] Quartarone E, Mustarelli P. *Energy Environ. Sci.*, **2012**, *5*, 6436.

[28] Quartarone E, Magistris A, Mustarelli P, Grandi S, Carollo A, Żukowska G.Z, Garbarczyk J.E, Nowiński J.L, Gerbaldi C, Bodoardo S. *Fuel Cells* **2009**, *9*, 349-355-15.

[29] Hughes CE, Haufe S, Angerstein B, Kalim R, Mähr U, Reiche A, Baldus M. *J.Phys.Chem. B.* **2004**, *108*, 13626-13631.

[30] Wasmus S, Kuver A. *J. Electroanal. Chem.* **1999**, *461*, 14–31.

[31] Aricò A.S, Srinivasan S, Antonucci V. *Fuel Cells* **2001**, *2*, 133–161.

[32] Han J, Liu H. *J. Power Sources* **2007**, *164*, 166–173.

[33] Yang C, Srinivasan S, Bocarsly a B, Tulyani S, Benziger JB. *J Memb Sci* **2003**, 237(1-2), 29-35.

[34] Alberti G, Casciola M, Capitani D. *Electrochim Acta* **2007**, 52(28), 8125-8132.

[35] Baglio V, Aricò AS, Di Blasi A, et al. *Electrochim Acta* **2005**, 50(5), 1241-1246.

[36] Aricò AS, Baglio V, Antonucci V, et al. *J Memb Sci* **2006**, 270(1-2), 221-227.

[37] Nicotera I, Angjeli K, Coppola L, Aricò AS, Baglio V. *Membranes* **2012**, *2*, 325-345.

[38] Nicotera I, Enotiadis A, Angjeli K, Coppola L, Ranieri GA, Gournis D. *J Phys Chem B* **2011,** 115(29), 9087-9097.

[39] Nicotera I, Enotiadis A, Angjeli K, Coppola L, Gournis D. *Int. J. Hydr. Ener.* **2012**, *37*, 6236-6245.

[40] Hallberg F, Vernersson T, Pettersson ET, Dvinskikh SV, Lindbergh G, Furó I. *Electrochim. Acta* **2010**, *55*, 3542-3549.

[41] Ji X, Yan L, Zhu S, Zhang L, Lu W. *J. Phys. Chem. B* **2008**, *112*, 15616-15627.

[42] Lufrano F, Baglio V, Staiti P, Antonucci V, Aricò AS. *J Power Sources* **2013,** 243, 519-534.

[43] Kim JH, Kim SK, Nam K, Kim DW. *J Membr Sci* **2012**, 415-416, 696–701.

[44] Kim Y, Choi Y, Kim HK, Lee JS. *J Power Sources* **2010**, 195,4653–4659.

[45] Nicotera I, Simari C, Coppola L, Zygouri P, Gournis D, Brutti S, Minuto FD, Aricò AS, Sebastian D, Baglio V. *J Phys Chem C* **2014**, 118, 24357−24368.

[46] Nicotera I, Kosma V, Simari C, D'Urso C, Aricò AS, Baglio V *J Solid State Electrochem* **2014**, 19 (7), pp 2053-2061.

[47] Cozzi D, de Bonis C, D'Epifanio A, Mecheri B, Tavares AC, Licoccia S. *J Power Sources* **2014**, 248, 1127–1132.

[48] de Bonis C, Cozzi D, Mecheri B, D'Epifanio A, Rainer A, De Porcellinis D, Licoccia S. *Electrochim Acta* **2014**, 147:418–425.

[49] Awang N, Ismail AF, Jaafar J, Matsuura T, Junoh H, Othman MHD, Rahman MA. React Funct Polym **2015**, 86, 248–258.

[50] Li L, Zhang J, Wang Y. *J Membr Sci* **2003**, 226, 159–167.

[51] Pandey RP, Shahi VK. *J Mater Chem A* **2013**, 1, 14375–14383.

[52] Lee KP, Arnot TC, Mattia D. *Journal of Membrane Science* **2011**, 370, 1-22.

[53] D. Winter, J. Koschikowski, M. Wieghaus, Desalination using membrane distillation: 375 (2011) 104–112.

[54] Ji X, Curcio E, Al Obaidani S, Di Profio G, Fontananova E, Drioli E. **2010**, 71, 76–82.

[55] Logan BE, Elimelech M. *Nature* **2012**, 488(7411), 313-319, 2012 and references therein.

[56] E. Brauns. *Desalination* **2009**, 237, 378-391.

CONCLUSIONS

Aim of the present research has been the development of proton conducting nanocomposite membranes to be considered as advanced electrolyte in proton exchange membrane fuel cells (both hydrogen, DHFC, and direct methanol fuel cells, DMFC) and able to tolerate a wide range of operating conditions. To this purpose a novel class of nanostructured materials were synthesized and tested as additives in Nafion polymer matrix. However, alternative polymers to perfluorosulfonated acid ionomers have been also examined. In particular: i) polybenzimidazole (PBI)-based membranes have been investigated for High Temperature FCs; ii) sulfonated Polyether Ether Ketone (sPEEK) and several nanocomposites have been tested for DMFCs applications.

In this research work a deep study of the transport properties of the water and methanol confined within the electrolyte membranes will be performed by NMR methods, including pulsed-field-gradient spin-echo (PFGSE), spectral analysis and spin-lattice relaxation time (T_1), together to a wide physico-chemical, mechanical and electrochemical characterization in order to achieve a systematic understanding at a fundamental level of the effects of dimensionality, architecture and organization of these nanofillers on the properties of the ionomers and to exploit this knowledge for the preparation of high performance electrolytes.

In this framework, a basic research on the molecular dynamics has been addressed by elaborating NMR data through a “two sites” model based on the fast exchange between “free” and “bound” water molecules. This model allowed the estimation the hydration numbers, i.e. the number of water molecules involved in the hydration shell of the hydrophilic groups of both polymer and filler, as function of temperatures and water content. The hydration numbers obtained are consistent with data reported in literature, demonstrating the strength of the model proposed.

Hybrid organic-inorganic fillers [***SWy-CNTs*** and ***organo-modified TiO_2***] have been proposed for the preparation of composite electrolyte for improved performances DHFCs. Homogeneous dispersion of both hybrid nanomaterials has found to improve the tensile strength, modulus, heat resistance, conductivity and water diffusion of the Nafion-based electrolytes in the region of high temperatures and very low water content. Consequently, nanocomposite membranes prepared during this PhD, are able to

extend the operative temperature of the DHFCs. Additionally, the surface functionalization of the fillers with hydrophilic groups, such as SO_3^-, increases the water retention capability in addition to a reinforcement of the polymeric network. The mechanical reinforcement of the membrane, and hence the reduction of the swelling properties, play an important role, especially in the temperature range 90–120 °C, where high humidification conditions can be still obtained at acceptable pressures of the cell.

Noteworthy behavior was demonstrated from the membranes containing SWy-oxCNTs-RSO_3H nanoadditives, able to guarantee a very high proton diffusion in "quasi-anhydrous" conditions. Proton mobility is ensured by a correct network created from the long nanotubes (well distributed through the clay nanoplatelets) appropriately decorated with acid groups: the best membrane reaches conductivities of **7×10^{-2} S cm^{-1}** @ 120 °C and 30% RH, one order of magnitude higher than pristine polymer, and a rather high value in the current panorama of the PEMFCs.

During my PhD thesis, the dispersion of 2D-layered nanomaterial [***Graphite Oxide (GO), Smectite Clays and Layered Double Hydroxides (LDHs)***] has been also suggested as effective strategy to reduce the methanol crossover, while maintaining an high proton conductivity, in polymer electrolyte for DMFCs. A procedure to attempt some preferential orientation of the fillers nanoplatelets in the polymer matrix has been also experienced.

Solution intercalation method was followed for the synthesis of the above composite membranes and the results demonstrated that, in most of the cases, highly homogeneous nanocomposites membranes were created and, regarding 2D-layered fillers, the individual layered nanofillers were uniformly dispersed in the continuous polymeric matrix.

It has been demonstrated that nanocomposite electrolyte where 2D-layered material are fully expholiated in the polymer matrix, could be a potential solution to some of the drawbacks presently affecting direct methanol fuel cells (DMFCs). Due to the strong interaction between water molecules and filler particles, also under low humidification, such nanocomposite electrolyte are capable of extending the operating temperature of a DMFC without any significant loss of conductivity. Remarkable

results were obtained on the composite Nafion-LDH. This hygroscopic filler demonstrates a very high proton mobility, ensured together with a reduced methanol diffusion due to a blocking effect of the layered nanoparticles dispersed in the polymer matrix. This behavior leads to improved DMFCs performances: a power density of **250 mW cm^{-2}** at 90 °C has been registered, which makes these materials quite promising, in comparison to other electrolytes. Besides, the experimental data suggest that a simple casting procedure developed by doctor blade (film applicator) produces a composite membrane in which the exfoliated lamellae of filler are distributed more regularly with a possible preferential orientation parallel to the film surface. So prepared membranes evidence a significant reduction of the diffusion of methanol and however, a high mobility of the water at high temperatures is still guaranteed.

The incorporation of the Titania-based nanoadditivies in the sPEEK polymer demonstrates considerable effects on the morphology and stiffness of the membranes, as well as on the transport properties and barrier effect to the methanol cross-over. In particular, the functionalization of the Titania nanoparticles by propylsulfonic acid groups promotes a higher reticulation between the polymeric chains, increasing the tortuosity of the methanol diffusional paths, so reducing the molecular diffusion, while the proton mobility increases being favored by the Grotthus-type mechanism. Outstanding improvements were found when using the sPEEK/TiO_2-RSO_3H composite membrane as electrolyte in a DMFC, in terms of reduced methanol crossover and higher current and power density delivered.

Regarding PBI, as alternative electrolyte for HT-PEMFCs, it has found that monomer sulphonation does increase the membrane stiffness by increasing the inter-chain crosslinks involving PA molecules and sulphonic groups. This, in turn, reduces the proton mobility with respect to PBI_5N, which is our PBI standard, where, the higher flexibility of the polymer chains favours the proton transport through a hopping-like mechanism.

Summarizing, the results obtained demonstrated that nanocomposite membranes prepared during this PhD research confer significant improvement to PEMFCs systems and an advance over the state of the art, both for DHFCs and DMFCs.

Due to the nature of our findings, as perspective future of this work, the nanostructured materials here described could be also tested as additives in cheaper polymers and/or with lower intrinsic methanol permeability.

Acknowledgements

Immeansurable appreciations and deepest gratitude for the help and the support are extended to the following people who, in one way or another, have contributed in making this study possible.

I am extremely grateful to Dr. Isabella Nicotera, for her excellent guidance, caring, patience, and providing me with an excellent atmosphere for doing research. I must thank her for believing in me. This experience was really important for my professional and personal training. Finally, but not less important, thanks because during the most difficult times when writing this thesis, she gave me the moral support and the freedom I needed to move on. I could not have imagined having a better advisor and mentor for my Ph.D study.

I owe my gratitude to Prof. Giuseppe Antonio Ranieri for providing me the opportunity to work in the Physical Chemistry Soft Matter Laboratory "Mario Terenzi" (PC_SM Mario Terenzi) of the Department of Chemistry and Chemical Technologies – CTC in the University of Calabria. Thanks for his scientific advice and for the many insightful discussions and suggestions. Sharing his knowledge with me he has challenged and enriched my ideas.

I would also like to thank Prof. Luigi Coppola and Dr. Cesare Oliviero Rossi. I am extremly thankful and indebted to them for sharing expertise, and sincere and valuable guidance and encouragement extended to me.

I am very grateful to Dr. Vasiliky Kosma, Dr. Assunta Spadafora, Dr. Paolino Caputo, Dr. Luigi Filippelli and Dr, Luigi Gentile, for their help, support and the enjoyable time we spent together. Without you my PhD would have been too lonely.

My sincere thanks also goes to Prof. Dimitrios Gournis and Prof. Steve Greenbaum, which provided me the opportunity to join their teams, and which gave access to their laboratory and research facilities. Without their precious support it would not have been possible to conduct part of this research.

Dr. Vincenzo Baglio from CNR-ITAE Institute (Messina,Italy) is acknowledged for their contribution to this work.Many thanks to Prof. Raffaele Giuseppe Agostino Dr. Alfono Policicchio from the Department of Physics(University of Calabria, Italy) for his significant help with the SEM measurements.

The financial support of the Italian Ministry for University and Research under the framework of the PRIN 2010-11 project "Advanced nanocomposite membranes and innovative electro catalysts for durable polymer electrolyte membrane fuel cells, NAMED-PEM" and of the European Commission, European Social Fund and Calabria Region are gratefully acknowledged.

Ma i miei ringraziamenti più importanti non possono che andare a loro...
… alla mia famiglia...
…. ad ognuno di loro che non ha mai smesso di credere in me e nei miei sogni…..
..... perché ogni mio successo è stato, è, e sarà sempre anche il loro successo!

APPENDIX A

Experimental Techniques

EXPERIMENTAL TECHNIQUES

During my experimental work three main experimental technique has been used in order to fully characterize the transport and mechanical properties of the material and the membranes prepared. Among them, the Nuclear Magnetic Resonance (NMR) has been widely applied in order to directly investigate water and methanol self diffusion coefficient. For this purpose different techniques, such as Pulsed Field Gradient (PFG) and High Pressure NMR, were applied on both pristine and nanocomposite membranes. Besides, Inversion Recovery and Spin Echo sequences allowed the relaxation times measurements, and one pulse to acquire NMR spectra.

The transport behavior of the prepared membranes was also characterized in terms of proton conductivity via Electrochemical Impedance Spectroscopy (EIS). Finally Dynamic Mechanical Analysis (DMA) has been used to investigate the mechanical properties of the polimer electrolyte. Both techniques are also described in this section.

4.1 NUCLEAR MAGNETIC RESONANCE (NMR)

Nuclear magnetic resonance (NMR) spectroscopy was first developed in 1946 by research groups at Stanford and M.I.T., in the USA. It is a powerful technique that that takes advantage of the magnetic properties of certain atomic nuclei interacting with magnetic fields, to determine physical and chemical properties of atoms or the molecules in which they are contained. As non-destructive and non-invasive technique, it can provide detailed information about the structure, dynamics, reaction state, and chemical environment of molecules with no alteration of the sample's structure. In

principle, NMR is applicable to any nucleus possessing spin. Classically, a nucleus of mass m_n and radius ***r,*** rotating with pulsation **ω**, has an intrinsic angular momentum (with module P) given by the following equation:

$$P = \omega\, m_n r2 = 2\,\pi\, m_n r^2/t_r \qquad \text{(Eq. 1)}$$

where t_r is the time of rotation. The angular momentum is also related to a magnetic momentum:

$$\mu = qP/\,2m_n \qquad \text{(Eq. 2)}$$

in which q is the charge and $q/2m_n$ is the giromagnetic ratio (γ) of the particle. The relationship between the angular momentum and the nuclear spin (I) is given by the equation:

$$\mathrm{P} = \hbar I \qquad \text{(Eq. 3)}$$

where $\hbar$ is the Planck constant. Replacing this last definition of angular momentum in Eq 3, it appears clear that the magnetic moment μ of a nucleus is directly proportional to I:

$$\mu = q\,\hbar I\,/\,2m_n = \gamma\hbar I \qquad \text{(Eq. 4)}$$

The magnitude of the spin quantum number (I) depends from the number of particles inside the nucleus, i.e. protons and neutrons. For nuclei in which the number of protons and the number of neutrons are both even, the spin is zero. When or the number of protons or neutrons within the nuleus is odd, it has half-integer spin (1/2, 3/2, 5/2). If the number of protons and the neutrons one are both odd the nucleus has integer value of spin. "I" values of some commonly occurring nuclei are given in Table 1.

Table 1. Some commonly nuclear spin quantum numbers.

I	***Nuclei***
0	**^{12}C, ^{16}O**
1/2	**^{1}H, ^{13}C, ^{15}N, ^{19}F, ^{29}Si, ^{31}P**
1	**^{2}H, ^{14}N**
3/2	**^{11}B, ^{23}Na, ^{35}Cl, ^{37}Cl**
5/2	**^{17}O, ^{27}Al**
3	**^{10}B**

It is worthy to note that ^{12}C and ^{16}O have $I = 0$, i.e. there is no angular momentum, no magnetic momentum and consequently no NMR spectra. When a magnetic field B_0 is applied to a nucleus with spin $\geq 1/2$, the nucleus will tend to precess about the direction of the magnetic field (see Fig 1).

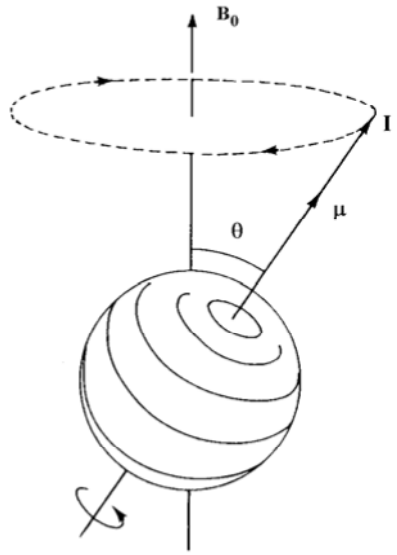

Figure 1. Spin precession around a constant magnetic field.

The precession arises from the intrinsic nuclear magnetic moment $\boldsymbol{\mu}$. $\boldsymbol{\mu}$ can have any orientation in space, but in an external magnetic field it aligns itself in such way as to minimize the energy of the system. The energy of this system is given by:

$$E = -\mu \bullet B_0 = -|\mu|\,|B_0|\cos\theta = -\mu_z B_0 \qquad \text{(Eq. 5)}$$

This equation can be rewritten as:

$$E = -\mu_z B_0 = -\gamma \hbar I_z B_0 \qquad \text{(Eq. 6)}$$

Therefore, the energy of this system depends on the z-spin vector. The quantization rule for I_z is:

$$I_z = m \qquad \text{(Eq. 7)}$$

where m can take the values $m = I, I\text{-}1, \ldots, -I$ and I is the nuclear angular momentum. There are $(2I+1)$ possible orientations for I_z and therefore the same number of energy levels. Hence, the energy of the system is:

$$E = -\mu_z B_0 = -m\gamma\hbar B_0 \qquad \text{(Eq. 8)}$$

and as result the energy difference between two consecutive energy levels is:

$$\Delta E = \gamma\hbar B_0 \qquad \text{(Eq. 9)}$$

which consequently is the minimum energy the system can absorb or emit.

Under the influence of B_0 the nucleus to precesses about the z-axis at a frequency ν. This frequency is called the Larmor frequency and is given by:

$$\nu_L = \gamma B_0 \qquad \text{(Eq. 10)}$$

The precession can be clockwise for $\gamma > 0$ or counterclockwise for $\gamma < 0$. According to this formula, Eq. 9 can be rewritten in term of the Larmor frequency as:

$$\Delta E = \hbar\, \nu_L \qquad \text{(Eq.11)}$$

Hence, energy transitions between the energy levels of the system involve absorption or emission of photons of energy ΔE [1]. Up to this point the behavior a single nucleus in a magnetic field has been only considered. To analyze the behavior of a collection of nuclei it is necessary to use statistical analysis. The $2I + 1$ states for spin-I nucleus are equally spaced, with energy gap $\hbar\gamma B_0$.

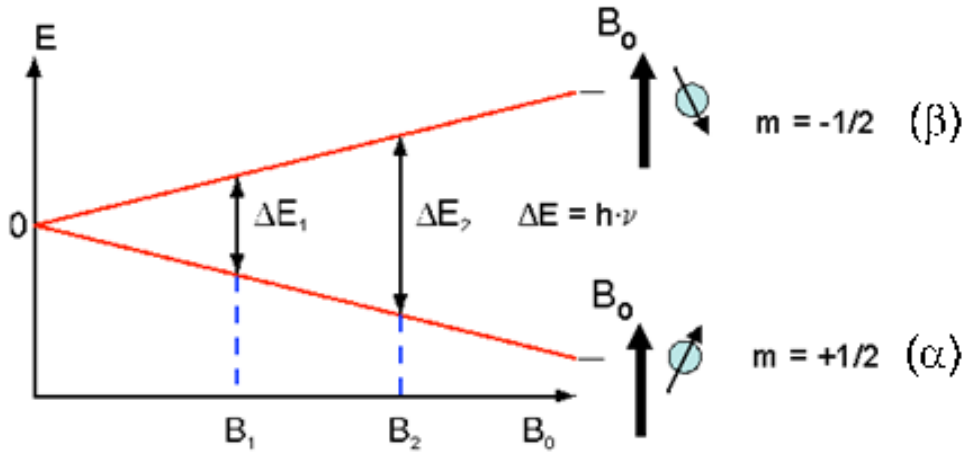

Figure 2. Energy of levels with mI = +1/2 and -1/2 as a function of increasing magnetic field strength. Note that when the field is zero, the different mI are degenerate (have the same energy).

Applying Boltzman statistics to a simple two state system (Figure 2) where I=1/2, and m=1/2, -1/2 results in:

$$\frac{N_\beta}{N_\alpha} = e^{-\frac{\Delta E}{k_B T}} \approx 1 - \frac{\Delta E}{k_B T} = 1 - \frac{\gamma \hbar B_0}{k_B T} \qquad \text{(Eq. 12)}$$

where N_β is the number of nuclei in the highest energy level, N_α is the number of nuclei in the lowest energy level and k_B is the Boltzmann constant. Generally, the population difference in a material at ambient temperature is approximately 10^{-6}.

The overall behavior of the spins in matter can be visualized in the following manner. Dividing the material onto small domains, each of the domains will have a net magnetization resulting from the sum of all the spins in the domains. The domain magnetization will randomly fluctuate in time, but the net magnetization of the material will be zero over time. When this material is introduced into a magnetic field, a small excess of the domain magnetizations will be generated which will be aligned parallel to the magnetic field at any instant time. As discussed previously, in fact, there are more magnetic moments aligned with the field than against it. This means that when all the opposing magnetic moments have cancelled each other out, the net population difference will create a bulk magnetization vector**,** also called the material's equilibrium magnetization vector (**M_0**), aligned along the direction of **B_0** (Fig. 3a).

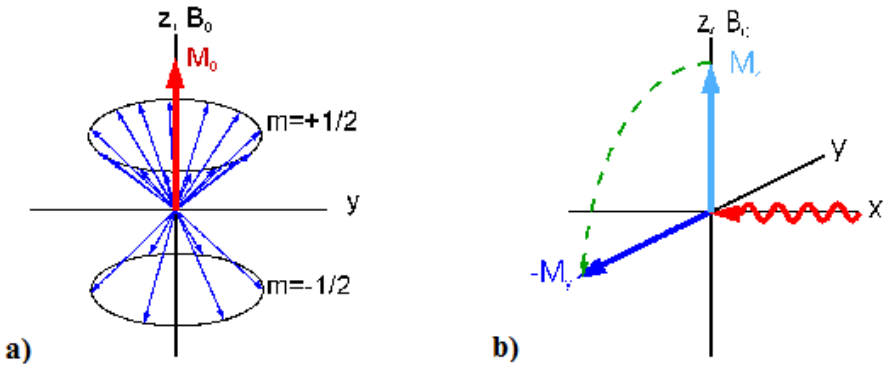

Figure 3. Schematic illustrations of: a) the net magnetization as a result of the addition of all spins in the system; b) effect of B1 on the magnetization vector.

Using this coordinate system, the total magnetization in the "z" direction (M_z) is equal to M_0, and the magnetization in the "x" and "y" directions (M_x, M_y) are 0. At this point, if a coil is used to produce an oscillating magnetic field **B_1** perpendicular to B_0, M_0 will

move away from the "z" direction, precessing at a frequency v_L and resulting in a net M_x and M_y (Figure 3b). B_1 is applied in the form of radio frequency (RF) pulses with resonance frequency v_L (eq. 10). In particular, the magnetic field B_1, influences the net magnetization of the overall samle due to changes in occupancy in the spin state. In other words M reflects the difference of the population between the upper and lower spin levels (for I = ½ nuclei system). The angle of rotation or flip angle of the magnetization vector is given by:

$$\theta=\gamma B_1 \tau \qquad \text{(Eq. 13)}$$

Applying an RF pulse that rotates the magnetization vector by 90° onto the x-y plane, M_z could also be reduced to zero. This is called a 90° pulse (Fig. 4) while the net magnetization in the x-y plane is called the transverse magnetization.

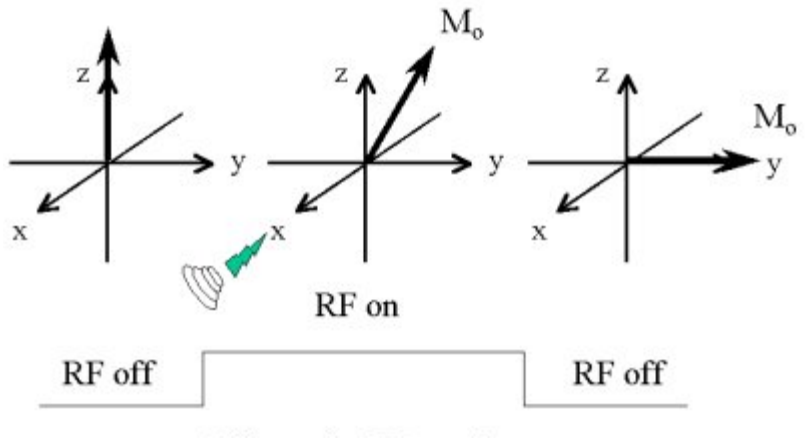

Figure 4. Effect on the net magnetization by a 90° RF pulse.

When a material is subjected to these conditions, it will emit radiation mainly in the form of an RF signal. The RF signal is received by the coil (same one used to generate B_1) and spectroscopically processed to extract information about the material in question.

The return of magnetization, M, to its equilibrium state is known as relaxation. There are three factors that influence the decay of M: magnetic field inhomogeneity, spin-lattice (longitudinal) T_1 relaxation and spin-spin relaxation (transverse) T_2 relaxation. T_1 relaxation is the mechanism by which the component of the magnetization vector along the direction of the static magnetic field reaches thermodynamic equilibrium with its

surroundings (the "lattice"). T_2 relaxation is the mechanism by which M_{xy}, the transverse component of magnetization vector, exponencially decays towards its equilibrium value of zero. The behavior of the magnetization vector as it returns to equilibrium can be described semi-classically by the Bloch equations[2], which are the equations of motion for the nuclear spin magnetization in the rotating frame.

$$dM_x/dt = \gamma[\boldsymbol{M}(t) \times \boldsymbol{B}(t)]_x - M_x(t)/T_2 \quad \text{(Eq. 14)}$$

$$dM_y/dt = \gamma[\boldsymbol{M}(t) \times \boldsymbol{B}(t)]_y - M_y(t)/T_2$$

$$dM_z/dt = \gamma[\boldsymbol{M}(t) \times \boldsymbol{B}(t)]_z - (M_z(t) - M_0)/T_1$$

where $\boldsymbol{M}$ is the magnetization vector and $\boldsymbol{B}$ is the magnetic field.

After an RF pulse is applied, the magnetization vector relaxes to its initial state along B_0 in the z-axis. This relaxation process is called the spin-lattice relaxation and it is characterized by a time T_1. The analytic solution the spin-lattice relaxation can be obtained from the Bloch equation for M_z:

$$dM_z/dt = -(M_z(t) - M_0)/T_1 \quad \text{(Eq. 15)}$$

The solution of equation (15) is:

$$M_z = M_0 \, (1 - e^{-\tau/T1}) \quad \text{(Eq. 16)}$$

In the x-y plane the magnetization is also affected by the presence of local field inhomogeneities. This causes each of the spin domains to experience a slightly different magnetic field. Therefore, the spin domains precess at different Larmor frequencies and start to dephase. This process is called spin-spin relaxation and is characterized by a time T_2. The analytic solution of the spin-spin relaxation process can be obtained from the Bloch equations for M_x and M_y.

$$dM_x/dt = -\omega M_y - M_x(t)/T_2 \quad \text{(Eq. 17)}$$

$$dM_y/dt = \omega M_x - M_y(t)/T_2$$

where $\omega = 2\pi\nu$. The solutions for these equations are:

$$M_x(t) = M_0 \cos(\omega\tau) \, e^{-\tau/T2} \quad \text{(Eq. 18)}$$

$$M_y(t) = M_0 \sin(\omega\tau) \, e^{-\tau/T2}$$

where M_0 is the magnitude of the spin magnetization. It should be mentioned that $T_2 \leq T_1$ and although these two processes have been discussed separately, they actually occur simultaneously.

There are two main processes that contribute to the decay of the transverse magnetization: molecular interactions (pure T_2 processes) and differences in the magnetic fields affecting by the spin domains (heterogeneous T_2 processes). The combination of these two effects is denoted T_2^*:

$$1/T_2^* = 1/T_2 + 1/T_{2(inhomogeneus)} \qquad \text{(Eq. 19)}$$

4.1.1 NMR Relaxation Measurements

T_1 measurements

As already mentioned, time constant T1 characterizes the rate of return to equilibrium of the z-compnent of the magnetization after perturbation. To determine the longitudinal relaxation time for T1, one of the most common pulse sequences used is the inversion recovery sequence[3]. The sequence consists of two RF pulses, π and π/2 respectively, separated by a relaxation time τ. (Fig. 5)

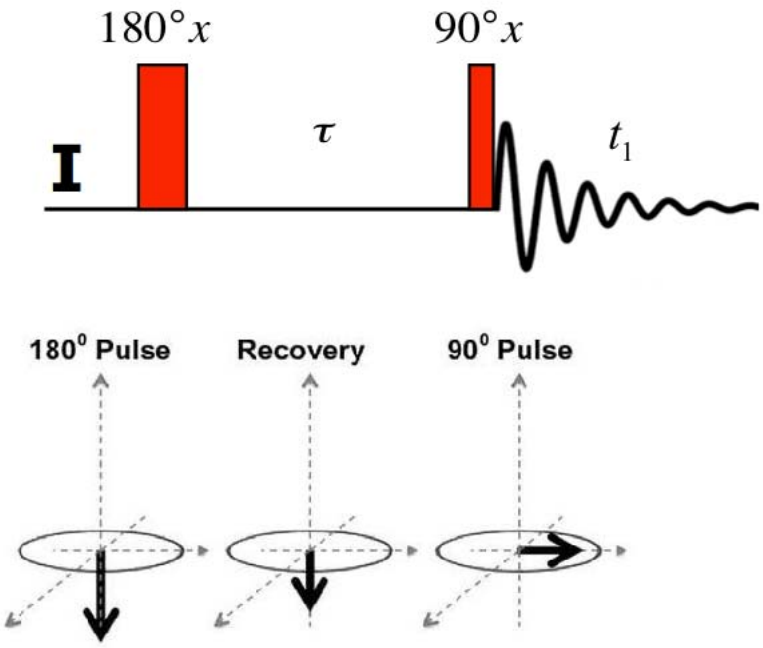

Figure 5. Inversion recovery sequence and magnetization vector evolution.

The first pulse, applied along the +x-axis, rotates the magnetization vector by π from the +z-axis to the –z-axis. In the delay τ between the pulses, the magnetization vector recovers along the z-axis towards its equilibrium value M_0 along the +z-axis. A second pulse is applied along the +x-axis after the delay time τ. The time interval τ is varied using approximately 12-15 values. The pulse rotates the magnetization vector by π/2 onto the y-axis, where its free induction decay is detected. The second pulse allows, thus, the spectrometer to detect the magnetization, since the spectrometer can only measure magnetizations in the x-y plane. In the inversion recovery sequence, the

magnetization vector intensity evolves as a function of τ and the characteristic spin-lattice relaxation time T_1. The time dependence of M_z follows:

$$M_z = M_0 (1 - 2e^{-\tau/T1}) \qquad \text{(Eq. 20)}$$

To prevent saturation of the spin system, the magnetization needs to be at equilibrium before a pulse sequence is applied. The value of the magnetization vector approaches M_0 as the relaxation time τ increases. Therefore, T_1 is of practical importance because it indicates the lowest time delay necessary between successive pulse sequences for the system to reach equilibrium. Usually, this delay time is approximately 5 T_1.

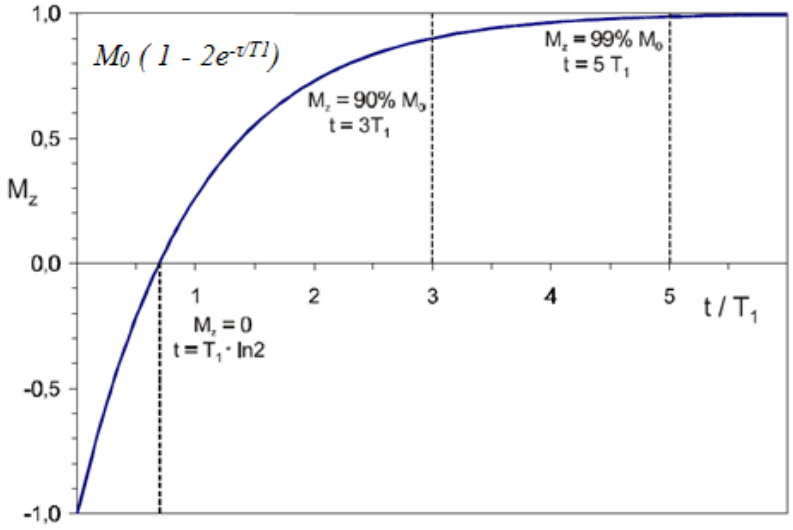

Figure 6. Longitudinal relaxation time, T_1, recovery curve.

T_2 measurements

The time constant T_2 determines the time it takes for the x and y components of the magnetization to equilibrate after perturbation. Whilst there are several more-elaborate techniques for measuring the spin-spin relaxation, T_2, most are based on the spin-echo pulse sequence, a schematic of which is shown in Figure 7. This technique was first developed by Hahn in 1950 [4] and consists of two rf pulses: one π/2 and the other π, separated by time –τ. Ideally, in a perfectly homogeneous static magnetic system, the perturbed magnetization returns to equilibrium by a dephasing of the coherences in the x-y plane during a time T_2, which is related to the spectrum line-width at half height.

However, in practice, the static magnetic field is not perfectly homogeneous; this causes nuclei in different regions of the sample to experience different fields and therefore precess at different frequencies. This precession results in additional dephasing of the spins in the x-y plane. In practice, $T_2 \leq T_1$.

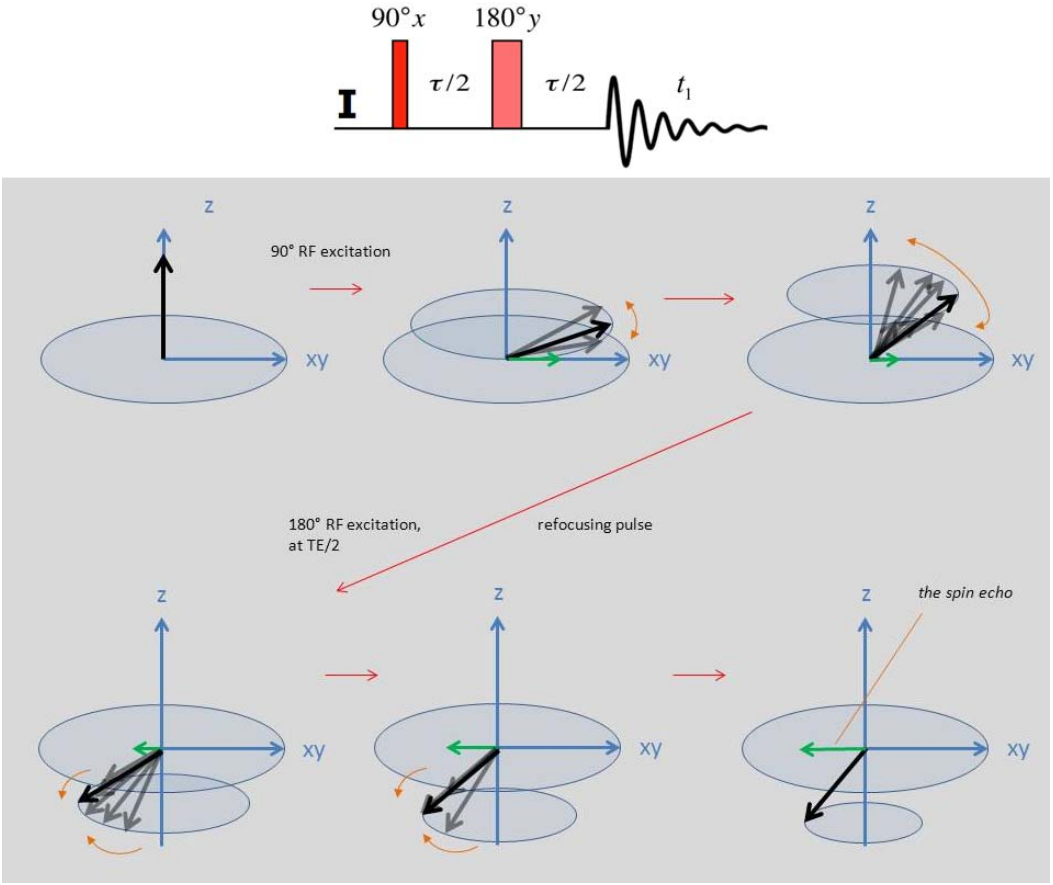

Figure 7. Spin-echo sequence and magnetization vector evolution.

The first pulse is applied along the +x-axis and rotates the magnetization vector by $\pi/2$ from the +z-axis to the –y-axis. In the interval τ, the spins dephase by a combination of local or external magnetic field inhomogeneities. Other effects such as spin-spin interactions or intermolecular interactions may contribute significantly to the spin dephasing. After the dephasing time τ, a second pulse is applied along the +y-axis. This pulse rotates the dephased spins by π, effectively reversing the dephasing process. At a time τ after the second pulse, the spins refocus and an echo is formed. In the spin echo

sequence, the magnetization vector intensity evolves as a function of τ and the characteristic spin-spin relaxation time T_2. (Eq. 21)

$$M_{(xy)} = M_0 e^{-\tau/T2} \qquad \text{(Eq. 21)}$$

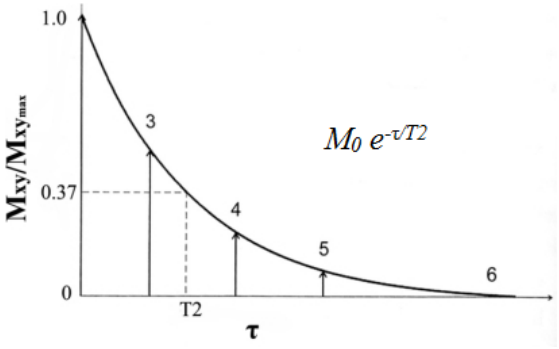

Figure 8. Transverse relaxation time, T_2, curve.

4.1.2 Temperature dependence of T_1 and T_2

An NMR state diagram is a curve of NMR relaxation time, be it spin–spin relaxation time (T_2) or spin–lattice relaxation time (T_1), versus temperature. Usually, relaxation times of liquids increase linearly with temperature. However, at very low temperatures or with solid materials, relaxation times behave drastically different. For solids, with rising temperature, T_2 changes little at low temperatures and increases rapidly above certain temperatures, characterized by a mirrored-L shape, while T_1 decreases rapidly to a certain point and rises again rapidly, characterized by a minimum (Figure 9).

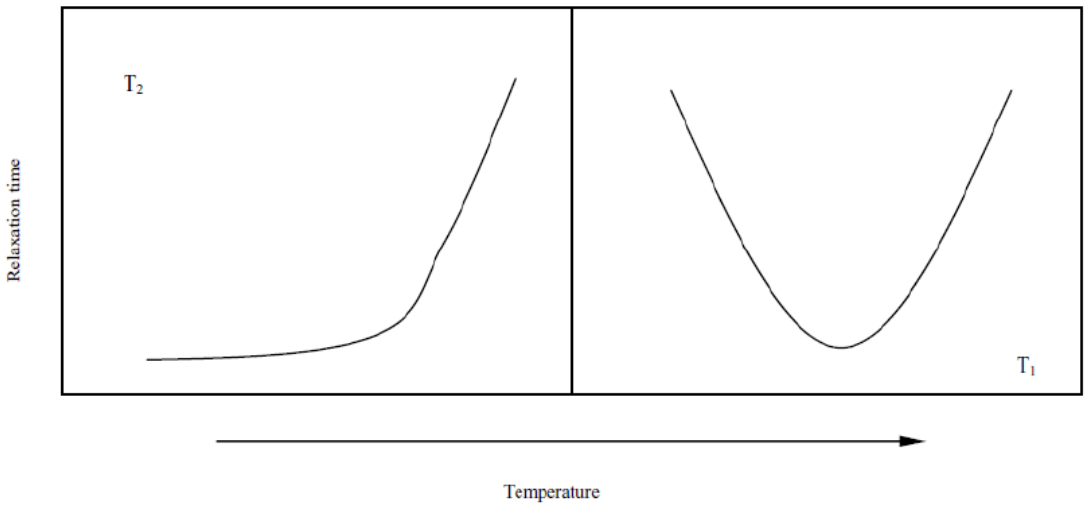

Figure 9. Schematic diagrams showing relaxation times of a material as a function of temperature.

Let us consider a high molecular weight polymer with side chain segments. When heated, some segments within the long chain of the polymer molecule are mobilized before the whole molecule starts moving. Further heating causes the entire molecule to move and become liquid. Two types of motions can be identified during the gradual heating, that is, segmental motion and molecular motion. At a certain low temperature, both motions are hindered severely or frozen; at higher temperatures, both motions may be activated. These 2 situations correspond to the solid state and liquid state, respectively. When the polymer is placed at a temperature where only the segmental motion is activated while the molecular motion is frozen, the state is called the rubbery state, and such state transition takes place at the glass–rubber transition temperature T_g. On further heating, the polymer in the rubbery state becomes a highly viscous liquid and starts flowing. The polymer moves into the visco-fluid state, and such transition takes place at the flow temperature T_f. Relaxation time is a function of the spin species and the chemical and physical environments surrounding the spins. Therefore, analysis of T_1 and T_2 of a sample will allow the study of the chemical and physical properties of the sample. A long T_1 or T_2 indicates a slow relaxation and a short T_1 or T_2 value indicates a rapid relaxation.

The dynamic motion of spins can be characterized by a correlation time τc, which is, roughly speaking, the minimum time required for the nuclear magnetic moment to

rotate 1 radian (1/2 π of a complete circle). In general,τc for non viscous liquid is very short. With water, for instance, τc is about 10^{-12} s. On the other hand, τc for solids is very long, about 10^{-5} s. Within limits, the slower the motion, the longer the τ_c, and the faster a perturbed spin system will relax. Thus, the relationship between the motional characteristics and NMR relaxation can be established through the relationship between τ_c and relaxation time, as described in the equations[5] 22 and 23:

$$\frac{1}{T_1} = K\left[\frac{\tau_c}{1+(\omega_0\,\tau_c)^2} + \frac{4\tau_c}{1+(2\omega_0\tau_c)^2}\right] \qquad \text{(Eq. 22)}$$

$$\frac{1}{T_2} = \frac{K}{2}\left[3\tau_c + \frac{5\tau_c}{1+(\omega_0\,\tau_c)^2} + \frac{2\tau_c}{1+(2\omega_0\tau_c)^2}\right] \qquad \text{(Eq. 23)}$$

$$K = \frac{3\mu^2}{160\pi^2}\,\frac{\hbar^2\gamma^4}{r^2}$$

K is a constant that includes a number of nuclear parameters and constants, and ω_0 is the resonance frequency. Figure 3.1.5 is a plot of τ_c versus relaxation time constants T_1 and T_2. The curves are similar to those in Figure 10 [6]. This is because, within limits, τ_c is related to temperature. Their relationship can be described by the equation 24:

$$\tau_c = \tau_{c0}\, e^{E_{act}/kT} \qquad \text{(Eq. 24)}$$

where E_{act} is the activation energy for rotational motion, k the Boltzmann constant, T the absolute temperature, and τ_{c0} is a constant.

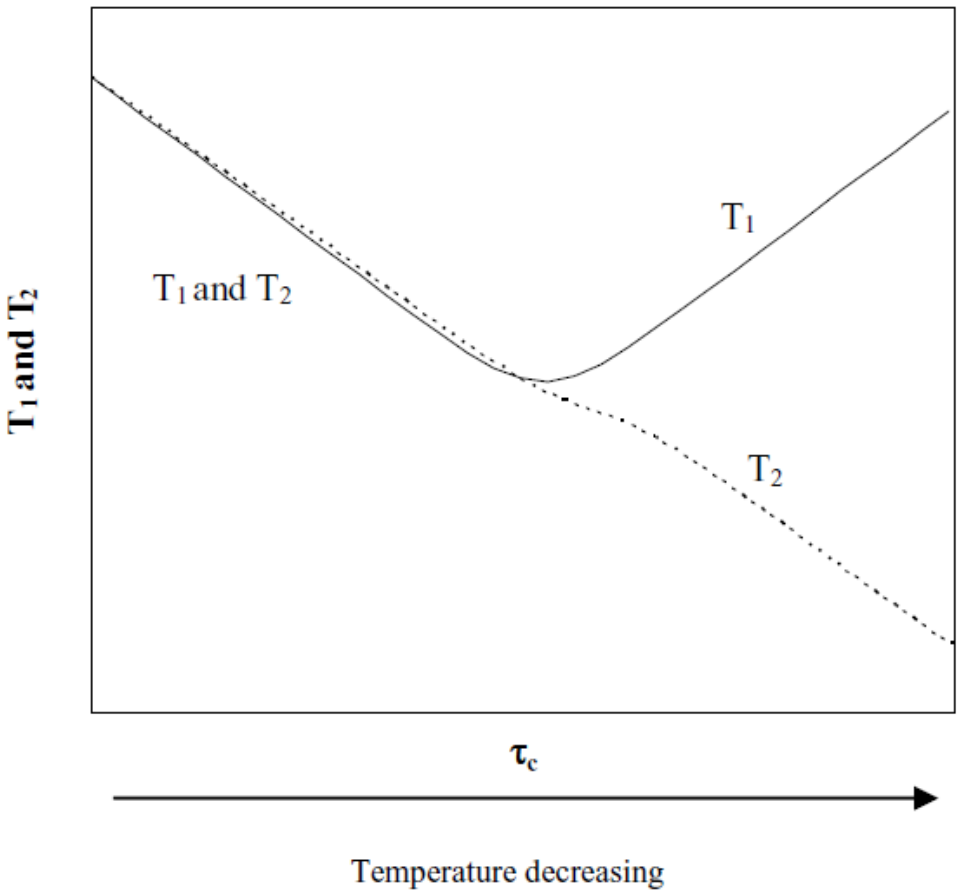

Figure 10. A generalized schematic diagram showing the relationship between relaxations time constants and correlation time.

Fundamentally, T_1, T_2, and equations 22 and 23 describe the rotational motions of nuclei. It is suggested that rotation of a probe molecule (e.g., water) in a viscous liquid should be coupled to the structural relaxation of the surroundings, which is largely determined by the translational diffusion properties and the structure of the neighboring molecules[7]. The fact that the product of correlation time and translational diffusion coefficient is a constant indicates that rotational and translational motions are closely related[7, 8]. Netz and others5 (2002) suggest that translational and rotational motions are controlled by a common mechanism. Therefore, T_1 and T_2 are conveniently coupled to molecular mobility; however, the relationship between relaxation times and molecular mobility depends on the nucleus being probed and surrounding systems[9, 10].

4.1.3 Self-Diffusion Measurements with NMR

As previously mentioned, NMR is a powerful noninvasive technique to obtain parameters of interest for fuel cell. NMR spectroscopy has provided information on the microscopic as well as macroscopic nuclear environments by determination of parameters such as relaxation times (T_1, T_2), self-diffusion coefficients (D), and structural information. One of its most important uses in the study of polymeric membranes has been to provide mass transport data of the diffusing ions or molecules through direct measurement of self-diffusion. It is the transport of particles or an ensemble of particles due to thermal motion, thus the particles feel no net driving force. Self-diffusion is classically described by the Stokes-Einstein equation:

$$D = \frac{k_B T}{f} \qquad \text{(Eq. 25)}$$

where T is the temperature, k_B is the Boltzman factor and f is the friction factor. For a spherical particle with hydrodynamic radius R_h immersed in a fluid of viscosity η, Stokes' law gives $f=6\pi\eta R_h$. The self-diffusion coefficient in a homogeneous system is related to the root mean square displacement of the ions/molecules by:

$$(\langle r^2 \rangle)^{1/2} = (2\, n\, D\, t_d)^{1/2} \qquad \text{(Eq. 26)}$$

where n is the number of dimensions a particle can move, t_d is the diffusion time and D is the self-diffusion coefficient.

Through the measurements of the self-diffusion coefficient, the ion conductivity of the electrolyte membrane can also be directly or indirectly obtained. In fact, ion conductivity is related to the self-diffusion coefficient by[11]:

$$\sigma = \frac{Dq^2 c}{k_B T} \qquad \text{(Eq. 27)}$$

where D is the self-diffusion coefficient, q the ionic charge, c the concentration of the ions, k_B is the Boltzmann factor and T the temperature.

As already mentioned, self diffusion coefficient of species or molecules can be directly measured by the NMR pulse gradient spin echo (PGSE) and pulse gradient stimulated echo pulse (PGSTE) sequences. The schematic for the PGSE technique is shown in Figure 11. The PGSE technique is a powerful non-invasive method for the determination of D. It can provide very accurate and quick measurement of D in multi-

component systems without the need for isotopic labeling based on is chemical shift difference of the diffusing specie. The technique was first developed by Hahn (1950)[4] and originally involved the use of a typical spin-echo-pulse sequence. In addition to this, a constant magnetic gradient was applied along the z axis. This method was later modified by Stejskal and Tanner (1965) in which they replaced the constant magnetic gradient by pulsed magnetic gradients[12-14]. The application of pulsed gradients as opposed to one that is constant eliminates the problem of large broadening of the signal in the presence of the static gradient. The NMR PGSE technique consists of two rf pulses: first π/2, then π. Following each rf pulse are magnetic gradients of strength g and duration δ, separated by time Δ.

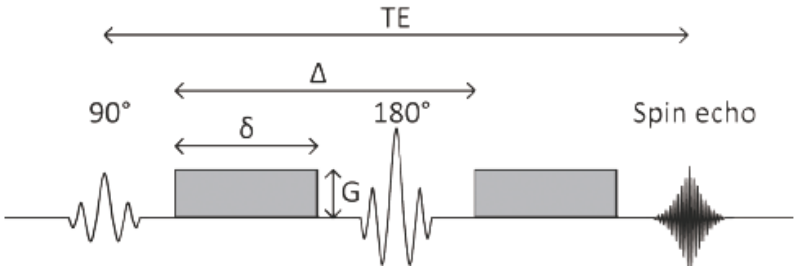

Figure 11. Schematic of the pulse gradient spin echo technique (PGSE) pulse sequence, which consist of two rf pulses (π/2 and π), separated by delay time τ, and each followed by a magnetic gradient pulse of magnitude g1, duration δ, and separation Δ [13].

The core of the NMR PGSE technique lies in the fact that in the presence of a magnetic field with superimposed magnetic gradients, a diffusing nucleus will experience changes in the magnetic field it experiences and its resulting phase. This change in phase results in attenuation of the magnetization M and the resulting attenuation factor is given by[12]:

$$M(g) = e^{-\gamma^2 g^2 D \delta^2 \left(\Delta - \frac{\delta}{3}\right)} \qquad \text{(Eq. 27)}$$

where D is the self-diffusion coefficient of the diffusing species, g is the gradient strength, and δ and Δ are the gradient pulse width and interval between gradient pulses, respectively. The expression above is for a fixed time between excitation and refocusing pulses. The attenuation of the spin echo versus gradient strength is shown for a representative system in Figure 12. In order to obtain D, the magnitude of g, Δ, τ, and γ

must be known. Typical values of δ are a few milliseconds, whilst Δ ranges from a few milliseconds to a few hundred milliseconds.

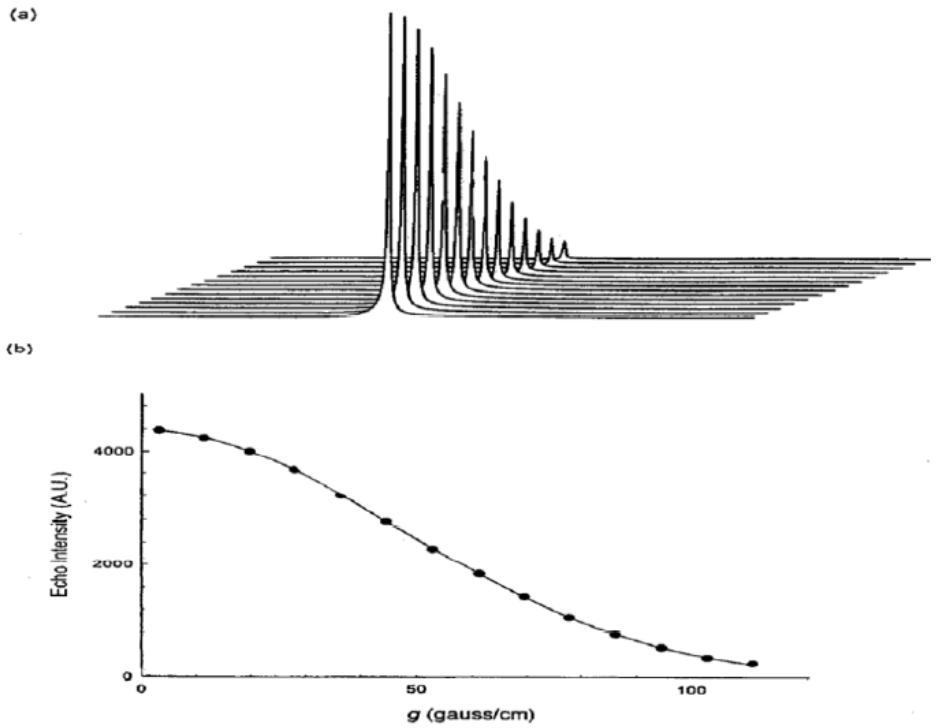

Figure 12. A representative 1H PGSE NMR decay profile and plot from which the diffusion coefficient is obtained[13].

Finally, the pulse gradient stimulated echo (PGSTE) pulse sequence, shown in Figure 13, is similar to the PGSE technique developed by J.E. Tanner in 1969 [15]. This pulse sequence is useful when $T_1 >> T_2$, where motion of molecules is slow compared with the period of the Larmor frequency[16] Determination of D by the PGSTE technique is also obtained by the equation used for the PGSE technique.

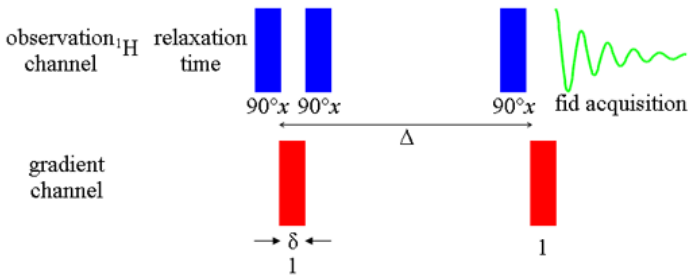

Figure 13. Schematic of the pulse gradient stimulated spin echo (PGSSE) pulse sequence.

4.1.4 High pressure NMR

One of the main interests in studying PEMs is to understand the behavior of ionic and molecular motion in them. In the case of PEMFCs, the characterization of water diffusion in the PEM membrane is important to understand the dynamics of the fuel cell. Primarily, molecular and ionic motion is affected by the temperature of the medium and the average available volume that molecules have for diffusion. These can be studied by variable temperature and pressure measurements, respectively[17]. To gain insight into the behavior of molecular motion it is important to separate both effects. This can be accomplished by independently controlling both temperature and pressure. Pressure, in particular, is an indispensible thermodynamic variable in the study of ionic conduction and ion diffusion[18, 19]. Accordingly, important information about PEM macroscopic properties could be obtained by measuring how various dynamic processes are affected by pressure[20]. Combining NMR with high-pressure can provide a wealth of information. In fact, the motion of the molecules and ions are accompanied by volume changes, which may be probed by changing the pressure. This method, pioneered by Benedek and Purcell in 1954, involves the application of hydrostatic pressure to the system being investigated in the presence of a static magnetic field[21]. The hydraulic fluid must contribute a minimal NMR signal and is used to transmit pressure from the pressure-generating system to the sample.

The dynamic parameter, represented by *A,* which may be the self-diffusion coefficient D, or the motional correlation time (which is related to the NMR spin-lattice relaxation time T_1), is associated to various motional processes by the Arrhenius equation:

$$A = A_0 e^{-G/RT} \qquad \text{(Eq. 28)}$$

where *R* is the universal gas constant, *T* is the absolute temperature and *G* is the Gibbs free energy

$$G = Q - ST + pV \qquad \text{(Eq. 29)}$$

Taking the logarithmic partial derivative of equation 28 with respect to pressure results in:

$$\left[\frac{\partial G}{\partial p}\right]_T = -RT\left[\frac{\partial ln(A)}{\partial p}\right]_T \qquad \text{(Eq. 30)}$$

One can now define:

$$\Delta V = -RT\left[\frac{\partial ln(A)}{\partial p}\right]_T \qquad \text{(Eq. 31)}$$

where ΔV is the activation volume, T is the temperature of the sample, P is the pressure and A could be either D is the diffusion coefficient or T_1 the spin lattice relaxation[20]. The activation volume is a parameter associated with molecular and ionic motion in a material, which quantifies the change in local volume as a molecule or ion diffuses[22]. It is of interest to quantify how the activation volume changes with temperature. This information gives insight into how the material structure changes with temperature and water or ion concentration. This type of measurement can be achieved with an experimental setup that allows independent pressure and temperature control. One must precise that the activation volume is, however, not directly related to an actual volume; instead it can be thought of as the pressure dependence of the activation energy [18]. A schematic of the experimental setup is shown below in Figure 14.

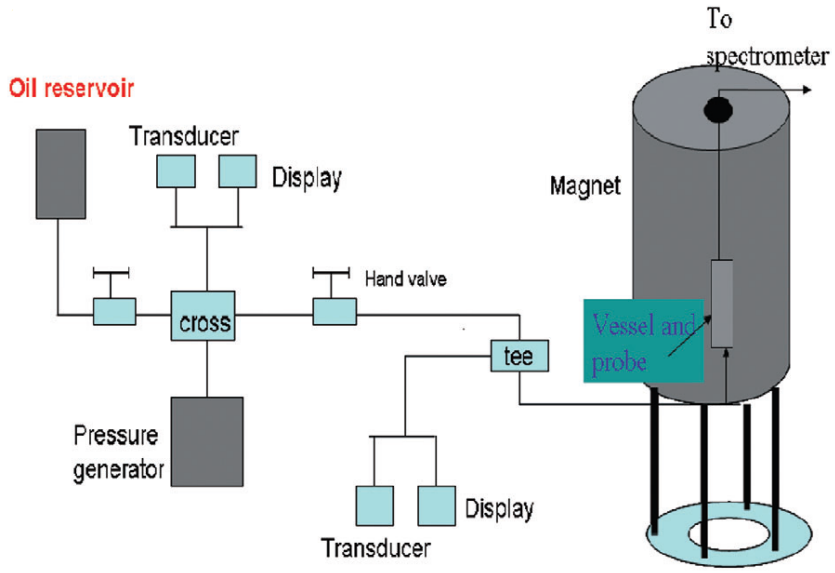

Figure 14. Schematic of the experimental setup for high-pressure NMR. The oil reservoir houses the pressurizing fluid, which is pressurized by the manual generator and sent to the vessel. The transducers allow determination of the pressure.

4.2 ELECTROCHEMICAL IMPEDANCE SPECTROSCOPY (EIS)

Electrochemical Impedance Spectroscopy (EIS) is a powerful characterization technique for investigating the electrical properties of materials and their interfaces with electronically conducting electrodes. It may be used to investigate the dynamics of bound or mobile charge in the bulk or interfacial regions of any kind of solid or liquid material: ionic, semiconducting, mixed electronic–ionic, and even insulators (dielectrics)[23]. In particular, for the investigation of the transport properties of polymeric membranes, EIS can be used to characterize limitations and improve the performance of the electrolyte. In fact, it allows to analyze in the frequency domain the different physical and chemical processes occurring in an investigated device, by imposing small harmonic perturbations to the system and measuring the impedance. Consequently, this technique can be used for in-situ and ex-situ studies which makes it a polyvalent and accurate tool by comparison with most of the classical electrochemical (steady-state) methods. A common application of EIS is the identification of the origin of the different potencial losses (charge transfer activation or "kinetic" losses, ion and electron transport or "ohmic" losses, and concentration or "mass transfer" losses) and their estimation[24-26] with the scope to optimize the devices design and to determine optimal working conditions.

4.2.1 Principles and Theory

The electrical resistance is the ability of a circuit element to resist the flow of electrical current. Ohm's law (Equation 32) defines resistance in terms of the ratio between voltage, E, and current, I.

$$R = \frac{E_{(t)}}{I_{(t)}} \qquad \text{(Eq. 32)}$$

While this is a well known relationship, its use is limited to only one circuit element -- the ideal resistor. An ideal resistor has several simplifying properties:

- ✓ It follows Ohm's Law at all current and voltage levels.

- ✓ Its resistance value is independent of frequency.
- ✓ AC current and voltage signals though a resistor are in phase with each other.

However, the real world contains circuit elements that exhibit much more complex behavior. These elements force us to abandon the simple concept of resistance, and in its place we use impedance, a more general circuit parameter. Like resistance, impedance is a measure of the ability of a circuit to resist the flow of electrical current, but unlike resistance, it is not limited by the simplifying properties listed above.

Electrochemical impedance is usually measured by applying an AC potential to an electrochemical cell and then measuring the current through the cell. Assume that we apply a sinusoidal potential excitation. The response to this potential is an AC current signal. This current signal can be analyzed as a sum of sinusoidal functions (a Fourier series).

Electrochemical impedance is normally measured using a small excitation signal. This is done so that the cell's response is pseudo-linear. In a linear (or pseudo-linear) system, the current response to a sinusoidal potential will be a sinusoid at the same frequency but shifted in phase (see Figure 15).

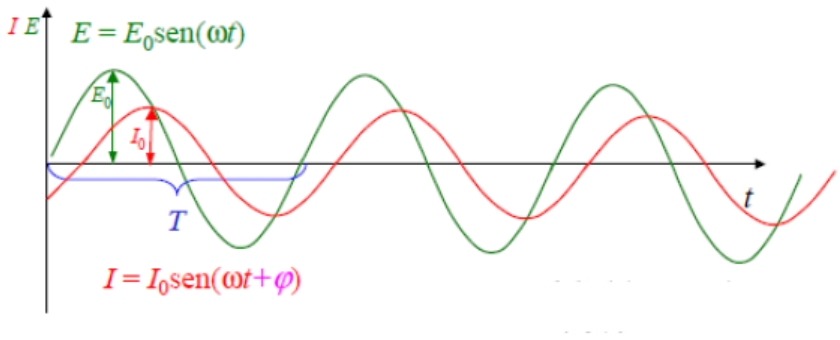

Figure 15. Sinusoidal Current Response in a Linear System.

The excitation signal, expressed as a function of time, has the form

$$E_{(t)} = E_0 \sin(\omega_t) \qquad \text{(Eq. 33)}$$

where $E_{(t)}$ is the potential at time t, $E_{(0)}$ is the amplitude of the signal, and ω is the radial frequency. The relationship between radial frequency ω (expressed in radians/second) and frequency f (expressed in hertz) is:

$$\omega = 2\pi f \qquad \text{(Eq. 34)}$$

In a linear system, the response signal, $I_{(t)}$, is shifted in phase (φ) and has a different amplitude than I_0.

$$I_{(t)} = I_0 \sin(\omega_t + \varphi) \qquad \text{(Eq. 35)}$$

An expression analogous to Ohm's Law allows us to calculate the impedance of the system as:

$$Z(\omega) = \frac{E_{(t)}}{I_{(t)}} = \frac{E_0 \sin(\omega t)}{I_0 \sin(\omega t + \varphi)} = Z_0 \frac{\sin(\omega t)}{\sin(\omega t + \varphi)} \qquad \text{(Eq. 36)}$$

The impedance is therefore expressed in terms of a magnitude, Z_0, and a phase shift, φ.

Let us assume we have an electrical element to which we apply an electric field *E(t)* and get the response *I(t)*, then we can disturb this system at a certain field *E* with a small perturbation *dE* and we will get at the current *I* a small response perturbation dI. In the first approximation, as the perturbation *dE* is small, the response *dI* will be a linear response as well (mirror at the tangent of the *I(E)* curve). If we plot the applied sinusoidal signal $E_{(t)}$ on the X-axis of a graph and the sinusoidal response signal $I_{(t)}$ on the Y-axis, the result is an oval (see Figure 16). This oval is known as a "Lissajous Figure". Analysis of Lissajous Figures on oscilloscope screens was the accepted method of impedance measurement prior to the availability of modern EIS instrumentation.

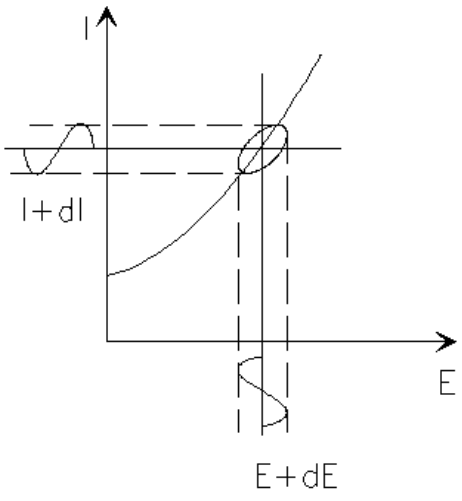

Figure 16. Origin of Lissajous Figure.

Using Eulers relationship:

$$e^{(j\,\varphi)} = cos\varphi \; + \; j\; sin\varphi \qquad \text{(Eq. 37)}$$

it is possible to express the impedance as a complex function. The potential is described as,

$$E_{(t)} \; = \; E_0 \; e^{(j\,\omega t)} \qquad \text{(Eq. 38)}$$

and the current response as

$$I_{(t)} \; = \; I_0 \; e^{(j\omega t \, - \, j\varphi)} \qquad \text{(Eq. 39)}$$

The impedance is then represented as a complex number,

$$Z_{(\omega)} \; = \; \frac{E_{(t)}}{I_{(t)}} \; = \; Z_0 \; e^{(j\,\varphi)} \; = \; Z_0 \; (cos\; \varphi \; + \; j\; sin\; \varphi) \qquad \text{(Eq.40)}$$

Look at the Equation above, the expression for *Z(ω)* is composed of a **real and an imaginary part**. If the real part is plotted on the X axis and the imaginary part on the Y axis of a chart, we get a "**Nyquist plot**" (see Fig. 17). Notice that in this plot the y-axis is negative and that each point on the Nyquist plot is the impedance Z at one frequency. On the Nyquist Plot the impedance can be represented as a vector (arrow) of length |Z|. The angle between this vector and the X-axis, commonly called the "phase angle", is *f* (= arg Z or φ).

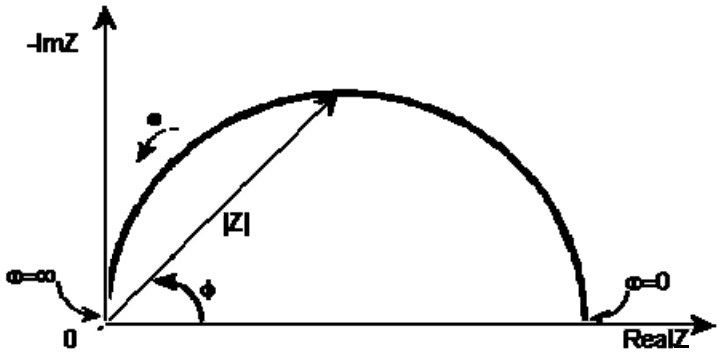

Figure 17. Nyquist Plot with Impedance Vector.

Nyquist plots have one major shortcoming. Looking at any data point on the plot, you cannot tell what the frequency used to record that point is not clearly expressed.

Low frequency data are on the right side of the plot and higher frequencies are on the left. This is true for EIS data where impedance usually falls as frequency rises (this is not true of all circuits). The Nyquist Plot in Figure 17 results from the electrical circuit of Figure 18. The semicircle is characteristic of a single "time constant". Electrochemical impedance plots often contain several semicircles. Often only a portion of a semicircle is seen.

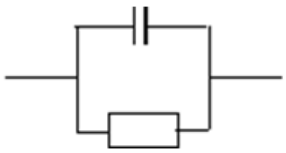

$$\frac{1}{Z} = \frac{1}{R} + \frac{1}{i\omega C}$$

Figure 18. Simple Equivalent Circuit with One Time Constant and relative formula for Equivalent impedance calculation.

Another popular presentation method is the "Bode plot". The impedance is plotted with log frequency on the x-axis and both the absolute value of the impedance *(|Z| =Z_0)* and phase-shift on the y-axis. The Bode plot for the RC circuit is shown below (Fig 19). Unlike the Nyquist plot, the Bode plot explicitly shows frequency information.

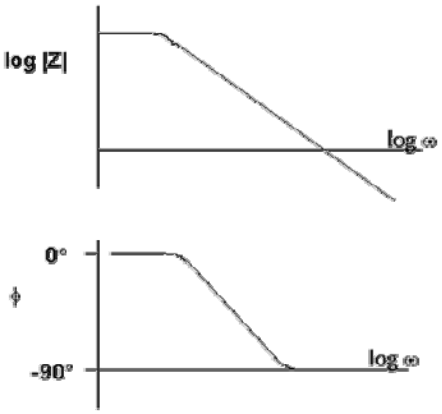

Figure 19. Bode Plot with one time constant.

Summerizing, Bode plots refer to representation of the impedance magnitude (or the real or imaginary components of the impedance) and phase angle as a function of frequency. Because both the impedance and the frequency often span orders of magnitude, they are frequently plotted on a logarithmic scale. Bode plots explicitly

show the frequency-dependence of the impedance of the device under test. A complex plane or Nyquist plot depicts the imaginary impedance, which is indicative of the capacitive and inductive character of the cell, versus the real impedance of the cell. Nyquist plots have the advantage that activation-controlled processes with distinct time-constants show up as unique impedance arcs and the shape of the curve provides insight into possible mechanism or governing phenomena. However, this format of representing impedance data has the disadvantage that the frequency-dependence is implicit; therefore, the AC frequency of selected data points should be indicated. Because both data formats have their advantages, it is usually best to present both Bode and Nyquist plots.

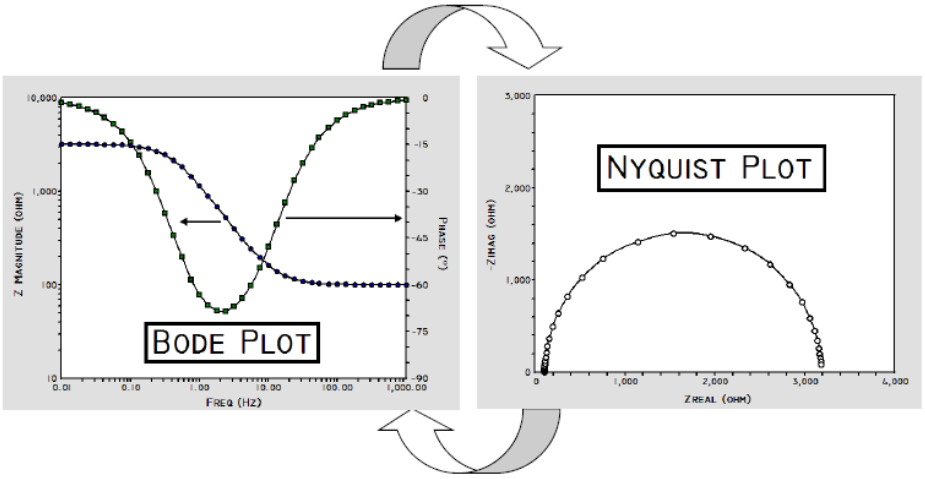

Figure 20. Comparison between Bode and Nyquist plots.

4.2.2 Linearity and Steady State of Electrochemistry Systems

By applying physically-sound equivalent circuit models, wherein physiochemical processes occurring within the device are represented by a network of resistors, capacitors and inductors, one can extract meaningful qualitative and quantitative information regarding the sources of impedance within the fuel cell. EIS is useful for research and development of new materials and electrode structures, as well as for product verification and quality assurance in manufacturing operations. Electrical circuit theory, however, can be usifully applied only when the operative condition allow

the system to work in linear and steady state conditions. It's well known that electrical circuit theory distinguishes between **linear** and **non-linear** systems (circuits). Impedance analysis of linear circuits is much easier than analysis of non-linear ones. A linear system is one that possesses the important property of superposition: if the input consists of the weighted sum of several signals, then the output is simply the superposition, that is, the weighted sum, of the responses of the system to each of the signals. Mathematically, let $y_1(t)$ be the response of a continuous time system to $x_1(t)$ ant let $y_2(t)$ be the output corresponding to the input $x_2(t)$.

Then the system is linear if:

1) The response to $x_1(t) + x_2(t)$ is $y_1(t) + y_2(t)$
2) The response to $ax_1(t)$ is $ay_1(t)$ ...

In the case of a potentiostated electrochemical cell, the input is the potential and the output is the current. Pratically, electrochemical cells are not linear, since then doubling the voltage will not necessarily double the current. However, Figure 21 shows how electrochemical systems can be **pseudo-linear**: looking at a small enough portion of a cell's current versus voltage curve, it appears to be linear. In normal EIS practice, a small (1 to 10 mV) AC signal is applied to the cell. The signal is small enough to confine the measurements to a pseudo-linear segment of the cell's current versus voltage curve. The cell's nonlinear response to the DC potential is not observed because in EIS only the cell current at the excitation frequency is measured.

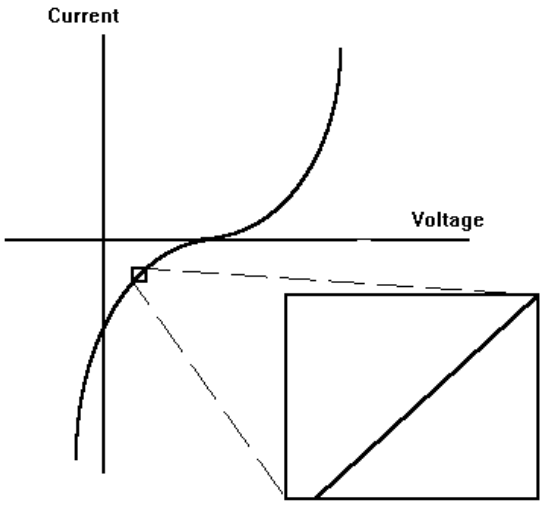

Figure 21. Current versus Voltage Curve Showing Pseudo-Linearity.

If the system is non-linear, the current response will contain harmonics of the excitation frequency. A harmonic is a frequency equal to an integer multipled by the fundamental frequency. For example, the “second harmonic” is a frequency equal to two times the fundamental frequency. Some researchers have made use of this phenomenon. Linear systems should not generate harmonics, so the presence or absence of significant harmonic response allows one to determine the systems linearity. Other researchers have intentionally used larger amplitude excitation potentials. They use the harmonic response to estimate the curvature in the cell's current voltage curve.

As already mentioned, another fundamental aspect of the EIS measurement is that the investigation should be conducted on steady state systems. Measuring an EIS spectrum takes time (often many hours). Accordingly, the system being measured must be at a **steady state** throughout the time required to measure the EIS spectrum. A common cause of problems in EIS measurements and their analysis is **drift** in the system being measured (see Fig. 22). In practice a steady state can be difficult to achieve. The cell can change through adsorption of solution impurities, growth of an oxide layer, build up of reaction products in solution, coating degradation, temperature changes, to list just a few factors. Standard EIS analysis tools may give wildly inaccurate results on a system that is not at a steady state

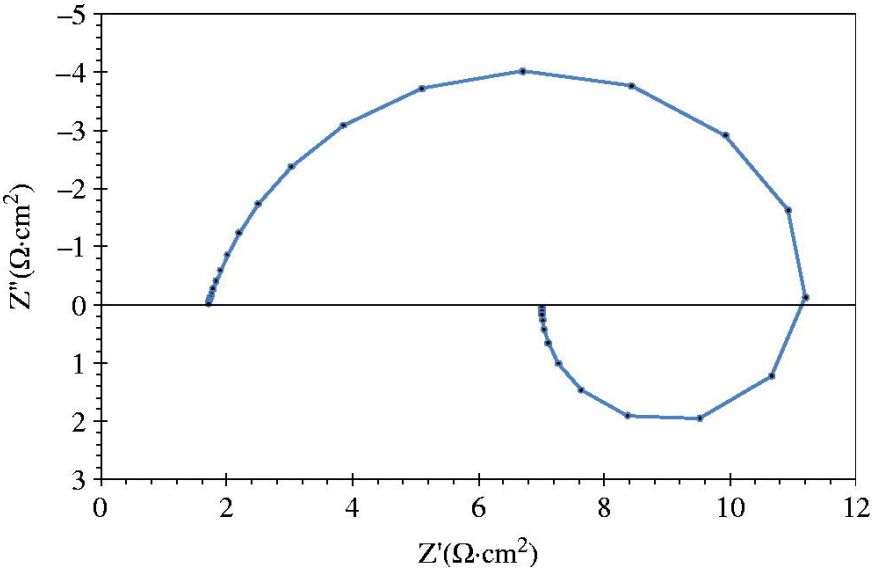

Figure 22. Drif of the impedance spectra.

4.2.3 Equivalent Electrical Circuits (EEC)

The experimental impedance spectra are usually interpreted in terms of equivalent electrical circuits (EEC) consisting of an assembly of resistances R, capacitances C and inductances I. Almosta all experimental impedance spectra in the right side of the complex plane can be fitted with an EEC provided that it contains enough R/C elements is series or in parallel. As a consequence, a multitude of more or less sophisticated EECs can be found in the literature to describe all possible forms of impedance spectra. However, in order to identify the origin(s) of voltage drop(s), the elements of the electrical circuit have to be consistent with the physical phenomena occurring in the cell. In addition, for their simultaneous independent estimation, the impedance parameters have to be decorrelated. Some knowledge of the impedance of the standard circuit components is therefore quite useful. The Table lists the common circuit elements, the equation for their current versus voltage relationship, and their impedance:

Table 2. circuit elements, the equation for their current versus voltage relationship, and their impedance

Component	Current Vs.Voltage	Impedance
Resistor	**E= IR**	**Z = R**
Inductor	**E = L dI/dt**	**Z = jωL**
Capacitor	**I = C dE/dt**	**Z = 1/jωC**

Notice that the impedance of a resistor is independent of frequency and has only a real component. Because there is no imaginary impedance, the current through a resistor is always in phase with the voltage.

The impedance of an inductor increases as frequency increases. Inductors have only an imaginary impedance component. As a result, an inductor's current is phase shifted 90 degrees with respect to the voltage.

The impedance versus frequency behavior of a capacitor is opposite to that of an inductor. A capacitor's impedance decreases as the frequency is raised. Capacitors also have only an imaginary impedance component. The current through a capacitor is phase shifted -90 degrees with respect to the voltage.

Very few electrochemical cells, however, can be modeled using a single equivalent circuit element. Instead, EIS models usually consist of a number of elements in a network. Both serial and parallel, shown in Fig. 23a) and b) respectively, combinations of elements occur. Fortunately, there are simple formulas that describe the impedance of circuit elements in both parallel and series combination.

For linear impedance elements in series the equivalent impedance can be calculated as:

$$Z_{eq} = Z_1 + Z_2 + Z_3 \qquad \text{(Eq. 41)}$$

For linear impedance elements in parallel one can calculate the equivalent impedance from:

$$\frac{1}{Z_{eq}} = \frac{1}{Z_1} + \frac{1}{Z_2} + \frac{1}{Z_3} \qquad \text{(Eq. 42)}$$

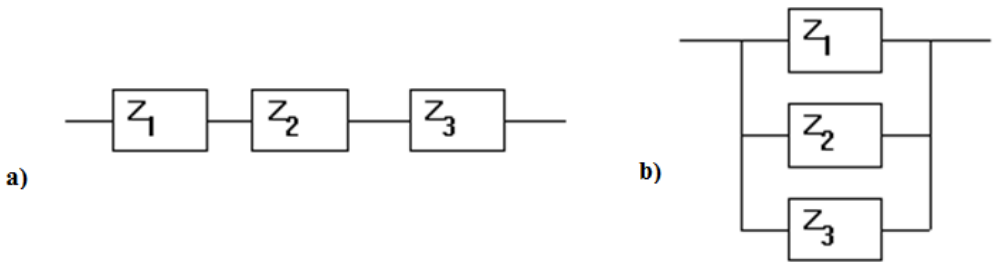

Figure 23. Schematic rapresentation of impedances a) in series and b) in parallel.

4.3 DYNAMIC MECHANICAL ANALISYS (DMA)

Dynamic mechanical analysis (abbreviated DMA, also known as dynamic mechanical spectroscopy) is a technique used to study and characterize materials. It is most useful for studying the viscoelastic behavior of the polymers. A sinusoidal stress is applied and the strain in the material is measured is measuring allowing one to determine the complex modulus. The temperature f the sample or the frequency of the stress are often varied, leading to variations in the complex modulus; this approach can be used to locate the glass transition temperature of the material, as well as to identify transitions corresponding to other molecular motions. Polymers composed of long molecular chains have unique viscoelastic properties, which combine the characteristics of elastic solids and Newtonian fluids. The classical theory of elasticity describes the mechanical properties of elastic solids where stress is proportional to strain in small deformations. Such response of stress is independent of strain rate. The classical theory of hydrodynamics describes the properties of viscous fluid, for which the response of stress is dependent on strain rate[27]. The viscoelastic property of a polymer is studied by dynamic mechanical analysis where a sinusoidal force (stress σ) is applied to a material and the resulting displacement (strain) is measured. For a perfectly elastic solid, the resulting strain and the stress will be perfectly in phase. For a purely viscous fluid, there will be a 90 degree phase lag of strain with respect to stress[28]. Viscoelastic polymers have the characteristics in between where some phase lag will occur during DMA tests[28].

Stress : $\sigma = \sigma_0 \sin(t_\omega + \delta)$ (Eq. 43)

Strain: $\varepsilon = \varepsilon_0 \sin t_\omega$ (Eq. 44)

Where ω is frequency of strain oscillation, t is time, δ is phase la between stress and strain. The storage modulus measures the stored energy, representing the elastic portion, and the loss modulus measures the energy dissipated as heat, representing the viscous portion. The tensile storage and loss moduli are defined as follows:

Storage Modulus: $E' = \frac{\sigma_0}{\varepsilon_0} \cos \delta$ (Eq. 45)

Loss Modulus: $E'' = \frac{\sigma_0}{\varepsilon_0} \sin \delta$ (Eq. 46)

Phase angle $\text{Tan}_{(\text{delta})}$: $tan\ \delta\ \frac{E''}{E'}$ (Eq. 47)

Similarly are also defined shear storage and loss moduli, G′ and G″.

Complex variables can be used to express the moduli E and G as follows:

$$E = E' + iE'' \qquad G = G' + iG'' \qquad \text{where } i^2 = -1$$

The instrumentation of a DMA consists of a displacement sensor such as a linear variable differential transformer, which measures a change in voltage as a result of the instrument probe moving through a magnetic core, a temperature control system or furnace, a drive motor (a linear motor for probe loading which provides load for the applied force), a drive shaft support and guidance system to act as a guide for the force from the motor to the sample, and sample clamps in order to hold the sample being tested. Depending on what is being measured, samples will be prepared and handled differently. Two major kinds of test modes can be used to probe the viscoelastic properties of polymers: temperature sweep and frequency sweep tests. A common test method involves measuring the complex modulus at low constant frequency while varying the sample temperature. A prominent peak in tan δ appears at the glass transition temperature of the polymer. Secondary transitions can also be observed, which can be attributed to the temperature-dependent activation of a wide variety of chain motions[29].

In semi-crystalline polymers, separate transitions can be observed for the crystalline and amorphous sections. Similarly, multiple transitions are often found in polymer blends. A sample can be held to a fixed temperature and can be tested at varying frequency. Peaks in tan δ and in E'' with respect to frequency can be associated with the glass transition, which corresponds to the ability of chains to move past each other. Note that this implies that the glass transition is dependent on strain rate in addition to temperature. Secondary transitions may be observed as well.

The Maxwell model provides a convenient, if not strictly accurate, description of viscoelastic materials. Applying a sinusoidal stress to a Maxwell model gives:

$$E'' = \frac{E\tau_0\omega}{\tau_0{}^2\,\omega^2+1} \qquad \text{(Eq. 48)}$$

where $\tau_0 = \frac{\eta}{E}$ is the Maxwell relaxtion time.

Thus, a peak in E'' is observed at the frequency $\frac{1}{\tau_0}$ [29].

A real polymer may have several different relaxation times associated with different molecular motions. Because glass transitions and secondary transitions are seen in both frequency studies and temperature studies, there is interest in multidimensional studies, where temperature sweeps are conducted at a variety of frequencies or frequency sweeps are conducted at a variety of temperatures. This sort of study provides a rich characterization of the material, and can lend information about the nature of the molecular motion responsible for the transition.

References

[1] Levitt M.H. *John Wiley & Sons*, ltd. March **2005**.

[2] Callaghan P.T. *Clarendon, Press, Oxford* **1991.**

[3] Fukushima E, Roeder S. *Addison Wesley Inc.* **1981**.

[4] Hahn E. L., *Physical Review* **1950**, 80, 580.

[5] Farrar T. C., *Madison: The Farragut Press*. **1989**, 211.

[6] Ruan R. R., Chen P. L. *Lancaster, Pa.: Technomic Publishing Co* **1998**.

[7] Bagchi B. *The Journal of Chemical Physics* **2001**, 115, 2207.

[8] Netz P. A., Starr F., Barbosa M. C., Stanley H. E. *Journal of Molecular Liquids* **2002**, 101, 159.

[9] Belton P. S., Delgadillo I., Gil A. M., Webb G. A., *Cambridge, U.K.: Royal Society of Chemistry* **1995**.

[10] Schmidt S. J. *Avances in Food and Nutrition Research* **2004,** 48, 1.

[11] Every H. A. *Ph.D. Diss*. Monash University, p 94. Australia **2001**.

[12] Stejskal E. O. *The Journal of Chemical Physics* **1965**, 43, 3597.

[13] Suarez S., Greenbaum S. *The Chemical Record* **2010**, 10, 377.

[14] Stejskal E. O., Tanner J. E. *The Journal of Chemical Physics* **1965,** 42, 288.

[15] Tanner J.E,*J. Chem. Phys.*, **1969**, 52.

[16] Callaghan P.T, *Principles of Nuclear Magnetic Resonance*, Oxford, **1991**.

[17] Jonas J. *Science* **1982**, 216, 1179-84.

[18] Jayakody J.R.P, Stallworth P.E, Managa E.S, Farrington-Zapata J, Greenbaum S.G. *J. Phys. Chem. B*, **2004**, *108*, 4260.

[19] Jayakody JRP, Khalfan A, Managa ES, Greenbaum SG, Dang TD, Mantz R, *J. Power Source*, **2006**, *156*, 195.

[20] Wu Y. *Ph.D. Diss*. City University of the City University of New York, p 38-9. New York **1998**.

[21] Benedek G.B, Purcell E.M. *J. Chem. Phys.*, **1954**, *22*, 2003.

[22] Chen R.S, Stallworth P.E, Greenbaum S.G, Fontanella J.J, Wintersgill M.C. *Electrochimica Acta* **1995**, 40(3), 309-13.

[23] Macdonald DD. *Electrochimica Acta* **2006**, 21, 1376-1388.

[24] Springer T., Zawodzinski T., Wilson M., Gottesfeld S. *J. Electrochem. Soc.* **1996**, 143, 587-599.

[25] Paganin V., Oliveira C., Ticianelli E., Springer T., Gonzalez E. *Electrochim. Acta* **1998,** 43, 3761-3766.

[26] Ciureanu M., Roberge R. *J. Phys. Chem. B* **2001**, 105, 3531-3539.

[27] Ferry J. D. Wiley (3 ed.) **1980**.

[28] Meyers M. A. Chawla K. K. *Prentice-Hall* **1999**.

[29] Young RJ, Lovell PA. *Introduction to Polymers* (2 ed.). Nelson Thornes **1991**.

APPENDIX B

Papers

I

"Clay-CNTs Hybrid Materials for Nanocomposite Membranes with Enhanced Proton Conductivity Under Low Humidity Conditions for PEMFCs"

Submitted to Journal of Membrane Science

Clay-CNTs Hybrid Materials for Nanocomposite Membranes with Enhanced Proton Conductivity Under Low Humidity Conditions for PEMFCs

C. Simari[1], Georgia Potsi[2], Alfonso Policicchio[3], Ida Perrotta[4], I. Nicotera[1*]

[1] *Dept. of Chemistry and Chemical Technologies, University of Calabria, Via P. Bucci 87036 Rende, Italy;*

[2]*Dept. of Material Science and Engineering, University of Ioannina,GR-45110 , Ioannina , Greece;*

[3] *CNISM and Dept. of Physics, University of Calabria, Via P. Bucci, 87036 Rende (CS), Italy*

[4] *Dept. of Biology, Ecology and Earth Science, University of Calabria, Via P. Bucci 87036 Rende, Italy;*

(*) isabella.nicotera@unical.it

Abstract

A new class of hybrid materials based on carbon nanotubes (CTNs) rooted on smectite clay (SWy) was synthesized by catalytic chemical vapor deposition (CCVD) method, and studied to be introduced in a perfluorosulfonic acid (Nafion®) membrane. Side-wall chemical oxidation and organo-functionalization of the CNTs was performed using organic ester molecules containing hydrophilic groups (-RSO_3H). SWy−CNTs nanoadditives were incorporated in the polymer by solution-precipitation method producing highly homogeneous nanocomposite membranes with outstanding mechanical properties. Materials were characterized by a combination of techniques (TGA, Raman, FT-IR, SEM, TEM and DMA), while a deep investigation on the water transport properties was performed by NMR methods (PFG and relaxation times). Membranes containing SWy-oxCNTs-RSO_3H nanoadditives are able to guarantee a very high proton diffusion in "quasi-anhydrous" conditions. Proton mobility is ensured by a correct network created from the long nanotubes (well distributed through the clay nanoplatelets) appropriately decorated with acid groups. Remarkable are the electrochemical results: the best membrane reaches conductivities of 7×10^{-2} S cm^{-1} @ 120 °C and 30% RH, one order of magnitude higher than pristine polymer, and a rather high value in the current panorama of the PEMFCs.

Keywords: *Clays-CNTs; hybrids materials; Nafion nanocomposites; NMR diffusion; PEMFCs.*

1 Introduction

Proton exchange membrane fuel cells (PEMFCs) are one of the most promising clean energy technologies. PEMFCs are especially developed as power source for an electric vehicle due to zero-CO_2 emission and high efficiency power generation.[1] However, today the large scale-up of polymer fuel cells is still limited by their incompatibility with the operating conditions of the automotive applications, namely working temperatures higher than 120°C and low humidification. Increasing the temperature would result in increased performance because of easier and more efficient water management, higher reaction rates to the electrodes, improved CO tolerance by the anode electro-catalysts, faster heat rejection rates and better systems integration.[2]

In PEMFC, the polymer electrolyte membrane (PEM) is one of the crucial components which strongly determine the cell performance. Nafion (a registered trademark of E. I. du Pont de Nemours and Co.) is the electrolyte that been most extensively studied.[3] It has excellent mechanical strength as well as high thermal and chemical stability, but it manifests a strong dependence of proton conductivity on hydration level, indeed conductivity dramatically declines as temperature rises above 80 °C and relative humidity/hydration decreases. Therefore, PEMFCs based upon PFSA have typically been operated in a temperature range 50-90 °C. due to the difficulty in maintaining membrane water content at temperatures at or above 100 °C. It is thus highly important to enhance the proton conductivity of the Nafion electrolyte membrane under low RH in order to accomplish higher PEMFCs performance. Over the last decade, attention has been focused on the study organic-inorganic additives include silica, heteropolyacids, metal oxides or solid state ionic conductors, and they are incorporated in the membrane by physical mixing or they are generated in-situ using sol–gel reactions as possible solution to enhance the hydration properties and conductivity of composite membranes at high temperatures. [4-12]

However, one of the major issue that is encountered in the dispersion of metal oxide particles in a polymer matrix is their aggregation in clusters more or less big, which cause obstruction to the water diffusional mobility, and thus to the protons. [13-14]

Recently, we have shown that nanoadditives layered based on smectite clays, are able to produce Nafion-composites completely exfoliated and therefore highly homogeneous and nanodispersed, with improved proton transport properties at high temperature and low humidity. [15-17] Additionally, the presence of two dimensional platelike silicate layers in the matrix of a polymer was of major interest due to the significant gains in thermal stability, mechanical and barrier properties of the resulting nanocomposites. [18,19] In polymer nanocomposite research, the basic aim is to enhance several properties of polymeric components by using molecular or nanoscale reinforcements in order to increase tensile strength, modulus, heat resistance and impact resistance. This aspect is particularly important in order to reduce membrane's swelling, because in the thermal

cycles any change in the water content will result in swelling and shrinkage of membranes, which can cause deterioration of the membrane-catalyst interface or even membrane breakage. One area of research has focused on using carbon nanotubes (CNTs) which, under the electronic percolation level, offer many opportunities for new composites thanks to their superior properties. Polymer/CNT composites combine exceptional mechanical, surface and multi-functional properties and have strong interactions with the matrix resulting from the nanoscale structure and the large interfacial area. [20,21] Zhang et al. [22] demonstrated that the incorporation of CNT–clay hybrid system into nylon-6 by simple melt blending leads to exfoliated nanocomposites with excellent mechanical properties. Compared with neat polymer, the tensile modulus and the tensile strength of the composite were greatly improved, by about 290 % and 150 % respectively, by the incorporation of only 1 wt % CNT–clay hybrid reinforcement. However, CNTs are generally insoluble in common solvents and polymers, and they agglomerate easily, forming entangled bundles which lead to many defect sites in the composites.

In this work, carbon nanotubes rooted on smectite layers are proposed as hybrid nanoadditives in order to provide outstanding functionalities to the resulting composite membranes by combining the features of both the clays and CNTs materials.[23]

Here, the produced CNTs developed on the clay surfaces were oxidized and then functionalized using organic ester molecules containing hydrophilic groups, such as $-SO_3^-$. The intent is to favour a "branched" structure between the hydrophilic pores inside the membrane, to facilitate the proton transport by a more efficient Grotthuss-type mechanism, from one acid site to another, in the dehydration state. Indeed, the mass transport in the electrolyte strongly depends on the structure at the molecular level, which determines the electrostatic interactions and the way in which ionic groups aggregate within the polymer network to form the clusters. Based on this, a one dimensional system like CNTs, homogeneously decorated with acid sites, most likely behaves differently from nanoparticles when dispersed in the polymer, because it could interact and modify the polymeric network structure.

Nanocomposites based on clays-CTNs additives are expected to improve significantly the water retention at high temperatures, and thus proton conductivity, since a high number of well dispersed hydrophilic sites are present either due to the functionalized CNTs and on the clay surfaces. Moreover, the sulfonilic groups on the nantubes should improve the chemical affinity with Nafion polymer providing composites with outstanding mechanical and thermal properties.

In the synthesis of such hybrid materials we used an natural smectite montmorillonite clay (SWy-2) as substrate for immobilizing the catalytic metal cations necessary for the development of the CTNs using the Catalytic Chemical Vapour Deposition (CCVD) method. [24]

Structural characterization of the synthesized materials and the nanocomposite membranes was achieved by a combination of powder X-ray diffraction, Raman and FTIR spectroscopies and

thermogravimetric analysis. The morphology was analysed by scanning electronic microscopy (SEM) and transmission electron microscopy (TEM), while the mechanical properties of the membranes were tested by dynamic mechanical analysis (DMA). Water/protons dynamics inside the electrolytes (recast Nafion and nanocomposites membranes) were investigated by NMR spectroscopy, in particular, Pulse Field Gradient (PFG) method was employed to obtain a direct measurement of water self-diffusion coefficients and inversion recovery sequence to measure the longitudinal relaxation times. These results were compared with the proton conductivities measured by impedance spectroscopy.

Nanocomposite membranes, prepared at various polymers to reinforcement loadings, showed good mechanical properties, excellent water diffusion behaviour and very high proton conductivity in drastic conditions both of temperature and humidity.

2 Experimental

2.1 Materials

The clay material used in this work was a natural smectite montmorillonite Wyoming clay, SWy-2, obtained from the Source Clay Minerals Repository, University of Missouri, Columbia. The cation exchange capacity (CEC), measured by the Co(II) procedure, is equal to 80 mequiv. per 100 g clay, charge density 0.6 e^{-1}/unit cell (unit cell is the Si_8O_{20} unit), and particle size around 200 nm. The structural formula is $Na_{0.62}[Al_{3.01}Fe(III)_{0.41}Mg_{0.54}Mn_{0.01}Ti_{0.02}](Si_{7.98}Al_{0.02})O_{20}(OH)_4$. Montmorillonite clay was fractioned to <2 μm by gravity sedimentation and purified by well-established procedures in clay science. [25]

Nafion, as a 20 wt% dispersion in water and lower aliphatic alcohols, was supplied by Aldrich. The organic compound used for the organo-functionalization of the CNTs was the 3-amino-1-propanesulfonic acid purchased from Aldrich.

2.2 Synthesis of Clay-CNTs hybrid materials

The synthetic procedure (illustrated in the Scheme 1) for the production of the clay-CNTs hybrid nanofillers used in this work consists of four steps, and retraces, for the initial two stages, those described by Tsoufis et al. [26]:

1) metal-exchange reaction for the preparation of an appropriate clay-substrate with catalytic metal centres (Fe and Ni);

2) growth of the CNTs on such clay-substrates;

3) oxidation reaction to obtain oxidized CNTs (ox-CNTs);

4) organo-functionalization reaction to obtain SWy-oxCTNs–RSO_3H.

For the first step, an homogeneous clay suspension in water was reacted with aliquots of nickel chloride and iron chloride aqueous solution ($NiCl_2 \times 6H_2O$ and $FeCl_3 \times 6H_2O$), concentration 0.1 M, such that, the amount of Ni-Fe cations added corresponds to 5 times the CEC of the clay. This allows to exchange all of the Na^+ ions present into the clay-galleries with bimetallic cations, obtaining a catalyst in which Fe^{2+} and Ni^+ ions are incorporated in the clay's structure. The final Ni-Fe-exchanged clay was separated by centrifugation, rinsed repeatedly with distilled−deionized water, and dried at room temperature in air. The resulting solid part was then subjected to calcinations at 450 °C for 4 hours, collected and grounded in fine powder.

This powder was, in a second step, used as substrate for the growth of the CNTs via Chemical Vapor Deposition by catalytic decomposition of acetylene in a fixed bed flow reactor at a temperature of 700 °C. In a typical run, a certain amount of catalyst powder was placed in an alumina crucible within a quartz tube, located in a horizontal tubular furnace and was heated up to the 700 °C under nitrogen atmosphere with acetylene as a carbon precursor. After the completion of acetylene flow, the ceramic boat was cooled down to room temperature.

Based on different reaction times in CVD (15 min and 30 min) it was possible to obtain two aliquots of hybrid materials loaded with different percentage of CNTs, as confirmed by thermogravimetric analysis showed later.

In the third step, an aliquot of Swy-CNTs powder was oxidized through refluxing in an acid solution of H_2SO_4-HNO_3 (3:1) mixture, to obtain the SWy-oxCNTs material. The oxidation of the CTNs is necessary for the organo-functionalization (fourth step) through, before an esterification reaction by reflux in thionyl chloride ($SOCl_2$) in dimethylformamide (DMF), and then followed by the addition of aliquots of propane amino sulfonic acid. After stirring for 24 h, the organo-modified CNTs were washed with water, separated by centrifugation and air-dried, obtaining the SWy-oxCNTs-RSO_3H powder.

At the end of this procedure, three types of hybrid materials were collected and tested as nanoadditives in a Nafion polymer matrix: SWy-CNTs, SWy-oxCNTs and SWy-oxCNTs-RSO_3H.

In Figure S1 of the Supporting Information are reported the FT-IR spectra to confirm the successful oxidation's and organo-functionalization's reactions of the CNTs.

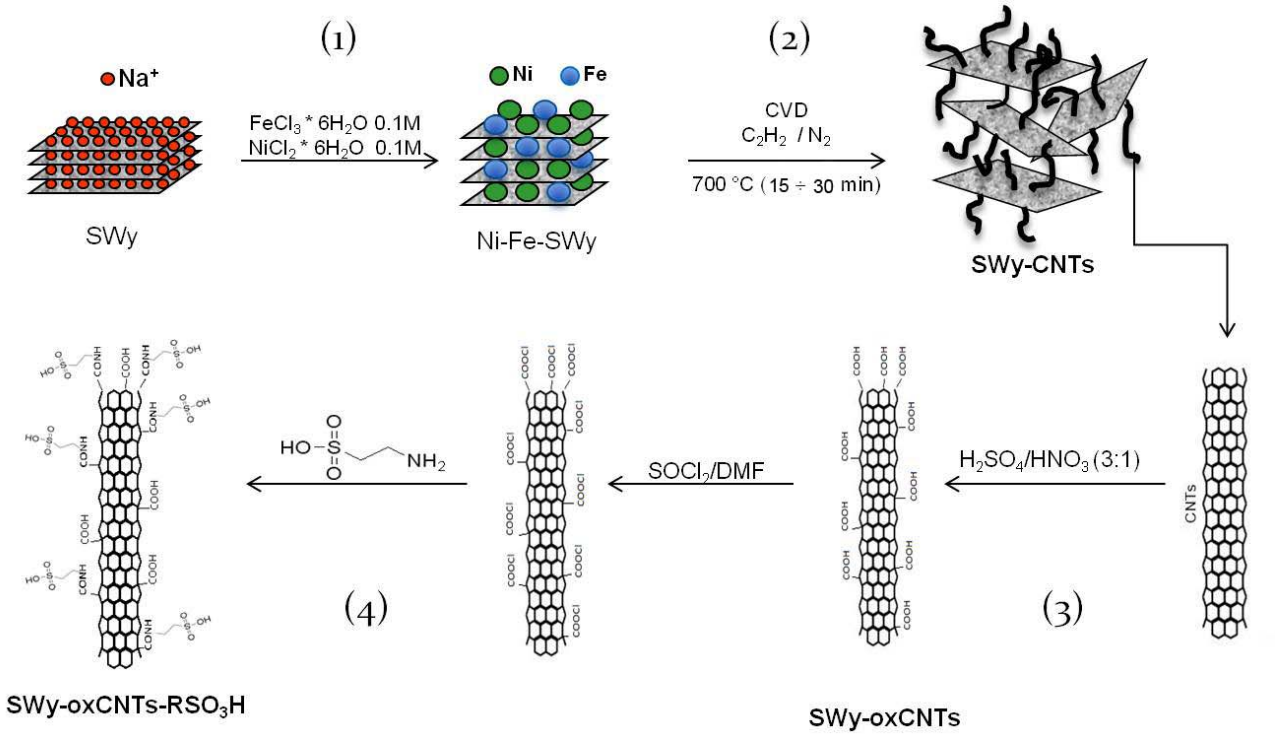

Scheme 1. Synthetic procedure for the production of clay-carbon nanotubes hybrid materials used as nanoadditives in Nafion polymer.

2.3 Preparation of Composite Membranes

Nafion hybrid nanocomposites were prepared by solvent casting method [27] by dispersing the fillers directly in the Nafion solution (mixture of water and propanol as purchased), ultrasonicated for 1 day, and stirred for another day at room temperature until a clear solution was obtained. After that, the dispersion was cast on a petri disk at 80 °C overnight to remove the solvents. The hybrid membranes were removed from the petri disk by immersing the glass plate in deionized water for several minutes. To reinforce the membrane, it was sandwiched and pressed between two Teflon plates and placed in an oven at 150 °C for about 15 min. All the membranes prepared were subsequently treated by rinsing in: 1) boiling HNO_3 solution (1 M) for 1 h to oxidize the organic impurities, 2) boiling H_2O_2 (3 vol%) for 1 h to remove all the organic impurities, 3) boiling in deionized water for 40 min three times, 4) boiling H_2SO_4 (0.5 M) for 1 h to remove any metallic impurities, and again 5) boiling in deionized H_2O for 40 min twice to remove excess acid. According to MacMillan et al. [28] an additional purification procedure was performed to ensure the removal of paramagnetic contaminants, which are particularly damaging to NMR experiments, such as the presence of copper that we found by electron paramagnetic resonance analysis. By this procedure membranes were soaked in ethylenediaminetetracetic acid (EDTA) solution (0.001 M) for 1 day followed by a thorough rinse. Then, they were soaked in HCl (2M) at 80 °C for 2 h

followed by boiling in freshly distilled–deionized water to remove any residual acids, and the treatment with EDTA was repeated. Finally, rinsing in boiled deionized water was carried out three times to remove residual EDTA and the membranes were stored at room temperature in the fully hydrated state.

2.4 Characterization Techniques

Infrared spectra were measured with an FT-IR 8400 spectrometer, in the region of 400-4000 cm^{-1}, equipped with a DTGS detector. Each spectrum was the average of 32 scans collected at 2 cm^{-1} of resolution. Membrane samples were measured as prepared. Thermogravimetric (TGA) analysis was performed using a Perkin Elmer Pyris Diamond TG/DTA. Fully dried and hydrated samples of approximately 5 mg were heated under nitrogen from 25 to 850 °C, at a rate of 10 °C/min and pressure drop in superheaters, steam flow and pressure, have been simultaneously collected from the own boiler instrumentation. Temperatures have been measured using Ni-Cr thermocouples with a relative error of 0.001% and pressure and pressure drop both with pressure transducers with a relative error of 0.02%.

The images of transmission electron microscopy (TEM) were obtained on JEM-1400 PLUS (JEOL Ltd./Japan) operating at 80 kV accelerating voltage. Samples for TEM were prepared by drying a drop of solution onto a carbon coated copper grid which was placed on a piece of paper to get rid of the excess solvent.

Scanning electron microscopy analysis was conducted with a QUANTA FEG 400 F7, FEI microscope. The SEM images were acquired collecting the backscattered electrons induced by using 10 keV electron beam and 0.4 mbar of water humidity. Test membranes were cracked under cryogenic conditions (after dipping in liquid nitrogen) in order to perform cross sectional analysis to estimate the homogeneity and nanodispersion of fillers across the membrane thickness.

NMR measurements were performed on a Bruker NMR spectrometer AVANCE 300 Wide Bore working at 300 MHz on ^{1}H. The employed probe was a Diff30 Z-diffusion 30 G/cm/A multinuclear with substitutable RF inserts. Water self-diffusion coefficients were measured by using the pulsed field gradient (PFG) method.[29] For the investigated samples, the experimental parameters, Δ and δ, are 10 and 1 ms, respectively. The gradient amplitude, g, varied from 10 to 1100 G cm^{-1}. In this condition the uncertainty in the self-diffusion measurements is ~ 3%. Longitudinal relaxation times (T_1) of water were measured on the same spectrometer by the inversion-recovery sequence (π-τ-$\pi/2$). Both self-diffusion and T_1 measurements were conducted by increasing temperature step by step from 20 to 130 °C, with steps of 20 °C, and leaving the sample to equilibrate for about 15 min. At the end of each experiment, the sample was left in the magnet at 130 °C for several hours, and further measurements of diffusion and T_1 were performed if the proton signal is still observable.

Prior to the NMR measurements, membranes were dried in oven, weighed and then immersed in distilled water. Upon being removed from the water they were quickly blotted dry with a paper tissue (to eliminate most of the free surface liquid). The water content value was determined using a microbalance and recorded as: $wu\% = [(m_{wet}-m_{dry})/m_{dry}] \times 100$.
At this point the membranes were loaded into a 5 mm NMR Pyrex tube and sealed.

In-plane conductivities of membranes were measured by impedance AC operational four-electrode system, adopting a commercial cell (BT-112, Scribner Associates Inc) fitted between the anode and cathode flow field of a fuel cell test hardware (850C, Scribner Associates Inc.). This allows controlling the sample temperature and relative humidity (RH). Humidification of the cell was accomplished by a humidification system (Fuel Cells Technologies, inc.) bubbling the fed gas (i.e. dry air) through stainless steel cylinders incorporated in the compact system and containing distilled water. The proton conductivity was measured in the temperature range 30-120 °C at different humidification conditions.

Finally, DMA measurements were made with a Metravib DMA/25 equipped with a shear jaw for films. Spectra were collected by applying a dynamic stress of amplitude 10^{-3} at 1Hz in the temperature range between 25 °C and 200 °C with a heating rate of 2 °C/min.

3 Results and discussion

3.1 Structural and morphological characterization

The amount of CNTs growth on the clays surfaces strongly depends from the reaction times in the CVD camera: two aliquots of SWy-CNTs were collected, after 30 minutes and 60 minutes of reaction time, respectively. The thermogravimetric analysis (TGA) is useful method to determinate with good precision the percentage of carbon yield by the following Equation (1) [30] :

$$\%\ yield = \frac{\text{weight loss (from 400 °C to 700 °C)}}{100-\text{weight loss}} \times 100 \qquad (1)$$

TGA curves in Figure 1 for the two materials demonstrate the different percentage of CNTs' loading on smectite clays, i.e. the weight loss between 400 °C and 700 °C proves a percentage yield of 32% (Fig 2a) and 5% (Fig 2b), respectively. Additionally, both fillers display analogous and well-defined DTG peaks with an oxidation temperature of CNTs above 550 °C. In general, higher oxidation temperatures are always associated with purer, less defective samples. [31] Then, based on the weight loss at low temperatures, between 300 °C and 400 °C of the TG diagrams, the amount of amorphous carbon is very low, i.e. less than 4 wt.%. Therefore, these results prove that the CNTs developed on the mineral surface possess a good overall quality.

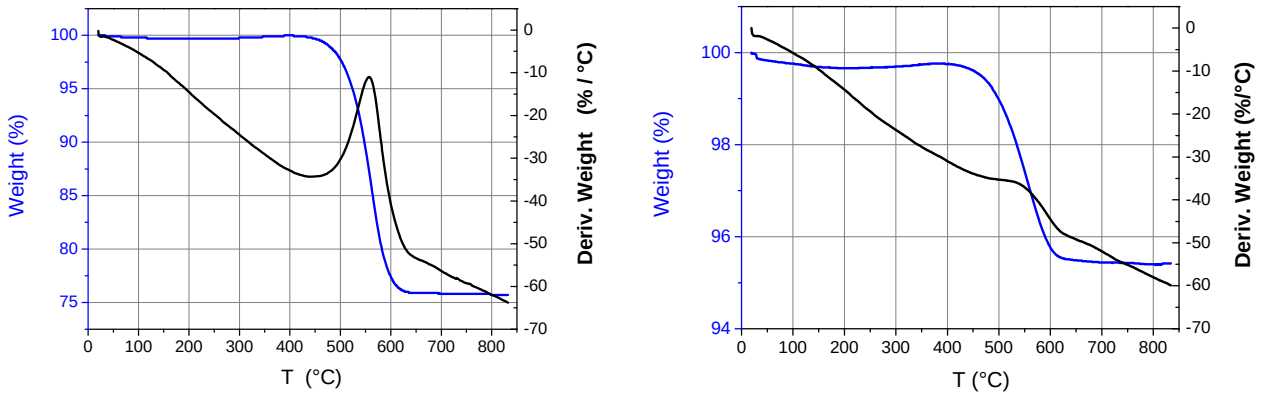

Fig. 1. TG curves derived from SW-CNTs with 32% of yield (on the left) and SW-CNTs with 5% of yield (on the right).

A further corroboration of the quality of the CNTs grafted on the clay's platelets is given by the Raman spectra analysis, reported in Figure S2 of the Supporting Information.

Morphological analysis of the synthesized hybrids nanoadditives, was carried out by Transmission Electron Microscopy (TEM). TEM measurements, performed in all CCVD products, revealed the presence of carbon nanotubes on the clays platelets. TEM images of two representative products, SWy-oxCNTs-RSO_3H at 32% (first row) and 5% (second row) of yields, respectively, are shown in Figure 3. Other images are shown in Figure S3 of the Supporting Information. From these photos is clear the higher amount of nanotubes grafted on clay's platelets in the sample at higher yield. Also it shows that the yield of 5% is an average of a sample rather inhomogeneous in which there are platelets with more nanotubes and others with less. Finally, the average diameter of the carbon nanotubes is between 20 and 30 nm while the length is quite variable.

The nanocomposite membranes were obtained by dispersion of the nanoadditives inside the Nafion polymeric matrix at 1 wt% of filler loading respect to the polymer. The composites with the functionalized CNTs were also prepared at higher loading, 2 wt% and 3wt%, to investigate its effect. Table 1 summarize all the membranes prepared for this study.

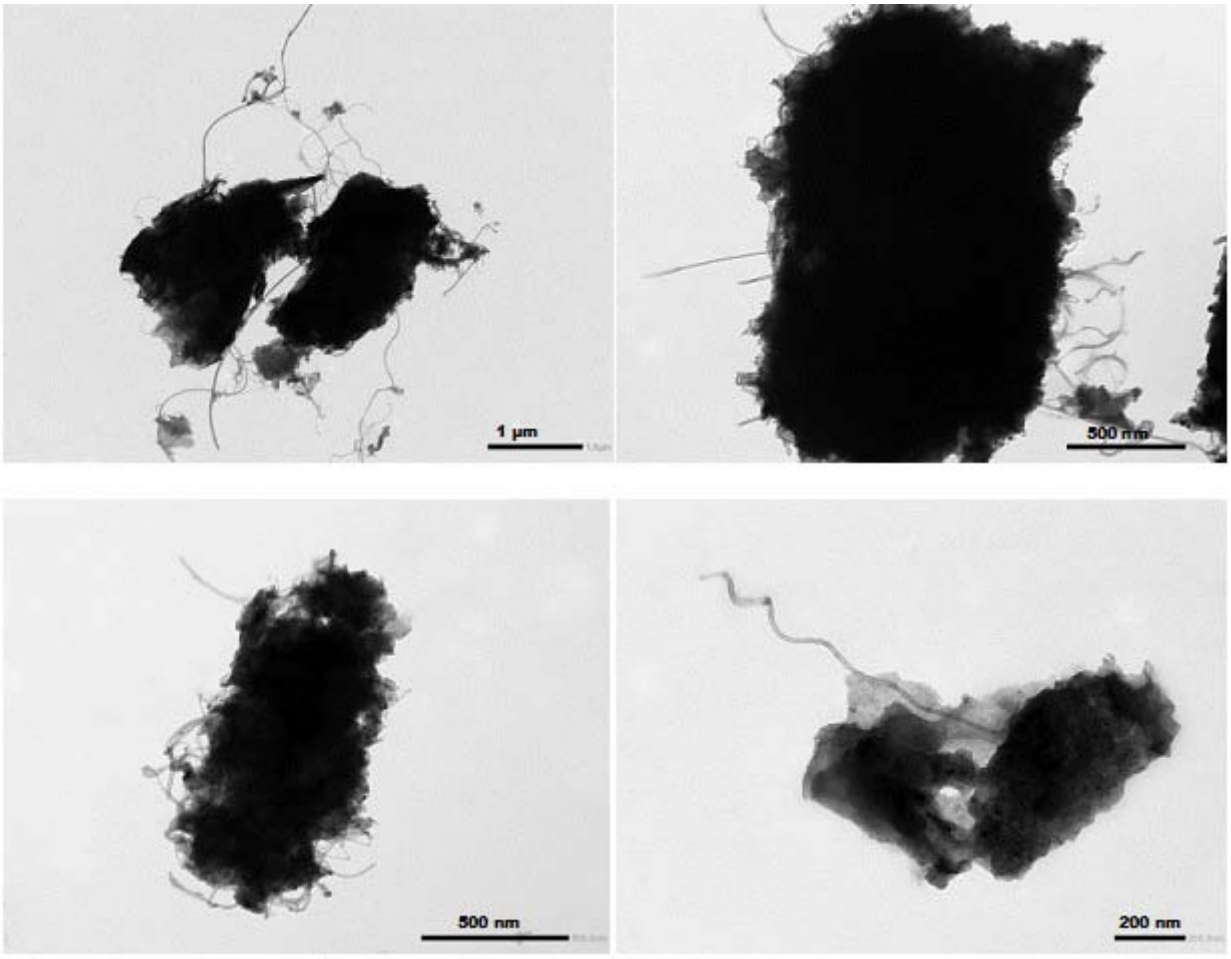

Fig. 2: TEM images of the products SWy-oxCNTs-RSO_3H at 32% (first row) and 5% (second row) of yields, respectively.

Table 1. *Nafion –based composite membranes prepared with the clay-CNTs materials*

nanofillers	*Composite Membranes*	*Filler loading (wt%)*
SWy-CNTs (yield 5%) SWy-CNTs (yield 32%)	N/SWy-CNTs(y5) N/SWy-CNTs(y32)	1
SWy-oxCNTs (yield 5%) SWy-oxCNTs (yield 5%)	N/SWy-oxCNTs(y5) N/SWy-oxCNTs(y32)	1
SWy-oxCNTs-RSO_3H (yield 5%) SWy-oxCNTs-RSO_3H (yield 32%)	N/SWy-oxCNTs-RSO_3H(y5) N/SWy-oxCNTs-RSO_3H(y32)	1 2 3

Scanning Electron Microscopy (SEM) coupled with BSE (back scattered electrons) technique was used to investigate the morphology of the composite membranes. The procedure developed by our

laboratory for the preparation of Nafion composite membranes with carbon-based fillers [27], allows to obtain highly homogeneous films with an extraordinary nanodispersion of the additive, without formation of agglomerates or clusters, as it can see from the SEM images in Figure 3. Here, the cross-sectional analysis of some representative composites membranes were performed. There is a good dispersion of the filler and the membranes are uniform, smooth and homogeneous on the whole volume. For each SEM picture, a BSE image was also acquired, in order to analyse some evident spots present inside the membrane. Since heavy elements (high atomic number) backscatter electrons more efficiently than light elements (low atomic number), and thus appear brighter in the image, BSE are used to detect contrast between areas with different chemical compositions, therefore, it allows to better visualize and discriminate between t the polymeric membrane from silicate clay agglomerates. The picture in false colours in Figure 3(b) is obtained as a superposition of SEM (greyscale) and BSE (yellow-to-blue intensity scale) images, in order to evidence that only some sporadic inhomogeneities (blue spots) due to small clusters of clays are present in the polymeric film. Other similar images are shown in Figure S4 the Supporting Information.

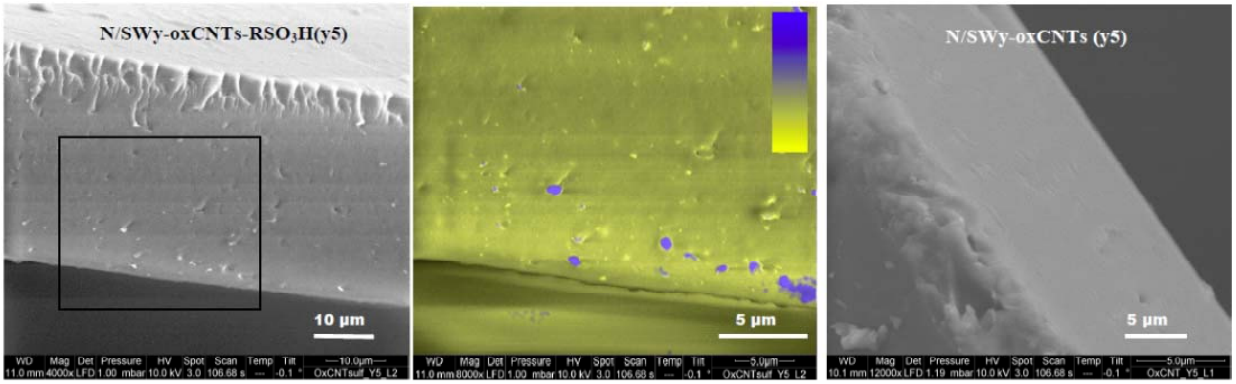

Figure 3. SEM images of representative composites membranes: (a) a cross setion view of the N/SWy-oxCNTs-RSO_3H(y5) membrane; (b) false colours SEM+BSE map of the region framed in (a) putting in evidence the clays clusters distribution (the yellow-to-blue colour bar spans from the lowest BSE intensity to the highest one); and (c) cross sectional view of the N/SWy-oxCNTs (y5) membrane.

The water absorption ability of the composites respect to the filler free Nafion membrane is displayed in the histogram of Figure 4. A first consideration is that the presence of carbon nanotubes reduces the hydrophilic ability of the clay itself on which are grafted, so much that the composite also containing only 1 wt% of this material, absorbs very low amount of water compared to the polymer recast. This is undoubtedly tied to the character hydrophobic of the CNTs. Instead, the oxidation and the subsequent functionalization, creates a highly hydrophilic material, and the composites can absorb almost 40% more water than the Nafion. The second observation relates the percentage of yield of CNTs developed on the plans of clay: the composite membranes produced

with fillers with 32% of yield basically show a lower hydrophilic capacity. This may be due more to an effect of hindrance/obstruction that limits the volume of the spheres of hydration of the nanoparticles.

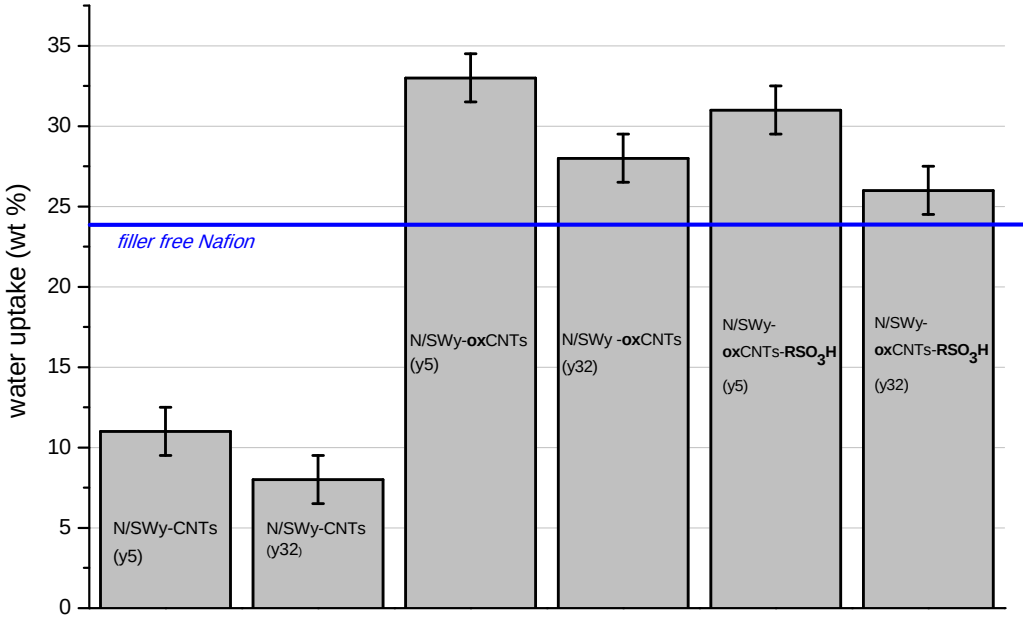

Fig. 4: Water uptakes of the composites membranes recorded as: $wu\% = [(m_{wet}-m_{dry})/m_{dry}] \times 100$.

3.2 NMR investigation

The hydration degree is the main factor that governs the proton conductivity in a polymer membrane, because the transport mechanism of the protons can occur through a diffusional mechanism or a "hopping" mechanism, related to its long-range and short-range mobility, respectively. NMR spectroscopy is widely used in this work to investigate the molecular dynamics of water confined in the membranes, as it allows an analysis of the translational motions on long-range by the direct measurement of the self-diffusion coefficients (Pulse Field Gradient technique), and a study of the roto-vibrational molecular motions through measurement of the relaxation times (T_1 and T_2). Figure 5 displays the self-diffusion coefficients on hydrated membranes (at their maximum water uptake), in the temperature range 20-130 °C. In this graph a comparison with recast Nafion is shown in order to evaluate the effect of the fillers.

The nanocomposites containing the SWy-CNTs additives show diffusion coefficients that are almost two orders of magnitude lower than filler-Nafion. This result was expected for the reasons

outlined above on their poor hydrophilic ability. The oxidation of the CNTs results in an increase of the material's hydrophilicity, consequently the water diffusion of membranes containing SWy-oxCNTs get close to that of pristine Nafion in the temperature region 20-80 °C. But, what is remarkable is the behaviour of the diffusion at high temperatures. Whereas the recast Nafion exhibits a collapse of the diffusion, due to the well-known dehydration of this polymer above 80 °C, the composite membranes based on oxidized nanotubes and, even more, those organo-functionalized, are able to maintain high values of D, and this means that they can keep a certain amount of water of hydration capable of ensuring the proton transport.

As described in the experimental part, these measurements are conducted on membranes loaded in a classic NMR tube and they are not provided of any hydration, if not the water absorbed initially at room temperature. The graph shows also the values of D acquired at 130 °C hourly, leaving the sample at this temperature in the magnet for long time. In these conditions, the ^1H signal, which comes from the water alone (being the polymer perfluorinated), is almost absent in the recast Nafion and in composites with CNTs not oxidized, whereas in the other composites it is a well detectable to still perform a PFG experiment and to derive a value of D.

It is clear that the best results seem to be given by the membranes containing SWy-oxCNTs-RSO_3H, demonstrating as the organo-modification of the CNTs' surface, with molecules bringing sulfonic acid groups, increases the number of hydrophilic sites nanodispersed inside the polymer matrix, and are able to guarantee a very high water diffusion, even after long time at 130 °C.

The increasing of the CTNs yield, from 5% up to 32%, on the clay's surface, doesn't improve the proton mobility, maybe due to some obstruction effect inside the hydrophilic pores of the membranes. This is confirmed by longitudinal relaxation time (T_1) measurements shown in Figure 6. NMR longitudinal (or spin-lattice) relaxation times (T_1), compared to diffusion, reflects more localized motions including both translation and rotation on a time scale comparable to the reciprocal of the NMR angular frequency (few nanoseconds). T_1 quantifies the energy transfer rate from the nuclear spin system to the neighbouring molecules (the lattice). The motion of the nuclei in the lattice causes a fluctuating magnetic field to the site of the nuclear spin involved. In the case of spin-½ nuclei (protons), the most common source of this fluctuating field is dipole-dipole interaction. The stronger the interaction, the quicker the relaxation (shorter T_1). [32] Therefore, higher T_1 values suggest more facile molecular rotational and translational motion, and generally T_1 increases with the temperature.

The three plots in Figure 6 show the relaxation times measured on the various hydrated membranes, in the temperature range 20-130 °C, and are compared to those of Nafion recast. In the case of N/SWy-CNTs (Figure 6a), the low amount of water absorbed by these membranes, in particular for 32% of yield, implies that water molecules are strongly "bound" to the hydrophilic groups of the Nafion, so the spin-lattice relaxation is very fast (T_1 shorter). In composites with CNTs oxidized

(Figure 6b), T_1 are longer, means that water molecules are freer to move, and this result is more marked for the fillers with a yield of 5%. Finally, in composites with CNTs sulfonated (Figure 6c), slight differences between y5% and y32% are found only at high temperatures, i.e. when the amount of water is reduced after the evaporation, therefore, an impediment to the roto-translational movements is more likely in composite with higher concentration of nanotubes.

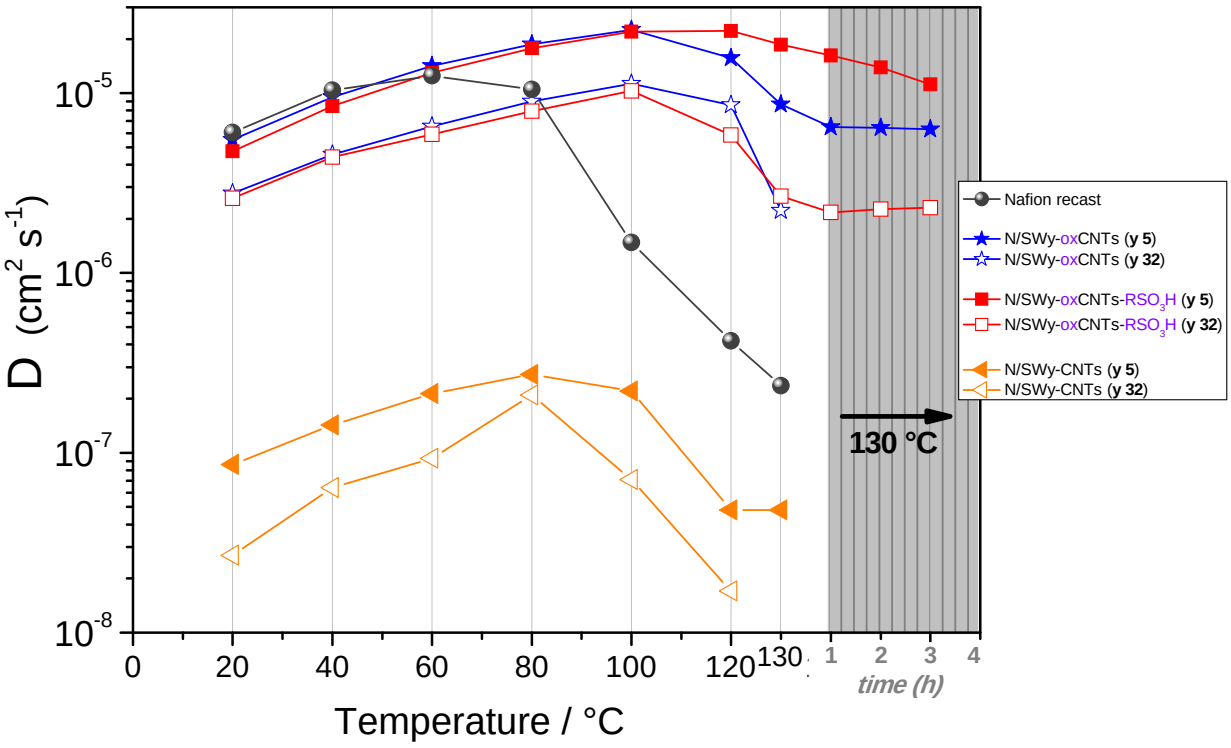

Fig.5: Self-diffusion coefficients as function of the temperature (from 20 °C up to 130 °C) of the water confined in recast Nafion and clay-CNTs composites membranes. In the graph are also plotted the data collected at 130 °C after several hours.

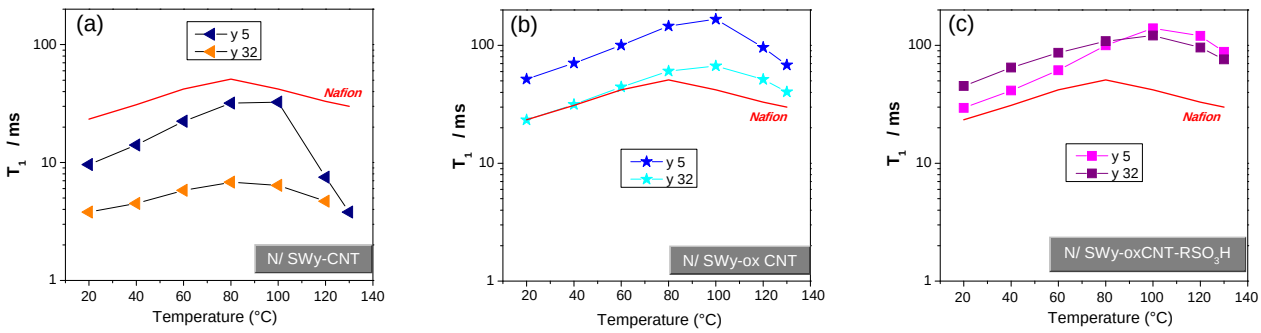

Fig.6: Longitudinal relaxation times (T1) vs. temperature of the water confined in Nafion recast and in composite membranes: (a) N/SWy-CNTs (yield 5 and 32 %); (b) N/SWy-oxCNTs (yield 5 and 32 %); (c) N/SWy-oxCNTs-SO_3H (yield 5 and 32 %).

The results obtained so far show that the composite N/SWy-oxCNTs-SO_3H(y5) is certainly the most promising. For this nanoadditive, the effect of the loading with respect to the polymer was investigated. Accordingly, composite membranes at 2 wt% and 3 wt% were prepared and analysed, while, higher loading lead to inhomogeneous membranes, and therefore were not taken into account. In Figure S5 of the Supporting Information, the diffusion coefficients vs. temperature are shown. De facto, there is not a significant difference between the three loadings if not that at 2 wt% of loading there is a slight increase of water uptake of the membrane (from 31-32 wt% up to 37 wt%).

3.3 Proton conductivity

The proton conductivity of the clay-CNTs based nanocomposites was measured by the electrochemical impedance spectroscopy over the frequency range of 1 Hz to 1 MHz. In Figure 7a are displayed the proton conductivities measured in the temperature range from 30 °C up to 120 °C, and for three relative humidity conditions: 30%, 50% and 90%. Respect to filler-free Nafion, both composites with oxidized and sulfonated CNTs demonstrate to have higher proton mobility, confirming the same trend observed by NMR diffusion, and such difference is noteworthy as the operating conditions become more drastic, that are high temperatures and very low RH. For instance, at 120 °C and 30% RH, the Naf/SWy-oxCNTs-RSO3H reaches a proton conductivity of 0.03 S cm^{-1}. This is a very high value compared with composites reported in literature. [5, 33-36]
In "quasi-anhydrous" state of the membrane, the proton mobility can be ensured by a Grotthus-type mechanism, only if the correct network of interconnected acids sites is created inside the hydrophilic pores. This is what is expected from a material such as the one proposed, where long nanotubes (well distributed through the clay platelets), appropriately decorated with sulfonic groups, favour the formation of a network, through which protons can move. An excessive amount of nanotubes on the clay's surfaces (32% yield), cannot bring any benefits (see Figure 7 b and c) and as discussed already by NMR data: large amounts of CNTs leads to steric hindrance and occlusion confirming the reasoning about the need to create an appropriate arrangement. Instead, increasing the filler loading with respect to the polymer, from 1 to 3%, the proton conductivities grow, as shown in Table 2. The membrane with 3% of filler shows outstanding values, e.g. 0.07 S cm^{-1} @ 120 °C and 30% RH and 0.25 S cm^{-1}@ 120 °C and 90% RH.

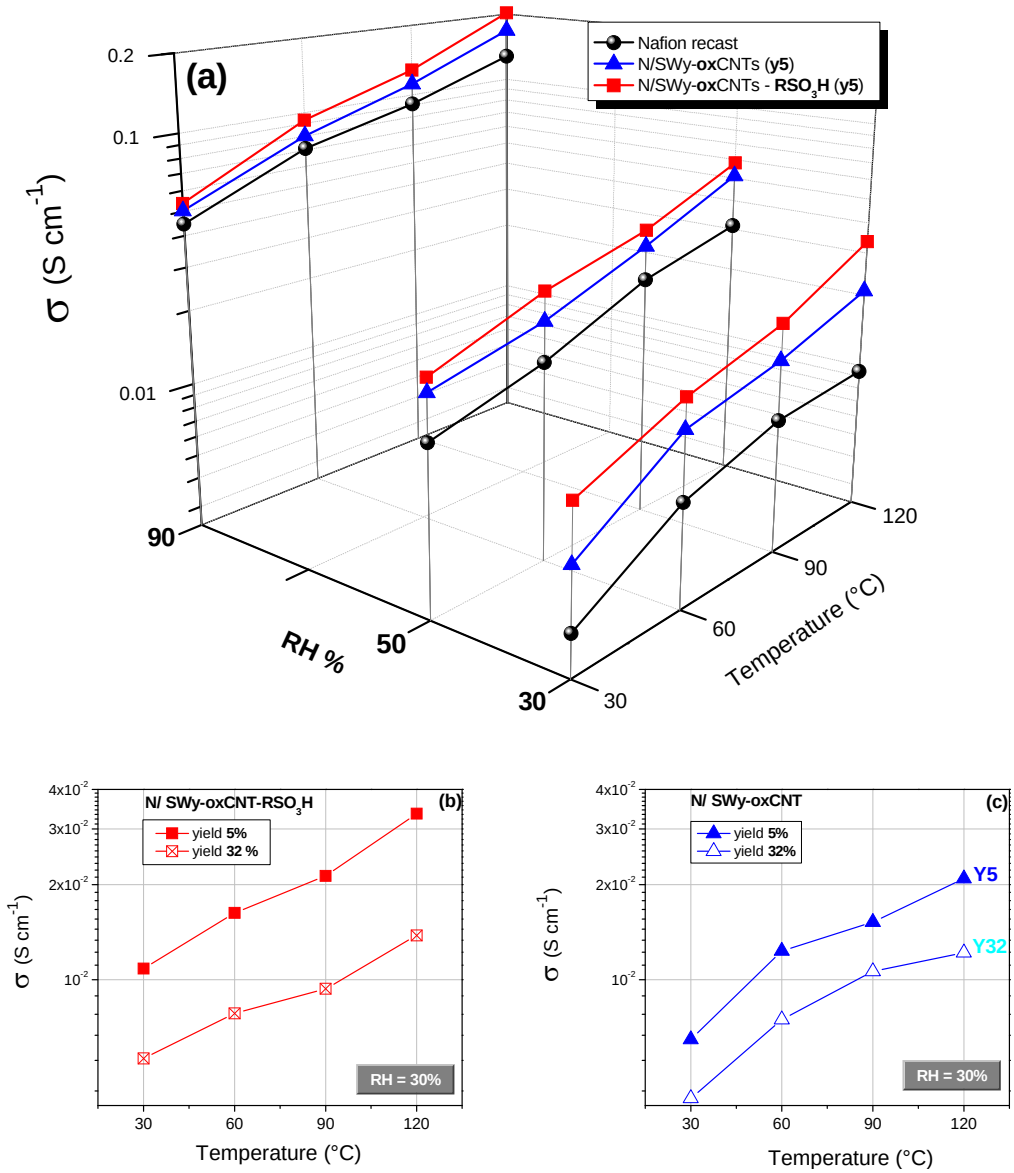

Fig. 7: (a) In-plane conductivities as a function of temperature and RH%, of three representative membranes: Nafion recast, Naf/SWy-oxCNTs (y5) and Naf/SWy-oxCNTs-RSO_3H (y5). (b) and (c) Proton conductivities, at RH 30% in the temperature range 30-120 °C, of Naf/SWy-oxCNTs-RSO_3H and Naf/SWy-oxCNTs, respectively, at the two different CNTs yields rooted on the clay's surfaces.

Table 2: *Proton conductivity of* ***N/SWy-oxCNTs-RSO$_3$H(y5)*** *composites at different filler loading respect to the polymer*

T (°C)	***Proton Conductivity (×10^{-2} S/cm)***					
	@ 30%RH			**@ 90%RH**		
	Filler loading respect to Nafion ionomer					
	1 wt%	***2 wt%***	***3 wt%***	**1 wt%**	**2 wt%**	**3 wt%**
30	1.1	1.3	1.4	5.4	6.4	6.0
60	1.6	2.0	2.2	9.3	14.2	13.9
90	2.1	2.9	3.5	12.8	17.6	18.3
120	3.4	4.4	6.7	20.3	23.8	25.2

3.4 Dynamic Mechanical Analysis

Finally, the effect of such hybrid nanoadditives on the mechanical properties of the Nafion membrane was investigated by temperature ramp tests. Figure 8 put in comparison the temperature evolution of the storage moduli (E'/Pa) and Tan δ of filler-free Nafion and N/SWy-oxCNTs-RSO_3H membranes at both 5% and 32% of yield.

The nanocomposites exhibit higher storage moduli indicating that the filler produces membranes with higher solidity. Likely, this is related both to the presence of the nanohybrids within the pores of the polymer and strong interactions with the polymeric chains, therefore, the membranes can withstand high temperatures. At the same time, an increased amount of CNTs on the clay's surfaces improves the thermal stability of the electrolyte. This is also confirmed by the analysis of the Tan δ: the α–relaxation, characteristic of the polar group clusters of polymer [37-38], shifts at higher values for the composite membranes, from 120 °C of the recast Nafion up to about 132 °C at 5% of yield, and 165 °C at 32% of yield.

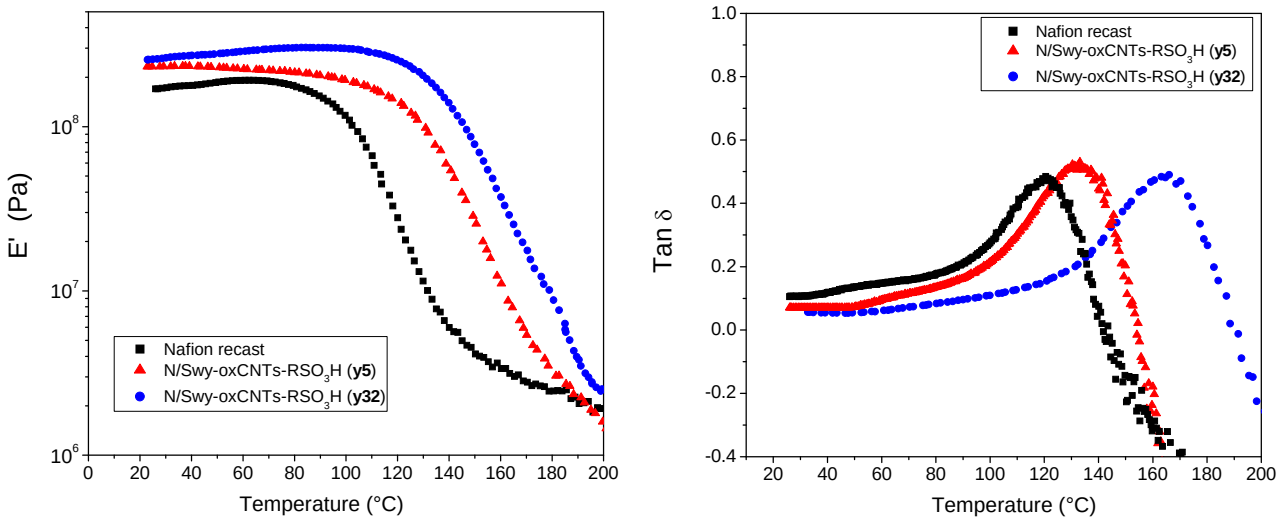

Figure 8. Storage moduli E' (on the left) and tan δ (on the right) versus temperature, from 20 to 200 °C, of filler free Nafion and of two nanocomposite membranes, N/SWy-oxCNTs-RSO_3H at 5% and 32% of yields, respectively.

4 Conclusions

Clay−CNTs hybrid materials were synthesized and novel Nafion-based composite membranes were prepared by solution-precipitation method and investigated for PEM fuel cells applications. Structural and morphological studies prove the successfully synthesis of the nanoadditives and the creation of highly homogeneous membranes.

The CNTs grown on the clays platelets were also oxidized and acid-functionalized. Indeed, unoxidized nanotubes, being substantially hydrophobic, cause very low water uptake of the resulting nanocomposite membranes, and so very low proton diffusion. On the contrary, their oxidation, and more, their organo-modification with alkyl-sulfonic groups (RSO_3H), show a significant effect on the proton transport properties of the nanocomposites, in particular in the region of high temperatures (above 100 °C). At 130 °C, in quasi-dehydrated state, the proton diffusion of the best nanocomposite membranes reach values of about 2×10^{-5} cm^2 sec^{-1}, i.e. two order of magnitude higher than filler-free Nafion.

Proton conductivity data are in perfect agreement with the NMR (diffusion and relaxation times) results, demonstrating as such hybrid membranes have higher proton mobility respect to filler-free Nafion, and the discrepancy is much higher as the operating conditions become more drastic, that are high temperatures and quasi-anhydrous state of the membranes. For instance, at 120 °C and 30% RH, the Naf/SWy-oxCNTs-RSO_3H (y5 and loading 3 wt%) exhibits a proton conductivity of 7×10^{-2} S cm^{-1}, a value very high if compared with other Nafion composites reported in literature, and gaining one order of magnitude respect to recast polymer. These outcomes are the consequence of the formation of an appropriate network which favour the proton mobility by a Grotthus-type mechanism. Finally, the mechanical investigation indicated that the adding of such hybrid nanoadditives to Nafion polymer produce membranes with higher solidity and extending their thermal stability since the α–relaxation of the polymeric matrix shifts at higher temperatures.

5 Acknowledgements

This work was realized with the financial support of the Italian Ministry of Education, Universities and Research (PRIN 2010-2011, prot. 2010CYTWAW_001) in the framework of the Project NAMED-PEM “Advanced nanocomposite membranes and innovative electrocatalysts for durable polymer electrolyte membrane fuel cells”.

The authors would like to thanks Prof. Dimitrios Gournis for his precious support in the synthesis of the materials.

Supporting Information

Supporting Information is available.

Bibliografia

[1] H. Zhang and P. K. Shen, "Recent development of polymer electrolyte membranes for fuel cells," *Chem. Rev.*, vol. 112, no. 5, pp. 2780–2832, 2012

[2] S. J. Peighambardoust, S. Rowshanzamir, and M. Amjadi, "Review of the proton exchange membranes for fuel cell applications," *Int. J. Hydrogen Energy*, vol. 35, no. 17, pp. 9349–9384, Sep. 2010.

[3] K. a Mauritz and R. B. Moore, "State of understanding of nafion.," *Chem. Rev.*, vol. 104, no. 10, pp. 4535–85, Oct. 2004.

[4] F. Damay and L. C. Klein, "Transport properties of Nafion^{TM} composite membranes for proton-exchange membranes fuel cells," *Solid State Ionics*, vol. 162–163, pp. 261–267, Sep. 2003.

[5] N. C. Rosero-Navarro, E. M. Domingues, N. Sousa, P. Ferreira, and F. M. Figueiredo, "Protonic conductivity and viscoelastic behaviour of Nafion® membranes with periodic mesoporous organosilica fillers," *Int. J. Hydrogen Energy*, vol. 39, no. 10, pp. 5338–5349, Mar. 2014.

[6] M. Casciola, G. Bagnasco, a. Donnadio, L. Micoli, M. Pica, M. Sganappa, and M. Turco, "Conductivity and Methanol Permeability of Nafion-Zirconium Phosphate Composite Membranes Containing High Aspect Ratio Filler Particles," *Fuel Cells*, vol. 9, no. 4, pp. 394–400, Aug. 2009.

[7] C. YANG, "A comparison of physical properties and fuel cell performance of Nafion and zirconium phosphate/Nafion composite membranes," *J. Memb. Sci.*, vol. 237, no. 1–2, pp. 145–161, Jul. 2004.

[8] M. B. Satterfield, P. W. Majsztrik, H. Ota, J. A. Y. B. Benziger, and A. B. Bocarsly, "Mechanical Properties of Nafion and Titania / Nafion Composite Membranes for Polymer Electrolyte Membrane Fuel Cells," *J. Polym. Sci.*, pp. 2327–2345, 2006.

[9] A. D'Epifanio, M. A. Navarra, F. C. Weise, B. Mecheri, J. Farrington, S. Licoccia, and S. Greenbaum, "Composite Nafion/sulfonated zirconia membranes: effect of the filler surface properties on proton transport characteristics.," *Chem. Mater. a Publ. Am. Chem. Soc.*, vol. 22, no. 3, pp. 813–821, Feb. 2010.

[10] I. Nicotera, K. Angjeli, L. Coppola, A. Enotiadis, R. Pedicini, A. Carbone, and D. Gournis, "Composite polymer electrolyte membranes based on Mg–Al layered double hydroxide (LDH) platelets for H2/air-fed fuel cells," *Solid State Ionics*, vol. 276, pp. 40–46, 2015.

[11] H. Xiuchong, T. Haolin, and P. Mu, "Synthesis and Performance of Water-Retention PEMs with Nafion-Intercalating-Montmorillonite Hybrid," *J. Appl. Polym. Sci.*, vol. 108, pp. 529–534, 2008.

[12] Z. Chen, B. Holmberg, W. Li, X. Wang, W. Deng, and R. Munoz, "Nafion/Zeolite Nanocomposite Membrane by in Situ Crystallization for a Direct Methanol Fuel Cell," *Chem. Mater.*, vol. 18, no. 24, pp. 5669–5675, Nov. 2006.

[13] K. T. Adjemian, R. Dominey, L. Krishnan, H. Ota, P. Majsztrik, T. Zhang, J. Mann, B. Kirby, L. Gatto, M. Velo-Simpson, J. Leahy, S. Srinivasan, J. B. Benziger, and A. B. Bocarsly, "Function and Characterization of Metal Oxide−Nafion Composite Membranes for Elevated-Temperature H 2 /O 2 PEM Fuel Cells," *Chem. Mater.*, vol. 18, no. 9, pp. 2238–2248, May 2006.

[14] G. Mohammadi, M. Jahanshahi, and A. Rahimpour, "Fabrication and evaluation of Nafion nanocomposite membrane based on ZrO2–TiO2 binary nanoparticles as fuel cell MEA," *Int. J. Hydrogen Energy*, vol. 38, no. 22, pp. 9387–9394, Jul. 2013.

[15] I. Nicotera, A. Enotiadis, K. Angjeli, L. Coppola, G. A. Ranieri, and D. Gournis, "Effective improvement of water-retention in nanocomposite membranes using novel organo-modified clays as fillers for high temperature PEMFCs.," *J. Phys. Chem. B*, vol. 115, no. 29, pp. 9087–9097, 2011.

[16] I. Nicotera, K. Angjeli, L. Coppola, A. S. Aricò, and V. Baglio, "NMR and Electrochemical Investigation of the Transport Properties of Methanol and Water in Nafion and Clay-Nanocomposites Membranes for DMFCs," *Membranes (Basel).*, vol. 2, no. 2, pp. 325–345, 2012.

[17] K. Angjeli, I. Nicotera, M. Baikousi, A. Enotiadis, D. Gournis, A. Saccà, E. Passalacqua, and A. Carbone, "Investigation of layered double hydroxide (LDH) Nafion-based nanocomposite membranes for high temperature PEFCs," *Energy Convers. Manag.*, vol. 96, pp. 39–46, 2015.

[18] P. LeBaron, Z. Wang, and T. Pinnavaia, "Polymer-layered silicate nanocomposites: an overview," *Appl. Clay Sci.*, pp. 11–29, 1999.

[19] E. Burgaz, H. Lian, R. H. Alonso, L. Estevez, A. Kelarakis, and E. P. Giannelis, "Nafion–clay hybrids with a network structure," *Polymer (Guildf).*, vol. 50, no. 11, pp. 2384–2392, May 2009.

[20] Y.-L. Li, I. A. Kinloch, and A. H. Windle, "Direct spinning of carbon nanotube fibers from chemical vapor deposition synthesis.," *Science*, vol. 304, no. 5668, pp. 276–8, Apr. 2004.

[21] A. B. Dalton, S. Collins, E. Muñoz, J. M. Razal, V. H. Ebron, J. P. Ferraris, J. N. Coleman, B. G. Kim, and R. H. Baughman, "Super-tough carbon-nanotube fibres.," *Nature*, vol. 423, no. 6941, p. 703, Jun. 2003.

[22] W.-D. Zhang, I. Y. Phang, and T. X. Liu, "Growth of Carbon Nanotubes on Clay: Unique Nanostructured Filler for High-Performance Polymer Nanocomposites," *Adv. Mater.*, vol. 18, no. 1, pp. 73–77, Jan. 2006.

[23] K. Litina, A. Miriouni, D. Gournis, M. a. Karakassides, N. Georgiou, E. Klontzas, E. Ntoukas, and A. Avgeropoulos, "Nanocomposites of polystyrene-b-polyisoprene copolymer with layered silicates and carbon nanotubes," *Eur. Polym. J.*, vol. 42, no. 9, pp. 2098–2107, Sep. 2006.

[24] T. Tsoufis, P. Xidas, L. Jankovic, D. Gournis, A. Saranti, T. Bakas, and M. a. Karakassides, "Catalytic production of carbon nanotubes over Fe-Ni bimetallic catalysts supported on MgO," *Diam. Relat. Mater.*, vol.

16, no. 1, pp. 155–160, 2007.
[25] D. Gournis, A. Lappas, M. a. Karakassides, D. Többens, and A. Moukarika, “A neutron diffraction study of alkali cation migration in montmorillonites,” *Phys. Chem. Miner.*, vol. 35, no. 1, pp. 49–58, Jan. 2008.
[26] T. Tsoufis, L. Jankovic, D. Gournis, P. N. Trikalitis, and T. Bakas, “Evaluation of first-row transition metal oxides supported on clay minerals for catalytic growth of carbon nanostructures,” *Mater. Sci. Eng. B*, vol. 152, no. 1–3, pp. 44–49, Aug. 2008.
[27] A. Enotiadis, K. Angjeli, N. Baldino, I. Nicotera, and D. Gournis, “Graphene-based nafion nanocomposite membranes: enhanced proton transport and water retention by novel organo-functionalized graphene oxide nanosheets.,” *Small*, vol. 8, no. 21, pp. 3338–49, Nov. 2012.
[28] B. Macmillan, A. R. Sharp, and R. L. Armstrong, “N . m . r . relaxation in Nafion — the low temperature regime,” *Polymer (Guildf).*, vol. 40, pp. 2481–2485, 1999.
[29] E. O. Stejskal and J. E. Tanner, “No Title,” *J. Chem. Phys.*, vol. 42, pp. 288–292, 1965.
[30] S. Karakoulia, L. Jankovic, K. Dimos, D. Gournis, and K. Triantafyllidis, *Molecular Sieves: From Basic Research to Industrial Applications, Proceedings of the 3rd International Zeolite Symposium (3rd FEZA)*, vol. 158. Elsevier, 2005.
[31] S. Arepalli, P. Nikolaev, O. Gorelik, V. G. Hadjiev, W. Holmes, B. Files, and L. Yowell, “Protocol for the characterization of single-wall carbon nanotube material quality,” *Carbon N. Y.*, vol. 42, no. 8–9, pp. 1783–1791, Jan. 2004.
[32] C. Slichter, *Principles of Magnetic Resonance*, 3rd ed. New York, 1990.
[33] D. J. Kim, M. J. Jo, and S. Y. Nam, “A review of polymer–nanocomposite electrolyte membranes for fuel cell application,” *J. Ind. Eng. Chem.*, vol. 21, pp. 36–52, Jan. 2015.
[34] I. S. Amiinu, W. Li, G. Wang, Z. Tu, H. Tang, M. Pan, and H. Zhang, “Toward Anhydrous Proton Conductivity Based on Imidazole Functionalized Mesoporous Silica/Nafion Composite Membranes,” *Electrochim. Acta*, vol. 160, pp. 185–194, Apr. 2015.
[35] A. Donnadio, M. Pica, D. Capitani, V. Bianchi, and M. Casciola, “Layered zirconium alkylphosphates: Suitable materials for novel PFSA composite membranes with improved proton conductivity and mechanical stability,” *J. Memb. Sci.*, vol. 462, pp. 42–49, Jul. 2014.
[36] K. Ketpang, S. Shanmugam, C. Suwanboon, N. Chanunpanich, and D. Lee, “Efficient water management of composite membranes operated in polymer electrolyte membrane fuel cells under low relative humidity,” *J. Memb. Sci.*, vol. 493, pp. 285–298, Nov. 2015.
[37] V. Di Noto, R. Gliubizzi, E. Negro, and G. Pace, “Effect of SiO 2 on Relaxation Phenomena and Mechanism of Ion Conductivity of [Nafion/(SiO 2) x] Composite Membranes †,” *J. Phys. Chem. B*, vol. 110, no. 49, pp. 24972–24986, Dec. 2006.
[38] R. Herrera Alonso, L. Estevez, H. Lian, A. Kelarakis, and E. P. Giannelis, “Nafion–clay nanocomposite membranes: Morphology and properties,” *Polymer (Guildf).*, vol. 50, no. 11, pp. 2402–2410, May 2009.

Supporting Information

Clay-Carbon nanotubes hybrid materials for nanocomposite membranes with enhanced proton conductivity under humidification for PEMFCs

C. Simari[1], Georgia Potsi[2], Alfonso Policicchio[3], Ida Perrotta[4], I. Nicotera[1*]

The presence of CNTs on the clay's platelets and their oxidation/ functionalization was revealed by FT-IR spectroscopy. Figure S5 show the IR spectra of all the materials after each reaction step:

1) the spectrum of SWy mineral material presents the bands at 465 cm^{-1} and 1039 cm^{-1} , which correspond to Si−O and Si−O−Si vibrations of the clay lattice.

2) The bands in the region 1380-1400 cm^{-1} which appear in both the oxidized and non-oxidized samples (SWy-CNT and SWy-oxCTN), are ascribed either to carboxyl-carbonate structures or aromatic C=C bonds.

3) the strongest prove of the nanotube's oxidation after treatment with the mixtures H_2SO_4/HNO_3. is the appearance of the additional band at 1725 cm^{-1} of the C=O stretch vibrations of carbonyl and carboxyl groups.

4) Finally, the bands in the region around 2900 cm^{-1} confirm the presence of the organo-functionalization being typical of C-H stretch vibrations of the alkyl chains.

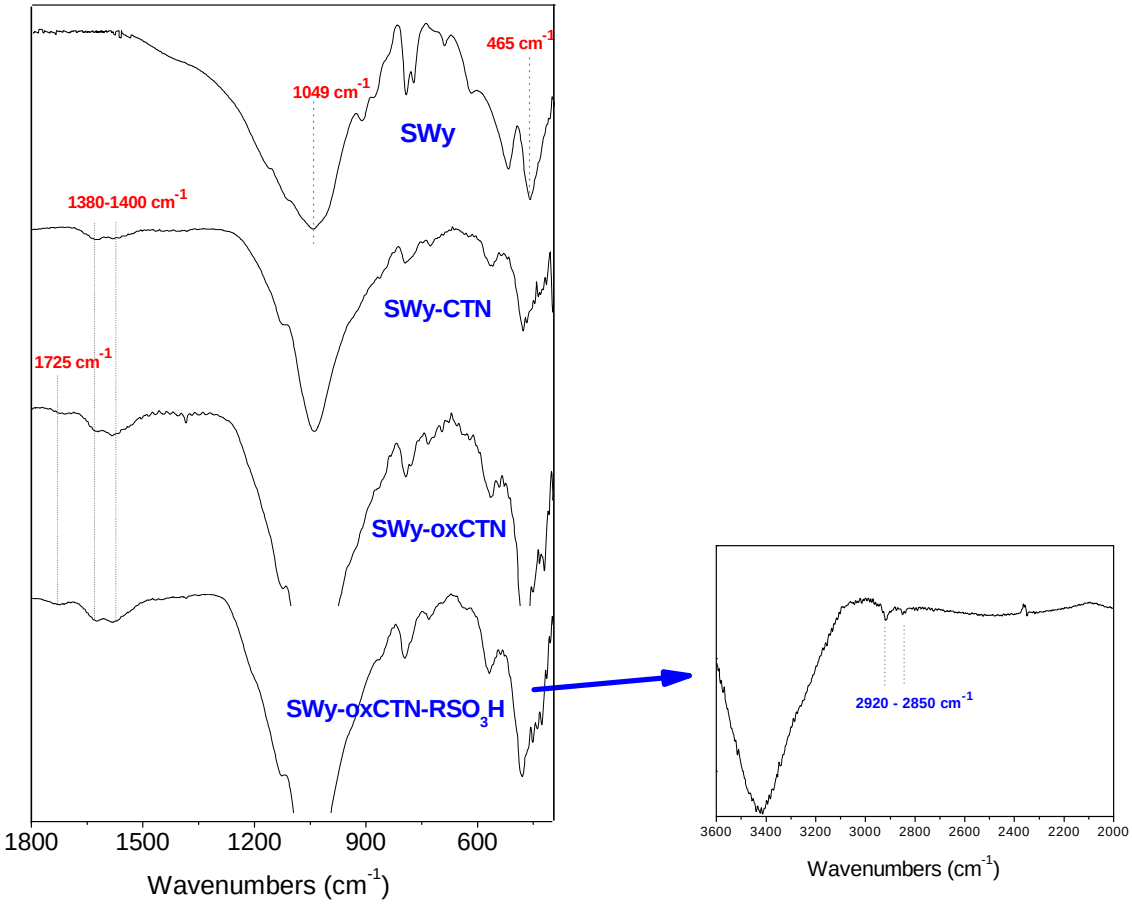

Figure S1. FT-IR spectra collected on pristine materials and final clays-CNTs nanofillers.

Raman spectroscopy is a powerful method for the characterization of the quality of the CNTs. Two characteristic CNTs peaks, at 1350 and 1595 cm^{-1} corresponding to graphite D- and G-bands respectively, are observed in the Raman spectra of the two SWy-CNTs synthesized materials (at 32% and 5% of yields). The G-band corresponds to the tangential stretching (E2g) mode of highly oriented pyrolytic graphite (HOPG), while the D-band originates from disorder in the sp_2-hybridized carbon atoms, characteristic for lattice distortions in the curved graphene sheets and/or tube ends. The relative intensity of the D and G-bands (I_D/I_G) reveals the degree of disorder in the graphite sheets and it can be used as a measure of the crystallinity of the synthesized CNTs.[1]
Before the oxidation reaction, the I_D/I_G value is 0.79, that increases up to 0.86 after oxidation.
These values are lower than those reported (ID/IG =0.85–1.3) in the literature and suggest high graphitization degree and thus good quality of the graphitic structures.[2]

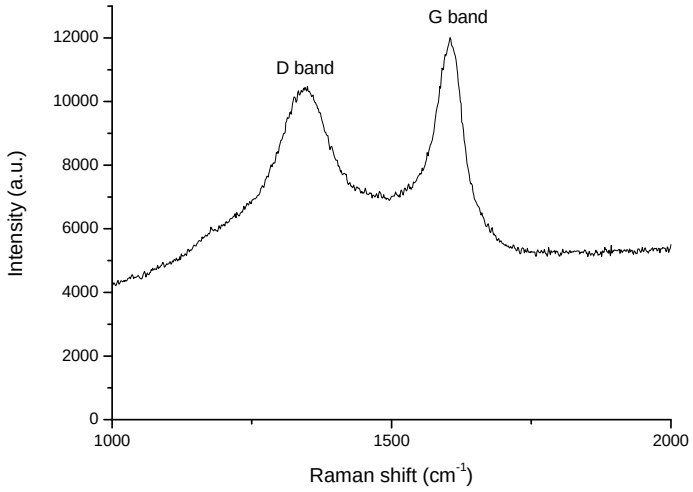

Figure S2. Characteristic Raman spectra of CNTs grown at 700 °C over Fe-Ni catalyst on SWy-clay's surface.

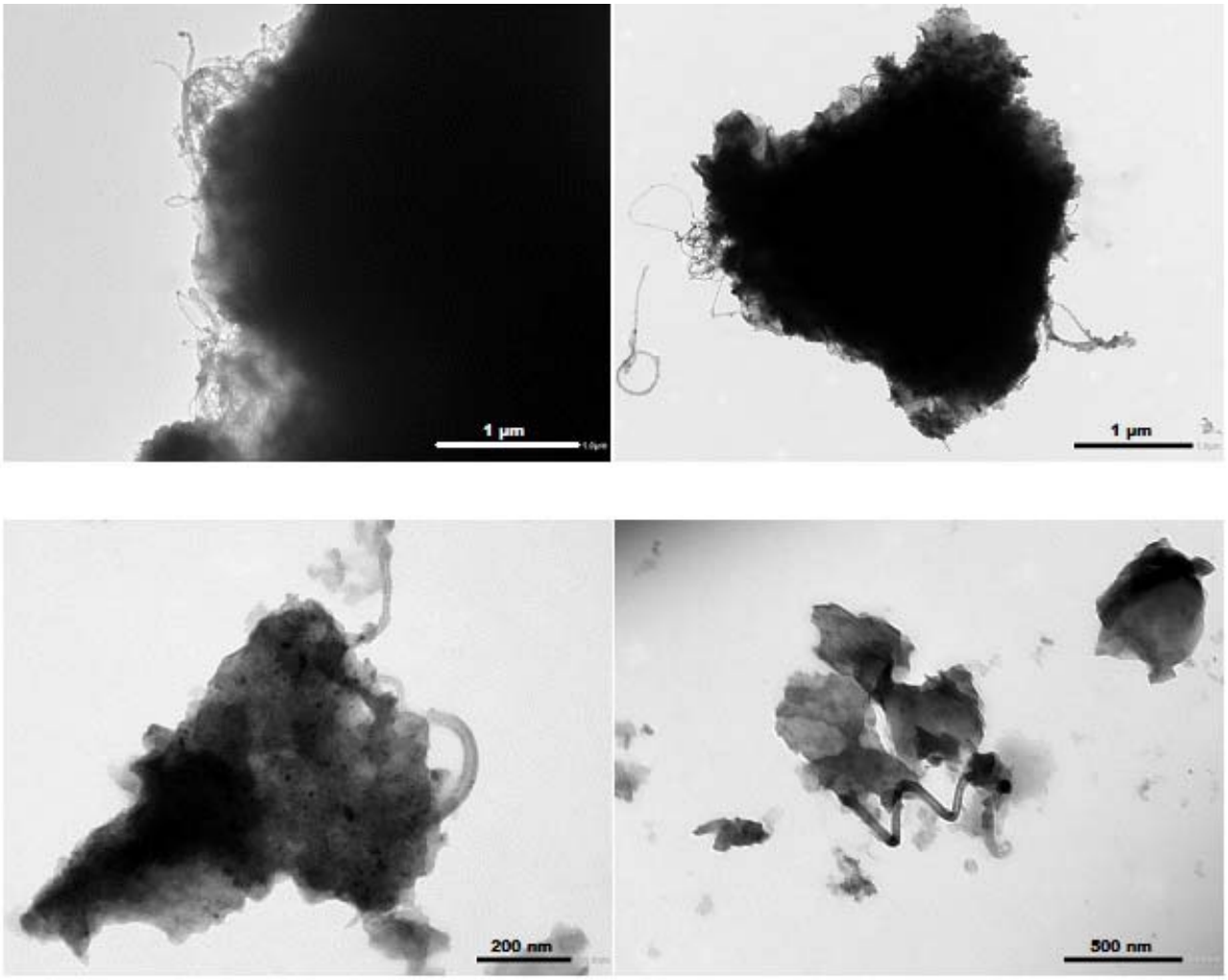

Figure S3. TEM images of the products SWy-oxCNTs-RSO_3H at 32% (first row) and 5% (second row) of yields, respectively.

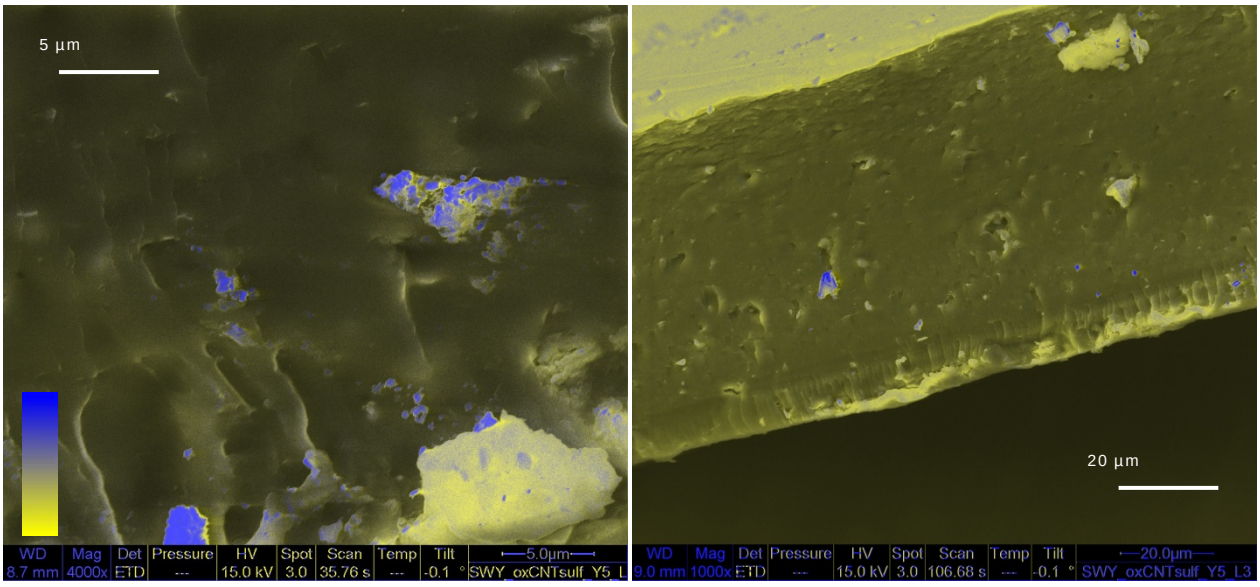

Figure S4. SEM-BSE images of representative composites membranes, N/SWy-oxCNTs-RSO3H(y5) and N/SWy-oxCNTs (y5), in false colours to put in evidence the clays clusters distribution. The yellow-to-blue colour bar spans from the lowest BSE intensity to the highest one.

The results obtained show that the composite N/SWy-oxCNTs-SO_3H(y5) is certainly the most promising. For this nano-additive, the effect of the loading with respect to the polymer, was investigated. Accordingly, composite membranes to 2 wt% and 3 wt% were prepared and analyzed, while, higher loading lead to inhomogeneous membranes, and therefore were not taken into account. In Figure S4, the diffusion coefficients vs. temperature is shown. De facto there is not a significant difference between the three loadings; the 2 wt% may be the best compromise, because it increases the water uptake from 31-32 wt% (in the loadings 1 and 3 wt%, respectively) at 37 wt%.

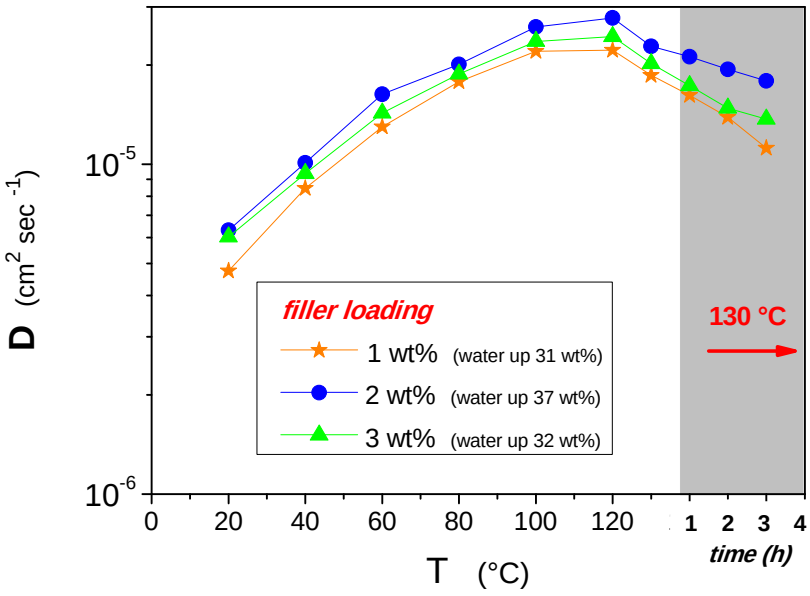

Figure S5: Self-diffusion coefficients as function of the temperature (from 20 °C up to 130 °C) of the water confined in N/SWy-oxCNTs-SO3H(y5) composites membranes at different filler to polymer loading. In the graph are also plotted the data collected at 130 °C after several hours.

References

[1] T. Tsoufis, P. Xidas, L. Jankovic, D. Gournis, A. Saranti, T. Bakas, and M. a. Karakassides, Diam. Relat. Mater. **2007**, 16, 155–160.

[2] a) Z. Xu, H. Wang, and J.-Y. Hwang, Carbon **2007**, 45, no. 4, pp. 873–879; b) V. Georgakilas, D. Gournis, M. A. Karakassides, A. Bakandritsos, and D. Petridis, Carbon **2004**, 42, 865–870.

II

"An NMR study on the molecular dynamic and exchange effects in composite Nafion/sulfated titania membranes for PEMFCs"

International Journal of Hydrogen Energy, **2015**, 40 (2), pp 14651–14660

INTERNATIONAL JOURNAL OF HYDROGEN ENERGY 40 (2015) 14651–14660

Available online at www.sciencedirect.com

ScienceDirect

journal homepage: www.elsevier.com/locate/he

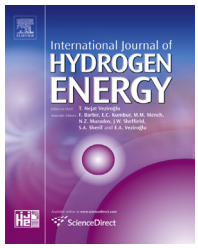

An NMR study on the molecular dynamic and exchange effects in composite Nafion/sulfated titania membranes for PEMFCs

Isabella Nicotera [a,*], *Vasiliki Kosma* [a], *Cataldo Simari* [a], *Giuseppe A. Ranieri* [a], *Mirko Sgambetterra* [b], *Stefania Panero* [b], *Maria Assunta Navarra* [b]

[a] *Department of Chemistry and Chemical Technologies, University of Calabria, via P. Bucci, 87036 Rende (CS), Italy*
[b] *Department of Chemistry, Sapienza University of Rome, Piazzale A. Moro 5, 00185 Rome, Italy*

ARTICLE INFO

Article history:
Received 13 March 2015
Received in revised form
24 June 2015
Accepted 25 June 2015
Available online 20 July 2015

Keywords:
Sulfated titania
Nanocomposite
PEMFC
Self-diffusion
NMR
Water dynamics

ABSTRACT

Sulfated titania nanoparticles were evaluated as inorganic additives in composite Nafion-based membranes, to be considered as advanced electrolyte in proton exchange membrane (PEM) fuel cells (FCs). Three different filler loadings respect to the polymer were comparatively investigated to elucidate the effect of the inorganic particles on membrane peculiar properties and finally establish the most effective electrolyte composition. Water dynamics were investigated by NMR spectroscopy, including pulsed-field-gradient diffusion and ^{1}H spectral analyses conducted as a function of temperature (20–130 °C), and by water content measurements, providing a general description of the water management inside the systems and of the effects of the fillers.

Due to its strong acidity and hydrophilicity, sulfated titania was found to improve both the water retention and diffusion in the composite membranes in respect to plain recast Nafion, in the whole range of investigated temperatures, with a significant impact in the region of high temperatures and very low water content.

In this work, self-diffusion coefficients data were interpreted in terms of a simple "two-sites" model involving exchange between relatively bound and mobile water sites to discuss the nature of water dynamics and the state(s) of the water (bound and free states) both inside composite and filler-free membranes, as well as its interaction with the hydrophilic polymer sites and particles surface. A quantitative analysis was elaborated to estimate the number of water molecules involved in the hydration shell of the hydrophilic groups of both polymer and filler, as function of the membrane water content. Despite the simplicity of this "bound/free water exchange" model, we obtain consistent values corresponding to about thirteen water molecules per sulfonic group.

* *Corresponding author*. Tel.: +39 0984 493379; fax: +39 0984 492044.
E-mail address: isabella.nicotera@unical.it (I. Nicotera).

http://dx.doi.org/10.1016/j.ijhydene.2015.06.137

Introduction

Proton exchange membrane fuel cells (PEMFCs) have been widely used as alternative mobile and stationary power sources. The proton exchange membrane (PEM) is a key component in this type of fuel cells, having the capability to transport protons from anodic to cathodic side. The development of high-performance electrolyte membrane is critical to the optimal power density and efficiency that a PEMFC can achieve because membrane ohmic loss is the major cause of overpotential in the fuel cell operational current range [1,2]. The state-of-the-art PEM is based on perfluorosulfonic acid (PFSA) polymers like Nafion, developed by DuPont, due to their good mechanical properties, excellent chemical stability and relatively high proton conductivity at highly hydrated conditions [3]. However, PEMFCs operating in the typical 60–80 °C temperature range face problems including poor carbon monoxide (from reformed hydrogen or methanol as fuels) tolerance and heat rejection [4]. These drawbacks can be overcome by increasing the operation temperature range up to 120 °C, but this leads to an unacceptable decrease in the proton conductivity of the electrolyte due to water loss and possible structural changes in the polymer. The most significant barrier to running a polymer electrolyte fuel cell at elevated temperatures is maintaining the proton conductivity of the membrane. Water is more easily lost at higher temperatures due to an increased vapor pressure, thereby resulting in a decreased proton conductivity. The conductivity of a dry membrane is several orders of magnitude lower than a fully hydrated membrane. Composite/hybrid membranes prepared by addition of organic/inorganic filler with high surface area to the Nafion matrix provide a promising alternative to pure perfluorosulfonic membranes for elevated temperature PEMFCs operation (>80–100 °C) [5–8]. In particular, inorganic acids, which can both act as a water reservoir into the polymer matrix and, in virtue of their acidity, provide additional pathways for proton transport inside the polymer, are a very attractive class of materials to be used as additive in Nafion matrices [9–11]. Among the inorganic acids, sulfated metal oxide have recently become subjects of intensive studies in PEM-related research field, due to their high stability, tunable morphological and structural properties and to the extraordinary acidity of some of these compounds, as, for instance, sulfate zirconium oxide [12–16], sulfate tin oxide [17,18] and sulfate titanium oxide [19].

The study of the water transport mechanism, and consequently of the H^+ ions within the electrolytic membrane, is one of the key aspects in the evaluation of these composite materials. Proton transport in water-containing media mainly occurs by two processes, typically referred to as *vehicle* and *Grotthus* mechanisms [20–22]. The first involves the protons diffusion on a vehicle, such as H_3O^+ ions, but is disadvantaged in dehydration state; the second is connected to rotation of water molecules within a constantly changing network of hydrogen bonds. It is also clear that most of the water absorbed in Nafion-like ionomers is very different from liquid water or bulk water.

The pulse field gradient (PFG) NMR is a powerful technique able to give insights into the dynamics of very complex systems. It was adopted in this work to obtain a direct measurement of the self-diffusion coefficients of water confined in filler-free Nafion membrane and in Nafion nanocomposites. This technique, together with the ^1H spectral analysis collected as a function of temperature and water content measurements, has provided a general description of the water management inside our systems, highlighting the specific role played by the filler, while a "bound water/free water exchange" model [23,24] was applied to interpret the water diffusion coefficients.

Experimental

Sulfated titania nano-particles, having an anatase crystallographic phase, were obtained following a 1-step sol–gel synthesis procedure already reported in a previous work of our group [19]. Briefly, H_2SO_4 (0.5 M; 6.4 ml) was added to a mixture of titanium isopropoxide (12.5 ml, Sigma–Aldrich) and 2-propanol (100 ml, Sigma–Aldrich) under vigorous stirring. After 2 h, the solution was filtered and calcined for 3 h at 400 °C. The synthesized powder had a homogeneous size distribution with particles diameter around 11 nm, as derived by the analysis of x-ray diffraction patterns [19].

To evaluate the surface acidity of the synthesized powders, ion exchange capacity (IEC) tests, providing the number of milli-equivalents of exchangeable protons per gram of sample, were performed by a classical titration method. Dry samples were immersed in NaCl aqueous solution and the exchanged protons were neutralized with a standard NaOH solution 0.1 N (Sigma Aldrich).

Nafion membranes were prepared following a solvent casting procedure. The commercial Nafion dispersion (5 wt% in water/alcohol, E.W. 1100, Ion Power, GmbH) was treated with *N,N*-dimethylacetamide (Sigma–Aldrich) at 80 °C in order to replace solvents. For composite membranes, the sulfated titania powder was added to the final Nafion solution and stirred to homogenize the dispersion. The mixture was casted on a Petri dish and dried at 90 °C to obtain self-standing membranes. Dry membranes were then hot pressed at 50 atm and 175 °C for 15 min. They were finally activated in boiling hydrogen peroxide (3 wt. %), sulfuric acid (0.5 M) and water.

The inorganic filler content was chosen to be equal to 2, 5 and 7 wt.% in respect to Nafion, resulting in three membrane samples hereafter labeled as M2, M5 and M7 respectively. Plain, additive-free Nafion membrane will be labeled as M0. Thickness of the various synthesized membranes, measured in dry conditions, ranged between 80 and 100 μm.

In-plane conductivity of membranes was measured by a DC operational four-electrode system, adopting a commercial cell (BT-112, Scribner Associates Inc) fitted between the anode and cathode flow field of a fuel cell test hardware (850C, Scribner Associates Inc.). This allows controlling the sample temperature and relative humidity (RH). Humidification of the cell was accomplished by bubbling the fed gas (i.e. nitrogen) through stainless steel cylinders incorporated in the compact system and containing distilled water. DC measurements, for the evaluation of membrane resistance as the slope of a linear plot of voltage versus current, were realized by a potentiostat

(885, Scribner Associates Inc.) connected to the fuel cell test system and operating under the integrated *FuelCell*® software.

NMR measurements were performed on a Bruker NMR spectrometer AVANCE 300 Wide Bore working at 300 MHz on ^{1}H. The employed probe was a Diff30 Z-diffusion 30 G/cm/A multinuclear with substitutable RF inserts. Spectra were obtained by transforming the resulting free-induction decay (FID) of single $\pi/2$ pulse sequences. The pulsed field gradient stimulated-echo (PFG-STE) method [25] was used to measure self-diffusion coefficients. This sequence is generally applied when the materials are characterized by a transverse relaxation time (T_2) considerably shorter than longitudinal relaxation time (T_1). The sequence consists of three 90° rf pulses ($\pi/2-\tau_1-\pi/2-\tau_m-\pi/2$) and two gradient pulses that are applied after the first and the third rf pulses, respectively. The echo is found at time $\tau = 2\tau_1 + \tau_m$. Following the usual notation, the magnetic field pulses have magnitude g, duration δ, and time delay Δ. The attenuation of the echo amplitude is represented by the following Eq. (1):

$$I(2\tau_1+\tau_m) = \frac{1}{2} I_0 exp\left[-\frac{\tau_m}{T_1} - \frac{2\tau_1}{T_2} - (\gamma g\delta)^2 D\left(\Delta - \frac{\delta}{3}\right)\right] \quad (1)$$

where D is the self-diffusion coefficient. The used experimental parameters were gradient pulse length $\delta = 1$ ms, time delay $\Delta = 10$ ms, and the gradient amplitude varied from 100 to 800 G cm^{-1}. The uncertainty in the self-diffusion measurements is ~3%. Measurements were conducted by increasing temperature step by step from 20 to 130 °C, with steps of 20 °C, and leaving the sample to equilibrate for about 15 min. All the membranes, before the NMR measurements, were dried in oven, weighed and then immersed in distilled water at room temperature. Upon being removed from the water they were quickly blotted dry with a paper tissue (to eliminate most of the free surface liquid). Then, the water uptake (wu) value was determined using a microbalance and recorded by Eq. (2):

$$wu\% = (m_{wet} - m_{dry})/m_{dry} \times 100 \quad (2)$$

At this point the membranes were loaded into a 5 mm NMR Pyrex tube.

Results and discussion

Fig. 1 displays the self-diffusion coefficients of water confined in the filler-free Nafion membrane and in the nanocomposites at different filler's loading, as a function of water content and temperature. In particular, the investigated

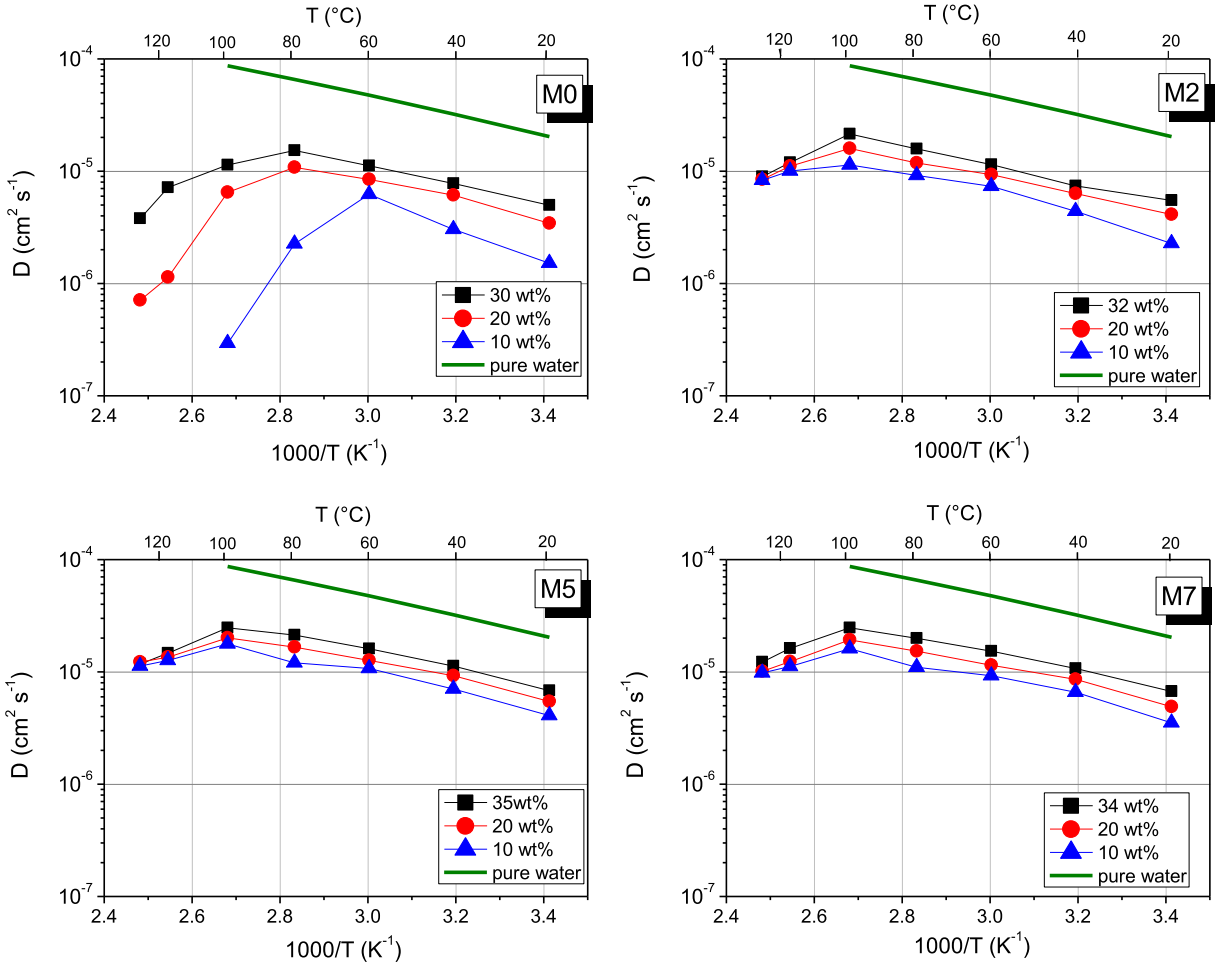

Fig. 1 – Arrhenius plot of the ^{1}H self diffusion coefficients of water in filler-free Nafion and Nafion composites membranes swelled at three water uptake (saturation, 20 wt% and 10 wt%), in the temperature range 20–130 °C. The pure-water diffusion coefficients are also plotted.

temperature range was 20–130 °C, and the analyzed water contents corresponded to the saturation condition (maximum membrane swelling), to a medium swelling of about 20 wt%, up to very low hydration condition, i.e. about 10 wt%, in order to explore the behavior of each system and the effect of the nano-additive in the various hydration states. Due to the strong correlation between the water content and mobility [7,26], as expected, D is inversely proportional to the water uptake.

The presence of the filler doesn't appreciably affect the water uptake capacity of the nano-composites with respect to filler free Nafion (M0), in fact the differences are very small: M0 30 wt%, M2 32 wt%, M5 36 wt% and M7 34 wt%. However, on the diffusion coefficients the effect of the inorganic additive is considerable if we observe the region high temperatures (above 100 °C) and, in particular for low hydration conditions. For instance, the slight decrease of the diffusion observed in the nano-composites over 100 °C, due to water evaporation, correspond to a brusque drop of the water mobility of almost two order of magnitude in the filler free membrane, starting already at 60–80 °C. Furthermore, when the water content is very low (10%), over 100 °C the proton signal is insufficient to perform diffusion measurements while, in all the three composites the diffusion remain high, without any appreciable differences respect to the filler loadings. Finally, one last noteworthy observation on these experimental data is that at 130 °C the values of the diffusion coefficients to different water uptake (*wu*) converge to a value almost identical.

These results clearly show the high retention capability of the sulfated titania material dispersed in the polymer matrix. It is also evident that the water diffusion in the composite membranes remains large at very low hydration state, being this reasonably attributed to the surface properties of the added inorganic particles. Indeed, sulfate functionalization on titania resulted in the formation of a very acidic compound, with an ion exchange capacity of 1.08 ± 0.03 meq g^{-1}, higher than the IEC value of the polymer adopted in this work (namely, 0.9 meq g^{-1} for Nafion 1100 EW). Since in Fig. 1 it is difficult (for the scale used) to appreciate the effect of filler loading on proton diffusion, we show further plots in the Supporting Information (Fig. S1), in which we compare all the membranes at the same *wu*. It appears quite clear that the composition corresponding to 5 wt% of filler can be considered as the most effective and promising for real application; in fact, an increase up to 7 wt% of loading does not lead to any improvement with respect to 5 wt% in terms of diffusion properties, likely disadvantaged by agglomeration processes of the particles.

The analysis of the temperature dependence of the water diffusivity, using Arrhenius equation in the temperature range in which the diffusion increases (20–100 °C for the composites, and up to 80 °C or 60 °C for recast Nafion), gives the corresponding activation energy (E_a) of diffusion process, which is the energy barrier for carrier transfer from one free site to another one. The values are reported in Table 1. On completely swelled membranes they range between 3.84 kcal/mol and 3.52 kcal/mol, in agreement with literature for Nafion-based electrolytes [27], with a clear dependence on the filler's loading, as can be seen in table moving from left to right. The increase of the activation energy with the decrease of the water uptakes is due to the reduced mobility associated with the presence of the confining pores. At lower hydration levels, i.e. with decreasing cluster sizes, the probability of hydrogen bond formation with neighboring acid groups increases. The reorientation of the protons in the solid-like sites requires the breaking of these bonds, therefore the activation energy associated with this motion increases [28,29].

Table 1 – Activation Energies (kcal/mol) calculated from the ^{1}H Self Diffusion Coefficient data as a function of water content.

Water uptake (wt%)	M0	M2	M5	M7
saturation	3,84	3,78	3,53	3,52
20%	3,91	3,63	3,50	3,63
10%	6,86	4,35	3,81	3,88

In a nutshell, in such polymer-based electrolytes, the two different proton transport mechanisms, vehicular and Grotthus, coexist, and the prevailing of one on the other depends from the hydration level inside the hydrophilic pores; consequently with minimum water content the structural diffusion starts to be a preferential path for proton diffusivity.

Accordingly, in M5 and M7 composites the activation energies remain almost unaffected by reducing the water content, meaning that a certain amount of water more "free" is available even at low hydration. Likely, the acid surface of the nanoparticles is exposed to the hydrophilic domains in the polymer, contributing to hydration of the composite. A continuous exchange of protons among the sulfonic and sulfate groups is expected, helping both retention and mobility at high temperature. This will be detailed later and confirmed on a quantitative model, but before, it is interesting to show the evolution of some proton spectra acquired during the heating on the membranes. In Fig. 2 (a) a representative spectral evolution collected on partially swelled M0 membrane (at 20 wt% of water uptake) is reported. Spectra were referenced against pure water set at 4.79 ppm [i.e., its chemical shift with respect to tetramethylsilane (TMS)] and were acquired with the same number of scans to compare their intensities. The proton signal is very wide, about 1 kHz, typical of solid-like configuration, due to the strong confinement of the water molecules within the hydrophilic pores. Clearly, this NMR peak is the convolution of "different" water signals (free and bound to the various hydrophilic groups) in fast rate of proton exchange [7,30]. By increasing temperature, the intensity of this peak decreases because of the water evaporation from the membranes. Finally, the small signal at 2.5 ppm comes from the background of the r.f. coil, visible when the proton signal of the sample has a very low intensity, deforming the peak.

The graphs (b) and (c) in Fig. 2 show the temperature dependence of signal's area, normalized to the initial water uptakes, for M0 and M5 membranes, respectively. The recast membrane, at low swelling degree (10 wt%), reaches the high temperatures in an almost dehydrated state, so that at 130 °C no signal is more detected. Instead, the composite membrane M5 maintains a sufficient hydration and, consequently, good proton diffusion. At higher water contents, both membranes have a loss of signal almost comparable. However, the data of diffusion at 130 °C showed higher proton mobility in the

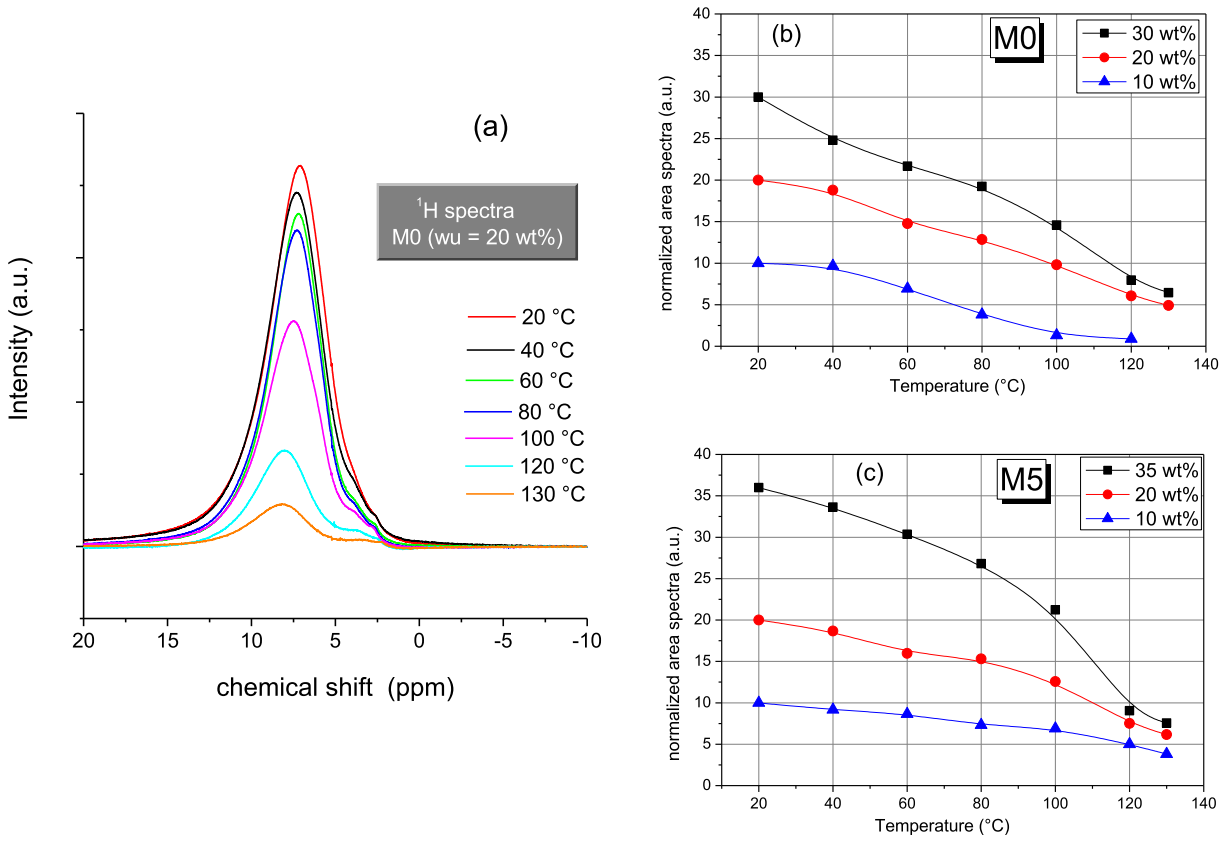

Fig. 2 – –Temperature evolution of ^{1}H NMR spectra of the water confined in filler-free Nafion (M0) acquired from 20 °C up to 130 °C (a). Plots of the peak areas normalized to the initial water uptakes vs. temperature for the sample M0 (b) and M5 (c).

composite. This means, in agreement with above, a greater contribution of free water (more mobile) to this NMR signal.

Such considerations are also supported by proton conductivity data. Measurements performed under low hydration level (i.e. RH = 40%) and relatively high temperature (i.e. 80 °C) revealed higher conductivity for the composite M5 membrane (i.e. 13.8 ± 2.0 mS cm^{-1}) compared with plain M0 membrane (i.e. 8.1 ± 0.5 mS cm^{-1}), this highlighting the contribution of water in proton transport.

The following model, applied to the diffusion data and proton spectra, tries to quantify and explain these aspects discussed so far.

Two sites model

The activation energies of Table 1, if compared with that of pure water (4.2 kcal/mol), are almost all slightly lower. The apparent decrease of the activation energy of diffusing water inside the membrane's pores with respect to the "unrestricted" water seems quite curious. Actually this outcome is an artefact associated with water loss from the membranes at higher temperature, and we will return on this point later.

It is well established that when solvent molecules (water in our case) diffuse in presence of macromolecules, their diffusion is slowed down by both the need to divert around macromolecules (obstruction effect) and any interactions with the same macromolecules that inhibit their motion (solvation or hydration), i.e. molecules are in the "bound state" [31,32]. Exchange of molecules between bound- and free-state results in an averaged diffusion coefficient D, which depends on the time fraction spent in each state, and expressed according by the Eq. (3):

$$D = (1 - P)\, D_f + P D_b \tag{3}$$

where, D_f and D_b are the diffusion coefficients of free and bound water, respectively, while P is the fraction of hydration water (water molecules involved in hydration of SO_3^- groups and/or hydrophilic sites of nanoparticles in the composite membranes). This approach is called the "bound water/free water exchange" representation [23,24,32]. It assumes that water molecules exist as "free" and "bound" water in rapid exchange compared with the NMR times involved in the experiment [33]. Now we use this simple model to analyze the diffusion data in order to determine the hydration number to the sulfonic groups, i.e. the water fraction in the bound state.

The self-diffusion coefficient of free water is defined as $D_f = f D_0$, where D_0 is the diffusion of the pure water and f is the so-called obstruction factor. The obstruction factor is a geometrical parameter depending on the particular structure and on the translational freedom degrees of water molecules, and its value ranges between zero (no diffusion) and 1 (free state) [34–36], that is, by increasing the translational freedom degrees of the molecules, the obstruction factor tends to be close to unity.

The evaluation of D_b is not an insignificant matter but it is assumed to be negligible compared to D_f and therefore approximated as zero. Therefore, Eq. (3) simplifies to:

$$D \approx (1-P)f \times D_0 \quad (4)$$

To establish the value of the obstruction factor for our system is not straightforward, while numerous are the models proposed for liquid crystalline systems and polymer solutions [31,37–41]. However, all these studies suggest that the obstructive effect of the polymer network is affected not only by the polymer content, but also by the morphology of the polymer network, including the spatial disorder of polymer molecules, and the validity of individual models depends on the macromolecular environment. In general, the theoretical approach considers a rigid sphere moving between two rigid solid surfaces, and the particle diffusion coefficient is then reduced by a factor expressed by the Faxén equation [41,42]: $D/D_0 = (1 - 2R_H/d_w)$ where D_0 is the bulk diffusivity, R_H is the hydrodynamic radius of the particle, and d_w is the distance between the plates.

In the "two sites" model, the decreasing in water diffusion coefficient is actually also due to the existence of a fraction of surface-associated water molecules, and the observed diffusion coefficient, assuming fast exchange between the two environments, is the average of the diffusion coefficients of the free and surface-associated molecules, as explained before.

One of most accredited models to describe the hydrated Nafion structure is the water-channel model proposed by Schmidt-Rohr and Chen [43,44], consisting in a cylindrical inverted micelles structure where the water molecules diffuse inside water channels (cylinders) of ~2.4 nm-diameter. For such structure, the obstruction factor calculated applying Faxen's formula with a water hydrodynamic radius of ~0.1 nm, is about 0.92. Therefore, by considering only the geometric confinement there would be a correction of only about 10% compared to free diffusion of water in bulk. This result is surely coherent for the observed efficient water diffusion in Nafion. The plot of diffusion ratios $\left(\frac{D}{f\,D_0}\right)$ versus temperature and versus membranes (at the water saturation) is given in Fig. 3.

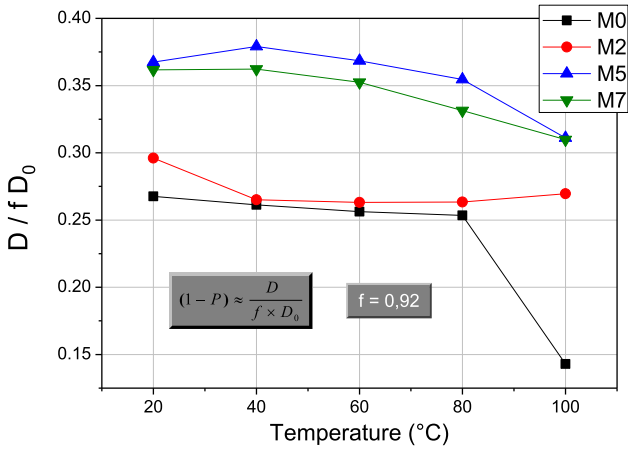

Fig. 3 – Diffusion ratios $\left(\frac{D}{fD_0}\right)$ versus temperature for the different samples in the temperature range 20–100 °C.

It is evident that our results can be interpreted in accordance with Eq. (4) by considering a temperature dependence of the free water molar fraction (1–P): we observe a slightly decreasing for the composites with temperature increasing, while it changes appreciatively, in particular above 80 °C, in the filler-free Nafion membrane.

These (1–P) data were used to calculate both bound (χ_b) and free (χ_f) water molar fractions for all the swollen membranes by considering their initial uptake. The results are listed in Table 2 where, the second column reports the maximum water uptake at 20 °C of each membrane and the third column shows the χ_f (free-water fraction) calculated as multiplication of (1–P) at 20 °C (got from the graph in Fig. 3) with the respective *wu*. The χ_b (bound-water fraction) is simply obtained as ($\chi_f - wu$). Additionally, we calculated the residual free-water amount in the membranes and the percentage of water driven from them at 100 °C, fourth and fifth columns of Table 2, respectively. χ_f was calculated like above [$(1-P)_{100°C} \times wu$] and the water loss in accordance with the following Eq. (5):

$$\%waterloss = \frac{freewater(20°C) - freewater(100°C)}{freewater(20°C)} \times 100 \quad (5)$$

From these values two aspects emerge:

i) the amount of bound-water is very similar for all the membranes (filler-free and composites Nafion) varying slightly from its average value (ca. 22 %wt);
ii) the water loss at 100 °C of the filler-free Nafion is the highest reaching almost the 50%, while the composites retain more water, and they lose no more than 15% of their initial water uptakes.

It is exactly this gradual water loss that provides an explanation for the apparently lower activation energies of water diffusion in the membranes compared to pure water. Even modest water loss at higher temperature gives a lower diffusion coefficient than would be obtained without losing water, thus yielding a decrease in the slope of the diffusion data. When comparing the results of ex-situ experiments to data drawn from in-situ conditions of an operating fuel cell (i.e. under controlled relative humidity conditions), one must exercise caution. The apparently smaller diffusion activation energy in the membranes is clearly an artefact.

Table 2 – Estimation of bound- and free-water fractions in membranes.

Membranes	*wu* (%wt) at 20 °C	χ_f χ_b at 20 °C	χ_f at 100 °C	Water loss
M0	30	8.1 21.9	4.3	~47%
M2	32	9.5 22.5	8.6	~9.5%
M5	36	13.2 22.8	11.2	~15%
M7	34	12.3 21.7	10.5	~15%

By taking into account of the above data and the area of the spectral signals, we attempted a quantitative analysis in order to estimate the number of water molecules involved in the hydration shell of the sulfonic acid groups of Nafion polymer, as well as of the sulfate groups on the nanoparticles. The SO_3^- groups present in the system originate from Nafion (EW 1100), therefore there are 0.9 mmol SO_3^- per 1 g of polymer, while the amount of exchangeable protons in SO_4^{2-}/TiO_2 are 1.08 mmol per 1 g of filler (see IEC evaluation).

Table 3 reports a schematic description of the calculations executed, before on the filler-free Nafion membrane and then on one composite sample, i.e. M5 membrane.

To calculate the hydration number at 130 °C, it was considered the integrals of the ^1H NMR signals, assuming that, at this high temperature, all the water present in the membrane (proportional to the area of the proton signal), is in the hydration shells to the hydrophilic groups.

The hydration numbers obtained by similar calculation for all the studied membranes are summarized in Table 4. As we can see, there are not any differences between composites and recast Nafion; the hydration numbers are nearly to 13H_2O/acid sites *mol/mol* in the maximum hydration state, and circa 4.5H_2O/acid sites *mol/mol* in the very low hydration state. These values are in agreement with the literature [43–45].

The results obtained are encouraging and indicate, therefore, that this relatively simple "two sites" model used to interpret the water diffusion data on pure Nafion and Nafion-composite membranes, was able to give a plausible description of the water distribution inside so complex systems.

As we reported above, the self-diffusion measurements were collected on membranes also at lower water uptakes, well below their saturation values, i.e. 20 wt% and 10 wt%, respectively.

With the decreasing of the water uptake, obviously both *bound* and *free* water molar fraction decrease, as shown in the histograms of Fig. 4(a). However, it is significant to observe as the ratio between these two molar fractions (χ_b/χ_f) changes among the membranes and with the water content (see Fig. 4(b)). For instance, in the recast Nafion the relative amount of free water is the lowest at all the water uptakes, and it drastically decreases at very low hydration. Additionally, this amount of free water evaporates completely above 100 °C. This outcome, as well as the trend of the composites, is entirely in agreement with the self-diffusion coefficients seen before. In other words, during the swelling there is a cluster expansion and a continuous redistribution of exchange sites and, in a fully hydrated sample there are fewer clusters but of larger size, with higher free/mobile water fraction.

Table 4 – Hydration numbers obtained on completely swelled membranes at 20 °C and at 130 °C.

Membranes	$h_{SO_3^-/SO_4^=}$ [*mol/mol*] 20 °C	$h_{SO_3^-/SO_4^=}$ [*mol/mol*] 130 °C
M0	13.6	4
M2	13.6	4.5
M5	13.3	4.4
M7	12.4	4.7

Finally, in Fig. 5 are shown the hydration numbers calculated for all the membranes at the various water contents. They range between 8 and 10 at 20 wt%, and between 4.5 and 6 at 10 wt% of water content, respectively. This regular reduction of the number of water molecules hydrating the sulfonic/sulfate groups is expected by decreasing the dimension of the hydrophilic pores and, to date, these values are consistent with data reported in literature. It is worth dwelling on the fact that the lower numbers obtained in the composite membranes compared to M0 (at 10 and 20 wt% of water uptake) are likely due to the framework described previously: the hydrophilic domains contain higher concentration of acid sites (SO_3^- and $SO_4^=$) and the quick exchange among the water molecules of the hydration shells, results in a reduction of the average hydration number.

Conclusions

A relatively simple "two sites" model was used to interpret the water diffusion data on pure Nafion and Nafion-composite membranes measured over a wide temperature range, where exchange between mobile and bound water sites leads to an average diffusion coefficient. Although the apparent low activation energy for diffusion in the membranes is determined to be an artefact associated with water loss, the model does provide a useful estimate of bound water behavior and plausible hydration numbers related to the hydrophilic groups of polymer matrix and to the nano-additive. The hydration number is essentially the same in all the completely swelled membranes, i.e. both filler-free Nafion and Nafion-composites contain approximately 13 water molecules per sulfonic and sulfonic/sulfate group, respectively, value in agreement with the literature. This result demonstrates as this inorganic

Table 3 – Water distribution and hydration numbers in M0 and M5 membranes.

M0 $wu = 30\ wt\% \rightarrow 16.7\ mmol\ of\ H_2O\left(=\frac{0.3\ g}{18\ g/mol}\right)$

At **20 °C**, $\chi_b = 21.9\%$ [*from* Table 2] ⇒ **12.2 *mmol***$\left(=\frac{0.219\ g}{18\ g/mol}\right)$;

$h_{SO_3^-} = \frac{12.2\ mmol}{(0.9\ mmol\ SO_3^-)} = 13.6$ H_2O/SO_3^-

At **130 °C** [*from normalized area of* ^1H *signal*] ⇒

$\chi_b = 6.45\%$ ⇒ **3.59 mmol** $\left(=\frac{0.0645\ g}{18\ g/mol}\right)$;

$h_{SO_3^-} = \frac{3.59\ mmol}{(0.9\ mmol\ SO_3^-)} = 4$ H_2O/SO_3^-

M5 $wu = 36\ wt\% \rightarrow 20\ mmol\ of\ H_2O\left(=\frac{0.36\ g}{18\ g/mol}\right)$

At **20 °C**, $\chi_b = 22.8\%$ [*from* Table 2] ⇒ **12.67 mmol**$\left(=\frac{0.228\ g}{18\ g/mol}\right)$;

$h_{SO_3^-,SO_4^=} = \frac{12.67\ mmol}{(0.9\ mmol\ SO_3^-)+[(1.08\times5\%)mmol\ SO_4^=]} = 13.3$ $H_2O/(SO_3^-, SO_4^=)$

At **130 °C**, [*from normalized area of* ^1H *signal*] ⇒

$\chi_b = 7.56\%$ ⇒ **4.2 mmol** $\left(=\frac{0.0756\ g}{18\ g/mol}\right)$;

$h_{SO_3^-,SO_4^=} = \frac{4.2\ mmol}{(0.9\ mmol\ SO_3^-)+[(1.08\times5\%)mmol\ SO_4^=]} = 4.4$ $H_2O/(O_3^-, SO_4^=)$

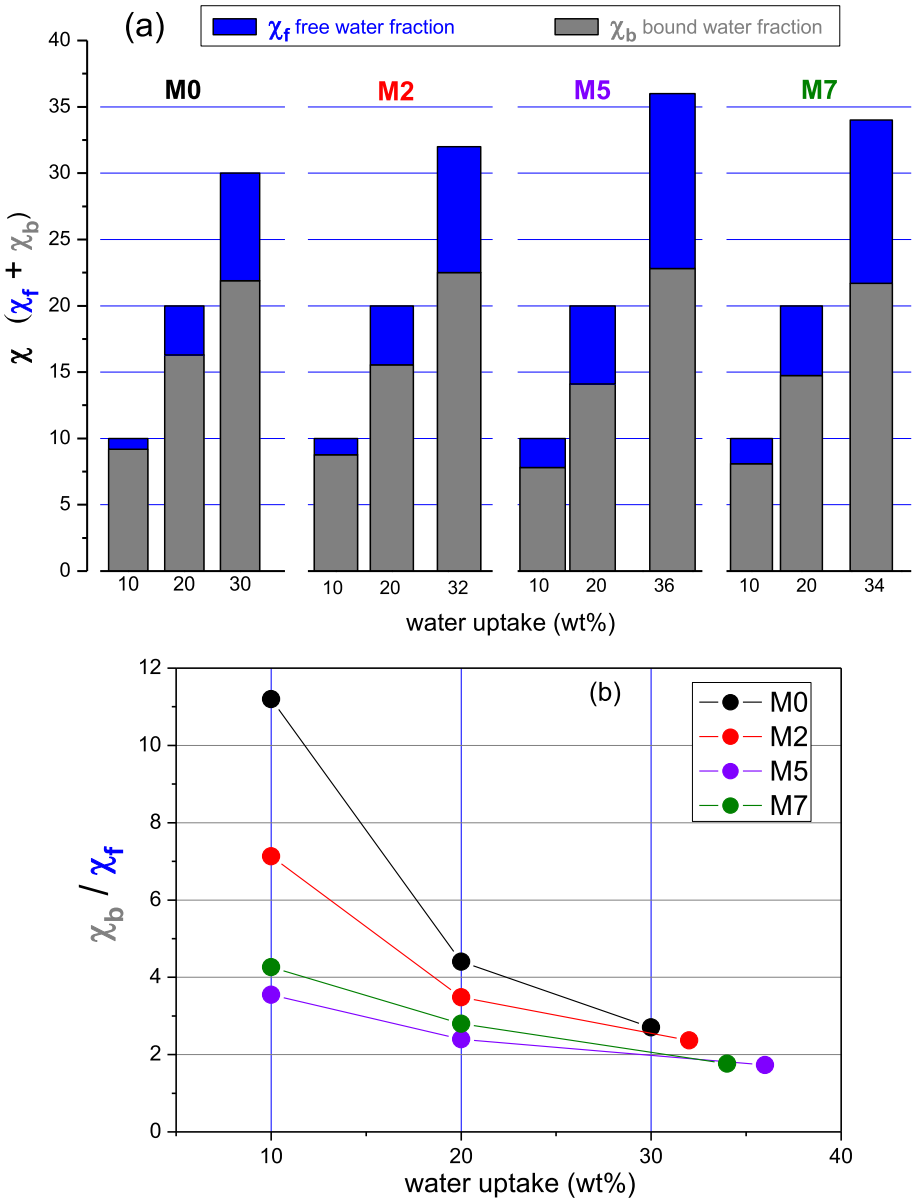

Fig. 4 – (a) Histograms showing the distribution of the bound- and free-water fractions in all the samples, at different initial water uptakes; (b) plot of the molar ratio between the bound water and free water fractions at the different water uptakes.

material added to the polymer increases the number of acid sites to be hydrated and, most important, to retain water even at high temperatures, as clear from the self-diffusion measurements.

Lower hydration numbers under smaller water uptakes (i.e. 10 and 20 wt%), associated with the composite systems compared to plain Nafion, could be the result of the dynamics of exchange of water molecules between the sulfonic and sulfate sites, although we cannot exclude morphology or structural changes of the polymer matrix induced by the filler particles. To verify this hypothesis, micrography and dynamic mechanical analyses are currently under consideration and the results will be reported in a future, next coming paper. In any case, the "two-sites" model and the analysis of the water self-diffusion coefficients had allowed to describe the nature of water dynamics and the state(s) of the water (bound and free states) both inside composite and filler-free membranes, as well as its interaction with the hydrophilic polymer sites and particles surface.

Improved water retention and higher free-water fractions were revealed in composite membranes, with special regard to the M5 sample which appears the most promising composition among those investigated. The free-water content related to this sample is probably the reason of its higher proton conductivity, compared to recast Nafion. On the basis of these considerations, the proposed composite membranes and, particularly, M5 sample, can be considered as effective, advanced electrolytes in operating fuel cell devices, with

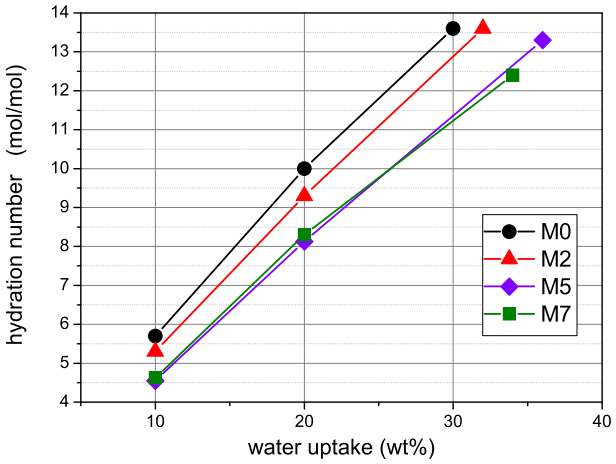

Fig. 5 – Hydration numbers calculated by the "two sites" model for all the membranes swelled at different water uptake at room temperature.

exciting perspectives in high temperature, low RH applications.

Acknowledgments

This work was realized with the financial support of the Italian Ministry of Education, Universities and Research (PRIN 2010-2011, prot. 2010CYTWAW_001) in the framework of the Project *NAMED-PEM* "Advanced nanocomposite membranes and innovative electrocatalysts for durable polymer electrolyte membrane fuel cells".

Appendix A. Supplementary data

Supplementary data related to this article can be found at http://dx.doi.org/10.1016/j.ijhydene.2015.06.137.

REFERENCES

[1] Jannasch P. Recent developments in high-temperature proton conducting polymer electrolyte membranes. Curr Opin Colloid Interface Sci 2003;8:96–102.
[2] Shyu JC, Hsueh KL, Tsau F. Performance of proton exchange membrane fuel cells at elevated temperature. Energy Convers Manag 2011;52:3415–24.
[3] Mauritz K, Moore RB. State of understanding of nafion. Chem Rev 2004;104(10):4535–85.
[4] Chandan A, Hattenberger M, El-kharouf A, Du S, Dhir A, Self V, et al. High temperature (HT) polymer electrolyte membrane fuel cells (PEMFC). A review. J Power Sources 2013;231:264–78.
[5] Ketpang K, Lee K, Shanmugam S. Facile synthesis of porous metal oxide nanotubes and modified nafion composite membranes for polymer electrolyte fuel cells operated under low relative humidity. ACS Appl Mater Interfaces 2014;6:16734–44.
[6] Nicotera I, Enotiadis A, Angjeli K, Coppola L, Gournis D. Evaluation of smectite clays as nanofillers for the synthesis of nanocomposite polymer electrolytes for fuel cell applications. Int J Hydrogen Energy 2012;37:6236–45.
[7] Nicotera I, Enotiadis A, Angjeli K, Coppola L, Ranieri GA, Gournis D. Effective improvement of water-retention in nanocomposite membranes using novel organo-modified clays as fillers for high temperature PEMFCs. J Phys Chem B 2011;115:9087–97.
[8] Enotiadis A, Angjeli K, Baldino N, Nicotera I, Gournis D. Graphene-based nafion nanocomposite membranes: enhanced proton transport and water retention by novel organo-functionalized graphene oxide nanosheets. Small 2012;8:3338–49.
[9] Uchida H, Ueno Y, Hagihara H, Watanabe M. Self-humidifying electrolyte membranes for fuel cells. Preparation of highly dispersed TiO_2 particles in nafion 112. J Electrochem Soc 2003;150(1):A57–62.
[10] Navarra MA, Fernicola A, Panero S, Martinelli A, Matic A. Effect of functionalized silica particles on cross-linked poly(vinyl alcohol) proton conducting membranes. J Appl Electrochem 2008;38(7):931–8.
[11] Adjemian KT, Dominey R, Krishnan L, Ota H, Majsztrik P, Zhang T, et al. Function and characterization of metal oxide-nafion composite membranes for elevated-temperature H_2/O_2 PEM fuel cells. Chem Mater 2006;18(9):2238–48.
[12] Navarra MA, Croce F, Scrosati B. New, high temperature superacid zirconia-doped Nafion composite membranes. J Mater Chem 2007;17:3210–5.
[13] Navarra MA, Abbati C, Scrosati B. Properties and fuel cell performance of a Nafion-based, sulfated zirconia-added, composite membrane. J Power Sources 2008;183:109–13.
[14] Navarra MA, Abbati C, Croce F, Scrosati B. Temperature-dependent performances of a fuel cell using a superacid zirconiadoped nafion polymer electrolyte. Fuel Cells 2009;9:222–5.
[15] D'Epifanio A, Navarra MA, Weise F, Mecheri B, Farrington J, Licoccia S, et al. Composite nafion/sulfated zirconia membranes: effect of the filler surface properties on proton transport characteristics. Chem Mater 2010;22:813–21.
[16] Giffin GA, Piga M, Lavina S, Navarra MA, D'Epifanio A, Scrosati B, et al. Characterization of sulfated-zirconia/Nafion® composite membranes for proton exchange membrane fuel cells. J Power Sources 2012;198:66–75.
[17] Scipioni R, Gazzoli D, Teocoli F, Palumbo O, Paolone A, Ibris N, et al. Preparation and characterization of nanocomposite polymer membranes containing functionalized SnO_2 additives. Membranes 2014;4:123–42.
[18] Brutti S, Scipioni R, Navarra MA, Panero S, Allodi V, Giarola M, et al. SnO_2-Nafion nanocomposite polymer electrolytes for fuel cell applications. Int J Nanotechnol 2014;11:882–96.
[19] Sgambetterra M, Panero S, Hassoun J, Navarra MA. Hybrid membranes based on sulfated titania nanoparticles as low-cost proton conductors. Ionics 2013;19:1203–6.
[20] Cohen B, Huppert D. Connection between proton abnormal conductivity in water and dielectric relaxation time. J Phys Chem 2003;107:3598.
[21] Eikerling M, Kornyshev AA, Kuznetsov AM, Ulstrup J, Walbran S. Mechanisms of proton conductance in polymer electrolyte membranes. J Phys Chem B 2001;105:3646–62.
[22] Kreuer K. On the development of proton conducting materials for technological applications. Solid State Ionics 1997;97:1–15.
[23] Nilson P, Lindman B. Water self-diffusion in nonionic surfactant solutions. Hydration and obstruction effects. J Phys Chem 1983;87:4756.

[24] Nilson P, Lindman B. Nuclear magnetic resonance self-diffusion and proton relaxation studies of nonionic surfactant solutions. Aggregate shape in isotropic solutions above the clouding temperature. J Phys Chem 1984;88:4764.
[25] Tanner JE. Use of the stimulated echo in NMR diffusion studies. J Chem Phys 1970;52(9):2523–6.
[26] Nicotera I, Zhang T, Bocarsly A, Greenbaum S. NMR characterization of composite polymer membranes for low-humidity PEM fuel cells. J Electrochem Soc 2007;154(5):B466.
[27] Gong X, Bandis A, Tao A, Meresi G, Wang Y, Inglefield PT, et al. Self-diffusion of water, ethanol and decafluropentane in perfluorosulfonate ionomer by pulse field gradient NMR. Polymer 2001;42:6485–92.
[28] MacMillan B, Sharp A, Armstrong R. An n.m.r. investigation of the dynamical characteristics of water absorbed in Nafion. Polymer 1999;40(10):2471–80.
[29] Pereira F, Vallé K, Belleville P, Morin A, Lambert S, Sanchez C. Advanced mesostructured hybrid Silica–Nafion membranes for high-performance PEM fuel cell. Chem Mater 2008;20(5):1710–8.
[30] Nicotera I, Simari C, Coppola L, Zygouri P, Gournis D, Brutti S, et al. Sulfonated graphene oxide platelets in nafion nanocomposite membrane: advantages for application in direct methanol fuel cells. J Phys Chem C 2014;118:24357–68.
[31] Coppola L, Muzzalupo R, Ranieri G. Temperature dependence of water self-diffusion in the gel phase of a potassium palmitate system. J Phys II 1996;6:657–66.
[32] Gottwald A, Creamer LK, Hubbard PL, Callaghan PT. Diffusion, relaxation, and chemical exchange in casein gels: a nuclear magnetic resonance study. J Chem Phys 2005;122(3):34506.
[33] Johnson CS. Effects of chemical exchange in diffusion ordered 2D NMR spectra. J Magn Reson Ser A 1993;102:214–8.
[34] Wang JH. Theory of the self-diffusion of water in protein solutions. A new method for studying the hydration and shape of protein molecules. J Am Chem Soc 1954;76:855.
[35] Chidichimo G, De Fazio D, Ranieri G, Terenzi M. Self-diffusion of water in a lamellar lyotropic liquid crystal: a study by pulased field gradient NMR. Chem Phys Lett 1985;117:514–7.
[36] Jonsson B, Wennerstrom H, Nilsson P, Linse P. Self-diffusion of small molecules in colloidal systems. Colloid Polym Sci 1986;264:77.
[37] Anderson DM, Wennerstrom H. Self-diffusion in bicontinuous cubic phases. L3 Phases Microemulsions June 1988;1990:8683–94.
[38] Poulos AS, Constantin D, Davidson P, Imperor M, Judeinstein P, Pansu B. A PGSE-NMR study of molecular self-diffusion in lamellar phases doped with polyoxometalates. J Phys Chem B 2010;114:220–7.
[39] Momot KI. Diffusion tensor of water in model articular cartilage. Eur Biophys J 2011;40:81–91.
[40] Dorenbos G, Morohoshi K. Chain architecture dependence of pore morphologies and water diffusion in grafted and block polymer electrolyte fuel cell membranes. Energy Environ Sci 2010;3:1326–38.
[41] Moreau P, van Effenterre D, Navaillesa L, Nalletb F, Rouxc D. Confined diffusion of hydrophilic probes inserted in lyotropic lamellar phases. Eur Phys J E 2008;26:225–34.
[42] Faxen H. Ann Phys 1922;4:89.
[43] Kreuer KD, Paddison SJ, Spohr E, Schuster M. Transport in proton conductors for fuel-cell applications: simulations, elementary reactions, and phenomenology. Chem Rev 2004;104:4637–78.
[44] Schmidt-Rohr K, Chen Q. Parallel cylindrical water nanochannels in Nafion fuel-cell membranes. Nat Mater 2008;7:75–83.
[45] Choi BG, Hong J, Park YC, Jung DH, Hong WH, Hammond PT, et al. Innovative polymer nanocomposite electrolytes: nanoscale manipulation of ion channels by functionalized graphenes. ACS Nano 2011;5(6):5167–74.

III

"Ion Dynamics and Mechanical Properties of Sulfonated Polybenzimidazole Membranes for High-Temperature Proton Exchange Membrane Fuel Cells"

Journal of Physical Chemistry C, ***2015***, *119 (18), pp 9745–9753*

THE JOURNAL OF PHYSICAL CHEMISTRY C

Article

pubs.acs.org/JPCC

Ion Dynamics and Mechanical Properties of Sulfonated Polybenzimidazole Membranes for High-Temperature Proton Exchange Membrane Fuel Cells

Isabella Nicotera,*[,†] Vasiliki Kosma,[†] Cataldo Simari,[†] Simone Angioni,[‡] Piercarlo Mustarelli,[‡] and Eliana Quartarone[‡]

[†]Department of Chemistry and Chemical Technologies, University of Calabria, via P. Bucci, 87036 Rende (CS), Italy

[‡]Department of Chemistry, University of Pavia and INSTM, Via Taramelli 12, 27100 Pavia (PV), Italy

Supporting Information

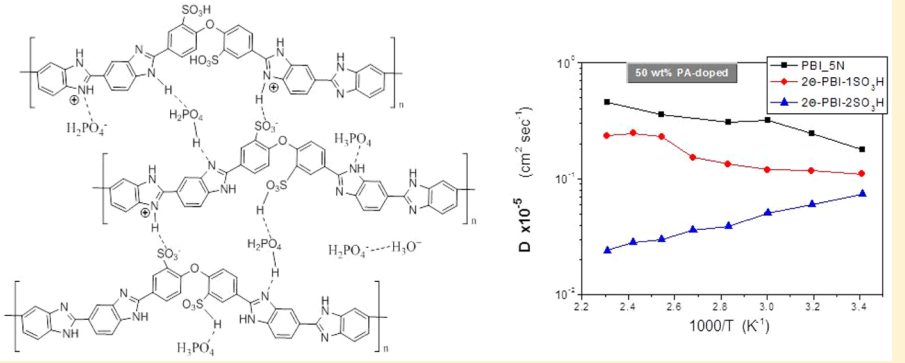

ABSTRACT: Polybenzimidazole (PBI)-based membranes are one of the systems of choice for polymer electrolyte fuel cells. Monomer sulphonation is one of the strategies suggested to improve proton transport in these membranes. We report a NMR and dynamic mechanical study aiming to investigate the effect of the sulphonation on the proton dynamics and the mechanical properties of the membranes. The analyses of ^{1}H self-diffusion coefficients and ^{1}H and ^{31}P spectra versus temperature show that sulphonation causes the formation of interchain cross-links, which involve phosphoric acid molecules and the sulfonic groups. This, in turn, reduces the proton mobility and, consequently, the ionic conductivity. The increase of the membrane stiffness with sulphonation is confirmed by dynamic mechanical analysis through the behavior of the storage modulus.

1. INTRODUCTION

Today the large scale-up of polymer fuel cells is still limited by their incompatibility with the operating conditions of the automotive applications, namely working temperatures higher than 130 °C and low humidification. The reasons for working at higher temperature are well-known.[1,2] First of all, CO poisoning of the catalyst remarkably decreases above 120 °C. In addition, the rates of H_2 and O_2 diffusion and their respective reactions are also observed to increase at elevated temperature. Furthermore, proton exchange membrane fuel cells (PEMFCs) working above 130 °C are preferable from the point of view of water and heat management. The most investigated polymers for use as the electrolyte in PEMFCs are perfluorosulfonic acid (PFSA) membranes such as Nafion, which for many years has been the reference target of the market. However, they do not totally fit the stringent requirements of the automotive market.[3] In spite of the wide spectrum of investigated systems, only three types of membranes may be actually considered for future industrial scale-up: (i) nanocomposite membranes, based on PFSA systems; (ii) hybrid systems based on proton-conducting ionic liquids (PCIL); (iii) acid−base membranes. Among the possible acid−base combinations, phosphoric acid (PA)-doped polybenzimidazole (PBI) is considered one of the systems-of-choice for the fabrication of proton-conducting membranes for high-temperature polymer fuel cells (HT-PEMFC).[4−15] Its main disadvantages, e.g., chemical degradation and acid leaching during operation, can be overcome by appropriate monomer tailoring and/or the addition of proper fillers.[6,16] We recently showed that mono- and polysulphonation of aryloxy-based PBI is a good method for obtaining high proton transport even at relatively low PA doping levels. This occurs at the expense of only a small reduction (∼15%) of the mechanical properties.[17,18] With respect to the nonsulfonated polymer membranes, in a wide range of relative humidity (from 20 to 70 RH%) the same conductivity values were generally obtained with half doping, whereas at the same PA levels conductivity enhancements of more than 1 order of magnitude were observed. In addition, we found notable differences between mono- and polysulphonation.

Received: February 2, 2015
Revised: April 17, 2015

DOI: 10.1021/acs.jpcc.5b01067
J. Phys. Chem. C XXXX, XXX, XXX−XXX

Scheme 1. Chemical Structures of the Polymers 2Θ-PBI-1SO_3H (Top Structure) and 2Θ-PBI-2SO_3H (Bottom Structure)

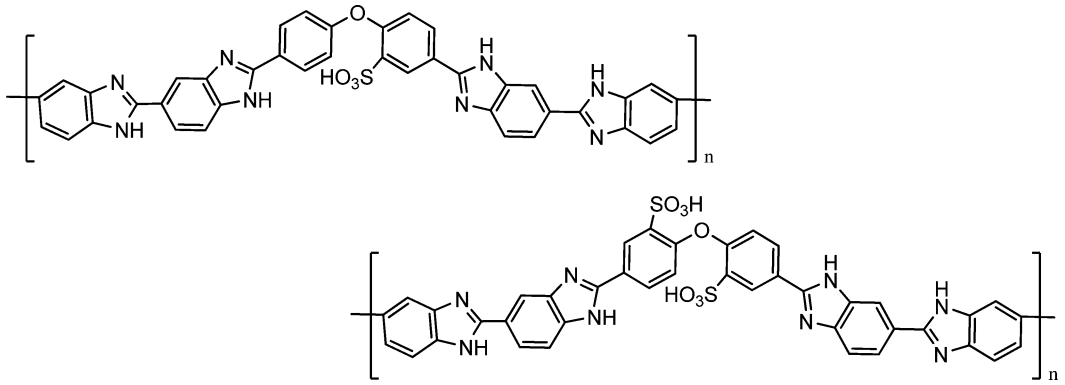

As an example, given the concentration of the PA solution used for the activation procedure, monosulphonation allowed higher doping and higher conductivity levels than polysulphonation. At the same time, however, when the same doping levels were accessible irrespective of the doping procedure, polysulphonation gave origin to higher conductivity values in a wide range of relative humidity values. In addition, no acid loss and membrane degradation were observed during electrochemical durability tests carried out on MEAs based on sulfonated systems, at least over 200 h of aging time.[18]

Whereas it is well-known that the transport mechanisms in PA−PBI electrolyte membranes may vary depending on the doping level,[6,19,20] our results pointed out the existence of a complex interplay among sulfonic groups, imidazole moieties, and phosphoric acid, which influences proton dynamics and ionic conductivity. A careful spectroscopic investigation is mandatory for obtaining a satisfactory knowledge of ion transport in these complex electrolytes.

Multinuclear solid-state NMR is a powerful spectroscopic technique and is particularly well-suited for investigating structure and dynamics in both hard and soft matter. In particular, in the case of polymer electrolyte membranes, proton interactions can be conveniently investigated by means of chemical shift and spin−lattice (T_1) and spin−spin (T_2) relaxation times. In addition, the pulse field gradient (PFG) technique allows the measurement of the self-diffusion coefficient, D, which can be directly related to ion mobility.[21,22] This combined information can help to shed light on ion transport mechanisms in complex electrolytes.

We report a detailed NMR study on two sulfonated polymer electrolyte membranes. The results have been compared with those of poly(2,2′-*m*-(phenylene)-5,5′-bibenzimidazole) (PBI_5N), which we consider our reference matrix for fuel cell applications.

2. EXPERIMENTAL SECTION

2.1. Membrane Preparation. Two mono- and disulfonated polymers were synthesized by means of a three-step reaction: (i) monomer synthesis, (ii) monomer sulphonation, and (iii) polymerization. The full synthetic procedure is reported in ref 18. In particular, the polymerization of the sulfonated monomers was carried out at 190 °C with a N_2 inlet for about 7 h in polyphosphoric acid (PPA) with a stoichiometric amount of 3,3′-diaminobenzidine. The solution then was poured into deionized water to precipitate tough and black filaments. The polymers were repeatedly washed with water and suspended in a 10% K_2CO_3 solution to remove traces of residual acid. The solids were again washed overnight in a Soxhlet apparatus and then dried under vacuum at 120 °C for 7 h. Yields greater than 70% were obtained for each polymer. Scheme 1 reports the chemical structures of the sulfonated PBI, labeled as follows: 2Θ-PBI-1SO_3H and 2Θ-PBI-2SO_3H. Intrinsic viscosities of 0.6 and 0.75 dL g^{-1} were obtained for the mono- and polysulfonated systems, which correspond to MWs of 570.1 and 650.0 g mol^{-1}, respectively, as reported in ref 18.

To obtain the membranes, proper amounts of polymer were dissolved in a mixture of DMA/*n*-butilamine/water at 180 °C in a sealed vessel under microwaves to reach a faster and more effective PBI dissolution. The resulting solution was poured in a Petri dish and heated through consequent drying steps, at 50 °C for 24 h and 120 °C for 10 h, so as to totally remove the solvents. The membranes were washed in hot water, doped with two different phosphoric acid concentrations, namely 50 and 70 wt %, for at least 72 h, even if an uptake plateau was reached after 24 h, and finally dried at 120 °C overnight to obtain the doping level, $N = n_{acid}/n_{mon}$. Film thicknesses of about 100 μm were obtained. The H_3PO_4 doping level, N, was calculated by weighing the membrane before and after the acid imbibition, as in the following relationship:

$$N = n_{acid}/n_{mon}$$

where n_{acid} is the PA moles absorbed by the polymer and n_{mon} the moles of the monomer unit.

2.2. Characterization Techniques. *2.2.1. NMR Spectroscopy.* NMR measurements were performed on a Bruker NMR spectrometer AVANCE 300 Wide Bore working at 300 MHz on ^1H. The employed probe was a Diff30 Z-diffusion 30 G/cm/A multinuclear with substitutable RF inserts. ^1H and ^{31}P spectra were obtained by transforming the resulting free-induction decay (FID) of single $\pi/2$ pulse sequences. The pulsed field gradient−stimulated echo (PFG-STE) method[23] was used to measure self-diffusion coefficients. This sequence is generally applied when the materials are characterized by a transverse relaxation time (T_2) considerably shorter than the longitudinal relaxation time (T_1). The sequence consists of three 90° rf pulses ($\pi/2-\tau_1-\pi/2-\tau_m-\pi/2$) and two gradient pulses that are applied after the first and the third rf pulses. The echo is found at time $\tau = 2\tau_1 + \tau_m$. Following the usual notation, the magnetic field pulses have magnitude g, duration δ, and time delay Δ. The attenuation of the echo amplitude is represented by the following equation:

$$I(2\tau_1 + \tau_m) = \frac{1}{2} I_0 \exp\left[-\frac{\tau_m}{T_1} - \frac{2\tau_1}{T_2} - (\gamma g \delta)^2 D\left(\Delta - \frac{\delta}{3}\right)\right]$$

DOI: 10.1021/acs.jpcc.5b01067
J. Phys. Chem. C XXXX, XXX, XXX−XXX

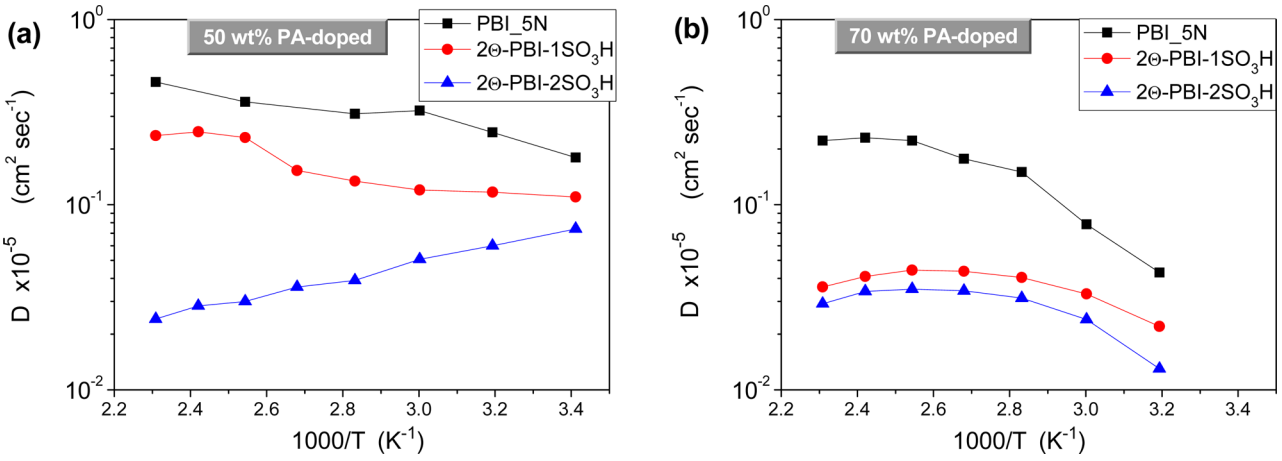

Figure 1. Arrhenius plots of the ^{1}H diffusion coefficients measured on the three membranes (PBI_5N, 2Θ-PBI-1SO$_3$H, and 2Θ-PBI-2SO$_3$H) activated with 50 wt % (a) and 70 wt % (b) of phosphoric acid (PA).

Scheme 2. Possible Interactions in the Sulfonated Membranes

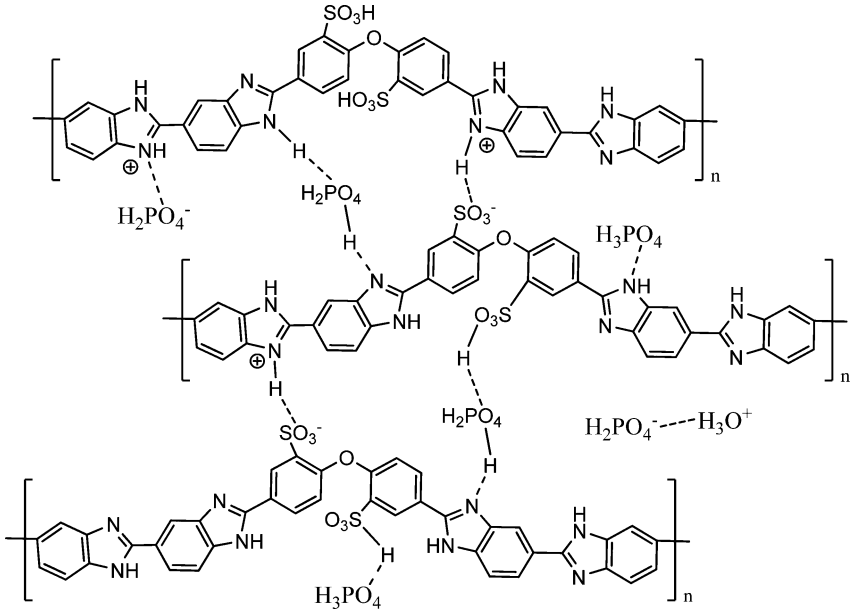

where D is the self-diffusion coefficient. The ^{1}H-T_2 is quite short (less than 3 ms); therefore, the used experimental parameters for ^{1}H diffusion coefficients measurements were gradient pulse length (δ) between 0.2 and 0.6 ms and time delay (Δ) between 80 and 270 ms; the gradient amplitude varied from 100 to 800 G cm^{-1}. The uncertainty in the self-diffusion measurements is ~5%. It is worth noting that a Gaussian proton self-diffusion has been observed (see the Supporting Information, Figure S1).

In the case of the ^{31}P nucleus, the T_2 is much shorter than ^{1}H, estimable to less than 1 ms; therefore, the diffusion measurements of ^{31}P were not possible with our experimental setup.

^{1}H and ^{31}P longitudinal relaxation times (T_1) were measured by the inversion−recovery sequence ($\pi-\tau-\pi/2$). Both self-diffusion and T_1 measurements were conducted by increasing temperature step-by-step from 20 to 180 °C, with steps of 20 °C, and leaving the sample to equilibrate for about 15 min.

2.2.2. Dynamic Mechanical Analysis. Dynamic mechanical analysis (DMA) measurements were made with a Metravib DMA/25 equipped with a shear jaw for films. Spectra were collected by applying a dynamic stress of amplitude 10^{-3} at the frequency of 1 Hz in the temperature range between 25 and 350 °C with a heating and cooling rate of 2 °C/min.

2.2.3. Impedance Spectroscopy. The proton conductivity was measured by means of both DC and AC techniques fixing the membrane to a four-point BekkTech conductivity cell connected to the test stand BekkTech 411 for the humidity and temperature control. In case of AC measurements, the impedance spectroscopy was carried out by using a frequency response analyzer (FRA Solartron 1255) connected to an electrochemical interface (Solartron 1287), over the frequency range 1 Hz to 1 MHz at a voltage of 100 mV. The impedance scans were performed at 120 °C ranging from 1.5 to 70% RH with a cell back-pressure of 2.0 bar. The films were allowed to equilibrate 1 h at each moisture level before the measurements. The impedance spectra were fitted with the Z-View 3.0 software (Scribner Associates, Inc.).

3. RESULTS AND DISCUSSION

3.1. Self-Diffusion Coefficients (D) and Spin−Lattice Relaxation Times (T_1). The Arrhenius plots of the ^{1}H self-diffusion coefficients measured on the membranes, activated at

DOI: 10.1021/acs.jpcc.5b01067
J. Phys. Chem. C XXXX, XXX, XXX−XXX

Table 1. Doping Levels (N) and Conductivity Values for the Two Membranes Activated with 50% and 70% PA Concentrations[a]

	50% PA concentration			70% PA concentration		
sample	N	$\sigma_{120°C\text{-}0\%RH}$ (mS/cm)	$\sigma_{120°C\text{-}50\%RH}$ (mS/cm)	N	$\sigma_{120°C\text{-}0\%RH}$ (mS/cm)	$\sigma_{120°C\text{-}50\%RH}$ (mS/cm)
PBI_5N	7.3	5	29	12	14	76
2Θ-PBI-1SO_3H	7	2	21	11.9	10	72
2Θ-PBI-2SO_3H	4.5	1	16	8.3	7	50

[a]Values obtained at 120 °C and 0% and 50% RH.

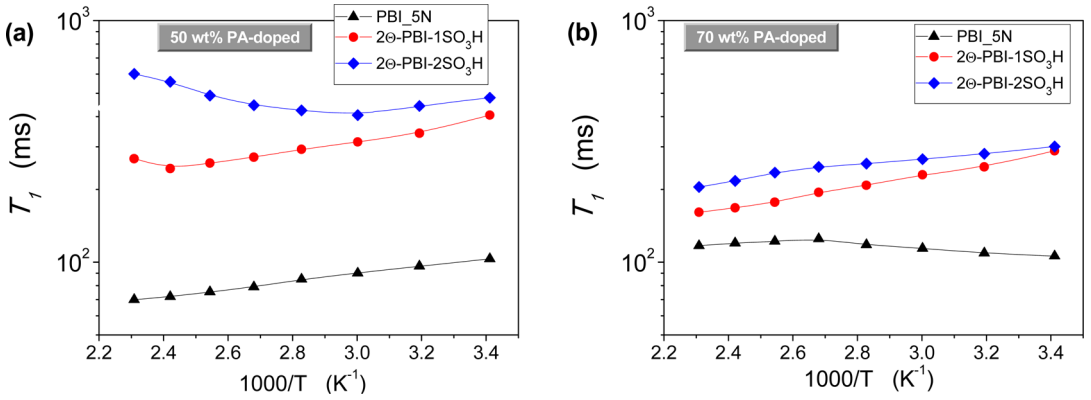

Figure 2. Arrhenius plots of the ^1H relaxation times (T_1) measured on the three membranes (PBI_5N, 2Θ-PBI-1SO_3H, and 2Θ-PBI-2SO_3H) activated with phosphoric acid concentration of 50 wt % (a) and 70 wt % (b).

50% and 70% PA concentrations, are shown in panels a and b of Figure 1, respectively. Diffusion measurements of ^{31}P were not possible within our experimental setup because of the very short spin−spin relaxation times. In all the investigated temperature range, proton diffusion in the sample PBI_5N is faster than that in the sulfonated membranes, and the observed differences are relevant, in particular at 70% PA concentration and high temperature. Moreover, the two sulfonated membranes score very different for 50% PA concentration, whereas the behaviors are similar in the case of 70% PA. To rationalize these results, we observe that (i) PBI_5N absorbs a higher amount of acid than the 2Θ-PBI-1SO_3H and 2Θ-PBI-2SO_3H membranes, although in the sulfonated polymer there should be a higher hydration level due to −SO_3H groups and (ii) the presence of sulfonic groups likely allows a greater cross-linking between the polymer chains (see Scheme 2), thus resulting in a stiffer membrane (see also the dynamic mechanical analysis results below).

A higher rigidity implies more difficult segmental motions of the polymeric chains, which in turn can also explain the decrease of swelling capacity (about 15% for both the sulfonated systems, as determined by thermogravimetric analysis measurements[18]). The behavior of the diffusion coefficients can now be interpreted as the effect of higher PA content and higher flexibility of the polymer chains in the PBI_5N sample, which favor the proton transport through a hopping-like mechanism, which will be further elaborated later.

The anomalous NMR temperature behavior of the 2Θ-PBI-2SO_3H membrane activated with 50% PA can be explained in terms of a more accentuated water loss not compensated by a high PA content. The activation of the membranes with 70% PA solution (Figure 1b) makes the proton mobility decrease with respect to 50% PA even if the solution uptake considerably increases. This could be due to possible complexation of the phosphate groups that effectively reduces the proton mass transport. On the other hand, activation with 70% PA solution allows higher values of the proton conductivity for both the membranes, as shown in Table 1. This indicates that carrier concentration is more relevant than mobility in determining the proton conductivity. Again, however, monosulphonation is more efficient than disulphonation in promoting proton transport.[17,18] We must stress that there is not control on the relative humidity inside the NMR probe during the PFG-STE experiments. Here we suppose that it was roughly at the equilibrium with the ambient humidity, which is in the range 30−50%.

The mechanism expected for the proton diffusion is the Grotthuss mechanism, which foresees a strong interaction among the H^+ ions and the lattice, i.e., with the phosphates and with active groups on the polymer. Figure 2 shows the Arrhenius plots of the ^1H spin−lattice relaxation times (T_1) measured in the various membranes. T_1 quantifies the rate of transfer of energy from the nuclear spin system to the neighboring molecules (the lattice). The motion of the nuclei in the lattice causes a fluctuating magnetic field to the site of the nuclear spin involved. In the case of spin-1/2 nuclei, the most common source of this fluctuating field is dipole−dipole interaction. The larger the interaction, the quicker the relaxation (shorter T_1). In the investigated temperature range, T_1 slightly decreases with the heating, and large plateaus are observed. However, in the case of the 2Θ-PBI-1SO_3H and 2Θ-PBI-2SO_3H membranes activated with 50% PA, it is possible to indicate a temperature range at which the T_1 minima occur: 333−353 K for the 2Θ-PBI-2SO_3H and 393−413 K for the 2Θ-PBI-1SO_3H. We stress that in this T_1 representation, the presence of a minimum indicates the transition to the so-called motional narrowing regime, where the Hamiltonian interactions are averaged to their mean values by noncorrelated motions. In the PBI_5N sample, in contrast, the minimum probably falls outside the investigated temperature range. The increase of PA content further shifts the T_1 minimum at higher temperatures. In any case, for both the PA contents, the PBI_5N membrane displays a shorter T_1 than the sulfonated ones. This reflects a greater spectral density of interactions (i.e., higher density of fluctuating magnetic fields), which is due to a more efficient Grotthuss mechanism, in

DOI: 10.1021/acs.jpcc.5b01067
J. Phys. Chem. C XXXX, XXX, XXX−XXX

agreement with the behavior of the diffusion coefficients reported in Figure 1.

For the sake of comparison, Figure 3 shows the ^{31}P T_1 Arrhenius plot for all the membranes activated with 50% PA.

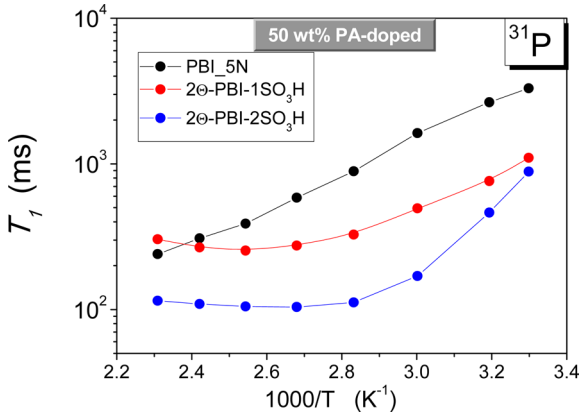

Figure 3. Arrhenius plot of the ^{31}P relaxation times (T_1) measured on the three membranes (PBI_5N, 2Θ-PBI-1SO_3H, and 2Θ-PBI-2SO_3H) activated with 50 wt % of phosphoric acid (PA).

Because of a partial membrane leaching observed on membranes activated at 70% PA, in particular at high temperature, the ^{31}P NMR investigation was focused only on the 50% PA-activated samples.

The T_1 minima for the sulfonated membranes do fall roughly in the same temperature range observed for the ^1H nuclei. Again, the T_1 of PBI_5N decreases linearly with the temperature, and no minimum can be observed in the explored temperature range. This result implies a strong correlation between the phosphorus and proton species. However, the trend of the three samples is reversed with respect to ^1H: the ^{31}P relaxation times in PBI_5N are the highest, whereas those in the 2Θ-PBI-2SO_3H are the lowest. This confirms that in the sulfonated membranes P nuclei do experience interactions with the polymer that are stronger than those in the PBI_5N one, in agreement with the evidence of slower proton diffusion in the sulfonated membranes. Moreover, the large uptake of PA in the PBI_5N suggests that most of these molecules are only weakly bound to the polymer chains, thus determining smaller restrictions on the P nuclei. This aspect will be further discussed by considering the ^{31}P spectra of these samples.

3.2. ^{31}P and ^1H NMR Spectra. The temperature evolution of the ^1H spectra acquired on the three membranes activated with 50 wt % PA concentration is shown in panels a, c, and e of Figure 4 for PBI_5N, 2Θ-PBI-1SO_3H, and 2Θ-PBI-2SO_3H, respectively. The proton spectra can be well fitted with two Lorentzian peaks (blue and red lines, while the green line is the cumulative fitted curve reported to check the agreement with the real spectrum represented by the black line), as shown in the figure for the signal acquired at 100 °C. The main peak (blue line) is narrower and centered at around 3−4 ppm, whereas the second peak (red line) is broader and centered at about 6−8 ppm. The first one could be associated with the more mobile "free" acid protons, and the second one to protons experiencing stronger interactions with the polymer. Figure 4b,d,f shows the behaviors of the areas of the two Lorentzian peaks versus the temperature. The area of these signals gradually decreases by increasing the temperature; significant fall of the intensity is registered even above 100−120 °C, where PA monomer condensation starts to take place (see below).[6]

Figure 5a shows the temperature evolution of the ^{31}P spectra, acquired from 20 to 160 °C, of the PBI_5N membrane activated with 50% PA concentration. By observing these spectra, we can clearly distinguish a main peak centered at 0 ppm with an asymmetric shoulder at higher frequency with chemical shift ∼5 ppm, a second peak at −14 ppm whose intensity increases with the temperature, and a third small peak at −27 ppm that appears above 140 °C.

The main peak at 0 ppm is due to orthophosphoric acid. The line width of this peak narrows as the temperature increases (see Figure 5b) because of the increased molecular mobility. The motional narrowing regime is reached at about 100 °C. The intensity of this peak increases up to about 100−120 °C and then decreases in favor of the signals at −14 and −27 ppm, which are assigned to the condensation products of the H_3PO_4, i.e., pyrophosphates and trypoliphosphates (or metaphosphates), respectively. The shoulder at 5 ppm is likely due to the phosphate molecules or anions strongly interacting with the polymer chains.[24]

The ^{31}P spectra of the 2Θ-PBI-1SO_3H and 2Θ-PBI-2SO_3H are slightly different from those of PBI_5N, as we can see in Figure 6. In the 2Θ-PBI-1SO_3H membrane, the shoulder on the left of the main peak is more relevant and almost not affected by the temperature as well as the pyrophosphates signal at −14 ppm, whereas the signal at lower frequency is absent. In the 2Θ-PBI-2SO_3H membrane, the main orthophosphate peak at 0 ppm and the shoulder at 5 ppm appear to be more overlapped, likely because of lower mobility and/or higher disorder. The signal at −14 ppm increases with the temperature. There is no evidence of the peak at −27 ppm, due to tripolyphosphates (or metaphosphates), likely because of sulfonic groups that strongly reduce the possibility of H_3PO_4 polycondensation.

The picture emerging from these data, determined by considering (i) the lower intensity of the pyrophosphate signal; (ii) the absence of the peak associated at higher oligomers, such as the trypolyphosphate one; and (iii) the considerable signal associated with phosphate molecules or anions interacting with the polymer backbone, confirms the hypothesis previously drawn from the D and T_1 data about the stronger interactions of the PA molecules with the sulfonic groups.

The thermal behavior of these membranes is reversible, but we observed a partial hysteresis, i.e., a time delay in achieving the original configuration after a thermal cycle, as reported in the Supporting Information (Figure S3). It is likely due to the kinetics of rehydratation which leads to the depolymerization of pyrophosphates and, if present, tripolyphoposphates or metaphosphates.

3.3. Dynamic Mechanical Analysis. The viscoelastic behavior of the three membranes was quantified in terms of the storage modulus, E'. Figure 7 shows the storage moduli versus temperature obtained on the membranes activated with 50 wt % PA. The values for all the samples are quite high (1 order of magnitude higher than Nafion)[25] because of the rigid backbones. Both the sulfonated membranes exhibit higher moduli compared to the PBI_5N, as expected on the basis of the NMR findings. In fact, the presence of sulfonic groups does cause stronger intermolecular interactions among the polymeric chains, which in turn inhibits segmental motions. The membranes activated with 70 wt % PA display a foreseeable reduction of the storage modulus (see the Supporting Information, Figure S2).

DOI: 10.1021/acs.jpcc.5b01067
J. Phys. Chem. C XXXX, XXX, XXX−XXX

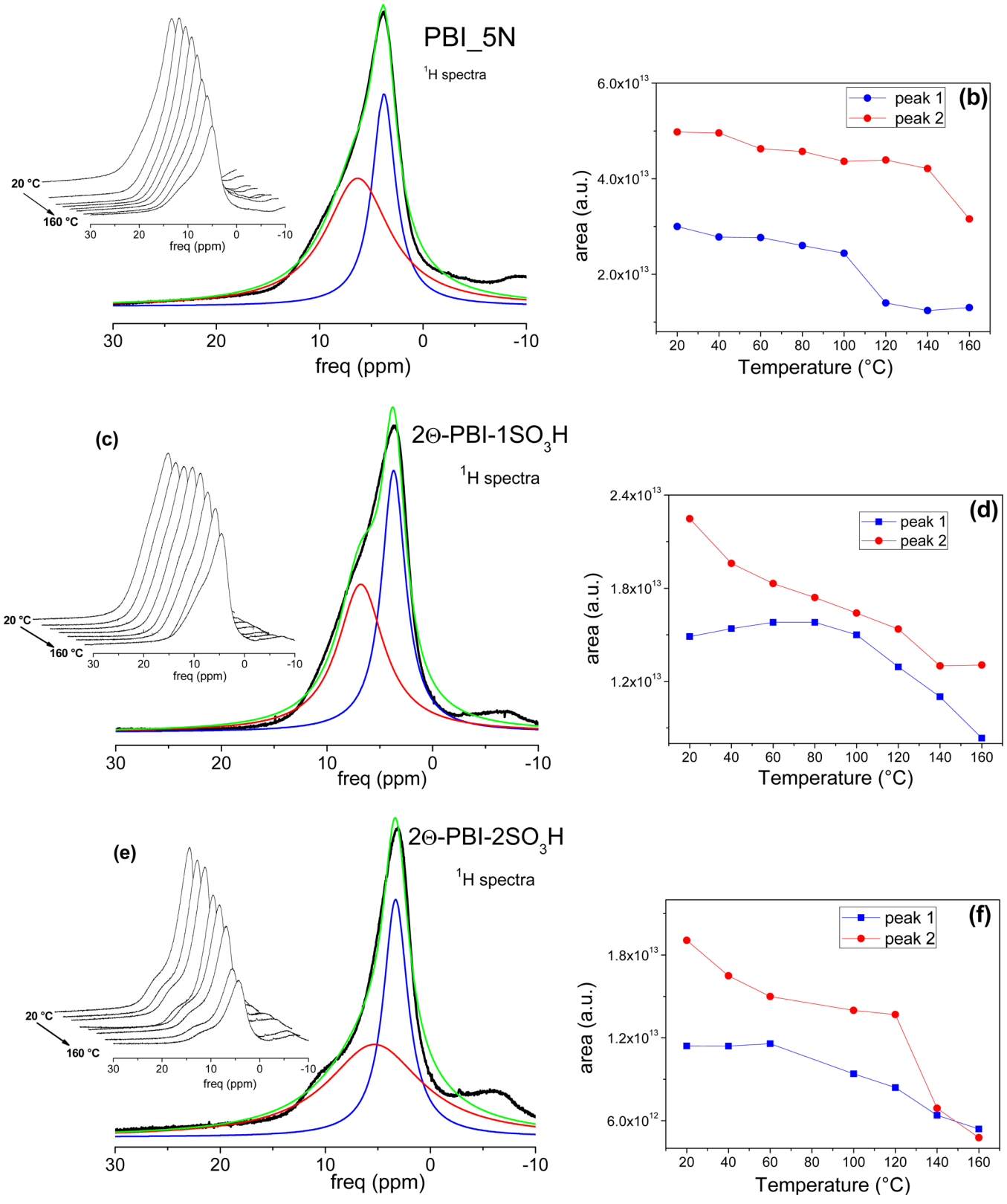

Figure 4. Temperature evolution and peak-fitting of the ^{1}H spectra for the samples (a) PBI_5N, (c) 2Θ-PBI-1SO$_3$H, and (e) 2Θ-PBI-2SO$_3$H. The blue and red lines are the fitting Lorentzian peaks, while the green line is the cumulative fitted curve. In the right column (panels b, d, and f), the plots of the peak area versus temperature for the three samples are reported.

As far as it concerns the effect of acid soaking on the mechanical properties of these systems, panels a and b of Figure 8 show two representative spectra for PBI_5N and 2Θ-PBI-1SO$_3$H, respectively, obtained on activated and nonactivated membranes, on a heating and cooling scan cycle. There are two main findings: (1) PA treatment leads to a reduction of the membrane stiffness. (2) A phenomenon of hysteresis is observed in the case of the activated membranes, i.e., in the cooling scan

DOI: 10.1021/acs.jpcc.5b01067
J. Phys. Chem. C XXXX, XXX, XXX−XXX

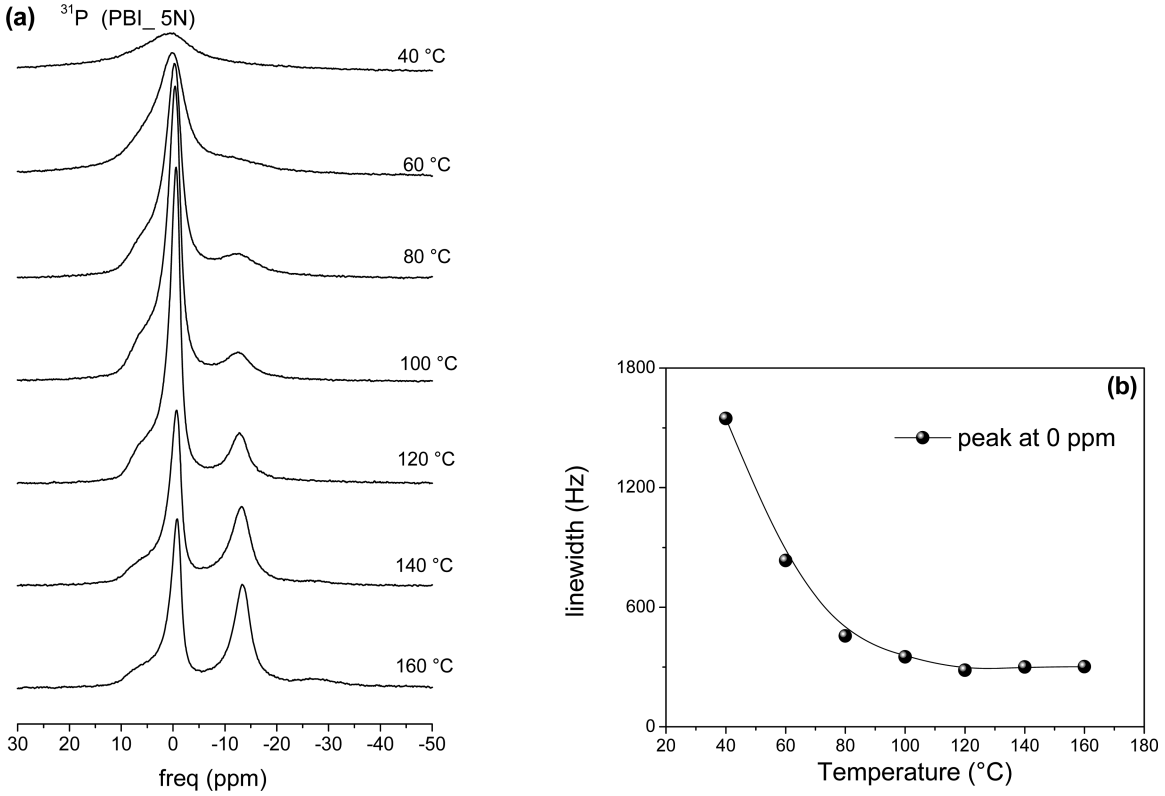

Figure 5. (a) Temperature evolution of the ^{31}P spectra, from 20 to 160 °C, for the PBI_5N membrane activated with 50 wt % PA concentration; (b) line width variations of the main peak (at 0 ppm) versus temperature.

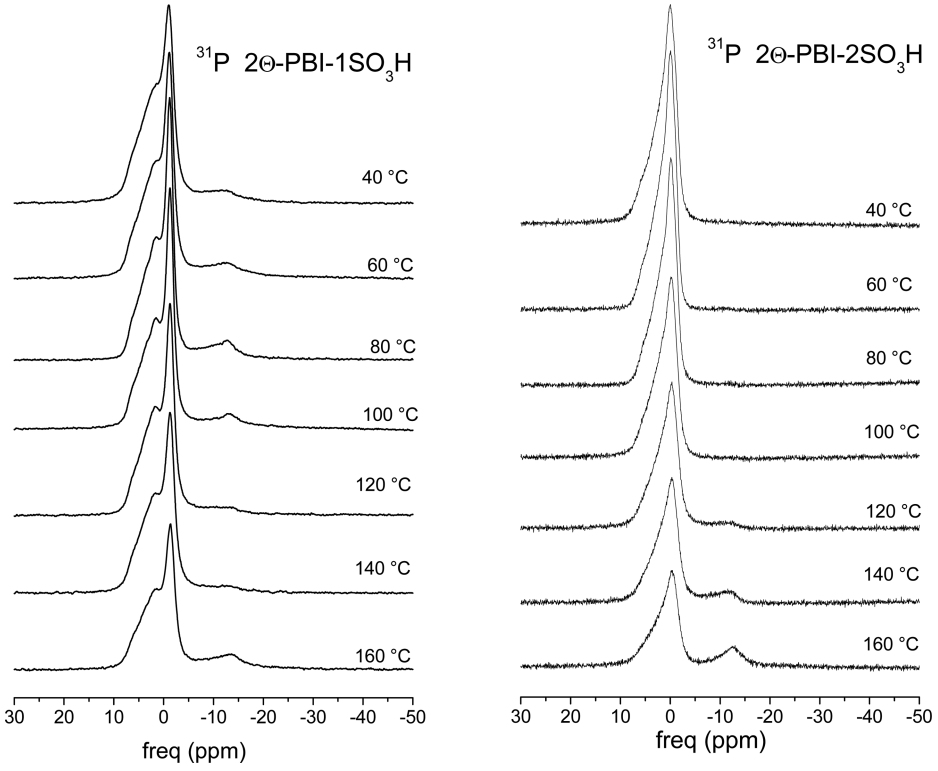

Figure 6. Temperature evolution of the ^{31}P spectra, from 20 to 160 °C, for 2Θ-PBI-1SO_3H (left panel) and 2Θ-PBI-2SO_3H (right panel) membranes activated with 50 wt % PA solution.

the storage modulus is much higher with respect to the heating scan, and it returns to its initial value only after several hours. This is in agreement with the thermal behavior observed on the ^{31}P NMR spectra and reported in the Supporting Information (Figure S3). Similar results were obtained for the 2Θ-PBI-2SO_3H membrane.

DOI: 10.1021/acs.jpcc.5b01067
J. Phys. Chem. C XXXX, XXX, XXX−XXX

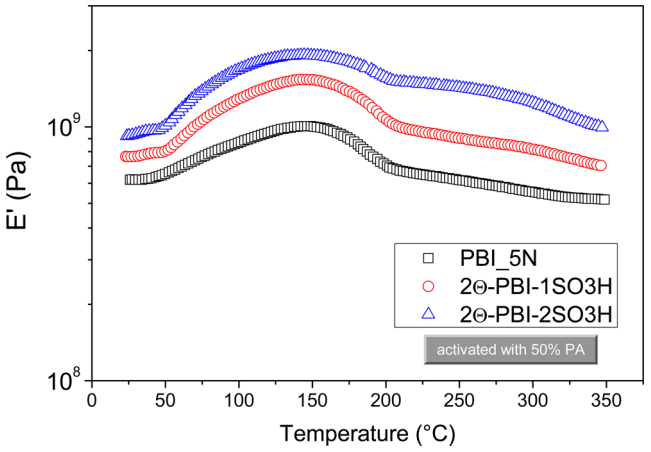

Figure 7. Storage moduli (E'), from 25 to 350 °C, obtained on the samples activated with 50% PA.

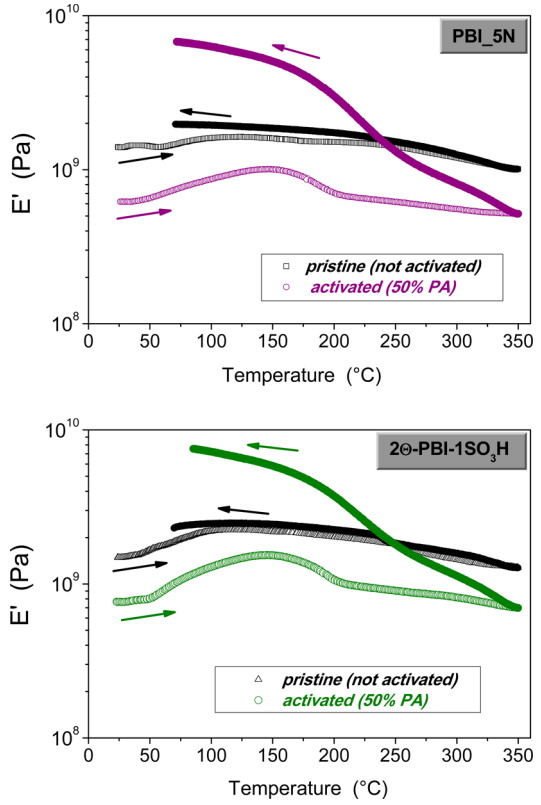

Figure 8. Temperature behavior of the storage moduli (E'), from 25 to 350 °C, performed on pristine membranes (not activated) and membranes activated with 50% PA: (a) PBI-5N and (b) 2Θ-PBI-$1SO_3H$.

4. CONCLUSIONS

We report careful NMR and dynamic mechanical analysis studies of sulfonated PBI membranes for applications in polymer fuel cells. Our main finding is that sulphonation does increase the membrane stiffness by increasing the interchain cross-links involving PA molecules and sulfonic groups. This, in turn, reduces the proton mobility with respect to PBI_5N, which is our PBI standard, in which the higher flexibility of the polymer chains favors the proton transport through a hopping-like mechanism. The effect is particularly evident when 70% PA concentration solution is used for the activation procedure. On the other hand, as previously reported by our group, the addition of sulfonic groups allows high conductivity values to be obtained at lower PA content with respect to the corresponding nonsulfonated aryloxy-based membranes. It is worth noting that ^{31}P NMR spectra acquired by conducting more thermal cycles evidenced some peculiar differences between the not-sulfonated and sulfonated PBI membranes, corroborating the hypothesis designed from the D and T_1 data about the stronger interactions of the PA molecules with the sulfonated polymer.

■ ASSOCIATED CONTENT

Ⓢ Supporting Information

Some representative decay lines of $[I(g)/I(0)]$ versus g^2 used to calculate the proton self-diffusion coefficients (D) in order to confirm the Gaussian self-diffusion behavior (Figure S1); the viscoelastic behavior (E' vs T) of the three membranes activated with 70 wt % PA (Figure S2; the storage modulus values are lower than the samples activated with 50% PA); ^{31}P MR spectra acquired on more thermal cycles on the 2Θ-PBI-$1SO_3H$ in order to demonstrate the thermo-reversibility of the systems (Figure S3). The Supporting Information is available free of charge on the ACS Publications website at DOI: 10.1021/acs.jpcc.5b01067.

■ AUTHOR INFORMATION

Corresponding Author

*E-mail: isabella.nicotera@unical.it. Tel.: +39-0984-493379. Fax: +39-0984-492044.

Notes

The authors declare no competing financial interest.

■ ACKNOWLEDGMENTS

This work was realized with the financial support of the Italian Ministry of Education, Universities and Research (Project PRIN 2011, NAMED-PEM).

■ REFERENCES

(1) Hogarth, W. H. J.; Diniz da Costa, J. C.; Lu, G. Q. Solid Acid Membranes for High Temperature (140 °C) Proton Exchange Membrane Fuel Cells. *J. Power Sources* **2005**, *142*, 223.

(2) Asensio, J. A.; Sanchez, E. M.; Gomez-Romero, P. Proton-conducting Membranes Based on Benzimidazole Polymers for High-temperature PEM Fuel Cells. A chemical quest. *Chem. Soc. Rev.* **2010**, *39*, 3210.

(3) Peighambardoust, S. J.; Rowshanzamir, S.; Amjadi, M. Review of the Proton Exchange Membranes for Fuel Cell Applications. *Int. J. Hydrogen Energy* **2010**, *35*, 9349.

(4) *2014 Annual Progress Report, DOE Hydrogen and Fuel Cells Program*. http://www.hydrogen.energy.gov/annual_progress14.html.

(5) Li, Q.; Jensen, J. O.; Savinell, R. F.; Bjerrum, N. J. High Temperature Proton Exchange Membranes Based on Polybenzimidazoles for Fuel Cells. *Prog. Polym. Sci.* **2009**, *34*, 449.

(6) Quartarone, E.; Mustarelli, P. Polymer Fuel Cells Based on Polybenzimidazole/H_3PO_4. *Energy Environ. Sci.* **2012**, *5*, 6436.

(7) Carollo, A.; Quartarone, E.; Tomasi, C.; Mustarelli, P.; Belotti, F.; Magistris, A.; Garlaschelli, L.; Righetti, P. P. Developments of New Proton Conducting Membranes Based on Different Polybenzimidazole Structures for Fuel Cells Applications. *J. Power Sources* **2006**, *160*, 175–180.

(8) Quartarone, E.; Magistris, A.; Mustarelli, P.; Grandi, S.; Carollo, A.; Żukowska, G. Z.; Garbarczyk, J. E.; Nowiński, J. L.; Gerbaldi, C.; Bodoardo, S.; Pyridine-based, P. B. I. Composite Membranes for PEMFCs. *Fuel Cells* **2009**, *9*, 349–355.

DOI: 10.1021/acs.jpcc.5b01067
J. Phys. Chem. C XXXX, XXX, XXX–XXX

(9) Ma, Y.-L.; Wainright, J. S.; Litt, M. H.; Savinell, R. F. J. Conductivity of PBI Membranes for High-Temperature Polymer Electrolyte Fuel Cells. *J. Electrochem. Soc.* **2004**, *151*, A8.
(10) Zhang, H.; Shen, P. K. Recent Development of Polymer Electrolyte Membranes for Fuel Cells. *Chem. Rev. (Washington, DC, U.S.)* **2012**, *112*, 2780.
(11) Li, J.; Zhao, Y.; Lu, W.; Shao, Z.; Yi, B. High-Temperature Proton-Exchange-Membrane Fuel Cells Using an Ether-Containing Polybenzimidazole Membrane as Electrolyte. *ChemSusChem* **2012**, *5*, 896.
(12) Yang, J.; Aili, D.; Li, Q.; Xu, Y.; Liu, P.; Che, Q.; Jensen, J. O.; Bjerrum, N. J.; He, R. Benzimidazole Grafted Polybenzimidazoles for Proton Exchange Membrane Fuel Cells. *Polym. Chem.* **2013**, *4*, 4768.
(13) Qjan, G. B.; Benicewicz, C. J. Synthesis and Characterization of High Molecular Weight Hexafluoroisopropylidene-containing Polybenzimidazole for High-temperature Polymer Electrolyte Membrane Fuel Cells. *J. Polym. Sci., Part A: Polym. Chem.* **2009**, *47*, 4064.
(14) Yang, J.; Li, Q.; Cleemann, L. N.; Jensen, J. O.; Pan, C.; Bjerrum, N. J.; He, R. Crosslinked Hexafluoropropylidene Polybenzimidazole Membranes with Chloromethyl Polysulfone for Fuel Cell Applications. *Adv. Energy Mater.* **2013**, *3*, 622.
(15) Mader, J. A.; Benicewicz, B. C. Synthesis and Properties of Random Copolymers of Functionalised Polybenzimidazoles for High Temperature Fuel Cells. *Fuel Cells* **2011**, *11*, 212.
(16) Mustarelli, P.; Quartarone, E.; Magistris, A. Membranes Based on Polybenzimidazole. In *Encyclopedia of Electrochemical Power Sources*; Garche, J. et al. eds.; Elsevier: Amsterdam, 2009; ISBN 0-444-52093-7.
(17) Villa, D. C.; Angioni, S.; Quartarone, E.; Righetti, P. P.; Mustarelli, P. New Sulfonated PBIs for PEMFC Application. *Fuel Cells* **2013**, *13*, 98.
(18) Angioni, S.; Villa, D. C.; Dal Barco, S.; Quartarone, E.; Mustarelli, P.; Tomasi, C.; Righetti, P. P. Polysulfonation of PBI-based Membranes for HT-PEMFCs: A Possible Way to Maintain High Proton Transport at a Low H_3PO_4 Doping Level. *J. Mater. Chem. A* **2014**, *2*, 663.
(19) Bouchet, R.; Siebert, E. Proton Conduction in Acid Doped Polybenzimidazole. *Solid State Ionics* **1999**, *118*, 287−299.
(20) Ma, Y. L.; Wainright, J. S.; Litt, M. H.; Savinell, R. F. Conductivity of PBI Membranes for High-Temperature Polymer Electrolyte Fuel Cells. *J. Electrochem. Soc.* **2004**, *151*, A8−16.
(21) Nicotera, I.; Simari, C.; Coppola, L.; Zygouri, P.; Gournis, D.; Brutti, S.; Minuto, F. D.; Aricò, A. S.; Sebastian, D.; Baglio, V. Sulfonated Graphene Oxide Platelets in Nafion Nanocomposite Membrane: Advantages for Application in Direct Methanol Fuel Cells. *J. Phys. Chem. C* **2014**, *118*, 24357−24368.
(22) Nicotera, I.; Enotiadis, A.; Angjeli, K.; Coppola, L.; Ranieri, G. A.; Gournis, D. Effective Improvement of Water-Retention in Nanocomposite Membranes Using Novel Organo-Modified Clays as Fillers for High Temperature PEMFCs. *J. Phys. Chem. B* **2011**, *115*, 9087−9097.
(23) Tanner, J. E. Use of the Stimulated Echo in NMR Diffusion Studies. *J. Chem. Phys.* **1970**, *52* (9), 2523−2526.
(24) Hughes, C. E.; Haufe, S.; Angerstein, B.; Kalim, R.; Mähr, U.; Reiche, A.; Baldus, M. Probing Structure and Dynamics in Poly[2,2′-(*m*-phenylene)-5,5′-bibenzimidazole] Fuel Cells with Magic-Angle Spinning NMR. *J. Phys. Chem. B* **2004**, *108*, 13626−13631.
(25) Enotiadis, A.; Angjeli, K.; Baldino, N.; Nicotera, I.; Dimitrios, G. Graphene-Based Nafion Nanocomposite Membranes: Enhanced Proton Transport and Water Retention by Novel Organo-functionalized Graphene Oxide Nanosheets. *Small* **2012**, *8*, 3338−3349.

DOI: 10.1021/acs.jpcc.5b01067
J. Phys. Chem. C XXXX, XXX, XXX−XXX

Ion Dynamics and Mechanical Properties of Sulphonated PBI Membranes for HT-PEMFCs

Isabella Nicotera [1*], Vasiliki Kosma [1], Cataldo Simari [1], Simone Angioni [2], Piercarlo Mustarelli [2], Eliana Quartarone [2]

[1] Department of Chemistry and Chemical Technologies, University of Calabria, via P. Bucci, 87036 Rende (CS), Italy

[2] Department of Chemistry, University of Pavia, and INSTM, Via Taramelli 12, 27100 Pavia, Italy

***** Author to whom correspondence should be addressed; E-Mail: isabella.nicotera@unical.it; Tel.: +39-0984-493379; Fax: +39-0984-492044.

SUPPORTING INFORMATION

As described in the experimental section, the NMR pulsed field gradient stimulated echo (PFG-STE) method was used to measure the ^{1}H self-diffusion coefficients in the membranes. The attenuation of the echo amplitude in this sequence is represented by the equation:

$$I(2\tau_1 + \tau_m) = \frac{1}{2} I_0 exp\left[-\frac{\tau_m}{T_1} - \frac{2\tau_1}{T_2} - (\gamma g \delta)^2 D(\Delta - \frac{\delta}{3})\right]$$

Figure S1 shows the decay lines of [I(g)/I(0)] vs. g^2(the other parameters are constants) which are used to calculate the self-diffusion coefficients (D), for some representative measurements performed.

We can observe that the decay lines are quite mono-exponential for all the systems as well as for all the investigated temperatures. This feature is very important in order to use the above equation to calculate D, and to confirm the Gaussian self-diffusion behaviour. Furthermore, it supports the consequence that in such complex systems, we measure only one diffusion value, which is a weighted average from the different protons species in fast rate of exchange.

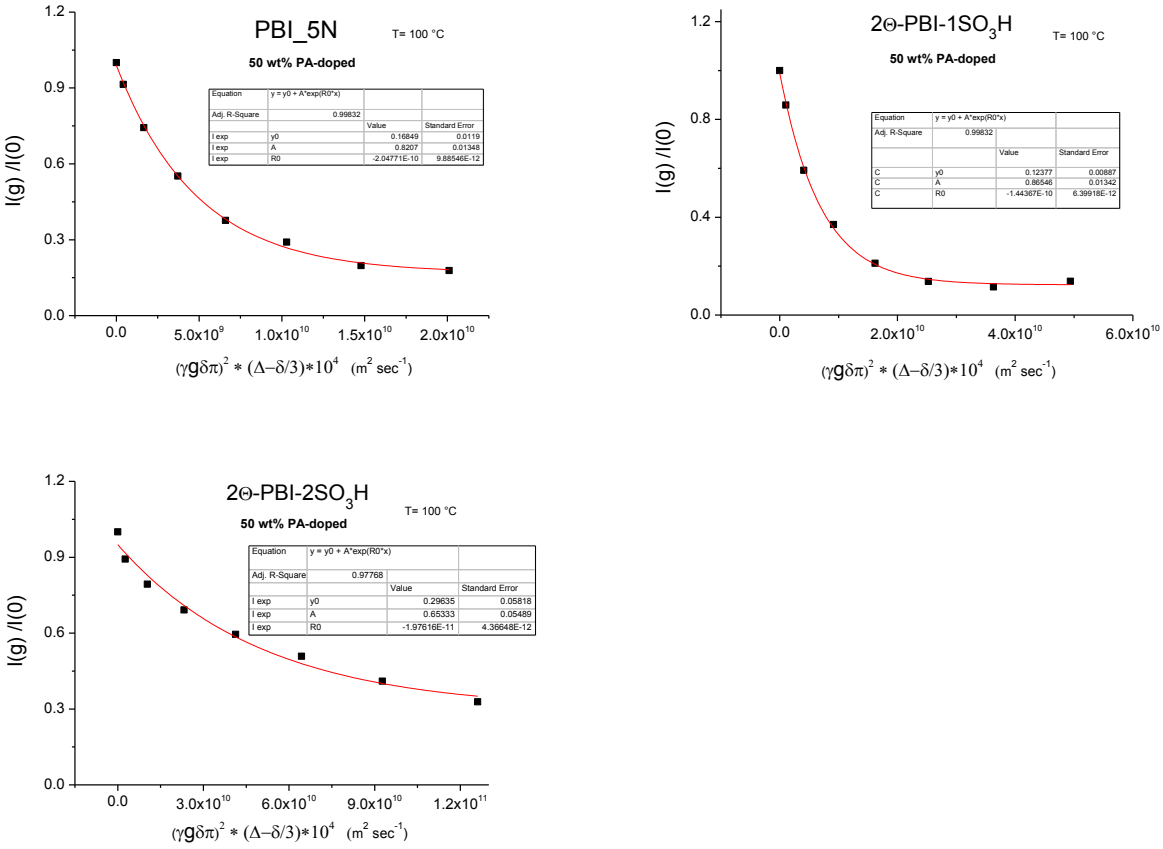

Figure S.1. *Decay lines of [I(g)/I(0)] vs. $(\gamma g\delta)^2(\Delta-\delta/3)$ of three PBI-based membranes.*

The viscoelastic behavior of the three membranes was quantified in terms of the storage modulus, E'. Figure S2 shows the storage moduli versus temperature obtained on the membranes activated with70 wt% PA. The values for all the samples are lower than the samples activated with 50% PA.

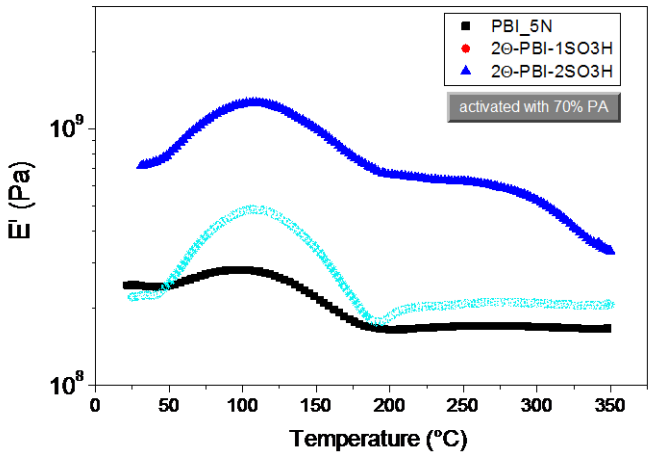

Figure S.2. *Storage moduli (E'), from 25 to 350 °C, obtained on the samples activated with 70% PA.*

By ^{31}P NMR spectra acquired on the three membranes, we performed a study on the reversibility of the systems after a thermal cycle: after the first thermal scan (from 20 °C up to 160 °C), the samples in the NMR tube were cooled down to room temperature, and then we followed the spectral changes in time during a second heating scan. Figure S.3 shows the spectra acquired on the sample 2Θ-PBI-1SO_3H, at two temperatures, 20 °C and 160 °C, after 3h (only for 20 °C) and after 24 h from the cooling. At 20 °C after 3 h (blue line) the signal is very low and broad, compared to the initial signal (black line) acquired in first thermal cycle. After 24 h (red line) it recovers more than half of the initial value. So there is a hysteresis phenomenon, i.e. the system needs a longer time to recover completely the initial condition. At 160 °C, after 24 h, the two signals are practically coincident. The same results were obtained also for the other two systems. It is likely due to the kinetics of rehydration which leads to the depolymerization of pyrophosphates and, if present, tripolyphoposphates/metaphosphates.

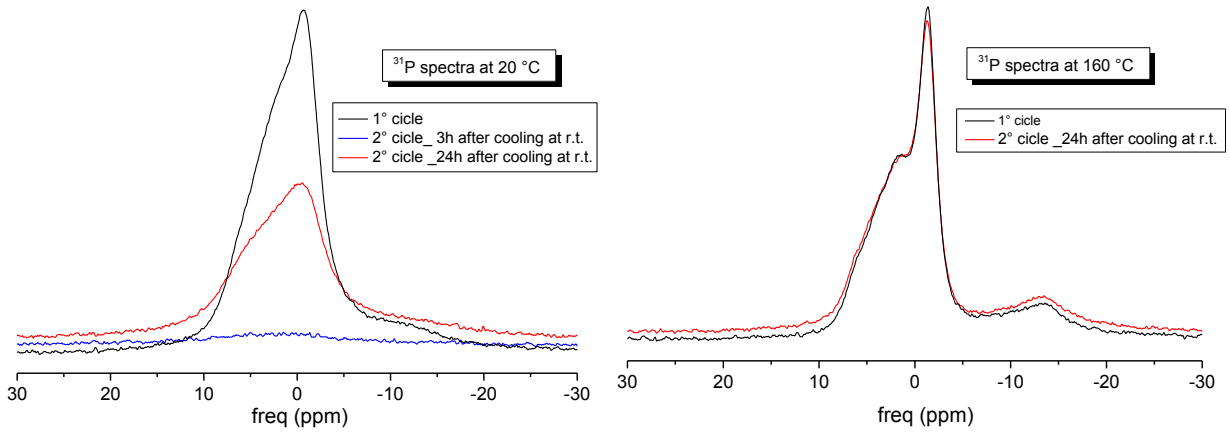

Figure S.3. *Time evolution of ^{31}P spectra acquired on the sample 2Θ-PBI-1SO_3H at 20 °C (on the left) and 160 °C (on the right), on the first thermal cycle, 3 h after the cooling at r.t., and 24 h after cooling at r.t.*

IV

"Sulfonated graphene oxide platelets in nafion nanocomposite membrane: Advantages for application in direct methanol fuel cells"

Journal of Physical Chemistry C, ***2014****, 118 (42), pp 24357-24368*

THE JOURNAL OF PHYSICAL CHEMISTRY C

Article

pubs.acs.org/JPCC

Sulfonated Graphene Oxide Platelets in Nafion Nanocomposite Membrane: Advantages for Application in Direct Methanol Fuel Cells

I. Nicotera,*[,†] C. Simari,[†] L. Coppola,[†] P. Zygouri,[‡] D. Gournis,[‡] S. Brutti,[§] F. D. Minuto,[∥] A. S. Aricò,[⊥] D. Sebastian,[⊥] and V. Baglio[⊥]

[†]Department of Chemistry and Chemical Technologies, University of Calabria, via P. Bucci, Cubo 14D, 87036 Rende (CS), Italy

[‡]Department of Material Science and Engineering, University of Ioannina, 45110 Ioannina, Greece

[§]Department of Science, University of Basilicata, V.le Ateneo Lucano 10, 85100 Potenza (PZ), Italy

[∥]Department of Physics, University of Calabria, via P.Bucci, Cubo 31 C, 87036 Rende (CS), Italy

[⊥]CNR-ITAE Institute, via Salita S. Lucia sopra Contesse, 5, 98126 Messina, Italy

Supporting Information

ABSTRACT: Graphene oxide (GO) is well known as an excellent amphiphilic material due to its oxygen-containing functional groups and its chemical tunability. By intercalation chemistry, organo-modified GO containing sulfonilic terminal groups were prepared and used as nanoadditive in Nafion polymer for the creation of hybrid exfoliated composites. The incorporation of hydrophilic 2D platelike layers in the Nafion membranes is expected to induce advantages in terms of thermal stability and mechanical and barrier properties (limitation of the methanol crossover by increased tortuosity and obstruction effect), although it may negatively affect the proton conductivity. In this work, we show how different preparation methods of the nanocomposites influence morphology, transport properties, and barrier effect to methanol. The hybrid membranes are characterized by powder X-ray diffraction and microscopies (SEM, TEM, and AFM). Water and methanol transport properties inside the nanocomposites are investigated by NMR spectroscopy (diffusivity and relaxation times), unveiling a reduction of the methanol diffusion and, nevertheless, an increase in the proton mobility and water retention at high temperatures. Finally, the electrochemical properties are investigated by direct methanol fuel cell (DMFC) tests, showing a significant reduction of the ohmic losses at high temperatures, extending in this way the operating range of a DMFC.

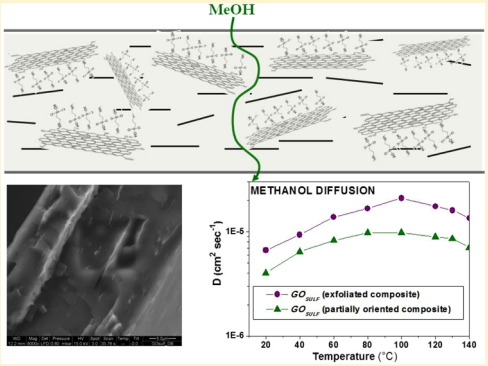

1. INTRODUCTION

Graphene is a one-atom-thick layer of sp^2 hybridized carbon atoms, tightly packed in a hexagonal crystal lattice: it constitutes the main basic building block of other graphitic nanostructures like graphite, fullerenes, and nanotubes. The extraordinary/unusual properties of graphene[1,2] bode well for a plethora of possible different applications ranging from electronics and spintronics but also as reinforcement in polymer composites, constituent of composite materials, or active element in sensors.[3−10] To realize this potential, efficient approaches for the production of large quantities of graphene are needed; currently one of the most promising is the chemical exfoliation of graphite passing the oxidation of the graphene sheets to form graphene oxide (GO).[8,11,12] GO is a layered material achieved through strong oxidation of graphite.[13−15] GO is characterized by the presence of oxygen-containing moieties, mostly hydroxyl and epoxy groups on the basal plane and carboxyl groups prevalently at the edges of the carbon sheets. These groups convert hydrophobic graphite into highly soluble graphite oxide in several polar and nonpolar solvents, including water.[16,17] By now the attachment of functional groups is exploited by the well-established intercalation chemistry leading to graphene-based hybrid materials for polymer composites, electrochemical sensors and biosensors, fillers in composite materials for engineering applications, supercapacitors, energy storage, and environmental applications.[8,18−26]

In the polymers research, during the last two decades large efforts have been devoted to the development of novel composites to enhance several properties of neat polymeric matrices using molecular or nanoscale reinforcement.[27] Homogeneous dispersion of the nanoadditives and the exploitation of their large surface area (per unit mass) to interact with the polymer are the key points to prepare polymer nanocomposites with improved mechanical, thermal, electrical, and barrier properties. In this regard, the production of graphene-based materials nanodispersed in a polymer matrix opens a new and interesting area in materials science.[28,29]

Received: August 9, 2014
Revised: September 17, 2014
Published: September 25, 2014

   dx.doi.org/10.1021/jp5080779 | J. Phys. Chem. C 2014, 118, 24357−24368

Nafion is a common electrolyte that has been most extensively studied in proton exchange membrane fuel cells (PEMFCs) for both vehicle applications and local on-site power generation system. PEMFCs would benefit from raising the operating temperatures above 100 °C due to the easier and more efficient water management, higher reaction rates, improved CO tolerance of the anode electrocatalyst, faster heat rejection rates, and better systems integration. In general, high temperature operation improves the performance and considerably reduces the volume and complexity of the fuel-cell system.[30,31] Recently, we prepared a series of novel nanostructured organo-modified layered materials based on GO and dispersed into Nafion matrix, demonstrating that these 2D nanofillers can control the nature of water confined in the nanosized ionic channels of Nafion.[32] As a result, hybrid nanocomposite membranes showed high proton mobility and water retention at temperature >100 °C.

Among PEMFCs, methanol-fed polymer electrolyte fuel cells (DMFCs) do not suffer many of the fuel storage problems typical of hydrogen-fed fuel cells (DHFCs). Being in the liquid state, like gasoline, methanol is also easier to transport and supply to the public using the existing infrastructures. DMFCs are well-suited for portable power applications for consumer electronics where the power requirements are low and the cost targets and infrastructure requirements are not as stringent as for automotive applications. However, methanol suffers from having a low boiling point (65 °C) and a high permeability in the PEMs, leading to a crossover effect. In this regard, the main challenge for DMFC development is to enhance proton conductivity with a parallel reduction of methanol crossover.[33]

The presence of hydrophilic 2D platelike layers in the polymeric matrix is of major interest due to the significant gains in thermal stability and mechanical and barrier properties of the resulting nanocomposites.[34] These physical modifications of the ionic clusters could be exploited to reduce the methanol crossover through obstruction effect and increased tortuosity of the fuel diffusion path; although, for a similar mechanism, the proton conduction may also decrease.

Therefore, appropriate functionalization of GO surfaces with amino derivatives having terminal hydrophilic acid groups, such as sulfonic, is expected to be an effective method to improve the proton transport by promoting the Grotthus-type mechanism, whereas the water "vehicular" transport mechanism, which strongly boosts the methanol crossover, may be reduced. The pictorial representation illustrated in Scheme 1 shows a conventional composite membrane where packages of layers keep their stacking with a minimal limiting effect on the methanol diffusion and without major positive effects for the protons mobility.[35,36] Conversely, the exfoliation of the layers and their dispersion throughout the continuous polymeric matrix may significantly increase the obstructions for the methanol crossover, and, as shown in figure, in the case of layers orthogonally oriented with respect to the diffusion path, the barrier effect could become noteworthy.

To this aim, here a detailed study of morphology structure and water and methanol transport properties of novel Nafion nanocomposite membranes based on sulfonated organo-modified GO (GO_{SULF}) is presented. An amine derivative containing sulfonic functional end group was covalently bonded via the amide functionality on the GO surfaces, and the resulting organo-modified GO nanofiller was incorporated in Nafion by solution intercalation. In the resulting nanocomposite, graphene-based nanoadditives are completely

Scheme 1. Representation of the Diffusion Pathway of Methanol Molecules through a Conventional, Exfoliated and Exfoliated/Aligned Nanocomposite Membrane, Respectively

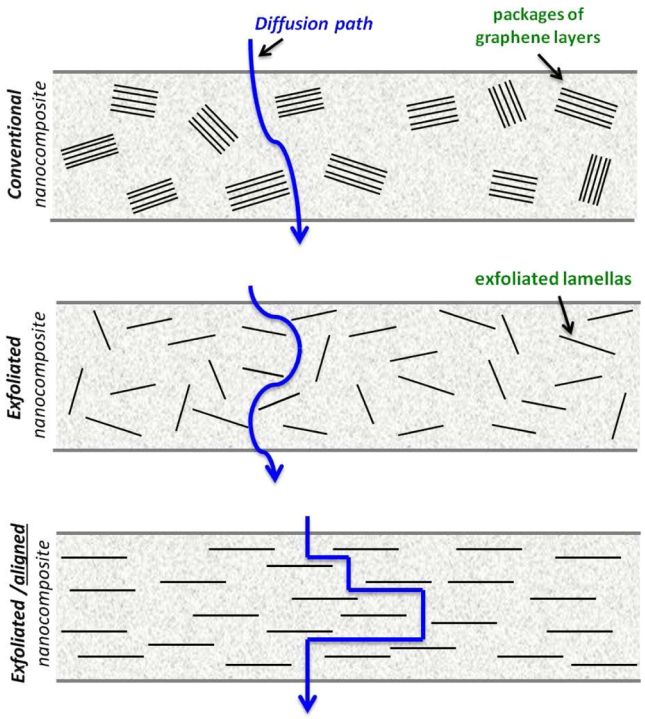

exfoliated, and an attempt to induce some preferential orientation to the GO_{SULF} lamellas in the polymer matrix was implemented by tuning the casting procedure of a very viscous dispersion.

As a final point, the electrochemical properties of the polymeric electrolytes were investigated by DMFC tests at high temperatures.

2. EXPERIMENTAL SECTION

2.1. Materials. Nafion as 20 wt % dispersion in water and lower aliphatic alcohols was supplied by Aldrich. The organic compound used for the synthesis of the organo-graphene oxide is 3-amino-1 propanesulfonic acid (acronym: SULF) purchased from Aldrich.

2.2. Synthesis of GO and Organo Derivative GO_{SULF}. Aqueous dispersions of GO were produced using a modified Staudenmaier's method[37] from graphite powder. In a typical synthesis, 10 g of powdered graphite (purum, powder ≤0.2 mm; Fluka) was added to a mixture of concentrated sulfuric acid (400 mL, 95−97 wt %) and nitric acid (200 mL, 65 wt %) while cooling in an ice−water bath. Potassium chlorate powder (200 g, purum, >98.0%; Fluka) was added to the mixture in small portions while stirring and cooling. The reaction was quenched after 18 h by pouring the mixture into distilled water, and the oxidation product was washed until the pH reached 6.0 and finally dried at room temperature. The above procedure was repeated three times, and according to elementary analysis data, the C/O atomic ratio of the resulting product is 2.6.[38]

For the preparation of GO_{SULF}, 100 mg of GO was dispersed in 100 mL of water, followed by the addition of an aqueous solution of the above amine derivative (300 mg of SULF in 40 mL of water). After stirring for 24 h, the product was separated

dx.doi.org/10.1021/jp5080779 | J. Phys. Chem. C 2014, 118, 24357−24368

by centrifugation, washed with water, and air-dried by spreading on a glass plate.

2.3. Preparation of Composite Membranes. Nafion hybrid nanocomposites were prepared by solvent casting method, as reported in the previous work,[32] by dispersing the filler directly in the Nafion solution (as purchased). However, in this work, to prepare "aligned" composites, as explained in the introduction, two different casting procedures of the polymer dispersion were followed (Scheme 2) and the resulting membranes were compared: (1) casting on a petridish (pd) and (2) spread a very viscous dispersion (after concentration of the initial dispersion) with a knife or doctor blade (kn).

Scheme 2. Casting Procedures Followed in Order to Prepare Membranes: Casting in a Petridish (left) and Spread with a Knife (right)

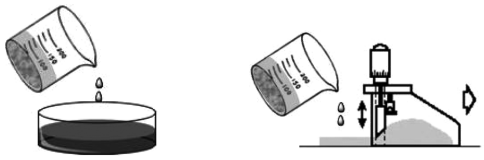

The cast dispersion then was placed in the oven at 40 °C overnight to remove the solvents. The reinforcement of the membranes and the acid activation is the same already reported.[32]

2.4. Characterization Techniques. *2.4.1. X-ray Diffraction.* The X-ray powder diffraction data were collected on a D8 Advanced Bruker diffractometer by using CuK_a (40 kV, 40 mA) radiation and a secondary beam graphite monochromator. The patterns were recorded in a 2-theta range from 2 to 60°, in steps of 0.02° and counting time 2 s per step.

2.4.2. Microscopy. Atomic force microscopy (AFM) experiments have been carried out on both the Naf/GOsulf-pd and Naf/GOsulf-kn samples. Prior to the AFM tests, membranes have been fully conditioned for 30 days in a closed vessel at 53% relative humidity (RH, water vapor back pressure above a saturated $Mg(NO_3)_{2(aq)}$ solution). The AFM study has been carried out by using a Park AFM XE120 instrument equipped with a home-modified universal closed liquid cell to allow a careful control of the RH condition upon scanning: measurements have been performed at RH = 53%. AFM scans have been carried out in tapping intermittent contact mode (TM). It is important to underline that phase−distance curves have been carefully monitored upon imaging to avoid the occurrence of unstable regimes and the rise of height artifacts in AFM topographies.[41] AFM images have been recorded on the two sides of the membranes to highlight possible differences: three different areas have been sampled on both membrane sides by recording at least five different magnifications in each zone. Scanning electron microscopy analysis was conducted with a QUANTA FEG 400 F7, FEI microscope. The SEM images were acquired collecting the backscattered electrons induced by using 10 keV electron beam and 0.4 mbar of water humidity. The SEM starting images are pretreated with a band-pass Fourier filter to delete high- and low-spatial-frequency noise; successively then the software computes the Fourier power spectra of the selected area and analyze results in polar coordinates. The power is measured, for each angle, using spatial filters.[39] Transmission electron microscopy (TEM) experiments have been carried out on the cross section of the composites membranes by using a Fei Tecnai cryo-TEM instrument: experiments have been carried out at 80 keV of electron beam acceleration and in liquid nitrogen cryo-condition to avoid membrane damage due to local heating.

2.4.3. NMR Spectroscopy. NMR measurements were performed on a Bruker NMR spectrometer AVANCE 300 Wide Bore working at 300 MHz on ^1H. The employed probe was a Diff30 Z-diffusion 30 G/cm/A multinuclear with substitutable RF inserts. Self-diffusion coefficients of water and methanol were performed by using the pulsed field gradient spin−echo (PFGSE) method based on the Stejskal−Tanner sequence.[40] For the investigated samples, the experimental parameters, Δ and δ, are 10 and 1 ms, respectively. The gradient amplitude, g, varied from 10 to 700 G cm^{-1}. Under this condition the uncertainty in the self-diffusion measurements is ∼3%. Longitudinal relaxation times (T_1) of water were measured on the same spectrometer by the inversion−recovery sequence ($\pi-\tau-\pi/2$). Both self-diffusion and T_1 measurements were conducted by increasing temperature step by step from 20 to 130 °C, with steps of 20 °C, and leaving the sample to equilibrate for ∼15 min. Prior to the NMR measurements, membranes were dried in oven, weighed, and then immersed in distilled water or in 2 M methanol solution at room temperature.[34] Upon being removed from the water they were quickly blotted dry with a paper tissue (to eliminate most of the free surface liquid).

The water content value was determined using a microbalance and recorded as

$$\text{uptake\%} = [(m_{wet} - m_{dry})/m_{dry}] \times 100$$

At this point the membranes were loaded into a 5 mm NMR Pyrex tube and sealed.

2.4.4. Electrochemical Tests. The electrodes were prepared according to the procedure described in a previous paper.[42] Pt black powder (Alfa Aesar) was used at the cathode, and PtRu black powder (Alfa Aesar) was used at the anode. A slurry composed of catalyst and water was mixed under sonication at 60 °C. Afterward, a 15 wt % of Nafion ionomer (5 wt %, Ion Power) with respect to the catalyst was added dropwise to the slurry. The obtained ink was deposited on a commercial GDL from E-TEK (LT-ELAT for the cathode and HT-ELAT for the anode). The electrodes (both anode and cathode) were prepared with a Pt loading of 1 mg cm^{-2}. The thickness of the membranes used for the electrochemical experiments in direct methanol fuel cells (DMFCs) was ca. 50 μm. Membrane-electrode assemblies (MEAs) were formed by hot-pressing the electrodes onto the membrane at 130 °C and 20 kg cm^{-2} for 90 s and subsequently installed in a fuel-cell test fixture of 5 cm^2 active area. The cell was connected with a DMFC test station from "Greenlight Innovation" for the single-cell polarization measurements and AC electrochemical impedance characterization. For these experiments, preheated aqueous 2 M methanol was fed to the anode chamber of DMFC through a pump, whereas humidified oxygen was fed to the cathode. Reactant flow rates were 2 and 100 mL min^{-1} for methanol/water mixture and oxygen stream, respectively. A pressure of 1.5 bar abs. at both anode and cathode was used at 90 °C, whereas it was increased up to 3 bar abs. at higher temperatures (120 °C). Single-cell performances were investigated by steady-state galvanostatic measurements.

dx.doi.org/10.1021/jp5080779 | J. Phys. Chem. C 2014, 118, 24357−24368

Scheme 3. Schematic Representation of the Synthetic Procedure for GO_{SULF} Nanofiller

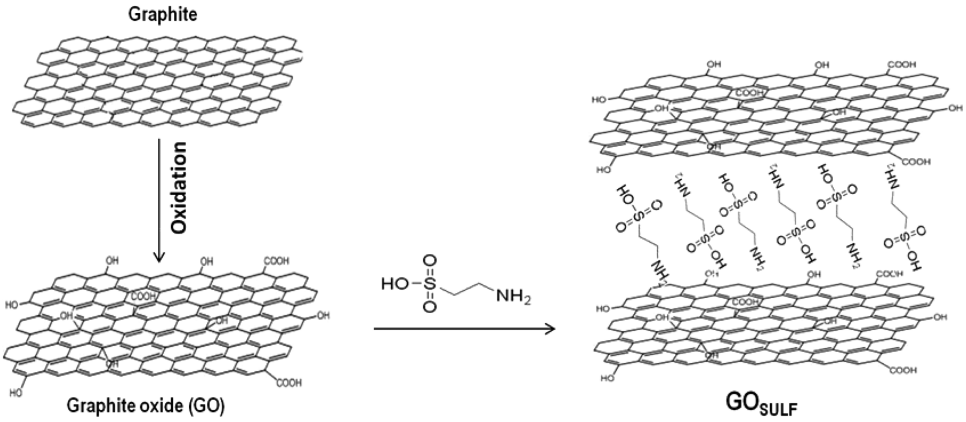

3. RESULTS AND DISCUSSION

3.1. X-ray Study of Organo-GO and Hybrid Nanocomposite Membranes. The starting material was produced by oxidizing powdered graphite to obtain exfoliated hydrophilic single-layer flakes of GO. This was then reacted with a sulfonated amine derivative, which binds covalently to the GO surfaces via nucleophilic substitution reactions[43,44] of the amine end group of the derivative with the epoxy groups of GO (Scheme 3), resulting in the formation of an organo-modified GO nanofiller, GO_{SULF}.

XRD measurements were applied to confirm the successful intercalation of SULF molecules on the GO interior and also to evaluate the type of composites created upon incorporation of the hybrid nanofillers in the Nafion matrix. An increment of the d_{001} value, as compared with the parent GO, is observed in the pattern of GO_{SULF} (Figure 1a) due to the successful insertion of the SULF molecules in the interlayer space of the layered material. From the equation: $\Delta = d_{001} - 6.1$ Å, where 6.1 Å is the thickness of the GO layer,[45,46] the interlayer distance (Δ) can be calculated. The interlayer distance, which was 1.2 Å in the pristine GO, increased to 3.7 Å in the case of GO_{SULF} revealing the successful insertion of the organic molecules within the GO galleries. Figure 1 also shows the XRD patterns of the filler-free Nafion and the nanocomposite membranes prepared with GO and organo-GO nanofillers either by casting in a Petri dish or using a knife (Figure 1b). Apart from the characteristic wide peak centered at 18° due to Nafion polymer arrangement (crystalline peak scattering from the polyfluorocarbon chains of Nafion),[47] the absence of the 001 diffraction peak of GO at low 2θ angles in the diffraction patterns of all nanocomposites indicates the creation of fully exfoliated nanocomposites. In these structures, all individual graphene platelets have lost their stacking after mixing with the polymeric mass implying that the majority of graphene-based nanofillers is existing in fine dispersion between the polymer chains.[32]

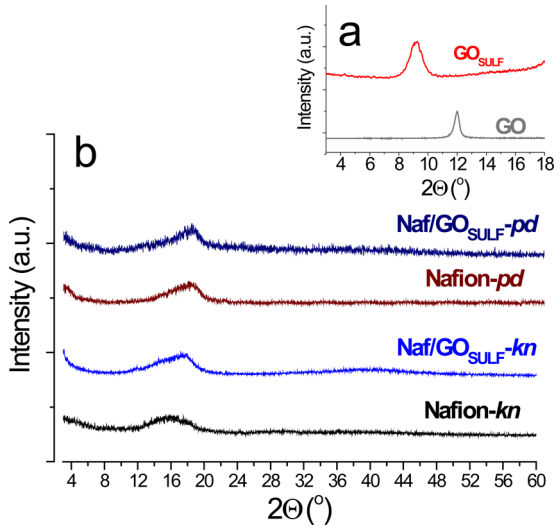

Figure 1. XRD patterns of (a) GO and GO_{SULF} and (b) Nafion filler free and composite membranes prepared by knife(kn) and by casting in Petri dish (pd).

3.2. Morphological Investigation. Morphological analysis of composite membranes exploited three microscopic techniques: SEM, TEM, and AFM. This multitechnique approach allowed us to fully highlight morphological differences between the films prepared by pd and kn procedures and to confirm the XRD results concerning the complete exfoliation and homogeneous dispersion of the filler within polymer.

Two examples of high-magnification AFM images are shown in Figure 2. Both topography and the corresponding phase image are reported. The Naf/GO_{SULF}-pd and Naf/GO_{SULF}-kn membranes show quite similar topographies and phase images with round-shaped aggregated pseudoparticles of homogeneous size (light regions) separated by darker areas. Because the phase signal is sensitive to variations in composition due to changes of the local elastic properties, this morphology is commonly attributed to the alternation of the hydrophobic (light regions)/hydrophilic (dark regions) domains across the membrane surface.[48−50] The typical diameter of the round-shaped domains in Nafion recast membranes ranges between 3 and 30 nm in diameter.[51] Apparently, the addition of sulfonated GO leads to the formation of a very homogeneous and smaller-in-size dispersion of the hydrophilic/hydrophobic domains on the membrane surfaces. The mean linear size (diameter) of the pseudo-round-shaped light particles (hydrophobic domains) is in both cases below 8 nm and for the Naf/GO_{SULF}-kn even smaller than 4 nm. Furthermore, various mid-to-high magnification AFM images of the Naf/GO_{SULF}-pd sample, recorded on both sides of the membrane, highlight the occurrence of aligned aggregation of round-shaped hydrophobic domains (light areas) with an apparent length of about 20−100 nm; similar superstructures are apparently missing on the surfaces of the Naf/GO_{SULF}-kn membrane.

dx.doi.org/10.1021/jp5080779 | J. Phys. Chem. C 2014, 118, 24357−24368

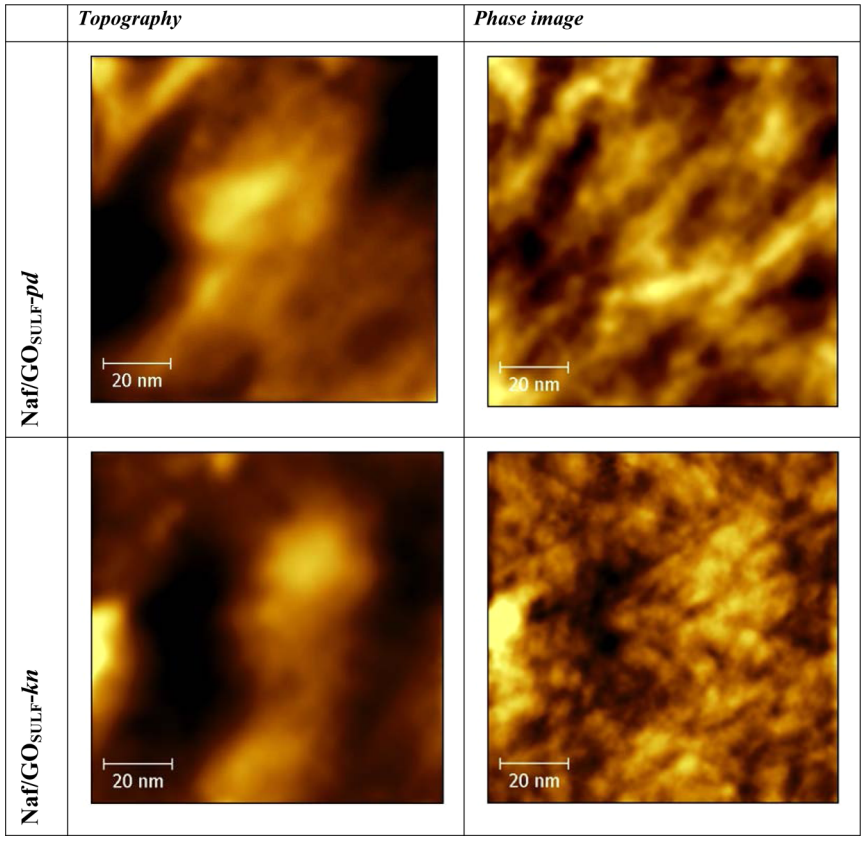

Figure 2. AFM topographies and phase images of the two Naf/GO$_{sulf}$-pd and Naf/GO$_{sulf}$-kn samples.

Because the composition of the two membranes is identical, the alteration of the overall morphology as well as the shrinking of the hydrophobic domain size is necessarily related to the manufacture procedure and thus to the corresponding possible different dispersion of the GO layers close to the surface. In fact the alteration of the recasting mechanism during membrane preparation as well as the solvent removal is expected to have a strong impact on the local organization of the ionic/hydrophobic domains in the final membrane and therefore in its hydration properties (water uptake and mobility).[52,53] Although highly speculative, one may suggest that the simple casting on a Petri dish may lead to a few random orientations of GO layers orthogonal to the membrane surface, capable of coordinating linear superstructures in the hydrophobic domains. This peculiar morphology is missing in the case of the Naf/GO$_{SULF}$-kn sample, thus possibly implying a preferential orientation parallel to the surface of the superficial GO layers.

Concerning TEM study, it is well known that when the dispersion in the polymer matrix concerns carbon-based materials the analysis is very difficult because of the insufficient contrast. In fact, in our knowledge there are no TEM images of similar composites in the literature. In Figure S1 of the Supporting Information we report some very clear pictures of both the Naf/GO$_{SULF}$-pd and Naf/GO$_{SULF}$-kn membranes. Because of the chemical homogeneity of the graphene filler with the polymer backbone, it was not possible to detect a clear evidence of the graphene sheets geometry in the cross-section of the composites membranes. However, these images demonstrate that these films have an extremely homogeneous dispersion of the graphene sheets without any agglomerates or clustering.

SEM images of Naf/GO$_{SULF}$-pd and Naf/GO$_{SULF}$-kn membranes cross-section obtained by cryo-cleavage are shown in Figure 3. The mapped morphology of the cross sections presents micrometer-sized cleavage planes whose orientation strongly depends on the casting procedure of the membrane.

At low magnification (Figure 3a), the kn-membranes show cleavage planes oriented parallel to their surface in the whole body. The cleavage planes in the pd-membranes have no preferential orientation. This qualitative result given by a visual inspection of the SEM images is supported by a quantitative comparison based on the Directionality algorithm of the NIMH-ImageJ open source software (http://fiji.sc/Directionality). The SEM images are rotated to have the membranes surface at 0°. The dispersion angle of membranes cleavage structures is depicted in the graphs reported in Figure 3b,f. It is rather evident that for pd-membrane there is not a preferential direction as the structures are disperse on a very broad angle and the distribution appears almost isotropic (graph f calculated on the image e). The analysis of the (4000×) SEM image (Figure 3a) shows instead that the *kn*-membrane has a sharp distribution of the cleavage planes orientation. The anisotropy can be estimated by a Gaussian peak fitting procedure (full line in graph b), and we get that, in this case, the mean direction relative to the surface is −6° with a fwhm angular dispersion of 33°. Similar analysis performed on images recorded at various magnification (from 3000× to 12 000×) on kn-membranes shows analogous results with average orientation close to 0° and fwhm dispersion of 35° (see Figure S2 in the Supporting Information), while no preferential direction is found for pd-membranes.

dx.doi.org/10.1021/jp5080779 | J. Phys. Chem. C 2014, 118, 24357−24368

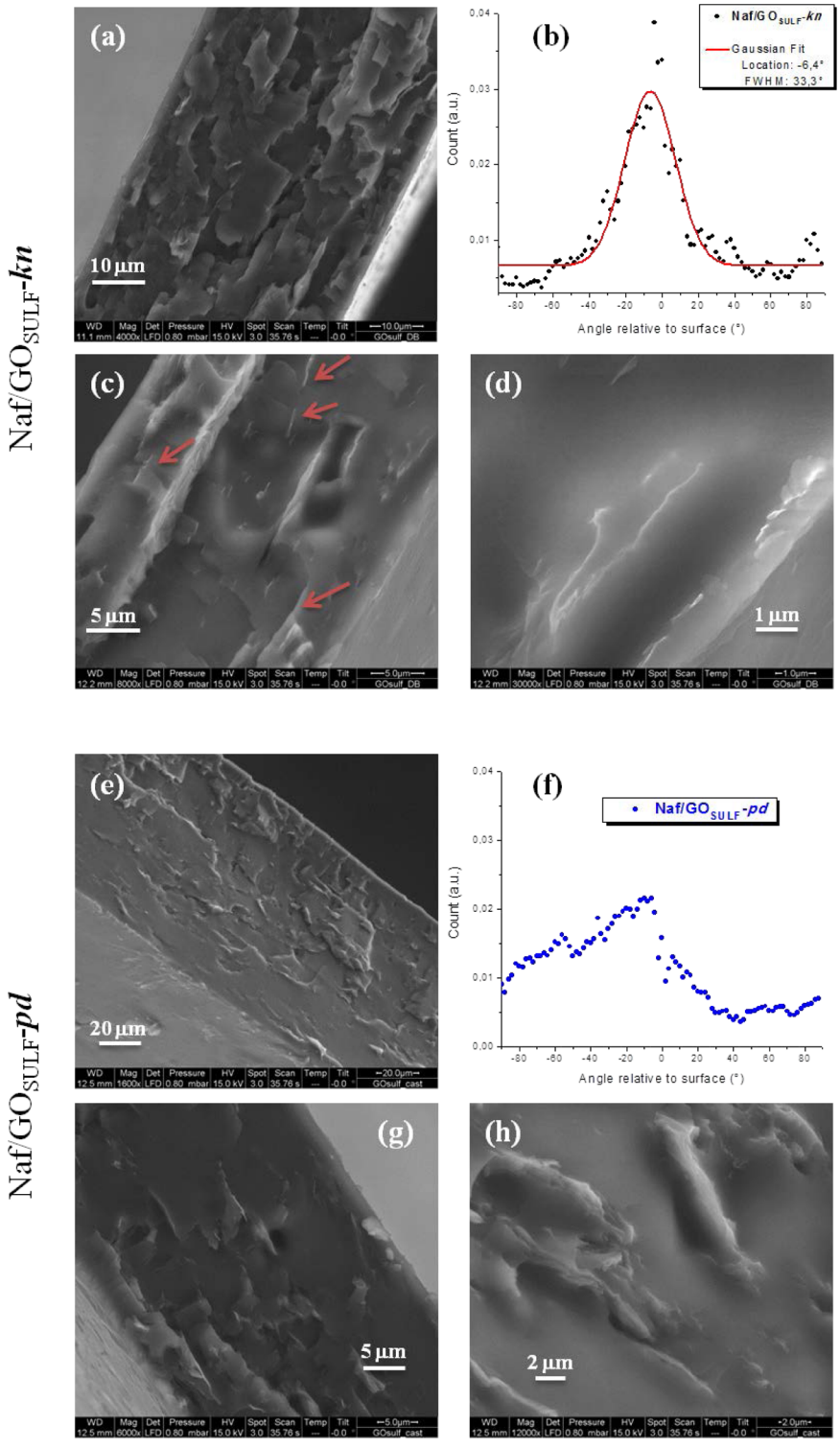

Figure 3. SEM images of the two Naf/GO$_{SULF}$-kn and Naf/GO$_{SULF}$-pd samples.

At high magnifications, we can observe some bright lines in the cross sections of the membranes (Figure 3d,h) that could be either attributed to stacking of GO following the same orientation distributions of the cleavage planes.

The results of this morphological analysis can be easily put in relation with the microstructure of the membranes. Apparently different morphologies of the composite membranes can be obtained by different casting procedures and a preferential direction is induced by the knife-casting procedure even though there is no direct evidence of alignment of the dispersed lamellae at the nanoscale.

3.3. NMR Investigation. Figure 4 displays the self-diffusion coefficients of water confined in filler-free and nanocomposite Nafion membranes measured by PFG-NMR technique in the temperature range 20−140 °C. In particular, the graph puts in comparison the water transport properties in completely swelled membranes prepared by casting in Petri dish (pd)

dx.doi.org/10.1021/jp5080779 | J. Phys. Chem. C 2014, 118, 24357−24368

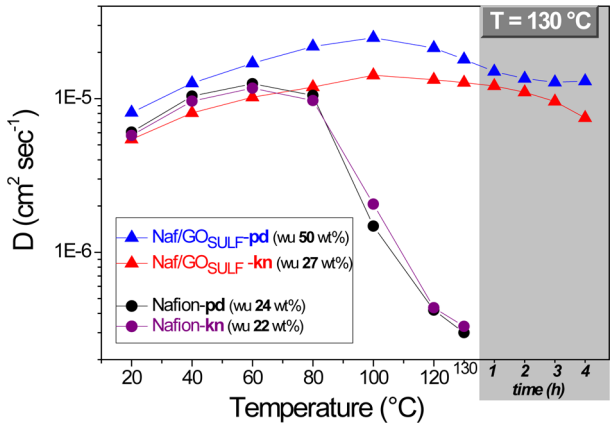

Figure 4. Water self-diffusion coefficients versus temperature (from 20 °C up to 130 °C) in completely swelled membranes of Nafion filler-free and GO_{SULF}-nanocomposite. Samples prepared by casting in petridish (pd) and by knife (kn) are compared and the water uptake is reported in the legend. In the graph the data collected at 130 °C after several hours are also plotted.

and by knife (kn). In the Figure the water uptakes of each sample recorded at the maximum swelling are also shown.

First, the advantages obtained from the dispersion of these organo-GO sheets in the Nafion polymer are evident, in particular, in the high temperature region: diffusion increases linearly up to 100 °C, and soon after, due to the evaporation of a certain amount of water from the membrane, it decreases slightly without abrupt drops after several hours at 130 °C. It is to be noted that in the NMR tube membranes are not humidified during the experiment and, in fact, the water diffusion in the filler-free Nafion decreases rapidly after 60−80 °C due to the fast water evaporation. In the composite membranes a certain amount of water (bound water) is kept likely due to the acids/hydrophilic sites of the filler, thus supporting the proton mobility.

Turning to the analysis of the effects of the casting method used to prepare the films, in the case of recast Nafion, only minor differences are observed between the two membranes. In fact, the water uptake is almost the same (24 wt % for pd and 22 wt % for kn), and the water diffusion coefficients are very similar. On the contrary, large difference is instead observed for the GO_{SULF} nanocomposites for both the amount of absorbed water, namely, 50 wt % in the pd-sample and almost half in the kn-sample (27 wt %), and the diffusion coefficients, appreciably lower in the kn-membrane, which are apparently strongly altered depending on the casting method adopted. These differences are likely due to the different morphology of the two composites and by the possible preferential orientation of the nanoadditives inside the polymer matrix that produces (a) a structural/morphological modification of the hydrophilic pores for which the water absorption is reduced even if there is the same nanomaterial dispersed and (b) a more regular distribution, through an obstruction phenomenon, that slows the diffusional motion of the water molecules, although the diffusion coefficients remain rather high at high temperature thanks to the Grotthus-type mechanism's contribution. On the basis of these observations, we verified the ability of these composite membranes to reduce the methanol diffusion to limit the crossover in the MEA, while maintaining high proton mobility.

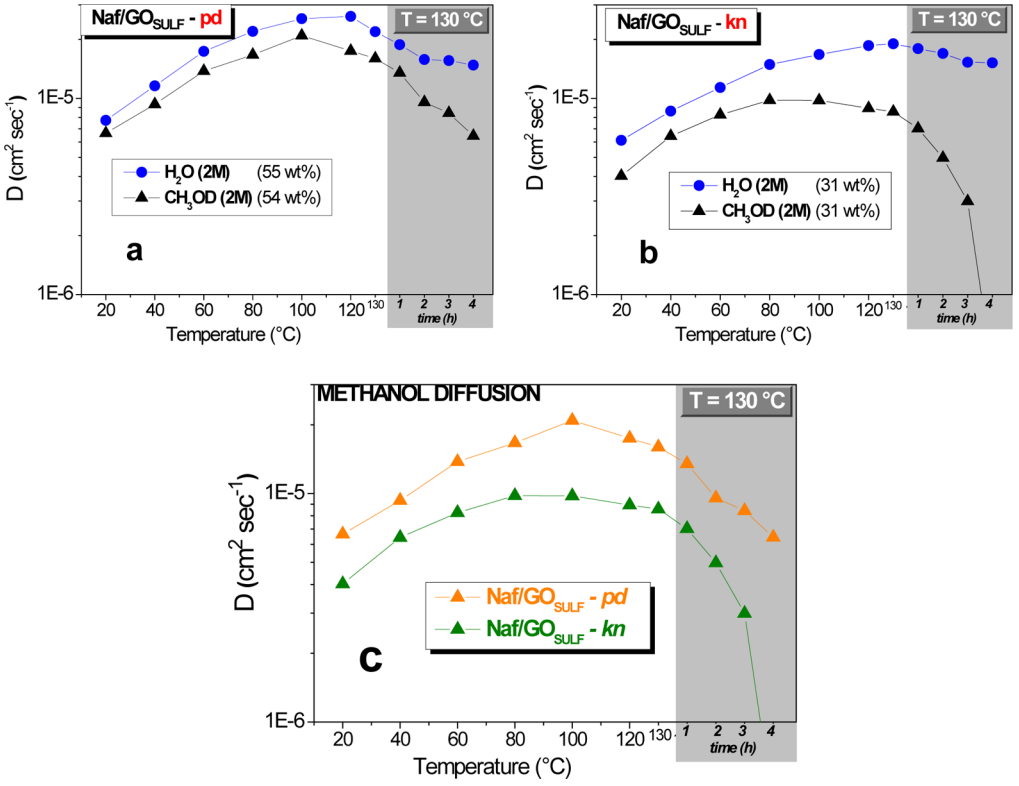

Figure 5. Self-diffusion coefficients of water and methanol in 2 M solution confined in Nafion-GO_{SULF} nanocomposite membranes prepared by (a) pd and (b) kn from 20 up to 130 °C. In the graphs are reported also the solution uptakes (wt %). The comparison of the methanol diffusion between the two membranes is shown in panel c. In each graph the data collected at 130 °C after some hours are also plotted.

dx.doi.org/10.1021/jp5080779 | J. Phys. Chem. C 2014, 118, 24357−24368

Recently, we reported the diffusion behavior of methanol in filler-free Nafion swelled in 2 M solution,[34] showing that at temperature >60 °C the diffusion coefficients of methanol are higher than water. This detrimental effect can be related to the different distribution of methanol and water molecules in the hydrophilic domains of the polymer membrane. Methanol molecules distribute preferentially close to the polymer backbone on the surface of the hydrophilic pores, whereas water molecules accumulate in their core. As a consequence, the acidic proton of methanol is only weakly bonded to the $-SO_3H$ groups, whereas water is strongly coordinated and it is therefore less mobile.[54,55] This outcome is clearly responsible of the methanol crossover observed in the DMFC operation.

The effect on water and methanol mobility of the incorporation of a layered filler in the polymeric matrix is shown in Figure 5, where the diffusion coefficients of water and methanol in 2 M solution are reported. The diffusion coefficients have been measured in swollen GO_{SULF} nanocomposites membranes, both pd (a) and kn (b), in the temperature range 20−130 °C. To decouple the NMR signals of methanol and water, the membranes have been equilibrated in solutions prepared with deuterated molecules, that is, mixture of CH_3OD/D_2O and CD_3OD/H_2O, respectively.[34] In this way, we can compare the mobility of water and methanol confined in membrane at the same solution concentration. To further clarification, the use of deuterated CH_3OD instead of CH_3OH is required due to the fast rate exchange of hydroxyl groups between water and methanol molecules during NMR time scales, which could affect the measurements.

We can observe that the water diffusion coefficients are at all temperatures larger than methanol for both the composite membranes, thus proving the beneficial blocking effect of the nanoparticles dispersed in the polymer. However, there are two crucial differences between the two composite membranes: (1) the solution uptake is also in this case very different, ∼55 wt % in GO_{SULF}-pd and ∼31 wt % in GO_{SULF}-kn, and (2) the discrepancy between water and methanol diffusion is larger for the kn-sample and increases as the temperature increases. On passing, it is likely that the larger uptake in the pd-sample accounts for the larger diffusion coefficients for both water and methanol observed in comparison with the kn-membrane.

In Figure 5c, the comparison between the diffusion coefficients of methanol in the two membranes is shown to highlight the remarkable reduction of the methanol molecules mobility in the kn-membrane. This experimental result also supports our hypothesis on a possible preferential orientation of the lamellae of GO in the polymer film driven by the casting procedure which induces (a) structural and morphological modification of the polymeric matrix and consequently of the hydrophilic domains, thus reducing the capability to absorb higher amount of water or solution, and (b) an increase in the tortuosity of the diffusional paths of both water and methanol molecules. However, different from the case of recast Nafion, the water diffusion in the composite membrane remains large likely due to the good retention capacity of the filler that boosts the proton transport by the Grotthus-type mechanism through the highly acid GO_{SULF} surfaces.

In Figure 6, the temperature variation of the NMR longitudinal (or spin−lattice) relaxation times (T_1) of (a) water and (b) methanol is shown for the two GO_{SULF}-nanocomposites swelled in methanol solution. T_1 values are more sensitive to more localized motions, in comparison with

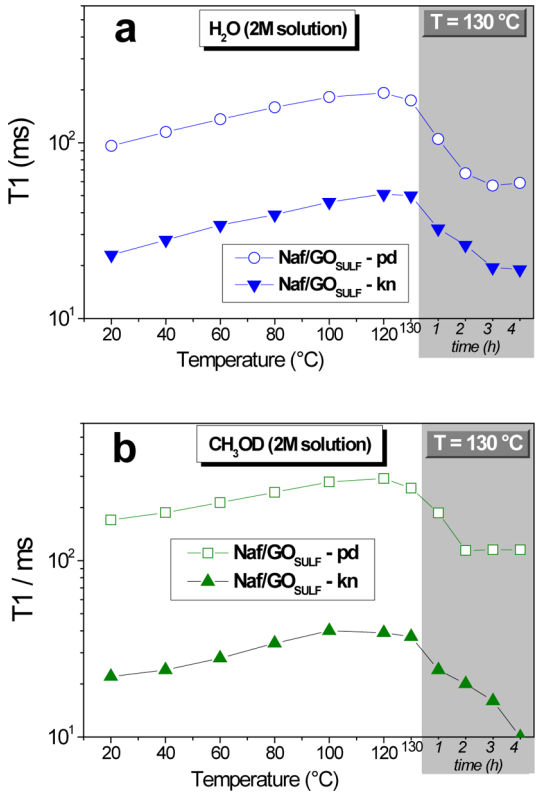

Figure 6. Longitudinal relaxation times (T1) of the water (a) and methanol (b) measured in the pd- and kn- composite membranes swollen in 2 M solution in the temperature range from 20 to 130 °C. In each graph, the data collected at 130 °C after some hours are also plotted.

standard diffusion, including both translation and rotation on a time scale comparable to the reciprocal of the NMR angular frequency (∼1 ns). Therefore, higher T_1 values suggest more facile molecular motions. The relaxation times of both water and methanol molecules in the pd-membrane are much higher than of kn-membrane in the entire temperature range investigated. This implies a greater local mobility (more translational and rotational degrees of freedom) of the solvent molecules in the first sample probably due to the poorer molecular interactions with the polymeric and particles sites. Once again, these data demonstrate that different casting procedures produce drastic effects on solvent mobility likely attributable to structural modifications, thus limiting water and methanol motions, confirming the diffusion behavior.

The analysis of the alterations of the ^1H NMR spectra of methanol and water at different temperatures can give further information on the solvents distribution in the membrane (both hydration and interactions) as well as on the evaporation dynamics. Figure 7 shows the temperature evolution of the proton spectra acquired on Nafion-GO_{SULF}-kn composite swollen in 2 M methanol solution from 20 to 130 °C (spectrum recorded at 130 °C after 4 h is also reported). In particular, the spectral lines of water (on the left) and methanol (on the right) are compared. These spectra were referenced against pure water and methyl protons, respectively, set at 0 kHz, and were acquired with the same number of scans. Because of the fluorinated character of the Nafion, the ^1H NMR signal arises essentially from the water and methanol absorbed by the membrane because the contribution of the hydrogen atoms of the sulfonic acid group and that of the

dx.doi.org/10.1021/jp5080779 | J. Phys. Chem. C 2014, 118, 24357−24368

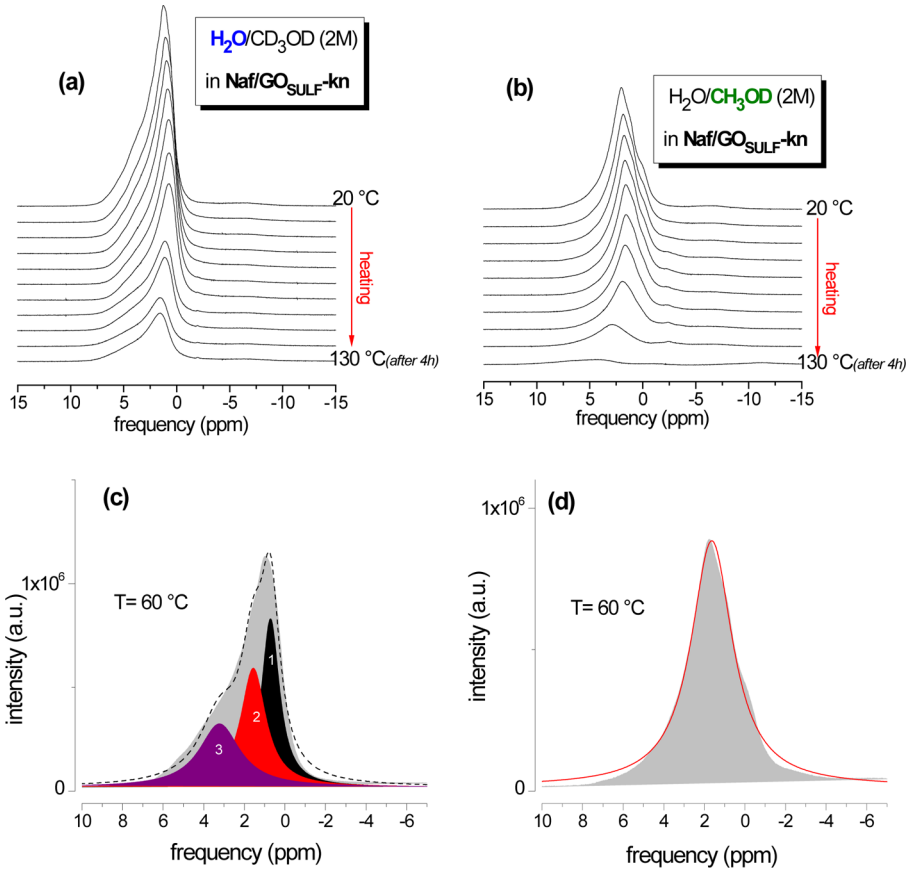

Figure 7. Evolution of proton spectra from water (a) and methanol (b) as a function of temperature on Nafion-GO_{SULF}-kn composite swollen in 2 M methanol solution. The spectra were referenced setting methyl protons and pure water at 0 ppm, respectively. Fitting of the NMR signal (c,d); see text.

organo-filler is practically negligible. Both signals are broader and more structured than in isotropically free liquid and, in particular, for the water signal, the shape is rather asymmetric (non-Lorentzian curve), implying a multiple components configuration, that is, different "types of water" coexist.

Water molecules are shared between the solvation sphere of the SO_3^- hydrophilic groups of Nafion polymer and of the organo-modified GO and bulk-like water (i.e., water molecules mainly interacting with each other). Because of the fast exchange with respect to the NMR observation time, the distinction between the different states of water within the hydrophilic pores is difficult. As a consequence, ^{1}H NMR shows only one structured signal; however, its shape and alterations are explicative of the chemical complexity. In all spectra, up to 130 °C, the asymmetric peak can be fitted using three Lorentzian peaks, as reported in Figure 7c: one narrow peak (blue), attributed to the bulk-like water, and two broad curves, assigned to the hydration water of the sulfonic groups of polymer and filler

Turning to the methanol signal, instead, it shows a rather symmetric shape, as also confirmed by the fitting analysis (Figure 7d), whereby the experimental data are nicely fitted with a single Lorentzian peak. This evidence supports the above-mentioned hypothesis concerning the homogeneous distribution of the methanol molecules over the surface of the ionic pores of the Nafion membrane.[56]

As a final point, it may be of interest to discuss the peculiar trend of the water and methanol self-diffusion coefficients and chemical shifts upon heating shown in Figure 8. This interesting behavior has been mentioned and discussed briefly by us in a previous publication,[32] and it is here analytically confirmed by a more extended analysis. What we observe is a straightforward and symmetric variation with temperature between self-diffusion coefficients and chemical shifts; that is, an increase in the chemical shift of the proton signals corresponds to an analogous and proportional reduction of the diffusion coefficient. The upfield shift of the proton resonance at higher temperature is likely due to higher environment acidity and stronger electrostatic interactions affecting water and methanol molecules, reducing their mobility.

3.4. Electrochemical Investigation. The electrochemical investigation was carried out in a single cell by recording the polarization and power density curves on the MEAs based on the different membranes at two temperatures, 90 and 120 °C (Figure 9a,b, respectively), feeding a 2 M methanol solution at the anode and oxygen at the cathode.

As can be observed, the maximum power density of the DMFC equipped with both composite membranes of Naf/GO_{SULF} increases slightly with temperature, while there is a significant drop of performance of the filler-free Nafion-based cell, from ~120 to ~60 mW cm^2 when the temperature increases from 90 to 120 °C. This outcome is clearly caused by the water evaporation from the membrane and, consequently, by an increase in the cell resistance (from 0.1 to 0.2 ohm cm^2). The electrochemical analysis, as well as the NMR study, highlights and confirms the exceptional water retention

dx.doi.org/10.1021/jp5080779 | J. Phys. Chem. C 2014, 118, 24357−24368

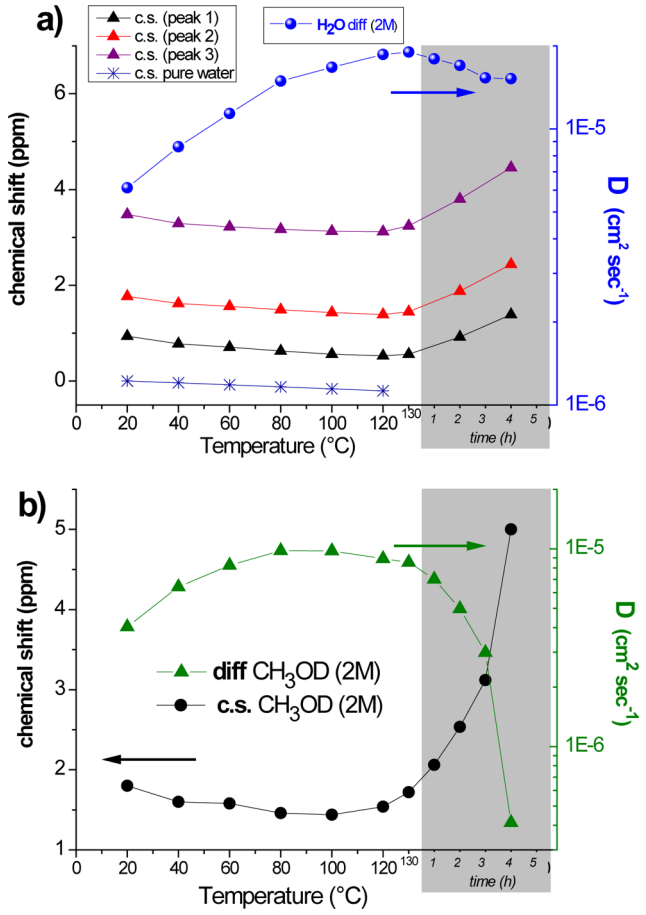

Figure 8. (a) Chemical shift versus temperature of the three Lorentzian peaks from fitting of the water spectra and the chemical shift of pure water. The graph shows also, on the right axis, the water (2M) diffusion coefficients data of Figure 5b. (b) Chemical shift versus temperature of the Lorentzian peak from fitting of the methanol spectra. The graph shows also, on the right axis, the methanol (2M) diffusion coefficients data of Figure 5b.

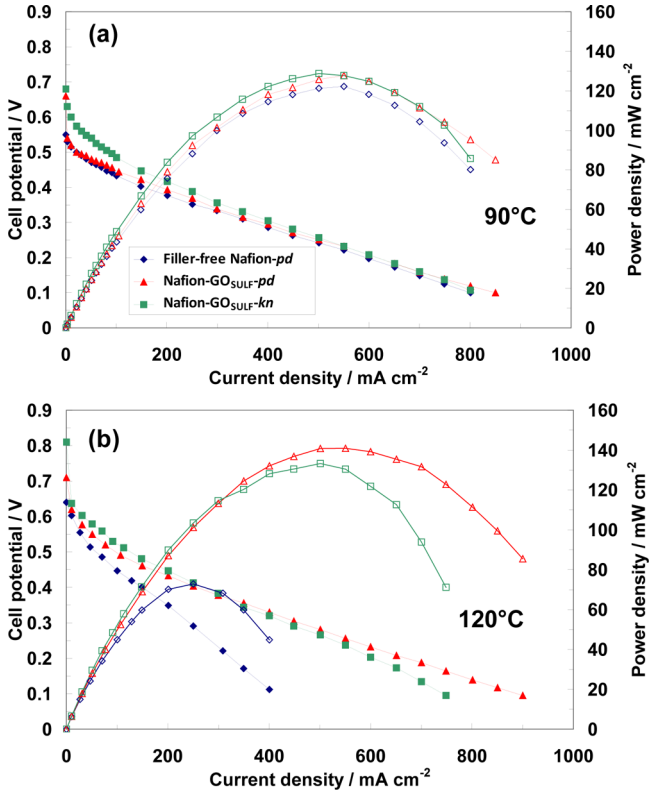

Figure 9. DMFC polarization and power density curves at 90 (a) and 120 °C (b) for the membrane-electrode assemblies equipped with composite and filler-free Nafion membranes.

properties at high temperatures of the organo-GO material dispersed in the polymeric matrix.

By going into detail, the performance at 90 °C (Figure 9a) is very similar for all the membranes, with a maximum power density close to 120 mW cm^{-2}. This value is lower than that obtained previously by our group with composite membranes using various inorganic fillers.[34,57−59] However, it is important to take into account the fact that different catalysts with a low Pt loading (1 mg cm^{-2}) on the electrodes have been used in the present analysis; also the thickness of the membranes used for the fuel-cell investigation was mostly different for the composite membranes previously reported in the literature. The most remarkable aspect in this graph is the variation of open-circuit potential (OCP) for the cells based on the different membranes. In a DMFC, the OCP is an important parameter to assess the methanol permeability of a membrane. The cell based on Nafion/GO_{SULF}-kn membrane showed a higher OCP (close to 0.7 V, taking into account the low thickness of the membrane used) and a lower polarization at low current densities compared with the other cells. In fact, Nafion/GO_{SULF}-pd membrane shows a comparable OCP value (>0.65 V), but the polarization losses at low current density are much more abrupt. Finally, the filler-free Nafion-based MEA shows a very low OCP (0.55 V). This result is a clear indication of the blocking effect toward methanol crossover of both composite membranes but with particular effectiveness for that one prepared by knife, as also evidenced from NMR methanol diffusion data, likely due to an increase in the tortuosity pathway.

Increasing the temperature to 120 °C (Figure 9b), as already said before, dehydration produced an increase in cell resistance with a consequent decrease in the performance for the filler-free Nafion membrane. A slight increase in power density is recorded with the GO-filler under these conditions, confirming the higher water affinity of these membranes, as shown by NMR experiments. The OCP and the potential at low current densities is higher for the cell equipped with Nafion/GO_{SULF}-kn membrane, confirming also at high temperatures the blocking effect of the well-distributed particles toward methanol permeation through an increase in the tortuosity pathway. Yet a slight increase in the cell resistance was observed for the MEA based on this membrane, as envisaged by the large slope of the $j-V$ curve. In fact, the maximum power density was reached with the membrane prepared by casting (Nafion/GO_{SULF}-pd), due to a good compromise between conductivity and methanol blocking effect. This result is perfectly in agreement with the diffusion data observed previously: higher water diffusion and retention of the membrane prepared by Petri dish ensure a lower resistance of the membrane (thus the possibility to produce high current density in a fuel cell), in particular at temperature over 100 °C, whereas a larger tortuosity effect of the kn-membrane produces a lower methanol crossover (thus high OCP and low potential losses at low current density). Thus, depending on the operating conditions selected for the DMFC stack (high voltage or high

dx.doi.org/10.1021/jp5080779 | J. Phys. Chem. C 2014, 118, 24357−24368

power), the most suitable preparation procedure for this kind of composite membranes may be applied.

4. CONCLUSIONS

Tailored organo-modified GO nanolayers bearing sulfonated functional groups were tested as nanoadditives for the creation of Nafion nanocomposite membranes in PEMFCs (HTFC and DMFC). Completely exfoliated Nafion nanocomposites were prepared by intercalation method, and a procedure to attempt some preferential orientation of the graphene nanoplatelets in the polymer matrix has been experienced. All of the experimental data (NMR, electrochemical, and microscopies) suggest that a simple casting procedure by film-casting procedure developed by film applicator produces a composite membrane in which the exfoliated lamellae of GO are distributed more regularly with a possible preferential orientation parallel to the film surface. This membrane evidences a significant reduction of the diffusion of methanol, and, however, a high mobility of the water at high temperatures is still guaranteed. Electrochemical experiments confirmed blocking effect toward methanol crossover of both the composites with respect to the filler-free Nafion due to an increase in the tortuosity pathway and demonstrated a marked extension of the operating temperature range of a DMFC toward high temperatures.

■ ASSOCIATED CONTENT

Supporting Information

TEM images obtained on the Naf/GO_{SULF}-kn and Naf/GO_{SULF}-pd composites membranes are shown in Figure S1. Figure S2 shows the Gaussian peak fitting procedure performed on SEM images recorded at various magnification (from 3000× to 12 000×) on Naf/GO_{SULF}-kn membranes. This material is available free of charge via the Internet at http://pubs.acs.org.

■ AUTHOR INFORMATION

Corresponding Author

*E-mail: isabella.nicotera@unical.it. Tel: +39-0984-493379. Fax: +39-0984-492044.

Notes

The authors declare no competing financial interest.

■ ACKNOWLEDGMENTS

This work was realized with the financial support of the Italian Ministry of Education, Universities and Research (Project: PRIN 2011, NAMED-PEM).

■ REFERENCES

(1) Novoselov, K. S.; Geim, K.; Morozov, S. V.; Jiang, D.; Zhang, Y.; Dubonos, S. V.; Grigorieva, I. V.; Firsov, A. A. Electric Field Effect in Atomically Thin Carbon Films. *Science* **2004**, *306*, 666−669.

(2) Geim, A. K.; Novoselov, K. S. The Rise of Graphene. *Nat. Mater.* **2007**, *6*, 183−191.

(3) Wu, J.; Pisula, W.; Müllen, K. Graphenes as Potential Material for Electronics. *Chem. Rev.* **2007**, *107*, 718−774.

(4) Balandin, A. A.; Ghosh, S.; Bao, W.; Calizo, I.; Teweldebrhan, D.; Miao, F.; Lau, C. N. Superior Thermal Conductivity of Single-Layer Graphene. *Nano Lett.* **2008**, *8*, 902−907.

(5) Kim, K. S.; Zhao, Y.; Jang, H.; Lee, S. Y.; Kim, J. M.; Kim, K. S.; Ahn, J.-H.; Kim, P.; Choi, J.-Y.; Hong, B. H. Large-Scale Pattern Growth of Graphene Films for Stretchable Transparent Electrodes. *Nature* **2009**, *457*, 706−710.

(6) Bae, S.; Kim, H.; Lee, Y.; Xu, X.; Park, J.-S.; Zheng, Y.; Balakrishnan, J.; Lei, T.; Kim, H. R.; Song, Y. Il; et al. Roll-to-Roll Production of 30-Inch Graphene Films for Transparent Electrodes. *Nat. Nanotechnol.* **2010**, *5*, 574−578.

(7) Tombros, N.; Jozsa, C.; Popinciuc, M.; Jonkman, H. T.; van Wees, B. J. Electronic Spin Transport and Spin Precession in Single Graphene Layers at Room Temperature. *Nature* **2007**, *448*, 571−574.

(8) Stankovich, S.; Dikin, D. a; Dommett, G. H. B.; Kohlhaas, K. M.; Zimney, E. J.; Stach, E. a; Piner, R. D.; Nguyen, S. T.; Ruoff, R. S. Graphene-Based Composite Materials. *Nature* **2006**, *442*, 282−286.

(9) Brey, L.; Fertig, H. Electronic States of Graphene Nanoribbons Studied with the Dirac Equation. *Phys. Rev. B* **2006**, *73*, 235411.

(10) Schedin, F.; Geim, a K.; Morozov, S. V.; Hill, E. W.; Blake, P.; Katsnelson, M. I.; Novoselov, K. S. Detection of Individual Gas Molecules Adsorbed on Graphene. *Nat. Mater.* **2007**, *6*, 652−655.

(11) Verdejo, R.; Barroso-Bujans, F.; Rodriguez-Perez, M. A.; Antonio de Saja, J.; Lopez-Manchado, M. A. Functionalized Graphene Sheet Filled Silicone Foam Nanocomposites. *J. Mater. Chem.* **2008**, *18*, 2221.

(12) Segal, M. Selling Graphene by the Ton. *Nat. Nanotechnol.* **2009**, *4*, 612−614.

(13) Brodie, B. C. Sur le poids atomique du graphite. *Ann. Chim. Phys.* **1860**, *59*, 466−472.

(14) Staudenmaier, L. Method of preparation of graphite-acid. *Ber. Dtsch. Chem. Ges.* **1898**, *31*, 1481−1499.

(15) Hummers, W. S.; Offeman, R. E. Preparation of Graphitic Oxide. *J. Am. Chem. Soc.* **1958**, *80*, 1339−1339.

(16) Bourlinos, A. B.; Gournis, D.; Petridis, D.; Szabo, T.; Szeri, A.; Dékány, I. Graphite Oxide: Chemical Reduction to Graphite and Surface Modification with Primary Aliphatic Amines and Amino Acids. *Langmuir* **2003**, *19*, 6050−6055.

(17) Dreyer, D. R.; Park, S.; Bielawski, C. W.; Ruoff, R. S. The Chemistry of Graphene Oxide. *Chem. Soc. Rev.* **2010**, *39*, 228−240.

(18) Bissessur, R.; Liu, P. K. Y.; Scully, S. F. Intercalation of Polypyrrole into Graphite Oxide. *Synth. Met.* **2006**, *156*, 1023−1027.

(19) Meng, N.; Zhang, S.; Zhou, N.; Shen, J. Biopolymer-Modified Graphite Oxide Nanocomposite Films Based on Benzalkonium Chloride-Heparin Intercalated in Graphite Oxide. *Nanotechnology* **2010**, *21*, 185101.

(20) Hagenmuller, P. Intercalation Chemistry and Chemical Bonding. *J. Phys. Chem. Solids* **1998**, *59*, 503−506.

(21) Shao, Y.; Wang, J.; Wu, H.; Liu, J.; Aksay, I. A.; Lin, Y. Graphene Based Electrochemical Sensors and Biosensors:A Review. *Electroanalysis* **2010**, *22*, 1027−1036.

(22) Wang, Y.; Shi, Z.; Huang, Y.; Ma, Y.; Wang, C.; Chen, M.; Chen, V. Supercapacitor Devices Based on Graphene Materials. *J. Phys. Chem. C* **2009**, *113*, 13103−13107.

(23) Chen, W.; Duan, L.; Zhu, D. Adsorption of Polar and Nonpolar Organic Chemicals to Carbon Nanotubes. *Environ. Sci. Technol.* **2007**, *41*, 8295−8300.

(24) Wang, L.; Lee, K.; Sun, Y.-Y.; Lucking, V.; Chen, Z.; Zhao, J. J.; Zhang, S. B. Graphene Oxide as an Ideal Substrate for Hydrogen Storage. *ACS Nano* **2009**, *3*, 2995−3000.

(25) Guo, J.; Wang, R.; Tjiu, W. W.; Pan, J.; Liu, T. Synthesis of Fe nanoparticles@graphene composites for environmental applications. *J. Hazard. Mater.* **2012**, *225−226*, 63−73.

(26) Jin, Z.; Lomeda, J. R.; Price, B. K.; Lu, W.; Zhu, Y.; Tour, J. M. Mechanically Assisted Exfoliation and Functionalization of Thermally Converted Graphene Sheets. *Chem. Mater.* **2009**, *21*, 3045−3047.

(27) Paul, D. R.; Robeson, L. M. Polymer nanotechnology: Nanocomposites. *Polymer* **2008**, *49*, 3187−3204.

(28) Kuilla, T.; Bhadra, S.; Yao, D.; Kim, N. H.; Bose, S.; Lee, J. H. Recent advances in graphene based polymer composites. *Prog. Polym. Sci.* **2010**, *35*, 1350−1375.

(29) Potts, J. R.; Dreyer, D. R.; Bielawski, C. W.; Ruoff, R. S. Graphene-based polymer nanocomposites. *Polymer* **2011**, *52*, 5−25.

(30) Cleghorn, S. J. C.; Ren, X.; Springer, T. E.; Wilson, M. S.; Zawodzinski, C.; Zawodzinski, T. A.; Gottesfeld, S. Pem fuel cells for

transportation and stationary power generation applications. *Int. J. Hydr. Ener.* **1997**, *22*, 1137−1144.
(31) Ren, X.; Zelenay, P.; Thomas, S.; Davey, J.; Gottesfeld, S. Recent advances in direct methanol fuel cells at Los Alamos National Laboratory. *J. Power Sources* **2000**, *86*, 111.
(32) Enotiadis, A.; Angjeli, K.; Baldino, N.; Nicotera, I.; Dimitrios, G. Graphene-Based Nafion Nanocomposite Membranes: Enhanced Proton Transport and Water Retention by Novel Organo-functionalized Graphene Oxide Nanosheets. *Small* **2012**, *8*, 3338−3349.
(33) Arico, A. S.; Baglio, V.; Antonucci, V.; Nicotera, I.; Oliviero, C.; Coppola, L.; Antonucci, P. L. An NMR and SAXS investigation of DMFC composite recast Nafion membranes containing ceramic fillers. *J. Membr. Sci.* **2006**, *270*, 221−227.
(34) Nicotera, I.; Angjeli, K.; Coppola, L.; Aricò, A. S.; Baglio, V. NMR and Electrochemical Investigation of the Transport Properties of Methanol and Water in Nafion and Clay-Nanocomposites Membranes for DMFCs. *Membranes* **2012**, *2*, 325−345.
(35) Nicotera, I.; Enotiadis, A.; Angjeli, K.; Coppola, L.; Gournis, D. Evaluation of smectite clays as nanofillers for the synthesis of nanocomposite polymer electrolytes for fuel cell applications. *Int. J. Hydr. Ener.* **2012**, *37*, 6236−6245.
(36) Nicotera, I.; Enotiadis, A.; Angjeli, K.; Coppola, L.; Ranieri, G. A.; Gournis, D. Effective Improvement of Water-Retention in Nanocomposite Membranes Using Novel Organo-Modified Clays as Fillers for High Temperature PEMFCs. *J. Phys. Chem. B* **2011**, *115*, 9087−9097.
(37) Staudenmaier, L. Verfahren zur Darstellung der Graphitsäure. *Ber. Dtsch. Chem. Ges.* **1898**, *31*, 1481.
(38) Stergiou, D. V.; Diamanti, E. K.; Gournis, D.; Prodromidis, M. I. Comparative study of different types of graphenes as electrocatalysts for ascorbic acid. *Electrochem. Commun.* **2010**, *12*, 1307−1309.
(39) Liu, Z. Q. Scale space approach to directional analysis of images. *Appl. Opt.* **1991**, *30*, 1369−1373.
(40) Stejskal, E. O.; Tanner, J. E. Spin Diffusion Measurements: Spin Echoes in the Presence of a Time-Dependent Field Gradient. *J. Chem. Phys.* **1965**, *42*, 288−292.
(41) James, P. J.; Antognozzi, M.; Tamayo, J.; McMaster, T. J.; Newton, J. M.; Miles, M. J. Interpretation of contrast in tapping mode AFM and shear force microscopy. A study of Nafion. *Langmuir* **2001**, *17*, 349−360.
(42) Baglio, V.; Stassi, A.; Matera, F. V.; Di Blasi, A.; Antonucci, V.; Aricò, A. S. Optimization of properties and operating parameters of a passive DMFC mini-stack at ambient temperature. *J. Power Sources* **2008**, *180*, 797−802.
(43) Gengler, R. Y. N.; Veligura, A.; Enotiadis, A.; Diamanti, E. K.; Gournis, D.; Jozsa, C.; van Wees, B. J.; Rudolf, P. Large-yield preparation of high-electronic-quality graphene by a langmuir-schaefer approach. *Small* **2010**, *6*, 35−39.
(44) Yang, H. F.; Shan, C. S.; Li, F. H.; Han, D. X.; Zhang, Q. X.; Niu, L. Covalent functionalization of polydisperse chemically-converted graphene sheets with amine-terminated ionic liquid. *Chem. Commun.* **2009**, 3880−3882.
(45) Bourlinos, A. B.; Gournis, D.; Petridis, D.; Szabó, T.; Szeri, A.; Dékány, I. Graphite oxide: Chemical reduction to graphite and surface modification with primary aliphatic amines and amino acids. *Langmuir* **2003**, *19*, 6050−6055.
(46) Stankovich, S.; Dikin, D. A.; Piner, R. D.; Kohlhaas, K. A.; Kleinhammes, A.; Jia, Y.; Wu, Y.; Nguyen, S. T.; Ruoff, R. S. Synthesis of graphene-based nanosheets via chemical reduction of exfoliated graphite oxide. *Carbon* **2007**, *45*, 1558−1565.
(47) Mauritz, K. A.; Moore, R. B. State of understanding of Nafion. *Chem. Rev.* **2004**, *104*, 4535−4585.
(48) Bussian, D. A.; O'Dea, J. R.; Metiu, H.; Buratto, S. K. Nanoscale current imaging of the conducting channels in proton exchange membrane fuel cells. *Nano Lett.* **2007**, *7*, 227−232.
(49) He, Q.; Kusoglu, A.; Lucas, I. T.; Clar, K.; Weber, A. Z.; Kostecki, R. Correlating humidity-dependent ionically conductive surface area with transport phenomena in proton-exchange membranes. *J. Phys. Chem. B* **2011**, *115*, 11650−11657.
(50) James, P. J.; Antognozzi, M.; Tamayo, J.; McMaster, T. J.; Newton, J. M.; Miles, M. J. Interpretation of contrast in tapping mode AFM and shear force microscopy. A study of Nafion. *Langmuir* **2001**, *17*, 349−360.
(51) James, P. J.; Elliot, J. A.; McMaster, T. J.; Newton, J. M.; Elliott, A. M. S.; Hanna, S.; Miles, M. J. Hydration of Nafion studied by AFM and X-ray scattering. *J. Mater. Sci.* **2000**, *35*, 5111−5119.
(52) Scipioni, R.; Gazzoli, D.; Teocoli, F.; Palumbo, O.; Paolone, A.; Ibris, N.; Brutti, S.; Navarra, M. A. Preparation and characterization of nanocomposite polymer membranes containing functionalized SnO_2 additives. *Membranes* **2014**, *4*, 123−142.
(53) Brutti, S.; Scipioni, R.; Navarra, M. A.; Panero, S.; Allodi, V.; Giarola, M.; Mariotto, G. SnO_2-Nafion® nanocomposite polymer electrolytes for fuel cell applications. *Int. J. Nanotechnol.* **2014**, *11*, 882−896.
(54) Hallberg, F.; Vernersson, T.; Pettersson, E. T.; Dvinskikh, S. V.; Lindbergh, G.; Furó, I. Electrokinetic transport of water and methanol in Nafion membranes as observed by NMR spectroscopy. *Electrochim. Acta* **2010**, *55*, 3542−3549.
(55) Ji, X.; Yan, L.; Zhu, S.; Zhang, L.; Lu, W. Methanol distribution and electroosmotic drag in hydrated poly(perfluorosulfonic) acid membrane. *J. Phys. Chem. B* **2008**, *112*, 15616−15627.
(56) Adamovic, I.; Gordon, M. S. Methanol-water mixtures: A microsolvation study using the effective fragment potential method. *J. Phys. Chem. A* **2006**, *110*, 10267−10273.
(57) Baglio, V.; Di Blasi, A.; Aricò, A. S.; Antonucci, V.; Antonucci, P. L.; Nannetti, F.; Tricoli, V. Investigation of the electrochemical behaviour in DMFCs of chabazite and clinoptilolite-based composite membranes. *Electrochim. Acta* **2005**, *50*, 5181−5188.
(58) Baglio, V.; Di Blasi, A.; Aricò, A. S.; Antonucci, V.; Antonucci, P. L.; Trakanprapai, C.; Esposito, V.; Licoccia, S.; Traversa, E. Composite mesoporous titania nafion-based membranes for direct methanol fuel cell operation at high temperature. *J. Electrochem. Soc.* **2005**, *152*, A1373−A1377.
(59) Staiti, P.; Aricò, A. S.; Baglio, V.; Lufrano, F.; Passalacqua, E.; Antonucci, V. Hybrid Nafion-silica membranes doped with heteropolyacids for application in direct methanol fuel cells. *Solid State Ionics* **2001**, *145*, 101−107.

Sulfonated Graphene Oxide Platelets in Nafion Nanocomposite Membrane: Advantages for Application in Direct Methanol Fuel Cells

I. Nicotera[1]*, C. Simari[1], L. Coppola[1], P. Zygouri[2], D. Gournis[2], S. Brutti[3], F.D. Minuto[4], A.S. Aricò[5], D. Sebastian[5], V. Baglio[5]

[1] Dept. of Chemistry and Chemical Technologies, University of Calabria, 87036-Rende (CS), Italy;
[2] Dept. of Material Science and Engineering, University of Ioannina, 45110-Ioannina, Greece;
[3] Dept. of Science, University of Basilicata, V.le Ateneo Lucano 10, 85100 Potenza (PZ), Italy;
[4] Dept. of Physics, University of Calabria, 87036-Rende (CS), Italy;
[5] CNR-ITAE Institute, via Salita S. Lucia sopra Contesse, 5, 98126 Messina, Italy;

* Author to whom correspondence should be addressed; E-Mail: isabella.nicotera@unical.it;
Tel.: +39-0984-493379; Fax: +39-0984-492044.

SUPPORTING INFORMATION

Figure S1 shows some TEM images obtained on the Naf/GO_{SULF}-*kn* and Naf/GO_{SULF}-*pd* composites membranes. Both membranes show an highly homogeneous morphology in cross section without evident alteration in the light/dark random patterning from the surface to the bulk. The different patterning between the *pd* and *kn* membrane cannot be easily put into correlation to real alteration of the morphology as it may also depend on the effective local thickness of the membrane that may vary across the sample. Unfortunately due to the chemical homogeneity of the graphene filler with the polymer backbone it was not possible to detect clear evidence of the graphene sheets in the cross section for both membranes. One may speculate that this is an indirect evidence of the highly homogenous incorporation of the filler within the membranes without apparent clustering of the graphene sheets.

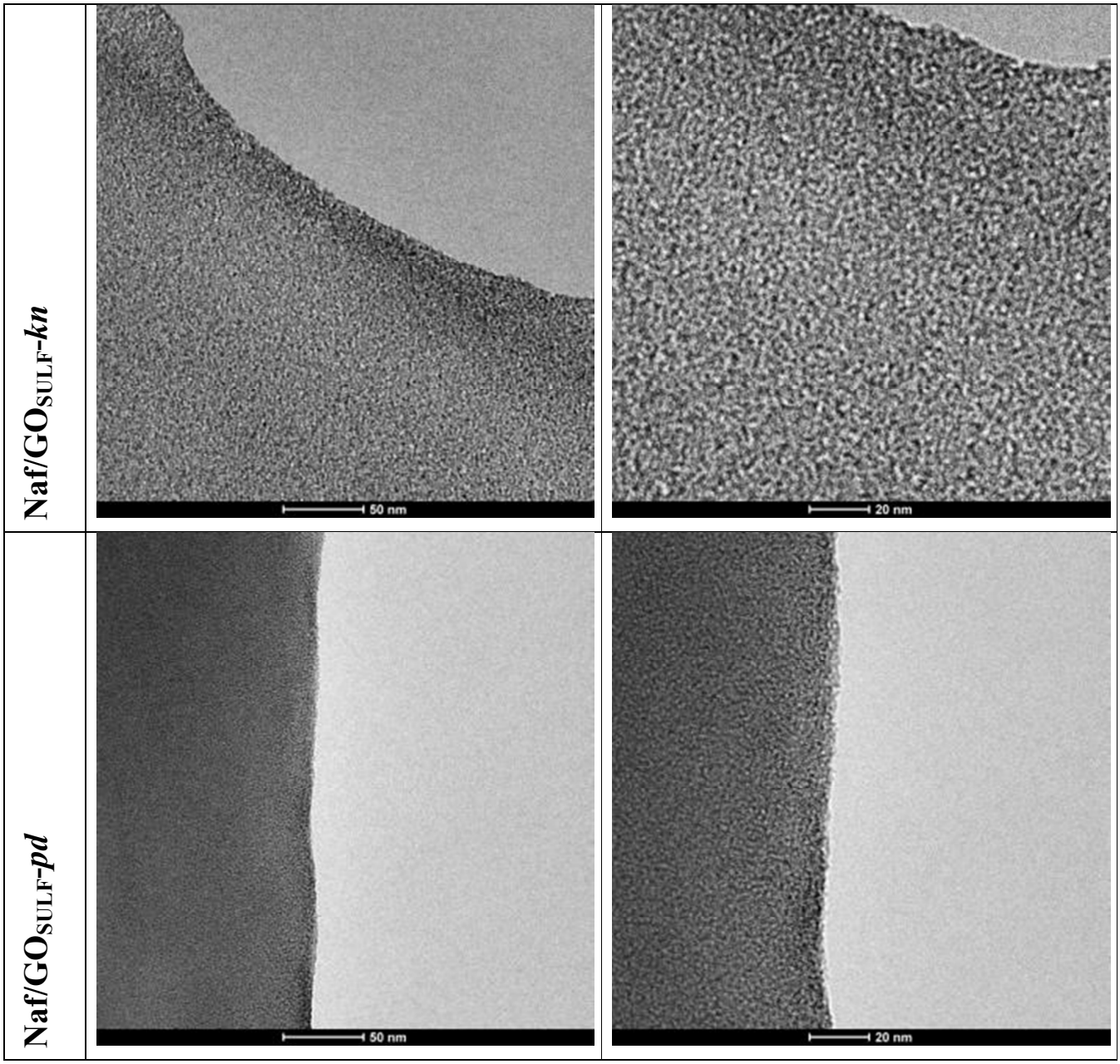

Figure S1. *TEM images of the cross sections of Naf/GO$_{SULF}$-kn and Naf/GO$_{SULF}$-pd membranes.*

Figure S2 shows the Gaussian peak fitting procedure performed on images recorded at various magnification (from 3,000x to 12,000x) on Naf/GO$_{SULF}$-kn membranes. As we can see, we obtain analogous results with average orientation close to 0° and FWHM dispersion of 35°.

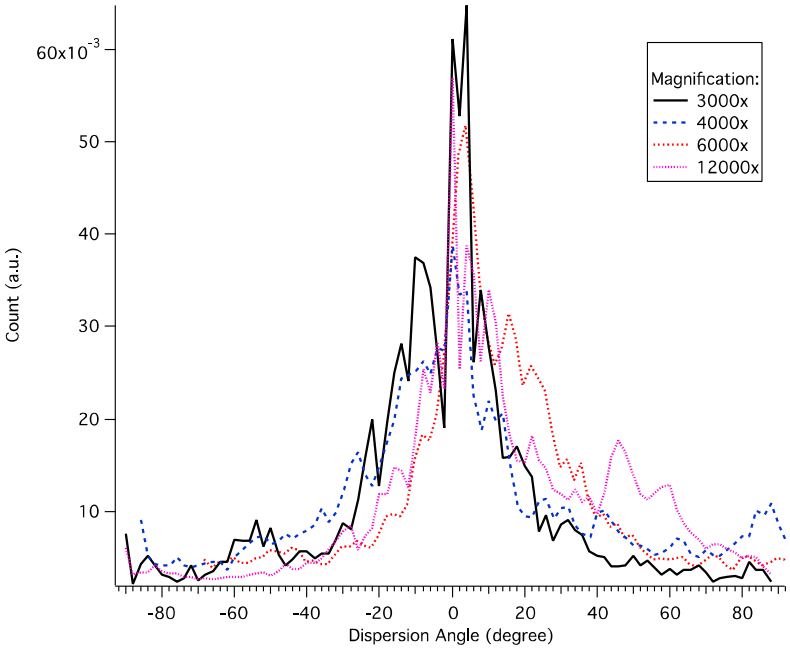

Figure S2. *Gaussian peak fitting analysis performed on images recorded at various magnification (from 3,000x to 12,000x) on Naf/GO$_{SULF}$-kn membranes.*

V

"Methanol and proton transport in layered double hydroxide and smectite clay-based composites: influence on the electrochemical behavior of direct methanol fuel cells at intermediate temperatures"

Journal of Solid State Electrochemistry, ***2014****, 19 (7), pp 2053-2061*

J Solid State Electrochem (2015) 19:2053–2061
DOI 10.1007/s10008-014-2701-y

ORIGINAL PAPER

Methanol and proton transport in layered double hydroxide and smectite clay-based composites: influence on the electrochemical behavior of direct methanol fuel cells at intermediate temperatures

I. Nicotera · V. Kosma · C. Simari · C. D'Urso · A. S. Aricò · V. Baglio

Received: 21 November 2014 / Revised: 1 December 2014 / Accepted: 2 December 2014 / Published online: 14 December 2014

Abstract Composite membranes based on Nafion with the inclusion of cationic and anionic nanoclays, Laponite, and layered double hydroxide (LDH), respectively, were used to increase the operating temperature of a direct methanol fuel cell (DMFC). The electrochemical behavior of the hybrid nanocomposites was investigated in a single cell at different temperatures (from 90 to 110 °C), and the results were compared with those obtained on the filler-free Nafion membrane. Cell resistance measurements showed a significant improvement of the water retention capability at intermediate temperature for the composite membranes, in particular the LDH-based one. This feature was investigated and explained by a thorough NMR study (diffusometry, relaxometry, and ^{1}H spectral analysis) on the different membranes. Furthermore, the dispersion of 2D plate-like nanolayers in the polymeric matrix demonstrates to be a physical barrier, considerably reducing the methanol mobility through an increase of the tortuosity of the diffusional paths of methanol molecules.

Keywords LDH · Nanoclay · Composite Nafion membrane · Methanol crossover · Direct methanol fuel cell · NMR

I. Nicotera (✉) · V. Kosma · C. Simari
Department of Chemistry and Chemical Technologies, University of Calabria, via P. Bucci, Cubo 14D, 87036 Rende, CS, Italy
e-mail: isabella.nicotera@unical.it

C. D'Urso · A. S. Aricò · V. Baglio (✉)
Istituto di Tecnologie Avanzate per l'Energia "Nicola Giordano" (CNR), via Salita S. Lucia sopra Contesse 5, 98126 Messina, Italy
e-mail: baglio@itae.cnr.it

Introduction

Direct methanol fuel cells (DMFCs) are good candidates as power sources for portable and auxiliary power unit applications [1–3]. They combine the merits of polymer electrolyte fuel cells fueled by hydrogen with the advantages of a liquid fuel, such as easy handling and high energy density. Despite these advantages, there are still technical barriers to overcome for their widespread commercialization [4], such as methanol crossover from anode to cathode through the proton exchange membrane. Methanol crossover not only leads to reduced fuel efficiency because of the direct chemical oxidation of methanol in the cathodic compartment but also decreases the fuel cell performance due to the presence of a mixed potential at the cathode [5–9].

In recent years, increasing interest has been devoted to the development of high-temperature DMFC systems. DMFC operation at elevated temperatures increases both methanol oxidation and oxygen reduction kinetics and simplifies water and thermal management. In this regard, composite membranes with the filler exhibiting strong affinity towards water molecules were largely used [10–15]. In fact, the role of an organic-inorganic filler is to improve the water retention in the membrane, allowing an increase of fuel cell operation temperature due to a suitable conductivity, and to reduce methanol crossover, through an increased tortuosity effect [16].

For this purpose, based on our recent experience [17, 18], this work focuses on two types of hydrophilic lamellar-type nanomaterials, for the development of hybrid membranes with improved suitable ionic conductivity, stability up to 130 °C, and low methanol crossover.

In general, the dispersion of 2D plate-like layers in a polymeric matrix is expected to behave as a physical barrier to the transport of a fluid, as well as to gain thermal stability and mechanical properties of the nanocomposite [17–19].

Additionally, the hydration properties of membranes are key characteristics that can influence fuel cell performance; therefore, appropriate highly hydrophilic nanoadditives may improve the water retention properties of the final composite membranes under low humidity conditions.

The proton exchange membrane fuel cell (PEMFC) architecture, as well as materials and components, has some common features for both hydrogen and methanol operation. Therefore, it could be attractive to develop a unique membrane product for a flexible use in terms of fuels (hydrogen, methanol, reformate gas), operating temperature, and application.

In the present work, two types of nanoclays, one cationic and one anionic, were studied as fillers in the Nafion polymer matrix: Laponite (synthetic clay) and layered double hydroxide (LDH).

Laponite is a smectite clay [20, 21] consisting of 1-nm-thick aluminosilicate platelets with a fixed negative charge, and neutrality is obtained, for example, by hydrated cations present in the galleries. The intercalation process in these systems is equivalent to ion exchange. The charge on the layers affects many fundamental properties of the clays, including water holding, cation fixation, swelling ability, cation exchange capacity (CEC), and high specific surface area. Laponite is characterized by a CEC=48 M equiv./100 g and a particle size of 20 nm.

Layered double hydroxides (LDHs) have the typical chemical structure of anionic (or hydrotalcite type) clay which can be represented as $[M_{1-x}^{(II)}\ M_x^{(III)}\ (OH)_2]^{x+}[A^{m-}_{x/m}]\cdot nH_2O$, where $M^{(II)}$ is a divalent metal cation (Mg, Mn, Fe, Co, Ni, Cu, Zn, Ga) and $M^{(III)}$ is a trivalent metal cation (Al, Cr, Mn, Fe, Co, Ni, and La). A^{m-} represents an interlayer anion, such as CO_3^{2-}, OH^-, NO_3^-, SO_4^{2-}, or ClO_4^- [22–24].

The anionic clay structure is similar to brucite $Mg(OH)_2$ and crystallizes in a layer-type lattice. Such LDHs have an anion exchange capacity, which depends on the isomorphic substitution of Mg^{2+} ions by higher-valence cations. As a consequence, the layers have a fixed positive charge and neutrality is obtained, for example, by hydrated anions present in the galleries [25]. For this work, Mg^{2+}/Al^{3+} LDH, with 2:1 metal ratio and NO_3^- anion, was chosen as nanoadditive. . The schematic representation of these two materials is shown in Scheme 1.

Composite membranes, indicated as Naf-Lap and Naf-LDH, were synthesized by a solution intercalation synthetic procedure with 3 % of filler loading with respect to the polymer. These membranes were investigated in direct methanol fuel cells operating at intermediate temperatures and low oxygen partial pressure (1.5 bar abs.) in order to assess the suitability of these electrolytes under conditions close to practical applications for auxiliary power units (APUs).

Greater understanding of the mechanism of ion and molecular transport in the membranes was achieved by NMR methods; ^1H spectral analysis; self-diffusion coefficients of water and methanol, measured using pulse gradient stimulated-echo (PGSTE); and spin-lattice relaxation times (T_1) of both solvents were also measured as a function of temperature.

Experimental

Materials, synthesis of nanofillers, and preparation of the composite membranes

Laponite (Lap) is a synthetic trioctahedral hectorite, produced by Laporte Industries Ltd with CEC 48 M equiv./100 g clay and a particle size of 20 nm.

LDH has been synthesized by co-precipitation of Mg^{2+} and Al^{3+} salts, in the presence of the appropriate anion, using an aqueous solution of sodium hydroxide. The Mg^{2+}:Al^{3+} metal ratio was adjusted to 2:1. In particular, in 100 mL of aqueous solution containing $Mg(NO_3)_2\cdot 6H_2O$ (0.05 mol), $Al(NO_3)_3\cdot 9H_2O$ (0.025 mol) and $NaNO_3$ (0.045 mol) were added dropwise in an aqueous solution of NaOH (2.5 M) until the

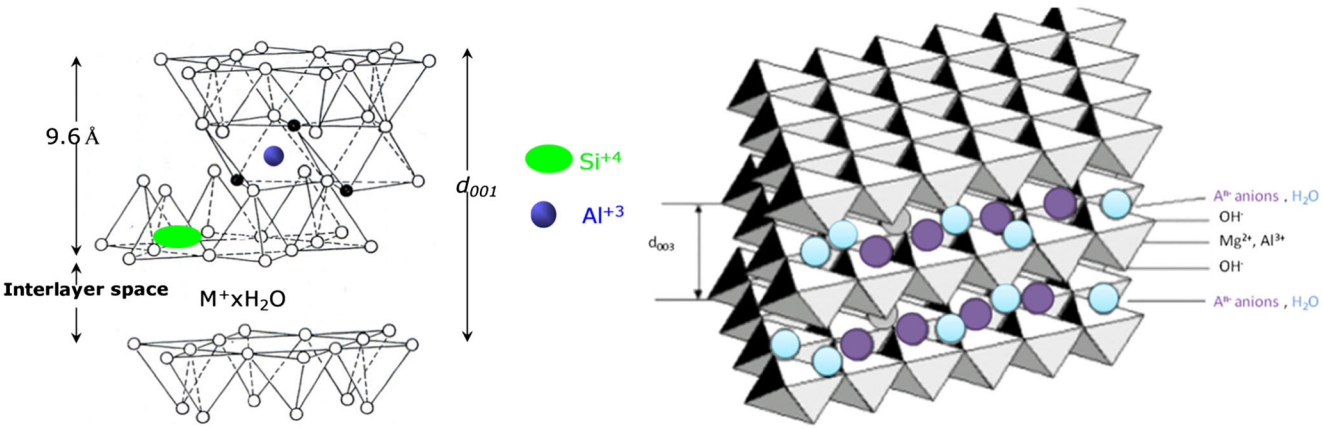

Scheme 1 Schematic representations of a smectite clay (*on the left*) and LDH (*on the right*) structures

pH value reached 10. The resulting precipitated LDH material was stirred at 60 °C for 24 h and subsequently separated by centrifugation, washed several times with water, and finally dried in air at 80 °C for 24 h. The synthetic procedure was done under nitrogen gas flow and using decarbonated-deionized water.

Concerning the Nafion-based composite membranes, we have used Nafion solution (20 wt% in a mixture of lower aliphatic alcohols and water) purchased from Aldrich, and the preparation procedure was a solving casting method followed by acid activation, as described elsewhere [18, 20].

Characterization techniques

NMR measurements were performed on a Bruker NMR spectrometer AVANCE 300 Wide Bore working at 300 MHz on ^{1}H. The employed probe was a Diff30 Z-diffusion 30 G/cm/A multinuclear with substitutable RF inserts. Spectra were obtained by transforming the resulting free-induction decay (FID) of single $\pi/2$ pulse sequences. The pulsed field gradient stimulated-echo (PFG-STE) method [26] was used to measure self-diffusion coefficients of water and methanol. This sequence is generally applied when the materials are characterized by a transverse relaxation time (T_2) considerably shorter than the longitudinal relaxation time (T_1). The sequence consists of three 90° RF pulses ($\pi/2$-τ_1-$\pi/2$-τ_m-$\pi/2$) and two gradient pulses that are applied after the first and the third RF pulses, respectively. The echo is found at time $\tau=2\tau_1+\tau_m$. Following the usual notation, the magnetic field pulses have magnitude g, duration δ, and time delay Δ. The attenuation of the echo amplitude is represented by the following (Eq. 1):

$$I(2\tau_1+\tau_m)=\frac{1}{2}I_0\exp\left[-\frac{\tau_m}{T_1}-\frac{2\tau_1}{T_2}-(yg\delta)^2D\left(\Delta-\frac{\delta}{3}\right)\right] \quad (1)$$

where D is the self-diffusion coefficient. The used experimental parameters were: gradient pulse length δ=1 ms, time delay Δ=10 ms, and the gradient amplitude ranging between 100-800 G cm^{-1}. The uncertainty in the self-diffusion measurements is ~3 %.

Longitudinal relaxation times (T_1) of water and methanol were measured by the inversion-recovery sequence (π-τ-$\pi/2$). Both self-diffusion and T_1 measurements were conducted by increasing the temperature step by step from 20 to 130 °C, with steps of 20 °C, and leaving the sample to equilibrate for about 15 min. All the membranes, before the NMR measurements, were dried in an oven, weighed, and then immersed in distilled water and in various aqueous methanol solutions at room temperature. Upon being removed from the water, they were quickly blotted dry with a paper tissue (to eliminate most of the free surface liquid). The uptake value was determined using a microbalance and recorded as described in the following formula (Eq. 2):

$$\text{up}\,\% = \left[\left(m_{\text{wet}}-m_{\text{dry}}\right)/m_{\text{dry}}\right]\cdot 100 \quad (2)$$

At this point, the membranes were loaded into a 5-mm NMR Pyrex tube.

For the electrochemical characterization, the electrodes used were composed of commercial gas-diffusion layer-coated carbon cloth at the anode (HT-ELAT, E-TEK) and cathode (LT-ELAT, E-TEK). Unsupported Pt-Ru (Johnson-Matthey) and Pt (Johnson-Matthey) catalysts were mixed under ultrasounds with 15 wt% Nafion ionomer (Ion Power, 5 wt% solution) and deposited by a doctor blade technique onto the diffusion media for the anode and cathode, respectively. A Pt loading of 2 mg cm^{-2} was used for all electrodes, both anodes and cathodes. The membrane-electrode assemblies (MEAs) were obtained by a hot pressing method between electrodes and the different membranes (filler-free recast Nafion, Lap-Nafion, and LDH-Nafion composite membranes) at 130 °C and 30 kg cm^{-2} for 1.5 min. The thickness of the membranes used for the electrochemical tests was ca. 50 μm (±5 μm). The MEAs were tested in a 5-cm^2 single cell (Fuel Cell Tech., Inc.) connected with an Autolab PGSTAT 302 Potentiostat/Galvanostat (Metrohm) equipped with a frequency response analyzer (FRA). The impedance measurements were performed under potentiostatic control in a frequency range between 20 kHz and 0.1 Hz by frequency sweeping in the single sine mode. The amplitude of the sinusoidal excitation signal was 0.01 V. The series resistance was determined from the high frequency intercept on the real axis in the Nyquist plot. A 2-M methanol solution was fed at the anode under atmospheric pressure with a flow rate of 3 mL min^{-1}, whereas oxygen was fed at the cathode at a flow rate of 100 mL min^{-1} under 1.5 bar absolute of pressure. The performance of each MEA was measured under steady-state conditions in the temperature range 90–110 °C.

Results and discussion

Fuel cell characterization

The electrochemical investigation was carried out in a single cell by recording the ac-impedance spectra at different temperatures (from 60 to 110 °C) and the polarization curves in the temperature range from 90 to 110 °C, feeding a 2-M methanol solution at the anode and oxygen at the cathode. The cell resistance (corresponding to the high frequency intercept on the real axis in the Nyquist plot, not shown) was plotted as a function of temperature as shown in Fig. 1. The

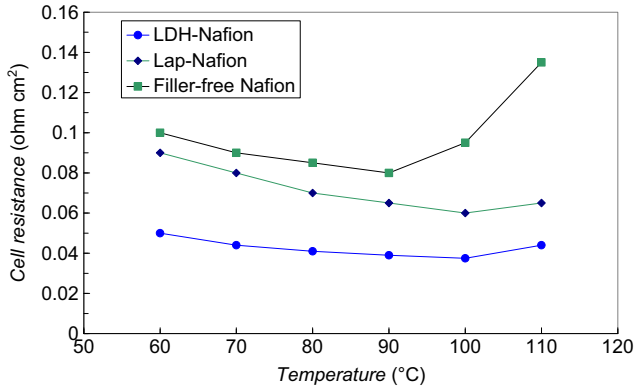

Fig. 1 Cell resistance values as a function of temperature for the cells equipped with the different membranes

decrease of cell resistance in the composite membranes indicates an increase of water retention caused by the fillers, in particular for the LDH-based membrane. This produces a higher performance of the MEAs based on the nanocomposites compared to the filler-free membrane, as can be observed in Fig. 2, where the polarization and power density curves obtained with the different membranes at 90 and 110 °C, respectively, are reported. The maximum power density of the DMFC equipped with the composite membranes slightly increases as the temperature increases, although the methanol solution is fed under atmospheric pressure and thus subjected to evaporation, whereas a decrease in performance is recorded for the filler-free membrane-based MEA. This latter phenomenon is due to water evaporation at a temperature higher than 100 °C and the significant increase of cell resistance at 110 °C (see Fig. 1). Instead, the MEAs equipped with the composite membranes show a smooth increase of cell resistance passing from 100 to 110 °C indicating a larger water retention capability.

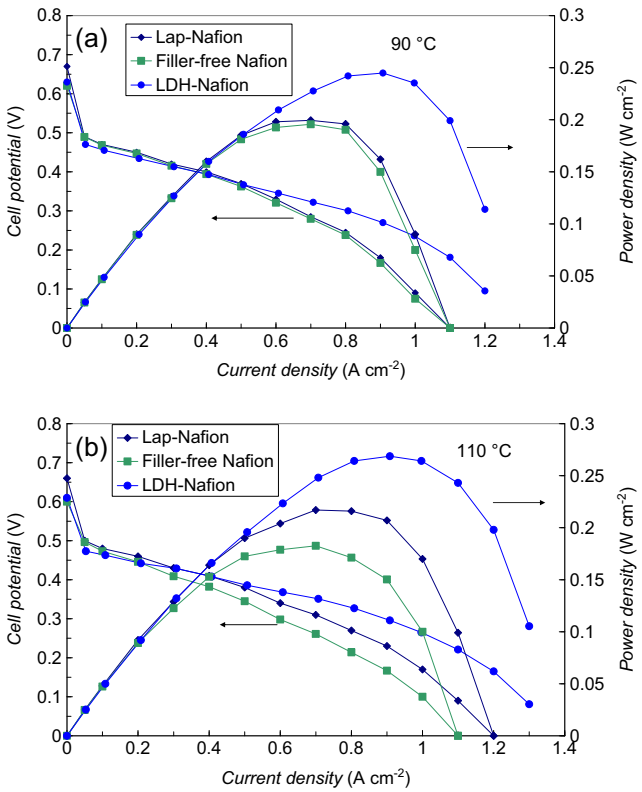

Fig. 2 DMFC polarization and power density curves at 90 (**a**) and 110 °C (**b**) for various membrane-electrode assemblies equipped with composite and filler-free membranes

The lowest cell resistance observed for the LDH-based membrane produced a power density of 250 mW cm^{-2} at 90 °C (Fig. 2a), which makes these materials quite promising, in comparison to other electrolytes reported in the literature [27], for a practical application. Increasing the temperature up to 110 °C (Fig. 2b), under atmospheric pressure at the anode, the water evaporation produces, as expected, a drastic decreasing of the performance for the filler-free Nafion membrane, whereas an increasing of power density is recorded with both nanocomposites under the same conditions. On the other hand, noteworthy is the performance achieved by using the Naf-LDH hybrid membrane as the electrolyte, confirming the exceptional water affinity of this nanoadditive and its beneficial effect when dispersed in the Nafion polymeric matrix, as confirmed by NMR experiments (see next paragraph).

NMR investigation

NMR spectroscopy was used in this work in order to investigate the transport properties of water and methanol confined in the membranes through measurements of the self-diffusion coefficients, spin-lattice relaxation times, and the ^{1}H spectra. An accurate comparison of the data obtained on the two composites and on the Nafion recast membrane was achieved, with the aim to understand the influence of the nanoadditives both on the polymer matrix structure and on the mobility of the solvent molecules (water and methanol).

For this study, the membranes have been equilibrated in aqueous methanol solution at the concentration of 2 M, so as to have the same conditions used in the DMFC cell. Furthermore, in order to discriminate in the NMR spectrum, the proton signals coming from water or methanol, we used deuterated molecules, i.e., a mixture of CH_3OD/D_2O and CD_3OD/H_2O for measuring methanol and water, respectively. In fact, although, for liquid mixtures, it is possible to differentiate spectroscopically (through their chemical shift) the methyl and hydroxyl protons when the solvents are confined inside nanometric pores, such as in polymeric membranes, the ^{1}H spectrum linewidth is huge; therefore, it is not possible to distinguish methanol and water. In support of this, Fig. 3a, b shows the temperature evolution (from 20 up to 130 °C) of the proton spectra acquired on the Naf-LDH composite membrane, swollen in 2 M methanol solution (CH_3OD/D_2O and CD_3OD/H_2O for methanol and water, respectively). Clearly, both signals are very wide, implying that both water and

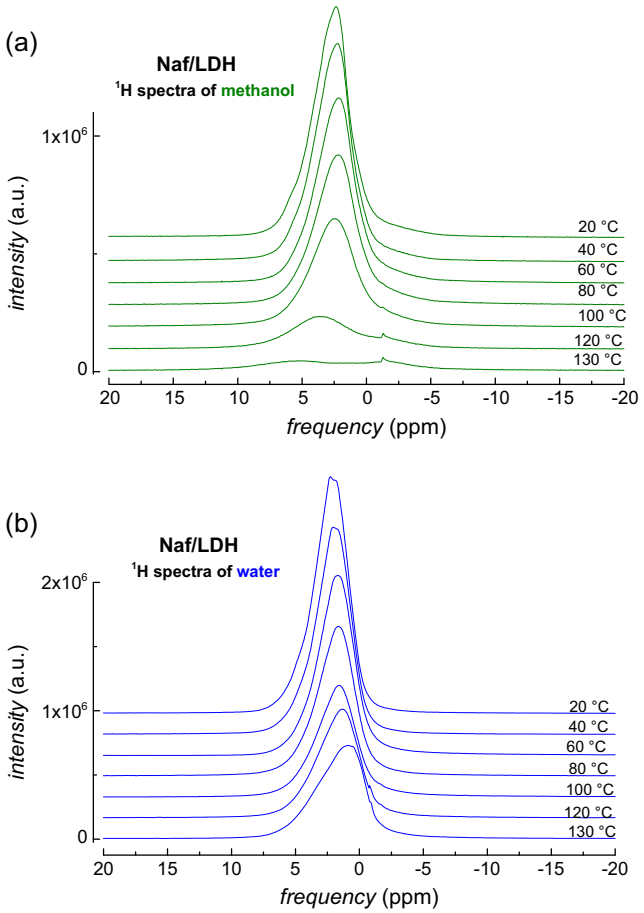

Fig. 3 Temperature evolution of ^{1}H spectra of methanol (**a**) and water (**b**) in Nafion-LDH composite swollen in 2 M methanol solution. The spectra were referenced, setting methyl protons and pure water at 0 ppm, respectively

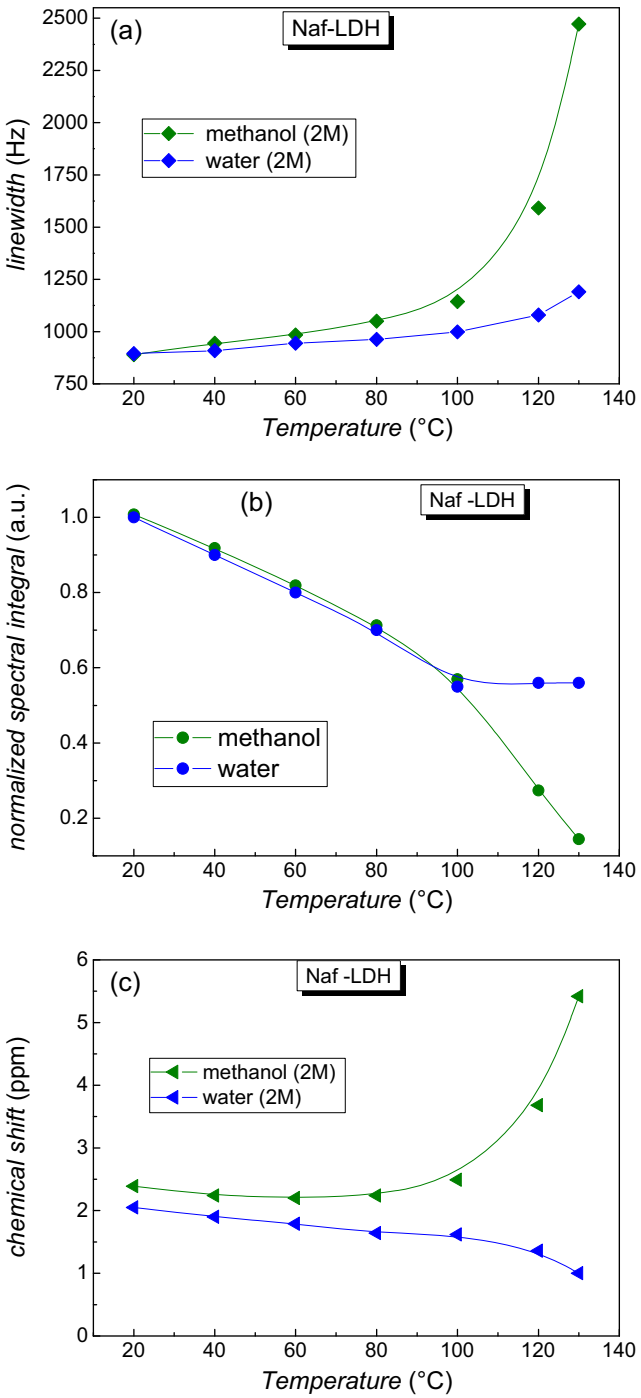

Fig. 4 **a** Linewidth versus temperature, **b** normalized spectral integral versus temperature, and **c** chemical shift versus temperature of the water and methanol ^{1}H spectra acquired on Nafion-LDH composite swollen in 2 M methanol solution

methanol molecules are nanoconfined and strongly interacting with both the functional groups of the polymer (sulfonic groups) and of the LDH. The information derived from this proton spectral study is summarized in the three plots of Fig. 4: linewidth (a), spectral integral (b), and chemical shift (c), versus temperature, respectively. The linewidths of the ^{1}H signals of methanol and water (Fig. 4a) are very similar at temperatures below 80 °C and ranged between 800 and 1000 Hz. At higher temperatures, they start to diverge, and at 130 °C, the methanol spectrum has a linewidth almost double that of the water signal. This outcome, together with the variation of the peak area in temperature, shown in Fig. 4b, demonstrates that above 100 °C, a large amount of methanol evaporates from the membrane, and the remaining is strongly interacting with the polymer, promoting line broadening. On the contrary, the water signal decreases linearly with the temperature due to evaporation, but in the range 100–130 °C, it remains constant and the linewidth slightly varies. This suggests that a considerable amount of water remains in the composite, and the "strength" of interactions between the water molecules and the functional groups of the system (polymer/filler) does not exhibit a substantial change from low to high temperatures.

To better understand the above, we need to take into account how water and methanol molecules are distributed inside the ionic pores of Nafion, specifically the micro-phase separation in which methanol-rich and water-rich spatial

domains are created [8, 28]. In the first ones, methanol molecules, because of their high chemical affinity with fluorine atoms, are aggregated close to the main polymeric backbone; hence, there is not any strong complexation of protons. Whereas in the latter domains, the water molecules are involved in the hydration shells of the SO^{3-} groups and of the "active" groups on the LDH layers; therefore, they fill the volume of pores. This can explain why the Naf-LDH composite appears to have good proton conduction at high temperatures, as we have seen from the electrochemical results and as will be confirmed from the diffusion measurements.

Also, the chemical shift plot (Fig. 4c) leads to the same conclusions; there is a strong dependence of the chemical shift from the temperature for methanol with a rough variation of the chemical environment at 100 °C, which can be attributed to the strong evaporation from the membrane. Additionally, as we have described elsewhere [17], there is an extraordinary relationship and an unpredicted symmetry between chemical shift behavior with the temperature and that of the self-diffusion coefficients, which will be shown below; increase of the chemical shift of the proton signals corresponds to an analogous and proportional reduction of diffusion.

On the other hand, the Laponite composite has shown a slightly different spectral behavior. We report in Fig. 5, in the same order of Fig. 4, linewidth (a), spectral integral (b), and chemical shift (c), versus temperature, respectively, for this second composite membrane. While the linewidth shows approximately the same behavior as seen above, integrals and chemical shift plots are quite different. As regards the temperature evolution of the integrals of the water and methanol signals, both decrease with the same slope; hence, both show a similar rate of evaporation from the membrane at least up to 130 °C. Also, the trend of the chemical shifts proceeds in parallel during the heating, without any strong variation as we have seen in the case of methanol inside the Naf-LDH composite. Additionally, the effect on the chemical shift, in particular for methanol, of the intercalated ions in the interlayer space of the two fillers is evident; in the anionic clay's composite, the ^{1}H signal is centered at ~2.5 ppm, while in the cationic clay's composite, the chemical shift is at ~4 ppm.

These differences observed between LDH and Laponite are likely connected to the chemical nature of the two clays; that is, in the case of LDH, favorable electrostatic interactions should occur between the negatively charged Nafion and the positively charged LDH platelets, whereas electrostatic repulsions are expected with the negatively charged Lap mineral. This could have an impact on the nanomorphology of the hydrophilic pores in the polymer matrix and should be taken into account in the analysis of the diffusional and motion data reported below.

Figure 6 displays the diffusion coefficients of water and methanol (in 2-M solutions) measured in the swollen membranes of Naf-LDH and Naf-Lap, respectively, in the range of

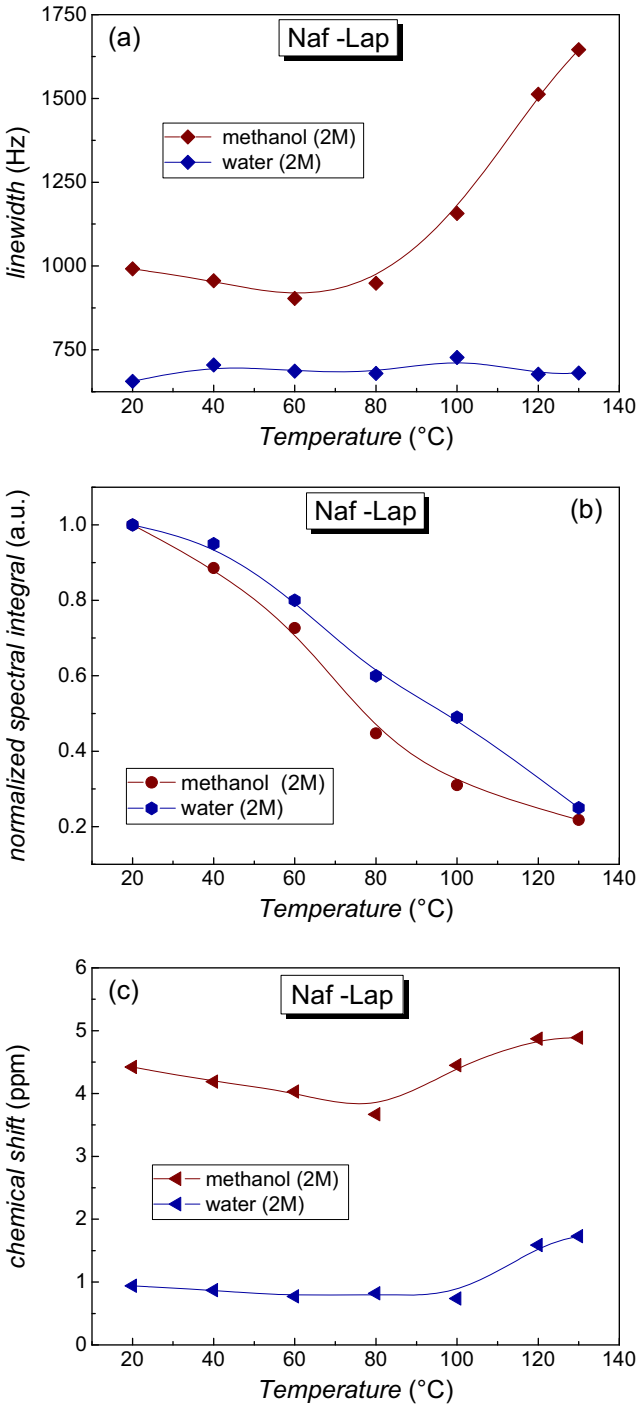

Fig. 5 **a** Linewidth versus temperature, **b** normalized spectral integral versus temperature, and **c** chemical shift versus temperature of the water and methanol ^{1}H spectra acquired on Nafion-Lap composite swollen in 2 M methanol solution

20–130 °C. The first important parameter to be considered before analyzing these data is the very dissimilar solution uptakes of the two nanocomposite membranes, 75 wt% for the LDH and only 30 wt% for the Lap.

Although the Naf-LDH membrane displays a very high uptake, the dimensional variations of the membrane, meaning

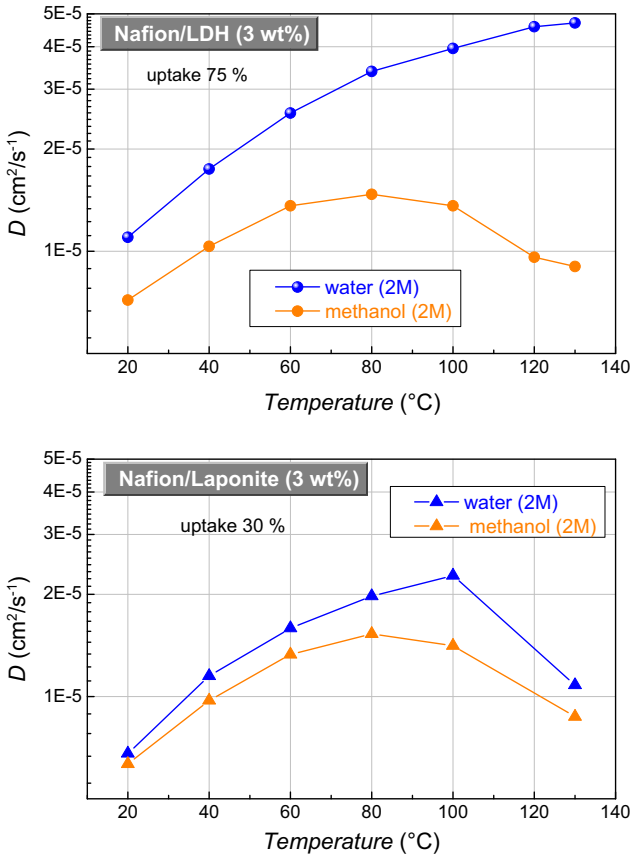

Fig. 6 Self-diffusion coefficients of water and methanol in 2 M solution confined in Nafion-LDH and Nafion-Lap nanocomposite membranes, from 20 up to 130 °C. In the graphs are reported also the solution uptakes (wt%)

the thickness and the area percentage variation upon swelling in the aqueous solution, are practically similar to that observed in the filler-free Nafion. This implies that most of the water is distributed in the interlayer space of the anionic clay, and that is why the observed water diffusion is not too much higher than the other composite, as in principle it was expected.

But, what is interesting to highlight is that, in both composite membranes, water diffusion is always higher than methanol in the whole investigated temperature range, proving the beneficial blocking effect of the nanoparticles dispersed in the polymer. This, absolutely, cannot be interpreted as something trivial if someone considers that for the filler-free Nafion, membrane swelled in 2 M solution (Fig. 7); above circa 60–80 °C, the diffusion coefficients of methanol are higher than those of water. This phenomenon can be attributed to the different distributions of methanol and water molecules in the hydrophilic domains of the polymer membrane, as we have already described above, where the acidic proton of methanol is only weakly bonded to the $-SO_3H$ groups, whereas water is strongly coordinated and it is therefore less mobile. This result is evidently responsible for the methanol crossover observed in the direct methanol fuel cell operation.

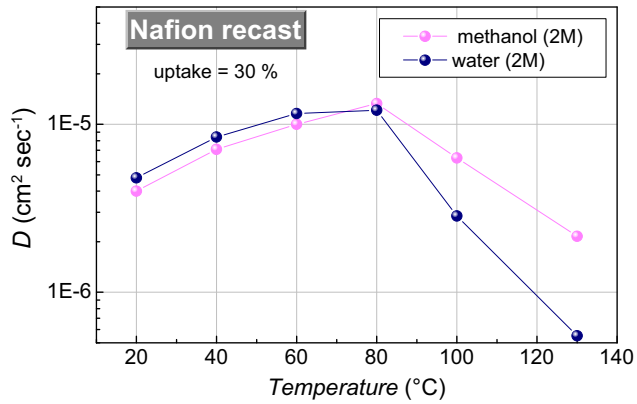

Fig. 7 Self-diffusion coefficients of water and methanol in 2 M solution confined in filler-free Nafion membrane, from 20 up to 130 °C. In the graph is also reported the solution uptake (wt%)

What appears to be reasonably safe to state is that the presence of layered nanoadditives, dispersed in polymeric matrix, is able to considerably reduce the methanol mobility through an increase of the tortuosity of the diffusional paths of both water and methanol molecules. However, differently to the case of recast Nafion, the water diffusion in the composite membrane remains large likely due to the good retention

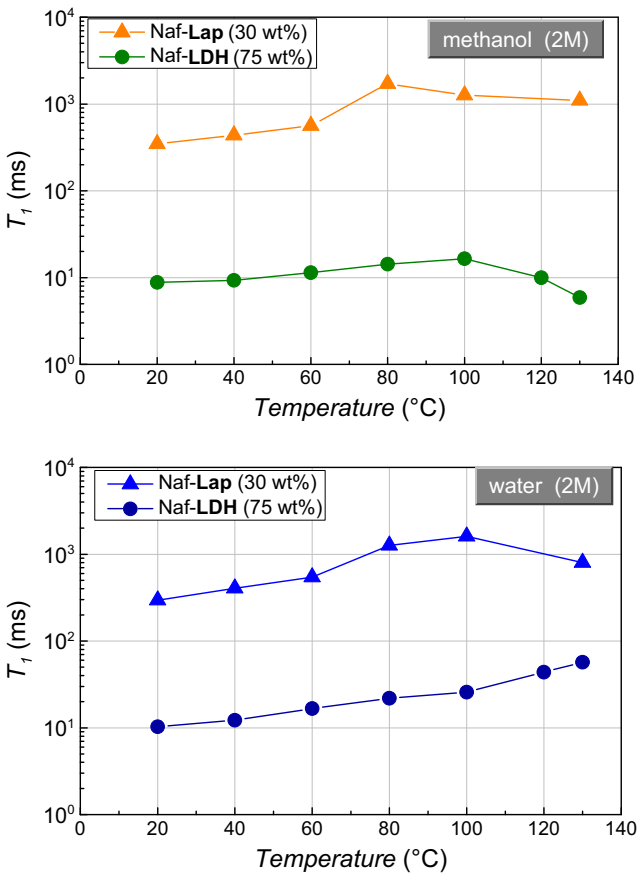

Fig. 8 Longitudinal relaxation times (T_1) of the methanol (**a**) and water (**b**) measured in the LDH and Lap composite membranes swollen in 2 M solution, in the temperature range from 20 up to 130 °C

capacity of the filler which favors the proton transport by the Grotthuss-type mechanism.

On the other hand, a certain difference between the two additives emerges here as also under operative cell. The anionic clay, likely due to the higher hydrophilicity and retention capability with respect to cationic clay, is able to maintain a very high water diffusion at high temperatures. The superior retention capability of the LDH has also been raised from the spectral analysis.

However, by considering also the electrostatic interactions between clay materials and polymer, discussed above, the favorable interactions in the LDH composite likely are able to originate a "bridge" for the proton diffusion, which instead is lacking with the Laponite clay. This aspect is supported also from the proton relaxation time measurements shown here.

The NMR longitudinal (or spin-lattice) relaxation times (T_1) give us a further information about the proton transport properties in these two composites. In Fig. 8, the temperature variation of T_1 of (a) methanol and (b) water is shown for the two nanocomposites.

T_1 values, compared to diffusion, reflect more localized motions including both translation and rotation on a time scale comparable to the reciprocal of the NMR angular frequency (~1 ns); therefore, higher T_1 values suggest more facile molecular motions.

Concerning the methanol (Fig. 8a), the relaxation times in the Lap membrane are much higher than those of the LDH membrane in all the temperature ranges investigated although the solution uptake of the LDH membrane is almost double. This implies a greater local mobility (more degrees of freedom) of the molecules in the Lap sample, which in turn can be attributed to the structuring and nanomorphology of the composite.

More interesting is the plot of the water (Fig. 8b) where, contrary to what we would expect in the light of data of diffusion, T_1 values in the LDH composite are shorter (almost two orders of magnitude) than those in the Lap composite. This provides additional evidence for stronger interactions between the water molecules and the LDH material and supports our interpretation of the diffusion data above, i.e., the proton mobility at very high temperatures is ensured prevalently through the Grotthuss mechanism which foresees a strong interaction between the H^+ ions and the lattice.

Conclusions

Composite membranes based on anionic (LDH) and cationic (Laponite) nanoclays have been demonstrated to be capable of extending the operating temperature of a DMFC without any significant loss of conductivity. This is due to the strong interactions between the water molecules and the clay materials, as shown by the NMR experiments and confirmed by the polarization curves recorded at intermediate temperature (110 °C) under low humidification conditions. Remarkable results were obtained on the composite Nafion-LDH. This hygroscopic filler demonstrates a very high water retention capability at high temperatures (most of the water molecules are distributed in the interlayer space of the material); therefore, the proton mobility is ensured together with a reduced methanol diffusion due to a blocking effect of the layered nanoparticles dispersed in the polymer. This would be a potential solution to some of the drawbacks presently affecting DMFCs as well as reformate-fuelled polymer electrolytes (PEMFCs), reducing electrode poisoning by adsorbed CO molecules, increasing both methanol oxidation and oxygen reduction kinetics, and simplifying water and thermal management.

Acknowledgments The authors acknowledge the financial support of PRIN 2010–2011 project "Advanced nanocomposite membranes and innovative electro-catalysts for durable polymer electrolyte membrane fuel cells (NAMED-PEM)."

References

1. Wasmus S, Kuver A (1999) Methanol oxidation and direct methanol fuel cells: a selective review. J Electroanal Chem 461:14–31
2. Aricò AS, Srinivasan S, Antonucci V (2001) DMFCs: from fundamental aspects to technology development. Fuel Cells 1:133–161
3. Aricò A, Baglio V, Antonucci V (2009) Direct methanol fuel cells: history, status and perspectives. In: Liu H, Zhang J (eds) Electrocatalysis of direct methanol fuel cells. WILEY-VCH Verlag GmbH & Co KGaA, Weinheim
4. Han J, Liu H (2007) Real time measurements of methanol crossover in a DMFC. J Power Sources 164(1):166–173
5. Paik Y, Kim S-S, Han OH (2008) Methanol behavior in direct methanol fuel cells. Angew Chem Int Ed 47(1):94–96
6. Neburchilov V, Martin J, Wang H, Zhang J (2007) A review of polymer electrolyte membranes for direct methanol fuel cells. J Power Sources 169(2):221–238
7. Kreuer KD (2001) On the development of proton conducting polymer membranes for hydrogen and methanol fuel cells. J Memb Sci 185(1):29–39
8. Ji X, Yan L, Zhu S, Zhang L, Lu W (2008) Methanol distribution and electroosmotic drag in hydrated poly(perfluorosulfonic) acid membrane. J Phys Chem B 112(49):15616–15627
9. Cui Z, Xing W, Liu C, Liao J, Zhang H (2003) Novel proton conducting composite membranes for direct methanol fuel cell. J Power Sources 57(1):24–29
10. Baglio V, Aricò AS, Antonucci V et al (2006) An NMR spectroscopic study of water and methanol transport properties in DMFC composite membranes: influence on the electrochemical behaviour. J Power Sources 163(1):52–55
11. Enotiadis A, Angjeli K, Baldino N, Nicotera I, Gournis D (2012) Graphene-based nafion nanocomposite membranes: enhanced proton transport and water retention by novel organo-functionalized graphene oxide nanosheets. Small 8(21):3338–3349
12. Yang C, Srinivasan S, Bocarsly AB, Tulyani S, Benziger JB (2003) A comparison of physical properties and fuel cell performance of

Nafion and zirconium phosphate/Nafion composite membranes. J Memb Sci 237(1–2):29–35
13. Alberti G, Casciola M, Capitani D (2007) Novel Nafion–zirconium phosphate nanocomposite membranes with enhanced stability of proton conductivity at medium temperature and high relative humidity. Electrochim Acta 52(28):8125–8132
14. Choi BG, Hong J, Park YC et al (2011) Innovative polymer nanocomposite electrolytes: nanoscale manipulation of ion channels by functionalized graphenes. ACS Nano 5(6):5167–5174
15. Baglio V, Aricò AS, Di Blasi A et al (2005) Nafion–TiO_2 composite DMFC membranes: physico-chemical properties of the filler versus electrochemical performance. Electrochim Acta 50(5):1241–1246
16. Aricò AS, Baglio V, Antonucci V et al (2006) An NMR and SAXS investigation of DMFC composite recast Nafion membranes containing ceramic fillers. J Memb Sci 270(1–2):221–227
17. Nicotera I, Simari C, Coppola L et al (2014) Sulfonated graphene oxide platelets in nafion nanocomposite membrane: advantages for application in direct methanol fuel cells. J Phys Chem C 118:24357–24368
18. Nicotera I, Enotiadis A, Angjeli K, Coppola L, Ranieri GA, Gournis D (2011) Effective improvement of water-retention in nanocomposite membranes using novel organo-modified clays as fillers for high temperature PEMFCs. J Phys Chem B 115(29):9087–9097
19. Song M-K, Park S-B, Kim Y-T, Kim K-H, Min S-K, Rhee H-W (2004) Characterization of polymer-layered silicate nanocomposite membranes for direct methanol fuel cells. Electrochim Acta 50(2–3): 639–643
20. Nicotera I, Enotiadis A, Angjeli K, Coppola L, Gournis D (2012) Evaluation of smectite clays as nanofillers for the synthesis of nanocomposite polymer electrolytes for fuel cell applications. Int J Hydrogen Energy 37(7):6236–6245
21. Herrera Alonso R, Estevez L, Lian H, Kelarakis A, Giannelis EP (2009) Nafion–clay nanocomposite membranes: morphology and properties. Polymer 50(11):2402–2410
22. Miyata S (1983) Anion-exchange properties of hydrotalcite-like compounds. In: *Clay and Clay Minerals* :305–311
23. Rives V (2001) Layered double hydroxides: present and future. Nova Publisher, New York
24. Cavani F, Trifir F, Vaccari A (1991) Hydrotalcite-type anionic clays: preparation, properties and applications. Catal Today 11(2): 173–301
25. Kim N, Kim Y, Tsotsis T, Sahimi M (2005) Atomistic simulation of nanoporous layered double hydroxide materials and their properties. I. Structural modeling. J Chem Phys 122(21):214713
26. Tanner JE (1970) Use of the stimulated echo in NMR diffusion studies. J Chem Phys 52(9):2523–2526
27. Lufrano F, Baglio V, Staiti P, Antonucci V, Aricò AS (2013) Performance analysis of polymer electrolyte membranes for direct methanol fuel cells. J Power Sources 243:519–534
28. Hallberg F, Vernersson T, Pettersson ET, Dvinskikh SV, Lindbergh G, Furó I (2010) Electrokinetic transport of water and methanol in Nafion membranes as observed by NMR spectroscopy. Electrochim Acta 55(10):3542–3549

VI

"Enhancement of proton mobility and mitigation of methanol crossover in sPEEK fuel cells by an organically modified titania nanofillers"

Under revision in Journal of Solid State Electrochemistry

Enhancement of proton mobility and mitigation of methanol crossover in sPEEK fuel cells by an organically modified titania nanofillers

Catia de Bonis [1], Cataldo Simari [2], Vassiliki Kosma [2], Barbara Mecheri [1], Alessandra D'Epifanio [1], Valentina Allodi [3], Gino Mariotto [3], Sergio Brutti [4], Sophia Suarez [5], Kartik Pilar [6], Steve Greenbaum [6], Silvia Licoccia [1], Isabella Nicotera [2*]

[1] Department of Chemical Science and Technologies, University of Rome "Tor Vergata", Via della Ricerca Scientifica, 00133 Rome, Italy.
[2] Department of Chemistry and chemical Technologies, University of Calabria, Via P. Bucci, 87036 Rende (CS), Italy.
[3] Dipartimento di Informatica, Università di Verona, Strada Le Grazie 15, Verona 37134, Italy
[4] Dipartimento di Scienze, Università della Basilicata, V.le dell'Ateneo Lucano 10, Potenza 85100, Italy.
[5] Department of Physics, Brooklyn College/CUNY, Brooklyn, New York 11210, United States.
[6] Department of Physics and Astronomy, Hunter College of the City University of New York, New York, New York 10065, United States.

***** Author to whom correspondence should be addressed; E-Mail: isabella.nicotera@unical.it; Tel.: +39-0984-493379; Fax: +39-0984-492044.

Abstract

An organically functionalized titania, TiO_2-RSO_3H, was evaluated as filler in sPEEK-based composite membranes for application in high temperature direct methanol fuel cells.
The presence of propylsulfonic acid groups covalently bound onto the TiO_2 surface and the nanometric nature of the additive were analyzed by Raman spectroscopy and transmission electron microscopy, respectively.
The properties of the sPEEK/TiO_2-RSO_3H composite membranes were compared with those of the pure sPEEK membranes and those of the sPEEK/TiO_2 composite membranes containing pristine titania nanoparticles at same filler content.
Water and methanol transport properties were investigated by NMR methods, including relaxation times and self-diffusion coefficients as function of temperature (up to 130 °C), and pressure (from 0 up to 2 kbar).
The incorporation of the nanoadditivies in the sPEEK polymer demonstrates considerable effects on the morphology and stiffness of the membranes, as well as on the transport properties and barrier effect to the methanol cross-over. In particular, the functionalization by propylsulfonic acid groups promotes a higher reticulation between the polymeric chains, increasing the tortuosity of the methanol diffusional paths, so reducing the molecular diffusion, while the proton mobility increases being favored by the Grotthus-type mechanism.
Conductivity measurements point out that the filler surface functionalization avoids the reduction of the overall proton conduction of the electrolyte due to the embedding of the low-conducting TiO_2.
Finally, remarkable improvements were found when using the sPEEK/TiO_2-RSO_3H composite membrane as electrolyte in a DMFC, in terms of reduced methanol crossover and higher current and power density delivered.

Keywords: SPEEK, nanocomposites, organically functionalized titania nanoparticles, NMR, DMFC.

Introduction

Direct methanol fuel cells (DMFC) have been recently considered as promising power sources for portable and transport applications due to the their high efficiency, high power density, compact cell design and low emissions [1, 2]. Proton exchange membranes (PEMs) are the key component of a DMFC: PEMs transfer protons from the anode to the cathode and act as a barrier to fuel crossover. However, technological barriers still need to be overcome for DMFC large-scale commercialization. In particular methanol permeation through the membrane [3] is one of most serious limitations since it leads to reduced energy conversion efficiency due to the direct chemical oxidation of methanol in the cathodic half-cell, and also causes cell operational failures.

Nafion is the most widely used membrane material due to its high thermal stability and good mechanical and electrochemical properties. However, it suffers a high permeability to methanol as well as a major decrease of the proton conductivity above 80 °C at low humidity, thus limiting its use in DMFCs. Several strategies have been developed to improve the performance of Nafion membranes, including the preparation of composites containing organically modified inorganic fillers, such as silica, clays, graphene oxide [4-7].

The use of an organic-inorganic hybrid compound offers the possibility to combine in a single material both the thermal and mechanical stability of inorganic component and the characteristic chemical of organic functional groups. The grafting of proper organic moieties on the filler surface reduces the proton conductivity loss of Nafion induced by the embedding of low-conducting inorganic particles. Furthermore, the enhanced interfacial compatibly with polymeric matrix can favor the uniform dispersion of filler at a nanometric scale level.

Recently, we have investigated composite membranes containing organically-modified titanium oxides thus obtaining electrolytes with better mechanical properties, reduced methanol permeability and higher power density delivered in a DMFC, with respect to unfilled Nafion membranes [8,9].

In the present work, this filler was tested in a polymer different from Nafion and a more comprehensive NMR analysis was performed, including the use of hydrostatic pressure as a thermodynamic variable, in order to understand the effect of the filler on the transport properties of methanol and water, and its interaction with this polymer. In fact, the use of hydrocarbon polymers alternative to Nafion is still one of the main targets to develop cheaper proton exchange membranes and with lower methanol permeability [10]. Aromatic main chain polymers such as poly(ether ketone), poly(phenylene sulphone), poly(ether sulphone) and poly(benzimidazoles) have been extensively studied as they are low-cost and high-performance materials that can be chemically modified to obtain proton-conducting electrolytes [11-14]. Among them, sulfonated polyetheretherketone (sPEEK) is interesting for applications in DMFCs because its microstructure

consists of narrower and less connected water filled channels compared to those of Nafion and this can help to reduce the problems related to methanol crossover and high water drag that occur in cell operative conditions [15]. The degree of sulfonation (DS) of sPEEK is a crucial parameter for its performance because the proton conductivity increases with the increment of DS, but the methanol crossover also increases, and the dimensional stability of the membrane worsens up to dissolution because of the excessive hydrophilicity of the ionomer.

Different methods have been developed to improve the proton conductivity limiting dimensional changes of sPEEK membranes, including the introduction of specific functional groups onto the ionomer backbone, and the preparation of polymer blends and organic-inorganic composites [16-19]. However, a limited attention has been focused on the investigation of the microstructural modifications of the ionomer in relation to the use of these strategies. The pristine sPEEK membrane has a distinct structuring and nanomorphology arising from self-organization of the sulfonated polymer chains into hydrophilic and hydrophobic domains. Concerning organic-inorganic composites, the embedding of inorganic component will affect the structure of water filled channels network, and hence the permeability to methanol and proton transport properties of the electrolyte [20-21].

In this work, sPEEK having DS=0.5 has been used as polymeric matrix to obtain composite membranes with adequate proton conductivity and good mechanical properties. Propylsulfonic-functionalized nanometric titania (TiO_2-RSO_3H) has been used as filler, in which aliphatic chains ending with sulfonic acid groups are covalently bound onto the oxide surface. The nanometric nature of the filler and the presence of bifunctional branches can increase the chemical-physical interactions with the polymer matrix. This is expected to favor the proton transport through the Grotthus-type mechanism, and to limit the vehicular transport mechanism, that facilitates methanol permeation through the membrane.

Fillers and membranes morphologies have been studied by transmission electron microscopy (TEM) and atomic force microscopy (AFM), respectively, and the vibrational features of the silylpropylsulfonic-functionalization on the grafted titania surfaces by Raman spectroscopy (RS).

The transport properties of water and methanol confined within the sPEEK and composite membranes have been studied by NMR methods in order to understand the molecular dynamics through direct measurement of the self-diffusion coefficients (D) and relaxation times (T_1) in a wide temperature range (25-130 °C). The goal is to evaluate how the ionic conduction is influenced by the polymeric structure and the nanofillers. Self-diffusion measurements on water and methanol have been also carried out under variable hydrostatic pressure conditions in order to probe

molecular motion and ionic diffusion processes associated with temperature-independent volume fluctuations. [22-25].

Finally, electrochemical characterization was carried out on the membranes to investigate their performance in fuel cell operative conditions. The influence of surface functionalization of the filler on proton conductivity of the membranes was probed by using ac-impedance spectroscopy. The functioning of these membranes in a real device, in terms of current and power density delivered, was tested by polarization measurements and their methanol permeability was evaluated by using linear sweep voltammetry.

Experimental Section

Materials

Polyetheretherketone (PEEK, 450 PF, MW=38,300 g/mol, 132 repeat units per mole) was purchased in powder form from Victrex. Pt (20 wt.%) and Pt/Ru (60 wt.%) black powders were supplied from Alfa Aesar. Nafion perfluorinated resin solution (5 wt.% in a mixture of lower aliphatic alcohols and water), polytetrafluoroethylene (PTFE), tetrabutylammonium hydroxide (TBAOH) and all other chemicals were purchased from Sigma-Aldrich.

Synthesis of fillers and sPEEK

Titania powder was prepared as previously described [26] to obtain the nanostructured oxide in the anatase phase with surface hydroxyl groups, such as to allow its subsequent functionalization. The surface chemistry of the oxide was investigated by X-ray photoelectron spectroscopy (XPS) and the relative peak area associated with of the oxygen species of the surface OH groups resulted to be 21% versus 73% of the peak deriving from O-Ti-O species of the framework.

The preparation of TiO_2-RSO_3H was then carried out following a two-steps synthetic pathway: *i)* introduction of mercaptopropyl moieties onto titania surface; *ii)* subsequent oxidation of the thiol groups into sulfonic acid groups to obtain propylsulfonic-functionalized titania [8]. The amount of functional groups in TiO_2-RSO_3H was determinated by CHNS/O elemental analysis and Neutron Activation Analysis (NAA) and was 2 wt.%, corresponding to 0.12 mmol/g.

SPEEK was prepared *via* aromatic electrophilic substitution following the procedure previously reported [17]. PEEK was reacted with H_2SO_4 (96%) controlling the temperature and reaction time. The degree of sulfonation of the product was evaluated by ^1H NMR and by titration and resulted to be DS=0.5.

Preparation of electrodes

The gas diffusion layer (GDL) was prepared according to the following procedure. A solution of water (4 mL), isopropyl alcohol (5.1 mL) and Vulcan XC-72R carbon black (0.25 g) was kept under magnetic stirring for 10 min and then mixed under sonication for 10 min. 29 μL of PTFE (60 wt.% in water) was added to the mixture that was kept under magnetic stirring for 10 min and mixed under sonication for 15 min. The solution was airbrushed on a carbon paper containing 30 wt.% of PTFE, until to reach a load of carbon black of 4.5 mg/cm^2. The electrode was pressed for 30 min at 90 °C under a load of 20 kg/cm^2 and put in oven at 70 °C for 30 min, at 120 °C for 30 min, at 280 °C for 15 min and at 350 °C for 30 min.

The ink of anode catalyst was prepared as follows. A slurry made of 6.7 mg of Pt/Ru powder and 61.1 μL of Nafion solution was kept under stirring for 1 hour. Then, 26.7 mg of glycerol and 3.22 mg of TBAOH were added and the mixture was stirred for 1 hour. Finally, 22 mg of glycerol was added and the solution was kept under stirring overnight.

The ink of cathode catalyst was prepared as follows. A slurry composed of 5 mg of Pt powder and 45.8 μL of Nafion solution was stirred for 1 hour. Then, 20 mg of glycerol and 2 mg of TBAOH were added and the mixture was stirred for 1 hour. Finally, 16 mg of glycerol was added and the solution was kept under stirring overnight.

The inks were distributed on the electrodes with GDL and dried overnight. The anode was prepared with a Pt/Ru loading of 4 mg/cm^2 and the cathode with a Pt loading of 1 mg/cm^2. The electrodes were pressed for 5 min at 90 °C under a load of 1 tons and treated in a standard activation procedure using H_2O_2 3 vol.% solution, 0.5 M H_2SO_4 solution and distilled water, boiling the samples for 1 h in each solution.

Preparation of Membranes

SPEEK-based composite membranes containing 10 wt.% of TiO_2 or TiO_2-RSO_3H were prepared by solution casting. In a typical procedure, sPEEK (250 mg) was dissolved in DMAc (20 mL) and the resulting solution was added to the filler/DMAc solution. The mixture was then heated to 80 °C under stirring until the volume was reduced to 5 mL, cast onto a Petri plate and heated to 80 °C overnight. Pure sPEEK membranes were also prepared. The membranes selected for polarization and methanol permeability tests had a thickness of ca. 100 μm. Before any characterization, all the membranes were treated in a standard activation procedure using 0.5 M H_2SO_4 solution and distilled water [17].

Characterization Techniques

Microscopy and Raman spectroscopy. Transmission electron microscopy (TEM) experiment was carried out on a FEI G2 20 HR-TEM equipped with a LaB_6 electron beam source, two 2D flat cameras (low resolution and high resolution) and a cold finger for cryo-TEM experiments. Sample

powders were suspended in hexane by repeated treatment in a ultrasonic bath and adsorbed on copper holey carbon film grids. TEM experiments were carried out at 200 kV electron energy and in cryo-conditions.

Atomic force microscopy (AFM) experiments were carried out by a Park AFM XE120 instrument equipped with a home-modified universal closed liquid cell to allow careful control of the RH condition upon scanning. Measurements were performed at RH = 33%. Prior to the AFM tests, membranes were fully conditioned for 30 days in a closed vessel at 33% relative humidity (RH, water vapor back pressure above a saturated aqueous $MgCl_2$ solution). The AFM study was carried out in tapping intermittent contact mode (TM). It is important to underline that phase-distance curves were carefully monitored upon imaging in order to avoid unstable regimes [27] and the rise of height artifacts in AFM topographies. Topographies and phase images were simultaneously recorded. Only phase images are reported in this communication because the membrane elastic response is highly sensitive to transitions from hydrophobic to hydrophilic domains and thus phase image is much more informative than topography. AFM images were recorded of both sides of the two membranes to highlight possible differences: three different areas were sampled on all membrane sides by recording at least 5 different magnifications in each zone. AFM images were studied analyzed by ImageJ software [28-29] in order to study the evolution of the size of the hydrophobic and hydrophilic domains. Our procedure required the analysis of at least three phase images with different magnification and the identification of more than 300 pseudo particles (hydrophobic and hydrophilic) for each. The size of the recorded particles were then analyzed by deriving for each membrane the particle size distribution and the cluster dimension mean values for both hydrophobic and hydrophilic domains.

Micro-Raman spectroscopy measurements were carried out in backscattering geometry using a single stage Horiba-Jobin Yvon spectrometer (model LABRAM HR), coupled to a He-Ne laser as excitation source (at 632.8 nm) and a notch filter for the Rayleigh line cut-off. The scattered radiation was dispersed by a diffraction grating having 600 lines/mm and detected at the spectrograph output by a multichannel detector, a CCD with 1024×256 pixels, cooled by liquid nitrogen, and with its maximum efficiency occurring in the red region. The wavenumber limit, due to the notch filter, was about 200 cm^{-1} on the low-energy side.

NMR Spectroscopy. NMR measurements were performed on a Bruker NMR spectrometer AVANCE 300 Wide Bore working at 300 MHz on ^1H. The employed probe was a Diff30 Z-diffusion 30 G/cm/A multinuclear with substitutable RF inserts. Spectra were obtained by transforming the resulting free-induction decay (FID) of single $\pi/2$ pulse sequences. The pulsed field gradient stimulated-echo (PFG-STE) method [30] was used to measure self-diffusion

coefficients. This sequence is generally applied when the materials are characterized by a transverse relaxation time (T_2) considerably shorter than longitudinal relaxation time (T_1). The sequence consists of three 90° rf pulses ($\pi/2$-τ_1-$\pi/2$-τ_m-$\pi/2$) and two gradient pulses that are applied after the first and the third rf pulses, respectively. The echo is found at time $\tau = 2\tau_1 + \tau_m$. Following the usual notation, the magnetic field gradient pulses have magnitude g, duration δ, and interpulse time delay Δ. The attenuation of the echo amplitude is represented by the following Eq. 1:

$$I(2\tau_1 + \tau_m) = \frac{1}{2} I_0 \exp\left[-\frac{\tau_m}{T_1} - \frac{2\tau_1}{T_2} - (\gamma g \delta)^2 D\left(\Delta - \frac{\delta}{3}\right)\right] \quad \text{(Eq. 1)}$$

where D is the self-diffusion coefficient. The used experimental parameters were gradient pulse length δ = 1 ms, time delay Δ =10 ms, and the gradient amplitude varied from 100 to 800 G cm^{-1}. The uncertainty in the self-diffusion measurements is ~ 3%.

Longitudinal relaxation times (T_1) of water and methanol were measured by the inversion-recovery sequence (π-τ-$\pi/2$). Both self-diffusion and T_1 measurements were conducted by increasing temperature step by step from 20 to 130 °C, with steps of 20 °C, and allowing the sample to equilibrate for about 15 min. All the membranes, before the NMR measurements, were dried in oven, weighed and then immersed in water and in aqueous methanol solutions (2 M concentration) at room temperature. Upon being removed from the water they were quickly blotted dry with a paper tissue (to eliminate most of the free surface liquid). The solvent content value was determined using a microbalance and recorded as described in the following formula (Eq. 2):

$$wu\ \% = [(m_{wet} - m_{dry}) / m_{dry}] \times 100 \quad \text{(Eq. 2)}$$

At this point the membranes were loaded into a 5 mm NMR Pyrex tube.

High pressure diffusion measurements were done on a Varian NMR spectrometer and an Oxford 300 Wide Bore magnet. A custom built Cu-Be probe was used with a Harwood Engineering high pressure pump to reach pressures of up to 2000 bar. 3M's Fluorinert FC-3283 electronic fluid was used as the hydraulic fluid to avoid hydrogen background. In order to isolate the membrane from the pressure-transmitting fluid, the samples were sealed in a polyethylene sheath. Due to the nature of the Cu-Be pressure vessel, the pulsed field gradient method cannot be used to obtain diffusion measurements [24]. Instead, the probe was lowered from the homogeneous field of the magnet into the fringe field, where the field strength was 1.9 T and the static magnetic field gradient was measured using the known self-diffusion coefficient of liquid water to be g = 30.041 T m^{-1}. Diffusion measurements were made using a Hahn spin-echo pulse sequence ($\pi/2$–τ–π–τ) [31]. Echo intensity was measured as a function of τ. The attenuation in echo intensity using the static field gradient follows Eq. 3:

$$I(2\tau) = I_o \exp\left[\frac{-2\tau}{T_2}\right] \exp\left[\frac{-2}{3}\gamma^2\tau^3 g^2 D\right] \quad \text{(Eq. 3)}$$

Heating tape around the probe and a thermocouple connected to a temperature controller allowed for temperature to be controlled simultaneously with high pressure.

Mechanical tests. Dynamic Mechanical Analysis (DMA) measurements were made with a Metravib DMA/25 equipped with a shear jaw for films. Spectra were collected by applying a dynamic strain of amplitude 10^{-3} at 1 Hz in the temperature range between 25 °C and 250 °C with a heating and cooling rate of 2 °C/min.

Ion Exchange Capacity Measurements. The ion exchange capacity (IEC) was determined by an acid-base titration. Disks of the membranes with known dry mass were equilibrated in 1.0 M NaCl aqueous solution for 24 h to replace the H^+ by Na^+ ions. The solution was titrated with 0.1 M NaOH (Aldrich, volumetric standard) using phenolphthalein as an indicator. IEC values (meq g^{-1}) were calculated by the following Eq. 4:

$$\mathrm{IEC} = \frac{V_{\mathrm{NaOH}} \times C_{\mathrm{NaOH}}}{m_{\mathrm{dry}}} \qquad \text{(Eq. 4)}$$

where V_{NaOH} is the added titrant volume at the equivalent point (mL), C_{NaOH} is the molar concentration of the titrant and m_{dry} is the dry mass of the sample (g).

Conductivity. Through-plane proton conductivity was measured by electrochemical impedance spectroscopy (EIS) using a multichannel potentiostat (VMP3 BioLogic Science Instruments). Disks of membranes were sandwiched between gas diffusion electrodes (E-Tek ELAT HT 140E-W with a Pt loading of 5 mg cm^{-2}). The proton conductivity was measured as a function of temperature at saturated water vapor pressure (100% relative humidity (RH)) in the frequency range from 1 Hz to 1 MHz, at an applied voltage of 25 mV. Before measurements, the samples were equilibrated overnight at room temperature and RH = 100%.

DMFC tests and MeOH permeation measurements. Membrane electrode assemblies (MEAs) were formed by hot-pressing the electrodes onto the membrane for 5 min. at 120 °C under a load of 1 ton and placed in a single cell (Fuel Cell Technologies, Inc.) with active area of 5 cm^2. A home-made test station was used to evaluate the MEA performance, feeding the cathode with humidified oxygen and the anode with a 2 M methanol solution. The feed supply of methanol was monitored by a KNF's Model FEM 1.10 TT.18 S diaphragm metering pump (flow rate: 2 mL min^{-1}). The oxygen supply was controlled by a MKS PR4000 mass-flow controller (flow rate: 150 sccm) and the humidifier temperature was set to ensure 100% RH of the gas. A pressure of 1 abs bar at both anode and cathode was used at 70 °C, whereas it was increased up to 2 abs bar at 90 °C). Polarization and power density curves were obtained using a Multichannel Potentiostat (VMP3 BioLogic Science Instruments).

Methanol permeation was evaluated by linear sweep voltammetry, measuring the steady-state limiting current density at cathode due to the oxidation of methanol permeating from the anode side.

The anode was fed by 2 M methanol solution and humidified N_2 was fed to the cathode. Limiting current density (J_{lim}) was measured applying a voltage from 0 to 1.3 V (scan rate: 2 mV s^{-1}).

Results and discussion

Morphological and spectroscopic investigation

The strong acid $–SO_3H$ groups were covalently bound onto the TiO_2 surface by bifunctional branches to enhance the proton conductivity of the oxide and to favor the interfacial interactions with polymer matrix to obtain a more uniform dispersion of filler in composite membranes.

TiO_2 and TiO_2-RSO_3H were preliminarily characterized by studying their physicochemical properties by completing the picture already published by some of us in ref. [8].

Transmission electron micrographies of the bare and grafted nanoparticles are shown in Figure 1.

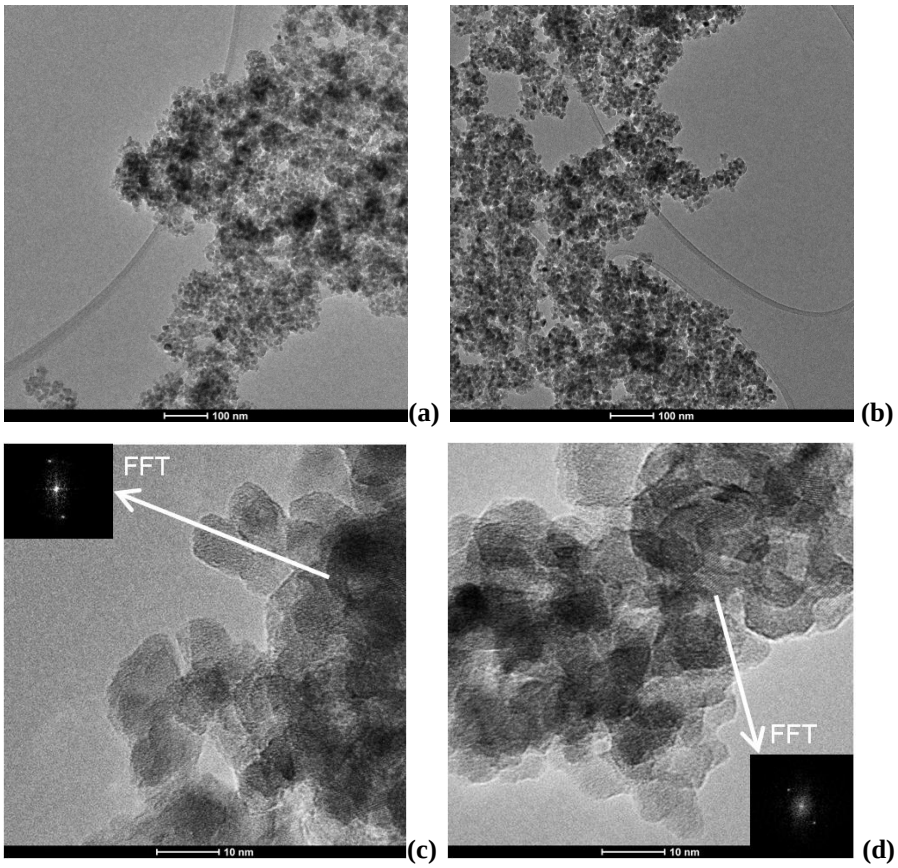

Fig 1 TEM images at low magnification of TiO_2 (a) and TiO_2-RSO_3H (b), and at high magnification together with Fast Fourie Transform (FFT) image of TiO_2 (c) and TiO_2-RSO_3H (d).

Samples are consist of nanometric round-shaped particles with very similar pseudospheric diameter. The two powders were morphologically very pure: no contaminations by larger particles, chunks or

other morphologies have been highlighted. The nanoparticle sizes are very homogenous: mean diameters of about 8-9 nm have been observed for both samples. The high resolution-TEM imaging confirms the homogenous morphology of the nanoparticles and their crystalline nature. Diffraction fringes were observed throughout the entire sample: the bright spots in the Fast-Fourier-Transform image of the nanoparticles, marked in the panels (c) and (d) of the same figure, are easily indexed to the alternation of 3.5A spaced (101) planes of the anatase lattice.

The success of the grafting procedure was tested by Raman spectroscopy: results for the bare and grafted titania nanoparticles are shown in the Figure 2.

Raman spectra highlight the occurrence of the typical vibrational features of the anatase lattice (396, 516 and 639 cm^{-1}) [32] and, for the TiO_2-RSO_3H grafted filler, also a single peak at 1046 cm^{-1} likely due to the symmetric stretching mode of SO^{3-} ion [33] and two peaks at about 2890 and 2936 cm^{-1} due to vibrational modes of the aliphatic chain [34].

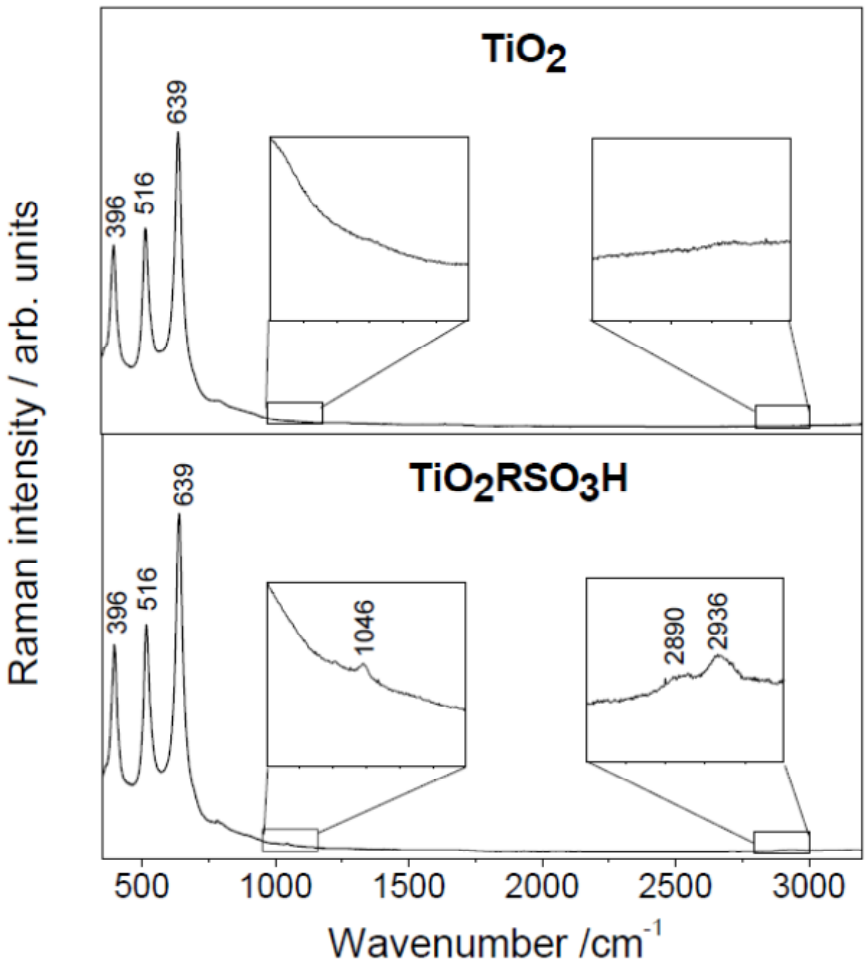

Fig 2 Raman spectra of the bare(top panel) and grafted (bottom panel) titania nanopowders. Note the occurrence of vibrational modes of both SO^{3-} ion and aliphatic chain in grafted powders.

Prior to proceed to advanced characterization by NMR and other techniques the morphologies of the pure sPEEK and the composite membranes were characterized by AFM at room temperature and 33% RH. Examples of phase images of the pure sPEEK and composite membranes are shown in the Figure 3 together with the statistical image analysis of the sizes of the dark and bright areas.

As expected the AFM phase images of the skin layer of the pure and composite sPEEK membranes show a regular alternation of elongated pseudocircular bright and dark areas. This alternation is related to the different hardness/elastic properties of the hydrophobic and hydrophilic domains [35-36]. Dark areas are assigned to softer regions, which represent the hydrophilic sulphonic group clusters whereas bright areas are attributed to the hard character of (a) the hydrophobic polymer matrix or (b) the filler nanoparticles [37]. The homogeneous dispersion of the dark/bright areas suggests a uniform dispersion of the filler nanoparticles and the lack of filler agglomeration on the membrane surface [37-39].

Analysis of the distributions of the bright and dark domains sizes suggests for both the hydrophobic and hydrophilic cases a lognormal distribution peaked between 11-13, 9-11 and 5-7 nm for the sPEEK, sPEEK/TiO_2 and sPEEK/TiO_2-RSO_3H samples, respectively, with a smooth decreasing tail due to few large pseudo-particles. Hydrophilic domains are in all cases slightly larger than the hard hydrophobic regions. The size of the hydrophilic domains as well as the hydrophobic ones shows a monotonic decreasing trend passing from pure sPEEK to the TiO_2 and the TiO_2-RSO_3H composite membranes. Apparently the incorporation of both inorganic fillers leads to a contraction of the cluster size on the membrane surfaces. This observation suggests that the interaction between the filler surfaces and the sulphonic acid groups of the polymer decreases the free volume of the hydrophilic regions which are able to contain water as similarly observed by Zhang et al. [40]. On the other hand it is likely that the reduced size of the hydrophobic/hydrophilic domains may lead to a more interconnected microstructure of the ion conducting channels thus possibly improving the homogeneity of the surface hydration [41].

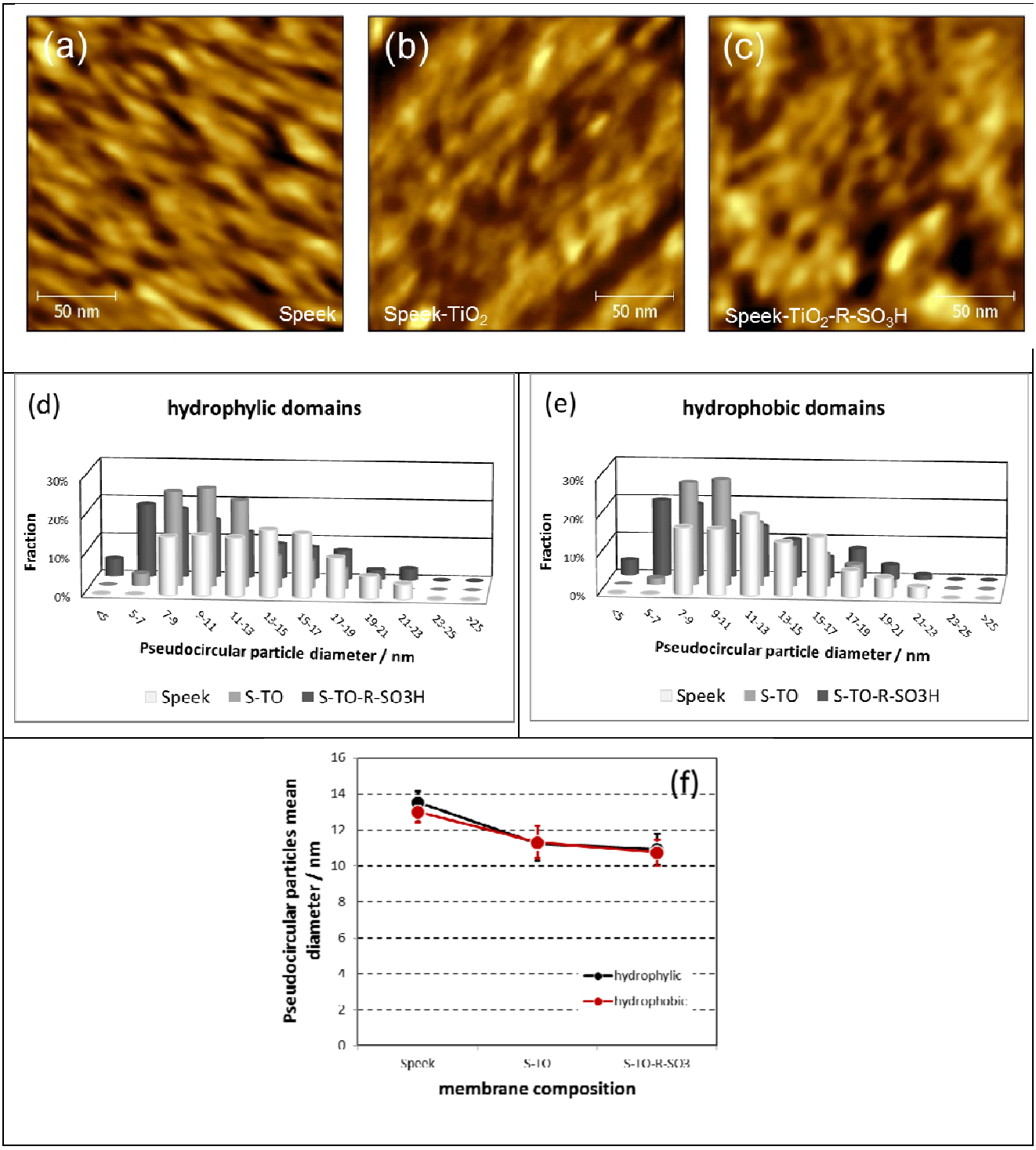

Fig 3 (a-b-c) AFM-phase images at RH 33% of pure sPEEK and composite membranes; (d) hydrophylic and (e) hydrophobic domain diameter distributions and (f) mean sizes

Dynamic Mechanical Analysis

The viscoelastic behavior of the membranes were quantified in terms of storage modulus, loss modulus and loss factor (*tan δ*). The measurements have been collected in the temperature range

between 25 °C and 250 °C, both in heating and in cooling scans. Figure 4(a) reports the temperature evolution of storage modulus of the sPEEK membrane and of the nanocomposites, sPEEK/TiO_2 and sPEEK/TiO_2-RSO_3H. The pure sPEEK shows *E'* modulus of 1.4 x10^9 Pa at room temperature and, during heating, it gradually decreases. sPEEK/TiO_2 has a comparable initial *E'* value, but it slightly increases upon heating up to about 80 ^oC, before declining. sPEEK/TiO_2-RSO_3H displays a larger storage modulus value (about 1.8 x10^9 Pa) and a plateau up to ca. 175 °C. These results demonstrate that the titania filler in the polymer matrix improves the mechanical properties of the membrane, and in particular, the particle's functionalization with silylpropylsulfonic groups further enhances the stiffness of the final composite. This beneficial effect is likely due to stronger intermolecular interactions between the polymeric chains. Upon cooling, the storage modulus in all the three samples recover the same initial values, thus suggesting a complete thermo-reversibility of the mechanical properties for these systems. Turning to the *tan δ* profile (Figure 4(b)), a simple alpha transition is observed for all samples in this temperature range, likely correlated to segmental motions of polymer backbone chains. Whereas for pristine sPEEK membrane, the glass transition temperature is at 228 °C, the nanocomposites both show a slight shift of the T_g to higher temperatures, in particular the sPEEK/TiO_2, and also a strong decreases in the loss tangent values from 1.6 to 0.7-0.8. This reduction is likely related to the higher stiffness of the nanocomposites respect to the filler-free membrane.

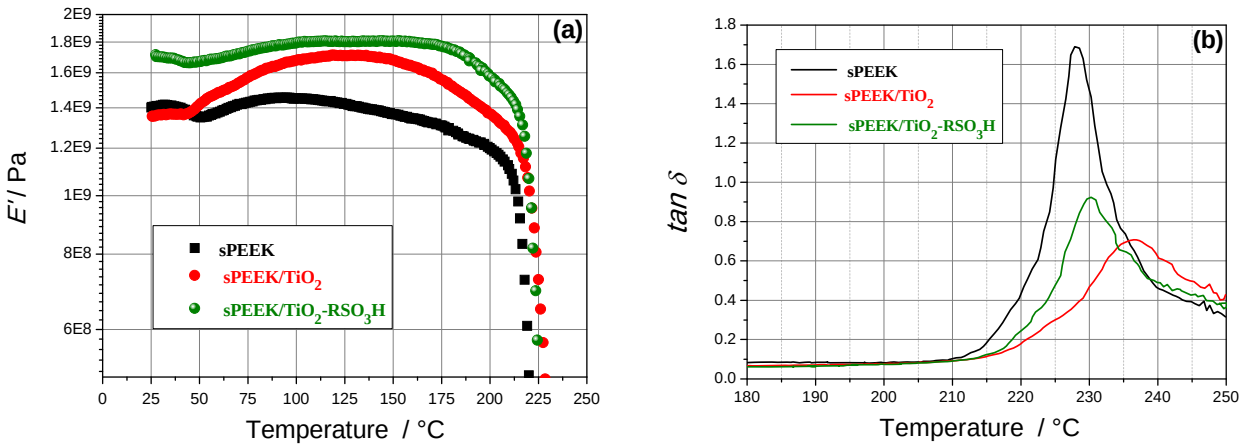

Fig 4 Storage modulus *E'* (a) and *tan δ* (b) versus temperature of pristine sPEEK and sPEEK/TiO_2 and sPEEK/TiO_2-RSO_3H nanocomposite membranes.

NMR Investigation

NMR technique has been applied in this study to investigate the transport properties of water and methanol confined in the membranes, with particular emphasis on the effect of the nanoadditivies.

Figure 5 displays the plots of the water self-diffusion coefficients (D) and the relaxation times (T_1) measured on completely swelled membranes, in the temperature range 20-130 °C.

At the maximum swelling, the percentage of water uptake is estimated to be 50% for sPEEK, 42% for the sPEEK/TiO_2 and 37% for the sPEEK/TiO_2-RSO_3H, respectively, as reported in the graph's legend. Apparently the nanocomposite membranes adsorb significant less amount of water compared to the recast sPEEK membrane. This swelling's reduction may well be related to the higher rigidity of the hybrid membranes, because the incorporation of fillers in the polymeric matrix, and especially the presence of sulfonic groups, allows a greater cross-linking between the polymer chains, with the result of a stiffer membrane, less able to swell.

The strong relationship between water uptake of the polymer electrolyte and self-diffusion coefficients is well known [42-44]: generally, at room temperature, electrolyte membranes that absorb more water exhibit higher diffusivity. However, in this case we observe higher water diffusion in the sPEEK/TiO_2 composite, even though the water uptake is smaller than the filler free sPEEK. Additionally, it increases up to 120 °C and then, due to the water evaporation, decreases rapidly.

At a first glance, it seems peculiar that the presence of sulphonic acid groups on the particles does not enhance the water mobility of the membrane. A possible explanation is that the polymeric chains strongly interact with the TiO_2-RSO_3H particles through the sulfonic groups with the result to reduce the filler's hydrophilic active area. This explanation matches well with the apparent reduction of the hydrophilic domain size due to incorporation of the filler and the possible reduction of the free volume able to contain water.

In fact, the sulfonic acid groups, bounded on an aliphatic chain before grafted in titania, may lead to a much better filler dispersion in the recast procedure due to the higher affinity with the organic solvent and polymeric chain.

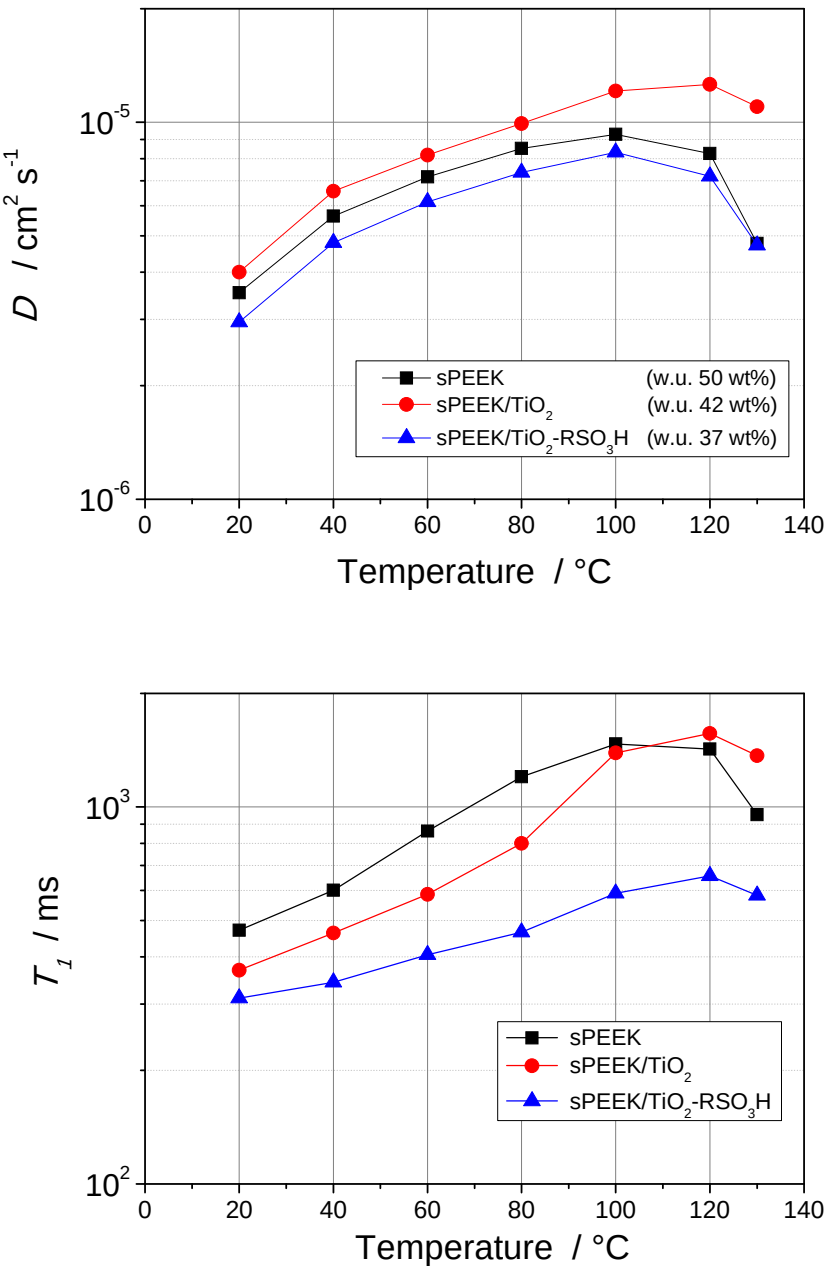

Fig 5 Self-diffusion coefficients (top) and longitudinal relaxation times (bottom) of water measured in in completely swelled membranes, in the temperature range 20 - 130 °C.

Further information about the molecular dynamics is provided by measurements of longitudinal (or spin–lattice) relaxation times (T_1). T_1 is more sensitive to localized motions in comparison with standard diffusion, including both translation and rotation on a time scale comparable to the reciprocal of the NMR angular frequency (~1 ns). As the molecular correlation time τ_c depends on temperature, a minimum in T_1 is often observed when $\varpi\tau_c \sim 1$, where ϖ is the NMR frequency [45].

In the temperature range investigated, well above the T_1 minimum, i.e. in the so-called extreme narrowing limit ($\varpi\tau_c << 1$), higher T_1 values suggest more facile molecular motions.

In both the composites, T_1 values are shorter than the pristine sPEEK in almost all the temperature range investigated. This provides an evidence for stronger interactions between the water molecules and the nanoadditives, in particular when they are sulfonated, decreasing their molecular motions. This can be hypothesized in the case of sPEEK/TiO_2-RSO_3H composite to explain the low T_1, and it is in agreement with the conductivity data reported in the next section.

Turning to the methanol dynamics throughout the membranes, apparently the use of titania nano-filler leads to major alterations. Figure 6 displays the diffusion coefficients of water and methanol measured in the swollen membranes of sPEEK (a), sPEEK/TiO_2 (b) and sPEEK/TiO_2-RSO_3H (c), respectively, in the range of 20-130 °C.

For this study, the membranes were equilibrated in aqueous methanol solution at concentration of 2 M, so as to have the same conditions used in the DMFC cell. Furthermore, in order to discriminate in the ^1H NMR spectrum between the proton signals coming from water or methanol, we used deuterated molecules, i.e. mixture of CH_3OD/D_2O and CD_3OD/H_2O for measuring methanol and water, respectively [6,46].

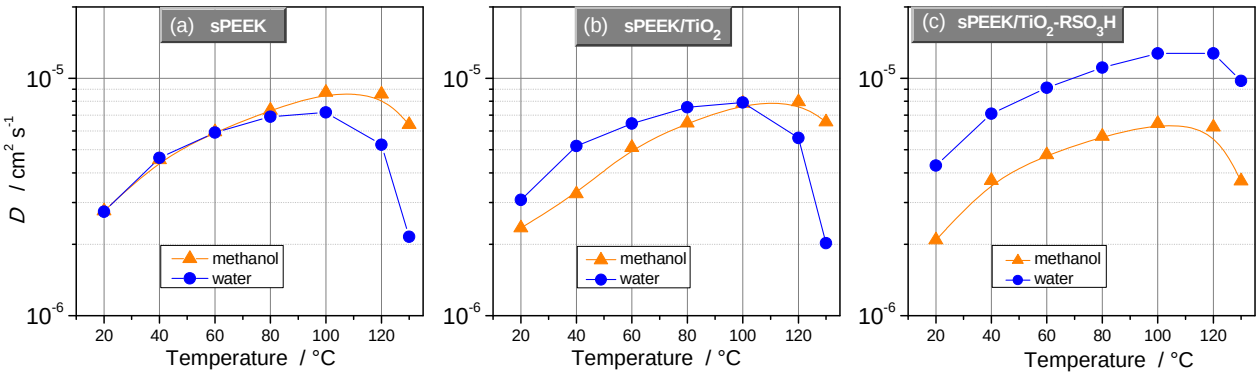

Fig 6 Self-diffusion coefficients of water and methanol in 2 M solution confined in sPEEK (a), sPEEK/TiO_2 (b) and sPEEK/TiO_2-RSO_3H (c) membranes, respectively, from 20 up to 130 °C.

Diffusion coefficients of water and methanol in the sPEEK membrane (Figure 6a), are overlapped up to 60 °C, and above this temperature the methanol mobility become much higher than that of the water. This behavior is consistent with the methanol crossover observed in the direct methanol fuel cell operation. The sPEEK/TiO_2 (Figure 6b) shows a different behavior where the water diffusion

dominates up to 100 °C, proving the beneficial methanol blocking effect of the nanoparticles dispersed in the polymer. However, above 100 °C, likely due to the solvents evaporation, we observe a brusque decline of the water mobility while the methanol molecules maintain a very high diffusion. On the other hand the sPEEK/TiO_2-RSO_3H membrane shows drastically improved performances: water diffusion is always larger than methanol in the whole investigated temperature range.

We can speculate that the sulfonilic groups on the titania particles interacting with the polymer chains cause a higher reticulation, reducing the dimension of the pores and significantly increasing the tortuosity of the diffusional paths of methanol molecules. Obviously, obstruction of the diffusion channels may also affect the diffusive path of bulk water. However protons can be transported additionally through a Grotthus-type mechanism that is likely enhanced in highly reticulated system: as a final result the water diffusion coefficients remain higher than methanol also at high temperatures. Additionally, we should be considered that methanol molecules have higher sterical hindrance than that of water molecules.

The concept of tortuosity and porosity of the membranes may be easily made quantitative by considering the ratio of the water self-diffusion coefficients in the ionomers (D) and the self-diffusion coefficient of pure water (D^0) according to the scaling equation (Eq. 5) [47-49]:

$$D = \frac{\varepsilon}{\tau} D^0 \qquad \text{(Eq. 5)}$$

Tortuosity τ and porosity ε are phenomenological scaling parameters. The porosity is by definition below 1; the tortuosity is defined above 1, where the value 1 would correspond to perfectly straight diffusion paths inside the membrane. The estimation of ε/τ ratios for the three membranes, sPEEK, sPEEK/TiO_2 and sPEEK/TiO_2-RSO_3H, was executed by considering the diffusion coefficients measured at 20 °C, obtaining the following values: sPEEK 0.17, sPEEK/TiO_2 0.20 , sPEEK/TiO_2-RSO_3H 0.14.

Such values confirm our description of such systems: the larger ratio for sPEEK/TiO_2 might correspond to a higher porosity, due to the Titania clusters dispersed, while the sulfonilic groups on the particles, through strong reticulations with the polymer, shrink the dimension of the pores, so the porosity is reduced and, likely, tortuosity increases.

Figure 7 shows the plot of the longitudinal relaxation times (T_1) vs. temperature of the methanol. These data confirm what affirmed above, i.e. in sPEEK/TiO_2-RSO_3H methanol shows the shorter T_1, implying that its local mobility is reduced, which in turn can be attributed to structuring and nanomorphology of the composite.

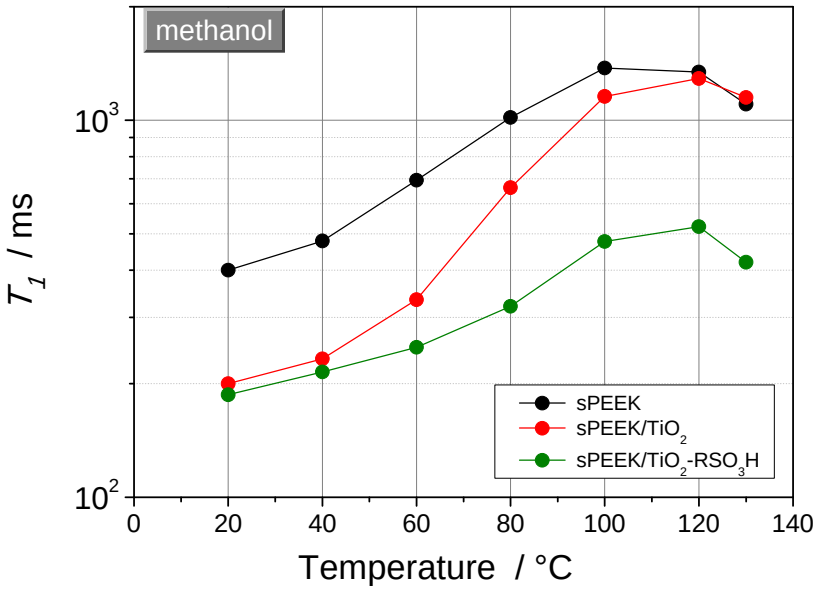

Fig 7 Longitudinal relaxation times (T_1) of methanol measured in the three membranes swollen in 2 M solution in the temperature range from 20 to 130 °C.

Finally, Figure 8 reports the high pressure NMR diffusion measurements performed on the membranes equilibrated in aqueous methanol solutions. The three plots compare methanol and water self-diffusion coefficients obtained as a function of the pressure from 1 atm. up to 2 kbar. The measurements were conducted at two different temperatures, 303 K and 328 K, but here only data at 328 K are shown. The aqueous methanol solution uptakes of the membranes were estimated to be about 55% for sPEEK, 44% for the sPEEK/TiO_2 and 38% for the sPEEK/TiO_2-RSO_3H, respectively. Also in this case, a picture similar to the previous cases is observed: dispersion of nanoparticles in the polymer matrix produces a structure that inhibits the methanol transport; moreover the functionalization of these particles with the RSO_3H groups, further enhances the obstruction effect.

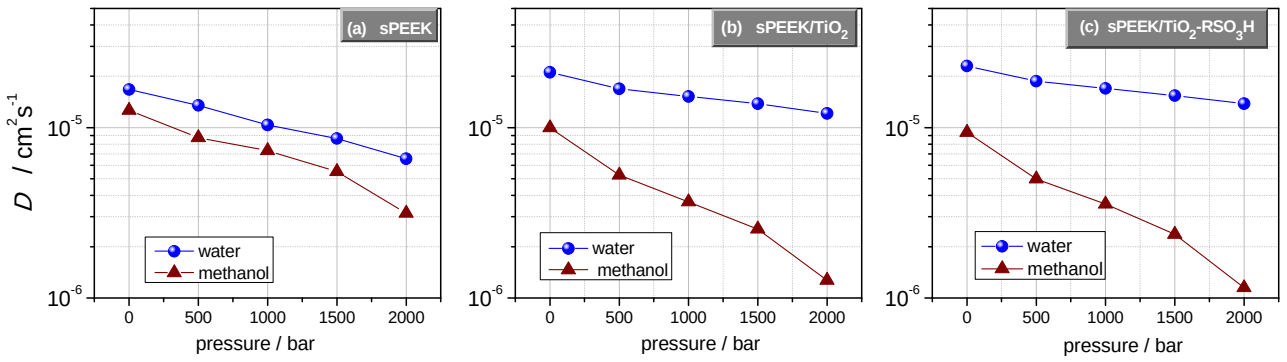

Fig 8 Self-diffusion coefficients of water and methanol in 2 M solution confined in sPEEK (a), sPEEK/TiO_2 (b) and sPEEK/TiO_2-RSO_3H (c) membranes, respectively, measured by high pressure SE–NMR technique from 0 up to 2 kbar, at 55 °C.

Table 1 reports the activation volumes of water and methanol in 2 M solution, respectively, calculated from the diffusion data for the pure sPEEK and the two composites according to Eq. 6:

$$\Delta v = -kT\left(\frac{\vartheta \ln D}{\vartheta P}\right)_T \qquad \text{(Eq. 6)}$$

Higher activation volume implies that more cooperative motion and hence larger change in local volume is required for the process of diffusion to occur within the membrane. This is consistent with interactions occurring between the methanol molecules and the surface of the nanoparticles. In fact, the activation volume of methanol increases in the composites, and the higher value is obtained for the sulfonated one. On the other hand, as expected, while the activation volume of water decreases in the composites, that of methanol increases.

Table 1. Activation Volumes* of water (2 M) and methanol (2 M) in the three membranes and at two temperatures.

Membrane	***Activation Volume (cm^3 mol^{-1})***			
	H_2O/CD_3OD (2 M)		D_2O/**CH_3OD** (2 M)	
	303 K	***328 K***	***303 K***	***328 K***
sPEEK	16.5	12.0	21.5	16.7
sPEEK/TiO_2	11.6	6.8	28.6	25.1
sPEEK/TiO_2-RSO_3H	10.4	6.3	30.2	25.6

* The error bar for these volumes is around +/-0.5 (since the error on *D* values of about 3%)

Electrochemical Investigation

The ion exchange capacity values of the membranes were measured to check the effect of the embedding of nanoadditivies. As shown in the Table 2, the IEC of the composites was lower than that of pure sPEEK. In particular, the sPEEK/TiO_2-RSO_3H membrane showed the lowest value, in agreement with the similar trend observed for the percentage of water uptake discussed previously for the NMR data (50% for sPEEK, 42% for the sPEEK/TiO_2 and 37% for the sPEEK/TiO_2-RSO_3H). This finding can be explained on the basis of filler/polymer interactions. The segregation of protogenic groups, due to H-bonding between the SO_3H groups of sPEEK and Si–OH and SO_3H groups of TiO_2-RSO_3H, reduces the amount of the ion exchange functionalities that are responsible for water and methanol uptakes.

The number of water molecules per sulphonic acid group was estimated by the following Eq. 7 and is reported in Table 2:

$$\lambda = \frac{n_{H2O}}{n_{SO3H}} = \frac{10 \times WU\%}{18 \times IEC} \quad \text{(Eq. 7)}$$

The decrement of λ value is consistent with narrowing of the ionic clusters for the composite membranes, as observed by AFM analysis.

Table 2. Ion exchange capacity (IEC) values and hydration number (λ) of the membranes

Membrane	IEC (meq/g)	λ
sPEEK	1.73	16
sPEEK/TiO_2	1.53	15
sPEEK/TiO_2-RSO_3H	1.44	14

The proton conductivity of the membranes was measured by EIS and the resulting plots are shown in Figure 9. As pointed out by the comparison of data relative to the sPEEK/TiO_2 and sPEEK/TiO_2-RSO_3H membranes, the functionalization of TiO_2 avoids the reduction of the overall proton conductivity of the electrolyte due to the use of non-conductive inorganic filler.

In the whole investigated temperature range, the sPEEK/TiO_2-RSO_3H membrane showed a conductivity similar to that of pure sPEEK, up to 0.04 S cm^{-1} at 100 °C, despite its lower values of IEC and water self-diffusion coefficient. This behavior can be explained considering that in the sPEEK/TiO_2-RSO_3H membrane, the presence of silylpropylsulfonic groups onto TiO_2 surface leads to a highly reticulated microstructure creating tortuosity and narrowing of the diffusional paths of water molecules. It is thus expected that the contribution to proton conductivity due to vehicular mechanism, that is the diffusion of protonated water molecules, will be smaller and the relative contribution of the Grotthus-type mechanism will be larger.

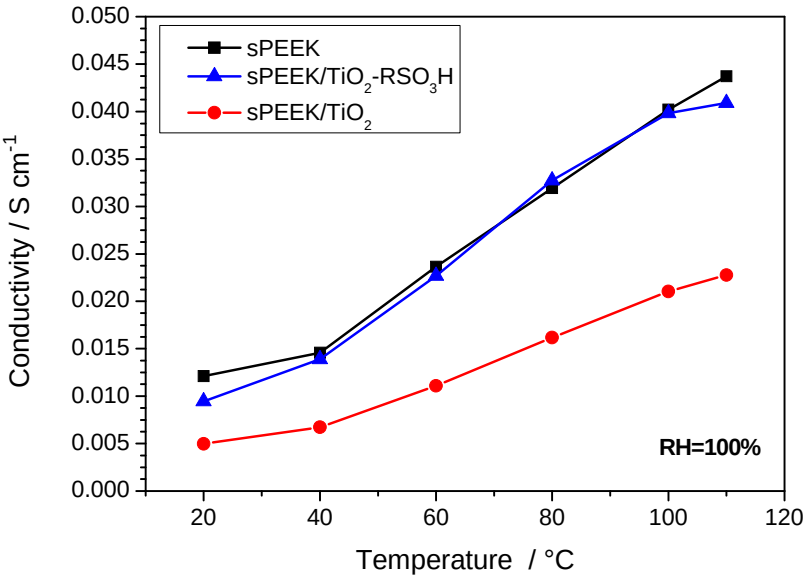

Fig 9 Proton conductivity of pure sPEEK and composite membranes.

DMFC single cell measurements were carried out to test the functioning of these membranes in a real device. To check the methanol permeability, steady-state limiting methanol oxidation current density (J_{lim}) through the membranes was measured. Figure 10 displays the voltammetric curves resulting from electro-oxidation of methanol permeating through the membranes, the J_{lim} value corresponds to the current density plateau.

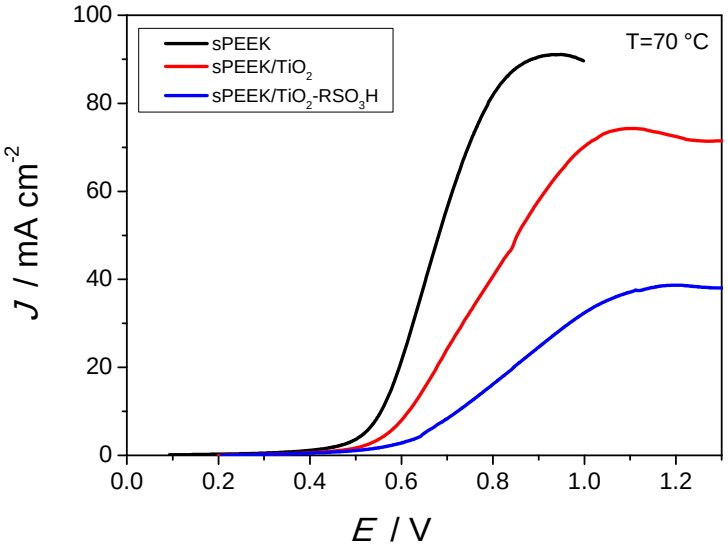

Fig 10 Voltammetric curves for the oxidation of methanol permeating through the membranes exposed to a 2 M methanol feed, at 70 °C.

Methanol permeability decreased in both the composite membranes and, in particular, sPEEK/TiO_2-RSO_3H showed the lowest permeability, in agreement with its lowest value of methanol self-diffusion coefficient. The physical cross-linking between the functionalized titania nanoparticles and the polymer chains reduce the size of the hydrophilic channels and thus effectively decreases the methanol permeability that strongly depends on the size and tortuosity of diffusional channels network [50].

Finally, Figure 11 shows polarization curves (*I-V*) and power density (*PD*) of the membranes, at 70 °C and 1 abs bar.

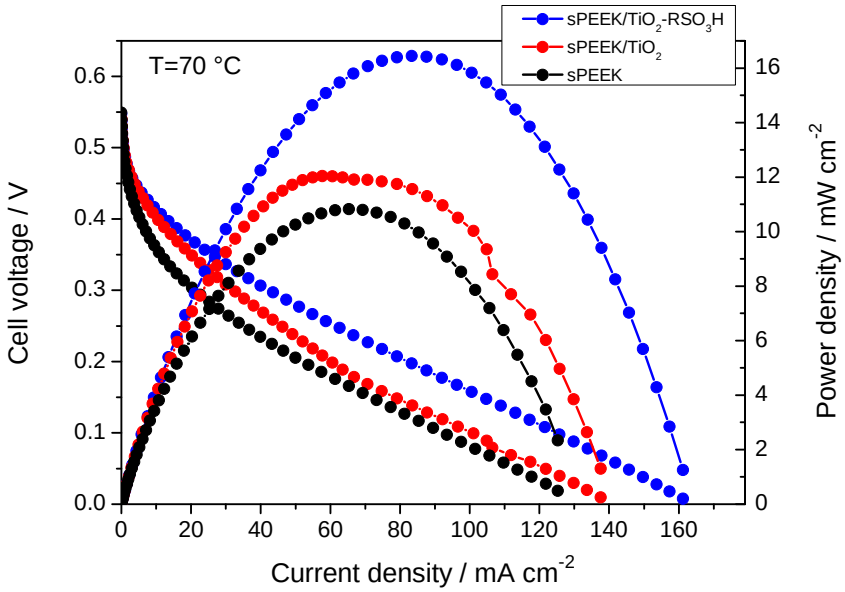

Fig 11 DMFC polarization and power density curves at 70 °C for the MEA equipped with composite and pure sPEEK membranes.

The sPEEK/TiO_2-RSO_3H composite showed better performance than those of the other membranes, in terms of higher power density delivered and reduced methanol crossover. These results are in agreement with the diffusion data previously observed. In this membrane, a larger tortuosity of the diffusive path produces a lower methanol crossover and lower potential losses at low current density. Furthermore, the higher water mobility with respect to that of methanol and the significant contribution of the Grotthus-type mechanism to the proton conductivity ensure a lower resistance and thus the possibility to produce higher current density in a DMFC.

The polarization and power density curves of the membranes, recorded at 90 °C and 2 abs bar, are shown in Figure 12.

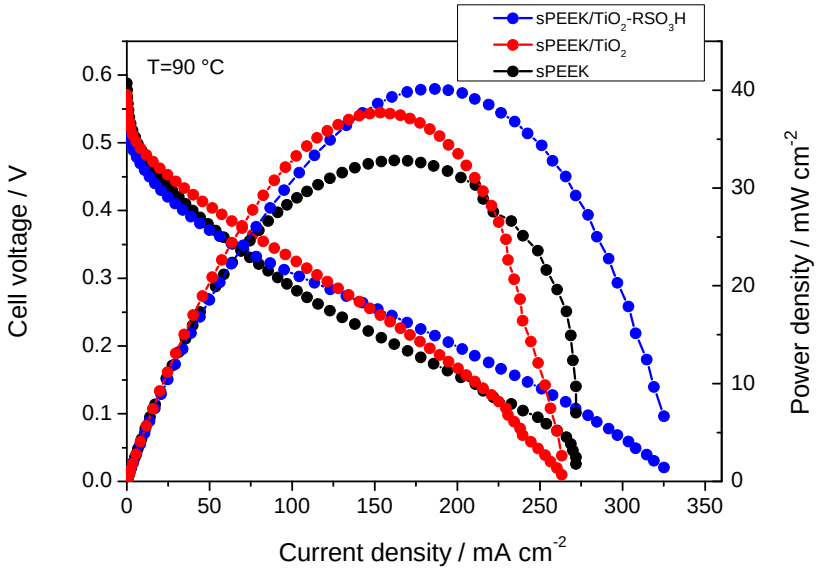

Fig 12 DMFC polarization and power density curves at 90 °C for the MEA equipped with composite and pure sPEEK membranes.

As can be observed, the maximum *PD* of the cell increase with increment of the temperature and pressure for all the sPEEK-based membranes. In detail, the sPEEK/TiO_2-RSO_3H composite showed the best performance also in these operating conditions (PD_{max} = 40 mW cm^{-2} and $I_{(0.2\ V)}$ = 200 mA cm^{-2}), with a *PD* improvement of 20% with respect to the pure sPEEK membrane. As highlighted by NMR measurements, the sPEEK/TiO_2-RSO_3H membrane showed the highest value of the water self-diffusion coefficient and the lowest value of that of methanol, in comparison with the other membranes. This is consistent with the highest current and power density by the cell equipped with the sPEEK/TiO_2-RSO_3H composite.

Conclusions

Propylsulfonic acid functionalized titania TiO_2-RSO_3H was chosen as nanoadditive for the preparation of sPEEK-based composites because the presence of bifunctional branches on the filler surface affects the structuring and nanomorphology of hydrophilic and hydrophobic domains within the membrane, and hence the properties of the electrolyte.

Mechanical analysis performed on the membranes demonstrate that the presence of titania nanoparticles functionalized with silylpropylsulfonic groups enhances the stiffness of the composite, likely due to higher intermolecular interactions among the polymeric chains. This results

in a higher reticulation of the polymer matrix, increasing the tortuosity of the diffusional paths for methanol transport, as highlighted from the NMR investigation. On the other hand, the proton acid of water can be transported through the Grotthus-type mechanism, much more favored in the highly reticulated system.

The functionalization of TiO_2 avoids the detrimental effect on overall proton conductivity of the membranes due to embedding of the low-conducting ceramic oxide in the polymer matrix. Conductivity measurements showed that the sPEEK/TiO_2-RSO_3H membrane exhibits conductivity values similar to those of pure sPEEK and higher than those of sPEEK/TiO_2 membrane in spite of its lower values of water self-diffusion coefficient and ion exchange capacity.

DMFC tests highlighted that the composites show lower methanol permeability than that of pure sPEEK membrane and, at the same filler content, the membranes incorporated with sulfonic acid functionalized titania exhibit much lower methanol permeability as compared with those incorporated with pristine titania nanoparticles.

In conclusion, the higher water mobility with respect to that of methanol within the sPEEK/TiO_2-RSO_3H membrane and the considerable contribution to the proton conductivity due to the Grotthus-type mechanism lead to a good cell response when this electrolyte is used in a DMFC, in terms of reduced methanol crossover and higher current and power density delivered.

This last result is really outstanding if we consider that sPEEK membranes, in general show very good methanol resistance and mechanical properties but at the same time suffer from lower proton conductivity compared to Nafion. Using finally the sulfonated titania filler we have managed to achieve low methanol permeability without sacrificing the conducting performance of the membrane.

ACKNOWLEDGMENTS

This work was carried out with the financial support of the Italian Ministry of Education, Universities and Research (Project: PRIN 2011, NAMED-PEM). The NMR measurements at Hunter College were supported by a grant from the U.S. Office of Naval Research.

References

1. Wasmus S, Kuver A (1999) Methanol oxidation and direct methanol fuel cells: a selective review. J Electroanal Chem 461:14–31
2. Aricò AS, Srinivasan S, Antonucci V (2001) DMFCs: From Fundamental Aspects to Technology Development. Fuel Cells 1:133–161
3. Han J, Liu H (2007) Real time measurements of methanol crossover in a DMFC. J Power Sources 164:166–173
4. Kim JH, Kim SK, Nam K, Kim DW (2012) Composite proton conducting membranes based on Nafion and sulfonated SiO_2 nanoparticles. J Membr Sci 415-416:696–701
5. Kim Y, Choi Y, Kim HK, Lee JS (2010) New sulfonic acid moiety grafted on montmorillonite as filler of organic–inorganic composite membrane for non-humidified proton-exchange membrane fuel cells. J Power Sources 195:4653–4659
6. Nicotera I, Simari C, Coppola L, Zygouri P, Gournis D, Brutti S, Minuto FD, Aricò AS, Sebastian D, Baglio V (2014) Sulfonated Graphene Oxide Platelets in Nafion Nanocomposite Membrane: Advantages for Application in Direct Methanol Fuel Cells. J Phys Chem C 118:24357−24368
7. Nicotera I, Kosma V, Simari C, D'Urso C, Aricò AS, Baglio V (2014) Methanol and proton transport in layered double hydroxide and smectite clay-based composites: influence on the electrochemical behavior of direct methanol fuel cells at intermediate temperatures. J Solid State Electrochem Doi 10.1007/s10008-014-2701-y
8. Cozzi D, de Bonis C, D'Epifanio A, Mecheri B, Tavares AC, Licoccia S (2014) Organically functionalized titanium oxide/Nafion composite proton exchange membranes for fuel cells applications. J Power Sources 248:1127–1132
9. de Bonis C, Cozzi D, Mecheri B, D'Epifanio A, Rainer A, De Porcellinis D, Licoccia S (2014) Effect of filler surface functionalization on the performance of Nafion/Titanium oxide composite membranes. Electrochim Acta 147:418–425
10. Awang N, Ismail AF, Jaafar J, Matsuura T, Junoh H, Othman MHD, Rahman MA (2015) Functionalization of polymeric materials as a high performance membrane for direct methanol fuel cell: A review. React Funct Polym 86:248–258
11. Mishra AK, Bose S, Kuila T, Kim NH, Lee JH (2012) Silicate-based polymer-nanocomposite membranes for polymer electrolyte membrane fuel cells. Prog Polym Sci 37: 842–869
12. Villa DC, Angioni S, Quartarone E, Righetti PP, Mustarelli P (2013) New Sulfonated PBIs for PEMFC Application. Fuel Cells 13:98–103
13. Roy A, Hickner MA, Einsla BR, Harrison WL, McGrath JE (2009) Synthesis and characterization of partially disulfonated hydroquinone-based poly(arylene ether sulfone)s random copolymers for application as proton exchange membranes. J Polym Sci Part A: Polym Chem 47:384–391
14. de Bonis C, D'Epifanio A, Di Vona ML, D'Ottavi C, Mecheri B, Traversa E, Trombetta M, Licoccia S (2009) Proton Conducting Hybrid Membranes Based on Aromatic Polymers Blends for Direct Methanol Fuel Cell Applications. Fuel Cells 9:387–393
15. Li L, Zhang J, Wang Y (2003) Sulfonated poly(ether ether ketone) membranes for direct methanol fuel cell. J Membr Sci 226:159–167
16. Laberty-Robert C, Valle K, Pereira F, Sanchez C (2011) Design and properties of functional hybrid organic–inorganic membranes for fuel cells. Chem Soc Rev 40: 961–1005
17. de Bonis C, D'Epifanio A, Di Vona ML, Mecheri B, Traversa E, Trombetta M, Licoccia S (2010) Proton-Conducting Electrolytes Based on Silylated and Sulfonated Polyetheretherketone: Synthesis and Characterization. J Polym Sci Part A: Polym Chem 48:178-2186
18. Mollà S, Compañ V (2014) Polymer blends of SPEEK for DMFC application at intermediate temperatures. Int J Hydrogen Energ 39:5121–5136
19. de Bonis C, D'Epifanio A, Mecheri B, Traversa E, Miyayama M, Tavares AC, Licoccia S (2012) Layered tetratitanate intercalating sulfanilic acid for organic/inorganic proton conductors. Solid State Ionics 227:73–79
20. Jones DJ, Rozière J (2008) Advances in the Development of Inorganic–Organic Membranes for Fuel Cell Applications. Adv Polym Sci 215:219–264

21. Alvarez A, Guzmán C, Carbone A, Saccà A, Gatto I, Passalacqua E, Nava R, Ornelas R, Ledesma-García J, Arriaga LG (2011) Influence of silica morphology in composite Nafion membranes properties. Int J Hydrogen Energ 36:14725-14733
22. Fontanella JJ, Edmonson CD, Wintersgill MC, Wu Y, Greenbaum SG (1996) High-Pressure Electrical Conductivity and NMR Studies in Variable Equivalent Weight NAFION Membranes. Macromolecules 29:4944-4951
23. Fontanella JJ, Wintersgill MC, Chen RS, Wu Y, Greenbaum SG (1995) Charge transport and water molecular motion in variable molecular weight nafion membranes: High pressure electrical conductivity and NMR. Electrochim Acta 40:2321-2326
24. Jayakody JRP, Stallworth PE, Mananga ES, Zapata JF, Greenbaum SG (2004) High Pressure NMR Study of Water Self-Diffusion in NAFION-117 Membrane. J Phys Chem B 108: 4260-4262
25. Nicotera I, Khalfan A, Goenaga G, Zhang T, Bocarsly A, Greenbaum S (2008) NMR investigation of water and methanol mobility in nanocomposite Fuel Cell membranes. Ionics 14:243–253
26. Licoccia S, Traversa E (2006) Increasing the operation temperature of polymer electrolyte membranes for fuel cells: From nanocomposites to hybrids. J Power Sources 159:12–20
27. He Q, Kusoglu A, Lucas IT, Clark K, Weber AZ, Kostecki R (2011) Correlating humidity-dependent ionically conductive surface area with transport phenomena in proton-exchange membranes. J Phys Chem B 115:11650–11657
28. Abramoff MD, Magalhaes PJ, Ram SJ (2004) Image processing with ImageJ. J Biophotonics International 11:36–42
29. Rasband WS (1997-2014) In: ImageJ, U. S. National Institutes of Health, Bethesda, Maryland, USA, http://imagej.nih.gov/ij/, 1997-2014
30. Tanner JE (1970) Use of the stimulated echo in NMR diffusion studies. J Chem Phys 52: 2523-2526
31. Stejskal EO, Tanner JE (1965) Spin Diffusion Measurements: Spin Echoes in the Presence of a Time-Dependent Field Gradient. J Chem Phys 42:288-292
32. Giarola M, Sanson A, Monti F, Mariotto G, Bettinelli M, Speghini A, Salviulo G (2010) Vibrational dynamics of anatase TiO2: Polarized Raman spectroscopy and ab initio calculations. Phys Rev B 81:1743051-8
33. Nakamoto K (1986) Infrared and Raman Spectra of Inorganic and Coordination Compounds, J. Wiley & Sons, New York
34. Silverstein R, Bassler G, Morrill TC (1991) Spectrometric identification of organic compounds, J.Wiley & Sons, Toronto
35. Kim Y, Hickner MA, Dong L, Pivovar BS, McGrath JE (2004) Sulfonated poly(arylene ether sulfone) copolymer proton exchange membranes: composition and morphology effects on the methanol permeability. J Membrane Sci 243:317-326
36. Ling X, Jia C, Liu J, Yan C (2012) Preparation and characterization of sulfonated poly(ether sulfone)/sulfonated poly(ether ether ketone) blend membrane for vanadium redox flow battery J Membrane Sci. 415-416:306-312
37. Xiao CY, Sun GM, Yan DY, Zhu PF, Tao P (2002) Synthesis of sulfonated poly(phthalazinone ether sulfone)s by direct polymerization. Polymer 43:5335-5339
38. Li X, Zhao C, Lu H, Wang Z, Na H (2005) Direct synthesis of sulfonated poly(ether ether ketone ketone)s (SPEEKKs) proton exchange membranes for fuel cell application. Polymer 46:5820-5827
39. Goalawit R, Chirachanchai S, Shishatckiy S, Nunes SP (2008) Sulfonated montmorillonite/sulfonated poly (ether ether ketone) (SMMT/SPEEK) nanocomposite membrane for direct methanol fuel cells (DMFCs). J Membrane Sci 323:337-346
40. Zhang Y, Shao K, Zhao C, Zhan G, Li H, Fu T, Na H (2009) Novel sulfonated poly (ether ether ketone) with pendant benzimidazole groups as a proton exchange membrane for direct methanol fuel cells. J Power Sources 194:175-181
41. Brutti S, Scipioni R, Navarra MA, Panero S, Allodi V, Giarola M, Mariotto G (2014) SnO2-Nafion® nanocomposite polymer electrolytes for fuel cell applications. Int J Nanotechnol 11:882-896
42. Nicotera I, Zhang T, Bocarsly A, Greenbaum S (2007) NMR characterization of composite polymer membranes for low-humidity PEM fuel cells. J Electrochem Soc 154:B466-B473
43. Nicotera I, Enotiadis A, Angjeli K, Coppola L, Ranieri GA, Gournis D (2011) Effective Improvement of Water-Retention in Nanocomposite Membranes Using Novel Organo-Modified Clays as Fillers for High Temperature PEMFCs. J Phys Chem B 115:9087–9097

44. Enotiadis A, Angjeli K, Baldino N, Nicotera I, Gournis D (2012) Graphene-based nafion nanocomposite membranes: Enhanced proton transport and water retention by novel organo-functionalized graphene oxide nanosheets. Small 8:3338-49
45. Slichter C (1990), Principles of Magnetic Resonance, Springer Series in Solid State Science, 3rd Ed, New York
46. Nicotera I, Angjeli K, Coppola L, Aricò AS, Baglio V (2012) NMR and electrochemical investigation of the transport properties of methanol and water in Nafion and clay-nanocomposites membranes for DMFCs. Membranes 2:325–345
47. Epstein N (1989) On tortuosity and the tortuosity factor in flow and diffusion through porous media. Chemical Engineering Science 44: 777-779
48. Pasquini AL, Ziarelli F, Viel S, Di Vona ML, Knauth P (2015) Fluoride ion-conducting polymers : ionic conductivity and fluoride ion diffusion coefficient in quaternized polysulfones. ChemPhysChem 10.1002/cphc.201500643.
49. Quartarone E, Mustarelli P, Magistris A (2002) Transport Properties of Porous PVDF Membranes J. Phys. Chem. B 106: 10828-10833
50. Pandey RP, Shahi VK (2013) Aliphatic-aromatic sulphonated polyimide and acid functionalized polysilsesquioxane composite membranes for fuel cell applications. J Mater Chem A 1:14375–14383

VII

"Probing membrane and interface properties in concentrated electrolyte solutions"

Journal of Membrane Science, ***2014****, 459, pp 177–189*

Journal of Membrane Science 459 (2014) 177–189

Contents lists available at ScienceDirect

Journal of Membrane Science

journal homepage: www.elsevier.com/locate/memsci

Probing membrane and interface properties in concentrated electrolyte solutions

Enrica Fontananova [a,*], Wenjuan Zhang [a], Isabella Nicotera [b], Cataldo Simari [b], Willem van Baak [c], Gianluca Di Profio [a], Efrem Curcio [d], Enrico Drioli [a,d]

[a] Institute on Membrane Technology of the National Research Council (ITM-CNR), c/o University of Calabria Via P. Bucci, cubo 17/C, 87036 Rende (CS), Italy
[b] Department of Chemistry and Chemical Technologies, Via P. Bucci, University of Calabria, 87036 Rende (CS), Italy
[c] Fujifilm Manufacturing Europe BV, Tilburg, The Netherlands
[d] Department of Environmental Engineering and Land and Chemical Engineering, University of Calabria Via P. Bucci, cubo 44A, 87036 Rende (CS), Italy

ARTICLE INFO

Article history:
Received 23 August 2013
Received in revised form
24 January 2014
Accepted 25 January 2014
Available online 17 February 2014

Keywords:
Concentrated electrolyte solution
Impedance
Interface
Ion exchange membrane
PGSE-NMR

ABSTRACT

This study deals with the membrane and interface electrical properties investigation by electrochemical impedance spectroscopy (EIS). The EIS is a powerful technique for characterizing electrical behavior of systems in which coupled electrical processes occur at different rates. A systematic study on the effect of solution concentration, temperature and velocity, on the electrical resistance of anion- and cation-exchange membranes (AEMs and CEMs) and their interfaces (electrical double layer and diffusion boundary layer), was carried out. At the best of our knowledge, for the first time electrolyte concentrations up to 4 M were used for the study of membranes and interface by EIS.

Moreover, Pulsed Gradient Spin Echo Nuclear Magnetic Resonance (PGSE-NMR) technique was used to measure the water self-diffusion coefficients in swelled membrane as a function of the solution concentration and temperature. These measurements gave additional important insights about the effect of the electrolyte solution and fixed charges concentration in membrane, on membrane microstructure and its transport and electrical properties.

1. Introduction

One of the major concerns of membranologists operating in the field of electro-membranes processes, is the depth knowledge of the membrane electrical and mass-transport properties. It is known that at the interface between a solid ionic conductor and a liquid electrolyte, physical and electrical properties change suddenly because of an heterogeneous charges distribution (polarization) which reduce the overall electrical conductivity of the system [1–3].

The membrane electrical resistance is usually measured by direct current (DC) method. In DC measurements the membrane is installed in a cell which consists of two chambers containing the testing solutions separated by the membrane. A DC signal is applied and the voltage drop across the membrane is measured. The electrical resistance is given by the slope of the current vs. the voltage drop curve, in agreement with Ohm's law [4]:

$$R = \frac{U}{I} \tag{1}$$

where R [Ω] is the resistance, U [V] is the voltage drop measured between the two sides of the membrane; I [A] is the current.

To obtain the membrane resistance, the resistance of the cell filled with the solution, but without the membrane, is subtracted from the resistance of the cell containing both, the solution and the membrane. The method is simple, but it is not able to distinguish the membrane from the interface resistance. On the contrary of the measurement in direct current, using an alternate current (AC) over a frequency range, it is possible to distinguish phenomena proceeding at different rates. Electrochemical Impedance Spectroscopy (EIS) is a powerful technique in which an AC is used to measure quantitatively the resistance to the charge transport in the bulk and interfacial regions of solid and liquid electrolyte materials [1,5–7].

In EIS experiments a sinusoidal electrical stimulus (voltage or current) is applied over a frequency range to a pair of electrodes and the response of the system under investigation is observed (current or voltage) by the same, or different electrodes. In the first case the configuration is indicated as two probes (or two electrodes) configuration; when two additional electrodes are used to collect the response of the system, the configuration is indicated as a four probes [1]. In membrane characterization field, the two probe configuration is usually applied when the membrane is pressed

* Corresponding author. Tel.: +39 098 449 2010; fax: +39 098 440 2103.
E-mail addresses: e.fontananova@itm.cnr.it, enrica.fontananova@cnr.it (E. Fontananova).

http://dx.doi.org/10.1016/j.memsci.2014.01.057

between two solid conductive electrodes, like in the case of the membrane electrode assembly (MEA) for fuel cells [8–11].

Despite some examples of the use of the two probes configuration can be found in literature for the study of the ion transport through a membrane separating two liquid electrolyte solutions [12–14], the four probe configuration is the most convenient and commonly used. The four probes, with respect to the two probes configuration, has the advantage to eliminate from the impedance spectra the contribution of the electrode injecting stimulus/electrolyte charge transfer resistance, focusing the probing on the membrane and its interface [15–21]. Impedance spectroscopy was also used for the in-situ non-destructive structural characterization of membranes and fouling phenomena [17,22–24]

Another possible configuration in EIS experiments consist in the use of three electrodes, but it is usually employed to characterize only one half of an electrolytic/electrochemical cell, or phenomena occurring on an electrode [25], but not to investigate membrane properties.

This study deals with the membranes and interface electrical properties investigation by EIS. A systematic analyses on the effect of solution concentration, temperature and velocity on the electrical resistance of anion and cation exchange membranes (CEMs and AEMs) and their interfaces, was carried out. At the best of our knowledge, for the first time electrolyte concentrations up to 4 M were used for the study of membranes and interface properties by EIS. Moreover, Pulsed Gradient Spin Echo Nuclear Magnetic Resonance (PGSE-NMR) technique was used to characterize AEMs and CEMs swelled in concentrated electrolyte solutions. NMR spectroscopy provides information on the microscopic, as well as, macroscopic nuclear environments by determination of parameters such as relaxation times, self-diffusion coefficients, and structural information.

The interest towards concentrated solutions lies in the high salinity-gradient power (SGP) that can be extracted by membrane-based energy conversion processes, like pressure-retarded osmosis (PRO) and reverse electrodialysis (RE). The maximum theoretical obtainable energy during the reversible mixed of a diluted stream with a saline concentrated solution, ranges from 0.75 kW-h/m^3 to 14.1 kW-h/m^3 of diluted solution, going from seawater (osmotic pressure 2.7 MPa) to Dead Sea water (osmotic pressure 50.7 MPa) as saline solution [26]. Concentrated solutions are produced in numerous industrial activities such as saltworks and salt mines. Membrane-based integrated systems open interesting perspectives for sustainable and efficient energy conversion using natural and abundant water resources. Brine solutions can be produced by reverse osmosis and/or membrane distillation of seawater [27–30], and they can be used as concentrated stream in SGP-RE stack employing as diluted stream sea or brackish water. This idea is at the basis of the European FP7 Project Reapower (www.reapower.eu), and it can offer a huge potential for the improvement of the electrical performance of SGP-RE system, which usually focus on the combination of fresh water, as the diluted solution, and seawater, as the concentrated solution. The use of concentrated solution allows to reduce the electrical resistance within the low concentration compartment of the SGP-RE stack, boosting the power that can be extracted from the SGP [26,31,32].

2. Materials and methods

2.1. Membranes samples

Three homogeneous reinforced cation exchange membranes (CEMs) and three homogenous reinforced anion exchange membranes (AEMs) produced by Fuji, were investigated (Table 1). Before the use the membranes were washed with a 0.5 M NaCl solution for 24 h changing the solution 4 times to remove residual traced of solvents and/or chemical agents. After this procedure the samples were indicated as “activated”.

2.2. Electrohemical impedance spectroscopy (EIS) experiments

In EIS experiments the response of a system to a sinewave voltage or current excitation is investigated in the frequency domain. Voltage ($U_{(\omega)}$ [V]) and current ($I_{(\omega)}$ [A]) depend from the circular velocity or circular frequency ω [s^{-1}] as follow:

$$U_{(\omega)} = U_o \sin \omega t \tag{2}$$

$$I_{(\omega)} = I_o \sin(\omega t + \varphi) \tag{3}$$

$$\omega = 2\pi\nu \tag{4}$$

where t [s] is the time, φ [°] is the phase shift between voltage and current, and the subscript o refers to the amplitude of voltage and current in phase, ν [s^{-1}] is the frequency.

By using the Euler form:

$$e^{j\varphi} = \cos \varphi + j \sin \varphi \tag{5}$$

where j is the imaginary number ($j = \sqrt{-1}$)

The impedance $Z_{(\omega)}$ [Ω] can be expressed in a form similar to Ohm's law:

$$Z_{(\omega)} = \frac{U_o e^{j\omega t}}{I_o e^{j(\omega t+\varphi)}} = \frac{U_o}{I_o} e^{j\varphi} = |Z| \cos \varphi + j|Z| \sin \varphi \tag{6}$$

where $|Z|$ is the impedance modulus.

The Eq. (6) indicates that the impedance is composed of two parts, i.e. the real part:

$$Z' = |Z| \cos \varphi \tag{7}$$

and the imaginary part:

$$Z'' = |Z| \sin \varphi \tag{8}$$

The real part of the impedance is the resistance, the imaginary part is called reactance [1,4].

Table 1
List and some experimentally determined properties of the membranes.

Membrane	Thickness (μm)*	Ion exchange capacity (mmol/g membrane)	Density of fixed charges (mol/L)*	Membrane areal resistance (Ω cm^2)**
Fuji-AEM-0150	166 ± 1	1.1 ± 0.1	2.2 ± 0.3	1.631 ± 0.001
Fuji-AEM-80045	129 ± 2	1.4 ± 0.1	3.8 ± 0.2	1.551 ± 0.001
Fuji-AEM-90025	109 ± 2	1.6 ± 0.3	2.9 ± 0.6	1.102 ± 0.001
Fuji-CEM-0150	170 ± 1	1.6 ± 0.1	3.4 ± 0.2	2.647 ± 0.001
Fuji-CEM-80050	114 ± 2	1.1 ± 0.1	2.4 ± 0.2	2.974 ± 0.001
Fuji-CEM-90026	113 ± 2	1.0 ± 0.3	1.8 ± 0.5	1.642 ± 0.001

* Conditions: NaCl 0.5 M, 20 °C.
** Conditions: NaCl 0.5 M, 20 °C, 2.8 cm s^{-1}.

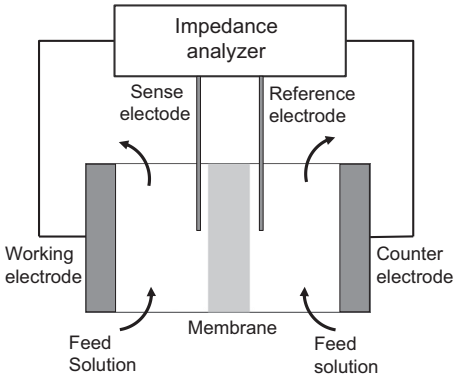

Fig. 1. Schematic view of the experimental set-up used for the EIS experiments.

In this work a four electrodes configuration was used with a home designed impedance cell having an active membrane area of 3.14 cm^2 (Fig. 1). The membrane disc was placed in vertical position.

The cell was fed by two gear pumps with two identical solutions (1 L for each solution), immersed in a thermostatic bath and kept under stirring, flowing along the opposite sides of the membrane. An AC current over a frequency range was injected through two planar electrodes (working and counter electrode) and the response of the system to the sinewave perturbation was measured by two reference electrodes (indicated as sense and reference) using a potentiostat/galvanostat combined with a frequency response analyzer, Metrohm Autolab Autolab PGSTAT302N. The voltage drop across the membrane was measured by positioning the two reference electrodes in symmetric Haber–Luggin capillaries having the tip close to the membrane surface. The cell was inserted inside a thermostatic Faraday cage connected to the potentiostat/galvanostat ground for proper shielding.

The sense and reference electrodes were Ag/AgCl Reference electrodes from Gamry Instruments; the Haber–Luggin capillaries were filled with KCl 3 M. The planar working and counter electrodes were made of Ag covered with a thin layer of AgCl by electro deposition. Milli-Q water (18.2 MΩ cm) was used to prepare all the solutions.

The EIS experiments were carried out in the frequency range 1000–0.01 Hz, with a signal amplitude of 10 mV. The electrical resistance [Ω] was multiplied for the active area [cm^2] to obtain the areal resistance [Ωcm^2].

Each sample, after activation, was immersed in the testing solution for 24 h to ensure a complete conditioning. The EIS spectra were fitted with the equivalent circuits [1,12] showed in Fig. 2, by the software Nova 1.9.16 by Metrohm Autolab B.V., using a non-linear least square procedure (convergence conditions: maximum number of iterations 1000; maximum number of iterations without improvement 50; maximum change in χ^2 (scaled) parameter 0.001). If not otherwise specified, the circuit A, was used. The membrane resistance (R_m) was obtained subtracting the solution resistance, obtained from blank experiments (i.e. without the membrane), from the membrane plus solution resistance (R_{m+s}). All the experiments have been repeated in triplicate.

2.3. Ion exchange capacity

The ion exchange capacity (IEC) was measured by acid–base titration. A sample of activated CEM or AEM was thoroughly washed with water to remove residual traces of salt on the surface and immersed respectively in a known volume of 0.1 M solution of HCl or NaOH for three days at 20 ± 2 °C. Then the membrane was removed and the exchanged solution was divided in three lots that were titrated respectively with 1 M NaOH or HCl solution until neutrality (pHmeter immersed in the solution).

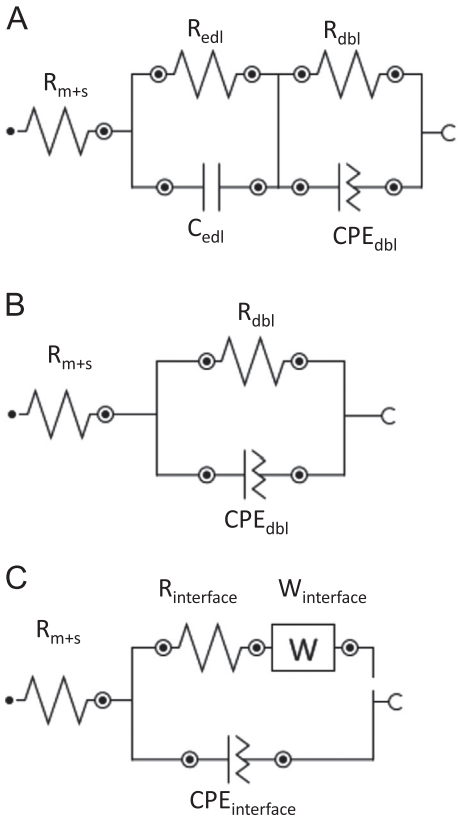

Fig. 2. Equivalent circuits used to fit the EIS spectra. The resistor is indicated as *R*; the capacitor as *C*; the constant phase element (a non-ideal capacitor) as CPE; the Warburg impedance as *W*. The subscript "*m+s*" is referring to membrane plus solution, the subscript "edl" to the electrical double layer; the subscript "dbl" to the diffusion boundary layer; the subscript "interface" indicates the global interface membrane/solution.

The IEC was calculated using the following equation:

$$IEC = \frac{\text{moles } H^+ \text{ or } OH^- \text{ exchanged}}{W_{dry}} \quad (9)$$

The dry weight of the membrane (W_{dry} [g]) was measured after the exchange, by washing the membrane thoroughly with water and drying the sample in a furnace at 80 °C for 2 days.

The procedure was repeated three times and the medium value was reported.

2.4. Membrane swelling

The membrane swelling was determined by immersing the activated samples in a NaCl solution (0.017 M; 0.5 M; 1 M or 4 M) for three days at a fixed temperature (20 °C; 30 °C or 40 °C). In the case of the swelling experiments with the 0.017 M NaCl solution, the activation procedure was carried out using this diluted solution instead of the 0.5 M solution.

The wet weight (W_{wet} [g]) was measured after swelling in the salt solution and rapid dipping of the membranes on the surface with paper tissue. The dry weight (W_{dry} [g]) was measured after the exchange procedure, as reported above.

The membrane swelling (*sw%*) was calculated using the following formula:

$$sw\% = \frac{W_{wet} - W_{dry}}{W_{dry}} 100 \quad (10)$$

The swelling and the IEC data were used to determine the density of the fixed charged groups (moles of fixed charged groups per volume of water in membrane, C_{fix} [mol/L]) at various

temperatures (20–40 °C) and solution concentrations (0.017–4 M):

$$C_{fix} = \frac{IEC}{sw\%}100 \quad (11)$$

2.5. PGSE-NMR analyses

NMR measurements were performed on a Bruker NMR spectrometer AVANCE 300 Wide Bore working at 300 MHz on ^{1}H. The employed probe was a Diff30 Z-diffusion 30 G/cm/A multinuclear with substitutable RF inserts. Spectra were obtained by applying the Fourier transform to the resulting free induction decay (FID) of a single $\pi/2$ pulse sequence. The $\pi/2$ pulse width was about 8 μs. One of its most important uses in the study of swelled membranes has been to provide mass transport data of the diffusing ions through measurement of water self-diffusion coefficient (D) by the NMR pulse gradient spin echo (PGSE) sequence [33] (Fig. 3A). The PGSE technique is a powerful non-invasive method for the determination of D in multi-component systems and consists of two rf pulses, Hahn-echo sequence ($\pi/2$–τ–π), with two identical pulsed-field gradients, the first applied between the 90° and 180° rf pulse (during the dephasing) and the second after the 180° rf pulse (during the rephasing) but before the echo. Following the usual NMR notation, the pulsed-field gradients have magnitude g, duration δ, and time delay Δ (different from the degree of ionic association). The attenuation of the echo amplitude is represented by the Stejskal–Tanner equation:

$$A(g) = A(0)e^{-\gamma^2 g^2 D\delta^2(\Delta - \delta/3)} \quad (12)$$

where D is the self-diffusion coefficient and γ is the nuclear gyromagnetic ratio and $A(0)$ is the amplitude of the echo at $g=0$. Note that the exponent in the equation is proportional to the mean-squared displacement of the molecules over an effective time scale ($\Delta-(\delta/3)$). For the investigated samples, the experimental parameters, Δ and δ, were 10 and 1 ms, respectively. The gradient amplitude, g, varied from 10 to 600 G cm^{-1}. In this conditions the uncertainty in the self-diffusion measurements was ~3%.

Finally, longitudinal relaxation times (T_1) were measured by the inversion-recovery sequence (π–τ–$\pi/2$) (Fig. 3B).

The time interval τ was varied using approximately 10–12 values. Immediately following the π pulse, the magnetization (M) was inverted. During the time interval, M relaxed back to thermal equilibrium at a rate of T_1^{-1}. The application of the $\pi/2$ rf pulse caused M to rotate from the z-axis into the x–y plane where the nuclear signal may be picked up by a receiver. The time dependence of Mz follows:

$$Mz = Mo(1-2e^{-\tau/T1}) \quad (13)$$

For the NMR measurements, two membrane samples were selected: Fuji-AEM-80045 and Fuji-CEM-80050. Each activated membrane was conditioned in the testing solution for 24 h, then it was removed from the solution and quickly blotted dry on the surface with a paper tissue. At this point the membrane was loaded into a 5 mm NMR Pyrex tube and put in the spectrometer. The measurements were conducted by increasing temperature step by step from 20 to 100 °C, and leaving the sample to equilibrate at each temperature for about 10 min.

3. Results and discussion

3.1. Effect of the solution velocity and temperature on the membrane and interface resistances

The membranes were characterized by EIS using a 0.5 M NaCl solution, simulating the seawater. The EIS spectra were fitted with

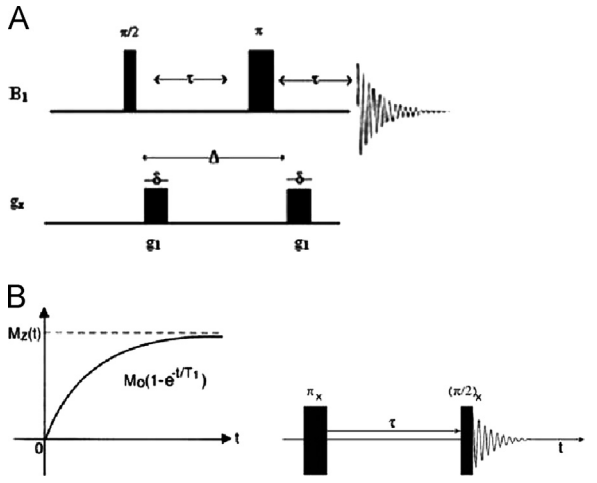

Fig. 3. Schematic of the pulse gradient spin echo technique (PGSE) pulse sequence (A); inversion recovery sequence (B).

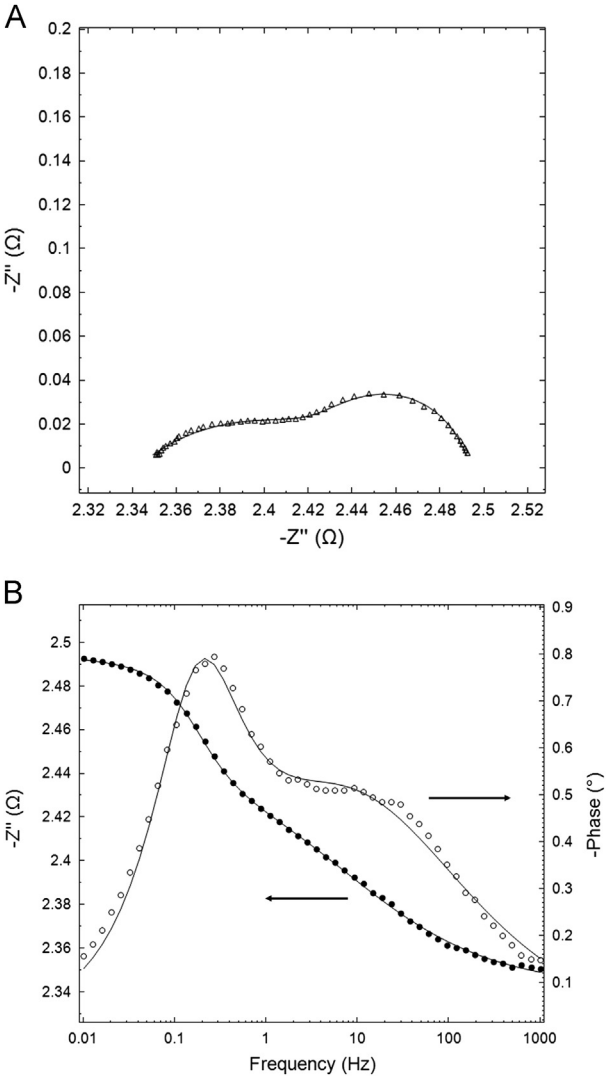

Fig. 4. Nyquist (A) and Bode plot (B) of the Fuji-CEM-0150 membrane measured in 0.5 M NaCl solution at 20 ± 1 °C and 2.8 cm s^{-1}. In (A): $Z'(\Omega)$ is the real part and $-Z''(\Omega)$ is the imaginary part of the impedance; in (B): $Z(\Omega)$ is the module of the impedance and Phase (°) is the phase shift between voltage and current. The experimental data (symbols) were fitted with the equivalent circuit of Fig. 2A (continuous line).

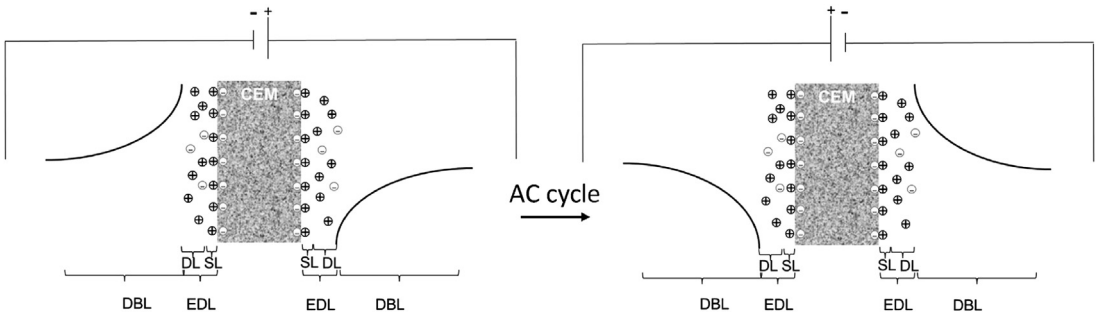

Fig. 5. Bipolar concentration polarization for a cation exchange membrane (CEM) immersed in an electrolyte solution during an AC cycle. Schematic view of the diffusion boundary layer (DBL) and the electrical double layer (EDL), composed by the Stern layer (SL) and the diffusion layer (DL). The continuous line in the DBL is the qualitative salt concentration profile.

the equivalent circuit of Fig. 2A. The Nyquist plot (Fig. 4A), which shows the imaginary part vs. the real part of the impedance, and the Bode plot (Fig. 4B), which represents the module of the impedance and the phase shift dependence vs. the frequency, provides a visual verification of the good agreement between the equivalent circuit proposed and the experimental data.

The circuit of Fig. 2A includes, in addition to the membrane and solution resistance (R_{m+s}) the contribution of the interfacial transfer resistance through the electrical double layer (R_{edl}) and the diffusion boundary layer (R_{dbl}). The formation of the electrical double layer is due to the presence of a net charge on the membrane surface which affects the ions distribution at the membrane/solution interface, resulting in an increase in the concentration of counter-ions (Fig. 5). The region over which this influence spreads out is called electrical double layer (EDL) [3,34,35]. The EDL is schematically composed by two layers: an inner layer, called *Stern layer* (SL), formed by ions strongly bound by electrostatic interactions with the membrane surface, and an outer layer, called *diffuse layer* (DL), constituted by loosely bond ions. The SL has a thickness in the order of Angstrom (one or two radius of solvated ions away from the surface); the DL has a thickness in the order of nanometer. The counter ions in the DL are less attracted to the charged surface because of the electrically screening of the SL, and they tend to diffuse into the liquid phase under the influence of electrical attraction and thermal motion. Fig. 5.

Moreover, concentration polarization phenomena occurs at the interface membrane/solution because of the flux difference between the co-ion and the counter-ion, as well as, because of the difference in transport number of the ions between the ion-exchange membrane (IEM) and the solution phase [36,37].

In a IEM the electrical current is transported almost exclusively by the counter-ions having a transport number in membrane tending to one. On the contrary, the co-ions are ideally excluded within the IEM due to the presence of fixed ions of the same sign (Donnan exclusion), and the transport number tends to zero. In the solution phase the current is transported both by co- and counter-ions and, in the case of symmetric salts, the transport number is 0.5 for both. As a consequence an additional layer, called diffusion boundary layer (DBL), having a thickness in the order of several hundred of micrometers, is formed (Fig. 5).

The membrane resistance did not change significantly with the solution velocity (Fig. 6). This behavior can be also easily appreciated comparing the Nyquist plot registered at different velocities (Fig. 7). The intercept with the real axis of the impedance at high frequency corresponds to the membrane plus solution resistance (R_{m+s}) and it was substantially independent from the solution velocity. On the contrary, the intercept at low frequency, which contains also the contribution of the interface ($R_{m+s}+R_{edl}+R_{dbl}$), was visibly reduced increasing the solution velocity. In particular, the resistance of the diffusion boundary layer decreased for all the samples with increasing solution velocity.

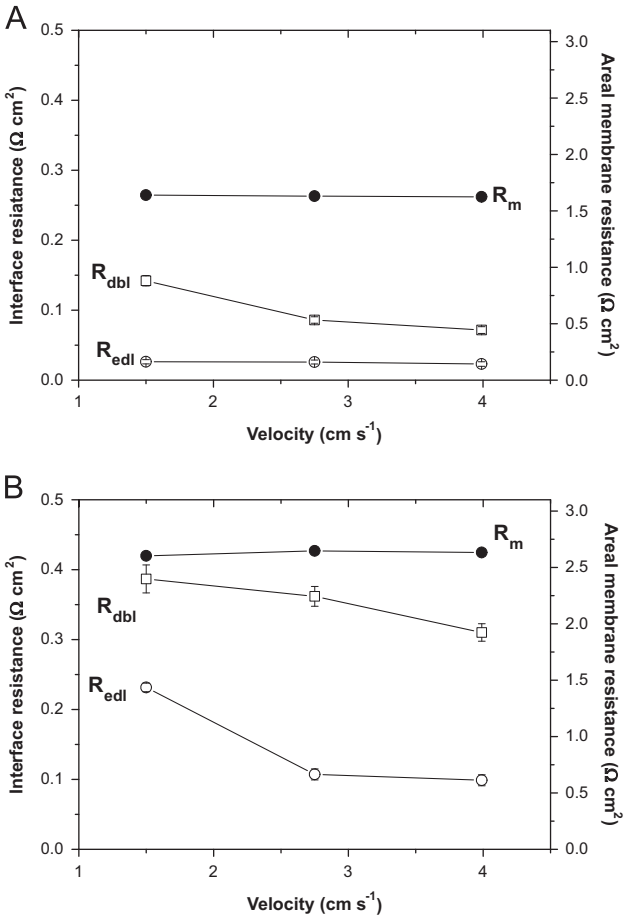

Fig. 6. Membrane (R_m) and interface (R_{edl} and R_{dbl}) areal resistances as a function of the solution velocity of the Fuji-AEM-0150 (A) and the Fuji-CEM-0150 (B). Conditions: 0.5 M NaCl, 20 ± 1 °C. Filled symbols, axes on the right for the R_m; empty symbols, axes on the left for the R_{edl} and R_{dbl}.

The bipolar concentration polarization during AC cycle caused by the buildup and depletion of ions at the interface, was time dependent. The contribution of the interfacial ionic charge transfer through the interface layers at low frequencies was greater than at high frequencies, because at high frequencies there is insufficient time for their formation.

The resistance of the membrane was the dominant resistance with respect the interfacial ionic charge transfer through the electrical double layer and the diffusion boundary layer ($R_m > R_{dbl} > R_{edl}$).

The velocity did not influence significantly R_{edl} in the case of the AEMs, but it had a not negligible effect in the case of CEMs.

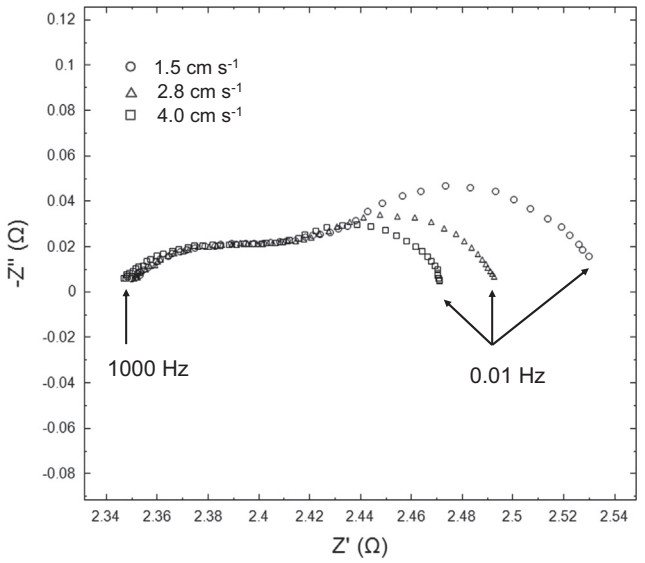

Fig. 7. Nyquist plot of the Fuji-CEM-0150 membrane measured in a 0.5 M NaCl solution at 20 ± 1 °C at different velocities: 1.5 (symbol: circle), 2.8 (symbol: triangle) and 4.0 cm s^{-1} (symbol: square).

This was probably due to a higher thickness of the DL in the EDL, with respect to the AEMs, which renders the influence of the tangential stress more relevant. The higher thickness of EDL of the CEM is related to the greater hydrodynamic radius of the counter-ion in the case of the CEMs with respect to the AEMs (respectively Na^+ and Cl^-).

The membrane and interface resistances of the CEMs, were higher in comparison with the AEMs resistances (Table 1). The higher resistances observed with the CEMs with respect to the AEMs were dependent from the lower mobility of the Na^+ ion with respect to the Cl^- (4.98×10^{-8} and 6.88×10^{-8} m^2 V^{-1} s^{-1} respectively at 25 °C [38]). This increased not only the membrane electrical resistance, but also the interface resistances where the counter-ions concentration was higher than co-ions.

The membrane areal resistance of the AEMs with 0.5 M NaCl decreased in the order: Fuji-AEM-0150 > Fuji-AEM-80045 > Fuji-AEM-90025. These results were in agreement with the decreasing thickness of the membranes in the same order (Table 1). This means that the reduction of the membrane thickness can contribute to reduce the electrical resistance. However, also the fixed charge density, the chemical nature and distribution of the fixed charged groups, are key factors for the membrane electrical resistance. In general, increasing the density of the fixed charged groups the ions migration through the membrane is expected to be more limited because of the stronger interactions of the mobile ions with the fixed ions [39]. For this reason, despite the Fuji-CEM-80050 and Fuji CEM-90026 had similar thickness, the electrical resistance of the second one was lower thanks to its lower density of the fixed charged groups

The resistance of the ion transport through the membrane, as well as through the interface, decreased with the temperature, because of the increasing ion mobility (Fig. 8). The effect of the temperature was more evident for the CEMs than for the AEMs.

3.2. Effect of the solution concentration on the membrane and interface resistances

In addition to the temperature and the solution velocity, another important factor able to influence the electrical resistance of the IEMs, was the solution concentration. Increasing the concentration from 0.5 M to 1 M resulted in a drop of the membrane and the interfacial ionic charge transfer resistances for the Fuji-AEM-90025 and the Fuji-CEM-90026 (Table 2).

In the case of the Fuji-AEM-80045 and Fuji-CEM-80050 membranes, the EIS experiments were conducted also with a 4 M NaCl solution. This solution simulates the seawater brine. With the 4 M solution the fitting with the model represented in the Fig. 2A did not converge for most of the experiments. Only in few cases, the model converged but it gave a R_{edl} values very low (in the order of few μΩ) or negative (without physical meaning), and the estimated error was very high (> 100%). On the contrary the experimental data were fitted reaching a good convergence with the equivalent circuit represented in Fig. 2B. As a consequence, it was possible to draw the conclusion that the contribution of the electrical double layer to the total resistance became negligible at 4 M NaCl. This behavior was in agreement with the reduction of the thickness of the electrical double layer increasing the solution concentration, because of the higher screening effect of the attractive electrical interactions between the counter-ions and fixed charged groups of the membrane, increasing the ions concentration in solution [40]. The thickness of the electrical double layer is approximately the Debye length, which is reciprocally proportional to the square root of the ionic strength of the solution, or ionic concentration in the case of symmetric electrolytes [41].

Also in the case of the 4 M solution, like for the 0.5 M solution, the ion transport resistance decreased with the increasing of the temperature (Fig. 8C and D).

Increasing the solution concentration from 0.5 M NaCl to 4 M, the membrane resistance decreased slightly for the Fuji-AEM-80045, and the resistance of the diffusion boundary layer increased (Table 2).

An opposite behavior was observed for the Fuji-CEM-80050: increasing the solution concentration the membrane resistance increased but the resistance of the diffusion boundary layer decreased (Table 2).

However, considering also the decreasing of the solution resistance, increasing the concentration up to 4 M, the effect on the total cell resistance ($R_{m+s}+R_{dbl}+R_{edl}$) was a net reduction. For example for the Fuji CEM-80050 at 20 ± 1 °C and 1.5 cm s^{-1} the total resistance decreased from 8.0 to 4.5 Ωcm^2, increasing the solution concentration from 0.5 to 4 M.

The increase of the membrane electrical resistance, was due to the membrane shrinking induced by the increasing solution concentration (Fig. 9A), with a consequent narrowing of the hydrophilic channels of the IEMs (pathway for the ions transport) [42]. In parallel, the fixed charge density increased with the reduction of the swelling degree and, as a consequence, the ion migration through the membrane was more difficult because of the stronger interactions with the fixed charged groups that can form isolated ionic domains not well interconnected each other [39,42].

The density of the fixed charges of the Fuji-CEM-80050 was lower than that of the Fuji-AEM-80045 over the entire range of concentration investigated (Fig. 9B). As a consequence, this membrane was more sensitive to shrinking going from the 0.5 to the 4 M solution with respect the Fuji-AEM-800445 (-21% of mass swelling vs. -7%) because of the higher osmotic pressure difference between the solution and the membrane (osmotic pressure of the 0.5 and 4 M NaCl solutions were respectively 2.5 MPa [43] and 22 MPa [44]).

The results obtained with the Fuji-AEM-80045 and Fuji-CEM-80050 tested with the 4 M NaCl solution, did not contradict the results obtained with the Fuji-AEM-90025 and Fuji-CEM-90026 tested with the 1 M NaCl solution.

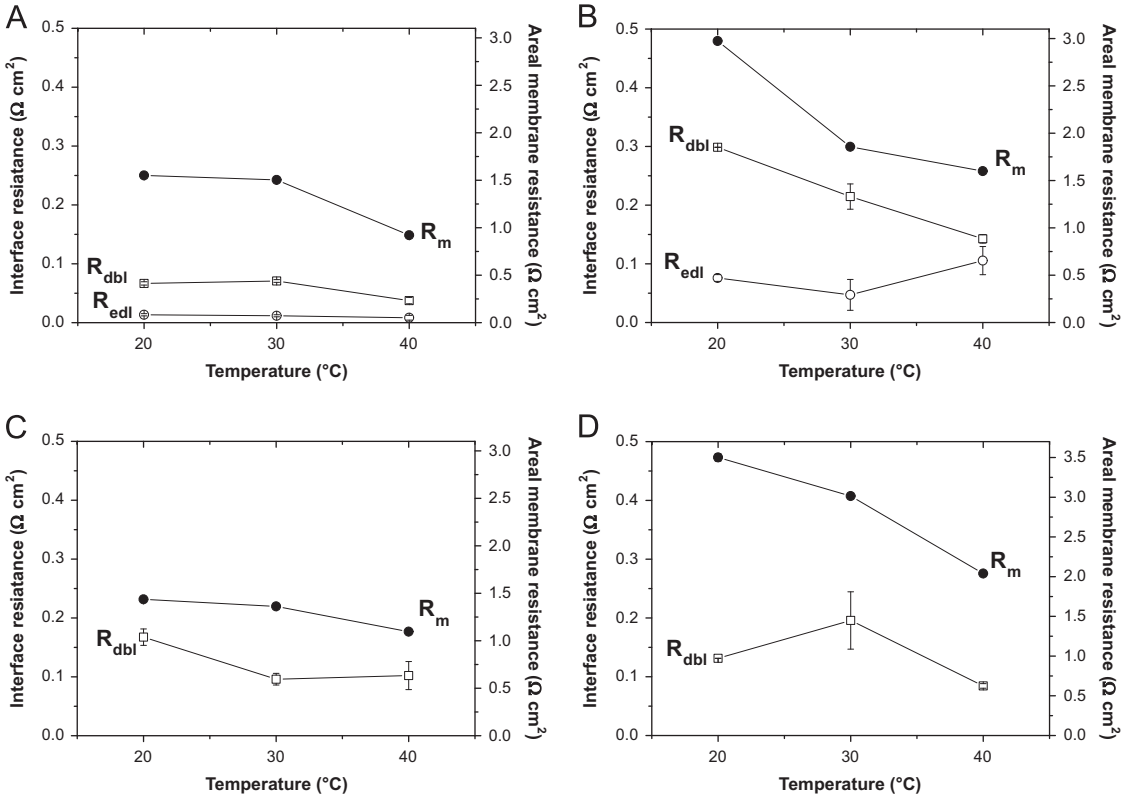

Fig. 8. Membrane (R_m) and interface (R_{edl} and R_{dbl}) areal resistances as a function of the temperature for the Fuji-AEM-80045 (A, C) and the Fuji-CEM-80050 (B, D). Conditions: 0.5 M NaCl in (A) and (B); 4 M NaCl in (C) and (D); solution velocity: 2.8 cm s^{-1}. Filled symbols, axes on the right for the R_m; empty symbols, axes on the left for the R_{edl} and R_{dbl}.

Table 2
Membrane (R_m) and interface (R_{edl} and R_{dbl}) areal resistances in NaCl solutions at various concentrations. Conditions: 2.75 cm s^{-1}, 20±1 °C.

Membrane	**0.5 M**			**1.0 M**		
	R_m (Ω cm²)	**R_{edl} (Ω cm²)**	**R_{dbl} (Ω cm²)**	**R_m (Ω cm²)**	**R_{edl} (Ω cm²)**	**R_{dbl} (Ω cm²)**
Fuji-AEM-90025	1.102±0.001	0.018±0.003	0.056±0.004	0.787±0.001	0.006±0.002	0.028±0.002
Fuji-CEM-90026	1.642±0.001	0.149±0.005	0.146±0.031	1.246±0.001	0.032±0.002	0.115±0.003
	0.5 M			**4.0 M**		
	R_m (Ω cm²)	**R_{edl} (Ω cm²)**	**R_{dbl} (Ω cm²)**	**R_m (Ω cm²)**	**R_{edl} (Ω cm²)**	**R_{dbl} (Ω cm²)**
Fuji-AEM-80045	1.551±0.001	0.013±0.002	0.067±0.003	1.436±0.001	–	0.167±0.014
Fuji-CEM-80050	2.974±0.001	0.076±0.006	0.299±0.010	3.501±0.050	–	0.131±0.001

In this second case, the membranes had an concentration of the fixed charged groups higher than the external solution (4.0 ± 0.4 for the Fuji-AEM-90025 and 2.5 ± 0.2 mol/L for the Fuji-CEM-90026 in NaCl 1 M at 20 °C), and the shrinking effect was moderate, leading to a favorable decreasing of the distance between the charged groups, but without isolating them each other. Moreover, it is well known that increasing the solution concentration the co-ion concentration in the IEM is increased, and to a first approximation is given for a monovalent salt by [45]

$$C_{co}^{m} = \frac{(C_s^s)^2}{C_{fix}} \tag{14}$$

The Eq. (14) is obtained from the Donnan equilibrium expression using the following assumptions, as described in the Ref. [45]:

the exponential function is 1, i.e.

$$e^{-(\Delta\pi \overline{V}_s / RT\nu_i z_i)} \cong 1 \tag{15}$$

the ratio of the activity coefficient in the solution and the membrane is 1, i.e.

$$\left(\frac{\gamma_{co}^{m}}{\gamma_{co}^{s}}\right)^{1/z_{co}} \left(\frac{\gamma_{cou}^{s}}{\gamma_{cou}^{m}}\right)^{1/z_{cou}} \cong 1 \tag{16}$$

and the counter ion concentration is close to the fixed ion concentration, i.e.

$$C_{cou}^{m} = C_{fix}^{m} + C_{co}^{m} \cong C_{fix}^{m} \tag{17}$$

where $\Delta\pi$ is the osmotic pressure difference between the solution and the membrane phase, C is the concentration, ν is the stoichiometric coefficient, z is the charge number, and $\overline{V}$ is the partial molar volume, the subscripts *i*, *co*, *cou*, *s* and *fix* refer to ions, co-ion, counter-ion, salt, and fixed ion of the membrane, the superscripts s and m refer respectively to membrane and solution.

Despite the obvious detrimental effect on the membrane permselectivity, the increase of the total ion concentration in

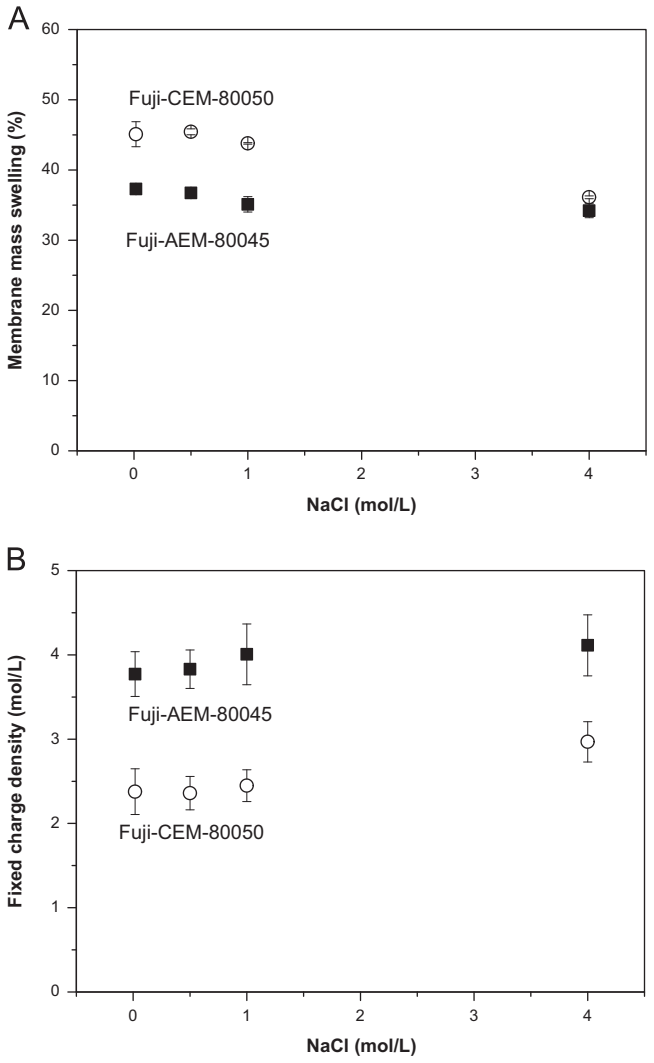

Fig. 9. Membrane mass swelling (A) and density of the fixed charges (B) of the Fuji-CEM-80050 and the Fuji-AEM-80045 as a function of the solution concentration. NaCl solution at 20 ± 1 °C.

membrane may have contributed to the reduction of the electrical resistance in the case of the test with the 1.0 M solution with respect to the test with the 0.5 M solution (higher number of current carriers).

For what concern the effect of the solution concentration on the interface resistances: increasing the concentration from 0.5 M to 1 M the resistance of both R_{edl} and R_{dbl} decreased.

However, increasing the external solution concentration from 0.5 to 4 M, the R_{dbl} increased while the R_m decreased in the case of the Fuji-AEM-80050, and the R_{dbl} decreased while the R_m increased, in the case of the Fuji-CEM-80045.

3.3. Diffusive behavior at zero solution velocity

A separate discussion of the impedance data measured at zero velocity is necessary. A peculiar feature of the spectrum registered at low frequency (< 0.1 Hz) was observed in the case of the 0.5 and 1.0 M NaCl solution, attributable to a diffusion control in the ion transport at the interface [46–49]. This phenomenon was due to the intensification of the bipolar polarization phenomena at the membrane/solution interface when the solution velocity was zero. The rising of the polarization phenomena was due to the absence of turbulences induced by the solution recirculation. The appearance of the diffusive component was reversible and it can be eliminated by restarting the solution recirculation. Various increasing and decreasing velocity runs were performed to confirm this point.

The Nyquist plot registered at frequency < 0.1 Hz with the membrane in 0.5 M solution, had an angle of about 45° (Fig. 10A and B). Moreover, plotting the absolute value of the real and imaginary part of the impedance (|Z'| and |Z″|) vs. $1/\sqrt{2\pi\upsilon}$ two straight and parallel lines were obtained and the slope of both lines was equal to the coefficient of the Warburg impedance σ [$\Omega\,s^{-1/2}$] [47–52]. Also with the 1.0 M solution a diffusive behavior can be observed in the Nyquist plot (Fig. 10C). In the case of the 4 M NaCl solution, the diffusive behavior was not visible in the impedance spectra because of the reducing of the thickness (and resistance) of the electrical double layer with the concentration (Fig. 10D).

The counter-ion diffusion coefficient (D_{ion} [$cm^2\,s^{-1}$]) was calculated according to the following equation [47–52]:

$$D_{ion} = \left(\frac{RT}{\sqrt{2}AF^2\sigma C_{fix}}\right)^2 \quad (18)$$

where R is the gas constant [8314 J K^{-1} mol^{-1}], T the temperature [K], A the membrane area [cm^2], F Faraday's constant [96485 A s mol^{-1}], σ the coefficient of Warburg impedance [$\Omega\,s^{-1/2}$] and C_{fix} is the concentration of the fixed charged groups in membrane [expressed as mol cm^{-3}].

The σ coefficient was obtained by fitting the impedance spectrum with the equivalent circuit showed in Fig. 2C. Despite in literature the Warburg impedance has been usually related to diffusion phenomena in DBL [51–54], in our opinion, the diffusive behavior is also related to phenomena occurring in the DL of the EDL. This hypothesis was formulated on the basis of the disappearance of the diffusive behavior testing the membranes in 4 M solution, e.g. in conditions in which the contribution of the EDL become negligible.

The Nova software returned the parameter Y^o [$S\,s^{½}$] which is related to the Warburg coefficient by the following relationship:

$$\sigma = \frac{1}{\sqrt{2}Y^o} \quad (19)$$

The calculated diffusion coefficient for the AEMs and CEMs depended from the reciprocal of the square of the density of the fixed charged groups in membrane (Eq. (15)). The bipolar polarization phenomena are expected to increase increasing the density of the fixed charged groups because of the higher attraction of the membrane for the counter ions. Moreover, increasing the fixed charge density the counter ions are "less free" to diffuse and the diffusion coefficient decreases. As a consequence, ion diffusion coefficient in a not ideal system, cannot be considered as an intrinsic parameter of the ion, and the effect of the chemical micro-environment cannot be overlooked. As a consequence the observed order in the ion diffusion coefficient for the AEMs was Fuji-AEM-0150 > Fuji-AEM-90025 > Fuji-AEM-80045 (Table 3). For the same reason, the order for the CEMs was Fuji-CEM-90026 > Fuji-CEM-80050 > Fuji-CEM-0150.

Also the increasing of the membrane electrical resistance favored bipolar polarization, because of the slower ion transport in membrane. This was the reason of the jump of the diffusion coefficient of the Fuji-CEM-90026 with respect to the other two CEMs (Table 3), because this sample had a significantly lower membrane electrical resistance, combined also with a lower density of the fixed charged groups. A third factor able to influence ion diffusivity is the ion mobility. The AEMs had a higher diffusion coefficient than the CEMs, and the values increased with the

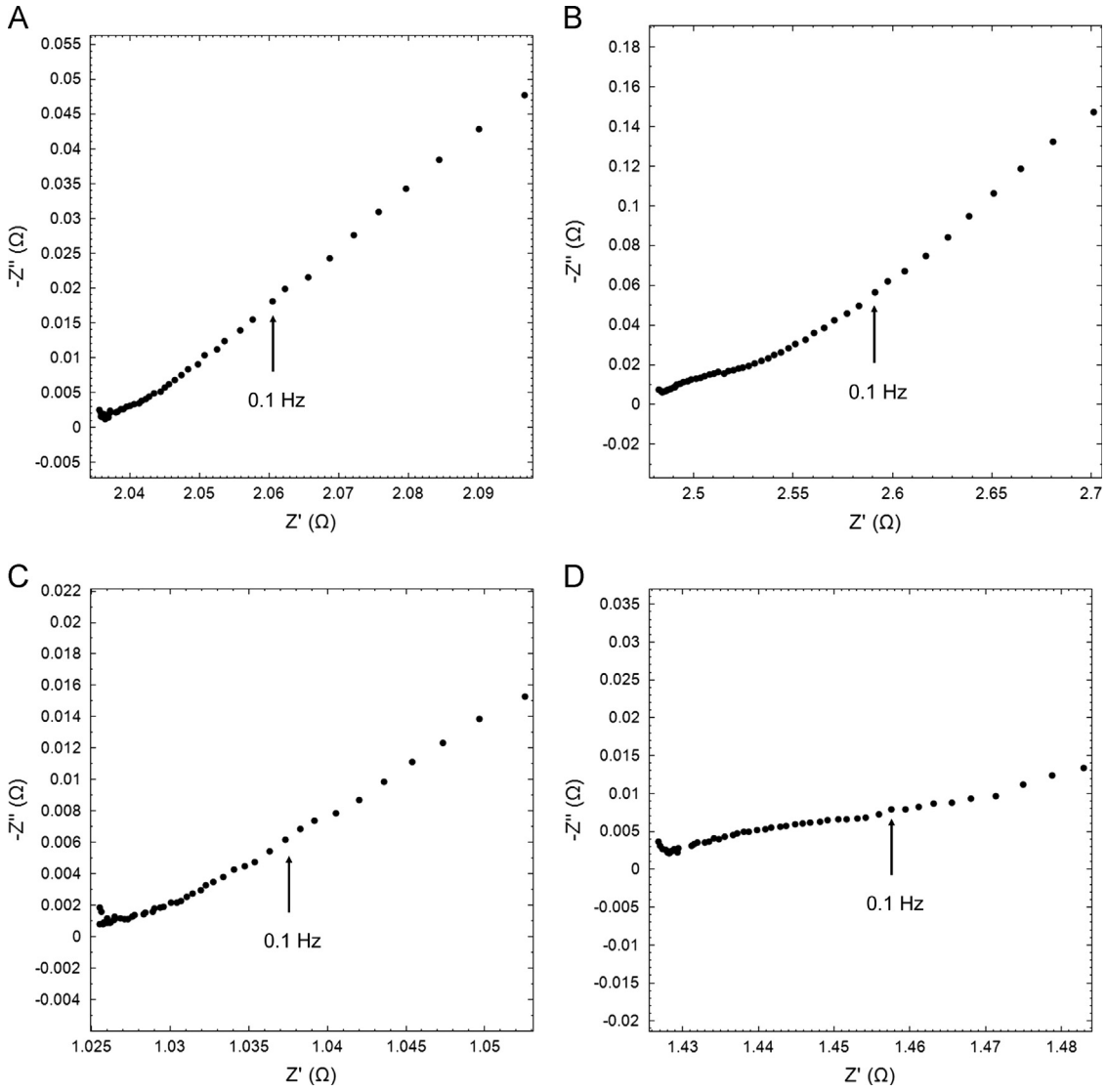

Fig. 10. Nyquist plot of the Fuji-AEM-80045 and the Fuji-CEM-80050 membranes measured in a 0.5 M (A and B respectively), Fuji-AEM-90025 in 1.0 M NaCl and Fuji-CEM-80050 in a 4.0 M NaCl solution (D) at zero solution velocity and 20 ± 1 °C.

Table 3
Ion diffusion coefficient obtained from impedance data registered at zero solution velocity

Membrane	Diffusion coefficient ($cm^2\ s^{-1}$) of Na^+ (for CEMs) and Cl^- (for AEMs)			
	@ 20 °C; 0.5 M NaCl	@ 30 °C (corr sw); 0.5 M NaCl	@ 40 °C (corr sw); 0.5 M NaCl	@ 20 °C; 1 M NaCl
Fuji-AEM-0150	4.61×10^{-6}	–	–	–
Fuji-AEM-80045	1.46×10^{-6}	1.60×10^{-6}	1.81×10^{-6}	
Fuji-AEM-90025	3.52×10^{-6}	–	–	1.74×10^{-5}
Fuji-CEM-0150	2.15×10^{-7}	–	–	–
Fuji-CEM-80050	3.83×10^{-7}	4.26×10^{-7}	6.89×10^{-7}	–
Fuji-CEM-90026	9.48×10^{-7}	–	–	4.57×10^{-6}

temperature. For what concern the effect of the solution concentration, increasing the concentration from 0.5 to 1 M, an increase in the diffusion coefficient was observed because of the increasing screening effect of the attractive electrical interactions between the counter-ions in the DL and fixed charged groups of the membrane. The ions in the DL are less attracted to the charged membrane surface and they tend to diffuse (back-diffuse) into the bulk phase under the influence of electrical attraction and thermal motion.

3.4. NMR investigation

The temperature evolution of the ^1H NMR spectra, collected from 20 °C up 100 °C on the Fuji-AEM-80045 and Fuji-CEM-80050

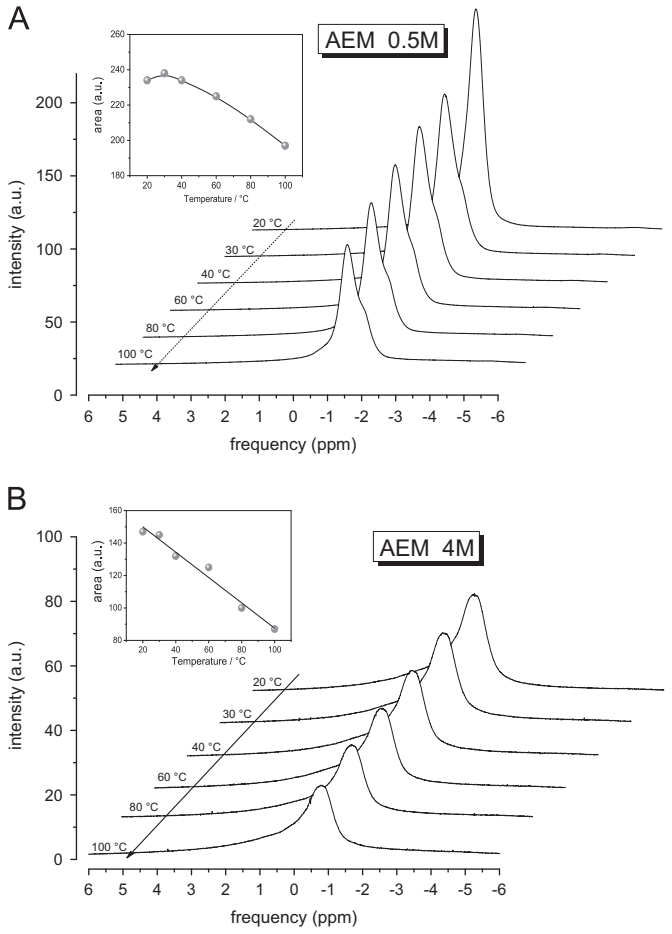

Fig. 11. Temperature evolution of ^{1}H–NMR spectra collected on the Fuji-AEM-80045 membranes swelled in water salt solution at two concentrations, 0.5 and 4 M. The inset shown the peak area vs. temperature.

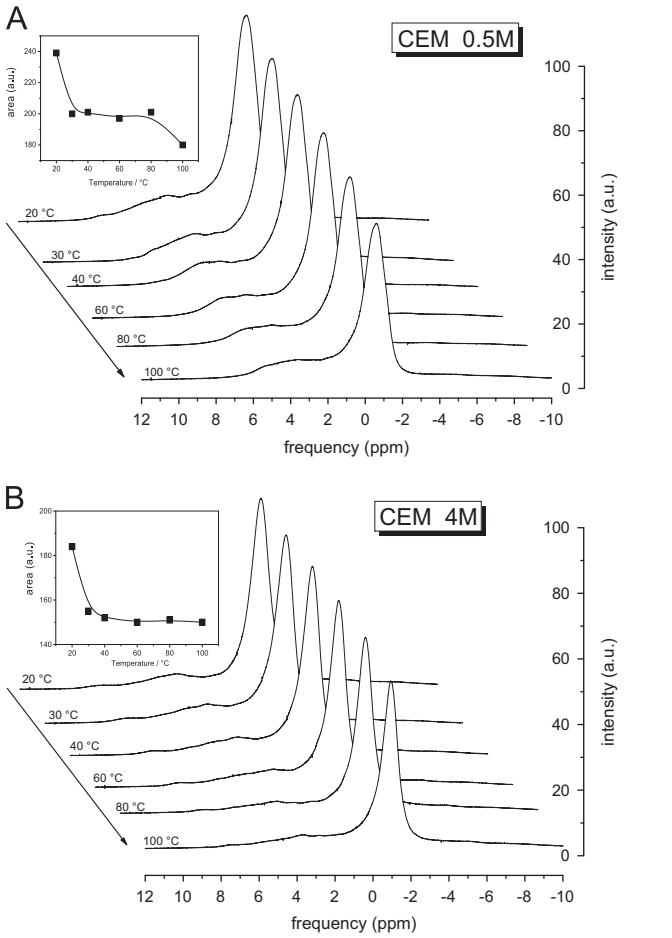

Fig. 12. Temperature evolution of ^{1}H–NMR spectra collected on the Fuji-CEM-80050 membranes swelled in water salt solution at two concentrations, 0.5 and 4 M. The inset shown the peak area vs. temperature.

membranes, swelled in 0.5 and 4 M NaCl solutions, are reported respectively in Figs. 11 and 12, respectively. All the spectra were acquired with the same number of scans ($ns=4$) and were referenced against pure water set at 0 ppm. The NMR signal essentially originates from the water of the salt solutions absorbed from the membranes, while, the proton signals of the polymer chains are basically "invisible", both because their intensity is very small compared to the signal intensity of the water, and because the dipolar spin-spin interactions make hugely broaden the spectral lines.

The proton's signal of both Fuji-AEM-80045 and Fuji-CEM-80050, was quite large (FWHM was about 1 kHz) and asymmetric, typical of a multiple components configuration, i.e., different "types" of water coexist in the system. Actually, water was involved in the hydration shells of the fixed ionic groups of the polymer matrix, as well as, of the mobile ions. However, the different states of water within the hydrophilic channels can be difficult to be discerned because of the fast rate of exchange and, for this reason, only one peak was seen. The intensity of this peak decreased with increasing temperature because of the water evaporation from the membrane (inset in Figs. 11 and 12 shown the peak area vs. temperature).

For the Fuji-AEM-80045 the proton signal of the membrane swelled with the 0.5 M solution was more intense and narrow than membrane swelled in 4 M (Fig. 11). This was due to the higher solution uptakes and to the greater amount of bulk/"free" water (water molecules not involved in the hydration shells of the ions), respectively. The bulk/"free" water originates a narrower Lorentzian signal and, by heating, it was reasonable to expect that this evaporates before, while the "bound" water was more retained in the membrane pores and the strong interactions cause a broadening of the NMR signal.

For the Fuji-CEM-80050, the spectral line for the two concentrations, was very similar and different from that observed in the anionic membrane (Fig. 12). Indeed, in the Fuji-CEM-80050 was present a peak quite Lorentzian accompanied by a broad shoulder in the region of higher frequency. The shape of the spectral line of water confined in membrane clearly depends on the structural and morphological nature of the membrane itself, such as hydrophilic channels size and ionic functional groups present within them, as well as by the nature (size and charge) of the solvated ions. In the CEM, the hydration of the Na^{+} cations involves a greater number of water molecules (hydration number is 5 ± 1), i.e. sodium ion has a greater hydrodynamic radius, than that of the Cl^{-} anions (hydration number is 1 ± 1). Furthermore, the different orientation of water molecules (H pointed toward anions and oxygen toward cations), which arises from the charge asymmetry of the water molecule, results in an effect on the chemical shift of water protons, as was clear from the spectra. The Fuji-CEM-80050 swelled in 0.5 M solution showed a more pronounced shoulder signal than the 4 M, probably imputable to the greater number of water molecules bounded to the ionic groups in the hydrophilic channels. Instead, the decrease of the total area of

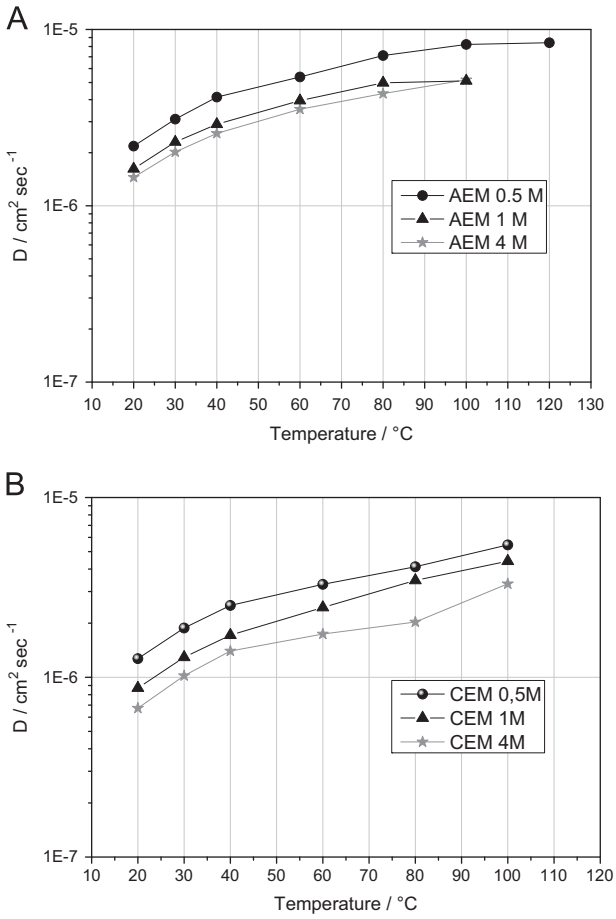

Fig. 13. Self-diffusion coefficients of water confined in completely swelled membranes, from 20 °C up to 100 °C. AEM indicates the Fuji-AEM-80045; CEM indicates the Fuji-CEM-80050.

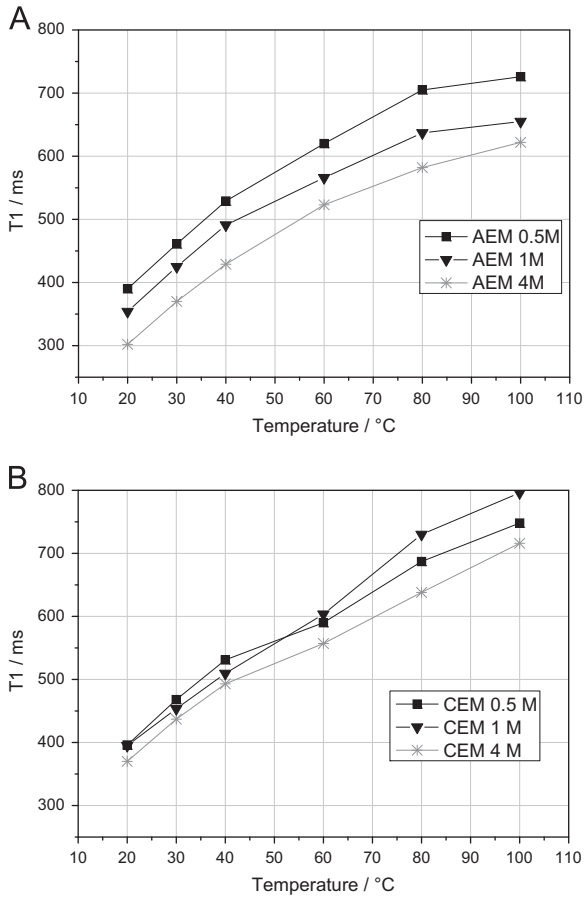

Fig. 14. Longitudinal relaxation times T1 as a function of the temperature (from 20 to 140 °C) of the water confined in completely swelled membranes. AEM indicates the Fuji-AEM-80045; CEM indicates the Fuji-CEM-80050.

the signal in temperature follows the same trend for both concentrations.

The self-diffusion coefficients (D) of water confined in the Fuji-AEM-80045 and Fuji-CEM-80050 swelled up to saturation in salt solutions at three different concentrations, 0.5 M, 1 M and 4 M, are reported in Fig. 13 as a function of temperature, from 20 °C up to 100 °C.

It is well established that when solvent molecules (water in this case) diffuse in presence of macromolecules, their diffusion is slowed down by both the need to divert around macromolecules (obstruction effect) and any interactions with the same macromolecules that inhibit their motion [55,56]

The latter effect, i.e. the interaction between solvent and macromolecules, may be termed solvation or hydration and we can affirm that the interacting molecules are in the "bound state". Exchange of molecules between bound- and free-state results in an averaged water diffusion coefficient D, which depends on the time fraction spent in each state. Additionally, in this case a salt solutions was present, so, water molecules are also involved in the hydration of sodium and chlorine ions and their transport by a vehicular mechanism.

From the data emerged that the ions mobility decreased with increasing the solution concentration while, overall, in the Fuji-CEM-80050, the water diffusion was lower than in the Fuji-AEM-80045.

The decreasing of D when the concentration of the solution increases was due to:

(i) the greater amount of ions that entails a greater number of hydration water molecules, then less mobile;

(ii) the reduction of hydrophilic channels size, that was correlated to the swelling/shrinking of the membrane and that brings a higher obstruction effect and at a reduction of the amount of "free" water.

Finally, as expected, the water diffusion in the AEM was higher than in CEM, since in the AEM, chlorine ions have a number of hydration much smaller than that of the sodium ion in the CEM, therefore, more "free" water in the first membrane and less in the second, at the same concentration.

Further information on the molecular dynamic of the molecules was provided by measurements of longitudinal (or spin-lattice) relaxation times (T_1), as reported in Fig. 14.

Compared to diffusion, T_1 reflects more localized motions including both translation and rotation on a time scale comparable to the reciprocal of the NMR angular frequency ($\sim$1 ns). As the molecular correlation time τ_c depends on temperature, a minimum in T_1 is often observed when $\overline{\omega}\tau_c \sim 1$, where $\overline{\omega}$ is the NMR frequency [57].

In the temperature range investigated, well above the T_1 minimum, i.e. in the so-called extreme narrowing limit ($\overline{\omega}\tau_c \ll 1$), higher T_1 values suggest more facile molecular rotational and translational motion.

In both two membranes, the T_1 values fall into the same range, between 300 and 800 ms, with an almost linear increase with the temperature. Respect to D, T_1 is less affected from the hydrophilic channels size, while the ionic interactions and the molecular aggregations are important. In fact, the solution concentration in the anionic membrane shows a well marked effect, less defined in

the cationic membrane. This could be attributed to the different ionic hydration (orientation of the water molecules in the hydration sphere, and hydration number).

4. Conclusions

The Electrochemical Impedance Spectroscopy is a powerful, non-invasive and non-destructive, technique to characterize the ion transport resistance through membranes and interfacial layers formed when an ion exchange membrane is in contact with an electrolyte solutions (electrical double layer and diffusion boundary layer). The cation exchange membranes were characterized by an higher electrical resistance in comparison with the anion exchange membranes in NaCl solutions. This behavior was explained considering the higher mobility of the Cl^- with respect to the Na^+ (the counter ions of the ion exchange membranes).

The areal membrane resistance was the dominant resistance in the whole range of solution concentration, temperature and velocity investigated (0.5–4.0 M; 20–40 °C; 0–4.0 cm s^{-1}) and it did not depend significantly from the velocity. On the contrary, the resistance of the diffusion boundary layer was reduced increasing the solution velocity.

A diffusive component in the ion transfer at the interface membrane/solution was evident operating in static conditions (zero velocity, no solution stirring), at concentrations $\leq$ 1.0 M.

It was demonstrated that increasing the solution concentration the resistance of the double electrical layer was reduced, and it became negligible at 4 M. This effect was due to the increasing screening of the attractive electrical interactions between the counter-ions and fixed charged groups of the membrane, increasing the concentration of the external solution.

Increasing the solution concentration from 0.5 to 4.0 M the membrane resistance decreases for the Fuji-AEM-80045 but increased for the Fuji-CEM-80050. An opposite behavior was observed for the resistance of the diffusion boundary layer. The increased electrical resistance in 4.0 M solution of the Fuji-CEM-80050 membrane was due to its low fixed charge density in comparison with the external solution, which induced an high osmotic pressure difference between the solution and the membrane phase, and the consequent membrane shrinking and narrowing of the hydrophilic channels pathway for the ions transport. As a consequence it was evident the importance to use membranes with a fixed charge density higher than the solution in the case of concentrated electrolyte solutions.

The relevant effect of the solution concentration on the membrane microstructure was confirmed by pulsed gradient spin echo (PGSE)-NMR technique. From the data clearly emerged that the water self diffusion coefficient decreased with increasing the solution concentration. In parallel the strong increase of fixed charged groups density, increased the resistance to the ion migration.

Acknowledgments

This work was partially funded in the framework of the REAPower project (Reverse Electrodialysis Alternative Power production) (www.reapower.eu), EU-FP7 programme (Project no. 256736).

References

[1] E. Barsoukov, J.R. Macdonald, Impedance Spectroscopy. Theory, Experiment, and Applications, Second Edition, John Wiley & Sons, New Jersey, 2005.
[2] N. Islam, N.A. Bulla, S. Islam, Electrical double layer at the peritoneal membrane/electrolyte interface, J. Membr. Sci. 282 (2006) 89–95.
[3] S. Sang, Q. Wu, K. Huang, A discussion on ion conductivity at cation exchange membrane/solution interface, Colloids Surf., A 320 (2008) 43–48.
[4] H. Strathmann, Ion-Exchange Membrane Separation, Elsevier, Amsterdam, 2004.
[5] H.G.L. Coster, T.C. Chilcott, A.C.F. Coster, Impedance spectroscopy of interfaces, membranes and ultrastructures, Bioelectrochem. Bioenergy 40 (1996) 78–96.
[6] T.C. Chilcott, M. Chna, L. Gaedt, T. Nantawisarakul, A.G. Fane, H.G.L. Coster, Electrical impedance spectroscopy characterization of conducting membranes, J. Membr. Sci. 195 (2002) 153–167.
[7] X. Dominguez-Benetton, S. Sevda, K. Vanbroekhoven, D. Pant, The accurate use of impedance analyses for the study of microbial electrochemical systems, Chem. Soc. Rev. 41 (2012) 7228–7246.
[8] G. Alberti, M. Casciola, L. Massinelli, B. Bauer, Polymeric proton conducting membranes for medium temperature fuel cells (110–160 °C), J. Membr. Sci. 185 (2001) 73–81.
[9] K.-V. Peinemann, S. Pereira Nunes, Membranes for Energy Conversion, Wiley–VCH, Chichester, 2008.
[10] E. Fontananova, F. Trotta, J.C. Jansen, E. Drioli, Preparation and characterization of new non-fluorinated polymeric and composite membranes for PEMFCs, J. Membr. Sci. 348 (2010) 326–336.
[11] E. Fontananova, V. Cucunato, E. Curcio, F. Trotta, M. Biasizzo, E. Drioli, G. Barbieri, Influence of the preparation conditions on the properties of polymeric and hybrid cation exchange membranes, Electrochim. Acta 66 (2012) 164–172.
[12] W. Zhang, U.E. Spichiger, An impedance study on Mg^{2+} selective membrane, Electrochim. Acta 45 (2000) 2259–2266.
[13] J. Benavente, A. Canas, M.J. Ariza, A.E. Lozano, J. de Abajo, Electrochemical parameters of sulfonated poly(ether ether sulfone) membranes in HCl solutions determined by impedance spectroscopy and membrane potential measurements, Solid State Ionics 145 (2001) 53–60.
[14] F. Treptowa, A. Jungbauerb, K. Hellgardta, Halide diffusion in polyaniline membranes, J. Membr. Sci. 270 (2006) 115–122.
[15] J. O'M. Bockris, F.B. Diniz, Aspects of electron transfer at a conducting membrane–solution interface, Electrochim. Acta 34 (1989) 561–575.
[16] J.S. Park, T.C. Chilcott, H.G.L. Coster, S.H. Moon, Characterization of BSA-fouling of ion-exchange membrane systems using a subtraction technique for lumped data, J. Membr. Sci. 246 (2005) 137–144.
[17] A. Antony, T. Chilcott, H. Coster, G. Leslie, In situ structural and functional characterization of reverse osmosis membranes using impedance spectroscopy, J. Membr. Sci. 425–426 (2013) 89–97.
[18] J.-S. Park, J.-H. Choi, J.-J. Woo, S.-H. Moon, An electrical impedance spectroscopic (EIS) study on transport characteristics of ion-exchange membrane systems, J. Colloid Interface Sci. 300 (2006) 655–662.
[19] P. Długołecki, P. Ogonowski, S.J. Metz, M. Saakes, K. Nijmeijer, M. Wessling, On the resistances of membrane, diffusion boundary layer and double layer in ion exchange membrane transport, J. Membr. Sci. 349 (2010) 369–379.
[20] Y. Xu, M. Wang, Z. Ma, C. Gao, Electrochemical impedance spectroscopy analysis of sulfonated polyethersulfone nanofiltration membrane, Desalination 271 (2011) 29–33.
[21] Yaoming Wang, Anlei Wang, Xu Zhang, Tongwen Xu, The concentration, resistance, and potential distribution across a cation exchange membrane in 1:2 (Na_2SO_4) type aqueous solution, Desalination 284 (2012) 106–115.
[22] J.M. Kavanagh, S. Hussain, T.C. Chilcott, H.G.L. Coster, Fouling of reverse osmosis membranes using electrical impedance spectroscopy: measurements and simulations, Desalination 236 (2009) 187–193.
[23] Y. Gao, W. Li, W.C.L. Lay, H.G.L. Coster, A.G. Fane, C.Y. Tang, Characterization of forward osmosis membranes by electrochemical impedance spectroscopy, Desalination 312 (2013) 45–51.
[24] J. Cen, J. Kavanagh, H. Coster, G. Barton, Fouling of reverse osmosis membranes by cane molasses fermentation wastewater: detection by electrical impedance spectroscopy techniques, Desalin. Water Treat. 51 (4–6) (2013) 969–975.
[25] T. Lopes, L. Andrade, H.A. Ribeiro, A. Mendes, Characterization of photoelectrochemical cells for water splitting by electrochemical impedance spectroscopy, Int. J. Hydrogen Energy 35 (2010) 11601–11608.
[26] B.E. Logan, M. Elimelech, Membrane-based processes for sustainable power generation using water, Nature 488 (7411) (2012) 313–319and references therein 488 (7411) (2012).
[27] K.P. Lee, T.C. Arnot, D. Mattia, A review of reverse osmosis membrane materials for desalination—development to date and future potential, J. Membr. Sci. 370 (2011) 1–22.
[28] D. Winter, J. Koschikowski, M. Wieghaus, Desalination using membrane distillation: experimental studies on full scale spiral wound modules, J. Membr. Sci. 375 (2011) 104–112.
[29] X. Ji, E. Curcio, S. Al Obaidani, G. Di Profio, E. Fontananova, Enrico Drioli, Membrane distillation–crystallization of seawater reverse osmosis brines, Sep. Purif. Technol. 71 (2010) 76–82.
[30] M. Tedesco, A. Cipollina, A. Tamburini, W. van Baak, G. Micale, Desalin. Water Treat. 49 (2012) 404–424.
[31] E. Brauns, Salinity gradient by reverse electrodialysis: effect of model parameters on electrical power output, Desalination 237 (2009) 378–391.
[32] E. Brauns, Finite elements-based 2D theoretical analysis of the effect of IEX membrane thickness and salt solution residence time on the ion transport within a salinity gradient power reverse electrodialysis half cell pair, Desalin. Water Treat. (2013) 1–15.
[33] E.O. Stejskal, J.E. Tanner Spin, Diffusion measurements: spin echoes in the presence of a time-dependent field gradient, J. Chem. Phys. 42 (1965) 288–292.
[34] R.J. Hunter, Zeta Potential in Colloid Science, Academic Press, London, 1981.

[35] J.A. Manzanares, W.D. Murpby, S. Maffè, H. Reiss, Numerical simulation of the nonequilibrium diffuse double layer in ion-exchange membranes, J. Phys. Chem. 97 (1993) 8524–8530.
[36] C. Larchet, S. Nouri, B. Auclair, L. Dammak, V. Nikonenko, Application of chronopotentiometry to determine the thickness of diffusion layer adjacent to an ion-exchange membrane under natural convection, Adv. Colloid Interface Sci. 139 (2008) 45–61.
[37] A.A. Moya, P. Sistat, Chronoamperometric response of ion-exchange membrane systems, J. Membr. Sci. 444 (2013) 412–419.
[38] S. Koneshan, J.C. Rasaiah, R.M. Lynden-Bell, S.H. Lee, Solvent structure, dynamics, and ion mobility in aqueous solutions at 25 °C, J. Phys. Chem. B 102 (1998) 4193–4204.
[39] K.A. Mauritz, R.B. Moore, State of understanding of nafion, Chem. Rev. 104 (2004) 4535–4558.
[40] K. Bohinc, V. Kralj-Iglic, A. Iglic, Thickness of electrical double layer. Effect of ion size, Electrochim. Acta 46 (2001) 3033–3040.
[41] W.B. Russel, D.A. Saville, W.R. Schowalter, Colloidal Dispersions, Cambridge University Press, Cambridge, 1989.
[42] K.D. Kreuer, On the development of proton conducting polymer membranes for hydrogen and methanol fuel cells, J. Membr. Sci. 185 (2001) 29–39.
[43] J.R. McCutcheon, R.L. McGinnis, M. Elimelech, Desalination by ammonia–carbon dioxide forward osmosis: influence of draw and feed solution concentrations on process performance, J. Membr. Sci. 278 (2006) 114–123.
[44] Y. Luo, B. Roux, Simulation of osmotic pressure in concentrated aqueous salt solutions, J. Phys. Chem. Lett. 1 (2010) 183–189.
[45] H. Strathmann, Electromembrane processes: basic aspects and application, in: Enrico Drioli, Lidietta Giorno (Eds.), Comprehensive Membrane Science and Engineering, vol. 2, Elsevier, Oxford, 2010, pp. 391–429.
[46] R.D. Armstrong, J.C. Lockhart, M. Todd, The mechanism of transfer of K^+ between aqueous solution and PVC membranes containing valinomycin, Electrochim Acta 31 (1986) 591–594.
[47] P.P. Prosini, M. Lisi, D. Zane, M. Pasquali, Determination of the chemical diffusion coefficient of lithium in $LiFePO_4$, Solid State Ionics 148 (2002) 45–51.
[48] A.A. Moya, Electric circuits modelling the low-frequency impedance of ideal ion-exchange membrane systems, Electrochim. Acta 62 (2012) 296–304.
[49] P. Sistat, A. Kozmai, N. Pismenskaya, C. Larchet, G. Pourcelly, V. Nikonenko, Low-frequency impedance of an ion-exchange membrane system, Electrochim. Acta 53 (2008) 6380–6390.
[50] Donald R. Franceschetti, J. Ross Macdonald, Richard P. Buck, Interpretation of finite-length-Warburg-type impedances in supported and unsupported electrochemical cells with kinetically reversible electrodes, J. Electrochem. Soc. 138 (1991) 1368–1371.
[51] N. Fouquet, C. Doulet, C. Nouillant, G. Dauphin-Tanguy, B. Ould-Bouamam, Model based PEM fuel cell state-of-health monitoring via ac impedance measurements, J. Power Sources 159 (2006) 905–913.
[52] S.A. Mareev, V.V. Nikonenko, A numerical experiment approach to modeling impedance: application to study a Warburg-type spectrum in a membrane system with diffusion coefficients depending on concentration, Electrochim. Acta 81 (2012) 268–274.
[53] M. Shi, Z. Chen, J. Sun, Determination of chloride diffusivity in concrete by AC impedance spectroscopy, Cement Concr. Res. 29 (1999) 1111–1115.
[54] F. Treptow, A. Jungbauer, K. Hellgardt, Halide diffusion in polyaniline membranes, J. Membr. Sci. 270 (2006) 115–122.
[55] L. Coppola, R. Muzzalupo, G.A. Ranieri, Temperature dependence of water self-diffusion in the gel phase of a potassium palmitate system, J. Phys. II 6 (1996) 657–666.
[56] A. Gottwald, L.K. Creamer, P.L. Hubbard, P.T. Callaghan, Diffusion, relaxation and chemical exchange in casein gels: a nuclear magnetic resonance study, J. Chem. Phys. 122 (2005) 34506–34515.
[57] C.P. Slichter, Principles of Magnetic Resonance, 3rd ed. Springer ed., Springer Series in Solid State Science, New York, 1990.

"La presente tesi è cofinanziata con il sostegno della Commissione Europea, Fondo Sociale Europeo e della Regione Calabria. L'autore è il solo responsabile di questa tesi e la Commissione Europea e la Regione Calabria declinano ogni responsabilità sull'uso che potrà essere fatto delle informazioni in essa contenute"